

Studies of b-associated production and muonic decays of neutral Higgs bosons at the ATLAS experiment within the Minimal Supersymmetric Standard Model

DISSERTATION

zur Erlangung des akademischen Grades
Doctor rerum naturalium
(Dr. rer. nat.)

vorgelegt
der Fakultät Mathematik und Naturwissenschaften
der Technischen Universität Dresden

von
Diplom-Physiker Markus Warsinsky
geboren am 23. April 1976 in Höxter



Gutachter : Prof. Dr. Michael Kobel
Prof. Dr. Markus Schumacher
Dr. Frank Krauss

Tag der mündlichen Prüfung: 15. September 2008
Tag der Einreichung: 25. Juli 2008

Abstract

This thesis presents a Monte Carlo study of neutral Higgs bosons of the Minimal Supersymmetric Standard Model (MSSM) decaying into muons at the ATLAS experiment at the CERN Large Hadron Collider. Signal and background processes are simulated using novel Monte Carlo generators that incorporate parts of higher order corrections and are expected to give a more accurate prediction than previous programs. The SHERPA Monte Carlo generator is validated for its use in the analysis and compared to results obtained with other programs. Where possible, the Monte Carlo event samples are normalized to higher order calculations. To increase the available Monte Carlo statistics, this study is based on the ATLAS fast detector simulation ATLFAST. Differences between ATLFAST and the detailed detector simulation of ATLAS are examined, and, where possible, correction procedures are devised.

A cut based analysis is performed assuming an integrated luminosity of 30 fb^{-1} , and optimized with respect to the discovery potential for MSSM Higgs bosons. The systematic uncertainties of the event selection and the Monte Carlo predictions are estimated. A method that can be used to estimate the background from data is presented and evaluated. Last, the discovery potential of the ATLAS experiment in the CP conserving benchmark scenarios of the MSSM is evaluated. One or more of the neutral Higgs bosons of the MSSM can be discovered in the muonic decay mode using 30 fb^{-1} of data for low masses of the pseudoscalar boson A^0 , if the model parameter $\tan\beta$ is at least 20. For higher masses of the A^0 , $\tan\beta$ would need to be significantly higher to ensure a discovery in the studied decay channel. The sensitivity of ATLAS to MSSM Higgs bosons is multiple times larger than the one of previous and currently running experiments.

Kurzfassung

Die vorliegende Arbeit präsentiert eine Monte Carlo Studie zu neutralen Higgs-Bosonen des Minimal Supersymmetrischen Standardmodells (MSSM) im myonischen Zerfallskanal am ATLAS Experiment am Large Hadron Collider des CERN. Signal- und Untergrundprozesse werden mit neuartigen Monte Carlo Ereignisgeneratoren simuliert, die Teile der Korrekturen höherer Ordnung beinhalten, und von denen eine verbesserte Vorhersage erwartet wird im Vergleich zu herkömmlichen Programmen. Der SHERPA Monte Carlo Ereignisgenerator wird auf seine Brauchbarkeit für die Analyse überprüft und mit Ergebnissen anderer Programme verglichen. Sofern möglich werden die erstellten Monte Carlo Datensätze mittels Rechnungen zu höheren Ordnungen normiert. Um eine hinreichend große Statistik von simulierten Daten zu erhalten wird die schnelle Detektorsimulation des ATLAS Detektors ATLFAST verwendet. Unterschiede zwischen der vollständigen Detektorsimulation und ATLFAST werden untersucht, und sofern möglich, Korrekturverfahren entwickelt.

Eine schnittbasierte Analyse wird durchgeführt unter der Annahme einer integrierten Luminosität von 30 fb^{-1} und optimiert mit Hinblick auf das Entdeckungspotenzial für MSSM Higgs-Bosonen. Die systematischen Unsicherheiten der Ereignisauswahl und der Monte Carlo-Vorhersagen werden abgeschätzt. Eine Methode zur Messung des Untergrundes in Daten wird vorgestellt und überprüft. Schliesslich wird das Entdeckungspotenzial des ATLAS Experiments in Vergleichspunkten für CP erhaltende Szenarien des MSSM ermittelt. Für niedrige Massen des pseudoskalaren Higgs-Bosons A^0 kann mindestens eines der neutralen Higgs-Bosonen des MSSM im myonischen Zerfallskanal entdeckt werden, sofern der Modellparameter $\tan\beta$ mindestens 20 ist. Für hohe Massen des A^0 muss ein wesentlich größeres $\tan\beta$ in der Natur realisiert sein, um eine Entdeckung im untersuchten Zerfallskanal zu ermöglichen. Die Sensitivität von ATLAS auf Higgs-Bosonen des MSSM ist um ein Vielfaches höher als diejenige bisheriger oder momentan laufender Experimente.

Contents

1	Introduction	1
2	Theoretical Foundations	5
2.1	The Standard Model	5
2.1.1	Quantum Electrodynamics	7
2.1.2	Electroweak Interactions	8
2.1.3	The Higgs Mechanism	11
2.1.4	Theoretical Constraints on the Higgs boson mass	15
2.1.5	Summary of the Standard Model	16
2.1.6	Limits of the Standard Model	16
2.2	Supersymmetry	19
2.3	The Minimal Supersymmetric Standard Model	20
2.4	The MSSM Higgs Sector	23
2.4.1	Radiative Corrections and Benchmark Scenarios	26
2.4.2	Properties of the Neutral Higgs Bosons for large $\tan\beta$	28
2.4.3	The Decoupling Limit	32
2.4.4	The “Intense Coupling Region”	33
2.4.5	Effects in the Benchmark Scenarios	33
3	Experimental Status of the Higgs Sector	35
3.1	The Standard Model Higgs Boson	35
3.1.1	Indirect Measurements	35
3.1.2	Direct Searches	35
3.1.3	ATLAS Discovery Potential for the Standard Model Higgs Boson	37
3.2	The Higgs Bosons of the MSSM	39
3.2.1	Indirect Measurements	39
3.2.2	Direct Searches	40
3.2.3	ATLAS Discovery Potential	42
4	The Large Hadron Collider	45
5	The ATLAS Experiment	49
5.1	Introduction	49
5.2	The ATLAS coordinate system	50
5.3	The Inner Detector	50
5.3.1	The Pixel Detector	52
5.3.2	The Semi Conductor Tracker	53
5.3.3	The Transition Radiation Tracker	53
5.3.4	Solenoid Magnet	55

5.4	The Calorimeters	55
5.4.1	Electromagnetic Calorimeter	56
5.4.2	Hadronic Calorimeters	58
5.5	The Muon Spectrometer	60
5.5.1	Precision Chambers	61
5.5.2	Trigger Chambers	62
5.6	Forward Detector Systems	62
5.6.1	The LUCID detector	62
5.6.2	The ZDC detector	63
5.6.3	The ALFA detector	63
5.7	Trigger and Data Acquisition	63
6	Event Simulation	65
6.1	Anatomy of a Hadron-Hadron Collision	65
6.2	Definition of Hadron Jets	67
6.3	Monte Carlo Generators	68
6.3.1	Matrix Elements	68
6.3.2	Parton Shower	68
6.3.3	Comparison of Matrix Element and Parton Shower	70
6.3.4	Matching of Matrix Element and Parton Shower	70
6.3.5	MC@NLO	72
6.3.6	Underlying event	72
6.3.7	Decays and QED radiation	73
6.4	Particle Filters	74
6.5	Detector Simulation	75
6.5.1	Detailed Simulation	75
6.5.2	Fast Detector Simulation	77
7	The Signal Process	79
7.1	Bottom Quark Associated Higgs Boson Production	79
7.1.1	Production Mechanisms	79
7.1.2	Inclusive Cross Section	81
7.1.3	Exclusive Cross Section	82
7.1.4	Simulation of b-associated Higgs Boson Production	83
7.1.5	Generator Studies	84
7.1.6	Comparison to Theory Predictions	90
7.1.7	Normalization	93
7.2	Direct Production	96
7.2.1	Monte Carlo Generators	97
7.2.2	Normalization	97
7.3	From Standard Model to MSSM	98
7.3.1	Cross Sections	98
7.3.2	Masses and Widths	99
7.4	Higgs Boson Decay Channels	99

7.5	Signal Characteristics	100
8	Background Processes	103
8.1	Z^0 + Jet Background	103
8.1.1	Z^0 + light and charm Jet	104
8.1.2	Z^0 + b Jet	106
8.2	W + Jet Background	110
8.3	Top Pair Production	111
8.4	Single Top Production	112
8.5	$Z^0 Z^0$ Production	112
8.6	WW Production	113
8.7	Multijet Background	113
9	Event Reconstruction	115
9.1	Muons	115
9.1.1	Reconstruction in FULLSIM	116
9.1.2	Reconstruction in ATLFAST	118
9.1.3	Dimuon Mass and Momentum Resolution	119
9.1.4	Muon Isolation	123
9.1.5	ATLFAST Efficiency correction	128
9.2	Jet Reconstruction	134
9.2.1	Jet Reconstruction in FULLSIM	134
9.2.2	Jet Reconstruction in ATLFAST	136
9.2.3	Jet Labeling	138
9.2.4	Jet Reconstruction Efficiency	138
9.2.5	Jet Fake Probability	144
9.2.6	Jet Calibration	145
9.2.7	Jet Resolution	150
9.2.8	Scalar Sum of Jet Momenta	151
9.3	Flavor Tagging	152
9.3.1	Life Time Tagging	153
9.3.2	b Tagging in ATLFAST	159
9.3.3	Updated Parameterization	160
9.3.4	Comparison between FULLSIM and ATLFAST	168
9.3.5	Influence of Pile-Up	170
9.3.6	Misalignment	172
9.4	Missing Transverse Energy	172
9.4.1	Reconstruction of \cancel{E}_T in FULLSIM	172
9.4.2	Reconstruction of \cancel{p}_T in ATLFAST	173
9.4.3	ATLFAST Correction	173
9.4.4	Influence of Pile-Up	177
9.5	Electrons, Photons, and Hadronic Taus	179
9.5.1	Electrons and Photons	179
9.5.2	Hadronic Taus	180

9.6	Overlap Removal	180
10	Event Selection	183
10.1	Preselection	183
10.2	Mass Window	186
10.2.1	The Mass Tail	190
10.3	Signatures with at least one tagged Jet	190
10.3.1	Missing Transverse Energy	191
10.3.2	Hadronic Activity	193
10.3.3	Muonic Variables	196
10.3.4	Selection	199
10.3.5	Influence of the Weight Cut	205
10.4	Signatures without tagged Jets	206
10.5	Trigger Requirements	211
11	Systematic Uncertainties	217
11.1	Normalization Uncertainties	217
11.1.1	Luminosity Uncertainty	218
11.1.2	Theory Uncertainties	218
11.1.3	Monte Carlo Statistical Uncertainty	218
11.2	Uncertainties of the Event Selection	220
11.2.1	Muons	220
11.2.2	Jets	223
11.2.3	B Tagging	224
11.2.4	Missing Transverse Energy	227
11.2.5	Electrons, Photons, and Hadronic Taus	228
11.3	Summary on Systematic Uncertainties	228
12	Background Estimation from Data	229
12.1	Basic Methods	229
12.1.1	Different Final States	230
12.1.2	Same Final State	230
12.2	Basic Fit Strategy	233
12.3	Analysis I (b tag)	234
12.3.1	Background Parameterization	234
12.3.2	Fit performance	236
12.4	Analysis II (b tag veto)	238
12.4.1	Parameterization	238
12.4.2	Fit Performance	240
12.5	Floating Higgs Boson Mass	243
12.6	Influence of the Mass Tail	244
13	Discovery Potential	245
13.1	Parameterization of Signal Efficiencies	246

13.1.1	Parameterization of Selection Efficiencies	247
13.1.2	Parameterization of the Mass Window Efficiency	247
13.2	Choice of Mass Window	251
13.3	Scan Procedure	252
13.3.1	Fit Stability	253
13.4	Calculation of Significances	254
13.4.1	Inclusion of Systematic Uncertainties	254
13.5	Results	257
13.5.1	Influence of the Mass Tail	265
13.5.2	Possible Improvements	266
13.6	Resolving Multiple Higgs Bosons	266
14	Conclusions and Outlook	271
A	Strong Interactions as Gauge Theory	273
B	Jet Algorithms	275
B.1	Recombination Schemes	275
B.2	Clustering algorithms	276
B.2.1	Cone algorithm	276
B.2.2	k_{\perp} Algorithm	276
C	Statistical Methods	279
C.1	Statistical Component of Systematic Variations	279
C.2	Calculation of Discovery Significances	281
C.2.1	Introduction	281
C.2.2	The Profile Likelihood	282
C.2.3	Probability Model	282
C.2.4	Application in the Analysis	283
C.2.5	Comment on Setting Limits	284
D	Tables of Systematic Uncertainties	285
D.1	Analysis I (b tag)	286
D.2	Analysis II (b tag veto)	290
	Bibliography	297

“Meinen Eltern.”

“To introduce something altogether new would mean to begin all over, to become ignorant again, and to run the old, old risk of failing to learn.”

Isaac Asimov, 1920–1992

1

Introduction

The subject of elementary particle physics is the study of the smallest known constituents of matter and their interactions with each other. Over the past 50 years a comprehensive, self-consistent description of all currently known phenomena in particle physics has been developed, which is called the *Standard Model*. Within the Standard Model, interactions between the constituents of known matter, which are spin $1/2$ fermions, are described in terms of a *local gauge theory* where forces are mediated by the exchange of spin 1 bosons.

The Standard Model is based on symmetries that seem to be realized in nature. It is tremendously successful and has been tested down to the level of the quantum corrections, and all its predictions have become true. However, within the Standard Model one of the most obvious properties of particles is difficult to describe: mass itself. It turns out that the underlying symmetries of the Standard Model remain only valid for massless particles. This is in contradiction to the experimental fact that elementary particles have a non-zero mass. For example the top quark has a mass of 172.6 GeV [1]¹, about the mass of a gold atom, and is at the same time regarded as an elementary, point-like particle.

Within the Standard Model a way has been devised to generate the masses by the so-called *Higgs mechanism*. It explains the origin of particle masses by their interaction with an omnipresent background field, the Higgs field, which permeates the whole universe. Within this theory, all particles must have been massless in the early universe, when the mean energy was very large. However, when the universe cooled down, the symmetries are *spontaneously* broken, and for an observer at present time the world looks no longer symmetric. However, the underlying symmetries of the Standard Model are still present, they are just in part hidden by the now much smaller energy scales.

In addition to generating the masses of the elementary particles while preserving the symmetries and the predictivity of the Standard Model, the Higgs mechanism predicts another physical particle, the spin zero *Higgs boson*.

Ever since the Higgs mechanism has been proposed in the 1960's, this particle has been searched for at particle accelerators and other experiments. No conclusive direct

¹Within this thesis a system of units is used where $\hbar = c = 1$.

observation of it has been made yet, thus ruling out a very light Higgs boson, since it would otherwise have been produced in previous experiments.

As mentioned before, the Standard Model is deeply rooted in symmetries. It is natural to explore whether these symmetries can be extended. One example of such extensions of the Standard Model is *Supersymmetry*, where for each fermion a bosonic partner particle is predicted and vice versa. Besides complementing the symmetries of the Standard Model, supersymmetry also promises to amend some of the aesthetic short-comings of the Standard Model. Also, within most supersymmetric theories, a candidate particle for the dark matter that makes up about 25% of the universe is predicted.

An example of a supersymmetric theory is the simplest extension of the Standard Model, the Minimal Supersymmetric Standard Model (MSSM), where only partner particles of the Standard Model particles are added, but nothing else. In addition to the existence of the supersymmetric partner particles, the MSSM predicts more than one physical Higgs bosons, three neutral and two charged ones.

From all experimental and theoretical evidence it is expected that the responsible mechanism for the generation of masses has to be found at the TeV scale. Up to now, this range in energy in particle collisions is only reached cosmic ray collisions with nuclei of the earth's atmosphere, but not in the controlled experimental environment of a particle accelerator.

This year, the Large Hadron Collider (LHC), will become the highest energy particle accelerator in the world. It will be capable of accelerating protons to energies of up to 7 TeV and colliding them, thus opening a gateway to the TeV scale. Due to this large increase in energy compared to former accelerators, and due to the expected unprecedented rate of interactions, the LHC will be able to produce the Higgs boson, if it exists.

One of the experiments at the LHC is the ATLAS experiment. It is a multipurpose detector designed and built by a multinational collaboration. It will exploit the full physics range offered by the LHC and is a very complex measuring device.

Although the LHC and ATLAS are not yet taking data, it is important to study the ATLAS capabilities for discovery of certain kinds of new phenomena using simulated data. Simulated data is used just as real data to verify the detector performance, develop analysis strategies, and evaluate the probability that ATLAS can discover a new phenomena, if these are realized in nature.

However, studies based on simulated events are only as good as the model used in the simulation. First there is the model of the proton-proton interaction. This is simulated using so-called Monte Carlo generators. In recent years, a number of novel Monte Carlo generators have been introduced that are expected to provide a better description of events. The simulated particles are then passed through a simulation of the detector, which in turn can only be of limited accuracy. Both steps will need extensive comparison with real data, once these are available.

Within this thesis a study of the ATLAS discovery potential for neutral Higgs bosons of the MSSM in the muonic decay mode is presented. Special emphasis is placed to obtain an improved description of the expected behavior of ATLAS and the proton-proton-collisions at the LHC. For this, new tools for the simulation of events and higher order corrections to obtain more accurate results are used. The ATLAS fast detector simulation is corrected where possible to account for differences to the full, more detailed simulation.

This thesis is organized as follows:

Chapter 2 gives an overview of the theoretical foundations of the Standard Model and the MSSM with a special emphasis on the Higgs sector.

Chapter 3 summarizes the current and expected future experimental status of the search for the Higgs boson(s).

Chapters 4 and **5** describe the LHC and the ATLAS experiment.

Chapter 6 summarizes some basic features of event simulation before describing the particularities of the relevant signal processes in **Chapter 7** and of the background processes in **Chapter 8**. The Monte Carlo generators used for the simulation are validated and normalizations to higher order calculations are proposed.

In **Chapter 9** the reconstruction performance of the ATLAS experiment is evaluated and correction procedures for the fast detector simulation are devised.

Chapter 10 describes a cut-based selection of neutral Higgs bosons of the MSSM.

Chapter 11 summarizes the experimental and theoretical systematic uncertainties of the predicted event yields.

In **Chapter 12** a data-based method to extract the background in the real experiment is discussed.

The **ATLAS discovery potential** for neutral MSSM Higgs bosons decaying into muons is evaluated in Chapter 13.

Chapter 14 closes with a summary and an outlook.

“Your theory is crazy, but it’s not crazy enough to be true.”

Niels Bohr, 1885–1962

2

Theoretical Foundations

2.1 The Standard Model

The subject of elementary particle physics are the constituents of matter and the interactions between them. Our present knowledge of these has culminated in the *Standard Model*. At present all experimentally observable phenomena are successfully described by this theory. According to the Standard Model the matter constituents are point-like particles with spin $1/2$. There are six leptons, the e , μ , τ with an electric charge of -1 in units of the elementary charge, and the corresponding chargeless neutrinos ν_e , ν_μ , ν_τ . There are 6 quarks with fractional charges: u , c , t with an electric charge of $2/3$, and d , s , b with an electric charge of $-1/3$. In addition, each particle has an corresponding anti-particle. These fundamental fermions are listed in Table 2.1 and can be grouped into three *generations* that show similar behavior. Stable macroscopic matter is built of particles of the first generation only. The only difference between the three generations are the very different masses (see Table 2.1), ranging from the almost massless neutrinos to the top quark that has about the mass of a gold atom. For the d , s , b quarks and the neutrinos, the interaction eigenstates are different from the mass eigenstates. In Table 2.1 the mass values are given for an effective neutrino mass, as seen in weak interactions (see below). For the quarks the mass eigenvalues corresponding to the eigenstates participating in strong interactions are listed.

Interactions between the fermions are described by four fundamental forces that are listed in Table 2.2. The *electromagnetic* force only acts on charged particles, the *strong* force only on the quarks and the *weak* interaction on all fermions. Within the Standard Model all forces but *gravity* are successfully described as a local quantum field theory, where the interaction is mediated by *gauge bosons* with spin 1, which are also listed in Table 2.2. Gravity, which is classically described as a geometric effect acting on all particles with energy [2], has not yet been successfully described in a consistent quantum field theory. Since it is too weak at presently reachable energy scales, it is neglected in the following. As for the fermions, the masses of the gauge bosons are very different. The gauge bosons of the weak interaction, the W^\pm and Z^0 are very massive, leading to a short-ranged interaction. On the other hand the photon γ is massless, and consequently the electromag-

Generation	Particle	Electric charge/e	Mass/GeV
1 st	e electron	−1	0.511 MeV
	ν_e electron-neutrino	0	$m_{\nu_e}^{\text{eff.}} \equiv \sqrt{\sum_i U_{ei} ^2 m_{\nu_i}^2} < 2 \text{ eV}$
	u up quark	+2/3	1.5-3.0 MeV
	d down quark	−1/3	3-7 MeV
2 nd	μ muon	−1	0.106 GeV
	ν_μ muon-neutrino	0	$m_{\nu_\mu}^{\text{eff.}} \equiv \sqrt{\sum_i U_{\mu i} ^2 m_{\nu_i}^2} < 0.19 \text{ MeV}$
	c charm quark	+2/3	1.25 GeV
	s strange quark	−1/3	25-55 MeV
3 rd	τ tau	−1	1.777 GeV
	ν_τ tau-neutrino	0	$m_{\nu_\tau}^{\text{eff.}} \equiv \sqrt{\sum_i U_{\tau i} ^2 m_{\nu_i}^2} < 18.2 \text{ MeV}$
	t top quark	+2/3	172.5 GeV
	b bottom quark	−1/3	4.2 GeV

Table 2.1: The fundamental fermions, their electric charges and masses [3]. The matrix elements U_{ei} , $U_{\mu i}$, and $U_{\tau i}$ connect the mass and weak eigenstates of the neutrinos. The corresponding matrix for the quarks is left out.

netic interaction has infinite range. Despite the fact that the eight gluons g are massless, the strong interaction is restricted to a short range. This results from the fact that the force between two quarks approaches a constant if one tries to separate them. This leads to the *confinement* of quarks inside bound states that have no net *color charge*, the mesons – consisting of a quark and an anti-quark, and the baryons – consisting of three quarks.

The Standard Model incorporates a number of symmetries, the most important being local gauge symmetries. It is based on the requirement that the Lagrangian describing a free particle is invariant under a gauge transformation of the fermion field. Global gauge symmetries lead to conserved quantities, e.g. the electric charge. Making the gauge symmetry local, one is forced to enter new quantum fields which can be identified with the gauge bosons, and interactions of these fields with matter. This concept has proved to exactly describe the fundamental interactions and will be discussed more closely in the following.

Interaction	relative strength	Range/m	Particle	Mass/GeV
Gravitation	10^{-39}	∞	graviton (?)	0
Electromagnetic	$1/137$	∞	photon (γ)	0
Weak interaction	$1/30$	$\approx 10^{-16}$	W^+, W^-	80.4
			Z^0	91.2
Strong interaction	1	$< 10^{-13}$	gluon (g)	0

Table 2.2: Fundamental interactions and the gauge bosons mediating them. The graviton is a hypothetical particle with spin 2, that has to appear in a quantum theory of gravity.

2.1.1 Quantum Electrodynamics

The simplest local gauge theory is quantum electrodynamics (QED). It is based on the $U(1)_{em}$ symmetry group which can be described mathematically as a phase transformation of the Dirac spinors of charged fermions. Starting from the Lagrangian density of a free Dirac field ψ (spin $1/2$) of mass m_f ,

$$\mathcal{L} = \bar{\psi}(i\gamma_\mu \partial^\mu - m_f)\psi, \quad (2.1)$$

where γ_μ are the Dirac matrices. One requires the Lagrangian to be invariant under a local phase transformation of the fermion field,

$$\psi(x) \rightarrow e^{iq\alpha(x)}\psi(x), \quad (2.2)$$

where q is the electric charge of the fermion in units of the elementary charge e , which can be identified as the coupling strength of the gauge group, and $\alpha(x)$ is an arbitrary phase that depends on the space-time coordinates. This can only be achieved by introducing a new vector field A_μ that transforms as

$$A_\mu(x) \rightarrow A_\mu(x) + \frac{1}{e}\partial_\mu \alpha(x), \quad (2.3)$$

and by replacing the derivative ∂_μ with the covariant derivative $D_\mu = \partial_\mu - iqeA_\mu$. The resulting Lagrangian

$$\begin{aligned} \mathcal{L}_{QED} = & \quad \bar{\psi}i\gamma^\mu \partial_\mu \psi && \text{kinetic energy of free fermion} \\ & + \quad qe\bar{\psi}\gamma^\mu A_\mu \psi && \text{interaction of fermion with } A_\mu \text{ field} \\ & - \quad m_f\bar{\psi}\psi && \text{fermion mass term} \\ & - \quad \frac{1}{4}F_{\mu\nu}F^{\mu\nu} && \text{kinetic energy of } A_\mu \text{ field} \end{aligned}, \quad (2.4)$$

with $F_{\mu\nu} = \partial_\mu A_\nu - \partial_\nu A_\mu$, is invariant under the gauge transformation. The requirement of local gauge symmetry has forced the introduction of a new vector field that interacts

with the fermion with a strength proportional to its electric charge q . It can be identified with the photon. To preserve local gauge invariance, any explicit mass term for the photon is forbidden, as such a term in the Lagrangian would need to be of the form $\frac{1}{2}M_\gamma^2 A_\mu A^\mu$ and would not be invariant under the gauge transformation. This prediction from QED is very well matched to the observation in nature: The photon does not have an observable rest mass, the current upper limit on it being $m_\gamma < 6 \cdot 10^{-26}$ GeV [3]. In contrast to the gauge boson itself, the masses of the fermions are not constrained to be zero by the $U(1)_{em}$ symmetry group, as the mass term $m_f \bar{\psi} \psi$ is gauge invariant.

Local gauge theories have several advantages from the theoretical point of view. Most importantly they are renormalizable [4], which means that any unphysical divergences occurring in higher orders of perturbation theory can be absorbed by redefining a finite number of physical parameters like the charge or mass of a particle. As this is guaranteed to hold in all orders of perturbation theory, local gauge theories are predictive. Physical observables can be calculated accurately and the theory be tested by experiment. QED has been tested successfully to very high levels of precision and all experiments agree with the prediction from theory. This enormous success of local gauge theory has inspired the development of gauge theories for the other interactions observed in nature.

2.1.2 Electroweak Interactions

It has not been possible to provide a consistent gauge theory that describes the weak interaction by itself. Instead, Glashow, Weinberg and Salam [5] developed a gauge theory that describes the electromagnetic and weak interactions in a common framework.

The first important requirement in describing weak interactions is that the underlying theory has to be a chiral gauge theory. This means, that the building blocks are (massless) left- and right-handed fermions:

$$\psi_L = \frac{1}{2}(1 - \gamma^5)\psi, \quad \psi_R = \frac{1}{2}(1 + \gamma^5)\psi. \quad (2.5)$$

In fact, it was observed that weak interactions involving the exchange of W bosons act only on left-handed fermions [6, 7]. The corresponding gauge groups have to be chosen in a way that this is reflected. The gauge group chosen is $SU(2)_L \times U(1)_Y$. The quantum number of the $SU(2)_L$ is the *weak isospin* T_W and the one for the $U(1)_Y$ the *weak hypercharge*.

The assignment of quantum numbers to the observed fermions now corresponds to assigning each of them into an irreducible representation of the gauge group. With respect to the $SU(2)_L$ group, the fermions are grouped into chargeless singlets and charged doublets. Since it is observed that the W bosons interact only with left-handed fermions, it is natural to assign the left-handed fermions to the doublets and the right-handed fermions to be singlets. Since weak interactions do not change color, it is not possible to mix quarks and leptons. Lorentz symmetry forbids mixing left- and right-handed fields. Since $U(1)_Y$ is an abelian group, it has only one-dimensional representations and the $SU(2)_L$ doublets and

	Generation				Quantum numbers			
	I	II	III		$SU(2)_L$	$U(1)_Y$	$U(1)_{em}$	
Quarks					T_W	T_W^3	Y_W	q
$Q_L^i = \begin{pmatrix} u_L^i \\ d_L^i \end{pmatrix}$	$\begin{pmatrix} u_L \\ d_L' \end{pmatrix}$	$\begin{pmatrix} c_L \\ s_L' \end{pmatrix}$	$\begin{pmatrix} t_L \\ b_L' \end{pmatrix}$	$1/2$	$+1/2$ $-1/2$	$+1/3$	$+2/3$ $-1/3$	
u_R^i	u_R	c_R	t_R	0	0	$+4/3$	$+2/3$	
d_R^i	d_R'	s_R'	b_R'	0	0	$-2/3$	$-1/3$	
Leptons								
$L_L^i = \begin{pmatrix} \nu_L^i \\ \ell_L^i \end{pmatrix}$	$\begin{pmatrix} \nu_{eL} \\ e_L \end{pmatrix}$	$\begin{pmatrix} \nu_{\mu L} \\ \mu_L \end{pmatrix}$	$\begin{pmatrix} \nu_{\tau L} \\ \tau_L \end{pmatrix}$	$1/2$	$+1/2$ $-1/2$	-1	0 -1	
ν_R^i	ν_{eR}	$\nu_{\mu R}$	$\nu_{\tau R}$	0	0	0	0	
ℓ_R^i	e_R	μ_R	τ_R	0	0	-2	-1	

Table 2.3: The fundamental fermions of the Standard Model and their electroweak quantum numbers. The index i corresponds to the generation.

singlets can have different hypercharges. This is done in such a way that the relationship

$$q = \frac{Y_W}{2} + T_W^3 \quad (2.6)$$

is valid, leading to the correct phenomenological predictions. Further, it can be shown, that with this assignment of hypercharges the Standard Model is a consistent theory, which has no net anomalies [8]. The fundamental fermions and their assignment to the doublets and singlets, along with their quantum numbers are shown in Table 2.3.

Right handed neutrinos have been added to the Standard Model particle content, although these are singlets under all Standard Model gauge groups. They are needed within the Standard Model only if the neutrinos are massive. Experimental results [9–12] show that they have a small rest mass. Non zero neutrino masses have no significant impact on the results of this work.

The Lagrangian expressed in these representations reads¹:

$$\mathcal{L} = i\bar{L}_L\gamma^\mu D_\mu L_L + i\bar{\ell}_R\gamma^\mu D_\mu \ell_R + i\bar{\nu}_R\gamma^\mu D_\mu \nu_R + i\bar{Q}_L\gamma^\mu D_\mu Q_L + i\bar{u}_R\gamma^\mu D_\mu u_R + i\bar{d}_R\gamma^\mu D_\mu d_R, \quad (2.7)$$

¹Summation over all three generations is implied and the generation index is suppressed here and in the following to reduce clutter. In addition, the designation ' denoting that the down type ($T_W^3 = -1/2$) quarks listed here are the electroweak eigenstates instead of the mass eigenstates is left out in the following.

with the $SU(2)_L \times U(1)_Y$ gauge transformation:

$$Q_L/L_L \rightarrow e^{\frac{i}{2}(\vec{\alpha}(x)\vec{\tau} + \beta(x)Y_W)} Q_L/L_L, \quad u_R/d_R/\ell_R \rightarrow e^{\frac{i}{2}\beta(x)Y_W} u_R/d_R/\ell_R, \quad (2.8)$$

where $\vec{\tau}$ consists of the three generators of the $SU(2)_L$ group, which can be represented by the Pauli matrices $\vec{\sigma}$, and Y_W is the hypercharge operator. The covariant derivative takes the form

$$D_\mu = \partial_\mu + ig \frac{\vec{\sigma}}{2} \vec{W}_\mu + ig' \frac{Y_W}{2} B_\mu, \quad (2.9)$$

where g and g' are the coupling constants of the two gauge groups. The gauge fields are $W_\mu^1, W_\mu^2, W_\mu^3$ for the $SU(2)_L$ and B_μ for the $U(1)_Y$. Inserting 2.9 into 2.7 gives the gauge invariant Lagrangian:

$$\begin{aligned} \mathcal{L} = & \bar{L}_L \left\{ i\partial_\mu - g \frac{\vec{\sigma}}{2} \vec{W}_\mu - g' \frac{Y_W}{2} B_\mu \right\} L_L + \bar{Q}_L \left\{ i\partial_\mu - g \frac{\vec{\sigma}}{2} \vec{W}_\mu - g' \frac{Y_W}{2} B_\mu \right\} Q_L \\ & + \bar{\ell}_R \left\{ i\partial_\mu - g' \frac{Y_W}{2} B_\mu \right\} \ell_R + \bar{u}_R \left\{ i\partial_\mu - g' \frac{Y_W}{2} B_\mu \right\} u_R + \bar{d}_R \left\{ i\partial_\mu - g' \frac{Y_W}{2} B_\mu \right\} d_R \\ & + \bar{\nu}_R i\partial_\mu \nu_R \\ & - \frac{1}{4} \vec{W}_{\mu\nu} \cdot \vec{W}^{\mu\nu} - \frac{1}{4} B_{\mu\nu} B^{\mu\nu}, \end{aligned} \quad (2.10)$$

where the field strength tensors are given by $B_{\mu\nu} = \partial_\mu B_\nu - \partial_\nu B_\mu$ and $\vec{W}_{\mu\nu} = \partial_\mu \vec{W}_\nu - \partial_\nu \vec{W}_\mu + ig \vec{W}_\mu \times \vec{W}_\nu$. As in the case for QED, gauge fields had to be introduced to obtain gauge invariance. However, these fields need to be identified with the physical bosons. W_μ^1 and W_μ^2 mix to the physical W boson states:

$$W_\mu^\pm = \frac{1}{\sqrt{2}} (W_\mu^1 \mp i W_\mu^2). \quad (2.11)$$

The B_μ field cannot be the γ , since it would couple to hypercharged neutrinos. Also the W_μ^3 field cannot be the Z^0 boson, which also couples to right-handed fermions. Rather the physical fields have to be mixtures of these two, and they can be expressed as:

$$\begin{pmatrix} Z_\mu \\ A_\mu \end{pmatrix} = \begin{pmatrix} \cos \theta_w & \sin \theta_w \\ -\sin \theta_w & \cos \theta_w \end{pmatrix} \begin{pmatrix} W_\mu^3 \\ B_\mu \end{pmatrix}, \quad (2.12)$$

where the θ_w is the *electroweak mixing angle*. The meaning and the size of this mixing will be explained more closely in Section 2.1.3.

An immediate problem is that the observed fermion and weak gauge boson states are massive with the exception of the photon. As explained before, gauge invariance forbids to introduce any explicit mass term for the gauge bosons. Furthermore, in contrast to QED, it

is also not possible to insert explicit fermion mass terms like

$$\mathcal{L}_{m_f} = m_f \bar{\psi} \psi = m_f (\bar{\psi}_L \psi_R + \bar{\psi}_R \psi_L), \quad (2.13)$$

as these mix left- and right-handed fermions and are also not gauge invariant under the $SU(2)_L \times U(1)_Y$ group. Therefore a dedicated mechanism had to be devised in the Standard Model to solve this problem, which will be explained in detail in the next section.

2.1.3 The Higgs Mechanism

In the 1960's Peter W. Higgs and others [13] found a mechanism to generate both the masses of the weak gauge bosons and the fermions within a gauge invariant framework. The principle of this mechanism is spontaneous symmetry breaking. This is always realized when the Lagrangian possesses a symmetry that is absent in the lowest energy state, which is also called the ground state or the vacuum. In case of the electroweak interaction the Lagrangian has the full $SU(2)_L \times U(1)_Y$ symmetry, whereas the ground state is only symmetric wrt. $U(1)_{em}$. This broken symmetry will lead to the emergence of *effective* mass terms for the weak gauge bosons, while retaining the full gauge invariance.

In the Standard Model electroweak symmetry breaking is accomplished by an additional scalar field, the Higgs field, with an appropriate potential. One of its components acquires a vacuum expectation value, thus spontaneously breaking the gauge symmetry. Fermions and gauge bosons interacting with this field acquire an effective mass while still preserving the gauge invariance of the theory.

In formulating the new Lagrangian for the theory, the following conditions have to be fulfilled:

- As the particle masses need to be generated by interactions with the scalar field, it needs to have non-vanishing hypercharge and weak isospin.
- The component of the scalar field containing the vacuum expectation value has to be neutral so that $U(1)_{em}$ remains unbroken.
- The self-interaction must be chosen so that it breaks gauge symmetry in the desired way and keeps the theory renormalizable. This restricts the mass dimension of the self-interaction terms to four or less.
- The representation of the scalar field must contain at least three degrees of freedom, otherwise the weak gauge bosons cannot be provided with the additional longitudinal polarization state corresponding to a massive particle.

The simplest representation of such a scalar field is a single complex isospin doublet

$$\Phi = \begin{pmatrix} \Phi^+ \\ \Phi_0 \end{pmatrix} = \begin{pmatrix} \Phi_3 + i\Phi_4 \\ \Phi_1 + i\Phi_2 \end{pmatrix}, \quad (2.14)$$

with a hypercharge of $+1$. The fields $\Phi_{1,2,3,4}$ are real fields, corresponding to four degrees of freedom. The electroweak Lagrangian 2.10 is supplemented by a kinematic term for the

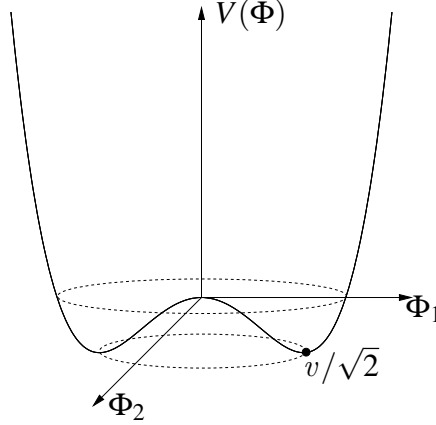


Figure 2.1: Visualization of the Higgs potential as a function of Φ_1 and Φ_2 .

Higgs field and a potential $V(\Phi)$, which are both gauge invariant:

$$\mathcal{L}_{Higgs} = (D_\mu \Phi)^\dagger (D^\mu \Phi) - V(\Phi), \quad (2.15)$$

$$V(\Phi) = -\mu^2 \Phi^\dagger \Phi + \lambda (\Phi^\dagger \Phi)^2. \quad (2.16)$$

The shape of the potential $V(\Phi)$ depends on the parameters μ^2 and λ . The latter has to be positive so that the total energy is bounded from below. For the case $\mu^2 < 0$, the lowest point of the potential corresponds to $\Phi_1 = \Phi_2 = \Phi_3 = \Phi_4 = 0$ and a zero vacuum energy. Only for $\mu^2 > 0$ spontaneous symmetry breaking occurs. The shape of the potential for this case is sketched in Figure 2.1 in dependence of two of the components. The minimum of the potential is now at non-zero values, although the potential is still symmetric wrt. the origin. This is the analogy of the still present – but broken – gauge symmetry. There is an infinite number of minima, defined by

$$\Phi^\dagger \Phi = \Phi_1^2 + \Phi_2^2 + \Phi_3^2 + \Phi_4^2 = \frac{\mu^2}{2\lambda} \equiv \frac{v^2}{2}, \quad (2.17)$$

with the vacuum expectation value $v = \mu/\sqrt{\lambda}$. In the Φ_1 - Φ_2 plane the minima form a circle and can be described by:

$$\Phi_{1,2}^{\min} = \sqrt{\frac{\mu^2}{2\lambda}} \exp(i\theta), \quad 0 \leq \theta \leq 2\pi. \quad (2.18)$$

From an arbitrary but fixed point in the minimum the symmetry is no longer present. Choosing one such point with only one non-vanishing field component, e.g.

$$\Phi_1^{\text{vac}} = \sqrt{\frac{\mu^2}{2\lambda}} = \frac{v}{\sqrt{2}}, \quad (2.19)$$

corresponds to spontaneous symmetry breaking. In this way the vacuum expectation value has non-vanishing hypercharge and isospin quantum numbers, thus spontaneously breaking both the $SU(2)_L$ and the $U(1)_Y$ gauge groups. The $U(1)_{em}$ gauge groups remains unbroken since the vacuum state has no charge.

The excitations of the field around the ground state have to be interpreted as particles. Seen from the chosen vacuum state there are three directions in which the energy is unchanged (in Figure 2.1 only one of these is visible). These correspond to massless bosons that would also be visible as non-vanishing values for Φ_2 , Φ_3 , and Φ_4 . They are called the Goldstone bosons and are unphysical states that can be removed by a gauge transformation, the so called *unitary gauge*. Their degrees of freedom are absorbed by the additional degrees of freedom that the weak gauge bosons acquire when becoming massive. In addition to these massless excitations, there is one massive excitation along the Φ_1 direction which can be parametrized as:

$$\Phi = \frac{1}{\sqrt{2}} \begin{pmatrix} 0 \\ v + H(x) \end{pmatrix}. \quad (2.20)$$

Inserting Eq. 2.20 into Eq. 2.15 and using the covariant derivative 2.9 leads to the following additional terms for the electroweak Lagrangian in the case of spontaneous symmetry breaking (SSB):

$$\mathcal{L}_{\text{Higgs}}^{\text{SSB}} = \frac{\lambda}{4} v^4 \quad (2.21)$$

$$+ \frac{1}{2} \partial_\mu H \partial^\mu H - \lambda v^2 H^2 - \lambda v H^3 - \frac{1}{4} \lambda H^4 \quad (2.22)$$

$$+ \frac{1}{8} (v + H(x))^2 \begin{pmatrix} W_\mu^1, W_\mu^2, W_\mu^3, B_\mu \end{pmatrix} \begin{pmatrix} g^2 & 0 & 0 & 0 \\ 0 & g^2 & 0 & 0 \\ 0 & 0 & g^2 & gg' \\ 0 & 0 & gg' & g'^2 \end{pmatrix} \begin{pmatrix} W^{1\mu} \\ W^{2\mu} \\ W^{3\mu} \\ B^\mu \end{pmatrix}. \quad (2.23)$$

The first term is a constant that has no consequence for particle dynamics, since the Euler-Lagrange equations contain only derivatives of the Lagrangian.

The second line corresponds to the Klein-Gordon equation for a scalar particle with mass $M_H = v\sqrt{2\lambda}$ that has both cubic and quartic self-couplings. This particle is called the Higgs boson and has not yet been found, but it is predicted by the electroweak Standard Model.

The last line in Eq. 2.21 contains mass terms for the vector bosons and couplings of the Higgs boson to them. As can be easily verified, the 4×4 mass matrix has rank three, so it has one eigenvalue of zero. The other three eigenvalues are non-zero but two of them are degenerate. This mass matrix describes one massless particle, two of equal non-zero mass, and one which is even heavier. This fits exactly to the photon, the W bosons and the Z^0 boson. The corresponding physical fields can be found by diagonalizing the mass matrix and yield the physical gauge bosons, as shown in Eq. 2.11 and Eq. 2.12. The electroweak

mixing angle is then:

$$\sin \theta_w = \frac{g'}{\sqrt{g^2 + g'^2}}. \quad (2.24)$$

The physical boson states have exactly the properties of the Z^0 and the γ , e.g. the γ does not couple to neutrinos. It should be noted that this is a direct consequence of the isospin and hypercharge assignments of the fermions and the Higgs field.

The gauge boson masses are:

$$M_{Z^0} = v \cdot \frac{\sqrt{g^2 + g'^2}}{2} \quad (2.25)$$

$$M_W = v \cdot \frac{g}{2} = M_{Z^0} \cdot \cos \theta_w \quad (2.26)$$

$$M_\gamma = 0. \quad (2.27)$$

The vacuum expectation value is known since it is related to the Fermi coupling constant G_F [14] that can be measured in beta decays:

$$v = \left(\sqrt{2} G_F \right)^{-\frac{1}{2}} \approx 246 \text{ GeV}. \quad (2.28)$$

For the couplings of the predicted Higgs boson to the gauge bosons one can derive:

$$g_{HWW} = g \cdot M_W \quad g_{HZ^0Z^0} = g \cdot \frac{M_{Z^0}}{\cos \theta_w} = g \cdot M_W. \quad (2.29)$$

The Higgs mechanism does not directly provide fermion mass terms. However it is possible to generate the masses in a gauge invariant way by using dimensionless Yukawa couplings of the fermions to the Higgs field. This can be done by adding the following term to the Lagrangian:

$$\mathcal{L}_{\text{Yukawa}} = \lambda_u \bar{Q}_L u_R \Phi + \lambda_d \bar{Q}_L d_R \tilde{\Phi} + \lambda_\ell \bar{L}_L \ell_R \Phi + \lambda_\nu \bar{L}_L \nu_R \tilde{\Phi} + \text{h.c.} \quad (2.30)$$

$$\stackrel{\text{Eq. 2.20}}{=} \frac{v}{\sqrt{2}} \cdot (\lambda_u \bar{u}_L u_R + \lambda_d \bar{d}_L d_R + \lambda_\ell \bar{\ell}_L \ell_R + \lambda_\nu \bar{\nu}_L \nu_R) + \text{h.c.} \quad (2.31)$$

$$+ \frac{1}{\sqrt{2}} \cdot (\lambda_u \bar{u}_L H u_R + \lambda_d \bar{d}_L H d_R + \lambda_\ell \bar{\ell}_L H \ell_R + \lambda_\nu \bar{\nu}_L H \nu_R) + \text{h.c.} \quad (2.32)$$

where $\tilde{\Phi} = i\tau_2 \Phi^*$ is the charge conjugated Higgs field which is needed to give mass to quarks with $T_W^3 = +1/2$. The last term in the second row corresponds to a Dirac mass term for the neutrinos, which can be generated in the Standard Model by interactions with the Higgs field. Another possible mass term for neutrinos would be a Majorana mass term, which is not included here.

The masses and the couplings of the Higgs boson to the fermions are then given by:

$$m_f = v \frac{\lambda_f}{\sqrt{2}}, \quad g_{Hf\bar{f}} = g \frac{m_f}{2M_W}, \quad (2.33)$$

where λ_f is the Yukawa coupling to the fermion f .

2.1.4 Theoretical Constraints on the Higgs boson mass

While the couplings of the Standard Model Higgs boson and therefore its branching fractions can be predicted, its mass remains a free parameter of the Standard Model. However, it is possible to place constraints on it by requiring the Standard Model to be a unitary, perturbative and stable theory up to an energy scale Λ where new physics might appear. A comprehensive discussion of these constraints can be found in [16].

In order that certain processes like $W^+W^- \rightarrow W^+W^-$ yield *unitary* scattering amplitudes, the Higgs boson mass has to be smaller than about 850 GeV.

Other constraints can be derived from radiative corrections to the quartic coupling parameter λ . From the need that the coupling remains perturbative, which means that *no trivial Landau pole* appears, up to a scale Λ an upper bound on the Higgs boson mass can be given. The Higgs boson mass can be limited from below by demanding λ to be positive up to the cut-off scale, i.e. that the *electroweak vacuum remains stable*.

The allowed region for the mass of the Higgs boson from these theoretical considerations is shown in Figure 2.2 in dependence of the scale Λ up to which the Standard Model is assumed to be valid and a stable and perturbative theory.

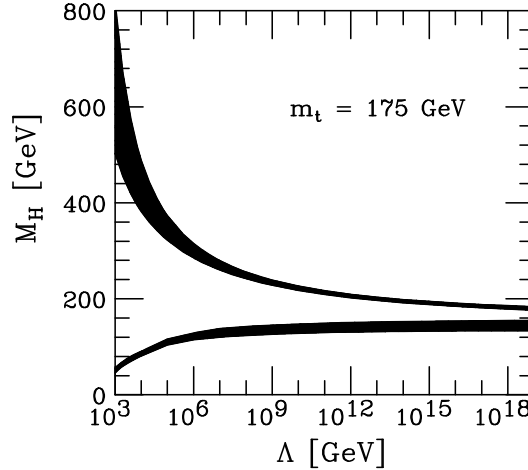


Figure 2.2: Theoretically allowed region for the Higgs boson mass in dependence of the cut-off scale Λ where physics beyond the Standard Model has to set in. The limits have been derived by demanding the quartic coupling λ to be positive and finite up to Λ (from [15]). The bands indicate the theoretical uncertainties.

If the Standard Model is assumed to be a valid effective theory up to the scale where gravity is predicted to become a strong force, which is called the Planck scale $M_{\text{Planck}} = 10^{19}$ GeV, the Higgs boson has to have a mass between 130 and 190 GeV.

In summary the theoretical expectation for the mass of the Standard Model Higgs boson is of the order of a few hundred GeV, which corresponds to the electroweak scale, which is set by the vacuum expectation value. This is further supported by indirect evidence for the mass of the Higgs boson, which will be further discussed in Chapter 3.

2.1.5 Summary of the Standard Model

The strong interaction is added to the Standard Model as a gauge theory with the gauge group $SU(3)_C$, which acts only on the quarks. Since it is a non-abelian gauge theory, the gluons themselves also carry charge, which is called color. More detail about the strong interaction as a gauge theory can be found in Appendix A.

The complete gauge group of the Standard Model is:

$$SU(3)_C \times SU(2)_L \times U(1)_Y,$$

which is spontaneously broken through a scalar field obtaining a vacuum expectation value to:

$$SU(3)_C \times U(1)_{em}.$$

For massless neutrinos, the Standard Model has 19 free parameters: Nine fermion masses, three mixing angles and one CP violating phase in the CKM matrix, the mass of the Z^0 , the Fermi coupling constant G_F , the gauge coupling constants α and α_s , the mass of the Higgs boson, and θ_{CP} , which is a possible CP violating parameter that occurs in strong interactions and is zero in the Standard Model. If neutrino masses are added as simple Dirac masses, as indicated previously, seven additional parameters – three masses, three mixing angle, and one CP violating phase – have to be added.

2.1.6 Limits of the Standard Model

The Standard Model as described in the previous sections is an immensely successful theory. It has been tested numerous times with increasing precision and seems to be valid also at the level of quantum corrections. The only missing particle predicted, the Higgs boson, should be within the discovery reach of the Large Hadron Collider. However, there is wide agreement that the Standard Model can only be an effective theory that is embedded within a larger, more fundamental theory. This is on the one hand evidenced by the large number of free parameters in the Standard Model. On the other hand, there are also remaining unsolved problems regarding the Standard Model, which are briefly discussed in the following.

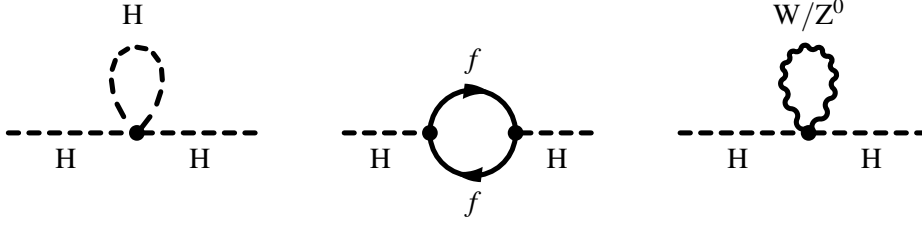


Figure 2.3: Examples of Feynman diagrams for one-loop corrections to the Higgs boson mass in the Standard Model.

The Hierarchy and Fine tuning Problem

One of the most astonishing features of the Standard Model is the large difference of natural scales in the theory. The electroweak scale is given by the vacuum expectation value $v = 246$ GeV, which is the same order of magnitude as the mass of the weak gauge bosons and the Higgs boson (if it exists). The other natural scale is the Planck scale² of 10^{19} GeV. This huge difference of scales is completely unexplained and is called the hierarchy problem [17].

The same problem, but in slightly different form arises when considering quantum corrections to particle masses. While the fermion and gauge boson masses are protected against large (quadratic) divergences by chiral and gauge symmetry [18], the same is not true for the mass of the Higgs boson. There is not even an approximate symmetry in the Lagrangian that would protect its mass. This can be seen in Eq. 2.16: Setting the parameter μ^2 , which is connected to the Higgs boson mass by $\mu^2 = 1/2 M_H^2$, to zero does not increase the symmetry of the Lagrangian. Figure 2.3 shows the Feynman diagrams responsible for the one-loop corrections to the Higgs boson mass. Calculating the corrections leads to terms of the form [18]:

$$\Delta M_H^2 \propto \pm \alpha (\Lambda_{\text{cut-off}}^2 - M_X^2) + \text{logarithmic terms.} \quad (2.34)$$

$\Lambda_{\text{cut-off}}$ is the cut-off parameter in the loop integral, α the coupling of the particle X in the loop to the Higgs boson, and M_X its mass. The sign of the correction depends on the spin of the particle. The cut-off parameter can be motivated by the assumption that the Standard Model is only an effective theory that is valid up to an energy scale where new physics set in and regularize the divergences. This new physics might be GUT-theories at a scale of $\Lambda_{\text{GUT}} = 10^{15-16}$ GeV. At the very latest the Standard Model has to break down at the Planck scale $\Lambda_{\text{Planck}} = 10^{19}$ GeV. Entering these high scales into Eq. 2.34 leads to corrections to the Higgs mass that are several orders of magnitude larger than the expected mass of the Standard Model Higgs boson, which should be at the electroweak scale. This has to be compensated by adjusting the bare mass accordingly in renormalization. As the same divergences reemerge in each order of perturbation theory, this *fine tuning* on the

²Also the scale of grand unification is expected to be not much smaller than the Planck scale, so even if a GUT theory exists in nature, the hierarchy problem remains.

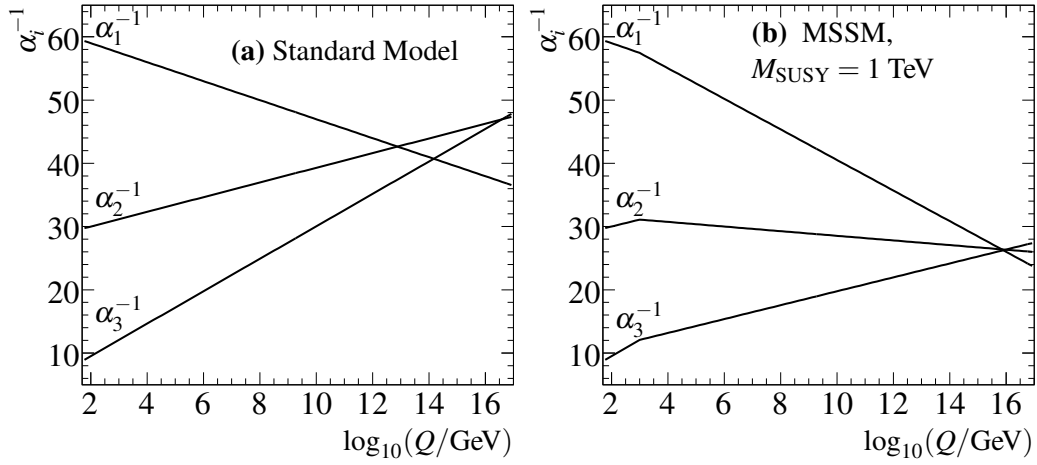


Figure 2.4: Evolution of the three gauge coupling constants with energy scale Q in (a) the Standard Model and (b) the minimal supersymmetric extension of the Standard Model with masses of the superpartners at the TeV scale. Shown is $\alpha_i^{-1} = 4\pi/g_i^2$. The evolution was calculated according to the formulas in Ref. [20], p. 199 ff.

order of 10^{-34} [17] has to be redone in each order. Since the only natural scale for the Higgs boson mass is the GUT-scale or the Planck scale, this is also called the *naturalness problem*.

Gauge Coupling Unification

Within the Standard Model the question remains why there are three gauge groups with three different coupling constants that seem to be unrelated to each other. Efforts have been done to unify all three gauge groups in one encompassing gauge group with only one gauge couplings and all fermions represented on equal footings. This *Grand Unified Theory* [19] would be realized at very high energies. Only at low energies the three interactions of the Standard Model seem to be different.

An indication of a grand unification would be if all coupling constants evolve with energy in such a way that they meet at the same point. If only the Standard Model particles enter the evolution equations for the couplings, they come generally close to each other at a scale of about 10^{13-14} GeV, but do not meet. This is shown in Figure 2.4 (a).

In the following one of the most interesting extensions of the Standard Model, Supersymmetry, is discussed.

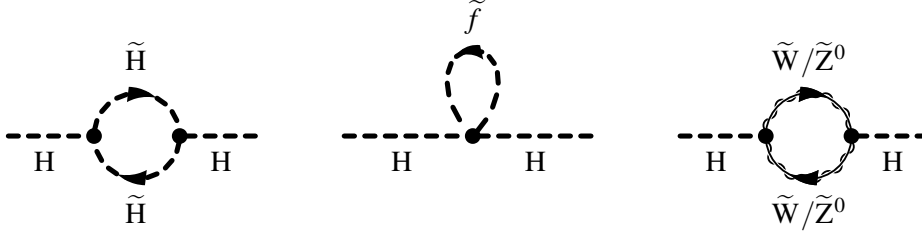


Figure 2.5: Feynman diagrams involving supersymmetric partner particles that cancel the quadratic divergences induced by the diagrams in Fig. 2.3.

2.2 Supersymmetry

Supersymmetry (SUSY) is a new symmetry connecting bosons and fermions. A SUSY transformation Q generates a fermionic state from a bosonic state and vice versa:

$$Q|\text{boson}\rangle = |\text{fermion}\rangle, \quad Q|\text{fermion}\rangle = |\text{boson}\rangle \quad (2.35)$$

In a supersymmetric theory, there has to be a fermionic partner particle to each boson with otherwise the same quantum numbers and vice versa. The Haag-Lopuszanski-Sohnius theorem [21] states that the largest symmetry incorporating an interacting unitary field theory has to be the direct product of Lorentz invariance, gauge symmetry and supersymmetry (SUSY). In this context it would be natural to expect that SUSY is realized in nature. In addition to this aesthetic argument, SUSY also solves parts of the problems of the Standard Model.

If there were supersymmetric partner particles, they would also lead to corrections to the Higgs boson mass that are depicted in Figure 2.5. Due to the spin difference of the superpartners, the quadratic divergences would be canceled exactly in all orders of perturbation theory. This would stabilize the Higgs boson mass and the electroweak scale.

Unfortunately no supersymmetric partner particles with the same mass as its corresponding Standard Model particle, e.g. a scalar partner of the electron with a mass of 0.511 MeV, have been observed in nature.

Supersymmetry must be a *broken* symmetry, which leads to different masses of the superpartners. If M and \tilde{M} are the Standard Model particle mass and the one of its supersymmetric partner, the summed correction to the Higgs boson mass is:

$$\Delta M_H^2 = \alpha (\tilde{M}^2 - M^2) \equiv \alpha \cdot M_{\text{SUSY}}^2. \quad (2.36)$$

If one requires to have corrections that are at most of the same order as the electroweak scale ($\mathcal{O}(100 \text{ GeV})$), then the mass scale of the SUSY particles has to be smaller than $\mathcal{O}(1 \text{ TeV})$. Such a low-scale supersymmetry with masses of the supersymmetric partner particles of a few TeV would solve the fine-tuning problem.

Standard Model particles	SUSY partners	Name of SUSY partners
$Q_L = \begin{pmatrix} u_L \\ d_L \end{pmatrix}$	$\tilde{Q}_L = \begin{pmatrix} \tilde{u}_L \\ \tilde{d}_L \end{pmatrix}$	left-chiral squarks
u_R, d_R^a	\tilde{u}_R, \tilde{d}_R	right-chiral squarks
$L_L = \begin{pmatrix} \nu_L \\ \ell_L \end{pmatrix}$	$\tilde{L}_L = \begin{pmatrix} \tilde{\nu}_L \\ \tilde{\ell}_L \end{pmatrix}$	left-chiral sleptons
ℓ_R	$\tilde{\ell}_R$	right-chiral sleptons
γ	$\tilde{\gamma}$	Photino
W^\pm	\tilde{W}^\pm	Winos
Z^0	\tilde{Z}^0	Zino
g	\tilde{g}	Gluinos
$\begin{pmatrix} H_1^+ \\ H_1^0 \end{pmatrix}, \begin{pmatrix} H_2^0 \\ H_2^- \end{pmatrix}$	$\tilde{H}_1^+, \tilde{H}_2^-, \tilde{H}_1^0, \tilde{H}_2^0$	Higgsinos

Table 2.4: Particle content of the MSSM. The superpartners mix to the mass eigenstates as described in the text. Generation indices for the fermions are suppressed.

SUSY with sparticle masses at the TeV scale would also solve the problem of gauge coupling unification. The additional supersymmetric partners have to be taken into account in the evolution of the couplings. The result is shown in Figure 2.4 (b) for the case of the minimal extension of the Standard Model to a supersymmetric theory. In this case, the three gauge couplings meet at a scale of $\mathcal{O}(10^{16} \text{ GeV})$.

2.3 The Minimal Supersymmetric Standard Model

The Minimal Supersymmetric Standard Model (MSSM) is the simplest supersymmetric extension of the Standard Model. It introduces new particles, but only those absolutely necessary to have a consistent supersymmetric theory and keeps the gauge groups of the Standard Model untouched. As none of the particles of the Standard Model can be identified as a superpartner, the particle spectrum is doubled. The MSSM is constructed as a $N = 1$ supersymmetry, which means that the superpartners for the gauge bosons and the Higgs boson(s) have spin $1/2$ and the superpartners of the fermions are scalar particles. A complete discussion of the construction of the MSSM Lagrangian is beyond the scope of

this summary and can be found in Refs. [18, 20, 22]. The particle content of the MSSM is summarized in Table 2.4.

Due to the chiral nature of the fermions, where the left- and right-handed fermions have different quantum numbers, each Standard Model fermion gets two distinct superpartners. E.g. the top quark gets the \tilde{t}_L and the \tilde{t}_R , the left- and right-handed stop quark. After electroweak symmetry breaking, these can mix to mass eigenstates \tilde{t}_1 and \tilde{t}_2 .

A potential superpartner of the right-handed neutrinos, the right-handed sneutrino, is left out here and in the following. It would have no effect on the Higgs sector of the MSSM.

In addition to the sparticles it is also necessary to introduce a second Higgs doublet field. Of these eight degrees of freedom, as in the Standard Model three are used to generate the gauge boson masses. The leftover five degrees of freedom manifest as five physical Higgs bosons, two charged ones and three neutral ones. This will be discussed in more detail in Section 2.4. The superpartners of the Higgs bosons, the Higgsinos, mix with the superpartners of the gauge bosons to the four charginos $\tilde{\chi}_{1,2}^\pm$ and the four neutralinos $\tilde{\chi}_{1,2,3,4}^0$.

When constructing the Lagrangian of the MSSM from these superfields, in which Standard Model partners and the superpartners are grouped together, it is not forbidden to construct terms that violate baryon and lepton number. Such terms are forbidden *ad hoc* by requiring an additional symmetry, called *R*-parity. It can be defined by the following relation:

$$R \equiv (-1)^{3B+L+2S}, \quad (2.37)$$

where B is the baryon number, L is the lepton number and S the spin of the particle. It can be easily verified that R is $+1$ for Standard Model particles and -1 for superpartners. Conservation of *R*-parity not only forbids baryon and lepton number violation – which would lead e.g. to proton decay – but also has the consequence that supersymmetric particles always have to be produced in pairs. In addition, there has to be a stable lightest supersymmetric particle (LSP). Due to cosmological constraints [17, 23] it cannot have electric or color charge and is frequently assumed to be the lightest neutralino. Since it would be neutral and only weakly interacting, it would be a prime candidate for the dark matter that is believed to provide around 25% of the energy of the universe [24].

As mentioned above, SUSY has to be a broken symmetry. Spontaneous breaking of supersymmetry would require to have a field of the MSSM to acquire a vacuum expectation value, just as in the Higgs mechanism. However it can be shown [25] that this would spoil the gauge invariance of the theory. Instead, it is assumed that some other fields at a higher mass scale spontaneously break SUSY. This breaking in a so-called *hidden sector* is then transported to the MSSM particles (the *visible sector*) via messenger fields. For a more detailed discussion of the hidden sector see Ref. [25]. The SUSY breaking scenarios are generally based on how the breaking is mediated to the visible sector. Among these are gravity mediation (mSUGRA) [26], gauge mediation (GMSB) [27], anomaly mediation (AMSB) [28], and gaugino mediation [29]. It is beyond the scope of this summary to discuss these in detail.

Instead of assuming an explicit breaking mechanism, in the MSSM *soft breaking* terms are explicitly added to the Lagrangian, which just parameterize the unknown breaking mechanism. These soft breaking terms are constructed by requiring gauge invariance, conservation of R -parity, and that no new quadratic divergences are created. This construction can be found in Ref. [22]. Among the soft breaking terms are (i) mass parameters for the Higgs fields, (ii) mass parameters for the gauginos of the three gauge groups, (iii) mass parameters of the sfermions, and (iv) trilinear couplings between the sfermions and the Higgs fields. Since most of these parameters can be complex, the mass parameters of the sfermions and the trilinear couplings are in general 3×3 matrices. This results in a large number of free parameters. An analysis of the number of physical degrees of freedom in Ref. [30] yields 105 new parameters in addition to the 19 of the Standard Model: In the sfermion sector 21 masses of the sfermions, 36 real mixing angles and 40 CP-violating phases, for the gauginos three real mass parameters (M_1, M_2, M_3) and two phases, and in the Higgs sector two real mass parameters and one phase. This huge parameter space is a direct consequence of the fact that the SUSY breaking mechanism is unknown. Since it is not possible to examine the whole 105-dimensional parameter space, the parameter space is commonly reduced by making some assumptions [30] that have almost no consequence for the phenomenology of the Higgs sector and can be motivated by theoretical arguments. These assumptions are:

- The masses of the gauge fermions are assumed to be real and the same at a grand unification (GUT) scale:

$$M_1(\Lambda_{\text{GUT}}) = M_2(\Lambda_{\text{GUT}}) = M_3(\Lambda_{\text{GUT}}) = m_{1/2}, \quad (2.38)$$

where $m_{1/2}$ is the common mass. This corresponds to the unification of the gauge couplings at Λ_{GUT} . The masses of the gauge fermions at low energies are then determined by renormalization group analysis, see [30].

- It is assumed that the scalar fermion masses and the trilinear couplings are diagonal, real, and universal for all three generations at the GUT scale. The common sfermion masses and trilinear couplings are called m_0 and A_0 . These assumptions reduce large effects beyond the Standard Model that would be present at tree-level, such as flavor changing neutral currents or additional CP violation, which are strongly limited by flavor observables.
- The Higgs mass parameters are assumed to be real at the GUT scale.

This reduces the number of additional parameters to five. Commonly the MSSM is only studied in this constrained form, also called the cMSSM. In the mSUGRA model [26] the high scale is not the GUT scale, but the Planck scale. This causes minor numerical differences for parameters at low energies. In addition to the assumptions above, in a mSUGRA model also the Higgs mass parameters m_1 and m_2 are identical to m_0 at the Planck scale, reducing the parameter space even further.

2.4 The MSSM Higgs Sector

In supersymmetry a second Higgs doublet field with opposite hypercharge ($Y = -1$) is needed. This has the following reasons:

- The superpartners of the Higgs field, the Higgsinos, would lead to the appearance of gauge anomalies [8], that are absent in the electroweak theory. Introducing a second Higgs doublet, these anomalies are canceled by the Higgsinos from the second doublet. Otherwise the renormalizability of the theory would be destroyed.
- The construction of supersymmetric Lagrangians, see e.g. [20], forbids the charge conjugate Higgs field $\tilde{\Phi} = i\sigma_2\Phi$ that is used in the Standard Model to describe the mass generation for the quarks with $T_W^3 = +1/2$. This is accomplished in the MSSM by the second Higgs doublet field, whose vacuum expectation value couples to the u, c, and the t quark.

Therefore, in the MSSM two Higgs fields with opposite hypercharge are postulated:

$$H_1 = \begin{pmatrix} H_1^1 \\ H_1^2 \end{pmatrix} \quad (Y = -1) \quad H_2 = \begin{pmatrix} H_2^1 \\ H_2^2 \end{pmatrix} \quad (Y = +1) \quad (2.39)$$

The Higgs potential in the MSSM is given by [22]:

$$V = \mu^2(|H_1|^2 + |H_2|^2) + \frac{g^2 + g'^2}{8}(|H_1|^2 - |H_2|^2)^2 + \frac{g^2}{2}|H_1^* H_2|^2. \quad (2.40)$$

The quartic Higgs self couplings are fixed by the gauge couplings, in contrast to the Standard Model, where it was a free parameter. This leads to the fact that the mass of the lightest Higgs boson has an upper limit.

The potential has only the trivial minimum $V = 0$ for $H_1 = H_2 = 0$, so there is no spontaneous symmetry breaking. To break the $SU(2)_L \times U(1)_Y$ symmetry, it is essential to break supersymmetry. This is also referred to as radiative breaking of the gauge group. At some high scale the potential is symmetric and has the trivial minimum. By SUSY breaking and the evolution of the parameters with energy the mass parameter μ^2 gets negative and the Higgs fields acquire vacuum expectation values, thus breaking the gauge symmetries. Adding the soft breaking terms to the potential yields [22]:

$$V = (\mu^2 + m_1^2)|H_1|^2 + (\mu^2 + m_2^2)|H_2|^2 - \sum_{i,j} \mu B(\epsilon_{ij} H_1^i H_2^j + \text{h.c.}) \quad (2.41)$$

$$+ \frac{g^2 + g'^2}{8}(|H_1|^2 - |H_2|^2)^2 + \frac{g^2}{2}|H_1^* H_2|^2, \quad (2.42)$$

with $\epsilon_{12} = -\epsilon_{21} = 1, \epsilon_{11} = \epsilon_{22} = 0$, where m_1, m_2 , and B are soft breaking parameters. Requiring the breaking of the gauge symmetry to $U(1)_{em}$ and having a potential that is

bounded from below, yields the following two conditions [18]:

$$(\mu B)^2 > (|\mu|^2 + m_1^2)(|\mu|^2 + m_2^2) \quad (2.43)$$

$$2|\mu B| < (|\mu|^2 + m_1^2) + (|\mu|^2 + m_2^2), \quad (2.44)$$

which can be fulfilled only for $m_1^2 \neq m_2^2$. If the Higgs mass parameters are the same at the GUT scale, as postulated in mSUGRA, the symmetry breaking occurs because of the different evolution for m_1^2 and m_2^2 , corresponding to radiative electroweak symmetry breaking. The two Higgs fields now acquire vacuum expectation values

$$\langle H_1 \rangle = \frac{1}{\sqrt{2}} \begin{pmatrix} v_1 \\ 0 \end{pmatrix}, \quad \langle H_2 \rangle = \frac{1}{\sqrt{2}} \begin{pmatrix} 0 \\ v_2 \end{pmatrix}, \quad (2.45)$$

where v_1 and v_2 can be assumed to be real and positive. The two vacuum expectation values add up quadratically to the value as in the Standard Model and their ratio is defined as:

$$\tan \beta \equiv \frac{v_2}{v_1}, \quad \sqrt{v_1^2 + v_2^2} = 246 \text{ GeV}. \quad (2.46)$$

The phenomenology of the MSSM Higgs sector is at tree level very dependent on $\tan \beta$. Minimization of the Higgs potential relates these parameters to the gauge couplings, the soft breaking parameters and the mass parameter μ :

$$\mu^2 + m_1^2 = \tilde{m}_3^2 \tan \beta + \frac{g^2 + g'^2}{4} (v_1^2 - v_2^2), \quad (2.47)$$

$$\mu^2 + m_2^2 = \tilde{m}_3^2 \cot \beta + \frac{g^2 + g'^2}{4} (v_1^2 - v_2^2), \quad (2.48)$$

with $\tilde{m}_3^2 \equiv -B\mu$. Thus, the Higgs sector at tree level is completely defined by only two parameters, which can for example be chosen as $\tan \beta$ and a mass scale, such as \tilde{m}_3^2 , or as it is usually done as the mass of one of the physical Higgs bosons.

The two complex Higgs doublet fields represent eight degrees of freedom. Just as in the Standard Model, three of these correspond to Goldstone bosons G^0, G^\pm that disappear in unitary gauge and are absorbed into the masses for the W^\pm and Z^0 bosons. The remaining five degrees of freedom have to be identified with physical Higgs bosons. Two of them are charged (H^\pm) and three are neutral, h^0 and H^0 with $CP = +1$ and A^0 with $CP = -1$. The Goldstone and Higgs bosons are mixtures of the components of the two Higgs fields with

same charge and CP quantum numbers:

$$\begin{pmatrix} G^- \\ H^- \end{pmatrix} = \begin{pmatrix} \cos \beta & -\sin \beta \\ \sin \beta & \cos \beta \end{pmatrix} \begin{pmatrix} H_1^2 \\ H_2^1 \end{pmatrix}, \quad (2.49)$$

$$\begin{pmatrix} G^0 \\ A^0 \end{pmatrix} = \sqrt{2} \begin{pmatrix} \cos \beta & -\sin \beta \\ \sin \beta & \cos \beta \end{pmatrix} \begin{pmatrix} \text{Im}(H_1^1) \\ \text{Im}(H_2^2) \end{pmatrix}, \quad (2.50)$$

$$\begin{pmatrix} h^0 \\ H^0 \end{pmatrix} = \sqrt{2} \begin{pmatrix} \cos \alpha & -\sin \alpha \\ \sin \alpha & \cos \alpha \end{pmatrix} \begin{pmatrix} \text{Re}(H_2^2) - v_2 \\ \text{Re}(H_1^1) - v_1 \end{pmatrix}, \quad (2.51)$$

$$G^+ = (G^-)^\dagger, \quad H^+ = (H^-)^\dagger, \quad (2.52)$$

where α is the mixing angle between the CP-even Higgs bosons. The mass eigenvalues and the mixing angle α are found to be [22]:

$$M_{H^\pm}^2 = \frac{1}{4} \left(g^2 + 2 \frac{\tilde{m}_3^2}{v_1 v_2} \right) (v_1^2 + v_2^2), \quad (2.53)$$

$$M_{A^0}^2 = \frac{\tilde{m}_3^2}{v_1 v_2} (v_1^2 + v_2^2) = \tilde{m}_3^2 (\tan \beta + \cot \beta) = M_{H^\pm}^2 - M_{W^\pm}^2, \quad (2.54)$$

$$M_{H^0, h^0}^2 = \frac{1}{2} \left[M_{A^0}^2 + M_{Z^0}^2 \pm \sqrt{(M_{A^0}^2 + M_{Z^0}^2)^2 - 4 M_{Z^0}^2 M_{A^0}^2 \cos^2 2\beta} \right], \quad (2.55)$$

$$\sin 2\alpha = -\sin 2\beta \left(\frac{M_{H^0}^2 + M_{h^0}^2}{M_{H^0}^2 - M_{h^0}^2} \right), \quad \cos 2\alpha = -\cos 2\beta \left(\frac{M_{A^0}^2 + M_{Z^0}^2}{M_{H^0}^2 - M_{h^0}^2} \right). \quad (2.56)$$

The masses of the gauge bosons and the fermions are:

$$M_{W^\pm} = \sqrt{\frac{g^2}{4} (v_1^2 + v_2^2)}, \quad M_{Z^0} = \sqrt{\frac{g^2 + g'^2}{4} (v_1^2 + v_2^2)}, \quad (2.57)$$

$$m_\ell = \frac{\lambda_\ell}{\sqrt{2}} v_1, \quad m_d = \frac{\lambda_d}{\sqrt{2}} v_1, \quad m_u = \frac{\lambda_u}{\sqrt{2}} v_2. \quad (2.58)$$

In contrast to the vacuum expectation values, all three neutral Higgs bosons couple to up- and down-type fermions since they are mixtures of the two Higgs fields. The pseudoscalar A^0 does not couple to the gauge bosons at tree level due to CP invariance. The coupling strengths are given relative to a Standard Model Higgs boson of the same mass in Table 2.5. The couplings fulfill the sum rules:

$$g_{h^0 d\bar{d}}^2 + g_{H^0 d\bar{d}}^2 = \frac{1}{\cos^2 \beta}, \quad g_{h^0 u\bar{u}}^2 + g_{H^0 u\bar{u}}^2 = \frac{1}{\sin^2 \beta}, \quad g_{h^0 VV}^2 + g_{H^0 VV}^2 = 1 \quad (2.59)$$

Φ	$g_{\Phi\bar{u}u}/g_{H^{\text{SM}}\bar{u}u}$	$g_{\Phi\bar{d}d}/g_{H^{\text{SM}}\bar{d}d}$	$g_{\Phi VV}/g_{H^{\text{SM}}VV}$
h^0	$\cos\alpha/\sin\beta$	$\sin\alpha/\cos\beta$	$\sin(\beta - \alpha)$
H^0	$\sin\alpha/\sin\beta$	$\cos\alpha/\cos\beta$	$\cos(\beta - \alpha)$
A^0	$1/\tan\beta$	$\tan\beta$	0

Table 2.5: Coupling strengths of the neutral Higgs bosons to up-type, down-type fermions, and gauge bosons relative to the coupling strength of a Standard Model Higgs boson with the same mass.

Examining the Higgs boson masses more closely yields the following relations between the masses of the Higgs bosons:

$$M_{h^0} \leq (M_{A^0}, M_{Z^0}) \leq M_{H^0}, \quad M_{W^\pm} \leq M_{H^\pm}. \quad (2.60)$$

The lightest Higgs boson is predicted to be lighter than the Z^0 boson. This has already been ruled out by the four LEP experiments [31]. However, the relations in Eq. 2.60 are given at tree-level only. When higher order corrections are taken into account, the upper bound on the mass of the lightest Higgs boson is shifted significantly. The most important radiative corrections come from loop diagrams involving top quarks and their scalar partners, and for high $\tan\beta$ also from the bottom quark and its scalar partners. Regardless of the radiative corrections, the mass of the lightest Higgs boson is bounded to be lower than about 135 GeV for arbitrary MSSM parameters. This is the result of the fixed quartic couplings in the Higgs potential. It should be noted that this limit depends significantly on the mass of the top quark.

2.4.1 Radiative Corrections and Benchmark Scenarios

At tree level, the MSSM Higgs sector depends only on two parameters that are usually chosen to be the mass of the pseudoscalar Higgs boson A^0 and $\tan\beta$. Through radiative corrections the Higgs sector also becomes sensitive to the soft breaking parameters of the MSSM. This will result in corrections to the Higgs boson masses. In addition the mixing angle α will change to an effective mixing angle α_{eff} .

Even when using the constrained MSSM the number of additional parameters is still five, which is impractical for experimental analysis. Instead *benchmark scenarios* have been defined that are designed to represent typical or experimentally challenging points in the parameter space. There are several sets of benchmark scenarios available.

One of these are the SPS scenarios [32], which have been designed to represent parameter regions that are typical for the phenomenology of the SUSY particles. They are more suitable for searches for SUSY particles and are defined in terms of supersymmetric parameters at some high scale, e.g. Λ_{GUT} .

In contrast to these scenarios, in [33] several benchmark scenarios have been defined that are specifically designed for the Higgs sector. They are not assuming any particular

SUSY breaking scenario, but instead take into account only constraints from the Higgs sector itself. They are not defined in terms of SUSY breaking parameters at the GUT scale, but rather by low energy parameters. These are chosen to have impact especially on the Higgs sector. As a consequence, these benchmark scenarios don't take into account any constraints from other observables, e.g. from electroweak precision data or B physics measurements. This means that it is not guaranteed that parts of the parameter space of these benchmark scenarios are not excluded by other measurements, such as the branching fraction of $b \rightarrow s\gamma$, which is sensitive to supersymmetric contributions.

The benchmark scenarios from [33] mostly affect only the properties of the lightest Higgs boson h^0 and have been designed to represent particularly difficult or unique points of the parameter space. As mentioned above, the main radiative corrections for the mass of the lightest Higgs boson, but also for the mixing angle α come from the $t\text{-}\tilde{t}$ - and for large $\tan\beta$ the $b\text{-}\tilde{b}$ -sector. Accordingly, the most important parameters are :

- m_t : The mass of the top quark.
- M_{SUSY} : The sfermion mass parameter at the electroweak scale, where it is assumed that these are identical for sbottom and stop squarks: $M_{\text{SUSY}} \equiv M_{\tilde{t}_L} = M_{\tilde{t}_R} = M_{\tilde{b}_L} = M_{\tilde{b}_R}$.
- X_t, X_b : The mixing parameters between the left and right handed stop and sbottom squarks. The off-diagonal elements of the mass matrices are proportional $X_t = A_t - \mu/\tan\beta$ and $X_b = A_b - \mu\tan\beta$. $A_{t,b}$ are the trilinear Higgs sfermion couplings and μ is the Higgs mixing parameter. In the benchmark scenarios it is assumed that the trilinear couplings are identical ($A_t = A_b$).
- M_2 , the $SU(2)_L$ gaugino mass parameter. The $U(1)_Y$ gaugino mass parameter M_1 is assumed to be related to M_2 by the GUT relation $M_1 = 5/3 \tan^2 \theta_W M_2$.
- $m_{\tilde{g}}$: At the two loop level the gluino mass enters.

The choice of parameters is shown in Table 2.6. The different scenarios are discussed in the following.

The $M_{h^0}\text{-max scenario}$ has been proposed already in [34] and has been chosen to maximize the mass of the lightest Higgs boson for a given M_{A^0} and $\tan\beta$. This leads to the smallest excluded parameter region from the LEP experiments [31].

In the *no-mixing* scenario the mixing in the $t\text{-}\tilde{t}$ -sector is assumed to be zero.

The *gluophobic scenario* is designed to suppress the main production mechanism of a light Higgs boson at the LHC, $gg \rightarrow h^0$. This is possible due to the cancellation of t and \tilde{t} loops [35]. This cancellation is more effective for small stop masses and large X_t .

The *small α_{eff}* scenario aims to reduce the coupling of the lightest Higgs boson to down-type fermions in certain regions of the parameter space, thus suppressing the main decay channels $h^0 \rightarrow b\bar{b}$ and $h^0 \rightarrow \tau\tau$.

In addition to these four CP conserving scenario, in the *CPX scenario* large complex phases are introduced to induce maximal CP violating effects in the Higgs sector [36]. The neutral Higgs bosons mix to mass eigenstates $h_{1,2,3}$. Instead of the mass of the A^0 , the mass of the H^\pm is chosen as scan parameter.

	benchmark scenario				
	$M_{h^0\text{-max}}$	no-mixing	gluophobic	small α_{eff}	CPX
$M_{\text{SUSY}}/\text{GeV}$	1000	2000	350	800	500
μ/GeV	200	200	300	2000	200
M_2/GeV	200	200	300	500	2000
$X_t^{\text{OS}}/\text{GeV}$	2000	0	-750	-1100	$A - \mu \cot \beta$
$m_{\tilde{g}}/\text{GeV}$	800	1600	500	500	1000
A/GeV	$X_t + \mu \cot \beta$	$X_t + \mu \cot \beta$	$X_t + \mu \cot \beta$	$X_t + \mu \cot \beta$	1000
$\arg(A, m_{\tilde{g}})$	0	0	0	0	$\pi/2$

Table 2.6: The numerical values of the input parameters in the four CP conserving benchmark scenarios. X_t is given in the on-shell scheme as used in the FEYNHIGGS program.

The radiative corrections used in this thesis are calculated using the FEYNHIGGS program (version 2.6.4) [37], which calculates the one loop and also the most important two loop corrections in the Feynman diagrammatic approach.

A detailed discussion of the impact of these higher order corrections is given in [38]. Among them are corrections to the relationship between the bottom quark mass and the bottom quark Yukawa coupling, which can arise from the bottom/sbottom sector especially for large $\tan \beta$. These are called Δ_b corrections. Also the mass relations between the neutral Higgs bosons, which are discussed in the following in a simpler approximation, can be modified slightly by higher orders. All relevant corrections are included in FEYNHIGGS.

2.4.2 Properties of the Neutral Higgs Bosons for large $\tan \beta$

Within this thesis especially the region of large $\tan \beta$ is of interest. In the following the properties of the neutral Higgs bosons in this region of parameter space are discussed. Large $\tan \beta$ are of special interest in the theory. Depending on the mixing in the t - \bar{t} sector, values of $\tan \beta \gtrsim 3 - 10$ are required to maximize the mass of the h^0 and thus evade the experimental constraints from the LEP experiments [31, 39]. In addition, if one requires the Yukawa couplings to unify at the GUT scale, values of $\tan \beta \approx m_t/m_b \approx \mathcal{O}(50)$ are favored [40]. Furthermore, in the constrained MSSM or mSUGRA model, all Higgs bosons have naturally rather small masses [41], making this an experimentally interesting region. Details of the following discussion can be found in Ref. [42].

The Higgs boson masses

As shown in Eq. 2.60 the mass of the lightest Higgs boson is bound to be below the mass of the Z^0 . Radiative corrections that in addition to the Standard Model parameters depend also on the soft breaking parameters as discussed in Section 2.4.1, bring this bound up to values of ≈ 130 GeV. In Ref. [42] an approximation of the full result that takes into

account only the main leading order corrections is given. In this approximation the masses of the neutral Higgs bosons are:

$$M_{H^0, h^0}^2 = \frac{1}{2}(M_{A^0}^2 + M_{Z^0}^2 + \varepsilon) \left[1 \pm \sqrt{1 - 4 \frac{M_{Z^0}^2 M_{A^0}^2 \cos^2 2\beta + \varepsilon(M_{A^0}^2 \sin^2 \beta + M_{Z^0}^2 \cos^2 \beta)}{(M_{A^0}^2 + M_{Z^0}^2 + \varepsilon)^2}} \right], \quad (2.61)$$

with $\varepsilon = \varepsilon(m_t, G_F, M_{Z^0}, \alpha_s, A_t, M_{\text{SUSY}}, \tan \beta)$. The full expression is given in Ref. [42], its exact form is not relevant for the following discussion. For $\tan \beta \gg 1$ the parameter ε remains finite and Eq. 2.61 can be approximated to:

$$M_{H^0, h^0}^2 = \frac{1}{2}(M_{A^0}^2 + M_{Z^0}^2 + \varepsilon \pm |M_{A^0}^2 - M_{Z^0}^2 - \varepsilon|). \quad (2.62)$$

In this approximation, there is a critical mass M_C of the A^0 boson, at which all three neutral Higgs bosons have the same mass. This corresponds to the maximal mass of the h^0 and the minimal mass of the H^0 . It is given by:

$$M_C = M_{h^0}^{\text{max}} = M_{H^0}^{\text{min}} = \sqrt{M_{Z^0}^2 + \varepsilon}. \quad (2.63)$$

At the same time, Eq. 2.62 implies that always at least two Higgs bosons are mass degenerate:

$$M_{A^0} \geq M_C \Rightarrow M_{H^0} = M_{A^0}, \quad M_{h^0} = M_C \quad (2.64)$$

$$M_{A^0} \leq M_C \Rightarrow M_{h^0} = M_{A^0}, \quad M_{H^0} = M_C \quad (2.65)$$

If the mass of the pseudoscalar Higgs boson is above the critical mass, the heavy Higgs boson H^0 has about the same mass. If it is below M_C , it is mass degenerate with the light scalar Higgs boson h^0 . This is shown in Fig. 2.6 in the M_{h^0} -max scenario for two different values of $\tan \beta$. The calculations were done using the FEYNHIGGS program.

Especially for the larger $\tan \beta$ the mass degeneracy is clearly visible. For smaller $\tan \beta$ it is still obvious, but only for $M_{A^0} \gg M_C$ or $M_{A^0} \ll M_C$.

The Higgs boson couplings

The radiative corrections to the effective mixing angle α_{eff} can be calculated in the same approximation to:

$$\tan 2\alpha_{\text{eff}} = \tan 2\beta \frac{M_{A^0}^2 + M_{Z^0}^2 - \varepsilon' / \sin 2\beta}{M_{A^0}^2 - M_{Z^0}^2 + \varepsilon / \cos 2\beta}. \quad (2.66)$$

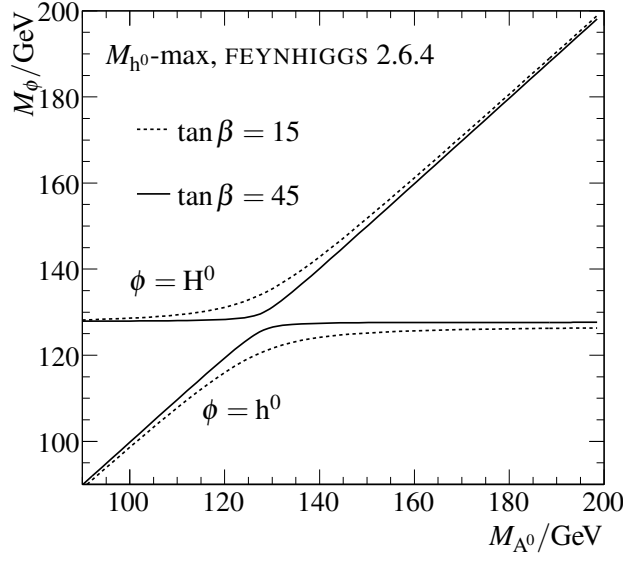


Figure 2.6: Masses of the neutral scalar Higgs bosons h^0 and H^0 versus M_{A^0} in the M_{h^0-max} scenario for $\tan\beta = 45$ (solid line) and $\tan\beta = 15$ (dashed line). The FEYNHIGGS program was used with a top quark mass of 172.5 GeV.

with $\varepsilon' = \varepsilon'(m_t, G_F, M_{Z^0}, \alpha_s, A_t, M_{SUSY}, \tan\beta, \mu)$. For $\tan\beta \gg 1$ the couplings can be approximated using two functions [42]:

$$f_1 = \frac{\varepsilon'/2}{M_{H^0}^2 - M_{h^0}^2}, \quad f_2 = \frac{M_{A^0}^2 + M_{Z^0}^2}{M_{H^0}^2 - M_{h^0}^2}. \quad (2.67)$$

The results are shown in Table 2.7. The coupling of the pseudoscalar Higgs boson A^0 to down-type fermions is proportional to $\tan\beta$, so it is enhanced. For $M_{A^0} > M_C$ the coupling of the H^0 , which is almost mass degenerate with the A^0 , to down-type fermions is also enhanced by $\tan\beta$. Its coupling to the vector bosons is suppressed since the coupling of the h^0 to vector bosons approaches unity and the sum rule Eq. 2.59 remains valid. At the same time the light scalar Higgs boson h^0 has Standard Model like couplings to up-type fermions and the gauge bosons. For $M_{A^0} < M_C$ it is exactly the other way around – the h^0 has couplings similar to the A^0 and the H^0 will be Standard Model like.

In summary, for high $\tan\beta$ at least two Higgs bosons are always almost mass degenerate, one of them being the A^0 . These two Higgs bosons will have enhanced couplings to down-type fermions and reduced couplings to vector bosons. This is also shown in Figure 2.7 which shows the values of decay widths into different types of fermions relative to those of a Standard Model Higgs boson with the same mass as a function of M_{A^0} in the M_{h^0-max} scenario for $\tan\beta = 30$. The increased coupling to down-type fermions for the A^0

case	Φ	$g_{\Phi\bar{u}u}/g_{H^{\text{SM}}\bar{u}u}$	$g_{\Phi\bar{d}d}/g_{H^{\text{SM}}\bar{d}d}$	$g_{\Phi VV}/g_{H^{\text{SM}}VV}$
$M_{A^0} > M_C, \tan\beta \gg 1$	h^0	+1	$-f_1 \tan\beta + f_2$	+1
	H^0	$f_1 - f_2/\tan\beta$	$\tan\beta$	$f_1 + (1 - f_2)/\tan\beta$
$M_{A^0} < M_C, \tan\beta \gg 1$	h^0	$-f_1 + f_2/\tan\beta$	$\tan\beta$	$-f_1 + (1 + f_2)/\tan\beta$
	H^0	-1	$-f_1 \tan\beta + f_2$	-1
both	A^0	$1/\tan\beta$	$\tan\beta$	0

Table 2.7: Approximative Coupling strengths of the neutral Higgs bosons to up-type, down-type fermions, and gauge bosons relative to the coupling strength of a Standard Model Higgs boson with the same mass for $\tan\beta \gg 1$ for the cases $M_{A^0} > M_C$ and $M_{A^0} < M_C$ (from Ref. [42]). The functions f_1 and f_2 are explained in the text.

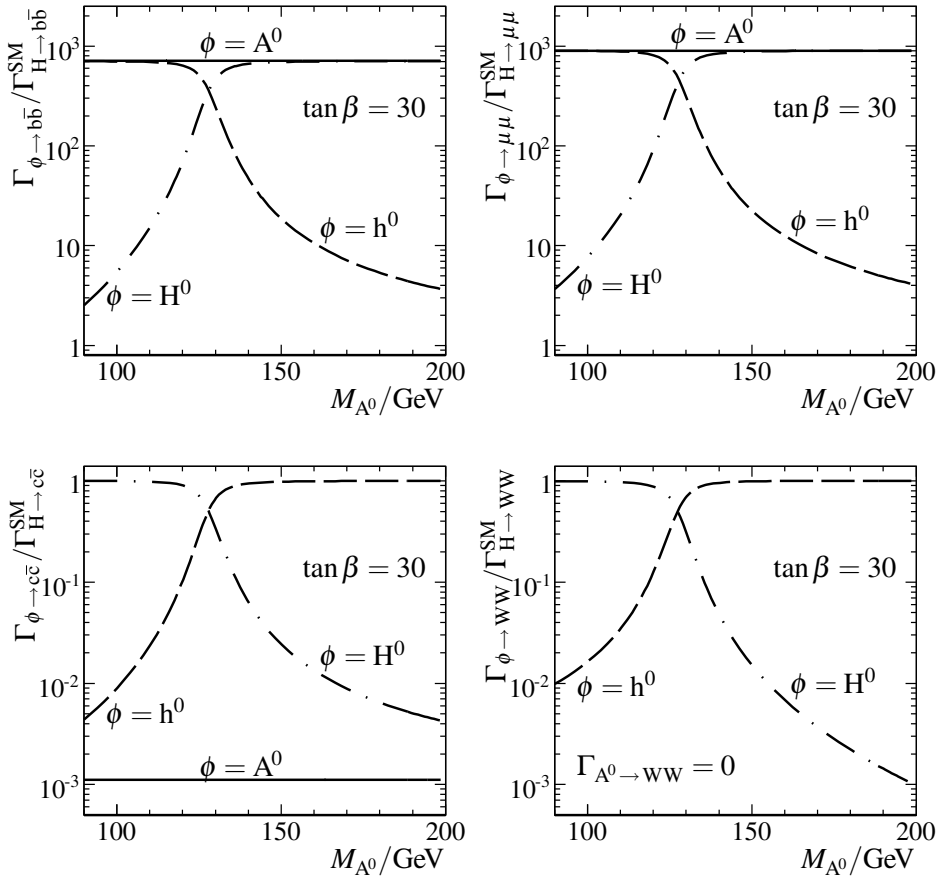


Figure 2.7: Ratio of the partial widths of the neutral MSSM Higgs bosons into $b\bar{b}$ (top left), $\mu\mu$ (top right), $c\bar{c}$ (bottom left), and WW to the value of a Standard Model Higgs boson with the same mass versus M_{A^0} . Solid line: A^0 , dashed line: h^0 , dash-dotted line: H^0 . FEYNHIGGS 2.6.4 was used assuming the M_{h^0} -max scenario and $m_t = 172.5$ GeV.

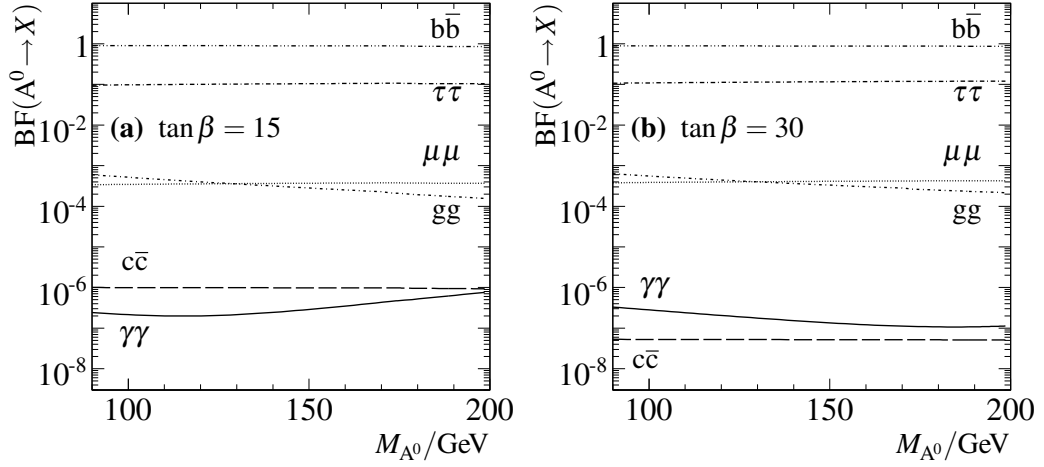


Figure 2.8: Branching fractions of the A^0 into $c\bar{c}$, $\gamma\gamma$, gg , $\mu\mu$, $\tau\tau$, and $b\bar{b}$ versus M_{A^0} for $\tan\beta = 15$ (a) and $\tan\beta = 30$ (b) in the M_{h^0} -max scenario. FEYNHIGGS 2.6.2 was used.

and the almost mass degenerate other Higgs boson is evident. Thus, the A^0 and the almost mass degenerate CP even Higgs boson decay predominantly into pairs of bottom quarks.

The branching fractions of the A^0 are shown in Figure 2.8 for two different values of $\tan\beta$. As the coupling is otherwise proportional to the fermion mass, the branching fractions into $\tau\tau$ and $\mu\mu$ are smaller according to the ratio of the squared masses.

Figure 2.9 shows the total decay width of the three neutral Higgs bosons as a function of M_{A^0} for two different values of $\tan\beta$. Again the CP-even Higgs boson that is almost mass degenerate with the A^0 has a very similar width. The total decay width is proportional to $\tan^2\beta$ since it is dominated by the partial width into $b\bar{b}$. As a consequence the width is significantly larger than for a Standard Model Higgs boson of the same mass for low masses. For high masses, depending on the value of $\tan\beta$, the width of a same mass Standard Model Higgs boson could be significantly larger. The Standard Model Higgs boson gets very large widths if it is massive enough to decay into WW or Z^0Z^0 . This is not the case for the A^0 and H^0 , since their couplings to the gauge bosons are suppressed in the region where their decay into massive vector bosons is allowed by kinematics.

In the following, two special cases of possible A^0 boson masses and the corresponding phenomenology are briefly discussed.

2.4.3 The Decoupling Limit

The decoupling limit is reached for an infinitely heavy A^0 . In this limit the two functions f_1 and f_2 become 0 and 1. This means that the h^0 will have exactly the Standard Model couplings and will be indistinguishable from the Standard Model Higgs boson. Since the H^0 and the H^\pm would be very massive as well, it would not be possible to confirm experimentally at the LHC that there is indeed a second Higgs doublet. The Higgs sector would look exactly like in the Standard Model.

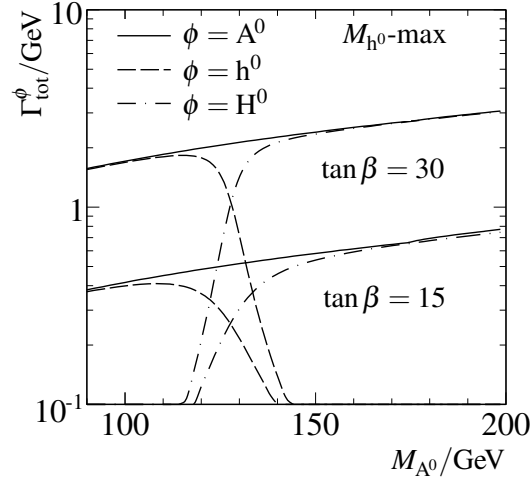


Figure 2.9: Total widths of the neutral Higgs bosons versus M_{A^0} for $\tan\beta = 15$ and $\tan\beta = 30$ in the M_{h^0} -max scenario. FEYNHIGGS 2.6.4 was used.

2.4.4 The “Intense Coupling Region”

Another interesting region of the parameter space is for $\tan\beta \gg 1$ and $M_{A^0} \approx M_C$. In this case all three neutral Higgs bosons would be almost mass degenerate, couple strongly to down-type fermions and their coupling to gauge bosons would be suppressed. In order to resolve the different Higgs bosons it is important to reconstruct the Higgs boson mass with a very high precision.

2.4.5 Effects in the Benchmark Scenarios

In this section, the benchmark scenarios are briefly analyzed for particularities wrt. the discussion of the previous session. Of largest importance for the study presented in this thesis are the mass differences between the neutral Higgs bosons and their coupling to b quarks. Figure 2.10 shows the mass relations as well as the ratios of the decay widths into $b\bar{b}$ to the one of a Standard Model Higgs boson of the same mass.

The M_{h^0} -max and no-mixing scenarios behave exactly as discussed previously: The A^0 is always mass degenerate with either the h^0 or the H^0 , and both of these show enhanced couplings to the b quark. The two scenarios only differ in the maximal h^0 mass and the enhancement of the coupling for a given $\tan\beta$, and consequently also in the total decay widths, which is higher in the no-mixing scenario.

For the gluophobic and small α_{eff} scenarios, the mass degeneracy is in part lifted by further radiative corrections, especially in the small α_{eff} scenario. As the “change-over” between the h^0 and the H^0 still lies at the old position, around the maximal h^0 mass, this leads to interesting effects: The A^0 and h^0 can both couple strongly to b quarks, while being a bit separated in mass. However, this separation does not become very large. This will become important later in the analysis.

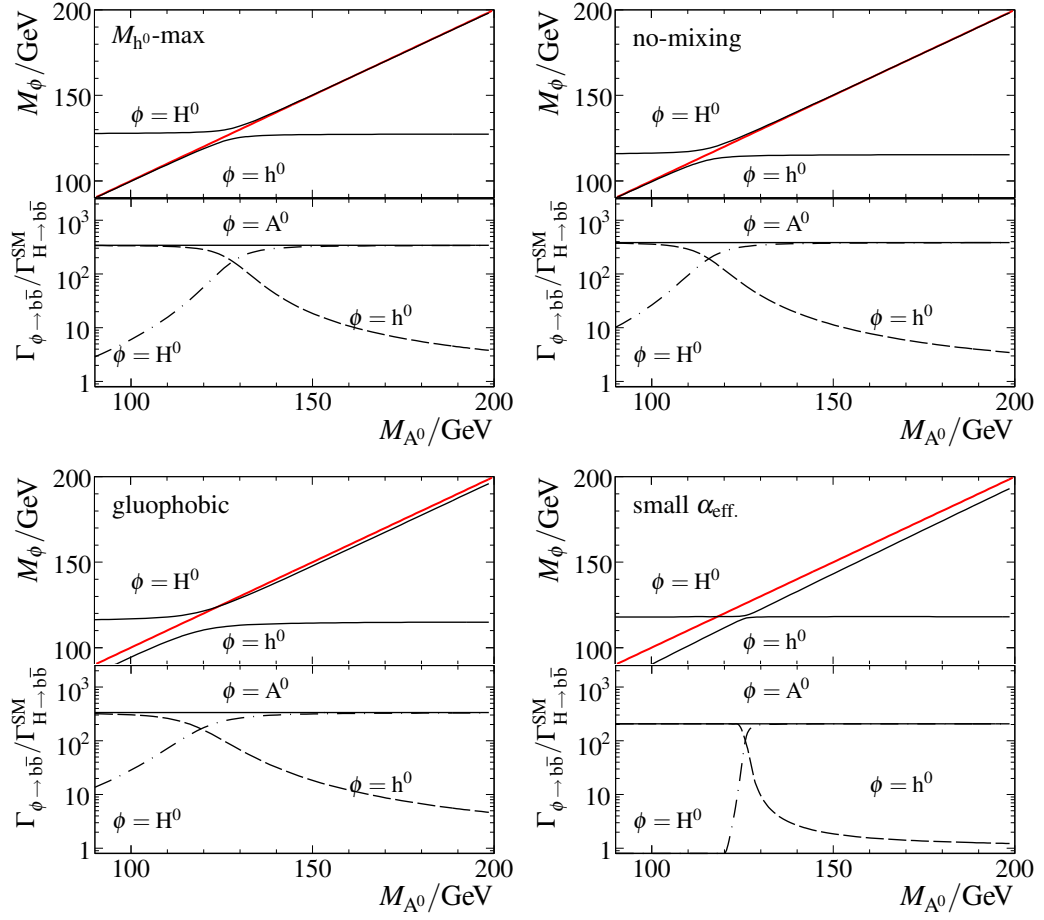


Figure 2.10: Masses and normalized decay widths to $b\bar{b}$ of the neutral MSSM Higgs bosons in dependence of the mass of the A^0 in the four CP conserving benchmark scenarios considered in this thesis, as calculated using FEYNHIGGS 2.6.4, for $\tan\beta = 30$ and $m_t = 172.5$ GeV. The red line shows $M_\phi = M_{A^0}$.

Another difference is also the “sharpness” of the change-over between the h^0 and the H^0 . This happens extremely fast for the small $\alpha_{\text{eff.}}$ scenario, and quite slowly for the gluophobic scenario.

In summary, in all four CP conserving benchmark scenarios the A^0 is always close in mass to either the h^0 or the H^0 , while both couple strongly to down-type fermions. The other scalar boson does not couple as strongly to b quarks and is around the maximal h^0 mass.

“The strongest arguments prove nothing so long as the conclusions are not verified by experience. Experimental science is the queen of sciences and the goal of all speculation.”

Roger Bacon, 1214–1292 or 1294

3

Experimental Status of the Higgs Sector

In the previous chapter an overview of both the Standard Model and the MSSM was given with a special emphasis on the Higgs sector. In addition to the theoretical constraints already discussed, the Higgs sector has already been probed for the past decades in experiments. No conclusive signal of a Higgs boson, neither with Standard Model properties nor beyond Standard Model signatures has been found yet, probably because the Higgs boson is too heavy to have been produced in previous collider experiments. In this chapter a short overview of existing indirect and direct searches for the Standard Model Higgs boson and the Higgs bosons of the MSSM is given. In addition the overall discovery potential of the experiments at the Large Hadron Collider, with an emphasis on the ATLAS experiment, is briefly discussed.

3.1 The Standard Model Higgs Boson

3.1.1 Indirect Measurements

Precision experiments that are not directly sensitive to the Higgs boson can nevertheless yield information through the influence of radiative corrections involving the Higgs boson. Assuming that the Standard Model is the correct theory, the Higgs boson mass can be deduced from electroweak precision observables, like the mass of the W boson or the electroweak mixing angle $\sin \theta_w$. The leading corrections entering are only logarithmic in M_H . The $\Delta\chi^2$ of a global fit of all Standard Model parameters to the precision observables is shown in Figure 3.1 in dependence of the assumed Higgs boson mass [43, 44]. Within the Standard Model a light Higgs boson is preferred. An upper limit on its mass can be derived as 160 GeV at the 95% confidence level.

3.1.2 Direct Searches

The Higgs boson has been searched for in collider experiments for the last decades. No signal was found, but it was possible to place lower limits on its mass assuming Standard

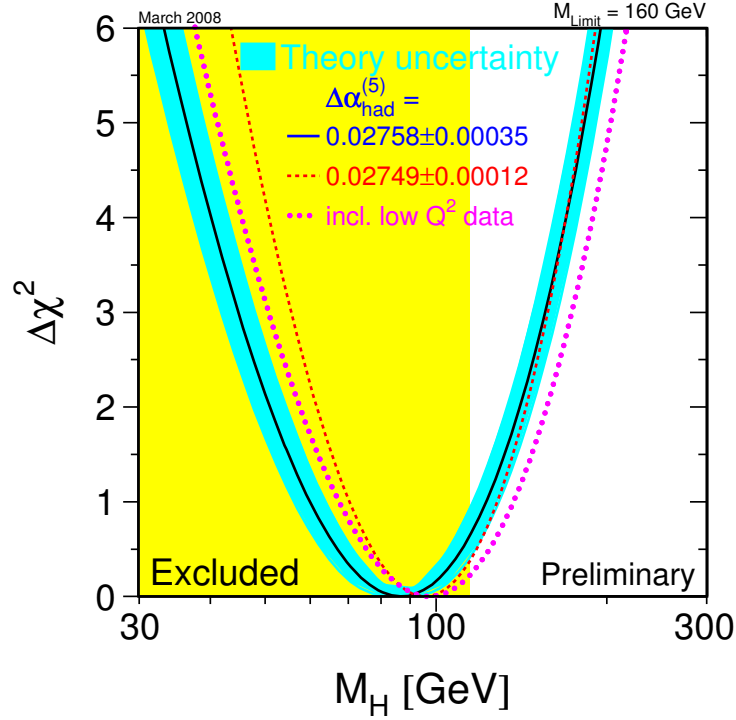


Figure 3.1: $\Delta\chi^2$ of a global fit of the parameters of the Standard Model to the data in dependence of the assumed Higgs boson mass M_H (from [44]). The shaded (yellow) region gives the range excluded by direct searches for the Higgs boson.

Model production cross sections. The four LEP experiments have searched for the Higgs boson in the processes $e^+e^- \rightarrow Z^0H$ and $e^+e^- \rightarrow \nu\bar{\nu}H$. No conclusive signal was found, instead a lower limit on the mass of the Standard Model Higgs boson was placed at [39]:

$$M_H > 114.4 \text{ GeV} \quad @95\% \text{ C.L.}, \quad (3.1)$$

which is also shown in Figure 3.1. The value for M_H most preferred by the electroweak precision data is already excluded by the direct searches for the Higgs boson.

Currently the two experiments CDF [45] and DØ [46] at the Tevatron proton-anti-proton collider are taking data.

The most important Higgs boson search channels at the Tevatron are $q\bar{q} \rightarrow W^\pm/Z^0 + H$ with $H \rightarrow b\bar{b}$ for low Higgs boson masses and $gg \rightarrow H$ with $H \rightarrow W^+W^-$ for higher masses.

The production cross sections, relative to the Standard Model one for the tested Higgs boson mass, that can be excluded using the currently analyzed datasets are shown in Figure 3.2. At the moment the two experiments are not yet sensitive to the Standard Model Higgs boson and the LEP limit could not yet be improved. During the next years the two experiments are expected to increase their data to a total amount of 8.5 fb^{-1} and they should

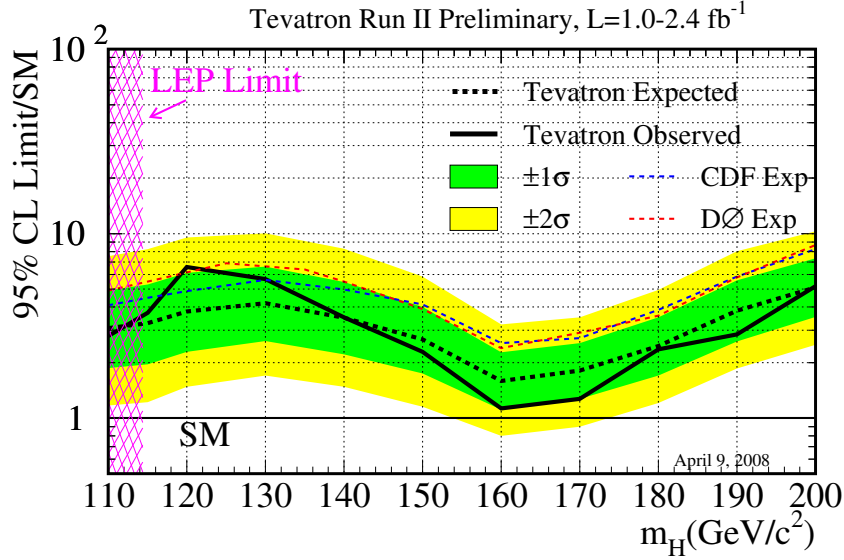


Figure 3.2: Current exclusion limits on the Standard Model Higgs boson from the Tevatron experiments CDF and DØ. The dashed lines show the production cross section in units of the Standard Model cross section that was expected to be excluded at the 95% CL in absence of a signal by CDF, DØ, and in the Tevatron combination respectively. The green and yellow shaded areas show the 1σ and 2σ uncertainties of the expected combined limit, and the solid line the observed excluded cross section (from [47]).

start to become sensitive to the Standard Model Higgs boson for masses just beyond the LEP limit and around 160 GeV.

3.1.3 ATLAS Discovery Potential for the Standard Model Higgs Boson

The search for the Higgs boson will be one of the prime physics goals of the Large Hadron Collider, which is described in Chapter 4. The most important production mechanisms for the Standard Model Higgs boson at the LHC are shown in Figure 3.3. They are:

- $gg \rightarrow H$ (gluon-gluon fusion, GGF):
This process occurs due to an effective coupling of the Higgs boson to gluons through a heavy quark loop, which is in the Standard Model case dominated by the top quark. Being already a loop process at lowest order, the higher order corrections are very important. The corresponding cross section is the largest over the whole allowed mass range of the Standard Model Higgs boson.
- $qq \rightarrow qqH$ (vector-boson fusion, VBF):
In this production channel, which has the second highest production cross section for $M_H < 800$ GeV, the Higgs boson is produced by the fusion of two electroweak gauge bosons, which are radiated off quarks. The scattered quarks can be detected as tagging jets in the forward detector region. As no color charge is exchanged between

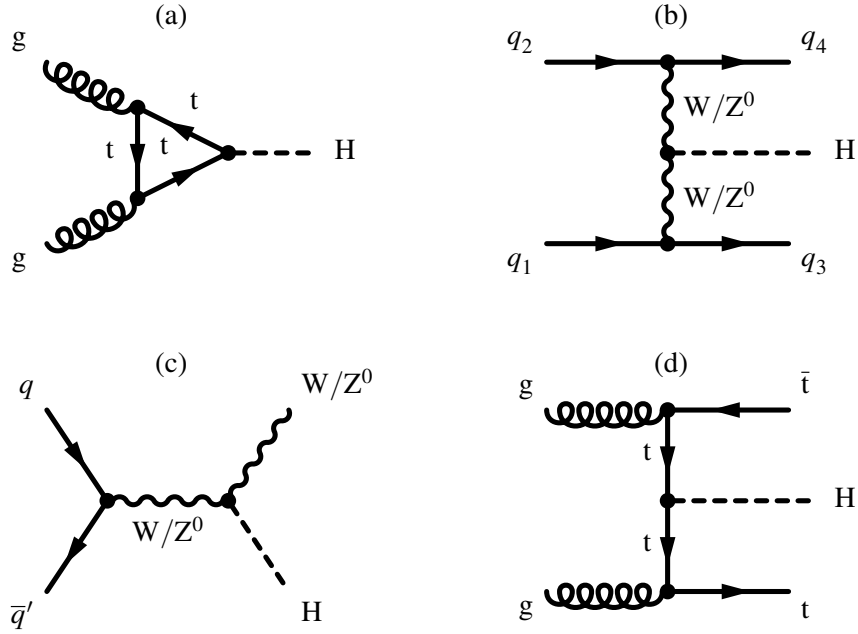


Figure 3.3: Selected Feynman diagrams for Standard Model Higgs boson production at hadron colliders. (a) gluon-gluon fusion $gg \rightarrow H$, (b) vector-boson fusion $qq \rightarrow qqH$, (c) Higgsstrahlung $q\bar{q} \rightarrow W/Z^0 H$, (d) top quark associated production $gg \rightarrow t\bar{t}H$.

the two quarks, only little hadronic activity is expected in the central detector region. This can be used to reject the background processes significantly and this production channel is the most important one for low Higgs boson masses.

- $q\bar{q} \rightarrow W/Z^0 H$ (Higgsstrahlung, WH and ZH):
Here the Higgs boson is radiated off an electroweak gauge boson. This process is more important at the Tevatron than at the LHC.
- $gg \rightarrow t\bar{t}H$ (top quark associated production, ttH):
In this mode, the Higgs boson is radiated off a pair of top quarks. The cross section is small, but the striking signature might allow to observe the Higgs boson in the decay $H \rightarrow b\bar{b}$ for masses below 120 GeV.

The ATLAS collaboration (see Chapter 5) has explored the discovery reach for the Standard Model Higgs boson in several production modes and decay channels. Figure 3.4 shows the expected signal significance [48] for an integrated luminosity of 30 fb^{-1} . Shown is only the mass range below 200 GeV which is clearly favored by electroweak precision data. The most difficult region for the LHC experiments will be at low masses, where quite a few channels have to be combined to ensure a discovery. For higher masses the decay channels $H \rightarrow W^+W^-$ and $H \rightarrow Z^0Z^0$ ensure a discovery with the same integrated luminosity up to a Higgs boson mass of 1 TeV. If the Standard Model Higgs boson exists, it will be discoverable at the 5σ level in the whole allowed mass range after a few years of running with well understood detectors.

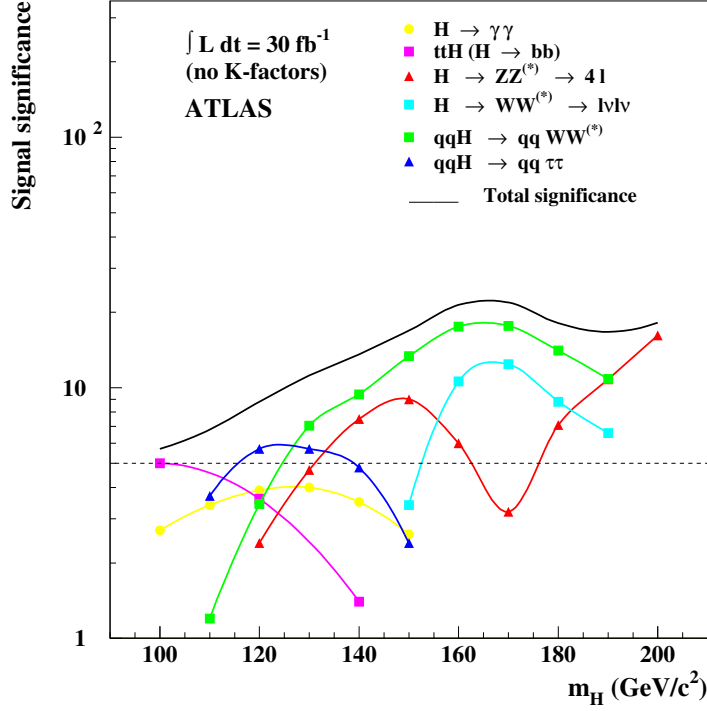


Figure 3.4: Significance for the Standard Model Higgs boson versus its mass in the ATLAS experiment for 30 fb^{-1} . Yellow: $gg \rightarrow H \rightarrow \gamma\gamma$, magenta: $gg \rightarrow t\bar{t}H, H \rightarrow b\bar{b}$, red: $gg \rightarrow H \rightarrow ZZ \rightarrow 4\ell$, light blue: $gg \rightarrow H \rightarrow WW \rightarrow \ell\nu_\ell\ell\nu_\ell$, green: $q\bar{q} \rightarrow q\bar{q}H, H \rightarrow WW$, dark blue: $q\bar{q} \rightarrow q\bar{q}H, H \rightarrow \tau\tau$. The black line gives the combined significance of all channels (from Ref. [48]).

3.2 The Higgs Bosons of the MSSM

3.2.1 Indirect Measurements

Just as in the Standard Model case, the Higgs bosons of the MSSM contribute to radiative corrections that can be measured also in low energy experiments. A recent analysis in Ref. [49] explored the preferred region of the mass of the lightest Higgs boson of the cMSSM. The performed χ^2 fit takes into account electroweak precision data, flavor physics observables, e.g. the branching fractions of $b \rightarrow s\gamma$ or $B^\pm \rightarrow \tau^\pm \nu_\tau$, and the abundance of Cold Dark Matter in the universe. The $\Delta\chi^2$ of this fit is shown in Figure 3.5.

The mass of the lightest Higgs boson from the fit turns out as:

$$M_{h^0}^{\text{cMSSM}} = 110_{-10}^{+8}(\text{exp.}) \pm 3(\text{theo.}) \text{ GeV}, \quad (3.2)$$

where the first uncertainty is experimental and the second theoretical. It should be noted that this analysis is valid only for the cMSSM, other SUSY scenarios might yield different results.

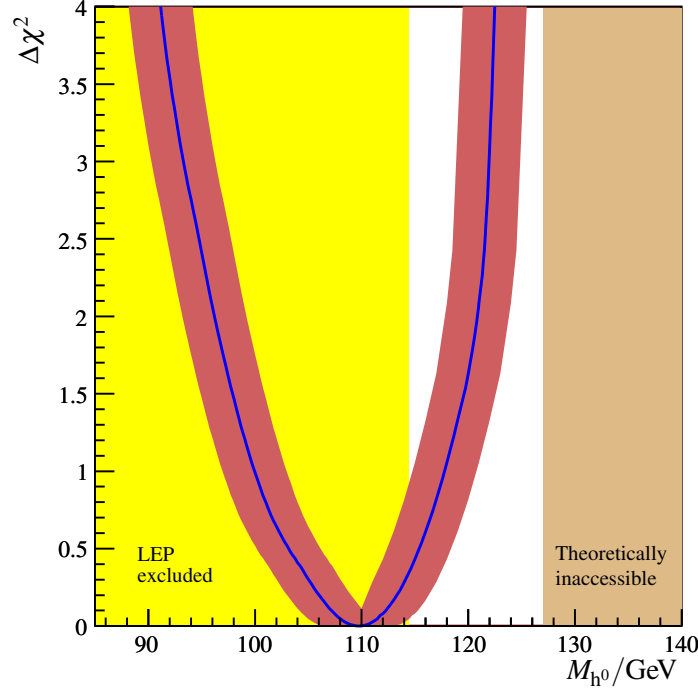


Figure 3.5: $\Delta\chi^2$ of a global fit of the parameters of the cMSSM versus the mass of the lightest Higgs boson. The yellow area shows the area excluded by the LEP experiments, the light brown area the theoretically not accessible region. The red area indicates the theoretical uncertainty. Taken from [49].

3.2.2 Direct Searches

Direct searches for the Higgs bosons of the MSSM have been made by previous experiments. The LEP experiments have performed searches in the processes $e^+e^- \rightarrow h^0 Z^0$ and $e^+e^- \rightarrow h^0 A^0$ [31]. No signal was found and the regions of the parameter space that could be excluded are shown in Figure 3.6 for the CP conserving benchmark scenarios. In the CPX scenario, there is no lower bound on the mass of the lightest Higgs boson from the LEP experiments.

It should be noted that these limits were derived using a top quark mass of 174.3 GeV. Using the latest result of 172.6 GeV [1] as in this thesis would result in a small increase of the excluded region. From the LEP experiments, the region of large $\tan\beta$ and $M_{A^0} > 95$ GeV is not excluded.

The CDF experiment has performed searches in bottom quark associated production with decays of the Higgs bosons into $b\bar{b}$ [50] and $\tau\tau$ [51]. The latter gives the best sensitivity at the moment. The excluded region is shown in Figure 3.7. The DØ experiment has obtained similar results [52, 53].

The Tevatron experiments are beginning to become sensitive to the region of $\tan\beta \approx 40 - 50$.

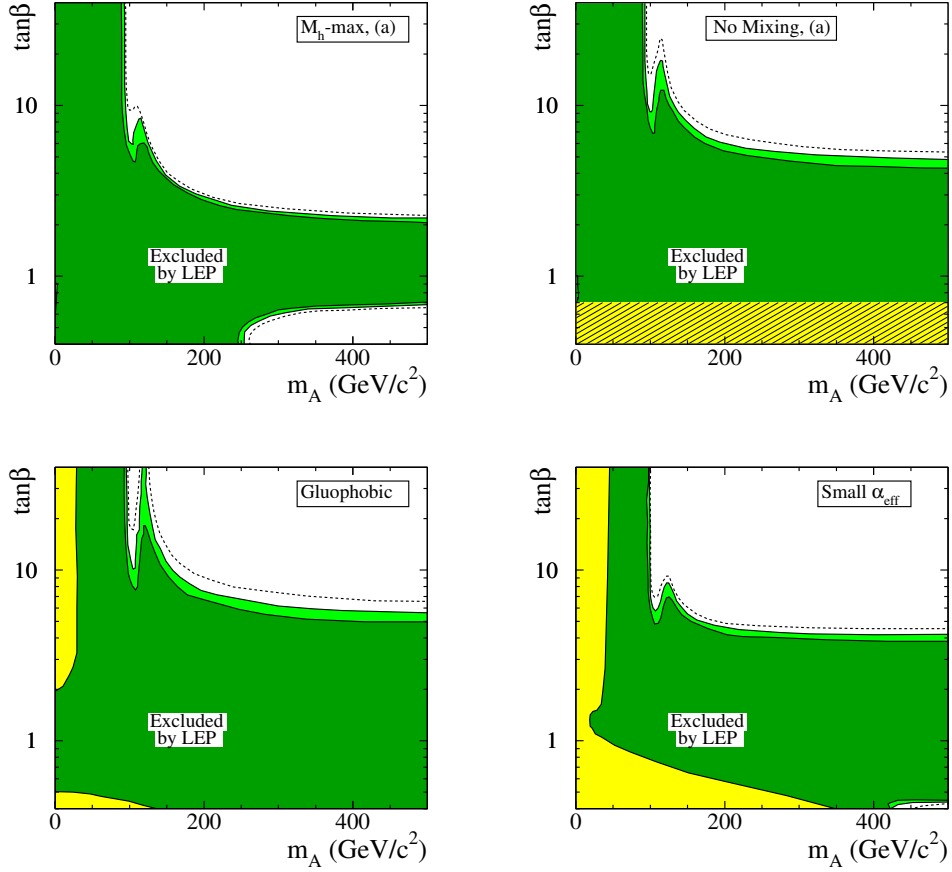


Figure 3.6: Excluded regions in the M_{A0} - $\tan\beta$ plane from the LEP experiments in CP conserving benchmark scenarios. The dashed lines indicate the regions that were expected to be excluded on basis of Monte Carlo simulations without signal. The dark green and light green regions correspond to excluded regions at the 99.7% and 95% confidence level. The hatched area corresponds to a region where a stable prediction of the MSSM Higgs properties is not possible in the no-mixing scenario. The yellow area is not accessible by the theory. A top quark mass of 174.3 GeV was used (from Ref. [31]).

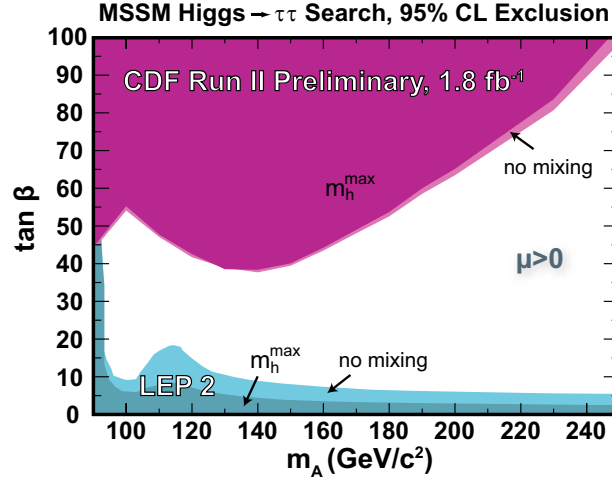


Figure 3.7: Excluded region in the M_{A^0} - $\tan \beta$ plane by the CDF experiment using 1.8 fb^{-1} of data in the M_{h^0} -max and no-mixing scenario (from Ref. [51]). The shaded regions are excluded at the 95% C.L.. The LEP exclusion region is also drawn.

3.2.3 ATLAS Discovery Potential

The ATLAS collaboration has examined the discovery potential for MSSM Higgs bosons in the benchmark scenarios [54, 55]. This study mostly consists of reinterpretations of studies done for Standard Model Higgs boson searches, but also of dedicated studies of MSSM Higgs bosons. In addition, for the heavier neutral Higgs bosons, the bottom quark associated production, which will be discussed in more detail in Chapter 7, with decays $A^0/H^0 \rightarrow \tau\tau$ and $\mu\mu$ has been investigated. The charged Higgs bosons can be discovered either in decays of the top quark $gg \rightarrow t\bar{t}$, $t \rightarrow H^+b$, or in the process $gb \rightarrow H^+t$, with subsequent decays $H^+ \rightarrow \tau^+\nu_\tau$ or $H^+ \rightarrow t\bar{b}$.

The results are shown in Figure 3.8 for the M_{h^0} -max scenario. The conclusion is that the ATLAS experiment will be able to discover at least one of the MSSM Higgs bosons in the complete parameter space using 30 fb^{-1} of well understood data (not shown in Figure 3.8). However in a part of the parameter space, only the h^0 will be discoverable, even with 300 fb^{-1} . This corresponds to intermediate $\tan \beta$ and large M_{A^0} , where the h^0 will be Standard Model like. Further studies [54] have shown that it will also be difficult to distinguish the h^0 from the Standard Model Higgs boson in large parts of this region. In the CPX scenario almost the whole parameter region is suitable for a discovery of at least one Higgs boson, except for a tiny region [55].

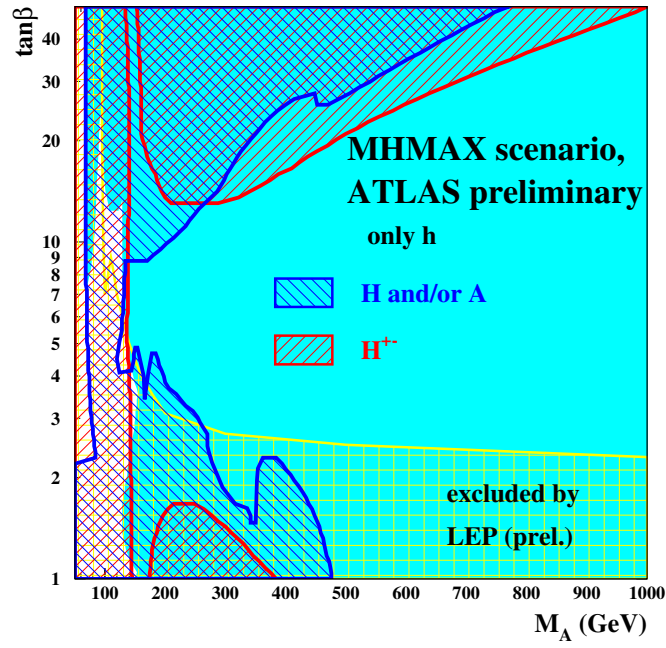


Figure 3.8: ATLAS discovery potential for MSSM Higgs bosons in the M_{A^0} - $\tan\beta$ plane of the M_{h^0} -max scenario assuming an integrated luminosity of 300 fb^{-1} (from Ref. [54]). The lightest Higgs boson can be discovered at the 5σ level in the light blue region. In the blue hatched region, also the H^0 and/or the A^0 , and in the red hatched region the charged Higgs bosons are discoverable.

“One Ring to rule them all, One Ring to find them...”

J.R.R. Tolkien, 1892–1973

4

The Large Hadron Collider

The Large Hadron Collider (LHC) [56] is currently nearing completion at the European Center for Particle Physics CERN¹ near Geneva, Switzerland. The LHC will be capable of accelerating two proton beams in opposite directions up to an energy of 7 TeV. Construction in the former LEP tunnel with a circumference of 27 km was started in 2001 and was completed in early 2008. At the time of this writing, all six of eight LHC sectors have already been cooled down to the temperature of supra-fluid helium of 1.9 K, with the other two currently being cooled down. Figure 4.1 shows a schematic view of the accelerator complex needed for the operation of the LHC.

¹Conseil Européen de la Recherche Nucleaire

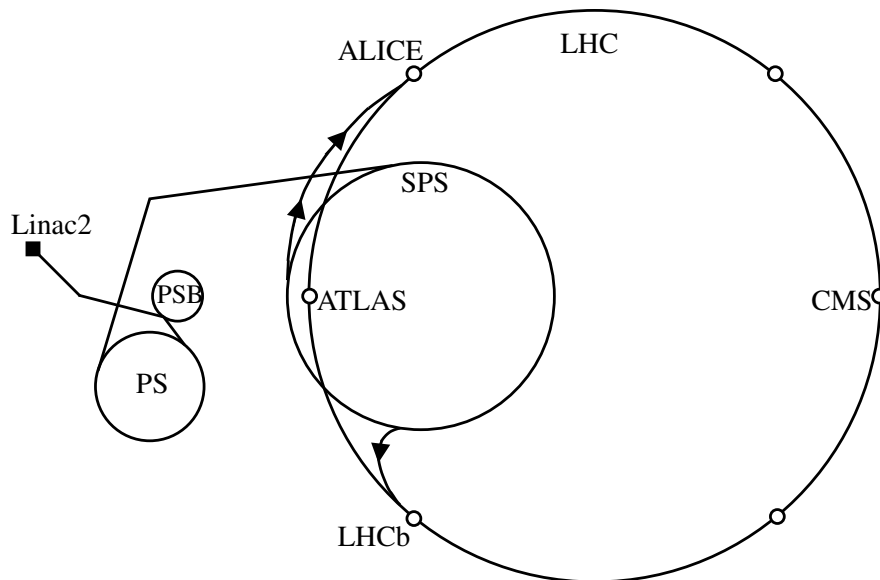


Figure 4.1: Schematic view of the CERN accelerator complex (not to scale).

The chain of acceleration of protons starts from a hydrogen source, from which the protons are accelerated in the Linac2 to 50 MeV. Subsequently, they are further accelerated by the BOOSTER (PSB), the PROTON SYNCHROTRON (PS) and the SUPER PROTON SYNCHROTRON (SPS) to energies of 1.4 GeV, 25 GeV and finally 450 GeV – the injection energy into LHC. The LHC itself consists of a system of in total 1232 superconducting NbTi dipole magnets with a maximal field strength of 8.34 T. These provide the bending power to keep the protons on a circular orbit. Since the two accelerated beams consist of same charge particles, the magnets have two independent magnetic channels that share the same yoke and cryostat vessel. Figure 4.2 shows a cross section of the dipole cryostat.

In addition to the dipole magnets, 392 main quadrupole magnets with gradients of 233 T/m provide the focusing strength to keep the beams at small diameters. About 7000 other corrector magnets are used in LHC. After injection of the protons, the energy is ramped up according to the synchrotron principle to the nominal operation energy of 7 TeV. The energy stored in the magnets during operation (≈ 11 GJ) has to be released safely in case of a magnet quench. This is accomplished by resistors that are switched into the circuit, heating eight tons of steel to about 300 °C. Some selected LHC machine parameters are shown in Table 4.1.

LHC is expected to be commissioned in late summer 2008. In the first pilot run of LHC the center-of-mass energy will be 10 TeV and the instantaneous luminosity is expected to be not larger than $10^{32} \text{ cm}^{-2} \text{ s}^{-1}$. In 2009 it is planned to run LHC at the nominal center-of-mass energy of 14 TeV.

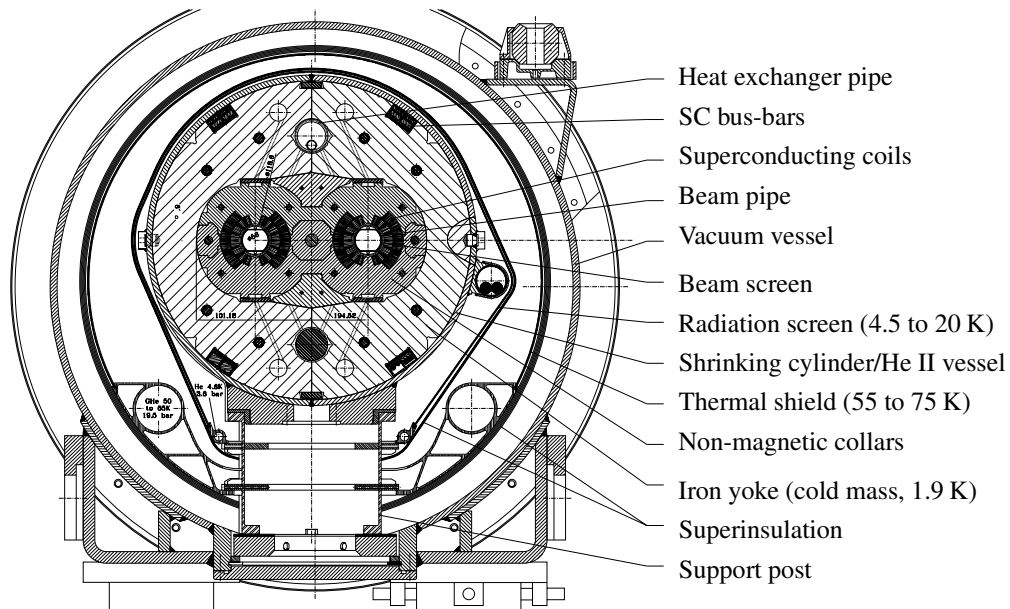


Figure 4.2: Cross-section of the LHC main dipole cryostat [57].

Parameter	Unit	Value at	
		low luminosity	high luminosity
Beam energy (injection)	TeV	0.45	
Beam energy (collision)	TeV	7	
Peak luminosity (IP1 and IP5)	$\text{cm}^{-2} \text{s}^{-1}$	1.2×10^{33}	10^{34}
expected integrated luminosity per year	fb^{-1}	10	100
Number of bunches		2808	
Bunch spacing	ns	25	
Number of protons per bunch		0.4×10^{11}	1.15×10^{11}
DC beam current	A	0.2	0.58
Stored energy per beam @ 7 TeV	MJ	126	362
Stored energy in magnets @ 7 TeV	GJ	11	

Table 4.1: Selected LHC machine parameters.

During later years, LHC operations can be divided into a low luminosity phase with an instantaneous luminosity of $10^{33} \text{ cm}^{-2} \text{s}^{-1}$ and a high luminosity phase leading to the design luminosity of $10^{34} \text{ cm}^{-2} \text{s}^{-1}$. This will be reached at the interaction points 1 and 5 where the multi purpose experiments CMS [58] and ATLAS [59] are located. In addition, two more specialized experiments are being built. These are LHC-b [60] which will address questions regarding CP-violation and properties of the b quark, and ALICE [61], which will study heavy ion collisions that will occur in a later phase of LHC operations. Smaller experiments intending to study particle production in the far forward direction are planned. These are LHCf [62] and TOTEM [63] which share the interaction points occupied by ATLAS and CMS, respectively.

Figure 4.3 shows the cross sections and event rates of selected processes versus the center of mass energy of a hadron collider. Obviously, the event rate in the LHC experiments will be dominated by “uninteresting” processes involving only the strong interaction. More interesting processes, like the production of electroweak gauge bosons, the top quark, or the Higgs boson, have much smaller cross sections. The extremely high event rates have placed very high demands on the design of the LHC detectors.

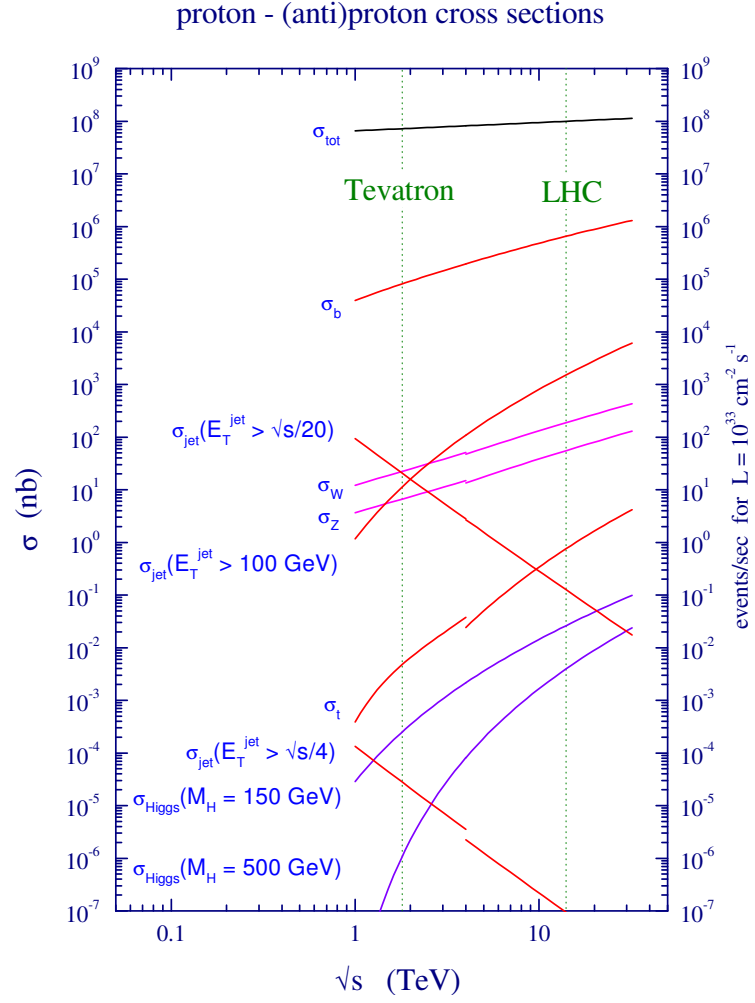


Figure 4.3: Production cross sections and event rates for an instantaneous luminosity of $10^{33} \text{ cm}^{-2} \text{ s}^{-1}$ versus \sqrt{s} of a proton-(anti)proton collider for selected processes. Discontinuities between the lines correspond to the change from proton-antiproton to proton-proton [64].

“Atlas was permitted the opinion that he was at liberty, if he wished, to drop the Earth and creep away; but this opinion was all that he was permitted.”

Franz Kafka, 1883–1924

5

The ATLAS Experiment

5.1 Introduction

The ATLAS¹ experiment is a multi purpose detector designed to study the full range of the LHC physics program. A sketch of the ATLAS detector is shown in Figure 5.1. It has a total height of 22 m, a length of 42 m and a weight of about 7000 metric tons.

¹A Toroidal LHC ApparatuS.

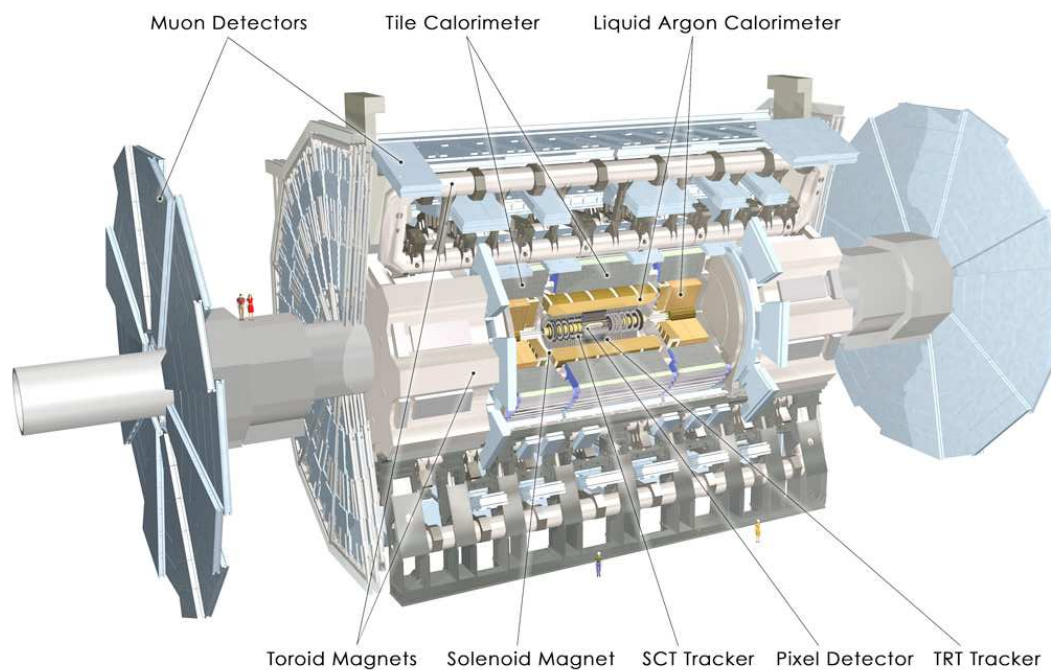


Figure 5.1: The ATLAS Detector [65].

ATLAS follows the concept of previous collider experiments, containing a central tracking detector in a solenoidal magnetic field, a hermetic calorimetry, and a muon spectrometer. Almost all produced particles – except non-interacting ones such as neutrinos – can be detected by ATLAS due to large coverage in solid angle. The parameters of LHC and the challenging physics program have placed very high demands on the design of each component. Especially the high rate at which collisions will occur and the high particle multiplicities resulting from the proton-proton collisions had to be taken into account in the design of all detector components. In the following the coordinates used in ATLAS and the individual sub-detectors are described. More detail can be found in [59, 65].

5.2 The ATLAS coordinate system

The Cartesian coordinate system in ATLAS is defined as follows: The y -axis points upwards, the x -axis points towards the center of the LHC ring, and the z -axis points along the beam direction forming a right-handed coordinate system. The azimuthal angle ϕ is defined as the angle to the x -axis in the xy -plane. In addition the distance to the z -axis in the transverse plane $R = \sqrt{x^2 + y^2}$ and the polar angle θ are used. θ is often replaced by the pseudorapidity, which is defined as:

$$\eta = -\ln\left(\tan\left(\frac{\theta}{2}\right)\right). \quad (5.1)$$

Particles going exactly in the beam direction would have a pseudorapidity of $\pm\infty$, while those going perpendicular to it have $\eta = 0$. For massless particles, the pseudorapidity is equal to the rapidity, which is a relativistic invariant under longitudinal boosts. Further, in QCD processes, particle densities tend to be flat in pseudorapidity, making this coordinate much more useful to analyze the data. Angular separations in 3-D between two objects are expressed in terms of $\Delta R = \sqrt{\Delta\eta^2 + \Delta\phi^2}$, where $\Delta\eta$ and $\Delta\phi$ are the separations in the corresponding variables. The helical tracks of charged particles in the uniform field of the inner detector are described by five parameters: $1/p_T$ – the inverse of the transverse momentum w.r.t. the beam axis, $\phi_0 = \tan^{-1}(p_y/p_x)$ at the point of closest approach (p.c.a.) to $x = y = 0$, d_0 – the transverse distance to the beam axis of the p.c.a., $\cot\theta = p_z/p_T$, and z_0 – the z position of the p.c.a..

5.3 The Inner Detector

The Inner Detector (ID) is a tracking detector designed to reconstruct the tracks of charged particles. Since it is situated inside a solenoidal magnetic field of 2 T, the momentum of charged particles with $p_T > 0.5$ GeV can be measured from the resulting curvature. By extrapolating a track back towards the interaction point, it is possible to reconstruct secondary vertices that are expected in jets containing B and D hadrons (“ b -tagging”). The ID is 5.5 m long, has a diameter of 2.3 m and covers $|\eta| < 2.5$. It is designed on the principle that close to the interaction point only a few, but very precise space points are measured

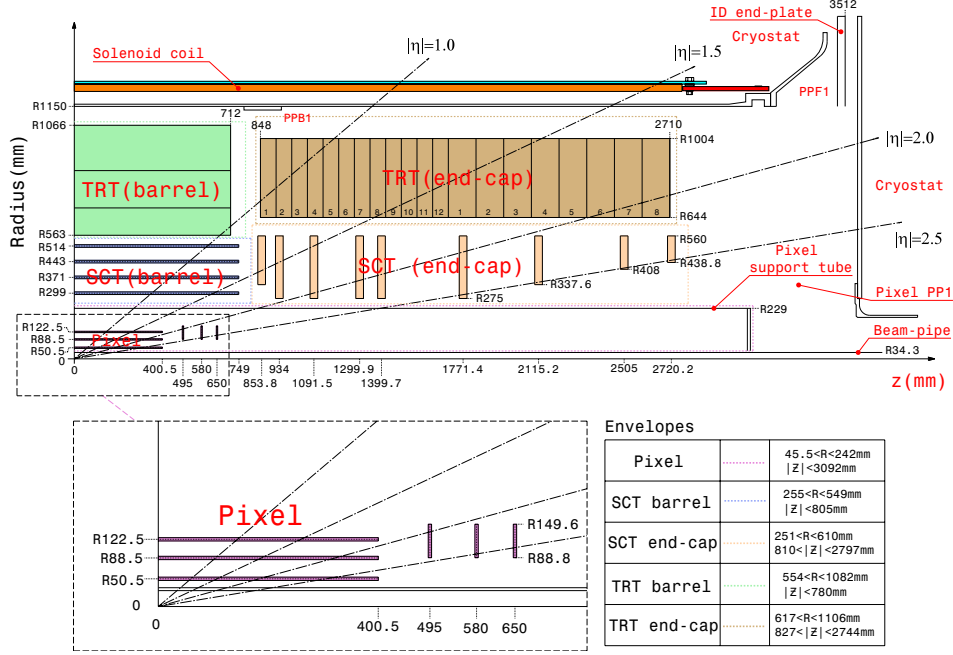


Figure 5.2: Schematic view of a quarter of the inner detector in the the yz plane showing the three sub-detectors and the corresponding coordinates. At the bottom a close-up of the pixel detector and a summary of the envelopes of the detector systems are given (from [65]).

with detectors with a high degree of segmentation, while at larger radii less precise detectors with a larger number of measurements along the particle track are used. This also minimizes the detector occupancy for the high track density expected at the LHC design luminosity, making readout and pattern recognition easier. The ID consists of three sub-detectors: A high resolution pixel detector, a micro-strip Semi Conductor Tracker (SCT) and a Transition Radiation Tracker (TRT). A schematic view of the inner detector is shown in Figure 5.2.

The expected resolutions of track impact parameters are [59]:

$$\sigma(d_0) = 11 \times \left(1 \oplus \frac{5.5}{p_T/\text{GeV} \sqrt{\sin \theta}}\right) \mu\text{m}, \quad (5.2)$$

$$\sigma(z_0) = 70 \times \left(1 \oplus \frac{1.4}{p_T/\text{GeV} \sqrt{\sin^3 \theta}}\right) \mu\text{m}. \quad (5.3)$$

The expected resolution of the momentum measurement of single particles is [59]:

$$\frac{\Delta p_T}{p_T} = 5 \times 10^{-5} p_T/\text{GeV} \oplus 0.01. \quad (5.4)$$

In the following the three sub-detectors of the ID are described in more detail.

5.3.1 The Pixel Detector

The pixel detector is the innermost tracking detector of ATLAS, giving high precision space points of charged particles close to the interaction region. A schematic view of the pixel detector is shown in Figure 5.2a.

It is a hybrid silicon pixel detector, consisting of three barrel layers and three forward disks on each side. The barrel layers consist of 1456 modules located at mean radii of 5.05 cm, 8.85 cm and 12.25 cm from the nominal beam position. The disks with 48 modules each are located on either side of the barrel modules at $z = \pm 49.5$ cm, $z = \pm 58.0$ cm, and $z = \pm 65.0$ cm. A pixel module consists of a silicon sensor and 16 FE-I2 readout-chips, each reading out 18×160 pixel cells. The sensor itself acts as a diode, which is depleted by an applied bias voltage. Charged particles traversing the depleted silicon material create electron-hole-pairs by ionization. The resulting electrons drift to the cathode side of the sensor, where they are collected in tiny bump bonds which connect the sensor with the readout-chips. In this way, the sensor is segmented into $16 \times 18 \times 160$ pixels with a size of $400 \times 50 \mu\text{m}^2$, resulting in 46080 pixels per module and about 80 million pixels in total. A schematic view of one pixel cell can be seen in Figure 5.2b. The spacial resolution of the pixel detector is expected to be $10 \mu\text{m}$ in $R\phi$, $115 \mu\text{m}$ in z for the barrel, and $10 \mu\text{m}$ in $R\phi$, $105 \mu\text{m}$ in R for the disks. The very high degree of segmentation is also necessary to cope with the high track density expected in high luminosity running conditions and at the same time provide a robust pattern recognition capability.

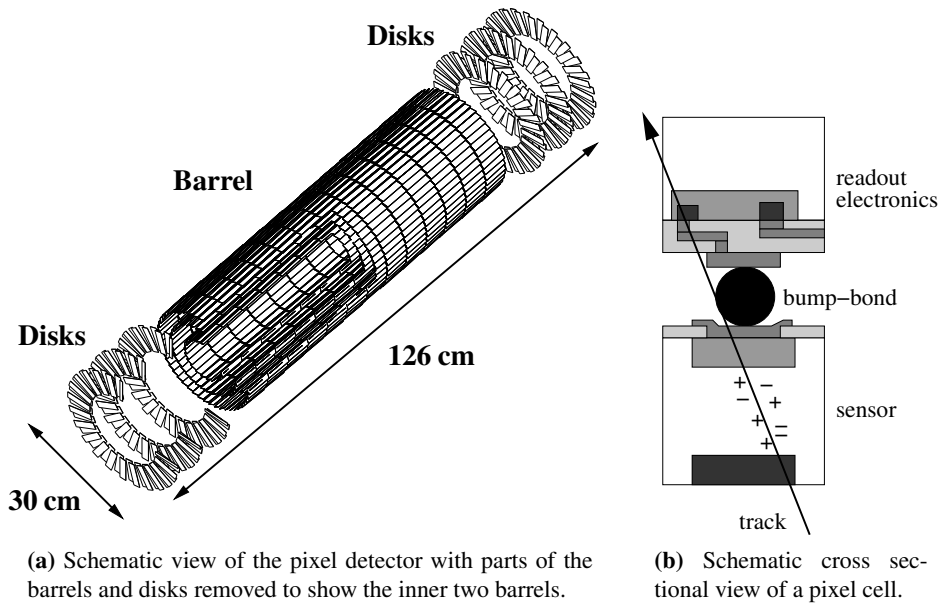


Figure 5.2: The pixel detector.

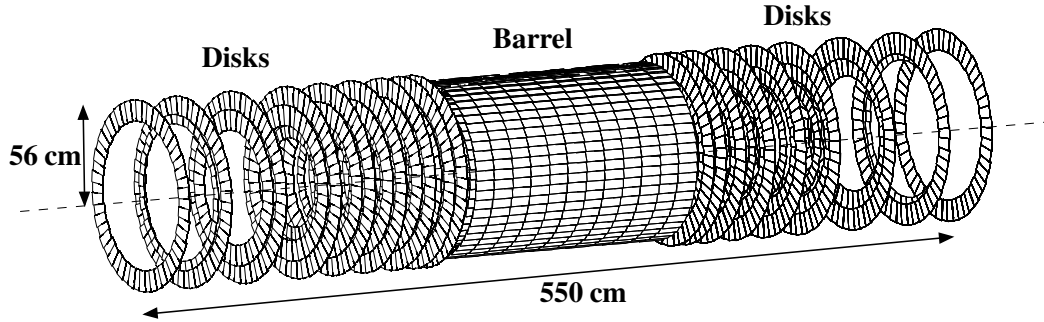


Figure 5.3: The Semi Conductor Tracker.

5.3.2 The Semi Conductor Tracker

The Semi Conductor Tracker (SCT) is another silicon tracking device, but in this case the modules are not segmented in pixels, but in strips. Each silicon detector has a size of $6.36 \times 6.40 \text{ cm}^2$ (in the barrel) and is segmented on the readout side into 768 strips with a pitch of $80 \mu\text{m}$. A module consists of four such sensors. Two detectors are wire-bonded together to form 12.8 cm long strips. Two such double-detectors are arranged back-to-back forming a 40 mrad stereo angle between the strips on the top and on the bottom to have access to the z coordinate of tracks. The layout of the SCT can be seen in Figure 5.3.

The modules described above are arranged in four barrel layers at mean radii between 30 cm and 52 cm, covering $|\eta| < 1.4$ and in nine disks on both sides of the barrels to measure tracks up to $|\eta| = 2.5$. The expected spatial resolution is $17 \mu\text{m}$ in $R\phi$ and $580 \mu\text{m}$ in the z direction. The total number of readout channels in the SCT is approximately 6.3 million. The coarser segmentation of the SCT is possible due to the lower track density at larger radii.

5.3.3 The Transition Radiation Tracker

The two high precision trackers are complemented by a less precise transition radiation tracker (TRT) that gives more space point measurements. On average it provides 36 measurements per track. It is build of straw tube detectors with diameters of 4 mm and a maximal length of 144 cm. In the center of each straw is a gold-plated tungsten-rhenium wire with a diameter of $50 \mu\text{m}$ that is placed on a positive high voltage. The straw tubes are filled with a gas mixture of 70% Xenon, 27% carbon dioxide and 3% oxygen with 5–10 mbar overpressure. A charged particle traversing a straw tube ionizes the gas. The produced electrons drift towards the wire with a constant velocity. Close to the wire the signal is amplified by an avalanche effect in the high electric field. With the known drift velocity, a drift circle can be calculated in which the particle must have passed the center of the straw tube. The expected spatial resolution is $130 \mu\text{m}$ per straw. In addition to the measurement of space points of charged particles, the TRT can also be used for particle

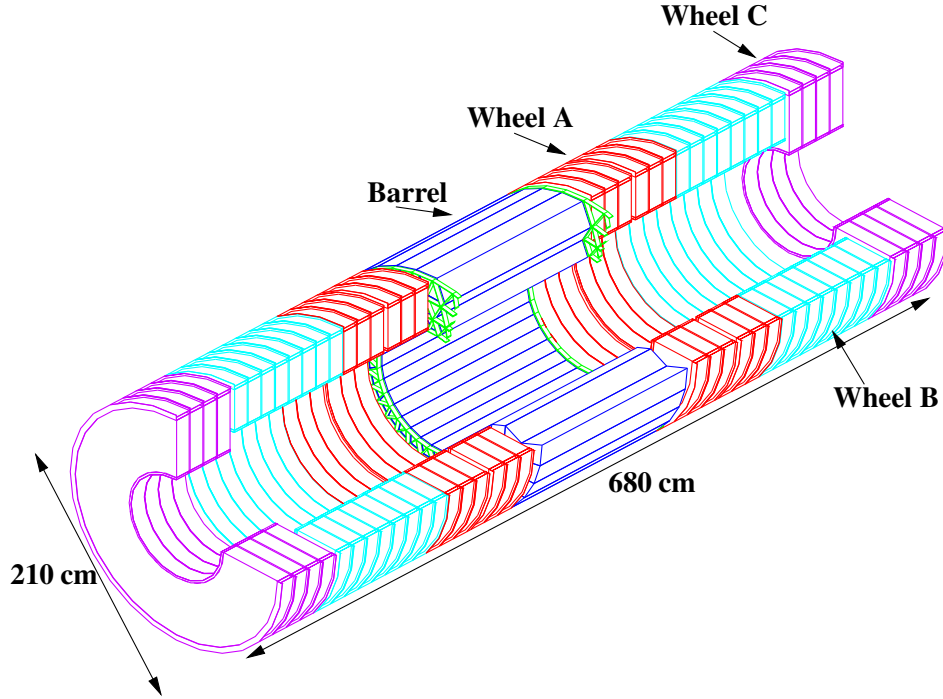


Figure 5.4: The Transition Radiation Tracker [59].

identification. The straw tubes are surrounded by a radiator material (polypropylene fibers in the barrel, foils in the end-cap) so that a traversing charged particle passes many boundaries with changes in the index of refraction. An ultra-relativistic particle ($\gamma \gtrsim 1000$) will emit transition radiation photons at these boundaries at small angles to the flight direction. The photons are then absorbed by the drift gas via the photoelectric effect due to the high Z of the Xenon, resulting in an additional signal in the hit straw. Ultra-relativistic particles leave in this way a higher amplitude signal in the TRT. Due to the low mass of the electron, this technique can be used to distinguish between electrons and pions over a wide momentum range, completely complementary to calorimetric information. The layout of the TRT is shown in Figure 5.4.

The barrel consists of about 50000 straws arranged in three rings with a total of 73 layers. It covers radii from 56 to 107 cm and $|\eta| < 0.7$. Larger pseudorapidities are covered by two end-caps, each built of 18 wheels which are grouped into wheel 'A' (6 disks), wheel 'B' (8 disks) and wheel 'C' (4 disks with smaller inner radii than the other two wheels). In these wheels the straw tubes are arranged radially. The full geometry as shown in Figure 5.4 would result in a coverage up to $|\eta| < 2.5$. The TRT 'C'-wheels are not installed in the initial ATLAS detector, but have been deferred for a possible later addition. This reduces the TRT acceptance to $|\eta| < 2.1$. The TRT has a total number of readout channels of about 351000.

5.3.4 Solenoid Magnet

The inner detector is placed inside a solenoidal magnetic field with a central field strength of 2 T. It is produced by a superconducting solenoid with an inner diameter of 2.46 m and an axial length of 5.3 m. The coil itself contains 10 km of Al:Cu:Nb:Ti wire in 1173 turns. The current necessary for operation is 7.73 kA and a total energy of 39 MJ will be stored in the magnet during operation. To reduce the material in front of the calorimeter, the solenoid shares a common cryostat with the liquid argon calorimeter.

5.4 The Calorimeters

The calorimeters are designed to absorb and measure the energy of all produced particles except muons and neutrinos. The calorimeters provide a measurement of the energies of electrons, photons and jets. By having a very large acceptance and uniformity of the calorimeters, it is possible to reconstruct also the missing transverse energy by summing over all other energies vectorially and taking the negative. Three different types of calorimeters are used: An electromagnetic calorimeter covering $|\eta| < 3.2$, a hadronic calorimeter in the barrel $|\eta| < 1.7$ and in the end-cap regions ($1.5 < |\eta| < 3.2$), and forward calorimeters ($3.1 < |\eta| < 4.9$). Figure 5.5 shows a view of the calorimeters, they are described in more detail in the following.

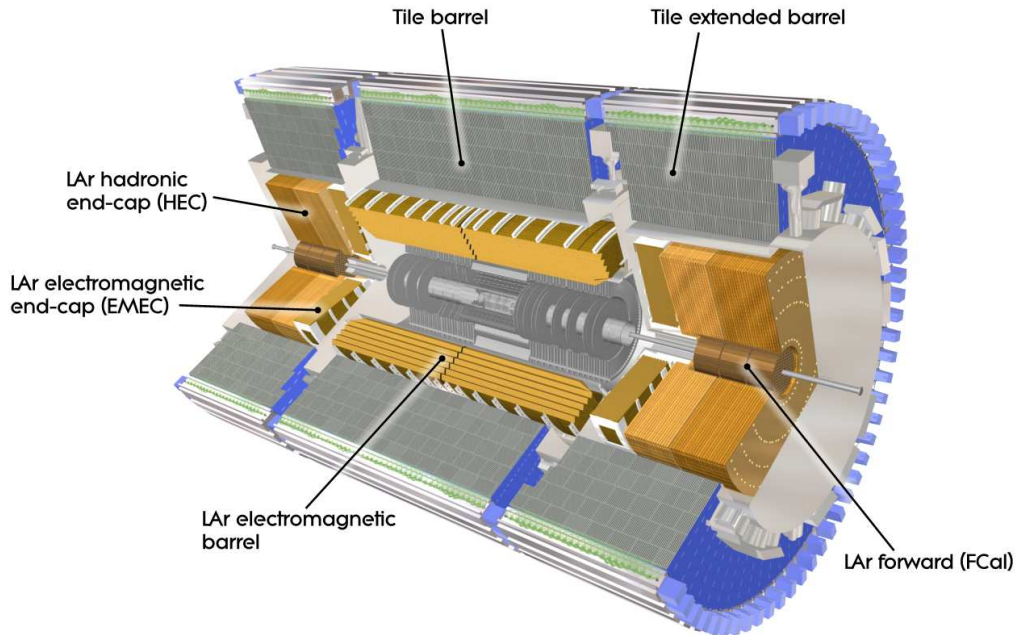


Figure 5.5: Overview of the ATLAS calorimeters [65].

Barrel			End-cap	
Longitudinal segmentation				
Presampler	1 layer	$ \eta < 1.52$	1 layer	$1.5 < \eta < 1.8$
Calorimeter	3 layers	$ \eta < 1.35$	2 layers	$1.375 < \eta < 1.5$
	2 layers	$1.35 < \eta < 1.475$	3 layers	$1.5 < \eta < 2.5$
			2 layers	$2.5 < \eta < 3.2$
Granularity ($\Delta\eta \times \Delta\phi$)				
Presampler	0.025×0.1	$ \eta < 1.52$	0.025×0.1	$1.5 < \eta < 1.8$
Cal. 1st layer	$0.025/8 \times 0.1$	$ \eta < 1.4$	0.050×0.1	$1.375 < \eta < 1.425$
	0.025×0.025	$1.4 < \eta < 1.475$	0.025×0.1	$1.425 < \eta < 1.5$
			$0.025/8 \times 0.1$	$1.5 < \eta < 1.8$
			$0.025/6 \times 0.1$	$1.8 < \eta < 2.0$
			$0.025/4 \times 0.1$	$2.0 < \eta < 2.4$
			0.025×0.1	$2.4 < \eta < 2.5$
			0.1×0.1	$2.5 < \eta < 3.2$
			0.050×0.025	$1.375 < \eta < 1.425$
Cal. 2nd layer	0.075×0.025	$1.4 < \eta < 1.475$	0.025×0.025	$1.425 < \eta < 2.5$
	0.050×0.025	$ \eta < 1.35$	0.1×0.1	$2.5 < \eta < 3.2$
			0.050×0.025	$1.5 < \eta < 2.5$
Cal. 3rd layer	0.050×0.025	$ \eta < 1.35$	0.050×0.025	$1.5 < \eta < 2.5$
# of readout channels				
Presampler	7808		768 \times 2	
Calorimeter	101760		31104 \times 2	

Table 5.1: Coverage, segmentation, and granularity of the electromagnetic calorimeters and the presampler.

and 0.5 cm in the end-caps precedes the electromagnetic calorimeter. In the transition region between the barrel and the end-cap cryostat ($1.0 < |\eta| < 1.6$) the material increases to $\approx 7 X_0$ and the presampler is supplemented by a scintillator slab. Table 5.1 lists the coverage, granularity, and segmentation of the EM calorimeter and the presampler. The design goal for the energy resolution of electrons and photons is [59]:

$$\frac{\sigma_E}{E} = \frac{0.1}{\sqrt{E/\text{GeV}}} \oplus 0.007. \quad (5.5)$$

In addition, the electromagnetic calorimeter is used to trigger on electrons and photons within $|\eta| < 2.5$.

5.4.2 Hadronic Calorimeters

The hadronic calorimeters together with the EM calorimeter are necessary to measure the energy of jets and hadronically interacting particles. The design goal for the energy resolution for jets is [59]:

$$\frac{\sigma_E}{E} = \frac{0.5}{\sqrt{E/\text{GeV}}} \oplus 0.03 \quad (|\eta| < 3.2), \quad (5.6)$$

$$\frac{\sigma_E}{E} = \frac{1.0}{\sqrt{E/\text{GeV}}} \oplus 0.10 \quad (|\eta| > 3.2). \quad (5.7)$$

Three different types of hadronic calorimeters are used in ATLAS, which are described in the following. Details about their respective coverage, longitudinal segmentation and granularity are listed in Table 5.2.

The scintillator tile calorimeter (TileCal) is a sampling calorimeter using iron as absorber and plastic scintillator plates (tiles) arranged in an alternating structure as active material. Particles reaching the calorimeter initiate showers, either electromagnetic ones or through inelastic hadronic interactions. The scintillator material is excited by the secondary particles of the shower and emits light. This light is transported by wavelength shifting fibers to photo-multipliers, producing an electronic signal. The tile calorimeter consists of a barrel ($|\eta| < 1.0$) and two identical extended barrel parts ($0.8 < |\eta| < 1.7$). The energy lost in the inactive materials in the gap between these calorimeters is sampled by the Inter-TileCal (ITC) scintillators. Radially, the tile calorimeter has an inner radius of 2.28 m and an outer radius of 4.25 m. The total thickness of the whole calorimeter system is 9.7 hadronic interaction lengths at $\eta = 0$. This ensures a good energy resolution also for high energetic jets as well as a good shielding against shower leakage reaching the muon system.

Due to the higher radiation density in the end-cap and forward regions, the hadronic calorimeter in the region $1.5 < |\eta| < 3.2$ is based on intrinsically radiation-hard LAr calorimeters. The Hadronic End-Cap (HEC) calorimeter is a copper-LAr calorimeter. It has a coarser granularity than the EM calorimeter, which is sufficient for measurements of hadronic showers.

The forward region ($3.1 < |\eta| < 4.9$) is also covered by LAr calorimeters. The forward calorimeter (FCal) is placed at about 4.7 m from the interaction point. It has to withstand very high radiation densities. The FCal consists of three sections on each side. The first is made of copper (FCal1) the outer two of tungsten (FCal2 & FCal3). The metal has regularly spaced longitudinal channels filled with concentric rods and tubes. The rods are at positive high voltage while the tubes and the metal matrix are grounded. The resulting gap is filled with liquid argon as active material.

Tile calorimeter	Barrel	Extended Barrel	
Coverage	$ \eta < 1.0$	$0.8 < \eta < 1.7$	
# of layers	3	3	
Granularity ($\Delta\eta \times \Delta\phi$)			
1st and 2nd layer	0.1×0.1	0.1×0.1	
3rd layer	0.2×0.1	0.2×0.1	
# of readout channels	5760	2048×2	
Hadronic LAr (HEC)		End-cap	
Coverage		$1.5 < \eta < 3.2$	
# of layers		4	
Granularity ($\Delta\eta \times \Delta\phi$)		0.1×0.1	$1.5 < \eta < 2.5$
		0.2×0.2	$2.5 < \eta < 3.2$
# of readout channels		2816×2	
Forward calorimeter			
Coverage		$3.1 < \eta < 4.9$	
# of layers		3	
Granularity ($\Delta x \times \Delta y/\text{cm}^2$)		FCal1: 3.0×2.6	$3.15 < \eta < 4.3$
		FCal1: $\approx \times 4$ finer	$3.10 < \eta < 3.15$
			$4.30 < \eta < 4.83$
		FCal2: 3.3×4.2	$3.24 < \eta < 4.50$
		FCal2: $\approx \times 4$ finer	$3.20 < \eta < 3.24$
			$4.50 < \eta < 4.81$
		FCal3: 5.4×4.7	$3.32 < \eta < 4.60$
		FCal3: $\approx \times 4$ finer	$3.29 < \eta < 3.32$
			$4.60 < \eta < 4.75$
# of readout channels		1762×2	

Table 5.2: Coverage and granularity of the hadronic and forward calorimeters.

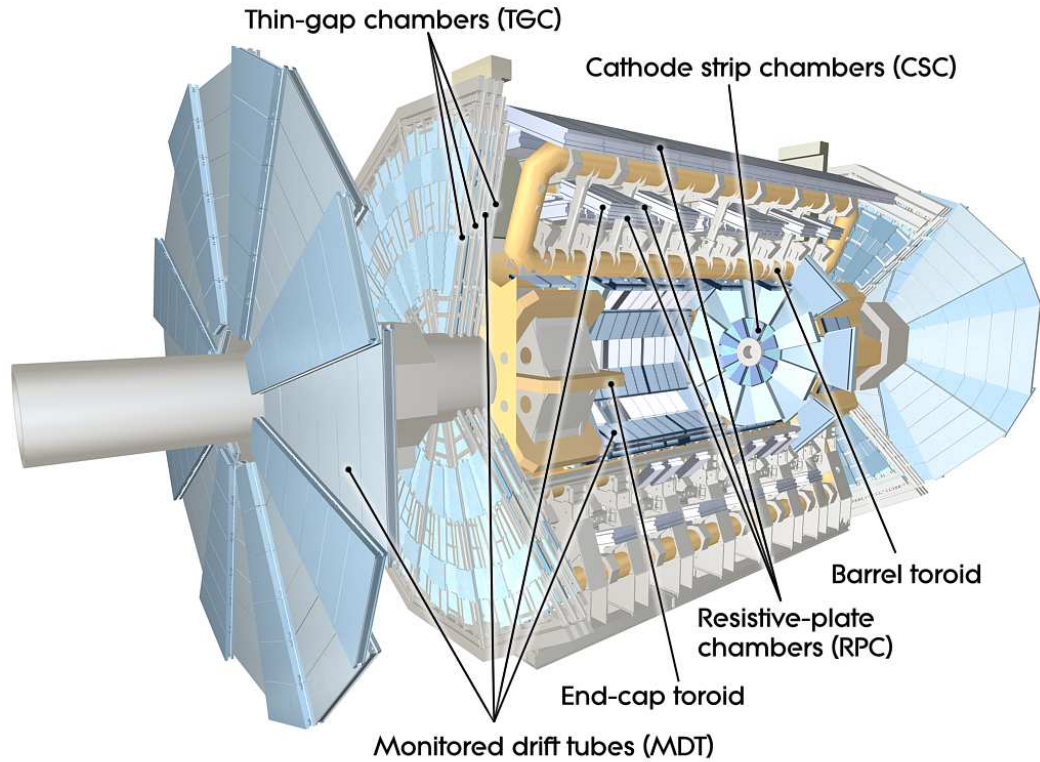


Figure 5.7: Cut-away view of the muon spectrometer [65].

5.5 The Muon Spectrometer

The muon spectrometer is one of the most outstanding features of ATLAS as it determines the outer dimensions of the detector and is shown in Figure 5.7. It is based on a large-scale magnetic field created by large superconducting air-core toroid magnets. These magnets provide a field that is roughly circular around the beam axis. The tracks of muons passing this field are bent in the Rz -plane, thus providing a measurement of the transverse momentum independent of the inner detector.

The magnet system has an overall length of 26 m and a diameter of 20 m. In the region $|\eta| < 1.4$ a bending power² of 2 to 6 Tm comes from a large barrel toroid (BT) that consists of eight superconducting magnet coils with a length of about 25 m and a width of about 5 m. In $1.6 < |\eta| < 2.7$ the bending power (1 to 8 Tm) is provided by two identical end-cap toroids (ECT) that are inserted in the BT. In the transition region ($1.4 < |\eta| < 1.6$) the bending power is caused by both the BT and the ECT but is generally lower.

The muon tracks are measured using a system of muon tracking chambers. There are generally 3 muon stations along a given muon track to provide a measurement of the sagitta

²The bending power is defined as the field integral over the azimuthal component of the magnetic field along a straight line between the inner and outer toroid radius.

	precision chambers		trigger chambers	
	MDT	CSC	RPC	TGC
coverage	$ \eta < 2.7$	$2.0 < \eta < 2.7$	$ \eta < 1.05$	$1.05 < \eta < 2.4$
Number of chambers	1150 (1088)	32	606 (544)	3588
Number of channels	354 000 (339 000)	31 000	373 000 (359 000)	318 000
resolution in η /mm	0.035	0.04	30	7 – 36
resolution in ϕ /cm	-	0.5	3	2 – 3
resolution in time/ns	750	4	20	20
area covered/m ²	5500	65	3650	2900

Table 5.3: Parameters of the four chamber types used in the muon detector. Numbers in brackets correspond to the initial layout of ATLAS.

of the deflected muons. The design goal is to have a 10% accuracy on muon momenta of 1 TeV at the highest luminosity. The chambers are divided into precision measurement devices that dominate the position and momentum resolution and trigger chambers that provide less accurate but very fast measurements. Table 5.3 gives an overview of the parameters of the muon chambers. Parts of the muon chambers have been deferred for a later addition. The different chamber types are described in more detail in the following.

5.5.1 Precision Chambers

Two types of chambers are used for the precision measurements of muon trajectories: Monitored Drift Tubes (MDT) and Cathode Strip Chambers (CSC). In the barrel they are located in three cylindrical layers around the beam axis at approximate radii of 5, 7.5, and 10 m. In the end-cap regions the three stations are installed horizontally at $|z| \approx 7, 10, 14$, and 21–23 m.

Over almost the whole pseudorapidity range ($|\eta| < 2.0$) the precision measurement is performed exclusively using MDTs. These consist of cylindrical drift tubes made of aluminum with a diameter of 3 cm. In the middle of each tube is a tungsten-rhenium sense wire with a diameter of 50 μm . The used drift gas is a mixture of 93% Argon and 7% carbon dioxide at a pressure of 3 bar. The total gas-filled volume is about 800 m³. The expected spatial resolution is 80 μm perpendicular to the wire direction, which corresponds to the Rz plane. Between three and eight layers of these drift tubes are combined in one chamber.

In the region $2.0 < |\eta| < 2.7$ with larger radiation and background levels, CSCs are used in the inner muon station due to their higher granularity and relative insensitivity to

neutron backgrounds. They are flat multiwire proportional chambers with 30 μm diameter tungsten-rhenium anode wires. The drift gas is 80% argon and 20% carbon dioxide with a total volume of 1.1 m^3 . The readout is done using a cathode segmented into strips. In combination with charge interpolation between neighboring strips a spatial resolution of 60 μm is reached.

5.5.2 Trigger Chambers

In addition to the precision chambers a system of chambers is used which have a better time resolution and can be used to trigger on muons with high transverse momenta. They also provide a measurement of the second coordinate since the MDTs provide no information in the wire direction.

In the barrel region, resistive plate chambers (RPC) are used in three layers located on both sides of the middle MDT layer. They consist of two resistive plates which are kept parallel to each other at a distance of 2 mm by insulating spacers. An electric field of 4.9 kV/mm is applied, leading to the formation of avalanches when an ionizing particle passes the gas volume. The gas used is a mixture of 94.7% $\text{C}_2\text{H}_2\text{F}_4$, 5% Iso- C_4H_{10} , and 0.3% SF_6 .

Thin Gap Chambers (TGC) are used for triggering in the end-cap region. They are located near the middle MDT wheel. The TGCs are similar to multiwire proportional chambers with both wire readout for the radial coordinate in the bending direction and azimuthal information by radial strips. They are operated in saturation mode providing a very quick response. The gas mixture is 55% carbon dioxide and 45% n-pentane with a total volume of 11 m^3 .

5.6 Forward Detector Systems

In addition to the described main ATLAS detector components, three smaller sub-detectors with acceptances in the very far forward region are planned [66]. These will be used for the measurement of the luminosity and for studies of forward physics such as diffraction.

5.6.1 The LUCID detector

The LUCID³ detector [67] will be the main instrument to measure the integrated luminosity of ATLAS runs and also to monitor online the instantaneous luminosity and beam conditions. It is installed at $|z| = 17$ m and consists of twenty aluminum tubes with a length of 1.5 m and a diameter of 15 mm filled with C_4F_{10} surrounding the beam pipe and pointing towards the interaction point. Particles traversing the tube will emit Cerencov light which is reflected down the tube and detected by photo-multipliers. The resulting amplitude is a measure for the number of particles coming from the interaction point and thus a measure of the luminosity. The fast response time allows for unambiguous measurements of individual bunch crossings.

³Luminosity measurement using Cerencov Integrating Detector.

5.6.2 The ZDC detector

The second forward subsystem is the zero-degree calorimeter (ZDC) [66]. It is located at $|z| = 140$ m directly behind the point where the LHC beam pipe is divided in two. It is located just after the split behind an absorber and is a tungsten-quartz sampling calorimeter. It is designed to measure neutral particles at a polar angle of 0° . Its main purpose is to provide a measurement of the centrality of heavy ion collisions, but it will also be used during proton running to study forward particle production and for machine tuning purposes.

5.6.3 The ALFA detector

The ALFA⁴ detector [66] is designed to measure the absolute luminosity scale. It consists of scintillating fiber trackers located inside roman pots at $|z| = 240$ m. The roman pots make it possible to measure elastically scattered protons down to angles of $3 \mu\text{rad}$. In this region the cross section can be computed very accurately by theory. In order to take such an absolute measurement, it will be necessary to have LHC run with special so-called β^* optics. These high β^* runs will have low instantaneous luminosities, but will provide a measurement of the absolute luminosity scale which is necessary to cross-calibrate the other detectors like LUCID.

5.7 Trigger and Data Acquisition

The bunch crossing rate of LHC of 40 MHz places very high demands on the trigger and data acquisition system of ATLAS. Along with the inelastic proton-proton interaction cross section this will correspond to an interaction rate of 1 GHz at design luminosity. Assuming an average event size of 1.5 Mbyte, this high rate has to be reduced to about 200 Hz based on technology and resource limitations. This required rejection against minimum bias processes has to coincide with a high efficiency to trigger on new physics and important Standard Model processes. The ATLAS trigger system consists of three distinct levels that are shown in Figure 5.8.

The first level (L1) consists of custom built pipelined electronics operating at the bunch crossing frequency. The two subsequent reduction levels are provided by the High-Level Trigger (HLT) which consists of two sub-levels: The Level 2 trigger (L2) and the Event Filter (EF). Each trigger level refines the decisions made at the previous levels and can also apply additional selection criteria since more latency time is available. The front-end readout electronics of each detector system have to contain pipeline memories in which the detector information is stored for the decision time of L1 - the L1 trigger latency of $2.5 \mu\text{s}$. A derandomizing buffer in which the data corresponding to a specific L1 trigger accept are stored before being sent to the following level reduces the maximum dead-time to 1%. After a L1 accept the data is shipped off the detector to the readout driver (ROD) and from there to the Higher Level Trigger. The L1 trigger searches for high transverse momentum

⁴Absolute Luminosity for ATLAS.

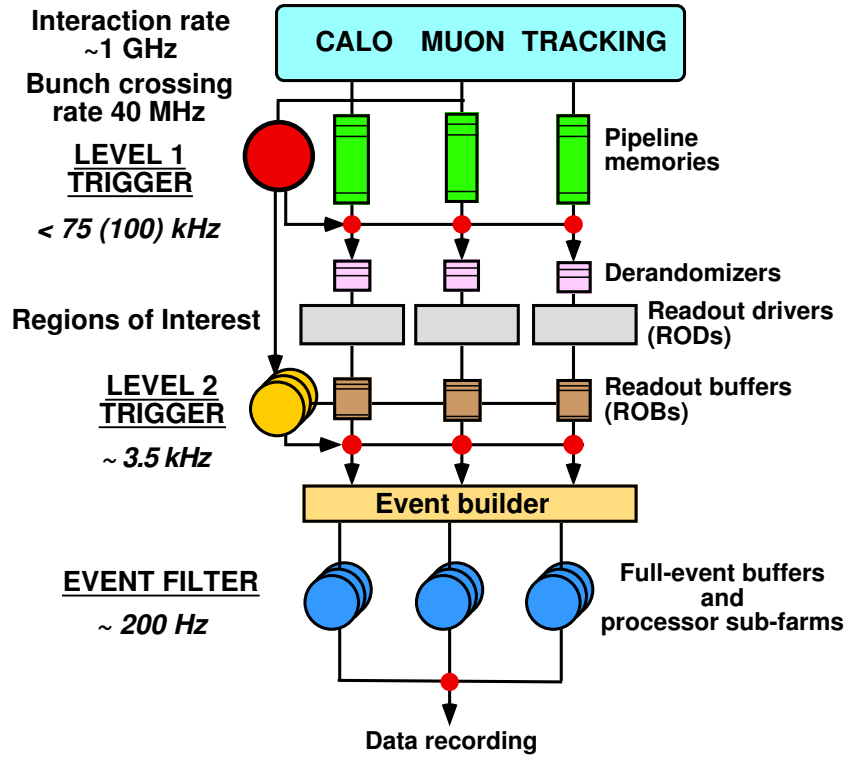


Figure 5.8: The ATLAS trigger system [59].

muons, electrons, photons, jets and hadronically decaying taus, as well as large missing or total transverse energy. It uses a reduced granularity information of the calorimeters and the information of the muon trigger chambers. Results from these two trigger processors are combined by a Central Trigger Processor using predefined trigger menus that combine different trigger elements. The maximum accept rate of L1 is 100 kHz. In addition to the trigger decision, the L1 trigger also defines regions-of-interest (RoI), which correspond to detector areas where interesting features have been found in the event. The selection of the L2 trigger is based on the RoIs given by L1. It has the full detector granularity available within a given RoI, which will on average correspond to 2% of the total event data. The L2 trigger will reduce the trigger rate to about 3.5 kHz. On a L2 accept the complete event is put together at full granularity using the event builder and passed on to the EF. It consists of a processor farm that runs offline analysis procedures on the complete event and can in this way reduce the event rate to 200 Hz. The data acquisition system is used to receive and buffer the event data corresponding to a L1 accept. It moves the data corresponding to a RoI to the L2 trigger and performs the event building at the L2 accept rate. The built events are passed to the EF and on selection moved to permanent storage.

“Any one who considers arithmetical methods of producing random digits is, of course, in a state of sin.”

John von Neumann, 1903–1957

6

Event Simulation

An important tool for experiments at particle colliders is the usage of simulated events. At the moment, since ATLAS is not yet taking data, simulated events are used to study the expected detector performance, develop analysis strategies, and in general prepare the experiment’s reconstruction software for the analysis of real data events. During operation of ATLAS, Monte Carlo samples will be of high importance to develop and refine procedures for the data analysis and to predict the background contributions to searches for phenomena beyond the Standard Model.

The study presented in this thesis is based on simulated, or as it is commonly called *Monte Carlo* events.

In this chapter, a brief introduction to the models used to describe hadron-hadron collisions is given first. Then basic concepts of the used Monte Carlo event generators are discussed in more detail. Last, a description of the ATLAS detector simulation is given.

6.1 Anatomy of a Hadron-Hadron Collision

The dynamics of hadron-hadron collisions are to a large extent governed by the properties of QCD. Even if particles not participating in strong interactions are produced, the dynamics of the initial state hadrons are very important. In general one is interested in a hard scattering process, that involves a high energy scale. This corresponds to short distance interactions that can be described by perturbative QCD. In this context, the partons (gluons and quarks) can be seen as free particles interacting with each other. On the other hand, the initial and final state have to be color neutral, since the strong coupling constant gets larger for larger distances (*confinement*). So in addition to this hard scale, there have to be softer processes connecting the hard interaction with the hadrons to be observed at large distances, corresponding to low energy scales.

The basic structure of a hadron-hadron collision is shown in Figure 6.1. It can be divided into several stages:

The fundamental interactions of *partons*, quarks and gluons, are known from the Lagrangian. But these do not appear as free particles due to confinement at low energy scales.

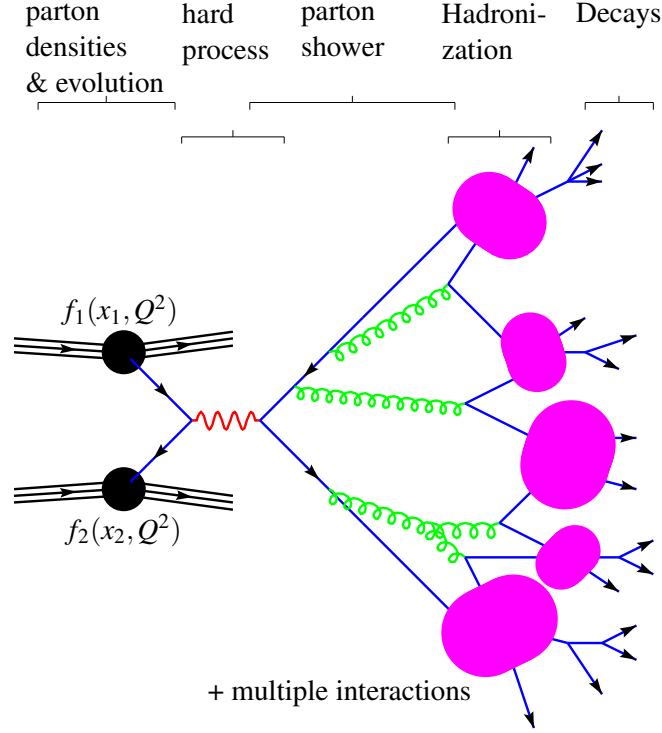


Figure 6.1: Basic structure of a proton-proton collision event (from [68]). The initial state parton shower and the multiple interactions have been left out for simplicity.

Instead hadrons, which can be seen as a bag of partons, can be brought to collisions. At sufficiently high center of mass energies the individual partons of each hadron are resolved and interactions between these can occur. In the collision, it is assumed that only one parton from each hadron participates in the *hard process*, e.g. W or H boson production. The (differential) cross section of the partonic process $\hat{\sigma}_{ij}$ for a scattering of a parton of species i with one of species j can be calculated from the underlying theory. To make the connection with the hadronic cross section, it is necessary to convolute this partonic result with the probability to find a parton with a momentum fraction x of the proton [64, 69]:

$$\sigma = \sum_{i,j} \iint dx_1 dx_2 f_i(x_1, \mu_f^2) f_j(x_2, \mu_f^2) \cdot \hat{\sigma}_{ij}. \quad (6.1)$$

The functions f_i are called the *parton density functions*, or pdf's, and represent the probability to find a parton of a specific flavor and with momentum fraction x of the hadron momentum¹, when the hadron is probed at an energy scale μ_f^2 , called the *factorization scale*. pdf's are not calculable from first principles in perturbative QCD and have to be determined experimentally. However, QCD can predict the evolution of the pdf's as a

¹Here the Breit frame is used, where it is assumed that the parton momentum perpendicular to the hadrons direction of flight is negligible.

function of the factorization scale. This is done in the DGLAP [70] *evolution* equations. Corrections from the emissions of gluons lead to large logarithms in the perturbative expansion. These can be *resummed* to all orders by renormalization into the pdf's themselves, leading to their dependence on μ_f^2 . However, finite non-universal terms from the corrections remain and appear as a power series in α_s . These terms then depend on another scale μ_r^2 , called the *renormalization scale*, which is the scale at which the running coupling α_s is evaluated. If the perturbative expansion could be done to all orders in α_s , the scale dependence would cancel exactly. In a sense, the choice of renormalization and factorization scales is arbitrary, but driven by the desire to not introduce large logarithmic terms. The residual scale dependence of a cross section is an indicator of the theory uncertainty of the prediction and on how good the perturbative expansion works.

A collision of partons implies accelerated color charges, which means that just as for accelerated electric charges, QCD bremsstrahlung has to occur. This emission can be either associated with the incoming partons, which is called initial-state radiation (ISR), or with outgoing partons, where it is called final-state radiation (FSR). This leads to a cascade of partons, which is also called a *parton shower*. The concept of the parton shower is discussed in more detail later.

The remnants of the protons, from which the partons participating in the hard collision have been taken, in general are left with a large fraction of the original energy and tend to continue in the original direction. They carry color charges that compensate the color exchanged in the hard process.

As the partons move apart from each other after the collision, they have to arrive at a length scale, where they can no longer be seen as free particles, but the confinement has to set in. This *hadronization* can not be modeled by first principles, since it involves non-perturbative aspects of strong interactions. Here, phenomenological models are used to describe the transitions from partons to hadrons.

Among the produced hadrons, there might be short lived particles that *decay* before they can be observed.

In addition to the hard interaction process, also other partons in the two colliding hadrons can undergo hard collisions, leading to *multiple interactions*.

6.2 Definition of Hadron Jets

At this point it is useful to introduce the concept of a *jet*. If a highly energetic parton moves into a certain direction, it is bound to radiate other partons, e.g. a quark may radiate off a gluon. As in QCD the radiation is in general in the flight direction, the hadrons emerging from the hadronization of the parton will also have the same general direction as the initial parton. Observable is a collimated jet of hadrons, where the initial quarks energy has been divided among the hadrons.

Jet algorithms are used to identify these jets. These are clustering algorithms, which try to group together particles that are close together. The two most widely used jet algorithms at hadron collider experiments are the *cone* algorithm and the k_\perp algorithm. They differ mostly in the used definition of “nearness”. The cone algorithm groups together particles

that are close to each other in (η, ϕ) space, while the k_{\perp} algorithm uses a resolution variable that depends on the relative transverse momentum. The two algorithms are described in more detail in Appendix B and in [71].

6.3 Monte Carlo Generators

In this section a brief overview is given of how the description of a hadron-hadron collision reflects in Monte Carlo generators. Within this overview, the description of the hard scattering process and the parton shower are discussed. Then some general concepts of merging these two phases and the implementation of higher order corrections in Monte Carlo generators are shown. Finally, the modeling of the multiple interactions is briefly summarized.

A detailed introduction into the physics of Monte Carlo generators is beyond the scope of this thesis. A more detailed introduction can be found in [72].

6.3.1 Matrix Elements

As described above, the hard process can be described using the Feynman rules following from the used interaction Lagrangian. The result is a *matrix element* (ME) for the process that is to be investigated. Leading order ME's, corresponding to Feynman diagrams not containing a loop, can be calculated in an automated way. This can be used to generate arbitrary processes given a set of Feynman rules.

However, there are also limits to the description of the event using only matrix elements. Processes like $q \rightarrow qg$ can in principle be included in a ME, but the obtained leading order matrix element has singularities for collinear and soft contributions of the radiated gluon. In perturbative expansions, these divergences in *real* emissions are in general canceled by divergences of the same type that occur in *virtual* corrections, where e.g. the gluon is reabsorbed by the same quark line. This is not the case for fixed order ME's and as a consequence, a ME can only describe well separated, energetic partons properly.

6.3.2 Parton Shower

Rather than using only the ME's, the ansatz generally used in Monte Carlo generators is a factorization of the whole process into a hard subprocess, described by a ME, and possible emissions of the in- and outgoing partons. The latter are described by the parton shower (PS).

The PS aims at describing the evolution of a parton from some high scale that is associated with the hard process, to a low scale where the hadronization takes place, in an *universal* way. The first major component of the PS technique are universal probabilities for a parton a to split into a pair of partons b and c at some evolution scale Q^2 . What kind of physical variable this evolution scale is, is a question of the implementation of the shower, as long as the divergences are correctly retained, i.e. the divergence has to be at $Q^2 \rightarrow 0$ (collinear divergence). Some examples of evolution variables are the virtualities

of the partons, the relative transverse momentum, or the relative angle between each other. Well separated partons have large Q^2 , collinear ones small Q^2 .

These probabilities can be obtained from the exact matrix elements by approximation in collinear and soft region. Defining the energy fraction that parton b receives of the initial partons energy as z , the probabilities are defined in a set of differential equations that are called the DGLAP equations [70], which are similar in structure to those governing the pdf evolution:

$$d\mathcal{P}_a = \frac{\alpha_s}{2\pi} \frac{dQ^2}{Q^2} P_{a \rightarrow bc}(z) dz \quad (6.2)$$

The *splitting kernels* $P_{a \rightarrow bc}$ are universal functions whose functional form only depends on the type of splitting, i.e. $q \rightarrow qg$, $g \rightarrow gg$, or $g \rightarrow q\bar{q}$. The exact form can be found in [72]. For this discussion it is only important that they are divergent for $z \rightarrow 1$ (except for $g \rightarrow q\bar{q}$). As expected the DGLAP equations still contain the collinear ($Q^2 \rightarrow 0$) and the soft divergences ($z \rightarrow 1$).

Using these probabilities it is possible to describe the parton shower as a series of consecutive branchings or emissions. However, the divergences are still present. In this way, the total probability of a parton to branch can be larger than one. This is cured by the second component of a parton shower, the *Sudakov form factor* [73].

The Sudakov form factor, or short Sudakov factor, is nothing else than a no-emission probability between two scales. Taking the DGLAP equations, the probability for a branching to occur in an infinitesimal scale- or, equivalently, time-interval δQ^2 is given by

$$P_{\text{branching}} = \sum_{b,c} \int_z \frac{d\mathcal{P}_a(z')}{dz'} dz' \cdot \delta Q^2. \quad (6.3)$$

The probability that nothing happens follows from conservation of probability as

$$P_{\text{no branching}} = 1 - P_{\text{branching}}. \quad (6.4)$$

Integrating over all small intervals gives an exponential factor for the probability that at a given time, corresponding to a certain scale Q^2 , no emission has occurred yet after starting from Q_{max}^2 [72]:

$$\Delta(Q_{\text{max}}^2, Q^2) = \exp \left(- \sum_{b,c} \int_{Q^2}^{Q_{\text{max}}^2} \frac{dQ'^2}{Q'^2} \int \frac{\alpha_s}{2\pi} P_{a \rightarrow bc}(z') dz' \right). \quad (6.5)$$

This is called the Sudakov form factor. The DGLAP evolution equation is now modified by a Sudakov factor on the right hand side. This corresponds to the conservation of probability: A branching can only occur, if it has not happened before. The Sudakov factor ensures that the total probability for a parton to branch does not exceed unity. This procedure has an analogy in radioactive decay: A nucleus can only decay at a given time, if it has not decayed before. Using the Sudakov factor as above, just yields the exponential law of radioactive decay.

In this way, the occurring large logarithms for collinear and soft parton configurations can be *resummed*. The Sudakov factor has an immediate probabilistic interpretation: a no-emission probability. It is immediately suited for a simulation of the PS, as it allows to randomly choose emission points in the shower evolution with a conserved probability. Also, since the PS provides an evolution from the large scale of the hard scattering process downwards, it gives a possible link to models of hadronization, which have to take over at a low scale where the strong coupling constant becomes non-perturbative.

For the initial state PS, the description is more complicated, since in this case the parton configurations at both ends of the parton shower are already known. The evolution is done in the opposite direction of time/scale. Using this *backwards* evolution a connection to the pdf's is formed, and only physically meaningful parton ensembles are generated. For a more complete discussion, see [72, 74].

6.3.3 Comparison of Matrix Element and Parton Shower

The matrix element description of a partonic final state has its limit in the case of soft or collinear configurations. This region of phase space is better suited for the description by the parton shower. For the visible final states, which will in general consist of jets emerging after the hadronization, the matrix element will be best for the general direction and distributions of well separated jets with high transverse momentum, while the parton shower should work best to describe soft jets and the internal structure of jets. In this respect, the two approaches are complementary to each other, and a combination of both is desirable. In combining the two approaches, care has to be taken that contributions from the ME and the PS are not counted multiple times.

6.3.4 Matching of Matrix Element and Parton Shower

A first approach to merge the PS and the ME is to correct the PS with the ME for an additional gluon emission by introducing a weight corresponding to the ratio between the coverage by the parton shower and the real emission matrix element. This procedure is called *matrix element correction* [72]. This approach works only for the first emission and the procedure is not generic for an arbitrary multi-parton final state.

Another, more ambitious approach is the merging of the ME and the PS. It aims at producing an automated way to combine ME's of different parton multiplicities, e.g. $0, 1, 2, \dots, n$, in a consistent way with the PS, without double counting any contributions. This works by separating the phase space into a region that is populated by the ME, and another one that is filled by the PS. The approach is generic, and can be applied to arbitrary processes and be implemented into automated Monte Carlo generators. In the following the CKKW algorithm as introduced in [75] for e^+e^- collisions and generalized to hadron hadron collisions in [74] is briefly described. More detail can be found in the quoted references and in [72].

The first thing to remember is that the differential cross sections as given by the ME for each multiplicity σ_i retain the soft and collinear divergences. So in order to have a meaningful result, one has to impose cuts on the parton configurations. These can for

example consist of a cut Q_{cut} on the resolution parameter of a k_{\perp} jet algorithm that acts on the final state partons. If this cut is lowered, the cross sections of each parton multiplicity rise without bounds due to the still present divergences. Without virtual corrections, no cancellation can take place, and there is no 'detailed balance' where a larger cross section of one jet multiplicity is compensated for by a smaller cross section of a lower multiplicity. This can also be understood in terms of the properties of the exclusive k_{\perp} jet algorithm (see Appendix B): If at some resolution scale i jets are present, and the scale is lowered, an additional jet at lower transverse momentum might appear or one of the already existing jets might be split in two. The event then has to be reclassified as a $i + 1$ jet event, without any change to the total cross section. The trick of the CKKW algorithm is to use Sudakov factors to ensure that this detailed balance takes place while retaining the matrix element description above Q_{cut} . This is done inspired by the next-to-leading logarithmic (NLL) jet rates as in [76], where the ME approximation by splitting functions is given. In the CKKW formalism the approximation is replaced by the complete ME.

The algorithm works as follows:

1. A parton multiplicity i is randomly chosen according to the relative cross section fulfilling the imposed cuts ($p = \frac{\sigma_i}{\sum_k \sigma_k}$). α_s is evaluated at Q_{cut} for this.
2. The ME partons are taken as input to an exclusive k_{\perp} jet algorithm [77], where the d_{cut} is raised successively. From the scales where two partons are merged into each other, a hypothetical parton shower history corresponding to this evolution is constructed. Only physically allowed mergings are used, e.g. a quark and an anti-quark of different flavors cannot be merged. This is continued down to the lowest input multiplicity.
3. A weight factor consisting of the product of the ratios of α_s at each of the imagined branchings to the one used in step 1 is applied, which corrects for the evolution of α_s .
4. For all propagator lines in the imagined shower history, Sudakov weights of the form $\Delta(Q_{\text{beg}}^2, Q_{\text{cut}}^2)/\Delta(Q_{\text{end}}^2, Q_{\text{cut}}^2)$ are introduced. Q_{beg}^2 is the scale at which the parton would have been produced (i.e. the scale at which the parton is merged with another in the k_{\perp} algorithm), and Q_{end}^2 the one where it either branches, or, if it is a final state parton, Q_{cut}^2 . This weight represents the lack of emissions with a scale larger than Q_{cut} between the branchings.
5. The generated parton configuration is kept randomly according to the combined Sudakov and α_s weight.
6. Now the ME parton configuration is evolved further by a parton shower, to add additional activity below Q_{cut} . In order to avoid double counting, any branchings that might occur above Q_{cut} are vetoed.

In [75] it is proved that the dependence on Q_{cut} cancels exactly at NLL accuracy, which is just the desired result. According to [64] the exact implementation of the matching procedure entails a number of choices that do not affect the resummation of the logarithms, but do affect the numerical predictions on the order of 20 to 30%.

In addition to the described algorithm, there are similarly working variations, like the Lönnblad scheme [78] or the MLM matching [79]. In [79] a comparison between the different approaches as implemented in different Monte Carlo generators is given.

The CKKW matching procedure has the huge advantage of being completely generic, it can be applied to any process of interest in an automated way. It is implemented in the SHERPA Monte Carlo generator [80] that is used extensively in this thesis.

6.3.5 MC@NLO

Another, much more ambitious approach has been taken in the Monte Carlo generator MC@NLO [81]. In this ansatz, also only the first hard emission is modeled by the real emission ME, but it also includes the virtual corrections, so that a complete next-to-leading order (NLO) result is obtained, that contains the first set of higher order corrections from perturbation theory. To obtain this, the NLO corrections to the leading order n -body matrix element are calculated, which will include real corrections with $n + 1$ partons, and n -body virtual ones. In a next step, it is calculated analytically, how a first, thus high scale, branching of a parton shower starting from the n -body topology would populate the $n + 1$ -body phase space. In this calculation, the Sudakov factor is excluded, since the large logarithms are not to be resummed already in this step. This analytical expression still contains the singularities, but these are the same as for the $n + 1$ -body matrix element. Subtracting the expression from the one for the $n + 1$ -body matrix element gives the 'true' $n + 1$ body events and the divergences cancel each other. One is left with n -body and $n + 1$ body events, which both give a finite cross section. To these event classes, normal parton showers can be added.

One technical disadvantage of this method is that the ME and the PS are only guaranteed to give exactly the same answer in the collinear or soft limit, but not in the whole phase space. This is solved in MC@NLO by adding a small fraction of events with negative weights. This will mean that MC@NLO will produce unweighted events, but only in the sense that the weights are mostly $+1$ and for about 10 to 15% of the events -1 , which has to be taken into account when predicting differential distribution, normalizing event samples, and calculating statistical uncertainties. One other disadvantage is that this procedure is not universal with respect to the process under consideration and the used PS. This means that each new process has to be implemented manually.

6.3.6 Underlying event

In contrast to e^+e^- collisions, the final state of a hadron hadron collision event does not only consist of the products of the hard scattering process. In addition there are the beam remnants and possible multiple interactions. In addition, ISR and FSR are linked together due to the color charges present between these. All these effects are to a large extent dominated by soft physics, which necessitates models for these components. In the following a short sketch of one model for multiple interactions, as implemented in the PYTHIA generator and in SHERPA in another form, is given. It is based on the model presented in [82]. More information on possible modeling of the underlying event can be found in [83].

The model is based on simulating (semi-)hard QCD $2 \rightarrow 2$ scattering processes. This type of events is dominated by t channel gluon exchange. Using only perturbative QCD, this type of processes is singular for vanishing transverse momentum of the outgoing par-

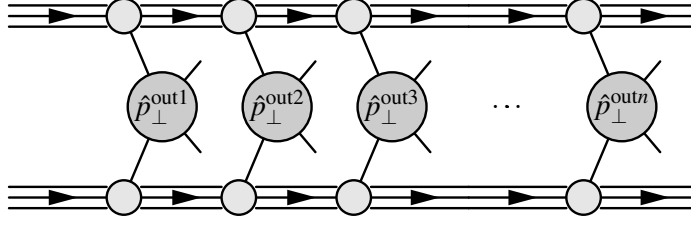


Figure 6.2: Schematic view of the multiple interactions modeling.

tons ($\hat{p}_{\perp}^{\text{out}}$). However, there has always to be a small transverse momentum scale, where non-perturbative effects have to set in. This can also be seen as the point where the wavelength of the exchanged gluon becomes so large that it “sees” the complete proton in a coherent way, and since the proton itself is color neutral, the cross section has to drop. This is modeled as a cut-off scale $\hat{p}_{\perp}^{\text{min}}$, below which no additional interactions are simulated. The probability to generate a $2 \rightarrow 2$ scattering at a transverse momentum scale $\hat{p}_{\perp}^{\text{out}}$ is given by the ratio of the $2 \rightarrow 2$ cross section at this scale to the total non-diffractive cross section.

The multiple interactions are then generated in a sequence of scatterings with decreasing transverse momentum scales, just as in a parton shower, which stops at the cut-off scale. This is depicted in Figure 6.2.

The underlying event models have been tuned to reproduce observables that have been measured at the Tevatron $p\bar{p}$ collider at a center of mass energy of 1.8 TeV and have to be extrapolated to the LHC. The most important parameter is the cut-off scale $\hat{p}_{\perp}^{\text{min}}$. It is extrapolated according to:

$$\hat{p}_{\perp}^{\text{min}} = \hat{p}_{\perp}^{\text{min}}(\text{ref.}) \cdot (s/s_{\text{ref.}})^{\alpha}, \quad (6.6)$$

where $\hat{p}_{\perp}^{\text{min}}(\text{ref.})$ is the cut-off scale at the reference energy $\sqrt{s_{\text{ref.}}}$, and α a rescale exponent, that is expected to be close to 0.16 [83].

In this thesis, the ATLAS default tunings are used for the PYTHIA generator [84] and for the multiple interactions model used in HERWIG [85], called JIMMY [86]. For the SHERPA generator, the default parameters of SHERPA 1.0.9 are used, but the reference cut-off scale is increased to 2.57 GeV instead of 2.45 GeV. This was done to get a similar charged hadron multiplicity as in the PYTHIA 6.2 model with the ATLAS tune [87]. Changing the cut-off at the reference scale of 1.8 TeV is known to change the prediction at the Tevatron as well. So in principle this tuning of the underlying event description does not reproduce the Tevatron data. After the turn-on of the LHC a renewed tuning of the available models to data will be necessary.

6.3.7 Decays and QED radiation

In addition to the described general-purpose Monte Carlo generators, two packages have been used in this thesis in the event generation that are more specialized. The first of these

two is TAUOLA, which is a dedicated decay library for τ leptons. It is used for all other Monte Carlo generators except for SHERPA. The second is PHOTOS, which is used to simulate QED final state radiation of resonances. It is used for all used Monte Carlo generators.

Table 6.1 lists the Monte Carlo generators used in this thesis along with the used versions.

6.4 Particle Filters

A parton shower Monte Carlo generator produces completely hadronized events, i.e. a set of stable particles with corresponding four-momenta and points of origin. To avoid having to simulate events that will in any case not be selected, commonly additional phase space cuts are applied. These can be either done already at the generator level, e.g. by specifying p_T and η cuts on certain final state particles, or by applying a filter on the generated events. This method assumes that the influence on the analysis of the events that are either already rejected by the generator cuts, or by the filtering algorithms, is negligible. Within this study, a *1 or 2 lepton filter* ($1\ell f$ and $2\ell f$) has been applied to some of the datasets. This filter requires at least one or two leptons (e or μ) with $p_T > 5$ GeV and $|\eta| < 2.7$. In addition, a *2 muon filter* ($2\mu f$), which corresponds to the $2\ell f$, but requiring at least two muons, and a filter on at least one decay sequence of the type $t \rightarrow Wb \rightarrow \ell \bar{\nu} b$ ($1tW\ell f$), are used for other Monte Carlo samples.

Generator	Version
SHERPA [80]	1.0.9
PYTHIA [84]	6.403
HERWIG [85]	6.510
JIMMY [86]	4.3
ACERMC [88]	3.4
TOPREX [89]	4.11
MC@NLO [81]	3.1
TAUOLA [90]	2.7
PHOTOS [91]	2.15

Table 6.1: Monte Carlo generators used in this work and their version numbers.

6.5 Detector Simulation

The output of a Monte Carlo event generator is not yet readily usable for performing analysis cuts, as any detector effects, like acceptance or resolution are missing. The produced particles have to be passed first through a simulation of the ATLAS detector. Figure 6.3 shows a flow chart of the complete simulation chain of ATLAS, where also the relationship to real events from the ATLAS detector are shown. In this flow chart, only the detailed simulation of the ATLAS detector is shown, which is described in the next section.

6.5.1 Detailed Simulation

The detailed simulation, in the following called FULLSIM, of the ATLAS detector relies on two main steps, the *simulation of hits*, which correspond to the deposited energy in the detector, and the *digitization*, where the response and data processing of the individual sub-detectors and their readout electronics is taken into account. More details can be found in [92]. At the end of the simulation chain are Raw Data Objects (RDO's), which can be passed on to the reconstruction software. These correspond to the same data format as real ATLAS events, that are obtained by conversion from the byte-stream format produced by the higher level trigger system.

The simulation of ATLAS events is based on the GEANT4 package [93], which has been tuned extensively for the use in ATLAS. GEANT4 gets a detailed description of the detector geometry from a dedicated database. The passage of particles through the detector volume is then simulated, and any secondary particles produced in interactions are added to the list of particles, until all particles either have stopped or left the detector volume.

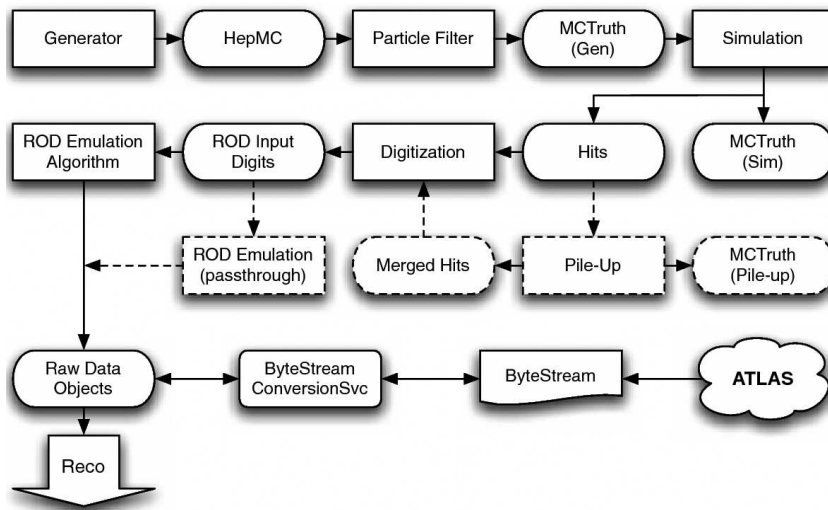


Figure 6.3: Data flow of the ATLAS event simulation. Rectangles represent processing stages and rounded rectangles represent objects within the ATLAS event data model (taken from [92]). Addition of pile-up and ROD (Read-Out Driver) emulation are optional.

Detector Subsystem	GEANT4 sim. time/kSI2ks
Inner Detector	144
EM Barrel Calorimeter	91
EM Endcap Calorimeter	393
Forward Calorimeter	155
Hadronic Barrel Calorimeter	29
Hadronic End cap Calorimeter	50
Muon Systems	21
Other (beam pipe, detector services, shielding)	124
Total Event	907

Table 6.2: CPU time for one event for the ATLAS detailed detector simulation of a QCD dijet sample with a 260-560 GeV leading jet (taken from [95]). A modern CPU core corresponds to 1.5 to 2.5 kSI2k.

In contrast to the Monte Carlo event generators, GEANT4 does not rely on the simulation of fundamental interactions, but rather uses macroscopic parameterizations or analytical calculations of energy loss mechanisms for particles traversing matter, so called transport models. More detail can be found in [94]. Table 6.2 shows the CPU time requirements of the detector simulation for hard QCD dijet events.

The digitization of the hereby produced hits is specific to each sub detector. At this level the response to the deposited energy is simulated on the level of the smallest detector units, like a pixel module, or a calorimeter cell. Inefficiencies or dead channels have to be included in this step.

Inclusion of Pile-Up and Cavern Background

At high instantaneous luminosity, in each bunch crossing in ATLAS, more than one pp pair can interact with each other due to the very large inelastic cross section of about 100 mb. At a luminosity of $10^{33} \text{ cm}^{-2} \text{ s}^{-1}$ 2.3, and at $10^{34} \text{ cm}^{-2} \text{ s}^{-1}$ 23 pile-up events are expected per bunch crossing. The majority of these pile-up events are just soft QCD dijet events that are overlayed on the hard scattering process that one wants to study. One can distinguish between in-time pile-up, corresponding to the same bunch crossing, and out-of-time pile-up, corresponding to previous bunch crossings. The latter is important as several detector components, such as the EM calorimeter integrate over multiples bunch crossings, as their read-out times are larger than the LHC bunch crossing interval of 25 ns.

In addition, cavern background has to be taken into account. This is a radiation background in the muon spectrometer caused by neutrons and photons in the ATLAS cavern that may degrade the muon spectrometer performance due to the larger occupancy noise.

Pile-up can be included on the hit level, where simulated hits of minimum-bias events are merged with the normal hits. Due to the very high CPU requirements of digitization

with pile-up, and because of pending software issues, not all event samples are available with overlaid pile-up.

Within this thesis, pile-up datasets were only available for selected processes with a much smaller statistics than samples of the same processes without pile-up. They are used to study the effects of pile-up on the quality of the event reconstruction. They correspond to an instantaneous luminosity of $10^{33} \text{ cm}^{-2} \text{ s}^{-1}$ and the simulated cavern background is five times higher than the prediction of the GCALOR [96] and FLUKA [97] simulation programs to account for the uncertainties of this prediction.

Misalignment

For the data samples used in this thesis, also misalignment has been simulated, which means that the detector elements have been intentionally misplaced in such a way as to resemble a possible real geometry of the ATLAS detector within the currently known uncertainties. However, in the used software release, also the reconstruction was done using exactly the same geometry version of ATLAS, which corresponds to using a perfectly aligned, as built detector. In the experiment, the alignment of ATLAS will be measured by using data events in a global fit procedure. However, this procedure was not yet available in the used software release.

6.5.2 Fast Detector Simulation

As shown in Table 6.2 the CPU time needed for one single event in FULLSIM is quite high. Depending on CPU and event, this process can take 5 to 15 minutes, with most time needed for the simulation of the EM calorimeter due to its very fine granularity.

As an alternative, a fast detector simulation, ATLFAST, has been developed [98,99]. It provides a very simplified approach to simulating the detector, where the four vectors of stable generator particles are smeared using resolution functions that have been determined in FULLSIM. More detail of the ATLFAST performance and its algorithms is shown in Chapter 9.

Reconstruction of electrons, photons and muons in ATLFAST is based on the Monte Carlo truth information, neglecting any fake reconstruction effects. Jets are obtained by summing the transverse energies of all particles in a simplified (η, ϕ) representation of the calorimeter and running a jet finding algorithm on the obtained cells. Identification of b and τ jets is done on a statistical basis, using the efficiencies and misidentification rates obtained in the detailed simulation. Missing transverse energy is calculated as well from the obtained objects after smearing and any unused “calorimeter” cells.

In this respect, ATLFAST bypasses the complete simulation and reconstruction chain, since its output are physics objects such as jets and muons. In its current version, it does not have any real reconstruction layer build in, and it can only be seen as an approximation of the detailed detector simulation. The main advantage of ATLFAST is its speed, the processing time needed for one event is less than 1 s.

Currently, within ATLAS other options for speeding up the detailed simulation are explored. Among these are efforts that try to treat showers in the calorimeters within GEANT4

differently [95], or replacing the calorimeter simulation with a simplified parameterization, while retaining a detailed simulation of the inner detector. These algorithms are currently in the validation phase and are not used in this study.

“I have only one eye, I have a right to be blind sometimes... I really do not see the signal!”

Horatio Nelson, 1758–1805

7

The Signal Process

In this chapter, the peculiarities of the description of the two relevant signal processes, the direct and b-associated production of a neutral Higgs boson with its subsequent decay into a muon pair are discussed. First the bottom quark associated production is described, where a brief overview of the available cross section calculations is given. The Monte Carlo event generators SHERPA and PYTHIA are compared and validated for their use in the analysis. A proposal to normalize the cross section according to higher order calculations is given. The direct production process is briefly discussed, also with a proposed higher order normalization. Last, the signature of the signal process is discussed.

7.1 Bottom Quark Associated Higgs Boson Production

In the Standard Model the associated production of the Higgs boson with bottom quarks proceeds via Feynman diagrams just as in Figure 3.3 (d), with the top quark replaced by a bottom quark. It is suppressed due to the much smaller Yukawa coupling of the b quark compared to the top quark. In the Standard Model this production channel will not be observable at the LHC due to its low cross section. However, as discussed in Chapter 2, there are regions of the MSSM parameter space (i.e. at large $\tan\beta$) where the Yukawa coupling of the b quark to neutral Higgs bosons is enhanced with $\tan\beta$. In this case the production cross section of bottom quark associated production is much larger (enhanced by $\tan^2\beta$), making it the dominant Higgs boson production channel.

7.1.1 Production Mechanisms

The perturbative calculation of b-associated Higgs boson production depends on which process is taken as the hard scattering process. The different Feynman diagrams are shown in Figure 7.1. The depicted production mechanisms differ mainly in whether the b quarks, which the Higgs boson is radiated off, are outgoing particles of the hard scattering process or not. It should be kept in mind that the b quarks that are ingoing particles in the matrix element, must have been produced by a gluon splitting into a $b\bar{b}$ quark pair, since the proton

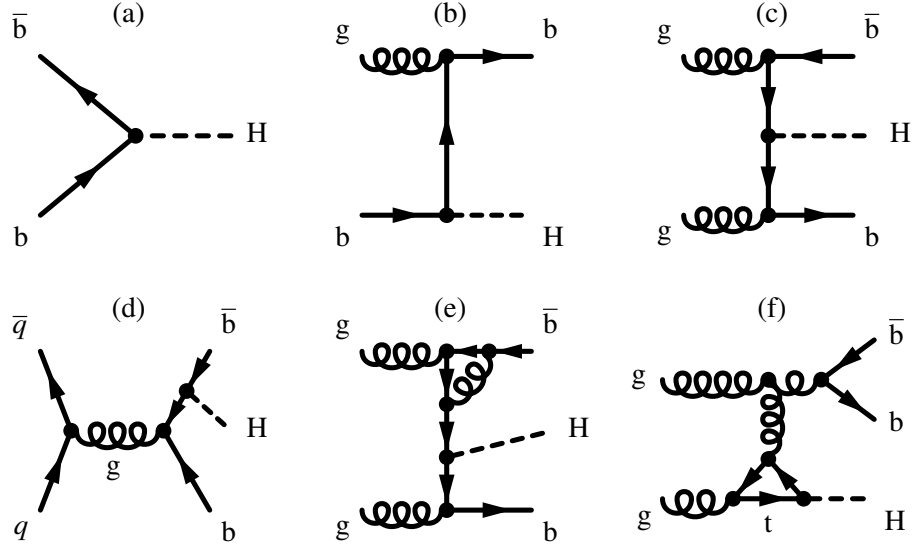


Figure 7.1: Example Feynman diagrams for b -associated Higgs boson production: (a) The process $b\bar{b} \rightarrow H$, (b) the process $bg \rightarrow bH$, (c) the process $gg \rightarrow b\bar{b}H$, (d) the process $q\bar{q} \rightarrow b\bar{b}H$, (e) NLO contribution to the $gg \rightarrow b\bar{b}H$ process, and (f) NLO contribution to the $gg \rightarrow b\bar{b}H$ process involving the top quark Yukawa coupling.

has no net b quark content. This can also be interpreted as introducing a b parton density function, or b -pdf. In the following, the different production mechanisms and the available higher order calculations are briefly discussed. Further detail can be found in [100].

The $gg \rightarrow b\bar{b}H$ process, shown in Figure 7.1 (c), has two gluons in the initial state. When using this process to calculate the cross section, collinear logarithms occur for phase space regions where the b quarks have small transverse momentum. In Ref. [100] it is discussed that these large logarithms enter the perturbative expansion as expansion parameter and might lead to poor divergence when calculating higher order corrections. This process should be most reliable in the case where both b quarks have large transverse momenta.

The $b\bar{b} \rightarrow H$ process, shown in Figure 7.1 (a), provides another way to deal with the collinear logarithms mentioned above. They are absorbed into a b -pdf and thus re-summed to all orders of perturbation theory. The result has no collinear divergences left. The intrinsically present final state b quarks, which come from a gluon splitting inside the proton, are given zero transverse momentum at lowest order. At higher orders they can acquire transverse momentum, e.g. in the process $bg \rightarrow bH$, which is a NLO contribution leading to an observable b quark. This process should be the best to describe the inclusive cross section where the observation of the b quark is not required, but also not vetoed.

Taking the $bg \rightarrow bH$ process, shown in Figure 7.1 (b), itself as the leading order one, is a mixture between the former two processes. Here one b quark will come from a bottom pdf and the other from the matrix-element description. It should be most reliable to use this process if one requires exactly one b quark at high transverse momentum.

The quark induced $q\bar{q} \rightarrow b\bar{b}H$ process (Figure 7.1 (d)) is negligible at LHC energies and contributes to less than 1% of the total cross section.

When higher order corrections to these diagrams are calculated, it should be noted that these do not necessarily have to include only diagrams like Figure 7.1 (e), where the Higgs boson is still radiated off a b quark. In the case of the $gg \rightarrow b\bar{b}H$ process, also loop diagrams like the one shown in Figure 7.1 (f) appear, which feature closed top quark loops involving the top quark Yukawa coupling. Within the Standard Model these corrections can have a significant effect due to the large top quark mass. In the MSSM at high $\tan\beta$ the coupling to the top quark is suppressed and these diagrams are less important.

The different calculation approaches disagree widely on the predicted cross section when using only leading order calculations. In recent years, using higher order calculations, this controversy has been remedied to a large extent [100]. In the following the results of these calculations are briefly discussed.

7.1.2 Inclusive Cross Section

The results for an inclusive total cross section, where a b quark at high transverse momentum is neither required nor vetoed, are summarized in Figure 7.2 as a function of the Higgs boson mass. The blue band corresponds to the NNLO¹ calculation of $b\bar{b} \rightarrow H$ [101]. The width of the band corresponds to the residual scale uncertainties when varying the renormalization and factorization scales from their default values $\mu_r = 4 \cdot \mu_f = M_H$. The red band shows a NLO calculation of $gg \rightarrow b\bar{b}H$ [102, 103]. The scale uncertainty for $gg \rightarrow b\bar{b}H$ is about 20 to 30%. It is much smaller for the $b\bar{b} \rightarrow H$ process, especially at high masses. This might be due to the remaining collinear logarithms in the $gg \rightarrow b\bar{b}H$ calculation.

¹In the following, when higher order calculations are given, it is implied that these are expansions in the QCD coupling constant α_s .

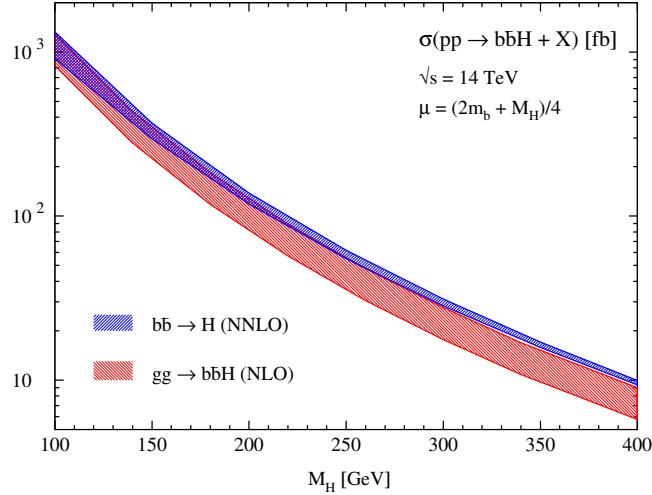


Figure 7.2: Inclusive cross sections for the process $b\bar{b} \rightarrow H$ [101] (blue hatched region) calculated at NNLO accuracy and $gg \rightarrow b\bar{b}H$ [102] (red hatched region) calculated at NLO accuracy. The width of the bands shows the theoretical uncertainty due to the remaining dependence on the renormalization and factorization scales. (Taken from [100].)

tion. However it should be noted that e.g. pdf uncertainties, especially for the bottom pdf have not been included in the shown uncertainties and there is reason to believe [104, 105] that the scale uncertainty alone underestimates the total uncertainty of the $b\bar{b} \rightarrow H$ cross section.

Nevertheless the two calculation approaches show satisfactory agreement. At large Higgs boson masses, the $b\bar{b} \rightarrow H$ prediction is higher than the one from $gg \rightarrow b\bar{b}H$. This is partially explained by the inclusion of closed top quark loops in the calculation of $gg \rightarrow b\bar{b}H$. The corresponding amplitude interferes destructively, lowering the cross section by about 9% for a Higgs boson mass of 120 GeV [100].

7.1.3 Exclusive Cross Section

For most experimental analyses the interesting cross section is not the inclusive total cross section, but the one with a b quark at high transverse momentum and inside the central detector region, since only in this case the jet emerging from the b quark can be reconstructed and identified. Figure 7.3 shows a comparison of cross section predictions requiring at least one b quark satisfying the requirement $p_T^b > 20$ GeV and $|\eta^b| < 2.5$ as a function of the Higgs boson mass. The blue band shows a NLO prediction for $bg \rightarrow bH$ [106], while the red band shows the NLO prediction for $gg \rightarrow b\bar{b}H$ [107]. The two calculations again show overlap within their systematic uncertainties. Again the calculation using a bottom pdf is slightly higher than the $gg \rightarrow b\bar{b}H$ prediction. Also in this case closed top quark loops were only included in the $gg \rightarrow b\bar{b}H$ calculation, lowering the cross section by about 13% for a Higgs boson mass of 120 GeV [100].

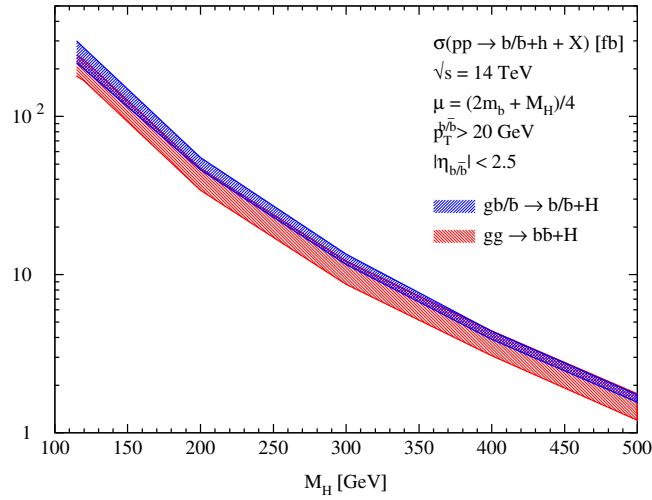


Figure 7.3: Exclusive cross sections for the process $bg \rightarrow bH$ [106] (blue hatched region) and $gg \rightarrow b\bar{b}H$ [107] (red hatched region) calculated at NLO accuracy. At least one b quark is required to have a transverse momentum of at least 20 GeV and be within $|\eta| < 2.5$. The width of the bands shows the theoretical uncertainty due to the remaining dependence on the renormalization and factorization scales. (Taken from [100].)

7.1.4 Simulation of b-associated Higgs Boson Production

Although the different processes for b-associated Higgs boson production have been evaluated extensively in higher order calculations, no NLO Monte Carlo generator is available yet for the signal process. It is also not yet implemented into MC@NLO, which is described in Section 6.3.5.

Instead one has to rely either on leading order Monte Carlo generators, or make use of generators that use some kind of matrix-element parton shower matching, like the CKKW algorithm. When using a simple, non-matched Monte Carlo generator, one cannot simply generate the $b\bar{b} \rightarrow H$, $bg \rightarrow bH$ and $gg \rightarrow b\bar{b}H$ separately and add them, since this would involve double counting between the different processes. Regions of phase space would be covered by both the matrix element and the parton shower. In order to really adequately describe the event sample, the analysis cuts have to be kept in mind. The process to be used is mainly determined by the number of b jets that are required to be tagged. In general, the analysis can be divided into two non-overlapping selections: One requiring at least one tagged jet, and one with zero tagged jets. Already this division is not mirrored by the described processes. The $bg \rightarrow bH$ processes should describe the case with exactly one tagged jet. The $b\bar{b} \rightarrow H$ process is best for the totally inclusive production, where also no veto on tagged jets is placed. So in principle, none of the described processes is perfectly suited for the experimental analysis. An exception would be requiring two jets to be tagged, where the $gg \rightarrow b\bar{b}H$ process would give the best description. Since this would severely reduce the signal cross section, this is not feasible.

An alternative is to use a matched generator, which can combine the different contributions without double counting. In this case the b quarks at low transverse momentum are described by the parton shower, which is equivalent to re-summing the large logarithms. b quarks at high transverse momentum are described by the matrix element in a region where it should be more reliable.

In the following both the PYTHIA generator as an example of an unmatched generator, and the SHERPA generator are discussed with respect to the description of b-associated Higgs boson production.

Signal Generation using the PYTHIA Monte Carlo Generator

The PYTHIA generator [84] is a versatile leading order Monte Carlo generator. In principle, PYTHIA can be used to generate the signal process using the $b\bar{b} \rightarrow H$, $bg \rightarrow bH$, and the $gg \rightarrow b\bar{b}H$ process. However, a specific subprocess has to be chosen, for using all three of them simultaneously would lead to double counting between the parton shower and the matrix element. So far, in ATLAS only the $gg \rightarrow b\bar{b}H$ process of PYTHIA has been used for event simulation in analyses of b-associated Higgs boson production [108, 109].

Signal Generation using the SHERPA Monte Carlo Generator

The SHERPA generator can in principle combine all three different production mechanisms via the CKKW matching algorithm, as described in Chapter 6. As a consequence no double counting will occur and the b jets at high transverse momentum, i.e. above the matching

scale Q_{cut} , are described by the exact matrix element, while b jets at low transverse momentum are modeled by the parton shower.

Due to these features, SHERPA (version 1.0.9) is used as the main generator for the associated production mode. The standard settings of SHERPA 1.0.9 were used, except that the underlying event was switched on and tuned as described in Section 6.3.6. The matching scale was set to 15 GeV to ensure that the region where parton shower and matrix element are matched is lower than possible analysis cuts. As described below, the matching between parton shower and matrix elements shows some imperfections for massive quarks. In Chapter 9 it is discussed that an acceptance cut on the transverse momentum of jets is applied at 20 GeV. Placing the matching scale somewhat lower than this cut avoids being sensitive to the imperfections.

The b quarks were assumed to be massless at the matrix element level. In addition, only Standard Model Higgs bosons were generated, using the masses and widths of the MSSM Higgs bosons. In this way any spin correlations due to the different CP quantum numbers were neglected, but these are expected to be small. The same is actually true for the PYTHIA generator, which also only generates a scalar Higgs boson in b-associated production.

7.1.5 Generator Studies

In the following some comparisons of the different Monte Carlo generators and of different generator versions and settings are presented. For the PYTHIA generator, the two processes $gg \rightarrow b\bar{b}H$ and $b\bar{b} \rightarrow H$ are chosen. The comparisons are done in the differential distributions of the Higgs boson, its decay products, the b quarks, and the b truthjets. Truthjets are formed using a k_{\perp} jet algorithm with $D = 1$, which clusters all stable generator particles except muons and neutrinos. Cuts on the transverse energy and the pseudorapidity of the truthjets are placed at $E_T > 7$ GeV and $|\eta| < 5.0$. A truthjet is flagged as a true b jet if a b quark (taken before hadronization, but after the parton shower) is found within $\Delta R < 0.4$ around the jet axis.

Comparison of SHERPA and PYTHIA

Figure 7.4 shows differential distributions of the Higgs boson and the decay muons for SHERPA and for the processes $gg \rightarrow b\bar{b}H$ and $b\bar{b} \rightarrow H$ in PYTHIA for $M_H = 150$ GeV.

The two different PYTHIA processes show remarkable similarity. SHERPA on the other hand gives a slightly harder transverse momentum distribution for the Higgs boson. The Higgs bosons are also produced slightly more central in Sherpa. This difference has only negligible influence on the transverse momentum and pseudorapidity of the decay muons since the mass of the Higgs boson (in this case $M_H = 150$ GeV) is much higher than its mean transverse momentum. Consequently the kinematics of its decay products are dominated by the Higgs boson mass, which is the same for the different generators.

Figure 7.5 shows the differential distributions of the leading and subleading b parton and the leading and subleading b truthjet.

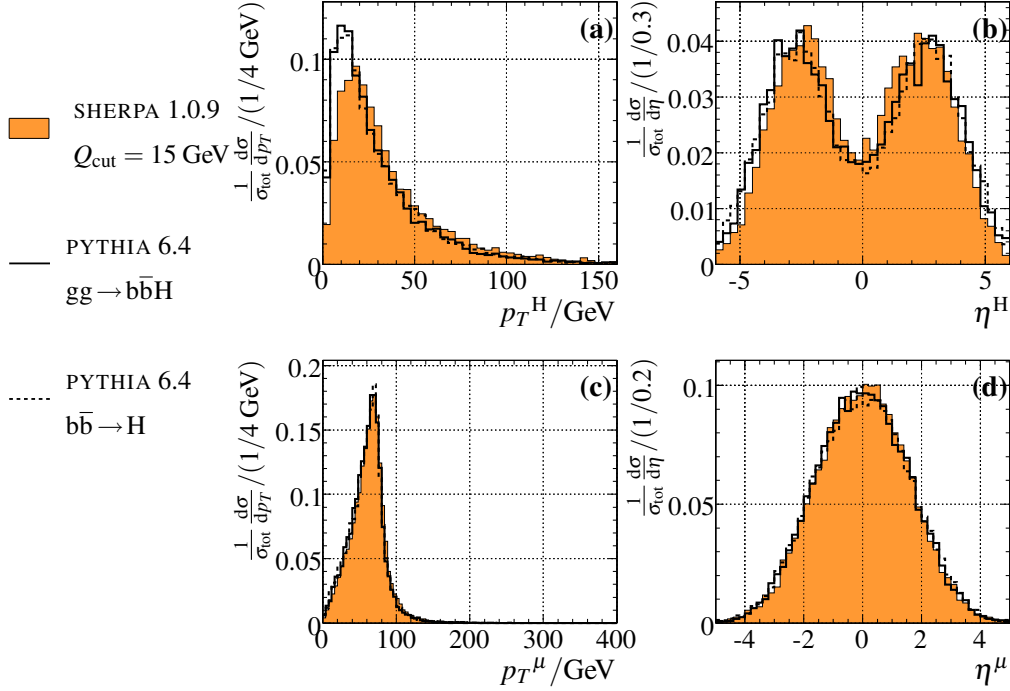


Figure 7.4: Truth differential distributions for $M_H = 150$ GeV. (a) Transverse momentum and (b) pseudorapidity of the Higgs boson. (c) Transverse momentum and (d) pseudorapidity of the decay muons. ■: SHERPA with $Q_{\text{cut}} = 15$ GeV, —: PYTHIA 6.4, $gg \rightarrow b\bar{b}H$,: PYTHIA 6.4, $b\bar{b} \rightarrow H$.

From these distributions, the reason for the larger transverse momentum of the Higgs boson in the SHERPA sample is evident. Both the leading b and the subleading b have a larger transverse momentum than in the PYTHIA samples. Since the Higgs boson has to recoil against these partons, it has to have a larger transverse momentum. In the p_T distribution of the leading b , a dip is visible just below the matching scale. It is more pronounced on parton level than on truthjet level. The effect is under investigation by the SHERPA authors, and it is planned to modify the handling of massive partons in the parton shower in future versions of SHERPA [110]. At the matching scale the parton shower and the matrix element description have to meet. Since the CKKW matching is still only an approximation, some imperfections at this point are to be expected. In this particular case, the effect is considerable and amounts to something like 20 to 30% in the spectrum. It is not clear at the moment, whether the deficit below the matching scale is somewhat compensated for by a surplus of jets at even lower transverse momentum, which would correspond to a peak-dip structure

However, in the region of interest for the analysis, where only b jets with a $p_T > 20$ GeV are used, the SHERPA spectra show no special features. The only point where the observed feature enters is in the absolute normalization, which is discussed in Section 7.1.7.

Regarding the two different PYTHIA samples, as expected, the $b\bar{b} \rightarrow H$ process shows slightly softer p_T distributions than the $gg \rightarrow b\bar{b}H$ process, since in the former case the b jets are produced by the parton shower.

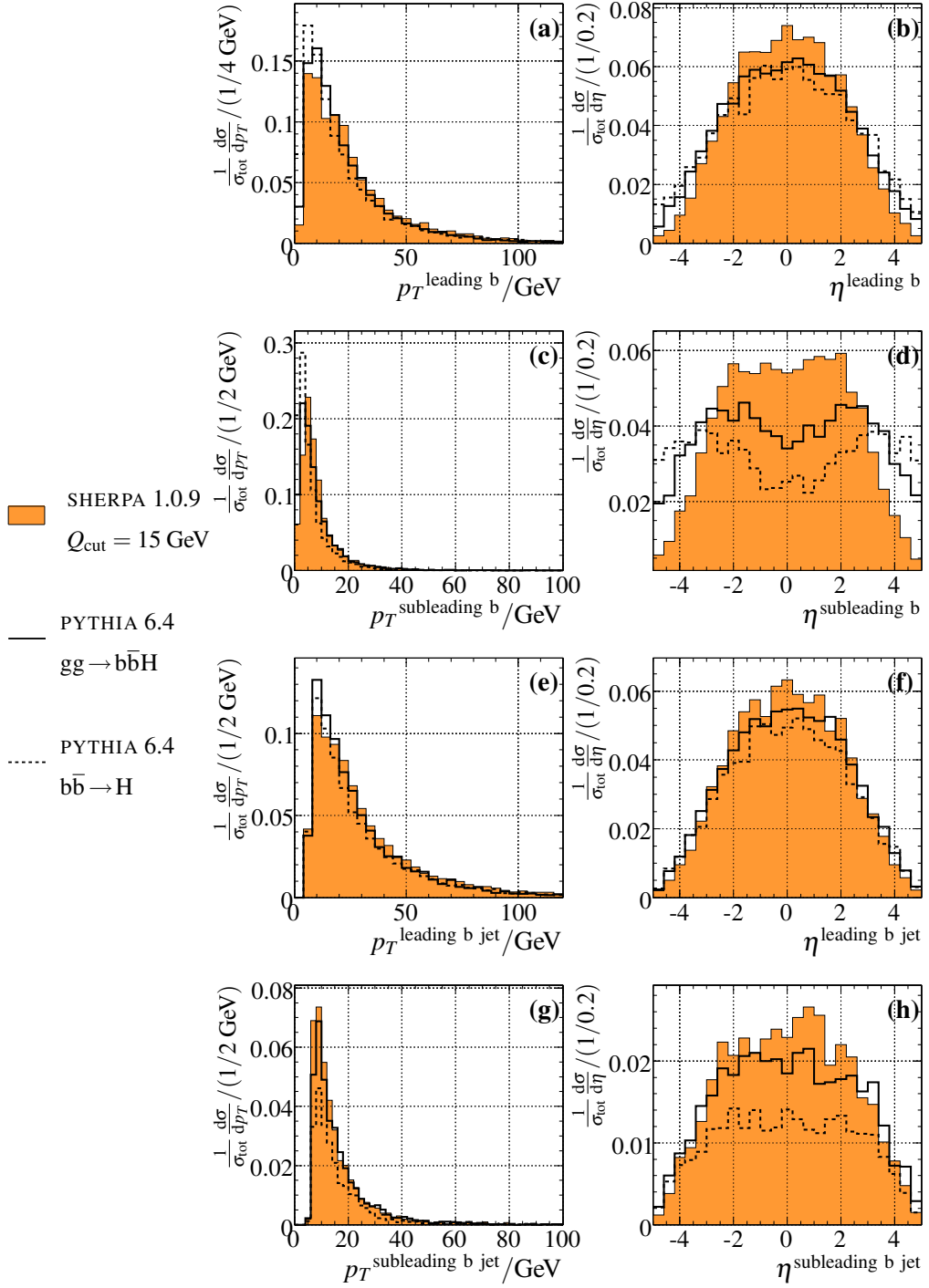


Figure 7.5: Truth differential distributions for $M_H = 150$ GeV. (a) Transverse momentum and (b) pseudorapidity of the leading b, (c) and (d) of the subleading b parton. (e) Transverse momentum and (f) pseudorapidity of the leading b truthjet (k_{\perp} algorithm, $D = 1$, $E_T > 7$ GeV, $|\eta| < 5$), (g) and (h) of the subleading b truthjet. ■: SHERPA with $Q_{\text{cut}} = 15$ GeV, —: PYTHIA 6.4, $gg \rightarrow b\bar{b}H$,: PYTHIA 6.4, $b\bar{b} \rightarrow H$.

Inconsistent Process Description in PYTHIA 6.3

The same comparison is done using the older PYTHIA 6.3 version. The differential distributions are shown in Figure 7.6. In this version, the $gg \rightarrow b\bar{b}H$ process gives a much harder p_T spectrum of the leading b quark and of the Higgs boson. This was traced back by the PYTHIA authors to a problem with the initial state parton shower. Its cutoff scale was set to \sqrt{s} , which is too high [111]. The problem was fixed in PYTHIA 6.403. Samples generated with PYTHIA 6.3 should be used with this problem in mind, since the produced b quarks will have too high transverse momenta. No PYTHIA 6.3 samples are used in this work.

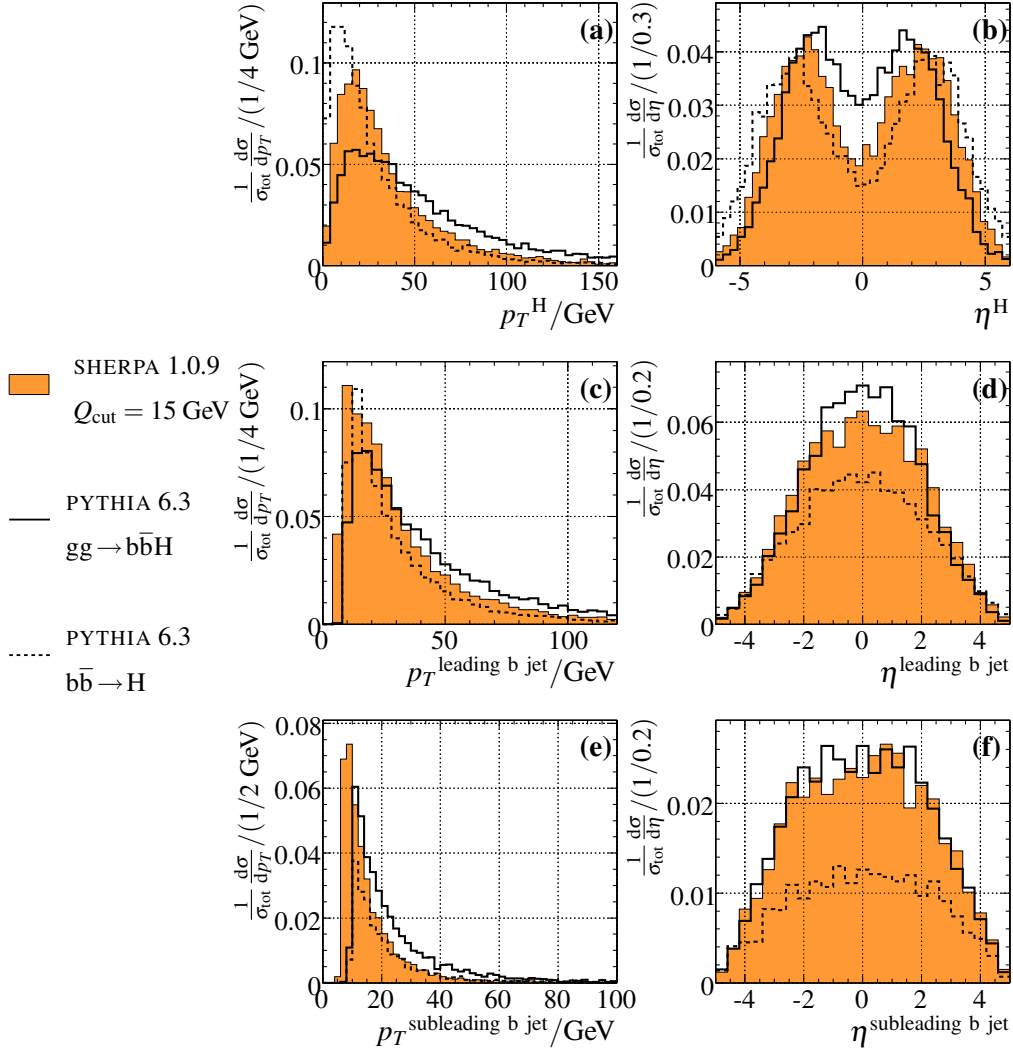


Figure 7.6: Truth differential distributions for $M_H = 150$ GeV. (a) Transverse momentum and (b) pseudorapidity of the Higgs boson. (c) Transverse momentum and (d) pseudorapidity of the leading b truthjet (k_\perp algorithm, $D = 1$, $E_T > 7$ GeV, $|\eta| < 5$), (e) and (f) of the subleading b truthjet. ■: SHERPA with $Q_{\text{cut}} = 15$ GeV, —: PYTHIA 6.3, $gg \rightarrow b\bar{b}H$, ⋯: PYTHIA 6.3, $b\bar{b} \rightarrow H$.

Variation of the Matching Scale in Sherpa

To study the effect of the matching scale on the differential distributions of the SHERPA generator, it is varied from its chosen standard value of 15 GeV to 20 GeV and 25 GeV. The resulting differential distributions are shown in Figure 7.7. The depression in the p_T spectrum of the leading b jet is directly related to the matching scale and its position varies accordingly, as can be seen in Figure 7.7 (c). The distributions of the Higgs boson do

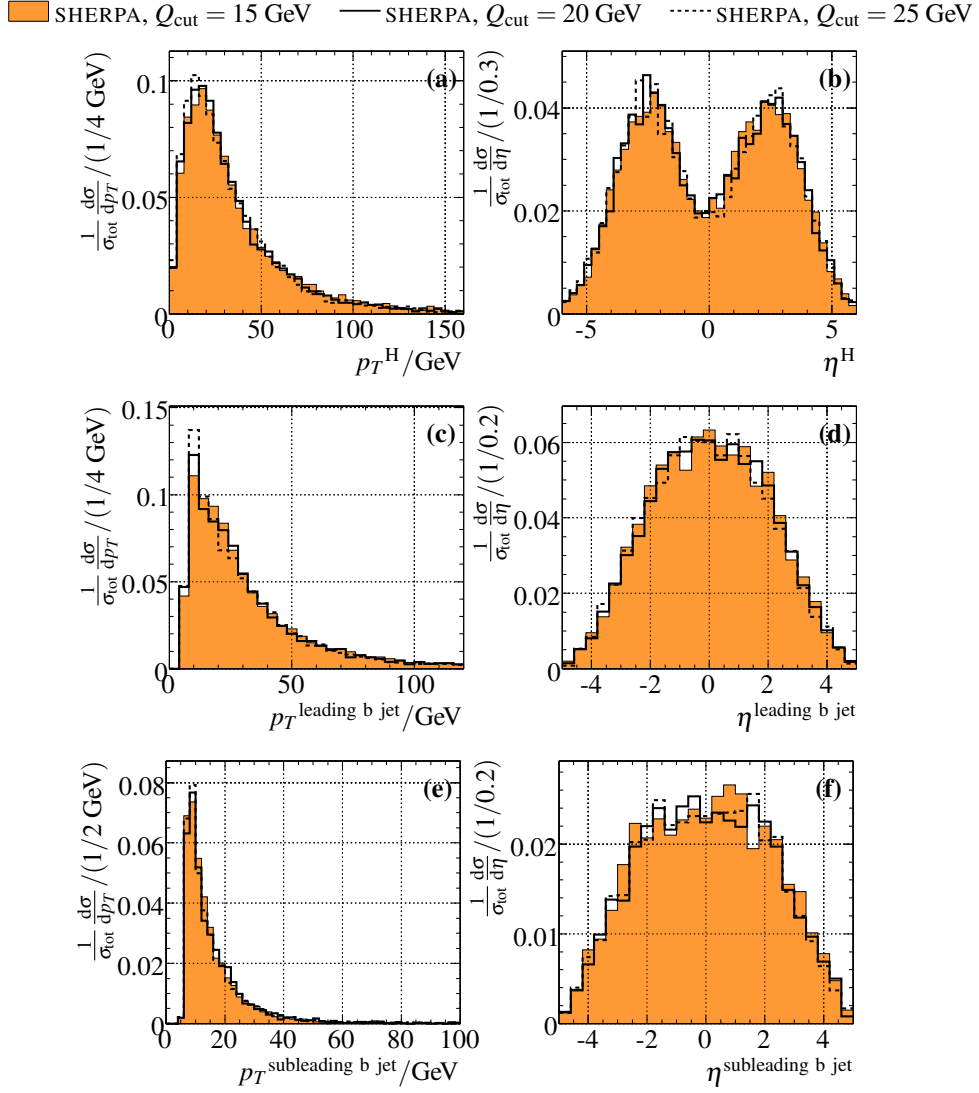


Figure 7.7: Truth differential distributions for $M_H = 150$ GeV. (a) Transverse momentum and (b) pseudorapidity of the Higgs boson, (c) and (d) of the leading b truthjet (k_\perp algorithm, $D = 1$, $E_T > 7$ GeV, $|\eta| < 5$), (e) and (f) of the subleading b truthjet. ■: SHERPA 1.0.9 with $Q_{\text{cut}} = 15$ GeV, —: SHERPA 1.0.9, $Q_{\text{cut}} = 20$ GeV,: SHERPA 1.0.9, $Q_{\text{cut}} = 15$ GeV.

not change significantly with the matching scale. To avoid placing the analysis cut in the problematic region, the matching scale is left at 15 GeV.

Massive b quarks in the Sherpa Matrix Elements

All SHERPA samples used in this analysis have been generated using massless b quarks in the matrix elements. A comparison between massive and massless b quarks is shown in Figures 7.8 and 7.9. PYTHIA 6.4, $gg \rightarrow b\bar{b}H$ is shown for comparison. The largest difference is at low transverse momentum, where the b quark mass is not small compared to p_T . The distributions of the b quarks above 20 GeV are less affected.

The observed differences are currently under investigation by the SHERPA authors [110], and in future SHERPA releases improvements in the handling of massive quarks in the parton shower are planned to be implemented.

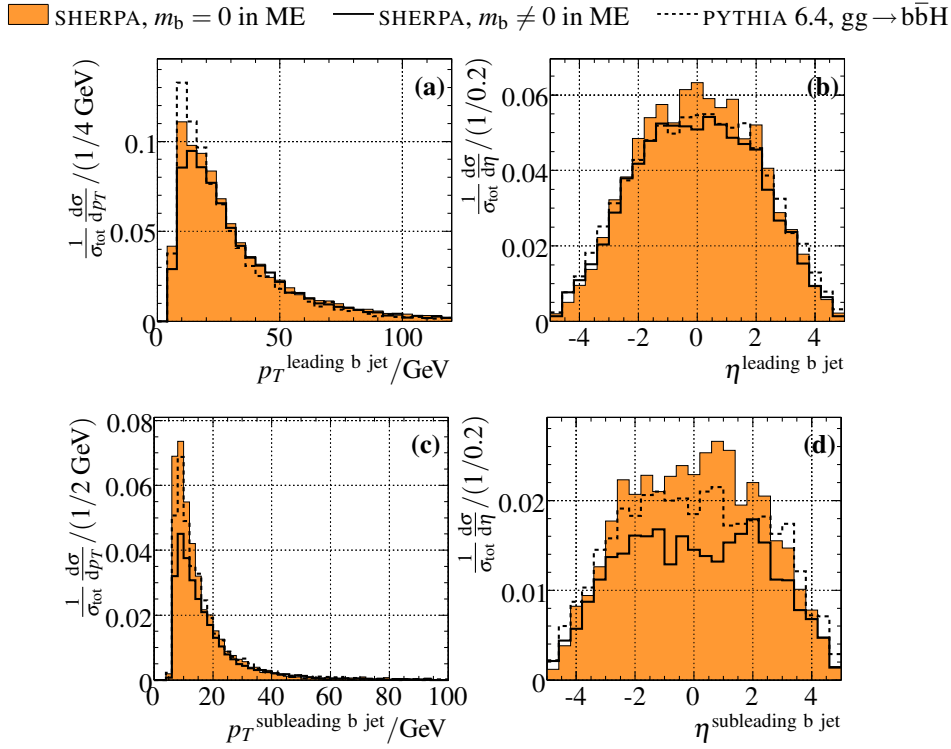


Figure 7.8: Truth differential distributions for $M_H = 150$ GeV. (a) Transverse momentum and (b) pseudorapidity of the leading b quark, (c) and (d) of the subleading b quark. ■: SHERPA 1.0.9, $Q_{\text{cut}} = 15$ GeV, $m_b = 0$ in matrix elements, —: SHERPA 1.0.9, $Q_{\text{cut}} = 15$ GeV, $m_b \neq 0$ in matrix elements, ⋯: PYTHIA 6.4, $gg \rightarrow b\bar{b}H$.

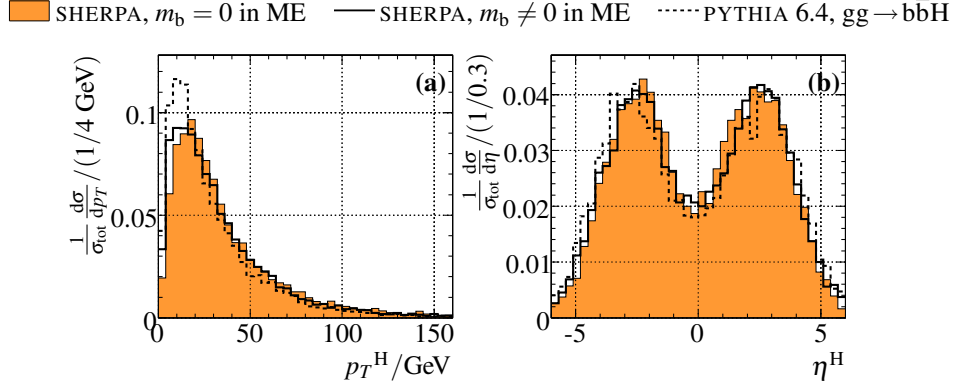


Figure 7.9: Truth differential distributions for $M_H = 150$ GeV. (a) Transverse momentum and (b) pseudorapidity of the Higgs boson. ■: SHERPA 1.0.9, $Q_{\text{cut}} = 15$ GeV, $m_b = 0$ in matrix elements, —: SHERPA 1.0.9, $Q_{\text{cut}} = 15$ GeV, $m_b \neq 0$ in matrix elements,: PYTHIA 6.4, $gg \rightarrow b\bar{b}H$.

7.1.6 Comparison to Theory Predictions

In general, since the two described generators still produce only leading order cross sections, it would be best to normalize the event samples to the cross section obtained by higher order corrections. SHERPA with the CKKW matching algorithm, already in the shape of the differential distributions includes parts of the higher order corrections, in the form of real emission of gluons.

Most important is in this respect the fraction of events that have a b jet at high p_T and in the central detector region, where it can be identified. To check with the theory predictions, the following study is done:

For the Monte Carlo generators, the fraction of events with exactly one b parton or jet with $p_T > 15$ GeV and $|\eta| < 2.5$ is calculated, which corresponds to the phase space inside which a b jet can in principle be reconstructed. The results vary only insignificantly (less than 5%) between a parton level and truthjet level analysis. In the following the truthjet analysis using k_\perp jets as described above is used.

For the theory estimate the cross section for the $bg \rightarrow bH$ process fulfilling the same cuts is calculated using the MCFM program [106, 112], which also uses a k_\perp clustering algorithm in its calculation. The two pdf sets MRST2002 [113] and MRST2004 [114] at NLO accuracy are used. To get a prediction of the one-jet rate, one has to divide by the inclusive cross section. For this the NNLO calculation of the $b\bar{b} \rightarrow H$ process [101] is used. This cross section is available in a parameterized form in FEYNHIGGS for the MRST2002 pdf set, where the NNLO pdf is used as corresponding to the NNLO calculation. In addition to this, the cross section using the MRST2004 pdf set was provided by the authors of [101]. For both calculations the renormalization scale and factorization scales are set to the recommended default of $\mu_r = 4\mu_f = M_H$.

calculation, pdf set	a_0	a_1	$a_2 \cdot 10^2$	$a_3 \cdot 10^4$	$a_4 \cdot 10^6$
$b\bar{b} \rightarrow H$, MRST2002	14.098	-0.83955	1.57237	-1.65728	0.0
$b\bar{b} \rightarrow H$, MRST2004	14.2702	-0.923215	2.41475	-4.30515	3.4509
$bg \rightarrow bH$ MRST2002	12.05	-0.6907	1.009	-0.988	0.09057
$bg \rightarrow bH$ MRST2004	12.19	-0.7096	1.120	-1.293	0.43540

Table 7.1: Parameters for the cross section parametrization for the two pdf sets.

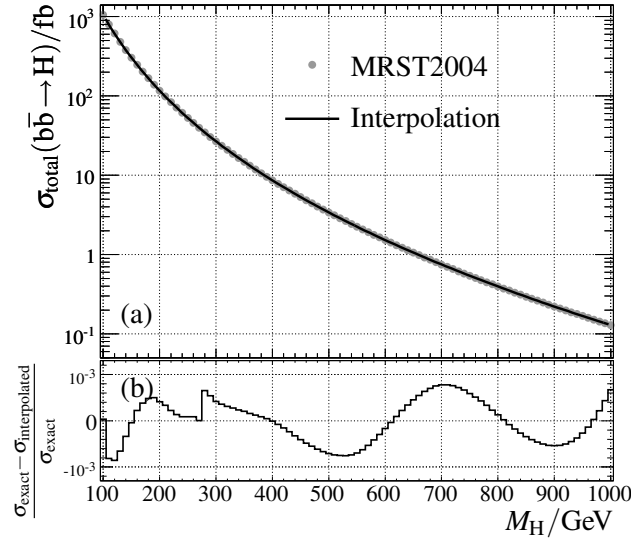


Figure 7.10: (a) Inclusive cross section for $b\bar{b} \rightarrow H$ versus the Higgs boson mass using the MRST2004 pdf set. The gray dots are the numerical results of the calculation in [101], the line shows a fit to this theory prediction. (b) Residuals between the fitted parametrization and the numerical values.

All cross sections were parameterized using the following function:

$$\sigma(m_H) = \exp \left(\sum_{i=0}^4 a_i \cdot \left(\frac{M_H}{\text{GeV}} \right)^{\frac{i}{2}} \right) \text{fb}. \quad (7.1)$$

The parameters are listed in Table 7.1, and Figure 7.10 shows as an example the interpolation of the numerical values for the $b\bar{b} \rightarrow H$ cross section using the MRST2004 pdf set.

The results of this comparison are shown in Figure 7.11 for SHERPA 1.0.9 and PYTHIA 6.4, where both the $gg \rightarrow b\bar{b}H$ process and the $b\bar{b} \rightarrow H$ process have been simulated.

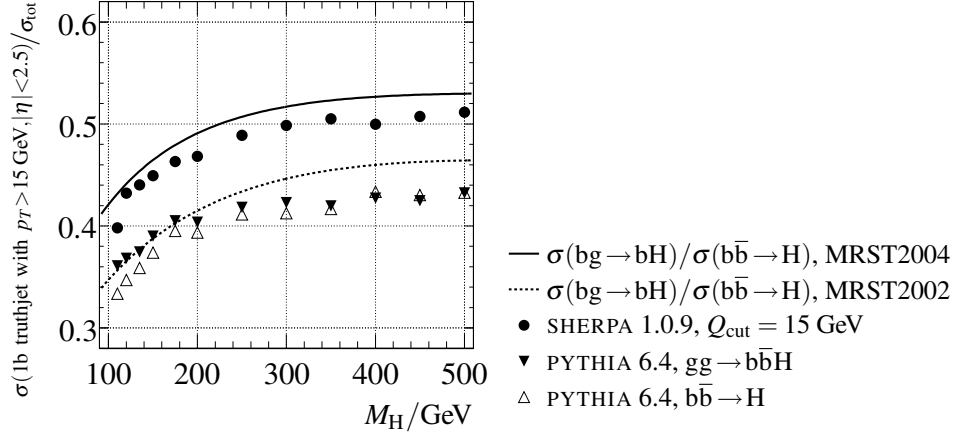


Figure 7.11: Fraction of events with exactly one b jet with $p_T > 15$ GeV and $|\eta| < 2.5$ versus the Higgs boson mass M_H . Circles: Result from Sherpa 1.0.9, $Q_{\text{cut}} = 15$ GeV. Upwards pointing triangles: Pythia 6.4, $b\bar{b} \rightarrow H$. Downwards pointing triangles: Pythia 6.4, $gg \rightarrow b\bar{b}H$. Solid line: $\sigma(gb \rightarrow bH, \text{NLO})/\sigma(b\bar{b} \rightarrow H, \text{NNLO})$ MRST2004, dashed line: same with MRST2002.

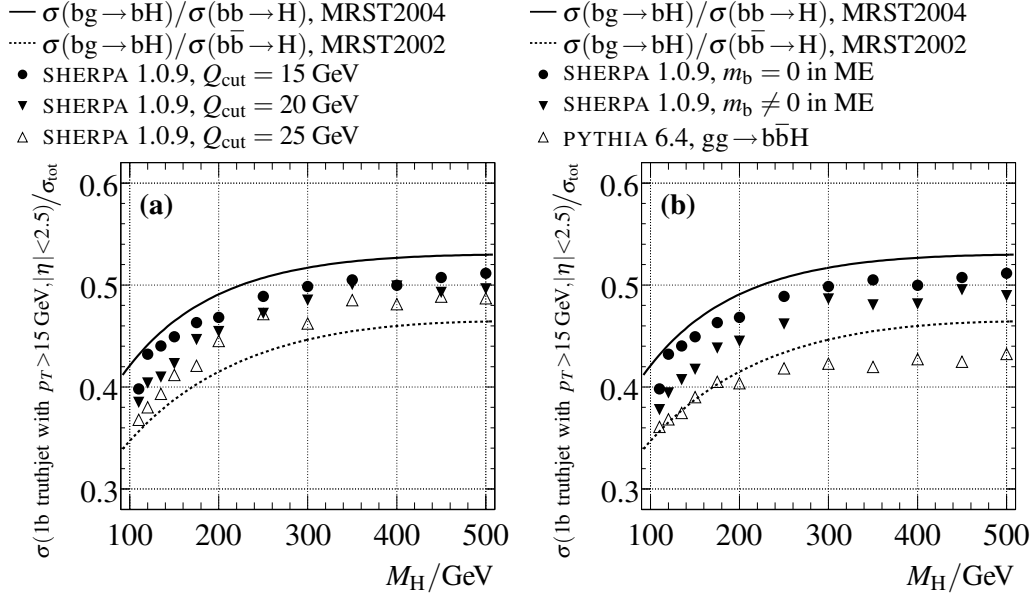


Figure 7.12: Fraction of events with exactly one b jet with $p_T > 15$ GeV and $|\eta| < 2.5$ versus the Higgs boson mass M_H . Solid line: $\sigma(gb \rightarrow bH, \text{NLO})/\sigma(b\bar{b} \rightarrow H, \text{NNLO})$ MRST2004, dashed line: same with MRST2002. Subfigure (a): Circles: Result from Sherpa 1.0.9, $Q_{\text{cut}} = 15$ GeV. Downwards pointing triangles: SHERPA 1.0.9, $Q_{\text{cut}} = 20$ GeV. Upwards pointing triangles: SHERPA 1.0.9, $Q_{\text{cut}} = 25$ GeV. Subfigure (b) Circles: Result from SHERPA 1.0.9, $m_b = 0$ in ME. Downwards pointing triangles: SHERPA 1.0.9, $m_b \neq 0$ in ME. Upwards pointing triangles: Pythia 6.4, $gg \rightarrow b\bar{b}H$.

As expected from the discussed differential distributions, SHERPA gives an about 15% higher one-jet rate than PYTHIA. Compared to the theory prediction, SHERPA seems to be better compatible with the MRST2004 pdf set, while PYTHIA shows better agreement with the prediction using MRST2002. The difference between the two pdf sets comes mainly from the $b\bar{b} \rightarrow H$ calculation. For this calculation, the results from MRST2002 and MRST2004 differ by about 15%. In $b\bar{b} \rightarrow H$ production, the bottom pdf enters the calculation twice and thus quadratically in the uncertainty.

If one takes the difference between the two pdf sets as a systematic uncertainty, one can conclude that both generators, SHERPA and PYTHIA agree with the one-jet rate of the theory predictions within the uncertainties. To rephrase it, the theory uncertainties are too large to discriminate between the two Monte Carlo generators.

However, given the features in the p_T spectra of the SHERPA generator, it has to be kept in mind that if the observed depression is really a region of phase space that is not properly filled, the seemingly larger one-jet rate might actually be a deficit in the zero-jet rate in SHERPA. Within the uncertainties, this cannot be conclusively proven at the moment.

Figure 7.12 (a) shows the dependence of the one-jet rate in SHERPA on the matching scale and Figure 7.12 (b) on the used matrix element description with massive or massless b quarks. Using a larger matching scale slightly decreases the one-jet rate of SHERPA. The same happens if massive b quarks are used in the matrix elements. This behavior matches to the observations in the differential distributions, as shown in Figure 7.7.

7.1.7 Normalization

This study aims at normalizing all used Monte Carlo samples to higher order calculations. It is most convenient to use an inclusive normalization in the b quark multiplicity, as the analysis itself can be divided into subsets containing zero or at least one identified b jet. Furthermore, the SHERPA generator contains at least part of the real emission of higher order calculations and is expected to give quite accurate differential distributions due to the used matrix element parton shower matching. In this sense an inclusive normalization is desirable, because if the shapes of differential distributions are properly described, everything needed is an accurate prediction of the total rate, which is given by the inclusive cross section.

This could be realized by using the $b\bar{b} \rightarrow H$ calculation that is available at NNLO. The scale uncertainties of this calculation reach from about 20% at low Higgs boson masses to 5% or less at high masses [101]. In addition, the difference between the MRST2002 and MRST2004 pdf sets can be used to estimate the pdf uncertainty. This leads to a total uncertainty of 25% to 12%. However, due to the observed feature of SHERPA at the matching scale, the validity of this approach can not be proven unambiguously.

An alternative method would be to normalize to the *exclusive* cross section. This would mean to take the cross section $\sigma_{\text{exclusive}}$ with one b at high transverse momentum and in the central detector region, and normalize the event sample in this region. Taking the fraction

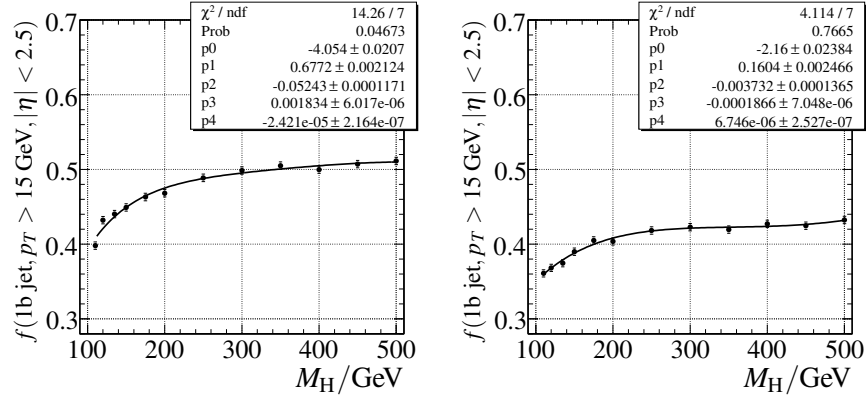


Figure 7.13: Fraction of events with exactly one b truthjet with $p_T > 15$ GeV and $|\eta| < 2.5$. Left: SHERPA 1.0.9 with $Q_{\text{cut}} = 15$ GeV, right: PYTHIA $gg \rightarrow b\bar{b}H$.

f of events fulfilling these cuts, one can get a total cross section by scaling:

$$\sigma_{\text{total}} = \frac{\sigma_{\text{exclusive}}}{f}. \quad (7.2)$$

In doing so, the one-jet rate is normalized correctly even if the matching scale problem has an influence on the total normalization. The uncertainty inflicted by the matching scale problem is in this approach shifted completely to the zero-jet rate, which might be estimated too high. In the following, this additional uncertainty is tolerated, as the more promising search channel is the one with at least one identified b jet.

To estimate $\sigma_{\text{exclusive}}$ the MCFM program (version 5.1) is used with a cut of 15 GeV on the transverse momentum and on $|\eta| < 2.5$ for the b jets. To get a consistent set of parton density functions with some of the background normalizations, the CTEQ6M [115] set is used. This also provides the possibility to estimate the pdf uncertainty since it contains 40 error sets, where parameters are varied. The resulting cross section is parameterized in dependence of the Higgs boson mass. The Higgs boson itself is assumed to have a negligible total width. This is not the case for a Standard Model Higgs boson with masses above twice the W boson mass. For the MSSM Higgs bosons it is a valid approximation for all $\tan\beta$ considered in this study, since the couplings of the heavy Higgs bosons A^0 and H^0 to the gauge bosons are suppressed in this region of parameter space.

The fraction f is determined using a k_{\perp} truthjet algorithm. The same parameterization as for the cross sections is used. Figure 7.13 shows the fitted fraction for SHERPA 1.0.9 with $Q_{\text{cut}} = 15$ GeV and for the PYTHIA $gg \rightarrow b\bar{b}H$ process. The parameterizations fit the discrete points well. This parameterization is only valid in the region $100 < M_H < 500$ GeV.

The theoretical uncertainties are estimated by varying the parameters in the MCFM program. The renormalization and factorization scales $\mu_r = M_H$ and $\mu_f = M_H/4$ are varied independently by a factor of two both in the upwards and in the downwards direction. Raising the renormalization scale results in a higher cross section and vice versa. The opposite

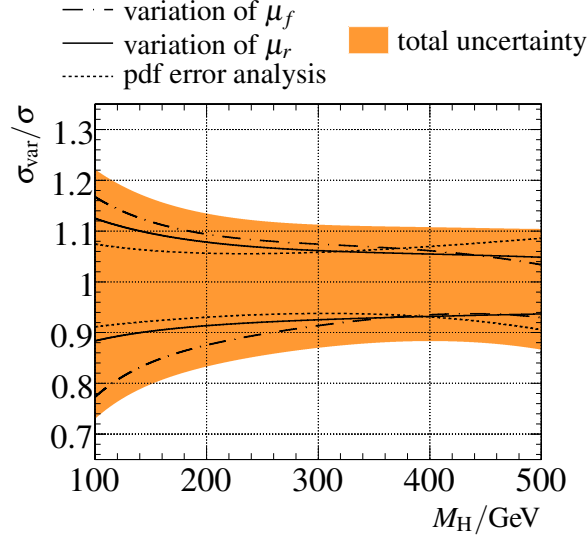


Figure 7.14: Theoretical uncertainties for the exclusive cross section of the $b\bar{g} \rightarrow bH$ process as estimated using the MCFM program in NLO with the CTEQ6M pdf set. Dash-dotted line: Variation of μ_f , solid line: variation of μ_r , dashed line: pdf uncertainty. Orange band: Total uncertainty.

behavior is observed for the factorization scale. The pdf uncertainty can be calculated by MCFM automatically, when the error sets of the CTEQ6M pdf are used. The total uncertainty is estimated by adding all three uncertainties in quadrature. The results are shown in Figure 7.14. For low masses the dominant uncertainty comes from the factorization scale. At high masses, the pdf uncertainty gets most important. The total uncertainty ranges from 20 to 25% at low masses to 10 to 12% at high masses.

Figure 7.15 shows the total cross section from the exclusive normalization in comparison with the NNLO results for $b\bar{b} \rightarrow H$ for the MRST2002 and MRST2004 pdf sets. The resulting total cross section is in excellent agreement with the prediction from $b\bar{b} \rightarrow H$ NNLO using MRST2004. It is slightly lower than the result using MRST2002.

Using this normalization procedure, one can be sure that the normalization of the one-jet sample is methodically correct. As at the moment it is not clear whether the matching scale feature results in a problem with the normalization, an additional systematic uncertainty to the zero-jet normalization has to be applied. For this a 15% uncertainty after all cuts is used, corresponding to the full difference between the inclusive cross sections using MRST2002 and MRST2004. This estimate is conservative, since the efficiency of tagging the low p_T b jets, which are dominating the sample, is rather low. This means that a lot of the b jets with $p_T > 15$ GeV will not be reconstructed as a b jet. This would dilute any normalization bias.

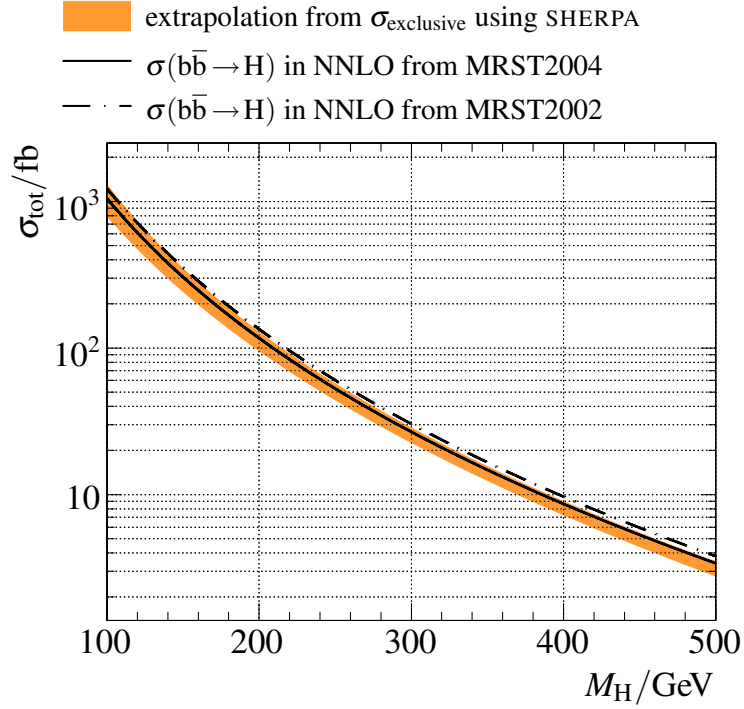


Figure 7.15: Total cross section for b associated Higgs boson production. Orange area: extrapolation from the exclusive cross section (MCFM, CTEQ6M) using the SHERPA one-jet rate. Solid line: $b\bar{b} \rightarrow H$ NNLO using MRST2004. Dash-dotted line: $b\bar{b} \rightarrow H$ NNLO using MRST2002.

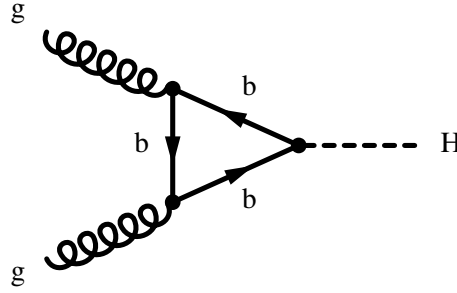


Figure 7.16: Feynman diagram for the direct Higgs boson production involving a bottom quark loop.

7.2 Direct Production

The other important production mechanism for neutral Higgs bosons of the MSSM for large $\tan\beta$ is the gluon-gluon-fusion, that was briefly discussed in Chapter 3. For large $\tan\beta$ the gluon-fusion process can take place via a bottom quark triangle, as shown in Figure 7.16.

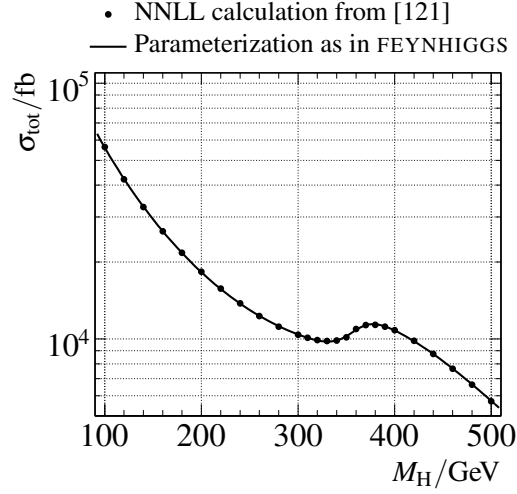


Figure 7.17: Cross section for the direct production of a Standard Model Higgs boson versus its mass. Dots: Values from [121]. Line: Parameterization as in FEYNHIGGS.

Since the direct production of a Higgs boson does not have a b quark in the final state, it is unlikely that such an event results in a jet being tagged as a b jet. This production channel is only relevant for the case where no b-tagged jet is required. As it turns out even in this case, the b associated production mode dominates, as the b jets are generally soft and can a lot of the times not be reconstructed. As a consequence, less emphasis was placed on the description of the direct Higgs boson production.

7.2.1 Monte Carlo Generators

For the direct production, the PYTHIA generator is used for two samples that were processed with the ATLAS detailed detector simulation. In addition, samples using MC@NLO (version 3.1) were generated, using ATLFAST.

7.2.2 Normalization

The first diagram entering the description of the gluon-gluon-fusion process already contains a loop. As a consequence, the higher order corrections are very important, e.g. the k-factor between leading order and next-to-leading order is about a factor of two. The process has been calculated in NNLO in [116, 117]. In Ref. [118] also differential distributions are calculated. In addition to these QCD corrections, electroweak higher order corrections have been calculated in [119, 120].

Within this work, the calculation in Reference [121] is used, which is a NNLL calculation, that is a NNLO result including soft-gluon re-summation. The MRST2002 pdf set was used and the renormalization and factorization scales set equal to the Higgs boson mass. This cross section is also available in a parameterized way in FEYNHIGGS. The values from Ref. [121] are shown along with the parameterization in Figure 7.17. As this

calculation is done for a Standard Model Higgs boson, the diagram involving a top quark loop dominates. The peak in the cross section around twice the top quark mass arises when two of the top quarks can be on their mass shell.

The relative scale uncertainty of this calculation is quoted as around 10% in [121]. In addition, differences between different pdf sets have been observed in [121] that can amount to around 10%. As a conservative estimate, a total uncertainty of 15% is assumed.

7.3 From Standard Model to MSSM

7.3.1 Cross Sections

The cross sections discussed in the previous sections have all been calculated for a Standard Model Higgs boson. These have to be modified to the MSSM case.

- For the b-associated production there are currently no complete supersymmetric corrections available. Instead a simplification is used. It is assumed that everything that is changed in the MSSM compared to the Standard Model are the effective Higgs boson couplings. Getting these from FEYNHIGGS and reweighting the cross sections takes into account vertex corrections from supersymmetric particles. Any corrections in the production mechanism itself are assumed to be negligible. This factorization ansatz has also been taken in [122, 123] and is expected to be a good approximation. It has also been used in the evaluation of the MSSM Higgs boson discovery potential for the ATLAS experiment [54]. In this way, the MSSM cross section can be obtained by scaling with the ratio of the partial widths into $b\bar{b}$ for the MSSM and for a Standard Model Higgs boson of the same mass:

$$\sigma_{b\bar{b}\phi}^{\text{MSSM}}(M_{A^0}, \tan\beta) = \sigma_{b\bar{b}H}^{\text{SM}}(M_\phi) \cdot \frac{\Gamma_{\phi \rightarrow b\bar{b}}^{\text{MSSM}}(M_{A^0}, \tan\beta)}{\Gamma_{H \rightarrow b\bar{b}}^{\text{SM}}(M_\phi)}, \quad \phi \in \{h^0, H^0, A^0\}. \quad (7.3)$$

The partial widths are calculated using FEYNHIGGS 2.6.4.

- For the direct production, a similar approach is used, but in this case the production cross section is taken directly from FEYNHIGGS. It uses the same Standard Model cross section as proposed in Section 7.2.2, but takes into account interference effects between bottom loops and other contributions in a more precise way than simply scaling with the ratio of partial widths. This feature is available in FEYNHIGGS starting in version 2.6.3.

Figure 7.18 shows as an example the production cross sections multiplied by the branching fraction into muons in the M_{h^0} -max scenario in dependence of M_{A^0} for $\tan\beta = 30$ and of $\tan\beta$ for $M_{A^0} = 150$ GeV.

The direct production cross section is significantly lower than the b-associated one. Although the cross section of the h^0 in the direct production seems to stay constant for large M_{A^0} , it has to be noted that the h^0 stays at the same mass for large M_{A^0} , and its

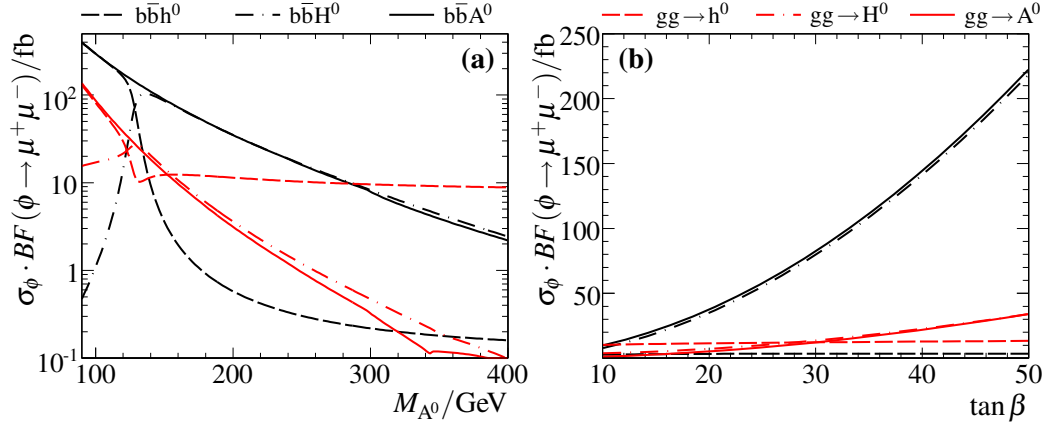


Figure 7.18: Production cross section times branching fraction into $\mu^+\mu^-$ of the neutral MSSM Higgs bosons in the M_{h^0} -max scenario vs. (a) M_{A^0} for $\tan\beta = 30$ and (b) $\tan\beta$ for $M_{A^0} = 150$ GeV. Solid lines: A^0 , dashed lines: h^0 , dash-dotted lines: H^0 . Black: b-associated production, red: direct production.

production cross section is more than one order of magnitude smaller than the b-associated cross section of the A^0 if it has approximately the same mass.

The dependence on $\tan\beta$ nicely shows the proportionality of the production cross section to $\tan^2\beta$.

7.3.2 Masses and Widths

For the PYTHIA event samples, the total decay widths of the generated A^0 resonances are calculated using the MSSM implementation in PYTHIA itself and the MSSM Higgs bosons are generated directly in PYTHIA. It should be noted that apart from the different widths, PYTHIA generates events according to the same matrix element as for the scalar Standard Model Higgs boson, also if a pseudoscalar A^0 is generated.

For the SHERPA and MC@NLO samples, Standard Model Higgs bosons are generated. As both generators allow to manually enter the Higgs boson decay width, the values obtained from FEYNHIGGS are used, so that in fact a Standard Model Higgs boson with the width of the corresponding MSSM Higgs boson is generated. Any possible differences in angular distributions due to the different CP quantum number of the A^0 are assumed to be negligible.

7.4 Higgs Boson Decay Channels

The Higgs bosons of the MSSM that are produced with a reasonable rate in the b-associated production couple strongly to down-type fermions. As shown in Chapter 2, the following decay channels are most important:

- $h^0/A^0/H^0 \rightarrow b\bar{b}$ has a branching fraction of about 90% for the Higgs bosons that are mass degenerate. However, this is a completely hadronic final state, which will make triggering on the signal events rather difficult. Also, the background from QCD multijet events is very large, and the invariant dijet mass resolution is moderate.
- $h^0/A^0/H^0 \rightarrow \tau\tau$ has a branching fraction of about 10%. It allows to trigger on the tau decay products efficiently and the QCD background is much lower. However, as in the decays of tau leptons always neutrinos appear, the reconstruction of the Higgs boson mass is difficult and depends on a good measurement of the missing transverse energy. This leads to a rather poor mass resolution of the order of a few ten percent.
- $h^0/A^0/H^0 \rightarrow \mu^+\mu^-$ has only branching fractions of the order of 10^{-4} , but in this channel a very clear signature is available. In addition, the mass resolution for a dimuon invariant mass is very good, so the Higgs boson mass can be reconstructing very accurately. This helps to reduce the background to acceptable levels.

7.5 Signal Characteristics

In the previous sections the main signatures of the signal process have already been shown:

- Two muons with opposite charge and high transverse momentum, that are isolated from other activity in the event, since they come from the Higgs boson decay. In contrast to this, muons coming from the decay of a hadron are expected to be within jets and are surrounded by hadronic activity. Since the Higgs boson has a low transverse momentum, the two muons in general have a large opening angle in the xy plane.
- No missing transverse energy since no hard neutrinos are involved.
- One or two b jets, mostly with low transverse momenta, except in the gluon-gluon-fusion production mode.
- No additional high p_T jets.

Figure 7.19 shows an event display of a simulated signal event for $M_{A^0} = 200$ GeV in the xy and Figure 7.20 in the ρz plane. Subfigures (a) show the complete ATLAS detector and subfigures (b) a closeup of the calorimeters and the inner detector. The detector components are labeled. Reconstructed tracks in the inner detector are marked in light blue, energy in the calorimeters in yellow, hits in the precision muon chambers in gray and hits in the trigger chambers in red. Only tracks with a minimal transverse momentum of 500 MeV are shown. This event has been simulated with PYTHIA 6.4 and includes pileup and cavern background for low luminosity running conditions ($L \approx 10^{33} \text{ cm}^{-2} \text{ s}^{-1}$). The two reconstructed muons are marked in red and green. The seemingly large occupancy, especially in the muon system, comes from the inclusion of pileup and cavern background, since the MDTs integrate over several bunch crossings. Nevertheless, due to the high granularity it is still possible to reconstruct the muon tracks. The event contains three reconstructed jets with a transverse momentum of at least 20 GeV. The jet directions are marked in the upper pictures. Two of these have indications of being a b jet. The third jet is at low transverse momentum and is most likely coming from pileup. The missing transverse energy is around 12 GeV, which is within the resolution very well compatible with zero.

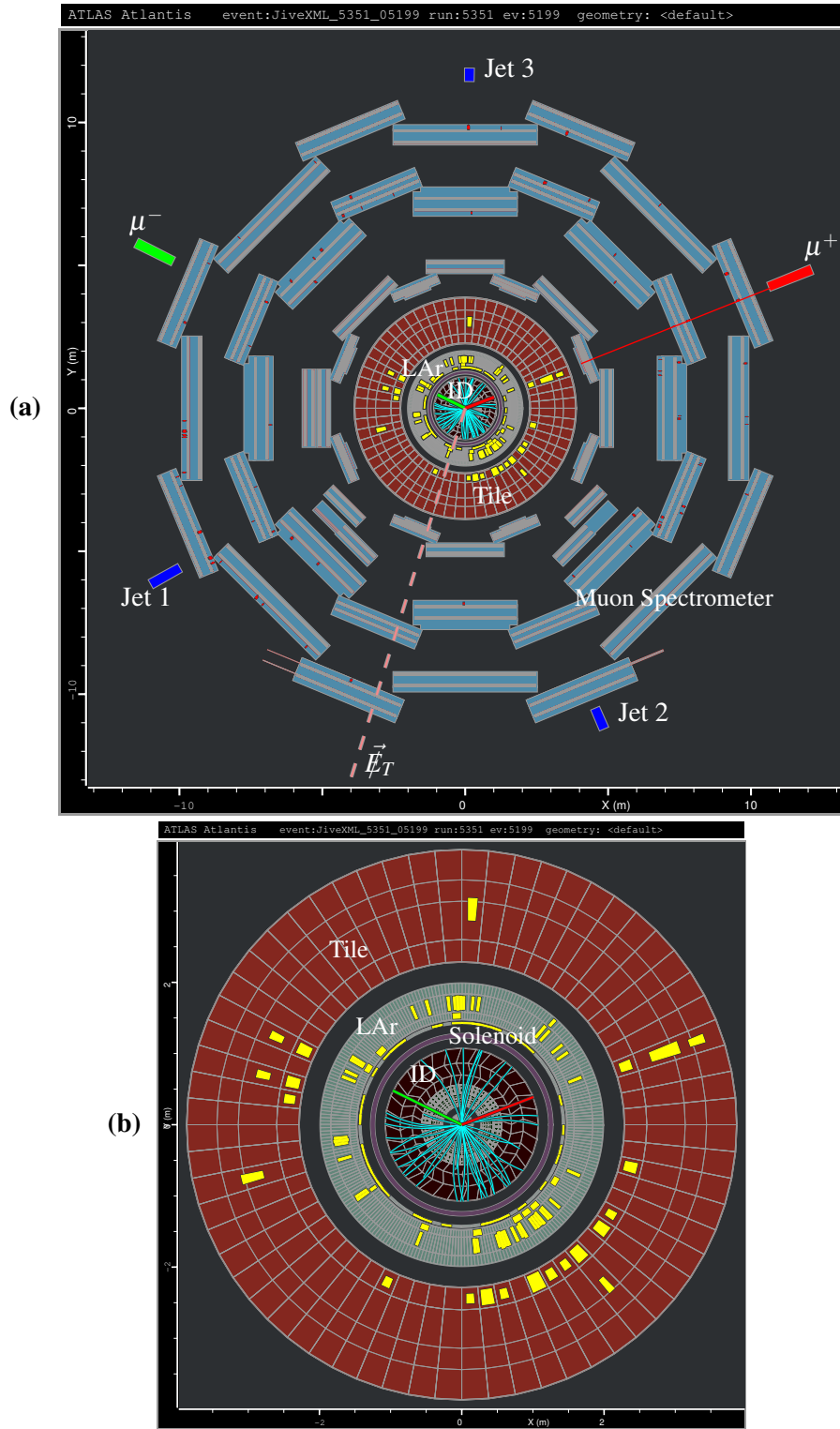


Figure 7.19: Event Display of a simulated $b\bar{b}A^0$ event in the xy -plane.

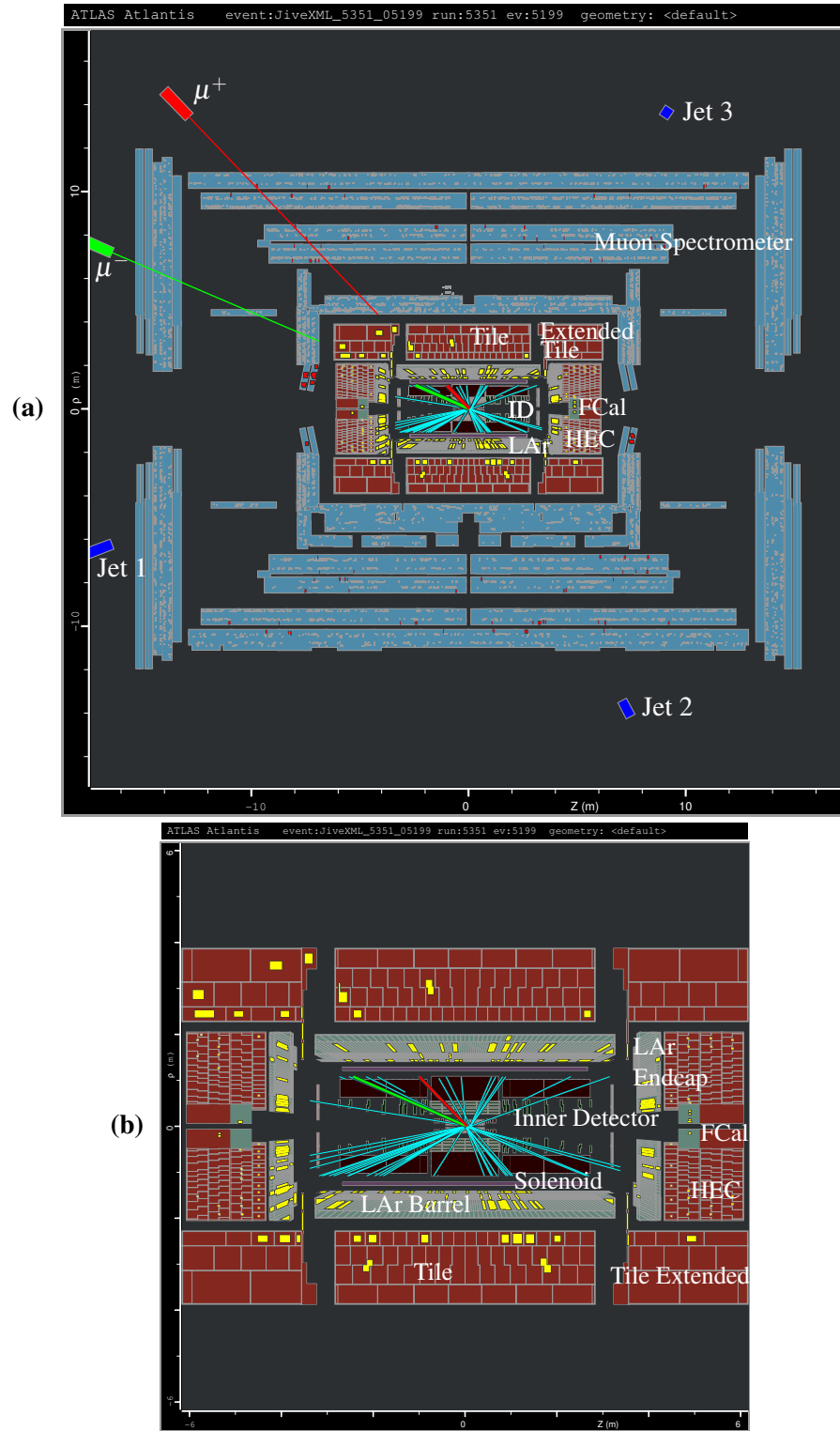


Figure 7.20: Event Display of a simulated $b\bar{b}A^0, A^0 \rightarrow \mu^+\mu^-$ event in the ρz -plane.

“O who knows what slumbers in the background of the times?”

Friedrich von Schiller, 1759–1805, *Don Carlos*, Act I, sc. i

8

Background Processes

In this chapter, the relevant background processes for the analysis of b-associated Higgs boson production in the MSSM are discussed. The Monte Carlo generators used to simulate these processes and the used normalizations are presented.

In deciding whether a Standard Model or MSSM process is a relevant background, one has to consider both its event topology and cross section. To qualify as a possible background process, there has to be a non-negligible probability that the signal topology is faked. One has to reconstruct two isolated muons with high transverse momentum, no significant missing transverse energy, and at least one jet. Since also light and charm jets can be misidentified as a b jet, these jets are a relevant background source.

The background processes can be sorted into two categories:

- Reducible backgrounds, which are backgrounds only because of experimental difficulties to distinguish them from the signal process, e.g. mistagging of light jets or a finite resolution of the measurement of missing transverse energy.
- Irreducible backgrounds on the other hand share almost all the properties of the signal, and can in principle never be fully reduced.

8.1 $Z^0 + \text{Jet}$ Background

A very important source of background is the production of a Z^0 boson¹ along with jets. Selected Feynman diagrams for this process are shown in Figure 8.1.

The Z^0 boson decays in about 3.37% of all cases into a $\mu^+\mu^-$ pair [3]. It has a total width of about 2.5 GeV [3], and since also a virtual γ can be produced instead of the Z^0 , the invariant mass of this $\mu^+\mu^-$ pair can be larger than the nominal mass of the Z^0 of 91.18 GeV. No neutrinos are produced, so no significant missing transverse energy is expected. In addition, one of the produced jets might be identified as a b jet, either due to misidentification of a light or charm jet, or because it is a real b jet.

¹In the following it is implied that a γ can be produced instead of the Z^0 . In fact the complete interference structure between the Z^0 and γ has been taken into account in the used Monte Carlo generators.

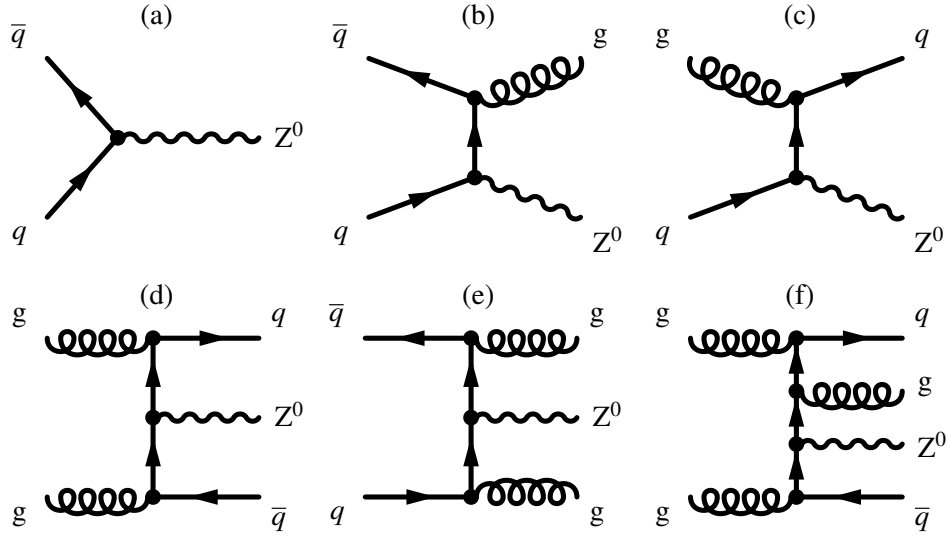


Figure 8.1: Selected Feynman diagrams for the production of a Z^0 boson together with 0, 1, 2 or 3 Jets.

8.1.1 Z^0 + light and charm Jet

In case that the jet produced along with the Z^0 boson is a light flavor or charm jet, this can fake the signal signature if the jet is misidentified as a b jet. Just as in the signal case, the produced jets in general have a low transverse momentum.

Monte Carlo Generator

This background is simulated using the SHERPA 1.0.9 event generator, because it can combine the different jet multiplicities in a consistent way, as described in Chapter 6. The standard settings of SHERPA are used, with the exceptions as described in Chapter 6. Up to three final state partons (no b quarks) are allowed in the matrix element, which means that higher multiplicities are populated exclusively by the parton shower. The matching scale is set to 20 GeV. To increase the fraction of events in which both muons are within in the detector acceptance, the muons from the Z^0 decay were required to be within $|\eta| < 3$ and to possess $p_T > 5$ GeV. In addition the invariant dimuon mass is required to be above 60 GeV.

Normalization

Studies at the DØ experiment [124] have shown that the SHERPA generator describes the properties of jets in Z^0 + jets events very well after normalizing to the total cross section. In this work, the Z^0 + jets background is normalized to the NLO cross section for inclusive Z^0 production as calculated by the MCFM program [112]. The MCFM program allows to place the same cuts on the muons originating from the Z^0 decay as those made in the

	$M_{\mu\mu} > 60 \text{ GeV}$ $p_T > 0 \text{ GeV}, \eta < \infty$	$M_{\mu\mu} > 60 \text{ GeV}$ $p_T > 5 \text{ GeV}, \eta < 3$	Ratio
	σ_{all}	σ_{reduced}	$\frac{\sigma_{\text{all}}}{\sigma_{\text{reduced}}}$
SHERPA 1.0.9	1322 pb	758 pb	1.75
MCFM 5.1, $Z^0 + X$, NLO	2021 pb	1190 pb	1.70

Table 8.1: Cross sections as obtained by the SHERPA generator for $Z^0 + 0 - 3$ jets and by the MCFM program, version 5.1.

event generation step. The CTEQ6M pdf set is used and the renormalization scale μ_r and factorization scale μ_f are set to the default value of M_{Z^0} . The cross sections as given by SHERPA and by MCFM are listed in Table 8.1.

The SHERPA cross sections are lower by a factor of about 1.5 compared to the NLO result. As these are leading order cross sections with a particular scale choice in the CKKW matching procedure, it has to be concluded that the SHERPA cross section should be replaced by the cross section from MCFM. Table 8.1 also shows the ratios of the cross sections with and without additional cuts on the muons. The difference amounts to about 2.5%, which is negligible compared to the theoretical uncertainties which are evaluated on the following.

The theoretical uncertainties are evaluated using the MCFM program, where the scale and pdf uncertainties are estimated by variation. For the pdf uncertainty the 40 error sets of the CTEQ6M pdf are used. This calculation is provided within MCFM. The resulting total pdf uncertainty is about 4%.

The scale uncertainties are estimated by varying the renormalization and factorization scales. The results are shown in Figure 8.2. Since the dependence on the renormalization and factorization scales is an artifact of the finite order of the calculation, the range used to estimate the uncertainties is arbitrary. To get an estimate, the cross section values at half and double the default scale choices are used.

The cross section used in this analysis for the $Z^0 + \text{light}$ background is:

$$\sigma_{Z^0 + \text{light, charm}} = 1190_{-14}^{+18}(\mu_r)_{-62}^{+38}(\mu_f)_{-70}^{+59}(\text{pdf}) \text{ pb} = 1190_{-94}^{+73} \text{ pb} \quad (8.1)$$

This number already includes the branching fraction of the Z^0 into a muon pair. The branching fraction as it is implemented into MCFM is within 1% of the world average of 3.366% [3], which is negligible compared to the theoretical uncertainties. The used cross section also agrees with NNLO cross sections from FEWZ [125] and a NNLO calculation in Ref. [126].

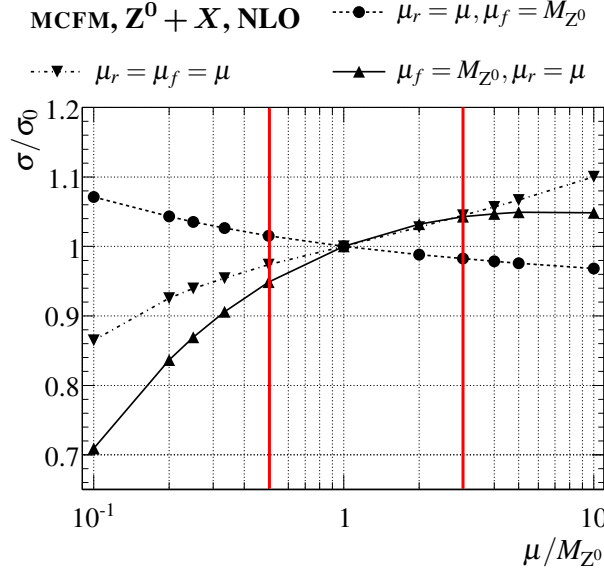


Figure 8.2: Dependence of the inclusive Z^0 production cross section computed by MCFM on the assumed renormalization μ_r and factorization scale μ_f . Dashed line with circles: variation of μ_f , solid line with upwards pointing triangles: variation of μ_r , dash-dotted line with downwards pointing triangles: simultaneous variation of μ_r and μ_f from the default value of M_{Z^0} . The red lines indicate the range used to estimate the uncertainties.

8.1.2 $Z^0 + b$ Jet

A special class of the Z^0 production background is the case where the Z^0 is produced in association with a b quark, since this constitutes an irreducible background to the signal process. In principle, it would have been possible to generate this background along the $Z^0 +$ light and charm jet background, by just including also the b quark in the matrix elements of the SHERPA generator. However, to get an increased statistics of the irreducible background, it is generated separately.

Monte Carlo generators

Event samples of this background can be generated using two different Monte Carlo generators. These are:

- The SHERPA generator is used with the same settings as for the signal process using massive b quarks in the matrix elements. Up to three outgoing strongly interacting particles are allowed in the matrix-element. All matrix-elements including in- or outgoing b or \bar{b} quarks are included. A mass cut on the invariant mass of the two muons is placed at 60 GeV. In addition, the muons are confined to be within $|\eta| < 3.0$ on matrix-element level to increase the fraction of events with both muons inside the

detector acceptance. The leading order cross sections of SHERPA are 30.7 pb with and 36.6 pb without the cut on $|\eta|$.

- ACERMC [88] is a matrix-element generator that can generate $Z^0 + b$ events. The parton-shower, underlying event and hadronization are later added using the PYTHIA generator. ACERMC has two different processes implemented:
 - The first consists of the leading order massive matrix-elements for the $gg \rightarrow Z^0 b \bar{b}$ and $q\bar{q} \rightarrow Z^0 b \bar{b}$ processes, which are most reliable if both b quarks have high p_T , see Chapter 7. Including a mass cut on the dimuon mass, this process yields a cross section of 28.1 pb.
 - The other process is a matched description of the $b\bar{b} \rightarrow Z^0$ and $bg \rightarrow Z^0 b$ processes [127], which is in the following called $Z^0 \oplus b$. Its cross section including the mass cut amounts to 63.8 pb. This process was not used for the analysis, but is mentioned here for completeness.

Figure 8.3 shows the differential distributions on parton level of the three different approaches.

SHERPA tends to slightly softer distributions in both the transverse momentum of the Z^0 and the leading b quark. However, the distribution of the leading b quark shows as for the signal process a dip around the matching scale that was chosen to be 15 GeV, see Chapter 7. For the subleading b quark, SHERPA shows a harder spectrum than both ACERMC processes. The matched $Z^0 \oplus b$ process of ACERMC has the softest spectrum of the sub-leading b quark, which is to be expected, since in this description the second b quark has to get its transverse momentum from the parton shower alone.

The two processes used in this analysis, SHERPA and ACERMC $gg/q\bar{q} \rightarrow Z^0 b \bar{b}$ show satisfactory agreement in the differential distributions.

Normalization

As for the signal process, it would be best to normalize to the inclusive cross section to produce a Z^0 together with b quarks. However, this calculation is not available at higher orders of perturbation theory. The reason for this difference to the signal process is that the Z^0 couples to light quarks with a similar coupling strength as to the b quark, which leads to additional diagrams compared to the case of the b associated Higgs boson production. These additional diagrams need to be computed using massive b quarks. No NLO calculations of these are available today. Instead, other possibilities for normalization are explored:

1. Use the same k -factor as for $Z^0 + \text{light}$ production. For the light jet case the SHERPA cross section had to be multiplied by a factor of 1.54, which can also be called a k -factor between the leading order cross section as given by SHERPA and the NLO cross section as given by MCFM. If one assumes that the b quark associated Z^0 production has similar NLO QCD corrections, one could use the same k -factor here:

$$\sigma_{\text{same } k\text{-factor}} = 47.3^{+2.9}_{-3.7} \text{ pb} \quad (8.2)$$

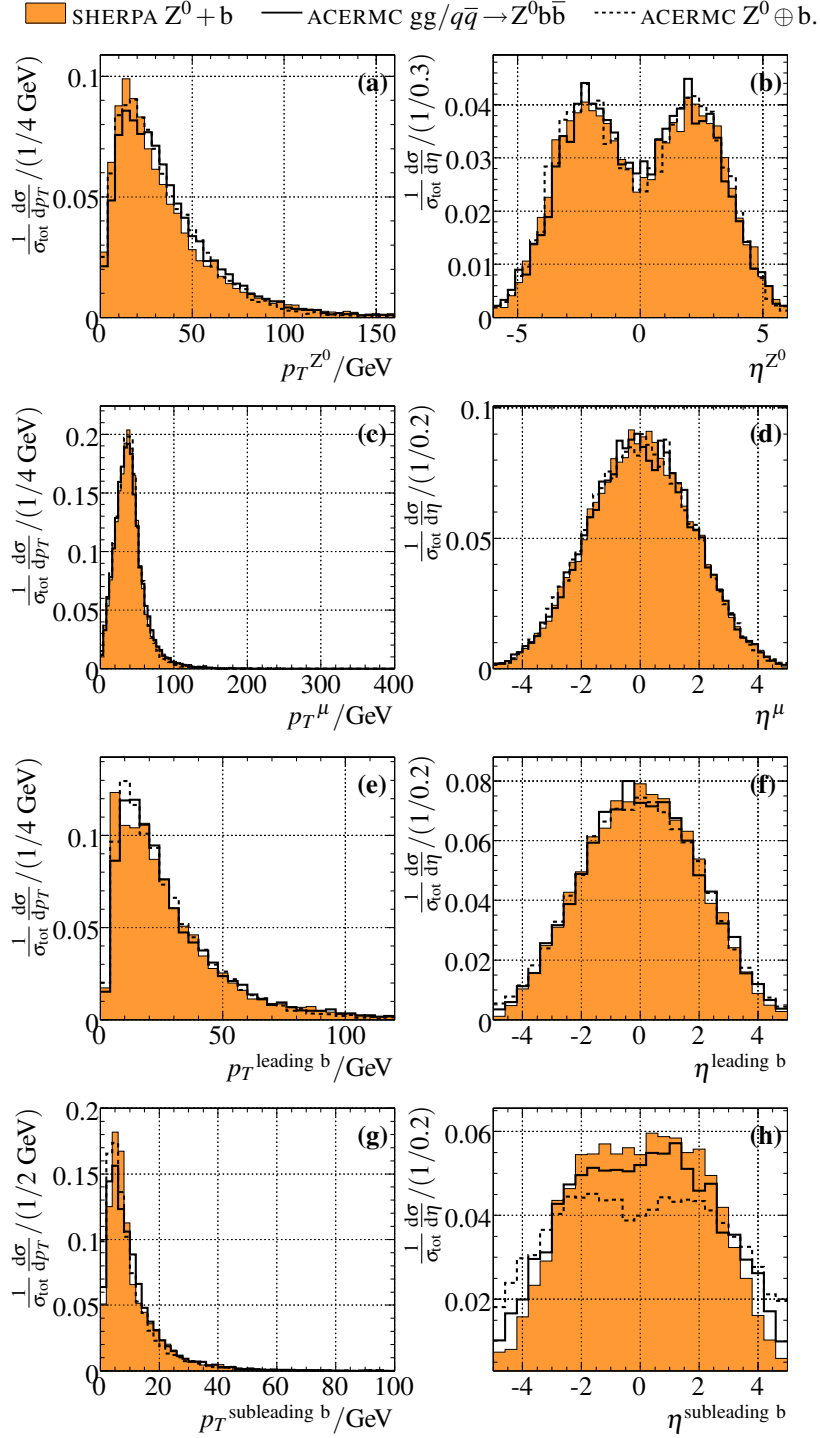


Figure 8.3: Truth differential distributions for $Z^0 + b$ background processes. (a) Transverse momentum and (b) pseudorapidity of the Z^0 boson, (c) and (d) of the muons from the Z^0 boson decay, (e) and (f) of the leading b quark, (g) and (h) of the sub-leading b quark. ■: SHERPA $Z^0 + b$, —: ACERMC $gg/q\bar{q} \rightarrow Z^0 b\bar{b}$,: ACERMC $Z^0 \oplus b$.

Process	order	cross section/pb
$b\bar{b} \rightarrow Z^0$	NNLO	1500
$q\bar{q} \rightarrow Z^0 b\bar{b}$	LO	120
$qb \rightarrow Z^0 qb$	LO	430
Sum		2050

Table 8.2: Inclusive cross sections for Z^0 production in association with b quarks as calculated in Ref. [128].

2. Use an inclusive cross section where part of the calculation is leading order. Reference [128] gives the inclusive production cross section of a Z^0 boson and a heavy quark. Here the process $b\bar{b} \rightarrow Z^0$ has been calculated in NNLO. The scale dependence of this cross section turns out to be very small. The additional processes $q\bar{q} \rightarrow Z^0 b\bar{b}$ and $qb \rightarrow Z^0 qb$ have been included only in leading order approximation, but integrated over the whole phase space to get an inclusive cross section. The numerical values are given in Table 8.2. As no scale uncertainties for the leading order cross

sections are given in Ref. [128], the theory uncertainty for the leading order part is assumed to be 50%, which is a conservative uncertainty for leading order cross sections. Taking the branching fraction of the Z^0 to $\mu^+\mu^-$ into account, one gets the inclusive cross section:

$$\sigma_{Z^0+(b)} = 75 \pm 8 \text{ pb} \quad (8.3)$$

To normalize the SHERPA event sample to this cross section, the additional cut on the muon pseudorapidity has to be taken into account and the accepted cross section is scaled down to:

$$\sigma_{Z^0+(b)}^{|\eta^\mu| < 3.0} = 63 \pm 7 \text{ pb}, \quad (8.4)$$

which is within two standard deviations compatible with using the same k-factor as for inclusive Z^0 production, especially when it is taken into account that no pdf uncertainties have been evaluated.

3. Normalize to the exclusive cross section. When calculating the exclusive cross section, where at least one b quark is required to be within the detector acceptance, it is possible to calculate the cross section in NLO accuracy. The results used here have been taken from Ref. [129], where the cross sections for the processes $gb \rightarrow Z^0 b$ and $q\bar{q} \rightarrow Z^0 b\bar{b}$ have been calculated requiring at least one b quark with a transverse momentum of 15 GeV or more and within $|\eta| < 2.5$, using the CTEQ6M pdf set. The

sum of the two cross sections is:

$$\sigma_{Z^0+\geq 1b, p_T > 15 \text{ GeV}, |\eta| < 2.5} = 1090_{-60}^{+70}(\mu_r)_{-100}^{+70}(\mu_f)_{-50}^{+30}(\text{pdf}) \text{ pb}, \quad (8.5)$$

where the uncertainties come from varying the renormalization and factorization scales and from the pdf error analysis. To normalize the SHERPA and ACERMC samples used, the fraction f of the events fulfilling the same phase space cut have to be determined in the event samples. This is done both on parton level and on the level of k_\perp truth jets that were matched within $\Delta R < 0.4$ to a b quark. Both results are found to be compatible, while the difference is used as an additional systematic uncertainty. The fractions are found to be:

$$f(\text{SHERPA}) = 0.59 \pm 0.03 \quad (8.6)$$

$$f(\text{ACERMC}) = 0.60 \pm 0.05 \quad (8.7)$$

Using these scale factors, the total cross sections including the branching fraction of the Z^0 to $\mu^+\mu^-$ are determined to be:

$$\sigma(\text{SHERPA}) = 52.3_{-6.6}^{+5.6} \text{ pb} \quad (8.8)$$

$$\sigma(\text{ACERMC}) = 61.1_{-8.8}^{+7.7} \text{ pb}, \quad (8.9)$$

where all uncertainties have been added in quadrature and the cross section for SHERPA takes the cut on the muons pseudorapidity into account. The cross section obtained in this way is within the uncertainties compatible with the one obtained from the other two approaches.

In the following, the result from the exclusive normalization (method 3) is used, since it provides the whole theory uncertainty. In addition any problems with the dip in the p_T distribution of the leading b quark are accounted for and in this way it is made sure that the cross section with one observable b quark is described adequately, just as for the signal process.

8.2 W + Jet Background

Instead of a Z^0 , also a W boson can be produced. The inclusive cross section for W production is predicted to be about a factor of ten higher than for Z^0 production. However, the W boson can decay only into a muon and a neutrino. To contribute to the background, a second muon would need to be reconstructed in the event. As described in Chapter 9, the rate of fake muons is very low. Consequently, the second muon would need to be a real muon, e.g. from the decay of a heavy flavor hadron. But in this case the muon is expected to be at small transverse momenta and non-isolated in the detector. In the following, it is assumed that the contribution of W production to the background is negligible.

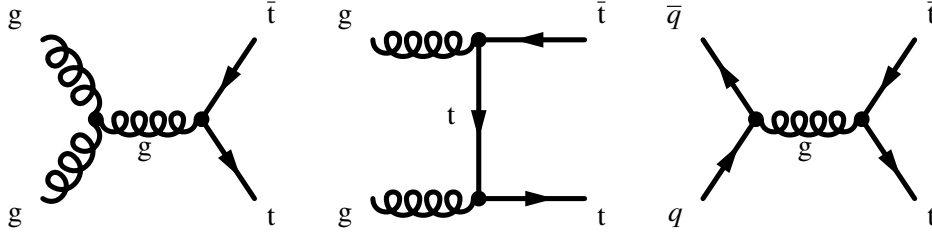


Figure 8.4: Leading order Feynman diagrams for $t\bar{t}$ production.

8.3 Top Pair Production

Another important background is the production of top quark pairs. The leading order Feynman diagrams for this process are shown in Figure 8.4.

Within the Standard Model the top quark decays with a branching fraction of almost 100% into a W boson and a bottom quark. The W boson can decay into a fermion anti-fermion pair. Its branching fractions are listed in Table 8.3.

In case both W bosons decay into muons, the final state signature of $t\bar{t}$ production can consist of two isolated muons with a high transverse momentum, and one or more b jets. The main difference to the signal process is the presence of neutrinos in the final state, leading to significant missing transverse energy. In addition to muons coming from W boson decays, muons can also originate from τ decays, where the τ leptons themselves come from the decays of a W boson. Also, mesons and baryons containing b quarks decay in around 10% of the cases into a muon.

The top quark pair production is simulated with the MC@NLO event generator (version 3.1).

MC@NLO gives an NLO $t\bar{t}$ production cross section of 774 pb. This agrees within the uncertainties with an NLO calculation in Ref. [130] yielding 794.1 ± 32 pb, where the MRST2002 pdf was used and the quoted uncertainty corresponds to the scale dependence. In Ref. [130] also the next-to-next-to-leading order soft gluon corrections are calculated (which is referred to as NLO+NNLL). The resulting cross section is 872.8 ± 15 pb, where again only the scale uncertainty is considered. Another calculation including the resummation of the next-to-leading logarithms (NLO+NLL) is given in Ref. [131] as 833^{+52}_{-39} pb, where again only the scale uncertainty is given.

Following the recommendation of the ATLAS top quark analysis group, the latter cross section is adopted, where the theory uncertainty is inflated to 12% to account also for pdf

Decay mode	$e^- \bar{\nu}_e$	$\mu^- \bar{\nu}_\mu$	$\tau^- \bar{\nu}_\tau$	hadrons
Branching fraction/%	10.75 ± 0.13	10.57 ± 0.15	11.25 ± 0.20	67.60 ± 0.27

Table 8.3: Branching fractions of the W^- boson. The branching fractions of the W^+ decay modes are the charge conjugates of the shown modes (from [3]).

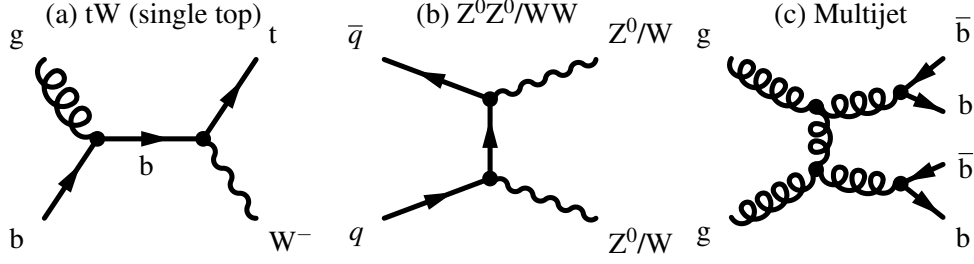


Figure 8.5: Selected Feynman diagrams for (a) single top production (tW), (b) $Z^0 Z^0$ production, (c) multijet heavy flavor production.

uncertainties:

$$\sigma_{pp \rightarrow t\bar{t}} = 833 \pm 100 \text{ pb.} \quad (8.10)$$

It should be noted that the used version of MC@NLO in combination with JIMMY does not allow to specify the W boson decay modes to be simulated. Instead, event filters are used to enhance the number of signal like events before detector simulation.

8.4 Single Top Production

Less important than the top quark pair production is the electroweak production of top quarks. The relevant Feynman diagram is shown in Figure 8.5 (a). Including the decay of the top quark, two W bosons are present which can lead to a $\mu^+ \mu^-$ pair². It has to be noted that the tW process shares the same final state as $t\bar{t}$ production, $W^+ W^- b\bar{b}$, where the \bar{b} comes from the gluon splitting in the proton that produced the b quark. In principle the complete six fermion final state has to be considered as a whole to get a correct prediction. This is not yet implemented into Monte Carlo generators.

The tW process is simulated using the TOPREX generator [89], version 4.11 with the renormalization and factorization scale set to $m_t/\sqrt{2}$. The parton shower, underlying event and hadronization are added using PYTHIA.

The production cross section as given by TOPREX is 56.54 pb. Instead of using this leading order cross section, the NLO+NLL cross section as calculated in Ref. [132] is used:

$$\sigma_{tW} = 66 \pm 2 \text{ pb} \quad (8.11)$$

8.5 $Z^0 Z^0$ Production

The pair production of Z^0 bosons, as shown in Figure 8.5 (b), where one Z^0 decays into a $\mu^+ \mu^-$ pair and one into a $b\bar{b}$ pair, is a possible background source. However, the produc-

²There are two further single top quark production processes, the s-channel and the t-channel, but neither of these two has two W bosons in the final state.

tion cross section is rather low, especially when compared to the much more important $Z^0 + \text{jets}$ background. The $Z^0 Z^0$ background was simulated using PYTHIA. One Z^0 was forced to decay into $\mu^+ \mu^-$ and the other to $b\bar{b}$ for a dataset in FULLSIM. A larger ATLFast dataset, where the second Z^0 was forced to decay into all accessible quark flavors was simulated to also estimate the contribution of this background to the analysis part requiring no identified b jet.

The Monte Carlo datasets are normalized using the NLO calculation in [133], where the cross section is given as 16.3 pb. Using the branching fractions of the Z^0 into muons, hadrons, and b pairs, yields the following cross sections:

$$\sigma_{pp \rightarrow Z^0 Z^0 + X \rightarrow \mu^+ \mu^- b\bar{b} + X} = 0.17 \pm 0.03 \text{ pb} \quad (8.12)$$

$$\sigma_{pp \rightarrow Z^0 Z^0 + X \rightarrow \mu^+ \mu^- q\bar{q} + X} = 0.77 \pm 0.15 \text{ pb} \quad (8.13)$$

A theory uncertainty of 20% on these cross sections is assumed, which is a conservative estimate compared to Ref. [133]. This background is of very small relevance after analysis cuts, even a 100% uncertainty would have no influence on the results presented in this thesis.

8.6 WW Production

A pair of W bosons can also be produced via diagrams as in Figure 8.5 (b). The cross section for W pair production is much larger than for Z^0 pair production, and in addition the branching fraction into muons is larger for the W than for the Z^0 . But as the W decays into a muon and a muon neutrino, there is missing transverse energy in the event. Also, there are no b jets to be expected. Correspondingly this background will only contribute in the case when no b jet is required.

W W production was simulated using the HERWIG [85] generator, version 6.510. The normalization was done to the NLO cross section, which is given in [133] as:

$$\sigma_{WW} = 121 \pm 24 \text{ pb} \quad (8.14)$$

An uncertainty of 20% is assumed, considering that the importance of this background is very low after analysis cuts are applied. The inclusion of this background has only a small influence on the results of this study.

8.7 Multijet Background

One possible background source, the QCD production of multijet events could not be simulated for this work. This can be a source of background especially in the case of the production of heavy flavor quarks, as shown in Figure 8.5 (c). The hadrons emerging from the produced b quarks after hadronization can decay into muons. But as these muons are

inside a jet, they can be suppressed by requiring the muons to be isolated. In addition, the muons from heavy quark decays have a low transverse momentum and consequently the dimuon mass will tend to be very low compared to the signal. Requiring a jet to be tagged as a b jet will reduce this background even further. However, due to the large cross section of QCD multijet production, it is not possible to generate enough Monte Carlo events to investigate this background and it is only assumed to be negligible. In practice, it will be necessary to estimate this background contribution directly from data.

“Peace is not unity in similarity but unity in diversity, in the comparison and conciliation of differences.”

Mikhail Gorbachev, 1931–present

9

Event Reconstruction

Just as in the real experiment, the Monte Carlo events are passed on to the ATLAS reconstruction software. As pointed out previously, the detailed simulation (FULLSIM) is very CPU intensive. As a consequence, it is not possible to process a sufficient number of events in FULLSIM, especially for the background processes due to their large cross sections. For the $Z^0 + \text{light background}$, a Monte Carlo sample corresponding to an integrated luminosity of 30 fb^{-1} would have to contain about 30 million events, corresponding to about 50 CPU years and in addition a very large amount of disk space would be needed. Instead, within this study, the $Z^0 + \text{light background}$ has almost exclusively been processed using ATLFast. ATLFast is known to be only an approximation of the detailed simulation and reconstruction of the ATLAS detector. Furthermore, recent changes in the simulation are not yet reflected within the parameterizations in ATLFast.

Nevertheless, this work needs to make use of ATLFast to obtain meaningful results that are not made useless by too small Monte Carlo statistics. In this chapter, the reconstruction performances of the main physics objects of interest, that are muons, jets, b jets, and missing transverse energy, for this study are reviewed. In addition to FULLSIM, comparisons with ATLFast are done, and where necessary, correction procedures to ATLFast are devised. In this way a set of ATLFast corrections is devised.

9.1 Muons

As discussed previously, due to the striking dimuon signature of the signal process, accurate and efficient reconstruction of muons is of high importance for this analysis. Important properties are the reconstruction efficiency, directly entering in the final event yield, the muon isolation efficiency and the mass resolution, which derives from the muon momentum resolution.

9.1.1 Reconstruction in FULLSIM

Muons in a momentum range from about 3 GeV to 3 TeV can be reconstructed in the ATLAS detector. Muons are minimal ionizing particles in this momentum range. Thus they leave a track in the inner detector, only a mip signal in the calorimeters and a track in the muon spectrometer. As a consequence, three different reconstruction strategies are available:

1. Stand-alone: In this mode the reconstruction of the muon tracks is based solely on information from the muon spectrometer, limited to the acceptance region of $|\eta| < 2.7$. The tracks are reconstructed in three steps. First the raw data of the MDT's and CSC's are pre-processed to form drift-circles (i.e. the radial distance of a particle track from the wire of a MDT) and clusters. In a next step, track segments are reconstructed. These are simple straight line tracks in a single MDT or CSC station. The search for these segments is seeded by a region of activity, which is defined by hits in the trigger chambers, and has a size of 0.4×0.4 in (η, ϕ) space. In a last step, the segments are used to built track candidates. This is done by starting with segments in the outer and middle stations and extrapolating these back through the magnetic field inwards. Segments in other stations matching reasonably are added to the track candidate. A final track-fitting procedure takes into account the geometry of the detector and the exact magnetic field along the trajectories. The muon-spectrometer track is propagated back to the interaction point. The energy loss in the calorimeters is taken into account by an algorithm which either uses a parameterization or the measured calorimeter energy. the latter is used only if it significantly exceeds the expectation and the muon track is isolated.

In this study, muon spectrometer tracks are used that have been reconstructed using the MUONBOY algorithm, of which more detail can be found in [134].

2. Combined: In the region $|\eta| < 2.5$ the muon spectrometer tracks can be combined with tracks reconstructed in the inner detector. This combination allows for a considerable improvement in the momentum resolution for muons with a transverse momentum below 100 GeV. In addition, fake muons arising e.g. from pion punch-through of the calorimeter and pion or kaon decays in flight are reduced.

The combination algorithm used in this study is the STACO algorithm, which statistically combines a muon spectrometer track with an inner detector track. The tracks are represented as five-vectors P_1 and P_2 that consist of the five measured track parameters with respect to the interaction point. The corresponding covariance matrices are called C_1 and C_2 . For each combination of a muon spectrometer track with an inner detector track, a combined track P is formed according to:

$$(C_1^{-1} + C_2^{-1}) \cdot P = C_1^{-1} \cdot P_1 + C_2^{-1} \cdot P_2, \quad (9.1)$$

with the covariance matrix

$$C = (C_1^{-1} + C_2^{-1})^{-1}. \quad (9.2)$$

An associated χ^2 variable is formed

$$\chi^2 = (P - P_1)^T \cdot C_1^{-1} \cdot (P - P_1) + (P - P_2)^T \cdot C_2^{-1} \cdot (P - P_2), \quad (9.3)$$

and only the combined track with the lowest χ^2 is kept. In this way the combined track automatically contains the best available information.

Within this study, only combined muons are considered, primarily due to better momentum resolution and due to the fact that ATLFast only provides parameterizations for combined muons.

3. Segment tags: In this muon reconstruction method, inner detector tracks are extrapolated outwards towards the muon spectrometer and are combined with segments in the inner stations. This leads to increased efficiency for low p_T muons ($p_T < 6$ GeV), since these might not reach the middle or outer muon stations, and for regions of reduced acceptance of the muon spectrometer. This is the case for $\eta \approx 0$ due to a gap in the muon chamber coverage to provide access for detector service, in the feet region of the detector due to support structures, and in the region of $|\eta| \approx 1.2$, where parts of the middle muon stations are not installed for initial data taking. The contribution of segment tags to the overall efficiency is expected to be only very limited for high p_T muons, and they have not been used in this study.

A muon identification method has to be very robust and efficient. It has to yield a high efficiency over a large acceptance region. In addition, the influence of pile-up and cavern background has to be small. For the chosen algorithm (STACO combined muons), the reconstruction efficiency and the muon fake probability have been studied. The reconstruction efficiency is defined as:

$$\epsilon_{\text{muon}} = \frac{\text{\# of reconstructed muons matched to a truth muon}}{\text{\# of truth muons}}, \quad (9.4)$$

and the fake probability as:

$$f_{\text{muon}} = \frac{\text{\# of reconstructed muons without matching truth muon}}{\text{\# of reconstructed muons}}. \quad (9.5)$$

Figure 9.1 shows the minimal distance in (η, ϕ) space between a truth muon and the closest reconstructed muon in a $b\bar{b}A^0$ ($M_{A^0} = 200$ GeV, PYTHIA) sample. The large peak for small values of angular separation corresponds to properly reconstructed muons. Based on this, a reconstructed muon is considered to be matched to a truth muon, if the ΔR distance is smaller than 0.1.

Figure 9.2 shows the obtained efficiencies and fake probabilities in the $Z^0 b\bar{b}$ (ACERMC) sample. The $b\bar{b}A^0$ sample yields similar results, but has a much lower statistics, so that the muon fake rate could not be accurately determined. As evident, the muon reconstruction is very efficient above $p_T = 20$ GeV. It decreases for low p_T and high $|\eta|$. Also the acceptance holes of the muon system at $\eta \approx 0$ and $|\eta| \approx 1.2$ are clearly visible. The slightly decreased efficiency for $\phi \approx -1$ and -2.2 corresponds to the feet region of the detector, where support structures lead to less muon chamber coverage. The fake probability is very

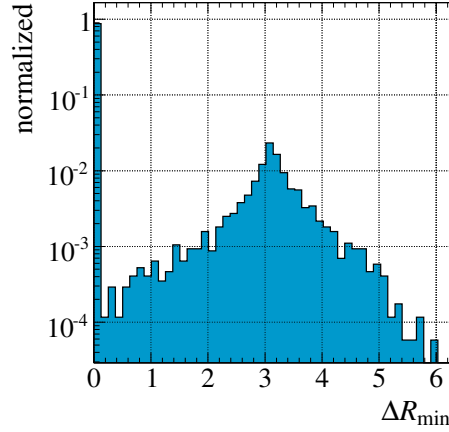


Figure 9.1: Minimal ΔR distance between a truth muon and a reconstructed muon in a $b\bar{b}A^0$ ($M_{A^0} = 200$ GeV, PYTHIA) sample.

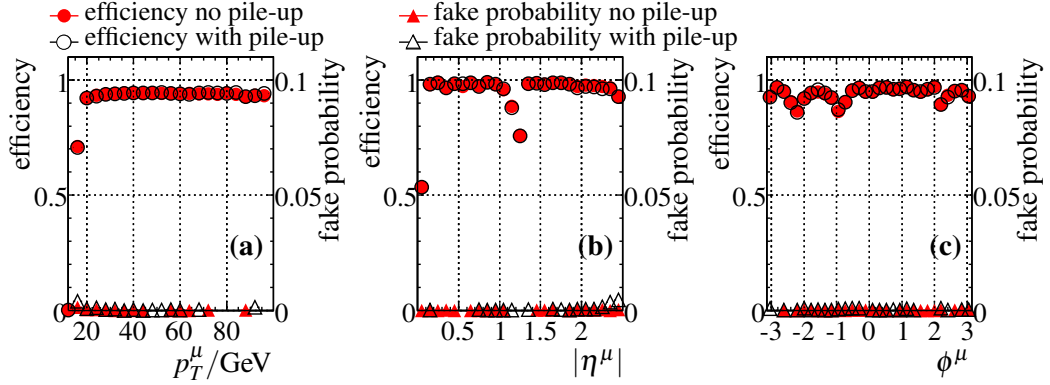


Figure 9.2: Muon reconstruction efficiency (circles) and fake probability (triangles) vs. (a) p_T^μ with $|\eta^\mu| < 2.5$, (b) $|\eta^\mu|$ with $p_T^\mu > 20$ GeV, and (c) ϕ^μ with $|\eta^\mu| < 2.5$ and $p_T^\mu > 20$ GeV, for a $Z^0b\bar{b}$ (ACERMC) sample. Closed symbols: Without, open symbols: including pile-up and cavern background. Matching criterion between truth and reconstructed muons: $\Delta R < 0.1$.

low over the whole region. The performance is robust against pile-up and does not change significantly.

9.1.2 Reconstruction in ATLFAST

The muon reconstruction in ATLFAST is much simpler. For each true muon with $p_T > 1.5$ GeV, the expected four vector after reconstruction is calculated. This is realized by applying a Gaussian resolution function that depends on p_T , η , and ϕ . Only the absolute value of the transverse momentum is smeared, the direction is not altered.

The used parameterization first consists of an analytical calculation of the muon p_T resolution in the muon spectrometer as a function of p_T , η and ϕ . This method neglects any non Gaussian effects, such as multiple scattering or pattern recognition errors. In addition, the layout of the muon spectrometer is taken into account. Similarly the energy loss of muons in the calorimeter is parameterized. Further, the inner detector p_T resolution is simulated using another smearing function. In complete analogy to the STACO algorithm used in FULLSIM, a combined muon is obtained by adding the inverse resolutions of the inner detector and the muon spectrometer in quadrature. More detail can be found in [98, 99].

After this smearing, muons with $p_T > 5$ GeV and $|\eta| < 2.5$ are kept. In the standard configuration of ATLFAST, no muons are discarded beyond these simple acceptance cuts. Thus, the muon reconstruction efficiency in the mentioned region is 100%. An option exists to randomly discard muons according to the reconstruction efficiencies found in detailed simulation, but the used parameterization leads to lower efficiencies than for the muon reconstruction used in FULLSIM. It has been obtained with an older software release and has not yet been updated. A correction for the discrepancy to FULLSIM is applied later in connection with the muon isolation.

9.1.3 Dimuon Mass and Momentum Resolution

As the signal processes consist of a comparably narrow resonance (the Higgs boson) decaying into a muon pair, a good dimuon mass resolution is essential for this analysis, as it will help significantly to reduce the backgrounds which are not expected to peak at the same mass values as the Higgs boson.

At this stage a first correction to the ATLFAST parameterizations is done. The smearing functions used in the current version of ATLFAST were obtained using an older detector description. In contrast to this, for the detailed simulation version used in this study, an updated detector layout is used, which includes more dead material, especially in the inner detector. As a consequence, the momentum resolution is underestimated by ATLFAST compared to FULLSIM. The most important variable, where this has a significant effect is the dimuon mass.

To estimate the difference and obtain a simple correction, signal datasets with a known input mass of the A^0 are used. Both in FULLSIM and in ATLFAST, the reconstructed muons coming from the Higgs boson decay are selected. This is done by requiring them to be within $\Delta R < 0.1$ of one of the two muons coming from the Higgs boson. In this way, both the reconstructed Higgs boson mass M_{rec} and the true Higgs boson mass M_{true} are found on an event by event basis¹. From this information, the relative mass resolution

$$\frac{M_{\text{rec}} - M_{\text{true}}}{M_{\text{true}}} \quad (9.6)$$

¹The true Higgs boson mass is not identical to the input mass due to non-zero total decay widths and possible QED final state radiation.

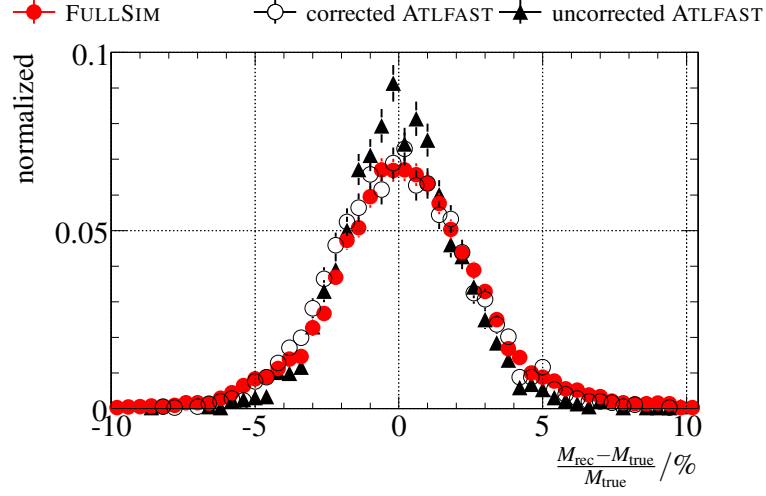


Figure 9.3: Relative mass resolution for $M_{A^0} = 200$ GeV, $b\bar{b}A^0$ (PYTHIA) for FULLSIM (filled circles), uncorrected ATLFast (triangles) and corrected ATLFast (open circles).

can be calculated. The result is shown in Figure 9.3 for an input mass of $M_{A^0} = 200$ GeV. ATLFast underestimates the mass resolution by about 25%.

A simple method has been developed to correct for this effect: An additional Gaussian smearing in $1/p_T$, which is the actual physical observable, is applied to the ATLFast muons with a resolution of 1.75%, which is optimized to give an agreement in the mass resolution. The result is also shown in Figure 9.3. The dimuon mass resolution now nicely coincides between FULLSIM and ATLFast. Any dependence on p_T and η of the resolution differences is neglected in this procedure.

Figure 9.4 shows a Gaussian fit applied to the relative mass resolution for FULLSIM and ATLFast, before and after the additional smearing. The fit is done only in the central region from -5% to $+5\%$. The agreement in the widths between FULLSIM and corrected ATLFast is good. The mean value for FULLSIM is about 0.2% higher than zero. This small shift is not reproduced in ATLFast. Since this amounts to a maximal shift of $O(0.5$ GeV), no correction in ATLFast is done. The more pronounced tails in FULLSIM cannot be described by a simple momentum smearing. Their source is at the moment not completely understood, but they amount only to a small fraction of events, which will not affect the analysis significantly.

The mass dependence of the correction is checked by applying the described procedure to signal samples with different input masses. Figure 9.5 shows the width of the fitted Gaussian against the input A^0 mass for FULLSIM, uncorrected ATLFast, and corrected ATLFast where the same correction has been applied for each mass point. Obviously the correction seems to be sufficient over the whole relevant mass range. The mass resolution is found to be proportional to the mass itself. This can be expected, if the muon momentum measurement is dominated by the sagitta resolution. In this case the relative momentum resolution is proportional to the momentum itself.

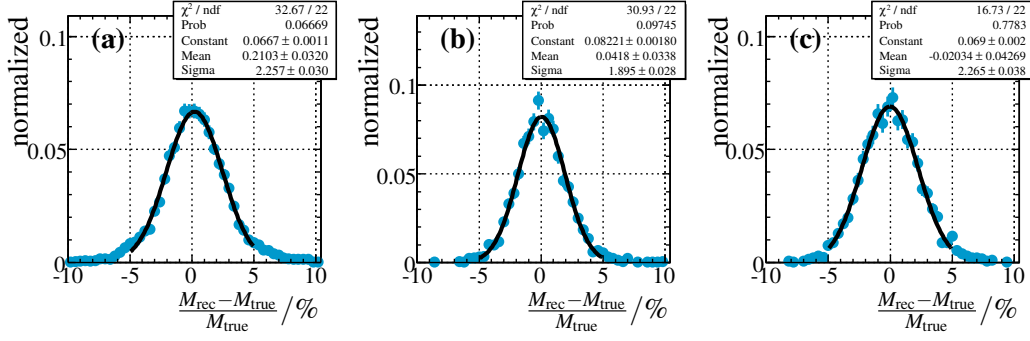


Figure 9.4: Relative muon momentum resolution and Gaussian fit to the central region.
(a) FULLSIM, (b) uncorrected ATLFast, (c) corrected ATLFast.

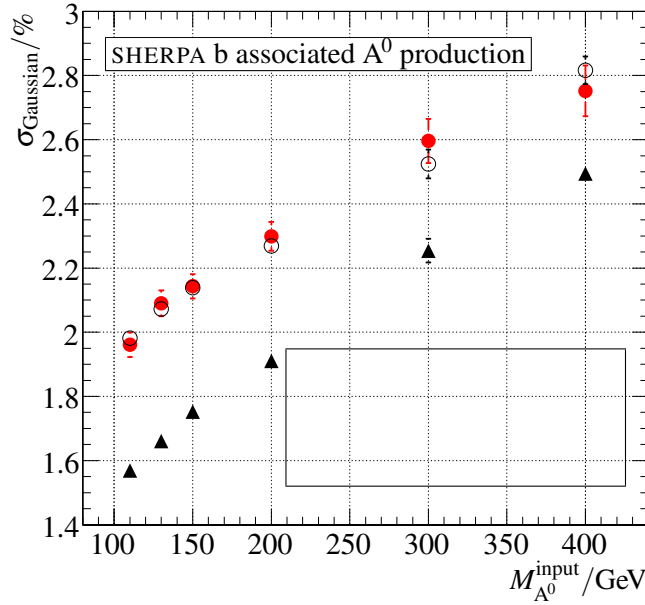


Figure 9.5: Relative muon mass resolution as obtained from a gaussian fit to the residuals versus the input A^0 mass. Triangles: ATLFast, open circles: corrected ATLFast (see text), closed circles: detailed simulation. SHERPA $b\bar{b}A^0$ samples.

The effect of the additional muon momentum smearing is illustrated in Figure 9.6 which shows the relative muon momentum resolution as a function of p_T and $|\eta|$ of the muons. Clearly the additional smearing in ATLFast gives much better agreement. The p_T dependence shows a tendency for the resolution being proportional to p_T , which is well described by ATLFast. Only at very low p_T , which are almost irrelevant for the analysis, a significant deviation from FULLSIM is seen. This could be due to additional multiple scattering contributions that are not included in the ATLFast parameterization.

The $|\eta|$ dependence of the muon momentum resolution shows that the central region is much better than the end-cap region. The resolution is worst for the transition region

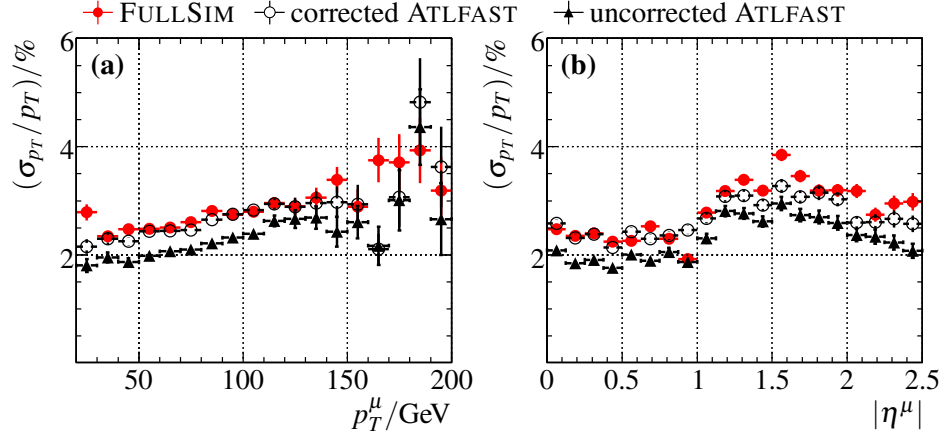


Figure 9.6: Relative muon momentum resolution versus p_T (a) and η (b) of the truth muon that could be matched to the reconstructed muon. Closed circles: FULLSIM, triangles: uncorrected ATLFast, open circles: corrected ATLFast. Sample: $b\bar{b}A^0$ ($M_{A^0} = 200$ GeV), PYTHIA.

between these two, which is expected, since here the magnetic field in the muon spectrometer is smallest, and in addition the missing muon chambers in the initial layout of ATLAS contribute to this effect. The momentum smearing corrects mostly only the central region, it is not as good for the end-caps. An $|\eta|$ dependent correction procedure would enable one to improve this situation, but this is not necessary for this analysis.

The influence of pile-up and cavern background on the quality of the mass reconstruction is checked using a signal sample with $M_{A^0} = 200$ GeV. The residual of the mass reconstruction is shown in Figure 9.7 with and without included pile-up. The mass resolution is not changed significantly under pile-up conditions.

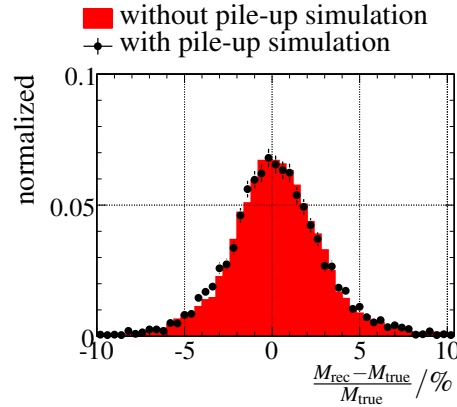


Figure 9.7: Dimuon mass residuals for a sample without (solid histogram) and with simulation of pile-up and cavern background (points). Signal sample $b\bar{b}A^0$, PYTHIA, $M_{A^0} = 200$ GeV.

9.1.4 Muon Isolation

Muons from the decay of the Higgs boson are not directly associated to any hadronic activity. This can only happen accidentally, in the case where the muon is by chance close to a jet. They can be called *isolated*. The same is true for muons coming from the decay of a Z^0 or W in the background processes. On the other hand, muons coming from decays of hadrons, especially from heavy flavor, are inside a hadronic jet and are not isolated. In order to suppress any background from the contribution of hadron decays, an isolation criterion has to be applied. This is also important to suppress $t\bar{t}$ background, since due to the b quarks present in $t\bar{t}$ events, a significant fraction of muons from hadron decays can be expected. However, the much more important background that is going to be rejected by requiring the muons to be isolated consists of the bulk of QCD multijet events. The cross section for this type of processes is huge, it can contain b jets, and thus also muons which may fake the signal signature. Due to the large cross sections it is not possible to generate sufficient Monte Carlo events to study this type of backgrounds. The muon isolation will need to be studied in more detail in data. Within this work it is assumed that the contribution from QCD multijets is negligible after isolation requirements.

Isolation in FULLSIM

In FULLSIM, the isolation can be done by requiring low activity in a region around the muon. This information can be obtained from tracks in the inner detector, or from the calorimeter. The latter is used in this work. The transverse energy in a ΔR cone around the muon axis in the calorimeter is reconstructed, and the expected energy loss of the muon is subtracted. Figures 9.8 (a–c) show the transverse energy in a $\Delta R = 0.4$ cone around the muon for different event samples and different truth origins of the muons.

Obviously, muons coming from hadron decays tend to have a larger energy in the isolation cone. A simple isolation criterion would now be to place a cut on the energy in the cone to define isolation. However, this can be improved even further: Muons from Higgs, Z^0 , or W decays tend to be at rather large transverse momentum. Muons from hadron decays on the other hand get only a fraction of the jet momentum and are at low transverse momentum. This is shown in Figures 9.8 (d–f) for different event samples. There is a clear separation between the two classes of muons. The information of both variables can be combined into one single variable by dividing the energy in the cone around the muon by the transverse momentum of the muon. This variable is shown in Figures 9.8 (g–h). Clearly the separation power between muons from heavy boson decays and from hadron decays is improved.

Figure 9.9 shows the rejection of muons from hadron decays versus the efficiency to retain muons from Higgs boson decays if the calorimeter energy around the muon normalized to its momentum is used as the isolation variable.

Larger cone sizes perform better than small ones in the sense that the rejection for a given efficiency is higher. The rejection against muons from hadron decays in $t\bar{t}$ events is much larger than for the same in $Z^0 b\bar{b}$ events. This is readily explained by the different event topology: $t\bar{t}$ events feature more jets and harder jets than $Z^0 b\bar{b}$.

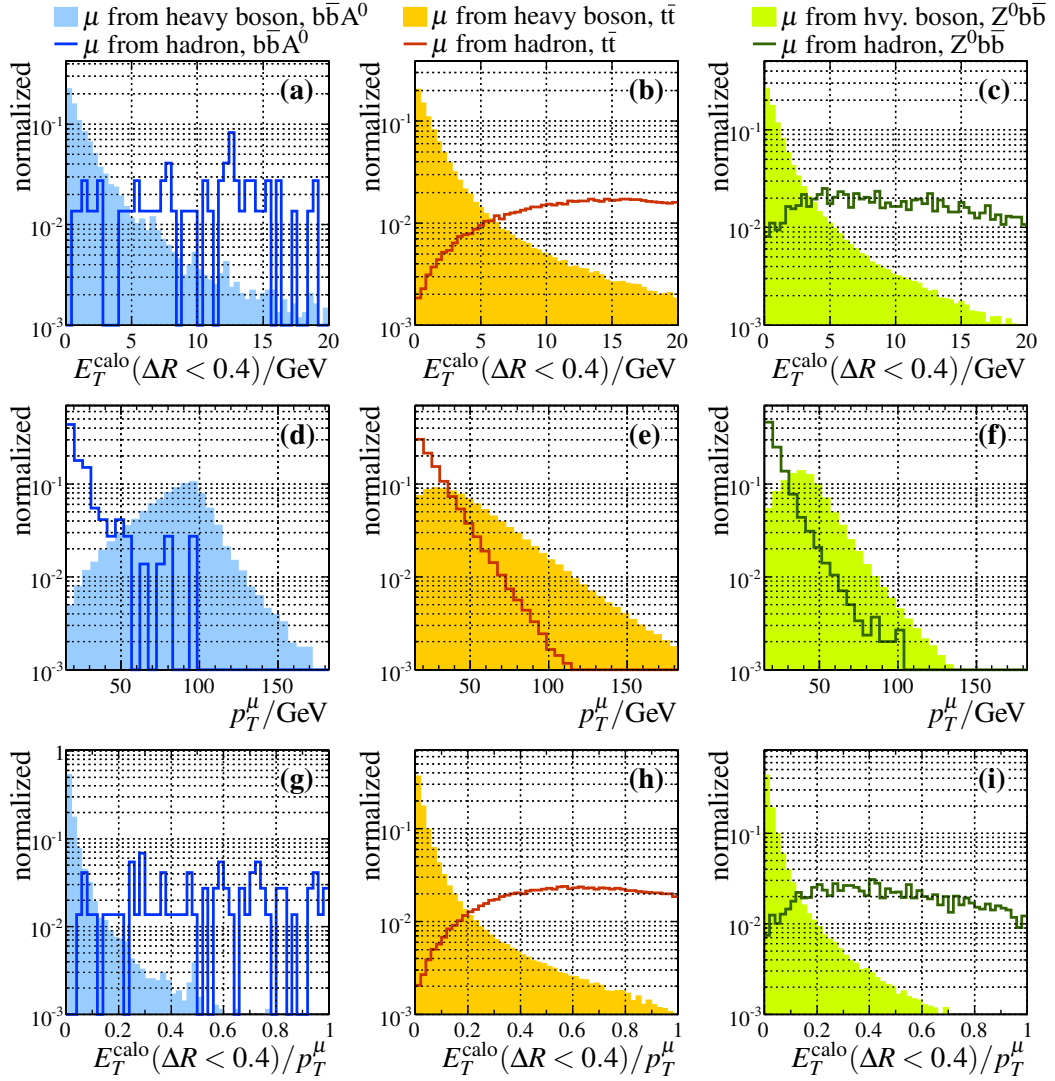


Figure 9.8: (a–c): $E_T^{\text{calo}}(\Delta R < 0.4)$ for muons coming from hadron decays (open histograms) and muons coming from the decays of a heavy boson (closed histograms). (d–f): p_T distribution of the muons. (g–i): $E_T^{\text{calo}}(\Delta R < 0.4)$ divided by the p_T of the muon. From left to right: $b\bar{b}A^0$ ($M_{A^0} = 200 \text{ GeV}$, PYTHIA), $t\bar{t}$ ($2\mu f$, MC@NLO), $Z^0 b\bar{b}$ (ACERMC).

The isolation criterion found in [135] is adopted for this analysis. It consists of the requirement:

$$E_T^{\text{calo}}(\Delta R < 0.4) < 0.2 \cdot p_T^\mu, \quad (9.7)$$

and is chosen to give an optimal suppression of the $t\bar{t}$ background while at the same time retaining more than 95% signal efficiency for a Higgs boson mass of 200 GeV. A re-

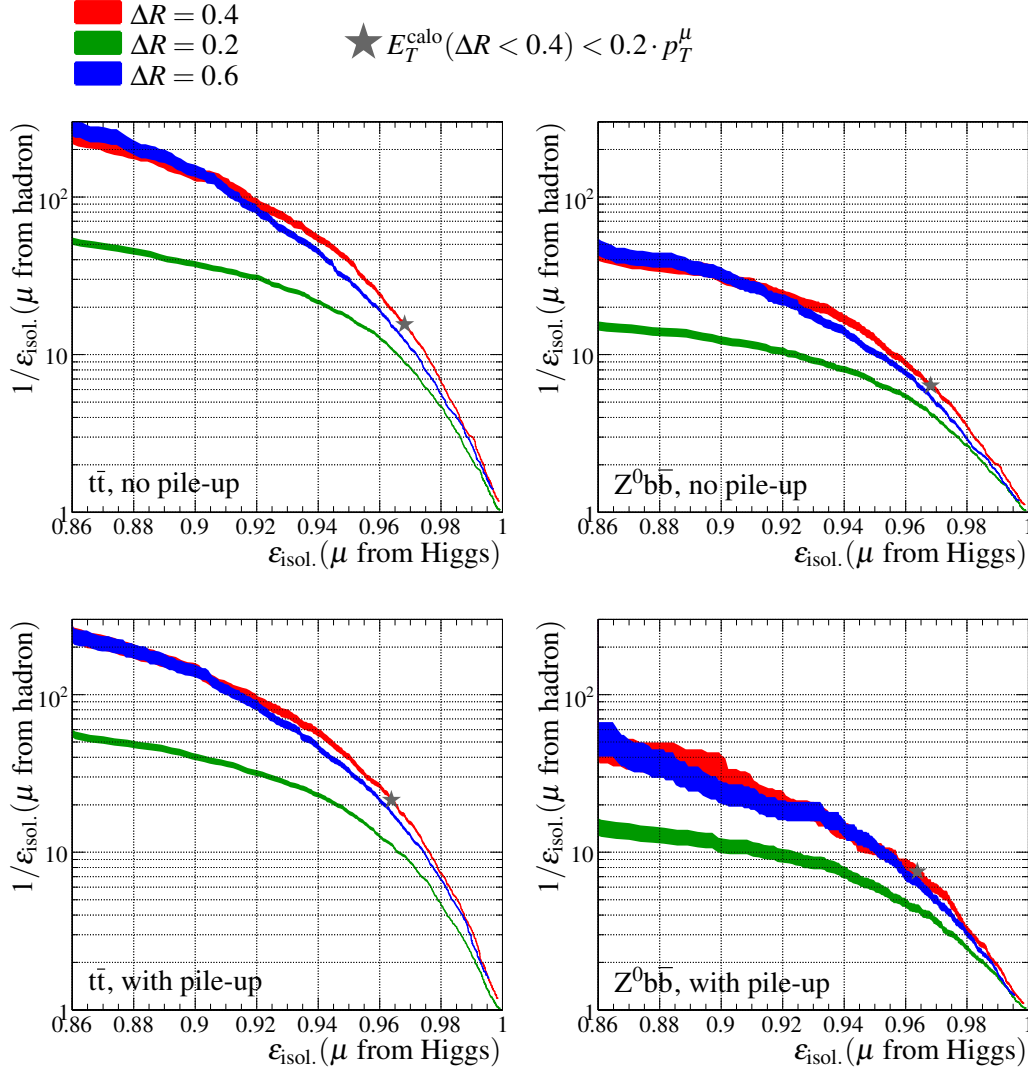


Figure 9.9: Rejection of muons from hadron decays versus isolation efficiency of muons from Higgs decays if the ratio of calorimeter energy in a cone around the muon divided by the muon momentum is used as isolation criterion. Green area: $\Delta R = 0.2$, red: $\Delta R = 0.4$, blue: $\Delta R = 0.6$. The gray star shows the chosen working point. Left column: Rejection of muons from hadron decays in the $t\bar{t}$ (MC@NLO) sample, right column: rejection of muons from hadron decays in the $Z^0 b\bar{b}$ sample (ACERMC). Top row: without pile-up, bottom row: with pile-up simulation. Efficiencies for muons from Higgs boson decays are taken from the $b\bar{b}A^0$ ($M_{A^0} = 200$ GeV, PYTHIA) sample.

optimization is not done. As it turns out, the remaining $t\bar{t}$ events relevant for the analysis are completely dominated by muons coming from the decays of W bosons. The background

contribution of muons from hadron decays is negligibly small for all Monte Carlo samples after requiring both muons to be isolated.

The chosen isolation criterion is also rather robust against pile-up effects. Pile-up can potentially decrease the isolation efficiency due to the extra energy deposited in the calorimeter. When pile-up is included, the efficiency for muons from Higgs boson decays decreases by only 1%. The rejection against muons from hadron decays even gets slightly better, which simply corresponds to a slightly different working point.

In contrast to the isolation criterion including a scaling by the muon transverse momentum, cutting solely on the transverse calorimeter energy in a cone around the muon yields significantly worse results. This is shown in Figure 9.10. Obtaining a similar rejection of muons from hadron decays would require to move to a significantly lower efficiency for muons from Higgs boson decays. In addition, the performance of this requirement seems to be influenced in an adverse way by the inclusion of pile-up. Especially the larger cone sizes yield a significantly reduced rejection for the same efficiency. This is due to the extra energy in the calorimeter if pile-up is included.

The rejection of QCD multijet events has been checked using samples of dijet events, which are separated in multiple p_T bins of the hard scattering and have been simulated with PYTHIA. Applying the standard isolation criterion, no event in any of these samples has a reconstructed $\mu^+\mu^-$ pair, both with $p_T^\mu > 20$ GeV. Limits to the 95% confidence level on the accepted cross section of this requirement are calculated using the poissonian statistics for a null-experiment. The parameters and the limits on the accepted cross sections are shown in Table 9.1. The limits on the accepted cross sections are still very large compared to the other background cross sections. However, it is expected that the QCD multijet background is well reducible and is neglected in the following.

Sample	p_T range	cross section	number of events	$\sigma_{\text{accepted}}^{\text{limit}} @ 95\% C.L.$
J0	8 – 17 GeV	17.6 mb	560 400	72.2 nb
J1	17 – 35 GeV	1.38 mb	352 350	9 nb
J2	35 – 70 GeV	93.3 μb	131 800	1.6 nb
J3	70 – 140 GeV	5.88 μb	325 050	41.6 pb
J4	140 – 280 GeV	308 nb	316 400	2.2 pb
J5	280 – 560 GeV	12.5 nb	279 900	10.2 fb

Table 9.1: p_T ranges, cross sections and number of events in the QCD dijet samples used for the updated b -tagging parameterization. The cross sections are the leading order values as obtained from PYTHIA. The last column gives the 95% confidence level on the accepted cross section when requiring exactly one $\mu^+\mu^-$ with $p_T^\mu > 20$ GeV and standard isolation requirements ($E_T^{\text{calo}}(\Delta R < 0.4) < 0.2 \cdot p_T^\mu$).

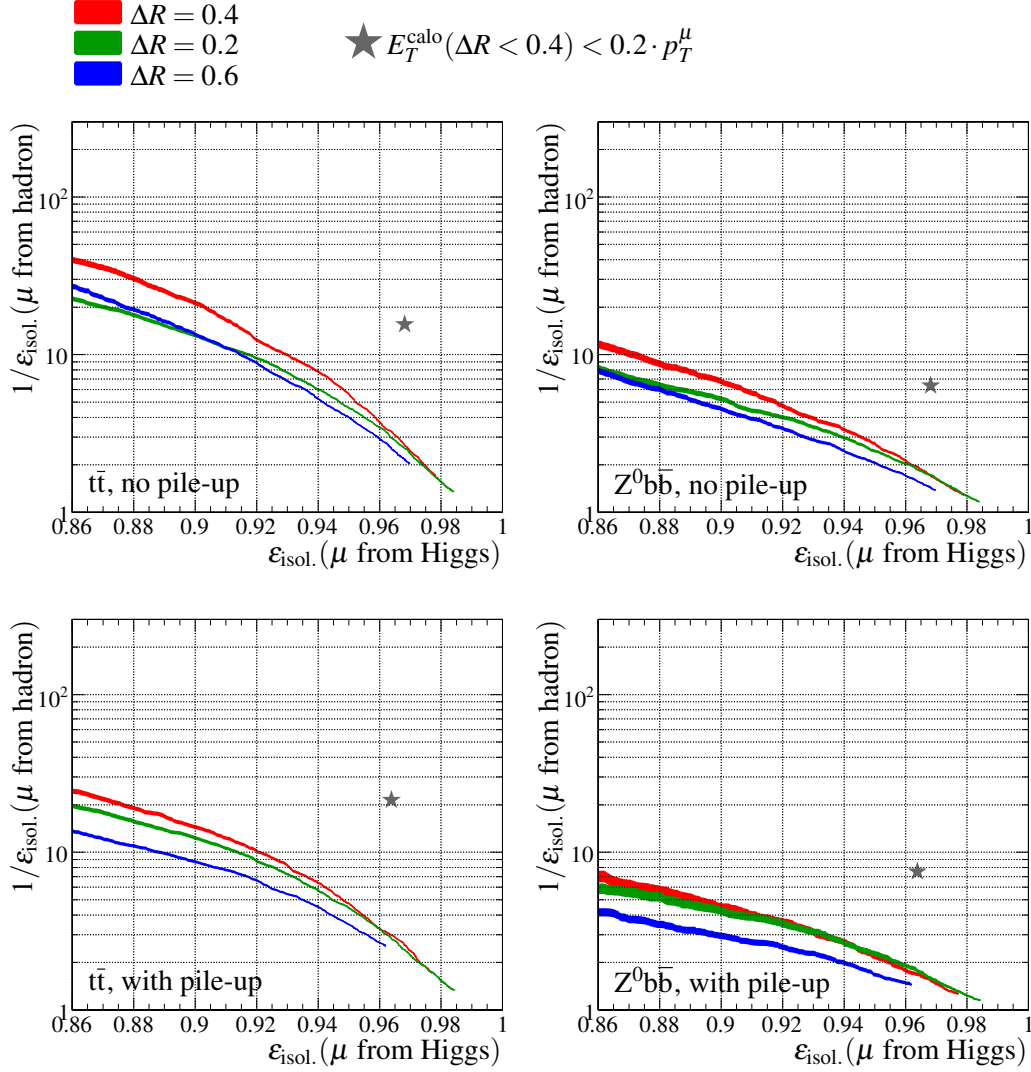


Figure 9.10: Rejection of muons from hadron decays versus isolation efficiency of muons from Higgs decays if the calorimeter energy in a cone around the muon is used as isolation criterion. Green area: $\Delta R = 0.2$, red: $\Delta R = 0.4$, blue: $\Delta R = 0.6$. The gray star shows the working point if using the calorimeter energy divided by the muon transverse momentum. Left column: Rejection of muons from hadron decays in the $t\bar{t}$ (MC@NLO) sample, right column: rejection of muons from hadron decays in the $Z^0 b\bar{b}$ sample (ACERMC). Top row: without pile-up, bottom row: with pile-up simulation. Efficiencies for muons from Higgs boson decays are taken from the $b\bar{b}A^0$ ($M_{A^0} = 200$ GeV, PYTHIA) sample.

Isolation in ATLFAST

Muon isolation ATLFAST is *digital*, in the sense that the information leading to the decision to call a muon isolated is not stored, only the result. In the standard configuration of

ATLFAST, the energy of all calorimeter cells (obtained in a simplified version of the ATLAS calorimeter, see Section 9.2.2), based on visible truth particles is used. The cone size is fixed to 0.2, and within this region less than 10 GeV transverse energy from truth particles is allowed. In addition, within $\Delta R < 0.4$, no ATLFAST cluster (see Section 9.2.2) is allowed. Muons failing this requirement are added to the four-vector of the cluster.

The efficiency of this isolation requirement for muons coming from Higgs bosons decays is significantly lower than the one in FULLSIM. For a Higgs boson mass of 200 GeV it is only about 92% compared to 96% in FULLSIM. This is primarily due to the cluster isolation requirement.

9.1.5 ATLFAST Efficiency correction

The ATLFAST isolation requirement is significantly different from the one that is used in FULLSIM. In addition, it is not possible to simply change the requirement in FULLSIM to meet the one from ATLFAST. This is primarily due to the cluster isolation requirement: The reconstruction efficiency of ATLFAST for low p_T jets is a lot higher than for FULLSIM. The minimal transverse energy for an ATLFAST cluster is only 5 GeV, compared to 10 GeV for a jet in FULLSIM. The only way to rebuild the ATLFAST isolation requirement in FULLSIM would be to use truthjets to mimic the cluster isolation. But this does not show the true capabilities of ATLAS to define isolated muons.

Instead of doing a more complicated correction procedure, in the following the only aim is to obtain identical efficiencies between FULLSIM and ATLFAST to select events of a given type. The selection involves requiring exactly one $\mu^+\mu^-$ pair, both muons isolated and with $p_T^\mu > 20$ GeV and with an invariant dimuon mass of at least 80 GeV. These cuts are expected to have a very high efficiency for signal events. The mass cut is applied to tune the efficiency only in the mass range of interest. Since the muon reconstruction efficiency in ATLFAST is one, a comparison of these cut efficiencies leads directly to a mean rate at which ATLFAST muons have to be removed in order to obtain the same event selection efficiency.

In this way a mean efficiency correction is applied, concerning the combined muon reconstruction and isolation efficiency $\epsilon_{\text{reco}} \times \epsilon_{\text{iso}}$. The needed additional inefficiency in ATLFAST might very well be sample-dependent, as the two isolation criteria in ATLFAST and FULLSIM are very different. The remaining differences constitute a systematic uncertainty of the ATLFAST modeling. It should be noted that in this way, parts of the ATLFAST isolation-inefficiency is compensated for by the lower muon reconstruction efficiency in FULLSIM.

Figure 9.11 shows the combined reconstruction and isolation efficiency for muons in the $Z^0 + \text{light}$ sample. For the corrected ATLFAST an additional muon inefficiency of 95.3% has been applied to yield the same mean event selection efficiency. Figure 9.12 shows the same result, but for the $b\bar{b}A^0$ ($M_{A^0} = 200$ GeV, SHERPA) signal sample. Here a slightly smaller additional inefficiency in ATLFAST of 97% is needed. The p_T dependence of the combined efficiency is rather well modeled by this simple correction. The structure in p_T obviously comes mostly from the isolation efficiency, as it is also present in ATLFAST: There is a rise in the efficiency up to a p_T corresponding to roughly half the mass of the

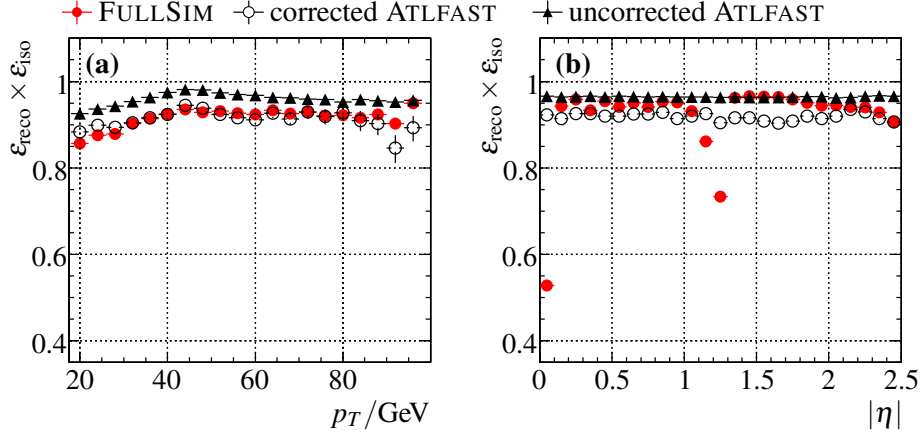


Figure 9.11: Combined muon reconstruction and isolation efficiency in the $Z^0 + \text{light}$ (SHERPA) sample for FULLSIM (filled circles), ATLFast (triangles) and corrected ATLFast with an additional muon inefficiency of 95.3%. In dependence of (a) p_T for $|\eta| < 2.5$ and (b) $|\eta|$ for $p_T > 20$ GeV of the truth muons.

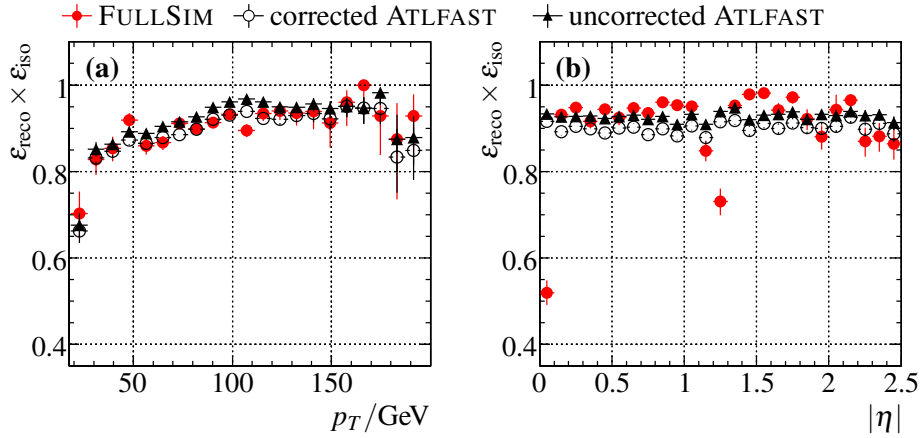


Figure 9.12: Combined muon reconstruction and isolation efficiency in the $b\bar{b}A^0$ ($M_{A^0} = 200$ GeV, SHERPA) sample for FULLSIM (filled circles), ATLFast (triangles) and corrected ATLFast with an additional muon inefficiency of 97%. In dependence of (a) p_T for $|\eta| < 2.5$ and (b) $|\eta|$ for $p_T > 20$ GeV of the truth muons.

simulated boson. This can be explained easily: The p_T distribution of a muon coming from a boson without a significant transverse momentum, as it is the case in these two samples, shows a maximum at half the boson mass. However, if in the decay one of the muons emits a hard *inner bremsstrahlung* photon, it will have a lower transverse momentum than usual. As QED radiation is emitted primarily in the direction of flight, this photon goes into the same direction as the muon and will deposit energy in the isolation cone, causing the muon to be falsely non-isolated. This explains the observed effect, but has not been verified in detail.

The acceptance holes in $|\eta|$ can obviously not be described by this simple correction. This would require a p_T , η , and ϕ dependent parameterization, which is not feasible in the scope of this work. But also this would not solve the large difference in the isolation requirements.

In the following a global correction factor that is chosen to be 97% is used instead of a sample dependent correction. Its value is optimized to minimize the deviations of the observed efficiencies. Table 9.2 shows the resulting efficiencies in FULLSIM, ATLFAST and their ratio for different signal and background datasets.

The largest deviations in the efficiencies are of the order of 4%. $t\bar{t}$ has a different topology (more and higher p_T jets) than the other samples and shows a slightly higher event selection efficiency in FULLSIM. For the other samples a tendency is visible that the ratio between ATLFAST and FULLSIM is correlated with the mass of the generated boson. This is investigated in more detail later.

The SHERPA signal samples show an about 2% higher efficiency in ATLFAST compared to the PYTHIA samples of the same mass. In contrast to this, the efficiencies in FULLSIM are very comparable. Obviously there is a modeling difference between these two generators. The fact that it only appears in ATLFAST points to it being caused by the cluster isolation requirement and thus to very low p_T hadronic activity. This might very well be a difference in the description of the underlying event.

Taking 2% as a systematic uncertainty on the additional ATLFAST inefficiency actually covers the complete range of deviations between FULLSIM and ATLFAST, as this corresponds to a change of 4% in the rate of two muons. But in addition to the raw efficiency, also the sample composition has to be checked. To do this, the selected events are categorized according to the truth origin of the reconstructed muons. As it turns out, only the $t\bar{t}$ sample has a significant fraction of events with at least one muon not coming from the decay of a heavy boson (Z^0 , W or A^0). All other samples have more than 99.9% of all muon pairs coming from the heavy boson decay. The composition of the $t\bar{t}$ sample is listed in Table 9.3 for FULLSIM and ATLFAST. Although the FULLSIM sample has a much larger fraction of muons coming from hadron decays than ATLFAST, the fraction itself is below 1%, and thus negligible. The other event fractions agree within 0.5%. In $t\bar{t}$ there is a significant fraction of events with at least one muon coming from the decay of a tau lepton. These tau leptons actually also come from the decay of a W boson, so the origin of these muons is the decay chain $W \rightarrow \tau \bar{\nu}_\tau \rightarrow \mu \bar{\nu}_\mu \nu_\tau \bar{\nu}_\tau$. Since they also come from the decay of a W , they are correctly classified as isolated. This shows that it is important not to generate $t\bar{t}$ events where the W bosons are forced to decay into muons, since one would otherwise neglect an important background source.

In addition to the total deviations of the efficiencies, which are covered by a systematic uncertainty of 2% in the muon efficiency correction of ATLFAST, there is also the possibility that the shape of the dimuon mass spectrum is different between FULLSIM and ATLFAST. As the effects are expected to be small, this cannot be studied using e.g. the available FULLSIM sample of $Z^0 + \text{light}$ and $Z^0 + b$, due to the very small statistics in FULLSIM. These samples are completely dominated by the Z^0 peak. Instead the mass dependence of the residuals is studied using signal samples at different masses in the following.

Dataset	Efficiency for $1 \mu^+ \mu^-$, $p_T^\mu > 20 \text{ GeV}$, $M_{\mu^+ \mu^-} > 80 \text{ GeV}$		
	$\epsilon_{\text{FULLSIM}}/\%$	$\epsilon_{\text{ATLFAST}}/\%$	$\frac{\epsilon_{\text{FULLSIM}}}{\epsilon_{\text{ATLFAST}}}$
$t\bar{t}$ ($2\mu\text{f,MC@NLO}$)	5.99 ± 0.03	5.81 ± 0.02	1.030 ± 0.006
$Z^0 + \text{light}$ (SHERPA)	62.9 ± 0.2	65.55 ± 0.02	0.960 ± 0.002
$Z^0 + b$ (SHERPA)	60.93 ± 0.16	62.92 ± 0.04	0.968 ± 0.003
$Z^0 b\bar{b}$ (ACERMC)	58.33 ± 0.09	58.84 ± 0.05	0.991 ± 0.002
$b\bar{b}A^0$ (110) SHERPA	69.1 ± 0.8	70.8 ± 0.5	0.98 ± 0.01
$b\bar{b}A^0$ (130) SHERPA	71.4 ± 0.7	73.2 ± 0.4	0.98 ± 0.01
$b\bar{b}A^0$ (150) SHERPA	73.8 ± 0.7	74.4 ± 0.4	0.99 ± 0.01
$b\bar{b}A^0$ (200) SHERPA	74.4 ± 0.7	74.0 ± 0.4	1.01 ± 0.01
$b\bar{b}A^0$ (300) SHERPA	75.1 ± 0.8	74.3 ± 0.6	1.01 ± 0.01
$b\bar{b}A^0$ (400) SHERPA	76.0 ± 0.7	73.1 ± 0.4	1.04 ± 0.01
$b\bar{b}A^0$ (110) PYTHIA	69.4 ± 0.7	69.0 ± 0.7	1.01 ± 0.01
$b\bar{b}A^0$ (130) PYTHIA	72.4 ± 0.7	71.1 ± 0.5	1.02 ± 0.01
$b\bar{b}A^0$ (150) PYTHIA	73.4 ± 0.6	71.0 ± 0.5	1.03 ± 0.01
$b\bar{b}A^0$ (200) PYTHIA	75.3 ± 0.5	72.7 ± 0.6	1.04 ± 0.01
$b\bar{b}A^0$ (300) PYTHIA	75.5 ± 0.8	72.2 ± 0.6	1.05 ± 0.01
$b\bar{b}A^0$ (400) PYTHIA	74.7 ± 0.6	70.88 ± 0.5	1.05 ± 0.01
$gg \rightarrow A^0$ (110) PYTHIA	65.9 ± 0.7	65.3 ± 0.5	1.01 ± 0.01
$gg \rightarrow A^0$ (200) PYTHIA	74.3 ± 0.5	72.0 ± 0.5	1.03 ± 0.01

Table 9.2: Selection efficiencies of signal and background samples in FULLSIM, ATLFAST and their ratio. A global additional muon inefficiency in ATLFAST of 97% is applied. Numbers in parentheses give the mass of the generated Higgs boson in GeV.

Isol. method	$f_{\text{good}}/\%$	$f_{\geq 1\text{from hadron}}/\%$	$f_{\geq 1\text{from } \tau}/\%$
FULLSIM	86.5 ± 0.2	0.8 ± 0.1	12.7 ± 0.2
ATLFAST	87.0 ± 0.11	0.09 ± 0.01	12.9 ± 0.1

Table 9.3: Fractions of selected events corresponding to different truth origins of the two muons in the $t\bar{t}$ ($2\mu\text{f,MC@NLO}$) sample: f_{good} : both muons are from W decays, $f_{\geq 1\text{from hadron}}$: at least one muon is from a hadron decay, $f_{\geq 1\text{from } \tau}$: at least one muon comes from a τ decay.

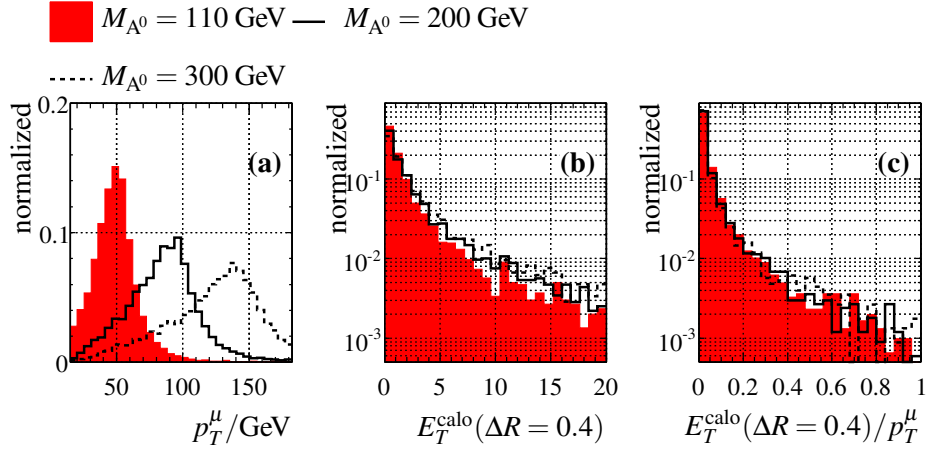


Figure 9.13: (a) Transverse momentum distribution of muons in $b\bar{b}A^0$, (b) distribution of calorimeter energy in a cone of $\Delta R = 0.4$ around the muon, with the muon energy loss subtracted, (c) calorimeter energy divided by the p_T of the muon. Solid histogram: $M_{A^0} = 110$ GeV, solid line: $M_{A^0} = 200$ GeV, dashed line: $M_{A^0} = 300$ GeV.

Figure 9.13 (a) shows the distribution of the transverse momentum of muons in $b\bar{b}A^0$ samples with different A^0 masses. A clear correlation with the Higgs boson mass is visible, according to the decay kinematics. Figure 9.13 (b) and (c) show the isolation energy in $\Delta R = 0.4$ and the isolation energy normalized to the muon transverse momentum, respectively. The higher the Higgs boson mass, and with it the transverse momentum, the higher is the energy deposited around the muon direction. Together with the increased muon momentum, this somewhat compensates when normalizing to the muon transverse momentum. This would explain the observed behavior: The FULLSIM isolation requirement is less sensitive to this effect than ATLFast, since it uses the normalized isolation energy. The source of the effect itself is not explained fully. It might be that there is a correlation between the muon momentum and the number and energy of emitted inner bremsstrahlung photons, which might spoil the isolation.

Figure 9.14 shows the isolation efficiency for muons coming from a Higgs boson decay in dependence of the mass of the generated Higgs boson for FULLSIM, ATLFast, and with an isolation requirement in FULLSIM mimicking the one in ATLFast expect for the cluster isolation. The standard FULLSIM isolation requirement yields a flat efficiency, whereas ATLFast and the modified FULLSIM criterion give an efficiency that decreases with the mass of the Higgs boson, as expected.

It has to be implied that the observed differences also give a slightly skewed invariant mass distribution of the $Z^0 + \text{light}$ and $Z^0 + b$ samples. This has to be investigated as a systematic uncertainty on the mass shape. To obtain a re-weighting function to alter the mass shape according to the differences, the ratio between the FULLSIM and ATLFast efficiencies is used. It is shown in Figure 9.15 in dependence of the generated mass along with a fitted first order polynomial. This function can be used to re-weight the dimuon mass distribution to investigate the effect of this systematic uncertainty.

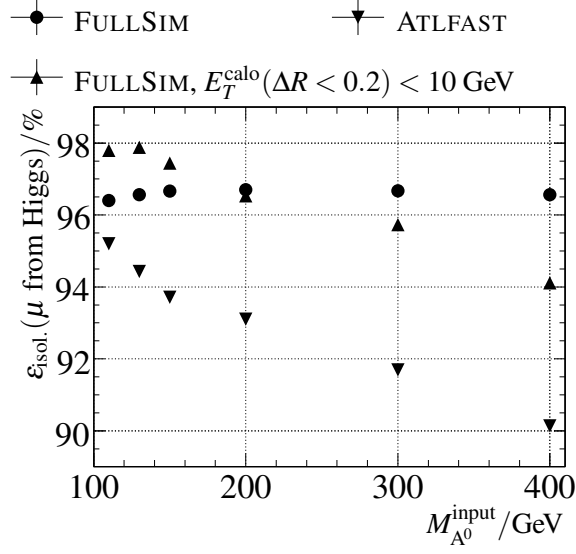


Figure 9.14: Isolation efficiency for muons from Higgs boson decays versus the generated Higgs boson mass. Circles: FULLSIM, standard isolation requirement, downwards pointing triangles: ATLFast, upwards pointing triangles: FULLSIM with the isolation requirement $E_T^{\text{calo}}(\Delta R < 0.2) < 10 \text{ GeV}$. The SHERPA signal samples are used.

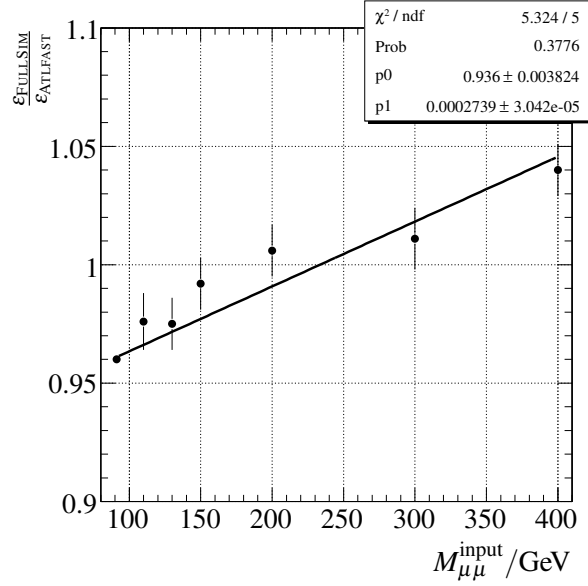


Figure 9.15: Ratio of the selection efficiency in FULLSIM to the one in ATLFast in dependence of the generated central mass of the resonance. The point at 91 GeV is from the $Z^0 + \text{light}$ (SHERPA) sample, the other from the $b\bar{b}A^0$ (SHERPA) samples.

9.2 Jet Reconstruction

The ATLAS calorimeter system, as described in Chapter 5 consists of different calorimeters, with a high granularity and several longitudinal samplings, especially within $|\eta| < 3.2$. But also the forward region $3.2 < |\eta| < 4.9$ is instrumented to reconstruct jets with sufficient precision. However, within this analysis, especially jets in the central detector region ($|\eta| < 2.5$) are of importance, as these can be identified as originating from the decay of a b quark (b jets).

In ATLAS, jets are purely calorimeter based objects, i.e. no use is made of the tracks reconstructed in the inner detector. In the following, the jet reconstruction in FULLSIM and in ATLFAST is first briefly discussed. Then, comparisons between key performance properties of jets are made between the two simulation approaches and simple correction methods are presented. The aim is to obtain a better agreement between FULLSIM and ATLFAST, not to get a perfect description by using ATLFAST.

9.2.1 Jet Reconstruction in FULLSIM

The basic procedure of jet reconstruction in ATLAS is shown in Figure 9.16. The fundamental building block from which everything starts is the calorimeter cell, which is first calibrated to the electromagnetic energy scale. In real data this will be possible using $Z^0 \rightarrow e^+e^-$ decays. The ATLAS calorimeters are in general not compensating, their ratio of electromagnetic to hadronic response is larger than one. Thus a calibration procedure to correct to the hadronic energy scale is necessary.

One basic choice is the type of objects used in the subsequent jet algorithm. The first possibility are *calorimeter towers*. These are formed by adding the energy content of all cells within a regular $\Delta\eta \times \Delta\phi = 0.1 \times 0.1$ grid. If a cell belongs to multiple towers due to the calorimeter geometry, its signal is divided between the towers. As the calorimeter baseline signal is subtracted online, this procedure can result in towers with negative energy due to noise fluctuations. These cannot be used for jet finding and are re-summed into nearby towers until the resulting tower has positive energy.

The second approach are *topological clusters*, which are described in [136, 137]. These aim at reconstructing three-dimensional energy depositions in the calorimeter. The algorithm is based on using cells with a signal above some threshold over its noise and adding nearest neighbors in an iterative procedure. After this clustering step, the cluster candidate is examined for local signal maxima and split in three dimensions if more than one maximum is found. Topological clusters have an inherent noise suppression, contrary to calorimeter towers. As this procedure is more complicated, it will require more careful validation in real data.

Jets, based either on calorimeter towers or topological clusters, are reconstructed using either a seeded cone ($E_T^{\text{seed}} > 2 \text{ GeV}$, $f = 0.5$, $\Delta R = 0.4$ or 0.7 , see Appendix B) or a k_\perp algorithm ($D = 0.4$ or 0.6).

The resulting jets are still calibrated to the electromagnetic scale and a hadronic calibration is necessary. This is done by applying a cell signal weighting similar to the original approach developed for the H1 calorimeter [138]. In this approach, all calorimeter cells

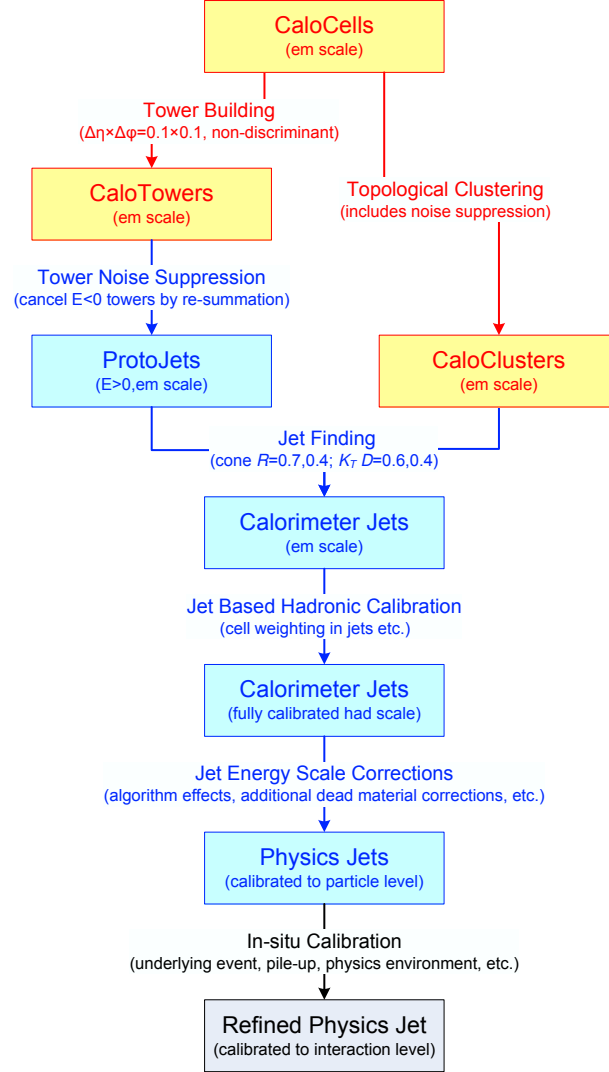


Figure 9.16: Jet reconstruction flow for calorimeter jets from towers or clusters (taken from [65]).

with four momenta (E_i, \vec{p}_i) , $E_i = |\vec{p}_i|$ are re-summed with weighting functions w that depend on the cell signal density $\rho_i \equiv E_i/V_i$ and the cell location in the calorimeter \vec{X}_i :

$$(E_{\text{jet}}, \vec{p}_{\text{jet}}) = \left(\sum_i^{N_{\text{cells}}} w(\rho_i, \vec{X}_i) E_i, \sum_i^{N_{\text{cells}}} w(\rho_i, \vec{X}_i) \vec{p}_i \right). \quad (9.8)$$

The weighting functions are derived using simulated QCD dijet events, where reconstructed jets (cone, $\Delta R = 0.7$) are matched to truth jets of the same size and the deviation

of the reconstructed from the truth jet energy is minimized in a global minimization of residuals.

This method absorbs all detector effects, including the impact of charged particles with a transverse momentum of less than 400 MeV, which do not reach the calorimeter due to the bending in the solenoidal magnetic field. Included are also energy losses in dead material, except those between the EM and hadronic calorimeter, which are corrected for. The calibration for other cone sizes and/or jet and clustering algorithms is derived using the same weighting functions, but the residual miscalibrations are corrected for by p_T and $|\eta|$ dependent correction functions, which again have been obtained from QCD dijet samples. The jets obtained in this way are calibrated to the level of the truth-particle jet. Not included are intrinsic effects of the jet algorithm, e.g. energy that is not included in the chosen cone size (out-of-cone energy), or physics effects like extra energy from the underlying event or pile-up. The calibration of these effects will have to be done in-situ to obtain a relationship that gives access to the hard parton momenta. This is of utmost importance in all analyses that strive to use or measure a mass that is reconstructed from a jet. In this analysis, this is not needed and no final jet energy scale calibration is applied.

Within this work, cone 0.4 jets build from calorimeter towers are used. This choice was first motivated by studies [139] showing that the b -tagging performance seems to be better using narrow jets. But most importantly, the jet reconstruction in ATLFAST (see below) is also based on cone 0.4 jets made up of calorimeter towers, though in a crude approximation. Generally, the choice of clustering algorithm (calorimeter towers or topological clusters) does not cause large differences, except in the forward part of the detector. In this analysis the main emphasis is on central jets, which are within the acceptance of the inner detector. Also, jets are not used for mass reconstruction, making their exact energy calibration less important.

In general, narrow jets (cone 0.4 or k_\perp 0.4) are preferable for analyses of final states with a lot of activity, e.g. $t\bar{t}$ events. Larger jets are needed when it is very important to collect all the jet energy, e.g. for reconstruction of the hadronic W mass in $W \rightarrow jj$, or in the measurement of QCD jet cross sections.

9.2.2 Jet Reconstruction in ATLFAST

ATLFAST gives a very simplified description of the ATLAS calorimeter. All stable generator particles are propagated through a perfectly homogeneous solenoidal magnetic field. The primary vertex is assumed to be at $(0,0,0)$. The impact point of all propagated particles on the calorimeter surface is calculated, any interactions with the detector material, like conversions, energy loss or multiple scattering are not taken into account. Effects of these are later on corrected by appropriate resolution functions.

The energies of electrons, photons and hadrons reaching the calorimeter surface are deposited in a calorimeter tower map with a size of 0.1×0.1 in $|\eta| < 3.2$ and 0.2×0.2 in $3.2 < |\eta| < 5.0$, that is sketched in Figure 9.17. No smearing is applied at this stage, and also no lateral or longitudinal shower development is simulated. There is no distinction between the EM and the hadronic calorimeter, and the response is assumed to be equal to one.

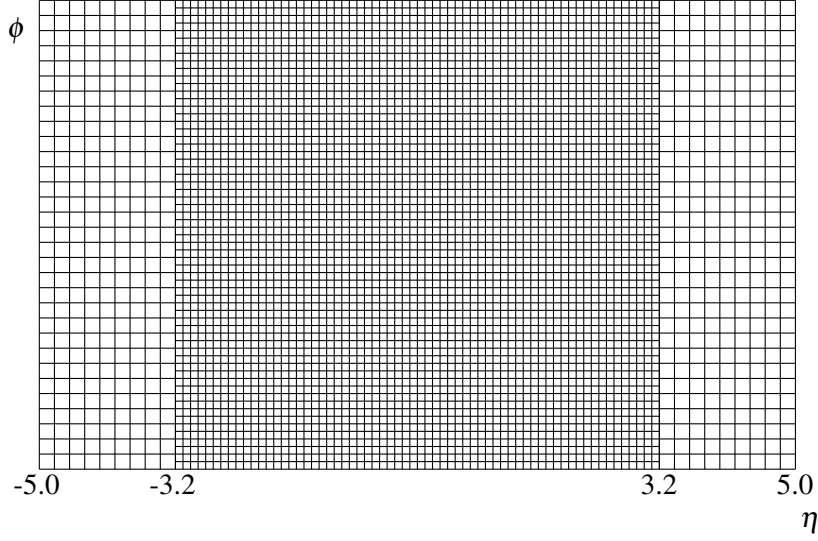


Figure 9.17: The ATLAS calorimeter as implemented in ATLFAS as a calorimeter tower map.

In a next step, *clusters* are formed from the deposited energies. This is done using a *simple* cone algorithm with $\Delta R = 0.4$. The algorithm is initiated by seeds with $E_T > 1.5$ GeV and applied to all seed towers in decreasing order of E_T . An important difference to the cone algorithm used in the detailed reconstruction is that it is a simple cone algorithm, which means that it is *not iterative*. This means that the jet axis is readjusted after the first step, but no new clustering step taking into account the moved axis is performed. In addition, in the ATLFAS jet algorithm, a particular calorimeter tower can only be associated to one cluster and the split-merge phase of the iterative cone algorithm is missing as well.

Only clusters with a minimum energy of 5 GeV are retained. After clusters assigned to originate from isolated electrons or photons are removed, and non-isolated muons are added to the corresponding cluster, the remaining clusters are considered as jets, if their transverse energy is larger than 10 GeV. The jet energy is taken to be the cluster energy, and is smeared according to the expected jet energy resolution, as given in Equations 5.6 and 5.7.

As the response of the ATLFAS is set to one by construction, no calibration of the reconstructed jets is necessary. In this sense they should be directly comparable to the globally calibrated jets from the detailed reconstruction. However, ATLFAS also contains the option to simulate the effect of an in-situ calibration of the jet energy scale, which also takes into account out-of-cone energy. This is accomplished by the ATLFASB package, which contains a parameterized correction factor. But as these factors are not readily available for the jets from detailed reconstruction, this calibration is not used in the following for consistency reasons. Although it would be possible to use the same calibration also for

full detector simulation, this approach was not taken, since no hadronic masses are used in the analysis.

9.2.3 Jet Labeling

It is sometimes useful to separate jets into different categories, depending on which type of parton they have originated from. Obviously, this is not possible in real data, but only on Monte Carlo events. Even here, the unique assignment of a jet to a parton is ambiguous at best, due to the effects of parton showers and hadronization. Nevertheless, a simple jet labeling procedure has been adopted in ATLAS which is described in the following.

The labeling of a jet is based on the distance between the jet axis and the quarks just before hadronization, i.e. after parton showering. If a b quark with $p_T > 5$ GeV is found within $\Delta R < 0.3$ of the jet, it is labeled as a b jet. If instead, a c quark or a hadronically decaying τ lepton is found using the same cuts, the jet is labeled as a c jet or a τ jet. If no b , c or τ is present satisfying these requirements, the jet is labeled as a light jet, where no difference is made between the remaining flavors. These jets are in the following called *udsg* jets.

One problem with this simple labeling procedure is that it does not take the event topology into account. If an *udsg* jet happens to be close to a b jet, it might still be labeled as an *udsg* jet. Tracks coming from the decay of a B hadron might be associated with it, thus altering the behavior of this type of jets. To take these effects into account, the jets labeled as *udsg* jets are split into two exclusive subclasses: One where no b , c or τ are found in a $\Delta R = 0.8$ cone around the jet axis, and those where a heavy quark or τ lepton is within this region. These two classes are in the following called *purified* and *non purified* *udsg* jets.

9.2.4 Jet Reconstruction Efficiency

As described, the jet reconstruction is fundamentally different between FULLSIM and ATLFAST. First of all, the used jet algorithms are different, especially as the ATLFAST algorithm is not iterative. Also the choice of seeds and the size of seed cells is very different, and ATLFAST does not take the exact geometry of the calorimeters and any material in front of the calorimeters into account. In this respect, differences in the jet reconstruction efficiency can be expected.

The jet reconstruction efficiency is compared by trying to find reconstructed jets within a ΔR cone of 0.4 around the jet axis of a truthjet (cone 0.4). The cone size is chosen to be rather large to take into account the non-iterative nature of the ATLFAST jet algorithm. Figure 9.18 shows the jet reconstruction efficiency in dependence of the p_T of the truthjet (left) and of the pseudorapidity (right) for the $Z^0 + \text{light}$ (SHERPA) sample.

Clearly the jet reconstruction efficiency is much higher in ATLFAST than in FULLSIM, especially at low transverse momenta and at high pseudorapidities. Since the b jets of the signal tend to have a small transverse momentum, this can be an important effect.

The rather large inefficiency at large $|\eta|$ is in part due to the rather large seed threshold ($E_T = 2$ GeV), which affects especially the calorimeter tower based jet reconstruction. Part

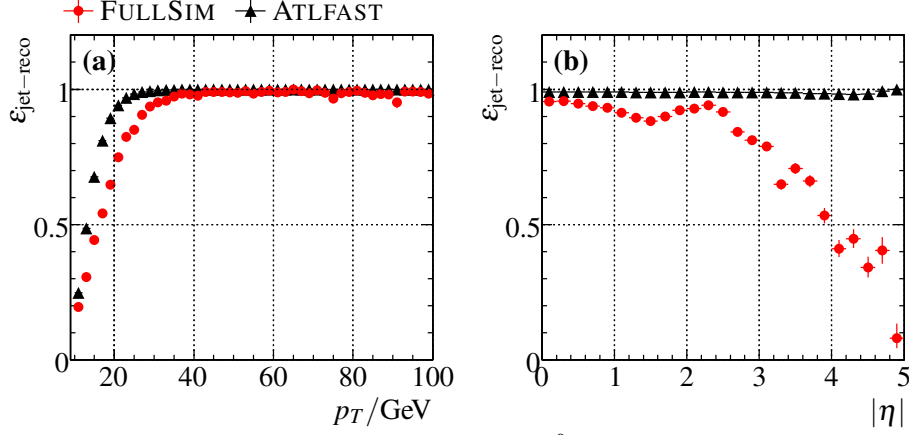


Figure 9.18: Jet reconstruction efficiency in the Z^0 + light sample for FULLSIM (red closed circles) and ATLFAS (triangles). (a): Versus the truthjet p_T in $|\eta| < 2.5$, (b): versus $|\eta|$ for $p_T > 20$ GeV.

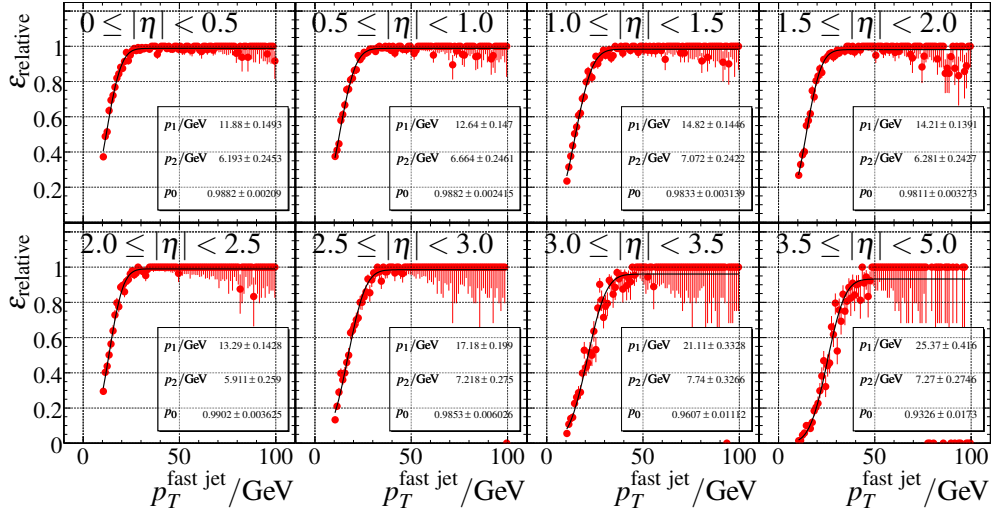


Figure 9.19: Relative jet reconstruction efficiency between ATLFAS and FULLSIM in eight different $|\eta|$ bins for the Z^0 + light jets sample (datapoints) and fitted step functions (lines).

of this inefficiency is recovered in recent ATLAS software releases where this threshold is lowered. Jets based on topological clusters also show an improved efficiency in this region.

A correction procedure is devised using the $Z^0 + \text{light jets}$ sample: On an event-by-event basis, for each ATLFAST jet a matching FULLSIM jet within $\Delta R < 0.4$ is looked for. In this way the *relative* jet reconstruction efficiency is calculated. This method has the advantage that it is independent of any miscalibrations between ATLFAST and FULLSIM. To take the detector geometry better into account, the relative efficiency is derived in dependence of the p_T of the ATLFAST jet in eight different $|\eta|$ regions. Figure 9.19 shows the resulting turn-on curves. In each $|\eta|$ region the turn-on curve is fitted with a step function:

$$\varepsilon_{\text{relative}}(p_T) = 0.5 \cdot p_0 \cdot \left(1 + \text{erf} \left(\frac{p_T - p_1}{\sqrt{2} p_2} \right) \right), \quad (9.9)$$

where erf is the Gaussian error function. The parameter p_0 is the efficiency in the plateau at high p_T , the parameter p_1 the p_T value where a relative efficiency of 50% is reached, and p_2 describes the steepness of the turn-on. To correct for the difference in jet reconstruction efficiencies, jets in ATLFAST datasets are removed randomly according to these fitted turn-on curves, that are taken as probabilities to retain an ATLFAST jet.

Figure 9.20 shows the resulting overall efficiencies for the $Z^0 + \text{light}$, $Z^0 + b$, $t\bar{t}$, and one exemplary signal sample in dependence of p_T and $|\eta|$ of the truthjet. The p_T dependence is only shown for jets within $|\eta| < 2.5$, corresponding to the acceptance for b jet identification. The $|\eta|$ dependence is shown only for jets with $p_T > 20$ GeV. The reconstruction efficiencies are now in reasonable agreement between FULLSIM and ATLFAST, especially in the central detector region. Beyond $|\eta| = 3$ significant deviations are visible. This is caused by the relatively coarse binning used for the parameterization of the relative efficiency, and could be improved by using a higher statistics Monte Carlo sample, thus allowing a finer binning. In this case, the parameterization only represents the mean efficiency in the range $3.5 \leq |\eta| < 5$.

There is also a small difference at low transverse momenta. This is due to a slightly different energy calibration between FULLSIM and ATLFAST (see below). As a consequence, if plotted versus p_T of the truthjet, the efficiencies seem to be different. The effect is much smaller above 20 GeV and disappears completely for high p_T , where the reconstruction efficiencies agree within 1%.

Figure 9.21 shows the $|\eta|$ distributions of all truthjets with $p_T > 20$ GeV. The pseudorapidity distributions between the different samples do not vary very strongly. In addition, the bulk of the cross section is at small $|\eta|$, where the reconstruction efficiency is well corrected and above 90%. At most, 10% of all jets have $|\eta| > 3.5$. The differences at large $|\eta|$ are expected to have only negligible influence on the event selection.

To quantify the remaining differences, the average jet reconstruction efficiency is best suited, as it will represent the actual influence on the event selection. The binning effects will introduce a slight bias in differential distributions, but this is unavoidable in this approach. The analysis itself is sensitive to mismodeling of the jet reconstruction efficiency in two ways: First, the efficiency in the acceptance region for b jets needs to be very well modeled, since any deviation here enters directly the accepted cross section. Jets beyond

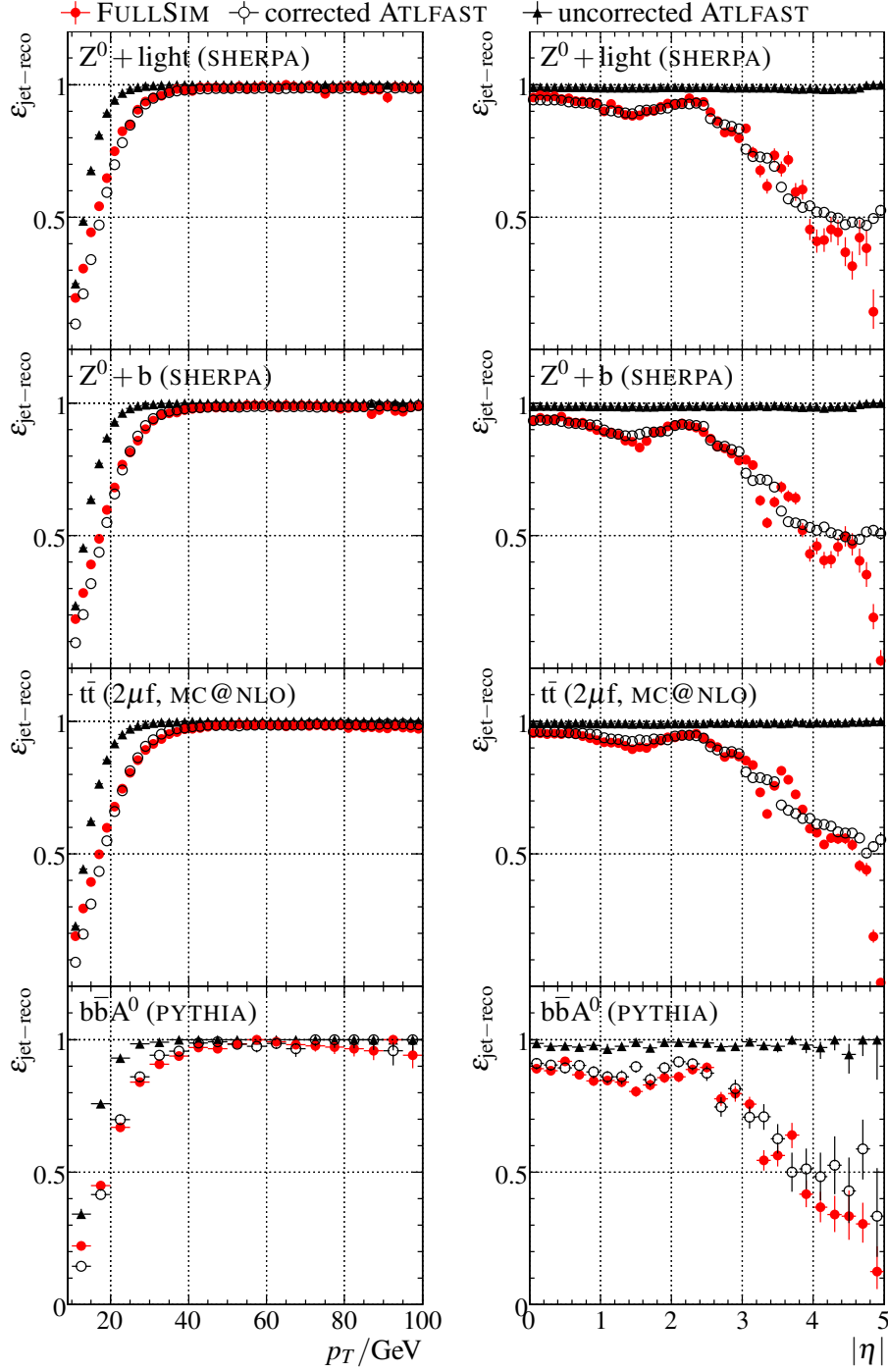


Figure 9.20: Jet reconstruction efficiency vs. p_T for $|\eta| < 2.5$ (left column) and $|\eta|$ for $p_T > 20$ GeV (right column). Closed (red) circles: FULLSIM, open circles: corrected ATLFast, triangles: uncorrected ATLFast. From top to bottom: $Z^0 + \text{light}$ (SHERPA), $Z^0 + b$ (SHERPA), $t\bar{t}$ ($2\mu\text{f}$, MC@NLO), $b\bar{b}A^0$ ($M_{A^0} = 200$ GeV, PYTHIA).

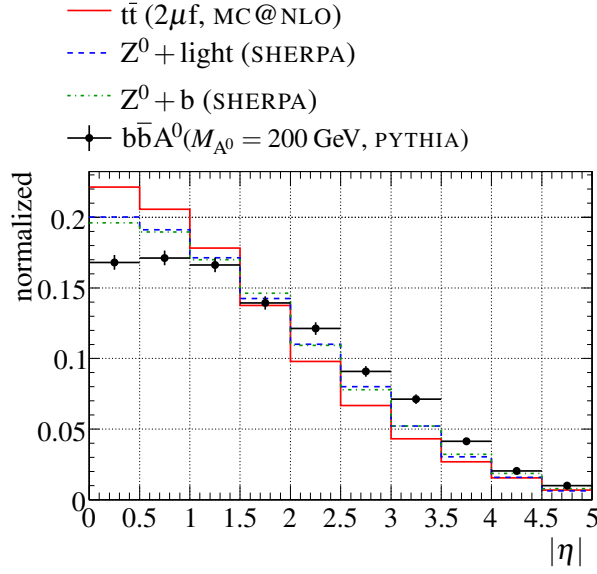


Figure 9.21: Truthjet $|\eta|$ distributions for $t\bar{t}$ (solid line), $Z^0 + \text{light}$ (dashed line), $Z^0 + b$ (dash-dotted line), and $b\bar{b}A^0$ (circles). A cut of $p_T > 20$ GeV is applied.

this acceptance cut of $|\eta| < 2.5$ cannot be identified as a b jet. They might still be used for other event shape variables, but as most jets are in the central detector region, a perfect modeling of the jet reconstruction in this outer region is not necessary. In the real experiment, it will be very difficult to get a quantitative handle on jets in the forward region.

Table 9.4 shows the average jet reconstruction efficiencies in these two regions for FULLSIM and corrected ATLFAST, as determined in background and signal samples. In the central region, the overall efficiencies agree to better than 2%, and also to 3% or better in the differential shapes. In the forward region, more sample dependence is visible. Especially the PYTHIA signal samples show deviations up to 10% here. Taking these deviations as a conservative estimate on the uncertainty of the jet reconstruction efficiency due to the remaining mismodeling of ATLFAST yields an uncertainty of about 3% on the total jet reconstruction efficiency. This is due to the fact that more than 75% of all jets are within $|\eta| < 2.5$, thus the impact of the mismodeling in the forward region is less important.

As the correction procedure has been derived on the $Z^0 + \text{light}$ jets sample, which contains almost no b jets, its application on b jets needs to be checked. This is partly done in the comparisons in the $Z^0 + b$ and $t\bar{t}$ samples, which contain significant fractions of b jets. In addition, the reconstruction efficiency of true b jets has been determined in the $Z^0 + b$ sample. This is done by requiring a b quark within $\Delta R = 0.3$ of the truthjet. The result for the $Z^0 + b$ sample is shown in Figure 9.22. The agreement for true b jets is on the same level as for the case where no requirement on any close-by b quarks is made.

sample	$ \eta < 2.5, p_T > 20 \text{ GeV}$			$ \eta > 2.5, p_T > 20 \text{ GeV}$		
	$\frac{\bar{\epsilon}_{\text{FULLSIM}}}{\%}$	$\frac{\bar{\epsilon}_{\text{ATLFAST}}}{\%}$	$\frac{\bar{\epsilon}_{\text{FULLSIM}}}{\bar{\epsilon}_{\text{ATLFAST}}}$	$\frac{\bar{\epsilon}_{\text{FULLSIM}}}{\%}$	$\frac{\bar{\epsilon}_{\text{ATLFAST}}}{\%}$	$\frac{\bar{\epsilon}_{\text{FULLSIM}}}{\bar{\epsilon}_{\text{ATLFAST}}}$
$Z^0 + \text{light}$ SHERPA	$92.8^{+0.2}_{-0.2}$	$92.10^{+0.02}_{-0.02}$	$1.010^{+0.002}_{-0.002}$	$72.1^{+0.6}_{-0.6}$	$72.8^{+0.1}_{-0.1}$	$0.99^{+0.01}_{-0.01}$
$Z^0 + b$ SHERPA	$90.5^{+0.1}_{-0.1}$	$91.01^{+0.03}_{-0.03}$	$0.995^{+0.002}_{-0.002}$	$68.9^{+0.4}_{-0.4}$	$70.8^{+0.1}_{-0.1}$	$0.97^{+0.01}_{-0.01}$
$t\bar{t}, 2\mu f$ MC@NLO	$93.52^{+0.05}_{-0.05}$	$94.64^{+0.03}_{-0.03}$	$0.994^{+0.001}_{-0.001}$	$77.6^{+0.2}_{-0.2}$	$78^{+0.1}_{-0.1}$	$0.995^{+0.003}_{-0.003}$
$b\bar{b}A^0(110)$ PYTHIA	$84.2^{+0.9}_{-0.8}$	$86.6^{+0.8}_{-0.8}$	$0.97^{+0.01}_{-0.01}$	60^{+2}_{-2}	68^{+2}_{-2}	$0.88^{+0.04}_{-0.04}$
$b\bar{b}A^0(200)$ PYTHIA	$86.2^{+0.5}_{-0.5}$	$88.1^{+0.7}_{-0.6}$	$0.98^{+0.01}_{-0.01}$	$64.8^{+1.3}_{-1.3}$	71^{+2}_{-2}	$0.91^{+0.03}_{-0.03}$
$b\bar{b}A^0(110)$ SHERPA	$89.0^{+0.8}_{-0.8}$	$88.9^{+0.5}_{-0.5}$	$1.02^{+0.01}_{-0.01}$	64^{+2}_{-2}	68^{+1}_{-1}	$0.94^{+0.04}_{-0.04}$
$b\bar{b}A^0(130)$ SHERPA	$89^{+0.7}_{-0.7}$	$89.0^{+0.5}_{-0.5}$	$1.01^{+0.01}_{-0.01}$	65^{+2}_{-2}	70^{+1}_{-1}	$0.93^{+0.03}_{-0.03}$
$b\bar{b}A^0(150)$ SHERPA	$89.2^{+0.7}_{-0.6}$	$89.9^{+0.5}_{-0.4}$	$0.99^{+0.01}_{-0.01}$	69^{+2}_{-2}	72^{+1}_{-1}	$0.96^{+0.03}_{-0.03}$
$b\bar{b}A^0(200)$ SHERPA	$89.7^{+0.6}_{-0.6}$	$91.3^{+0.4}_{-0.4}$	$0.98^{+0.01}_{-0.01}$	65^{+2}_{-2}	68^{+1}_{-1}	$0.95^{+0.03}_{-0.03}$
$b\bar{b}A^0(300)$ SHERPA	$90.3^{+0.6}_{-0.6}$	$91.1^{+0.5}_{-0.5}$	$0.99^{+0.01}_{-0.01}$	68^{+2}_{-2}	75^{+1}_{-1}	$0.91^{+0.03}_{-0.03}$
$b\bar{b}A^0(400)$ SHERPA	$91.2^{+0.5}_{-0.5}$	$92.3^{+0.3}_{-0.3}$	$0.99^{+0.01}_{-0.01}$	69^{+2}_{-2}	70^{+1}_{-1}	$0.98^{+0.03}_{-0.03}$

Table 9.4: Mean jet reconstruction efficiencies in the acceptance region of the inner detector ($|\eta| < 2.5$) and in the forward region ($|\eta| > 2.5$) and for a minimal jet p_T of 20 GeV.

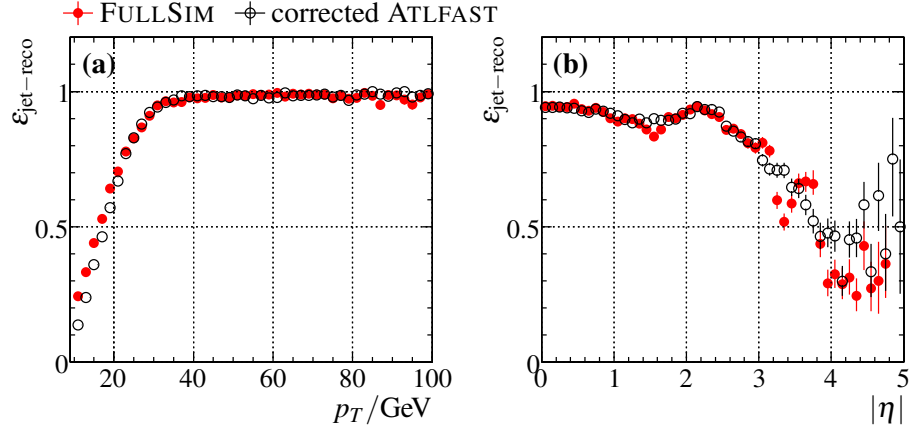


Figure 9.22: Jet reconstruction efficiency for true b jets in the $Z^0 + b$ (SHERPA) sample for FULLSIM (red closed circles) and corrected ATLFAST (black open circles). (a): Versus the truthjet p_T in $|\eta| < 2.5$, (b): versus $|\eta|$ for $p_T > 20$ GeV.

9.2.5 Jet Fake Probability

Another important figure of merit is the fake jet probability, which gives a measure on how probable it is for a given jet to be a fake jet. The fake probability is found by dividing the number of jets without a matching truthjet in $\Delta R < 0.4$ by the number of all jets. Figure 9.23 shows the fake probability in the $Z^0 + \text{light jets}$ sample in dependence of p_T and $|\eta|$ of the jets for events with exactly one isolated $\mu^+\mu^-$ pair, where each muon has $p_T > 20$ GeV. This requirement is done in order to avoid any ATLFAST jets where a muon from the Z^0 decay is added to a jet, since it is (falsely) non-isolated. This would result in

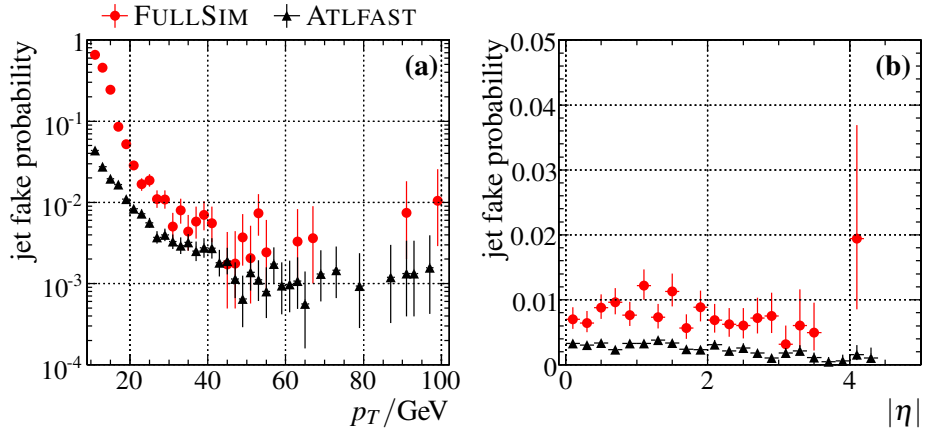


Figure 9.23: Jet fake probability in the $Z^0 + \text{light jets}$ sample for FULLSIM (red circles) and ATLFAST (black triangles) (a): Versus the jet p_T in $|\eta| < 2.5$, (b): versus $|\eta|$ for $p_T > 20$ GeV.

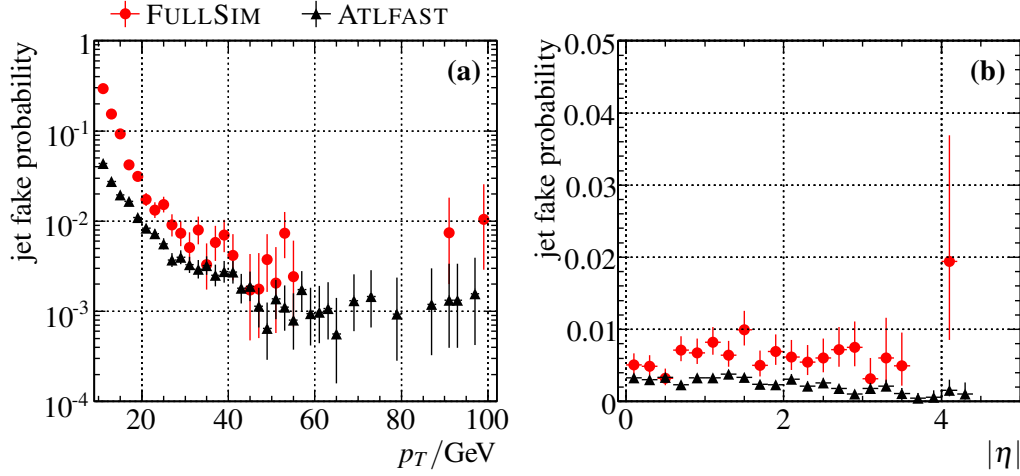


Figure 9.24: Jet fake probability in the Z^0 + light jets sample for FULLSIM (red circles) areas) and ATLFAST (black triangles) (a): Versus the jet p_T in $|\eta| < 2.5$, (b): versus $|\eta|$ for $p_T > 20$ GeV. Jets within $\Delta R < 0.3$ of an isolated muon are not considered.

jets that are completely dominated by the four momentum of the hard muon, which is not modeled at all in FULLSIM.

The jet fake probability at low p_T is a lot higher in FULLSIM than in ATLFAST. This is mostly due to a difference in the reconstruction algorithms: ATLFAST is completely blind to the energy loss of a muon in the calorimeter, whereas in FULLSIM it is possible that the jet finding algorithm *can* find the muon in the calorimeter. One solution to solve this problem would be to remove all jets that overlap with a reconstructed muon within a certain ΔR . But this is not desirable, since hadron decays into muons can result in a muon inside a jet. This removal should be restricted to isolated muons. In the following, jets are not considered if they are within $\Delta R < 0.3$ of the two isolated muons that are required in the event. It can be assumed that these are not from hadron decays, since the fake isolation rate is low, and any overlap between a jet and the muons is due to the jet finding algorithm finding the small energy deposition of the muon in the calorimeter. Figure 9.24 shows the resulting jet fake probability. The jet fake probability in FULLSIM decreases dramatically, but still a difference between FULLSIM and ATLFAST remains. Above a transverse momentum of 20 GeV, the modeling differences between FULLSIM and ATLFAST are no longer important, as the jet fake rate is below a few percent. Rather than randomly introducing fake jets into the ATLFAST samples, a general cut on the transverse momentum of jets at 20 GeV is applied. In this way the region of mismodeling is avoided.

9.2.6 Jet Calibration

Another important difference between jets in FULLSIM and in ATLFAST is a possibly different response and calibration. Though both algorithms should be calibrated to the same level, differences especially at low transverse momenta can remain. Such differ-

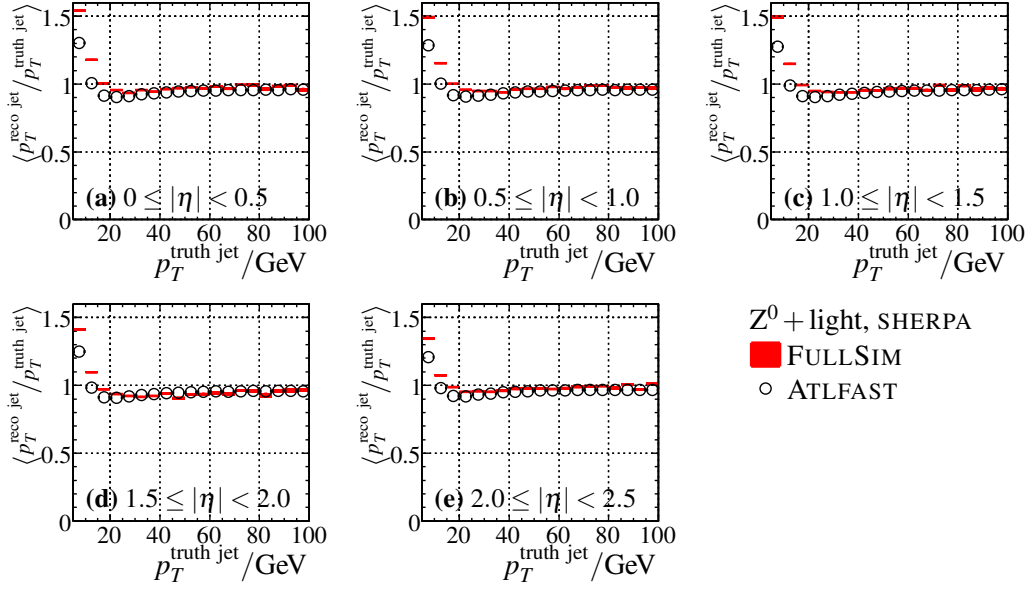


Figure 9.25: Jet response in dependence of p_T in five $|\eta|$ regions for the $Z^0 + \text{light}$ sample.

ences would mean that placing a p_T cut on a jet has a different effect in FULLSIM and in ATLFAST, since the cut would act on different equivalent truthjet momenta.

The level of miscalibration between FULLSIM and ATLFAST is investigated by looking at the mean value of the ratio of the transverse momenta between a reconstructed jet and the matching truth jet ($\Delta R < 0.4$). This mean is shown in dependence of p_T of the truthjet and in five different $|\eta|$ regions in Figure 9.25. The $Z^0 + \text{light jets}$ sample is used for this comparison. Generally the ATLFAST response is slightly lower than the one in FULLSIM. This might be due to the different jet algorithms. Above the chosen jet- p_T cut of 20 GeV, the agreement is better than 10%. It should be noted that, since the jet response is slightly lower than one, a jet- p_T cut of 20 GeV corresponds to slightly larger values of the p_T of the corresponding truthjet.

The larger deviations of the response from one below 15 GeV are a consequence of different reconstruction thresholds: In FULLSIM and in ATLFAST jets need to have a minimum transverse momentum of 10 GeV, the truthjets need only 7 GeV.

Although the level of miscalibration between ATLFAST and FULLSIM seems to be small at large p_T , it has a not negligible effect on the rates of reconstructed jets. This effect is most apparent in the $Z^0 + b$ sample, but can also be seen in other datasets. Figure 9.26 shows the reconstructed jet rate of true b jets in the $Z^0 + b$ sample. A preselection has been applied that consists of requiring exactly one $\mu^+\mu^-$ pair, each with $p_T > 20$ GeV and the standard isolation cut.

Despite the effort to correct the jet reconstruction efficiencies between ATLFAST and FULLSIM, the corrected ATLFAST has significantly too few jets at low transverse momentum than FULLSIM. At high transverse momentum the two predictions are very compa-

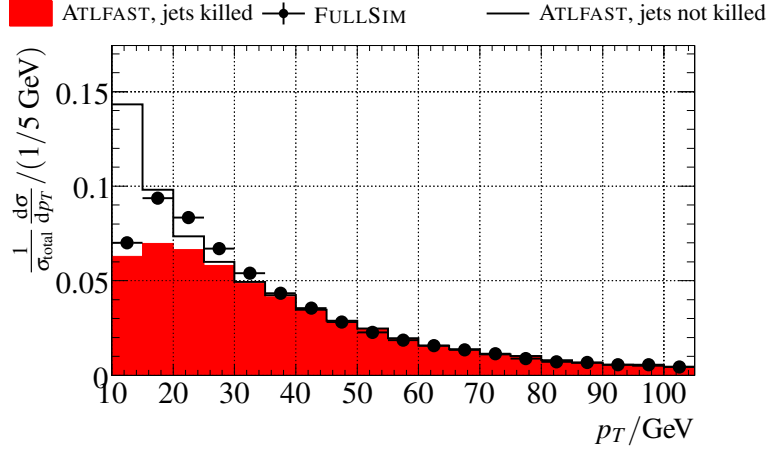


Figure 9.26: Jet rates of true b jets in the $Z^0 + b$ (SHERPA) sample. Solid histogram: ATLFAST with jet-killing, open histogram: ATLFAST without jet-killing, datapoints: FULLSIM. The jet rates have been normalized to the accepted cross section of the pre-selection cuts.

table. Leaving the jet-killing off does not improve the situation a lot above $p_T = 20$ GeV. Instead one gets a very large number of additional jets at very low transverse momentum, as expected from the larger efficiency in ATLFAST. This is a direct consequence of the miscalibration between ATLFAST and FULLSIM: The jet p_T spectrum is falling very rapidly. If the jet p_T measurement has a small difference between ATLFAST and FULLSIM, this results in a significant shift in the reconstructed spectrum. In principle this is in part taken care of in the jet-killing procedure, as the parameterization has been obtained vs. the transverse momentum of the ATLFAST jets. However, this parameterization has been obtained only for the $Z^0 + \text{light}$ sample, which is dominated by true udsg jets. In addition, the shifts in jet p_T needed to explain the differences are very small and within the uncertainties of the fitted jet turn-on curves. A more appropriate way of dealing with this effect would be to first find a correction for the ATLFAST jet energy scale and then find a new set of jet-killing corrections. But this is rather complicated and in addition might not lead to the desired results, as jets below $p_T = 10$ GeV are not reconstructed in ATLFAST. If the jet energy scale for low p_T jets is too small in ATLFAST, any jets below 10 GeV will not appear in the spectrum at all, leaving distortions in spite of the correction effort.

Instead a more phenomenological approach is taken: A global correction factor is applied to each ATLFAST jet, afterwards the jet-killing is applied using the new jet p_T . The correction factor is determined in such a way that the resulting jet rates are compatible with the FULLSIM result. As the jet energy scale difference between ATLFAST and FULLSIM can be dependent of the jet flavor, a different scaling factor is applied for b and other jets. In this way the remaining differences are simply parameterized. This rescaling approach is strongly driven by the difference in jet energy scales, but does not only correct this effect. Any other effects are simply parameterized in this way. It might very well be that the real difference in jet energy scales is underestimated, since applying the rescaling before the

jet-killing would overestimate the efficiency. The goal of this parameterization is only to improve the description above $p_T = 20$ GeV.

Obviously the needed rescaling factors have to be p_T dependent. At high transverse momentum no rescaling of the ATLFast jets is necessary. The following rescaling factor has been chosen:

$$r = 1.0 + C \cdot \exp\left(-\frac{p_T}{10 \text{ GeV}}\right). \quad (9.10)$$

The four vector of each ATLFast jet is rescaled using this multiplicative factor. The constant C is chosen to be 0.75 for true b jets and 0.325 for all others. To give a feeling for the size of the shift occurring, it is about 2 GeV for true b jets and 1 GeV for other jets for an original transverse momentum of 20 GeV. The latter number is of the same order as the binning of the histograms used to obtain the jet-killing parameterization, so it is within the systematic uncertainties.

Figure 9.27 shows the resulting jet rates before and after the momentum rescaling procedure for different types of jets and different samples. For all samples and types of jets a clear improvement of the description of jet rates is obtained. This is especially the case for true b jets. At low transverse momentum the improvement is not as good. For the first bin of the jet rate distribution the rescaled distribution seems to be worse than the unrescaled one. This is caused by the ATLFast jet cut-off at 10 GeV. Below this cut, no jets are reconstructed and cannot migrate to higher p_T , causing a seemingly worse behavior. Above $p_T = 20$ GeV the jet rates agree very well within 5 to 10%.

The largest differences are visible in the $Z^0 + \text{light}$ sample. The statistics is very limited, but true b jets in this sample show better agreement with the unrescaled ATLFast. This might be caused by another production mechanism of the b jets: For all other samples, b quarks occur at the matrix element level. For the $Z^0 + \text{light}$ sample, they have to be produced by the parton-shower. This might lead to significant kinematic differences leading to a different behavior of b jets in this sample. However, the effect is not statistically significant above 20 GeV.

For the $t\bar{t}$ sample the distribution of true b jets is a bit different between FULLSIM and the corrected ATLFast, but the effect is small.

In conclusion, the proposed rescaling procedure reproduces the FULLSIM jet rates very well for jets with (rescaled) transverse momentum of 20 GeV and more. For this analysis there is no need to find a more refined correction procedure. An obvious improvement would be to apply the rescaling dependent on the pseudorapidity or other event shape variables.

Although the correction procedure works properly in this case, it has to be noted that very small shifts of the jet momenta are enough to produce rather large differences. This is caused by the jet turn-on, which is in this region, and by the steeply falling p_T spectra. This underlines the fact that this analysis is very sensitive to the modeling of jet reconstruction efficiencies and the jet energy scales. If the real experiment also has miscalibrations compared to FULLSIM, this will lead to very similar differences as shown in this study. It will be very important to study these effects in data.

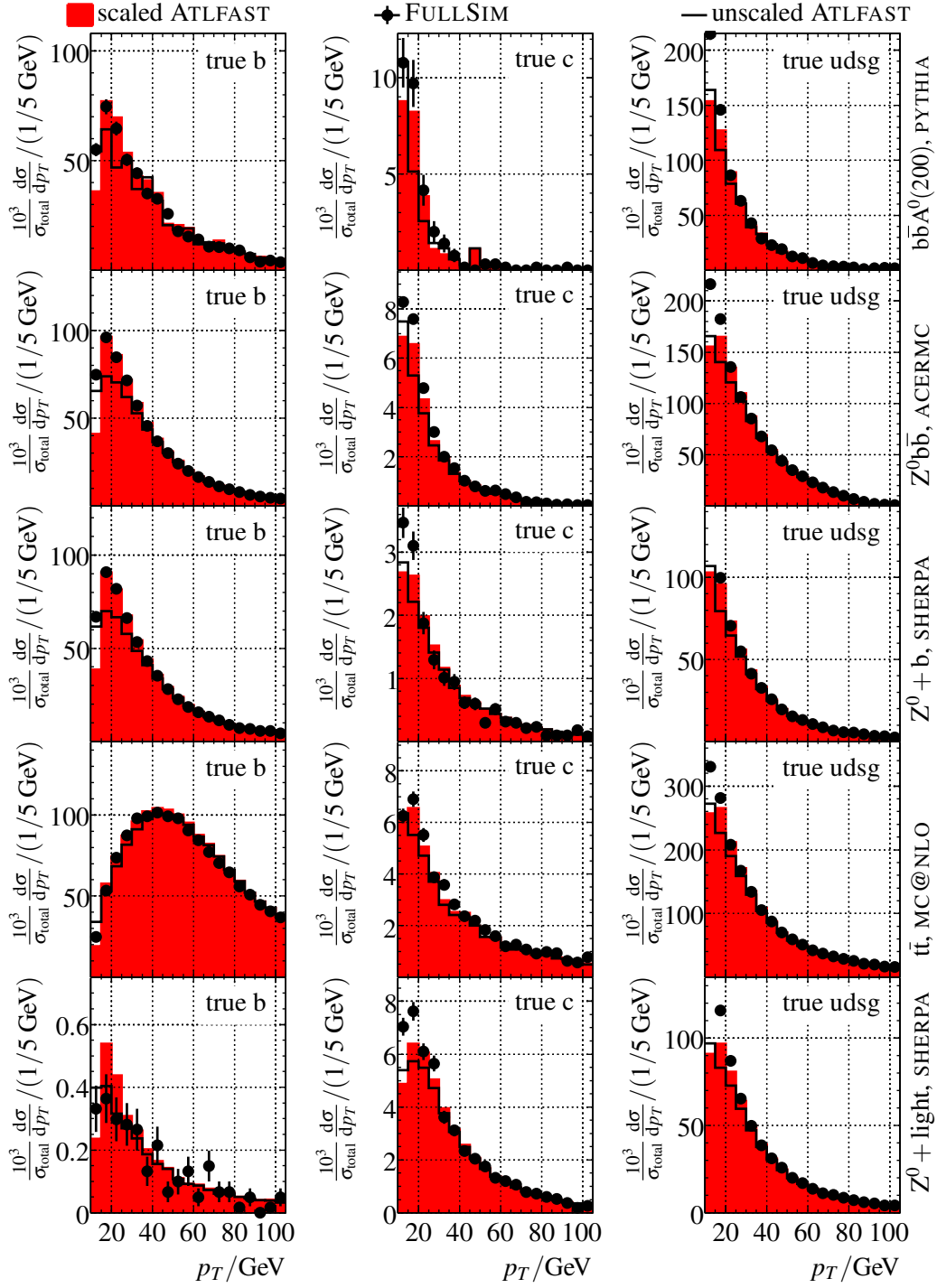


Figure 9.27: Jet rates for true b jets (left column), true c jets (middle column), and true udsg jets (right column). Solid histogram: Rescaled ATLFast, open histogram: ATLFast without rescaling, data-points: FULLSIM. From top to bottom: $b\bar{b}A^0$ ($M_{A^0} = 200$ GeV, PYTHIA), $Z^0b\bar{b}$ (ACERMC), $Z^0 + b$ (SHERPA), $t\bar{t}$ ($2\mu\text{f}$, MC@NLO), $Z^0 + \text{light}$ (SHERPA).

9.2.7 Jet Resolution

Last, the jet p_T resolution is compared. To quantify this, the width of the distribution of the difference between the jet p_T and the matched truth jet p_T , divided by the truth jet p_T is used. This corresponds directly to the relative jet p_T resolution. It is shown for different regions of pseudorapidity in dependence of the truth jet p_T in Figure 9.28 for the $Z^0 + \text{light}$ sample.

ATLFAST shows a slightly better resolution than FULLSIM, especially in the transition region between barrel and end-cap calorimeters ($1.25 < |\eta| < 1.75$). This effect is less pronounced in the forward detector regions. It has to be noted that although the resolution in transverse momentum is better for large $|\eta|$, this is not the case for the jet energy resolution: Jets in the forward direction have a much higher energy for a given transverse momentum than central jets.

The effect of this difference is two-fold: First it can influence the acceptance of a cut on the jet p_T . This effect is actually either corrected by the jet energy rescaling procedure described above, or it is negligible since the jet rates agree very well between FULLSIM and the corrected ATLFAST.

The second effect is that the jet energy resolution enters in the measurement, and especially the resolution, of missing transverse energy. In this respect it would be very helpful to correct also the jet energy resolution. But since unclustered energy can not be corrected in the same step, a correction of the missing transverse energy needs to be done anyway. For simplicity, this correction is only done once, for the missing transverse energy. The jet energy resolution in ATLFAST is left unchanged as a more accurate description is not needed.

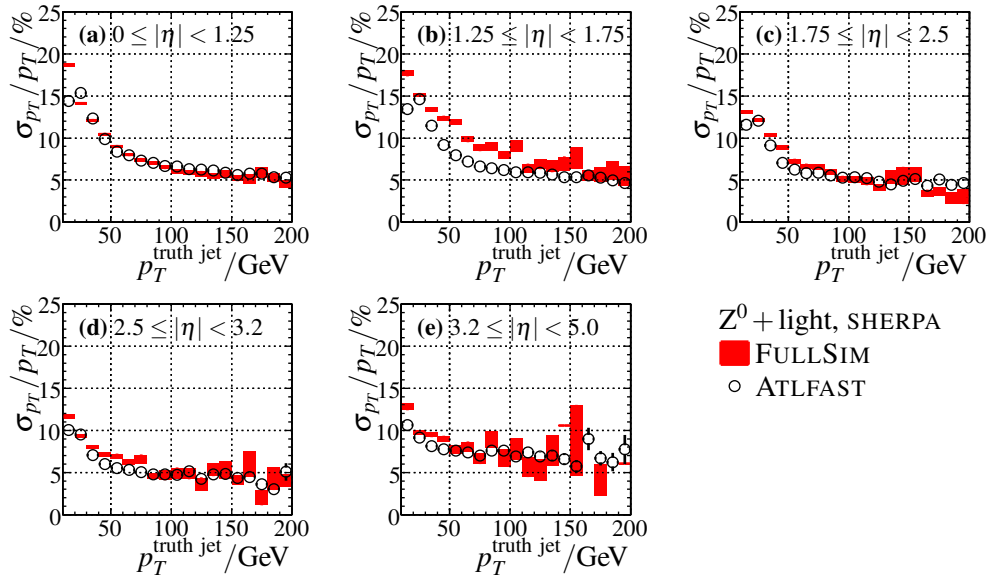


Figure 9.28: Relative jet p_T resolution in dependence of p_T in five $|\eta|$ regions for the $Z^0 + \text{light}$ sample.

9.2.8 Scalar Sum of Jet Momenta

One observable that is used in this analysis is the scalar sum of all jet transverse momenta, H_T . This is a useful variable to define both the “jettiness” of an event and to summarize how hard the jets in the event are. Events with only a few, soft jets tend to have small H_T , events with a lot of and/or hard jets have a large H_T . H_T is an example of an event shape variable. Due to the obvious modeling differences described in this section, in the following only jets with a minimal transverse momentum of 20 GeV but over the whole pseudorapidity region covered ($|\eta| < 5$) are used in the calculation of H_T .

Figure 9.29 shows the distribution of H_T calculated in this way after preselection cuts (one $\mu^+\mu^-$ pair, both isolated, $p_T > 20$ GeV) for FULLSIM and the corrected ATLFast. All distributions are normalized to the accepted cross section. The agreement between ATLFast and FULLSIM is good.

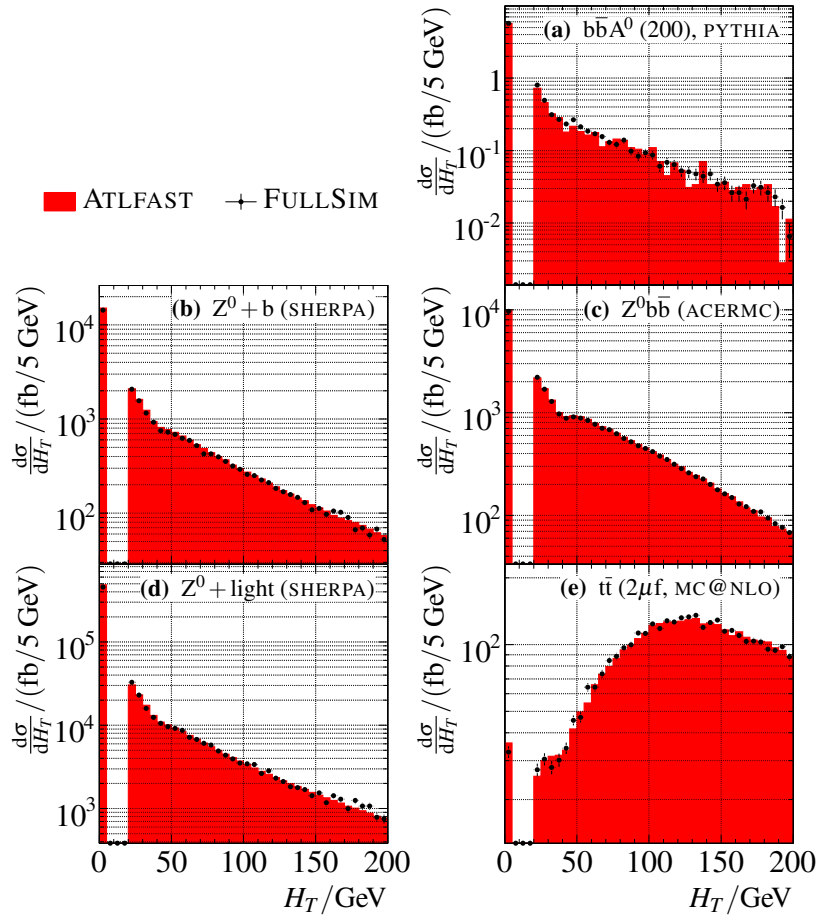


Figure 9.29: Distribution of H_T after preselection cuts for (a) $b\bar{b}A^0$ ($M_{A^0} = 200$ GeV, PYTHIA), (b) $Z^0 + b$ (SHERPA), (c) $Z^0 b\bar{b}$ (ACERMC), (d) $Z^0 + \text{light}$ (SHERPA), (e) $t\bar{t}$ ($2\mu\text{f}$, MC@NLO). Solid histogram: corrected ATLFast, points: FULLSIM.

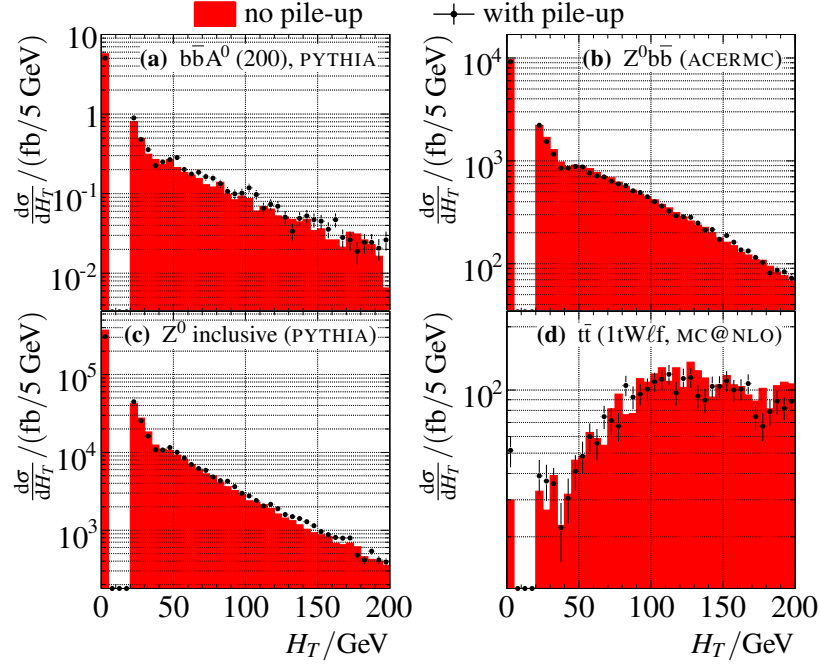


Figure 9.30: Distribution of H_T after preselection cuts for (a) bbA^0 ($M_{A^0} = 200 \text{ GeV}$, PYTHIA), (b) Z^0bb (ACERMC), (c) Z^0 inclusive (PYTHIA), (d) $t\bar{t}$ (1tWlf, MC@NLO). Solid histogram: without pile-up, points: with pile-up simulation.

Pile-up might lead to additional jets in the event which can have an influence on the reconstruction of H_T . Figure 9.30 shows the distribution of H_T normalized to the cross section after preselection with and without pile-up for those datasets for which pile-up samples are available. The distribution of H_T is very slightly shifted to higher values. A correction of this effect for ATLFast is not applied.

9.3 Flavor Tagging

A very important tool for the ATLAS physics program is the ability to tag reconstructed jets as arising from heavy flavor, especially from the fragmentation of b quarks. This is commonly called *b*-tagging, and is of utmost importance for many measurements and searches at the LHC, e.g. for $t\bar{t}$ analyses or searches for the Standard Model Higgs boson, which would decay dominantly into a pair of b quarks if its mass is not too large.

Within this study, *b*-tagging is also very important, as the b associated production process is dominant. Tagging one of the b jets reduces the backgrounds significantly. It should be noted that the b jets in the signal process are predominantly at low p_T , which is a challenging region of phase space for *b*-tagging.

The tagging of heavy flavor jets can be done based on different techniques, which make use of the properties of hadrons composed of heavy quarks. The different methods that are used in ATLAS are discussed in the following.

9.3.1 Life Time Tagging

A very important property of bottom hadrons is their relatively long life time due to the large suppression of quark mixing between the third and the other two generations. The mean decay length of bottom hadrons is of the order of 400 to 500 μm , which is significantly larger than for charmed hadrons. Taking into account the Lorentz boost, the mean decay length gets larger due to time dilatation. For a bottom hadron with an energy of a few dozen GeV, it can reach a few mm. The decay products of the bottom hadrons will not originate from the primary interaction point, as most of the other particles coming out of the fragmentation, but from a secondary decay point. This effect is enhanced by the fact that very often a bottom hadron decays among other particles into a charmed hadron, which travels further before decaying (*cascade decays*)². In addition, the mean charged multiplicity of bottom hadron decays is rather large (≈ 5.2 [140]), in contrast to charm hadrons (≈ 2.3 [141]) and hadrons consisting of light quarks.

In reconstructing the tracks of the charged particles and looking for *life time* information in them, i.e. indication for them to not have originated from the primary interaction point, b jets can be identified in an inclusive way without relying on specific decay modes.

In the following, some basic features of the life time tagging as used in ATLAS are discussed.

Tracking Algorithm

The track reconstruction algorithm used in ATLAS is too involved to describe in complete detail within this thesis. Here, only some basic concepts are discussed. More detail can be found in [142–145].

Track reconstruction in the inner detector has to deal with the very different three sub-detectors, Pixel and SCT as precision devices, and the TRT which provides more, but less precise measurements. In addition, the amount of material in the inner detector is quite large, limiting the resolution and efficiency at low transverse momentum due to multiple scattering.

The tracking can be divided into multiple steps. First, the raw data coming from the tracking detectors is preprocessed. Clusters in the Pixel and SCT are reconstructed, and the TRT drift time information is converted into calibrated drift circles. In addition, the two clusters from opposite sides of one SCT module are combined into one space point.

The default tracking algorithm then exploits the high granularity of the Pixel and the SCT detector to find tracks coming directly from the vicinity of the interaction point. Track

²As a side remark it should be noted that due to the lower mass of charmed hadrons, they will have at a given energy a larger Lorentz boost factor γ , resulting in decay lengths that are comparable to the ones of bottom hadrons. However, the decay multiplicity is smaller than for bottom hadrons, and the decay products are more boosted into the forward direction, making the c jets more difficult to be tagged.

cut on	value
p_T	$> 1 \text{ GeV}$
# of hits in Pixel+SCT	≥ 6
# of hits in Pixel	≥ 2
# of hits in innermost Pixel layer	≥ 1
transverse impact parameter	$ d_0 < 1 \text{ mm}$
longitudinal impact parameter	$ z_0 - z_{PV} \sin \theta < 1.5 \text{ mm}$
distance from jet axis	$\Delta R < 0.4$

Table 9.5: Track quality cuts for tracks used in lifetime tagging.

seeds are formed from a combination of space points in the three pixel layers and the innermost SCT layer. These seeds are extended into the SCT to form track candidates. These are fitted in a complete track fit, whose working procedure is documented in [142]. Ambiguities in how the clusters are assigned to tracks are resolved and fake tracks rejected, based on the number of shared clusters between different tracks and the number of holes, i.e. points in active detectors crossed by the track, but not having a cluster. The surviving tracks are then extended into the TRT, drift circles are added along a road around the track, and a final refit using the information of all three tracking detectors is done.

To increase the efficiency for secondary decays occurring inside the detector, e.g. the decays of K_S^0 , Λ , or photon conversions, a complementary track-finding is applied afterwards, which searches for unused track segments in the TRT. These track segments are extended inwards to collect space points in the silicon detectors.

Primary Vertex Reconstruction

Another important ingredient is the primary vertex of the event, for in order to identify the life time signature of bottom hadrons a starting point is necessary. The size of the luminous region inside ATLAS is rather small in the xy plane ($\approx 15 \mu\text{m}$), but more extended in z ($\approx 5.3 \text{ cm}$). In addition, it is not guaranteed by the LHC machine setup that the interaction region is centered around the center of the ATLAS coordinate system, e.g. in the xy plane deviations of about 1 mm can be expected.

The primary vertex is found by a set of dedicated algorithms, that are described in [143]. In case that more than one primary vertex is reconstructed, the one with the largest p_T sum of the attached tracks is chosen as the hard scattering vertex. This is especially important at higher luminosities, where more than one primary vertex can be present due to pile-up events.

Track Selection for Life Time Tagging

In order to reduce mismeasured and fake tracks, and to reject secondary tracks from K_S^0 , Λ and hyperon decays, additional requirements are placed on the tracks to be used in the b -tagging algorithms, which are listed in Table 9.5. d_0 and z_0 are the transverse and longitudinal impact parameters of the track. Regardless of the algorithm used to reconstruct a jet, which are strictly calorimeter based objects, reconstructed tracks within $\Delta R < 0.4$ of the jet axis are used for life time b -tagging.

Impact Parameter Tagging

One set of b -tagging algorithms using lifetime information are the impact parameter (IP) tagging algorithms. The basic premise of these is that tracks coming from a secondary (or tertiary) decay point do not necessarily point back towards the primary vertex, but will have a non-zero impact parameter.

To take into account resolution effects, the impact parameter is *signed*, which is depicted in Figure 9.31. It is positive if the track crosses the jet axis in front of the primary vertex and negative otherwise. Negative impact parameters can occur because of resolution effects, positive ones also because of resolution, but also due to true life time effects. In order to take into account the accuracy of the track reconstruction, commonly the impact parameter *significance* S_{d_0}/S_{z_0} defined as the impact parameter divided by its error is used. Figure 9.32 shows the distribution of the longitudinal impact parameter and its significance for $t\bar{t}$ events for true b , c and u jets. For the true b jets a clear tail towards high impact parameters is visible. Also the c jets show, as expected, some signs of non-zero life time.

The impact parameter tagging is implemented in various forms in ATLAS, mostly differing in whether only the transversal (IP2D), only the longitudinal (IP1D), or both (IP3D) impact parameters are used. Within this thesis, only results of the IP3D tagging algorithm are used. More detail can be found in [147].

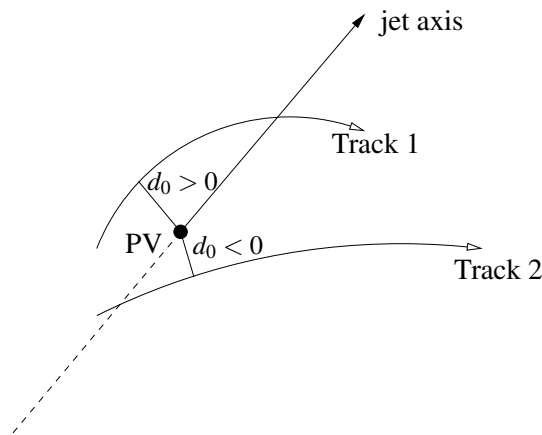


Figure 9.31: Definition of the sign of the impact parameter.

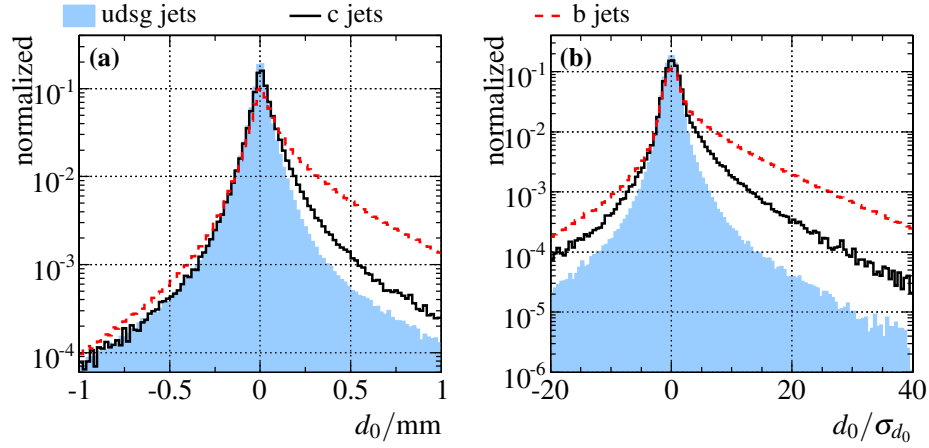


Figure 9.32: Distributions of the signed longitudinal impact parameter d_0 (a) and its significance d_0/σ_{d_0} (b) for tracks in b jets (red dashed line), c jets (solid black line) and udsg jets (blue shaded histogram) in $t\bar{t}$ events. Courtesy of [146].

To give a quantitative measure of the probability of the jet to be a b jet, a *likelihood ratio* method is applied. In this method, the distribution of the impact parameter significances is taken as a *probability density function*. Smoothed *reference histograms* for true b jets (P_b) and true light (u) jets (P_u) are prepared as a calibration of the tagging algorithm. In the case of the IP3D algorithm, these are two-dimensional in S_{d_0} and S_{z_0} . Each track assigned to a jet is given a weight according to the reference histograms:

$$w_{\text{track}}^i = \frac{P_b(S_{d_0}^i, S_{z_0}^i)}{P_u(S_{d_0}^i, S_{z_0}^i)} \quad (9.11)$$

A jet weight is constructed by taking the logarithmic sum of all track weights belonging to the jet:

$$w_{\text{jet}}^{\text{IP3D}} = \sum_i \log w_{\text{track}}^i. \quad (9.12)$$

According to the *Neymann Pearson Lemma* this is the optimal way of combining independent variables into a common measure. True b jets will tend to have large jet weights, while udsg jets will have small ones. The selection of a jet as a reconstructed b jet is then done by placing a cut on the value of the jet weight.

The reference histograms are at the moment still taken from Monte Carlo, but studies are underway on how to calibrate the *b*-tagging on data.

Secondary Vertex Tagging

The discrimination between b and udsg jets can be further enhanced by reconstructing the inclusive vertex from the bottom and possible subsequent charm hadron decay. Within

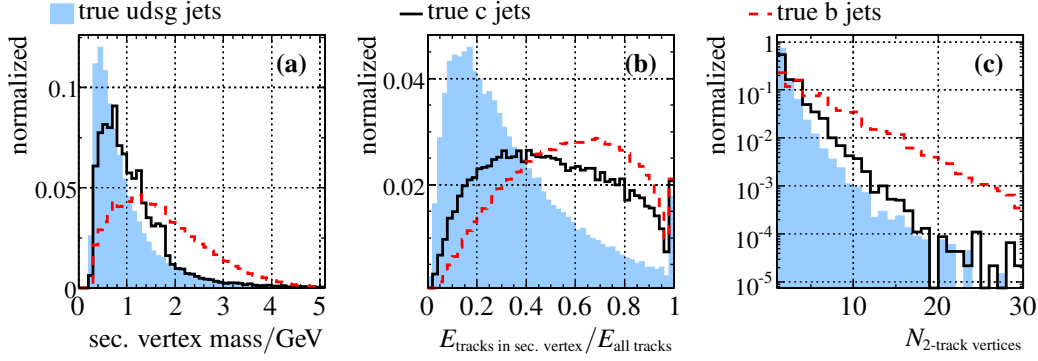


Figure 9.33: Properties of secondary vertex used for the secondary vertex tagger. (a): Secondary vertex mass, (b): fraction of track energy in the secondary vertex, (c): number of two track vertices formed. Red dashed line: true b jets, solid line: true c jets, shaded histogram: true udsg jets in the $t\bar{t}$ (1tW ℓ f, MC@NLO) sample. Courtesy of [146].

this algorithm, first all tracks with small impact parameters are discarded to remove those originating from the primary vertex. Then, all track pairs are combined that can be fitted to be coming from a good common vertex. At this stage, by exploiting the invariant mass of the two tracks forming the vertex and the location of the secondary vertex candidate, it is possible to reject K_S^0 and Λ decays, as well as interactions with detector material, such as photon conversions. All tracks from the two track vertices are then fitted to a common secondary vertex. To calculate a jet weight, just as in the case for the impact parameter based algorithms, it is necessary to know the probabilities of reconstructing a secondary vertex in a b jet ϵ_b and in a light jet ϵ_u . Furthermore, properties of the secondary vertex are used that are largely uncorrelated to the impact parameters of the tracks are used. These are the invariant mass of the secondary vertex, the ratio of the energy contained in the tracks forming the vertex to the sum of the energy of all tracks in the jet, and the number of two track vertices forming the secondary vertex. The distribution of these are shown in Figure 9.33 for $t\bar{t}$ events and can be used to calculate a jet weight:

$$w_{\text{jet}}^{\text{SV1}} = \begin{cases} \ln \frac{P_b \cdot \epsilon_b}{P_u \cdot \epsilon_u} & \text{if secondary vertex reconstructed} \\ \ln \frac{1 - \epsilon_b}{1 - \epsilon_u} & \text{else,} \end{cases} \quad (9.13)$$

where P_b and P_u are again probabilities obtained from reference histograms. Within this study the SV1 tagger is used, which takes into account correlations between the vertex mass and the energy fraction carried by the vertex by using two-dimensional reference histograms.

The secondary vertex tagger is more powerful than the purely impact parameter based taggers since it uses more information. However, it is expected to be less robust during initial data taking, since it not only uses more reference histograms, but also the secondary vertex reconstruction efficiencies for true b and true light jets are needed.

Combined Tagging

The weights of the IP3D and SV1 tagging algorithms are used in the following by summing them to a combined weight. At the moment, it is expected that this tagging algorithm will be the optimal one, i.e. it will yield the best rejection of light jets for a given efficiency to tag a b jet as such.

Figure 9.34 shows the distribution of the combined jet weight for a number of signal and background processes. As expected, true b jets tend to have large weights, while true udsg jets have smaller weights. True c jets, which are not used in obtaining the reference histograms, are in between the two. Differences in the weight distributions are mostly due to different p_T and η distributions of the jets in the different samples.

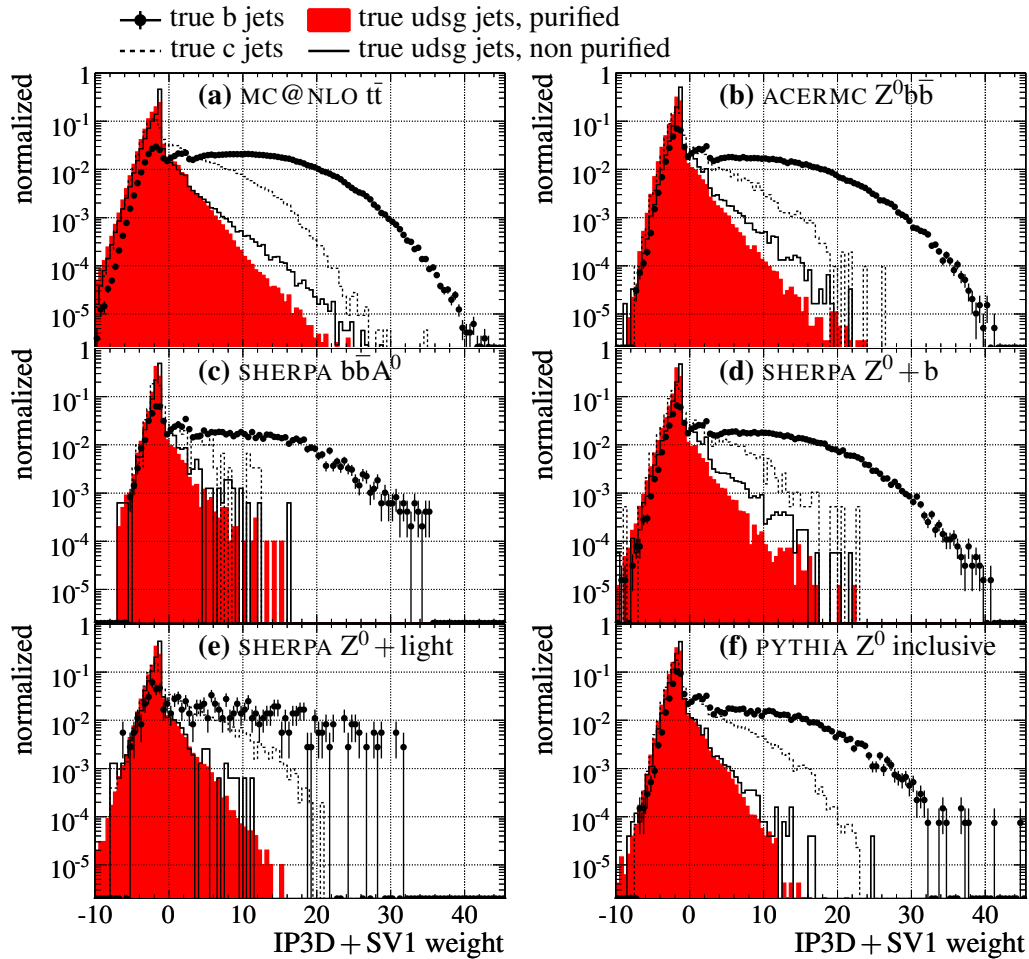


Figure 9.34: Distributions for different Monte Carlo samples of the combined jet weight (FULLSIM) for true b jets (points), true c jets (dashed line), true purified udsg jets (filled histogram), and true non-purified udsg jets (solid line).

9.3.2 b Tagging in ATLFAST

Although ATLFAST also contains a parameterization of the tracking performance in the inner detector, these tracks are not generally used. They are implemented for specific studies in B physics, but are not intended to be used for b -tagging. Instead, in ATLFAST a *statistical* b -tagging is applied, based on the Monte Carlo information of the jet flavor according to the labeling procedure. To do this, both the efficiency to tag a b jet as such, and the rejections of c jets, τ jets, purified and non-purified udsg jets are parameterized. The rejection is defined as the inverse of the tagging probability $R = 1/\epsilon$. The parameterization is based on FULLSIM Monte Carlo samples. In order to take different kinematic configurations into account, the efficiencies and rejections are parameterized in dependence of p_T and $|\eta|$ of the jet. Due to statistical reasons, this is done in bins of p_T and $|\eta|$ with the following binning:

$$|\eta| : [0.0, 0.5, 1.0, 1.5, 2.0, 2.5] \quad (9.14)$$

$$p_T/\text{GeV} : [10, 30, 45, 66.25, 100, 140, 180, 220, 260, \infty[\quad (9.15)$$

Due to historical reasons, the b -tagging efficiency in ATLFAST is set to a fixed value, while the rejections are then dependent of p_T and $|\eta|$. In FULLSIM this can only be realized by tuning the cut on the combined jet weight in each $(|\eta|, p_T)$ bin separately to obtain a fixed efficiency. The consequence is a weight-cut that is dependent on p_T and $|\eta|$.

In standard running of the used version of ATLFAST, the parameterization is done for the combined (IP3D+SV1) tagger, with a fixed efficiency $\epsilon_b = 60\%$.

However, the parameterization has been obtained using Monte Carlo samples processed with an older release of the ATLAS offline software (release 11 opposed to release 12 as used in this thesis). The main differences between the older software version and the newer one used to simulate the FULLSIM samples used in this study are an updated, more accurate description of the material present in the inner detector and also algorithmic changes in the tracking and b -tagging. As a consequence, the standard parameterization in ATLFAST does overestimate the b -tagging performance. This is shown in Figure 9.35, where the rejections of τ jets, c jets, purified, and non-purified light jets are shown in dependence of the p_T of the jet for a $t\bar{t}$ ($2\mu\text{f}$, MC@NLO) sample. The dependence on $|\eta|$ has been integrated out.

The standard parameterization overestimates the rejection of c jets and non-purified udsg jets by about 20 to 30%. For purified udsg jets, the performance is a factor of more than two worse in FULLSIM compared to ATLFAST. This is because of the impact of extra material in the inner detector, which leads to increased multiple scattering. In this way the impact parameter resolutions are worsened. For jets which contain true lifetime information, such as c jets, this effect is not as pronounced as for jets that only contain prompt tracks. This means that the rejection of purified udsg jets is degraded most, just as observed.

In addition, the reference histograms used for the b -tagging in FULLSIM are still based on the older software release with less material in the inner detector. They have only recently been updated to the newer detector description, but this optimization is not yet

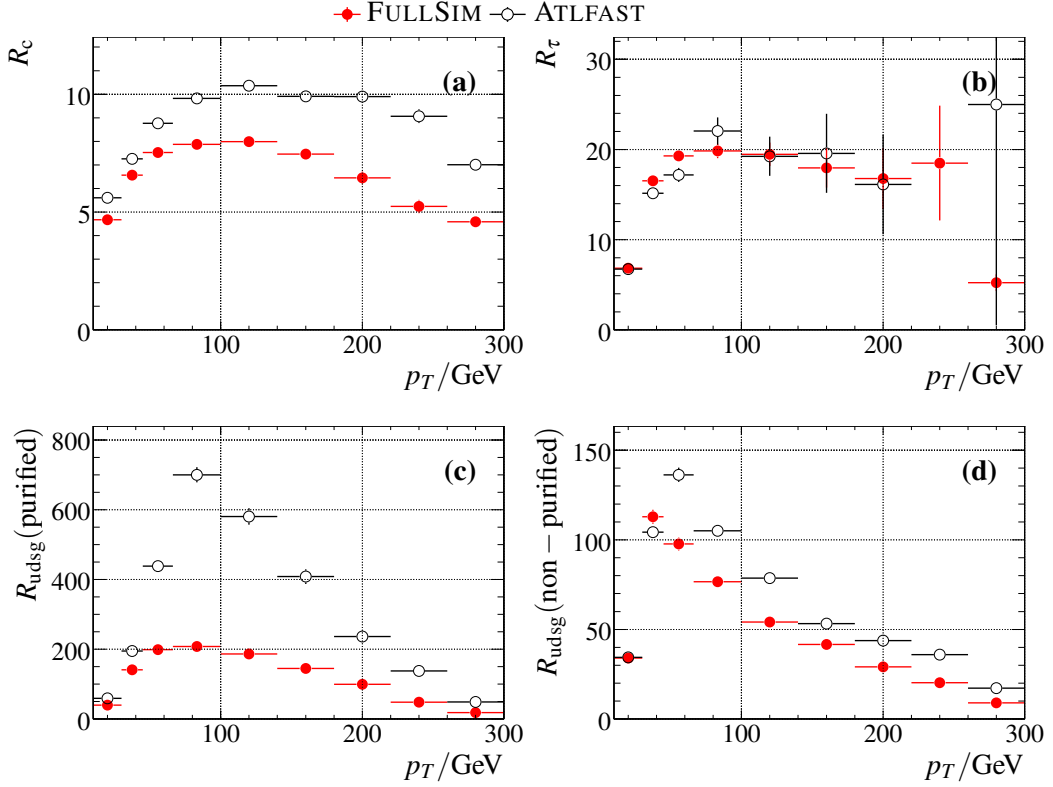


Figure 9.35: Rejections for a fixed b -tagging efficiency of 60% in the $t\bar{t}$ ($2\mu\text{f}$, MC@NLO) sample versus p_T of the jet. (a) Rejection of c jets, (b) rejection of τ jets, (c) rejection of purified udsg jets, (d) rejection of non-purified udsg jets. Closed circles: FULLSIM, open circles: ATLFAST, standard parameterization in ATHENA release 12.

applied to the FULLSIM samples used in this analysis. This could also contribute to the large degradation.

9.3.3 Updated Parameterization

In order to obtain a comparable b -tagging performance in FULLSIM and in ATLFAST, two points have to be taken into account: First the parameterization of efficiencies needs to be updated in order to reflect the latest changes in the b -tagging performance. Second, as in FULLSIM commonly b -tagging is applied not by choosing a fixed efficiency, but by choosing a specific weight cut, the parameterization needs to be done for a fixed cut on the jet weight. As it turns out, choosing a fixed jet weight cut is preferable, as it provides increased udsg jet rejection at low transverse jet momenta, where most of the $Z^0 + \text{light jets}$ background is concentrated.

The updated parameterization is derived from a mix of different Monte Carlo samples that have a very different topology. In this way, dependencies on the event topology are taken into account to some extent. The two sets of Monte Carlo samples are:

Sample	p_T range	cross section	number of events
J0	8 – 17 GeV	17.6 mb	560400
J1	17 – 35 GeV	1.38 mb	352350
J2	35 – 70 GeV	93.3 μ b	131800
J3	70 – 140 GeV	5.88 μ b	325050
J4	140 – 280 GeV	308 nb	316400
J5	280 – 560 GeV	12.5 nb	279900

Table 9.6: p_T ranges, cross sections and number of events in the QCD dijet samples used for the updated b -tagging parameterization. The cross sections are the leading order values as obtained from PYTHIA.

1. A $t\bar{t}$ (1tW ℓ f, MC@NLO) sample. This represents a rather crowded topology with a lot of jets in the event. In addition, the b jets from top quark decays and c and τ jets from W decays provide enough statistics to get a reasonable estimate for rejections of these. However, a $t\bar{t}$ sample has a very different topology from $Z^0 + \text{light}$ and $Z^0 + b$, where the jets tend to have a very small transverse momentum.
2. QCD dijets samples that were simulated using PYTHIA. These are generated in different ranges of p_T of the hard scattering process in order to take into account the steeply falling QCD cross section. Table 9.6 lists the samples used. This type of events should present a topology that is less crowded than $t\bar{t}$, since in this case only the two jets are expected which are expected to be well separated. However, the extraction of τ jet rejections is impossible.

The parameterization is now obtained from the sum of the $t\bar{t}$ and the QCD dijet samples. The $|\eta|$ binning is not changed compared to the old parameterization, as the η distribution of the jets in all samples is rather flat within $|\eta| < 2.5$. On the other hand, the p_T distribution of jets, especially in the $Z^0 + \text{light}$ sample, is falling very steeply. The bulk of the cross section is thus at low transverse momenta. If the binning of the parameterization is too coarse, this will lead to additional sample dependent b -tagging efficiencies and rejections just due to different p_T distributions. In order to avoid this effect, the p_T binning of the parameterization is made finer in the low p_T region:

$$p_T/\text{GeV} : [10, 15, 20, 25, 30, 35, 40, 45, 66.25, 100, 140, 180, 220, 260, \infty[\quad (9.16)$$

The high p_T region is left unchanged due to lack of statistics in the FULLSIM samples. The lowest two bins correspond to transverse momenta below the chosen jet p_T cut. In principle it would be possible to consider tagging jets in this region as well, but due to the observed differences between FULLSIM and ATLFast, this is not possible.

Before discussing the quality of the parameterization it is useful to summarize which part of it is most important for a proper description of the b -tagging in ATLFast. This cer-

tainly depends on the type of signal and background events. The b associated Higgs boson production, as well as $Z^0 + b$ and $t\bar{t}$ contain true b quarks, so one can expect the selection rate of a required tagged jet to be dominated by true b jets. The $Z^0 +$ light background on the other hand is dominated by u and d jets. It can also contain c jets (from the matrix-element) or b jets (from the parton shower). But in any case, the rejection of non-purified light jets is not expected to be overly important, since if a u or d jet is not well separated from a true heavy flavor jet, the heavy flavor jet is far more capable of causing a b tag. The rejection of τ jets is not necessary to be described in much detail, since the backgrounds do not contain any significant number of true τ jets after the first few selection steps.

Figures 9.36 to 9.40 show the efficiencies and rejection factor for true b , c , τ and u and d jets in the case of a cut on the combined jet weight of four. The b efficiency agrees in most of the phase space well between the $t\bar{t}$ and the dijets sample. Only at low and at high transverse momenta some disagreement is present. The parameterization itself is dominated by the $t\bar{t}$ sample due to the larger fraction of b jets in it. The differences to the dijet samples are about 5%, increasing to 10% in the outermost $|\eta|$ bin and at high transverse momentum. As the p_T distribution of b jets is falling, only a small fraction of events is affected by this uncertainty. The efficiency is lower at smaller p_T , since the flight distances of b hadrons get shorter and the impact parameter resolution gets worse for low p_T due to multiple scattering.

The rejection of c jets shows agreement on the level of 10% between the two samples. Curiously the rejection gets better for large $|\eta|$. This is caused by the larger amount of material that the tracks of the jets have to traverse in this region. This also causes some loss of b efficiency at high $|\eta|$.

The τ jet rejection is completely dominated by the $t\bar{t}$ sample, as the QCD dijets sample does contain only a minuscule amount of τ jets. Also, at large p_T and $|\eta|$ the parameterization is severely limited by the statistics of the $t\bar{t}$ sample. As τ jets do not play any significant role in the selection, this effect can be neglected. The rejection of purified u and d jets agrees on the level of 10% between the two samples. The same is definitely not true for non-purified u and d jets, where differences of 20% or even more are observed. This is probably due to the very different topology of the two event classes. In addition, the isolation cut of $\Delta R < 0.8$ to define purified and non-purified u and d jets is completely arbitrary, so these differences can be expected. A solution would be to provide a three-dimensional parameterization that also takes the distance to the next true heavy quark into account. Due to the limited statistics, this is not possible. However, as discussed before, non-purified u and d jets are not expected to play an important part of the background contribution to the analysis.

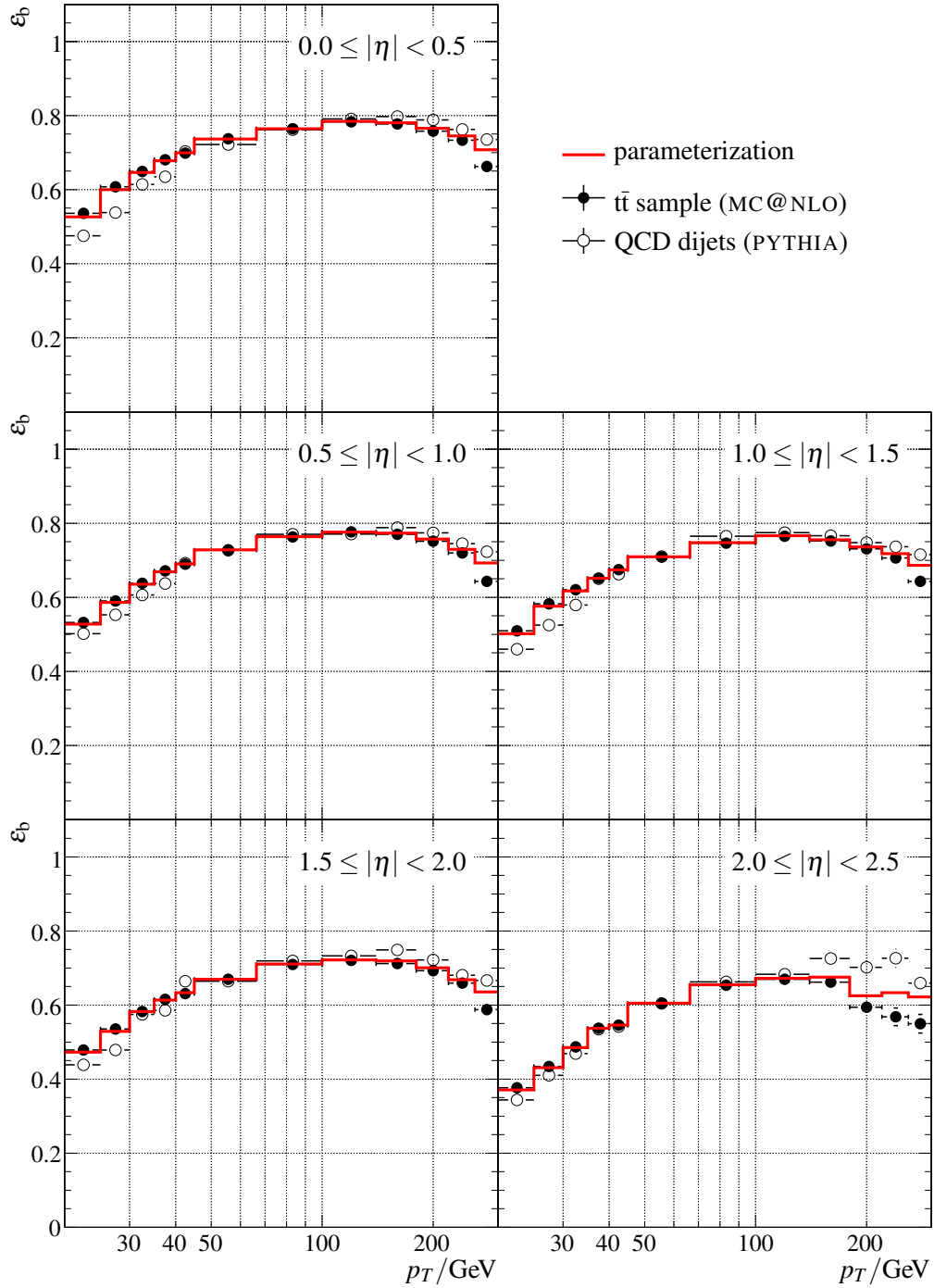


Figure 9.36: Parameterization of the b jet tagging efficiency for a weight-cut of four in dependence of p_T in five $|\eta|$ bins (red line). Closed circles: $t\bar{t}$ (1tWℓf, MC@NLO), open circles: QCD dijet (PYTHIA) samples.

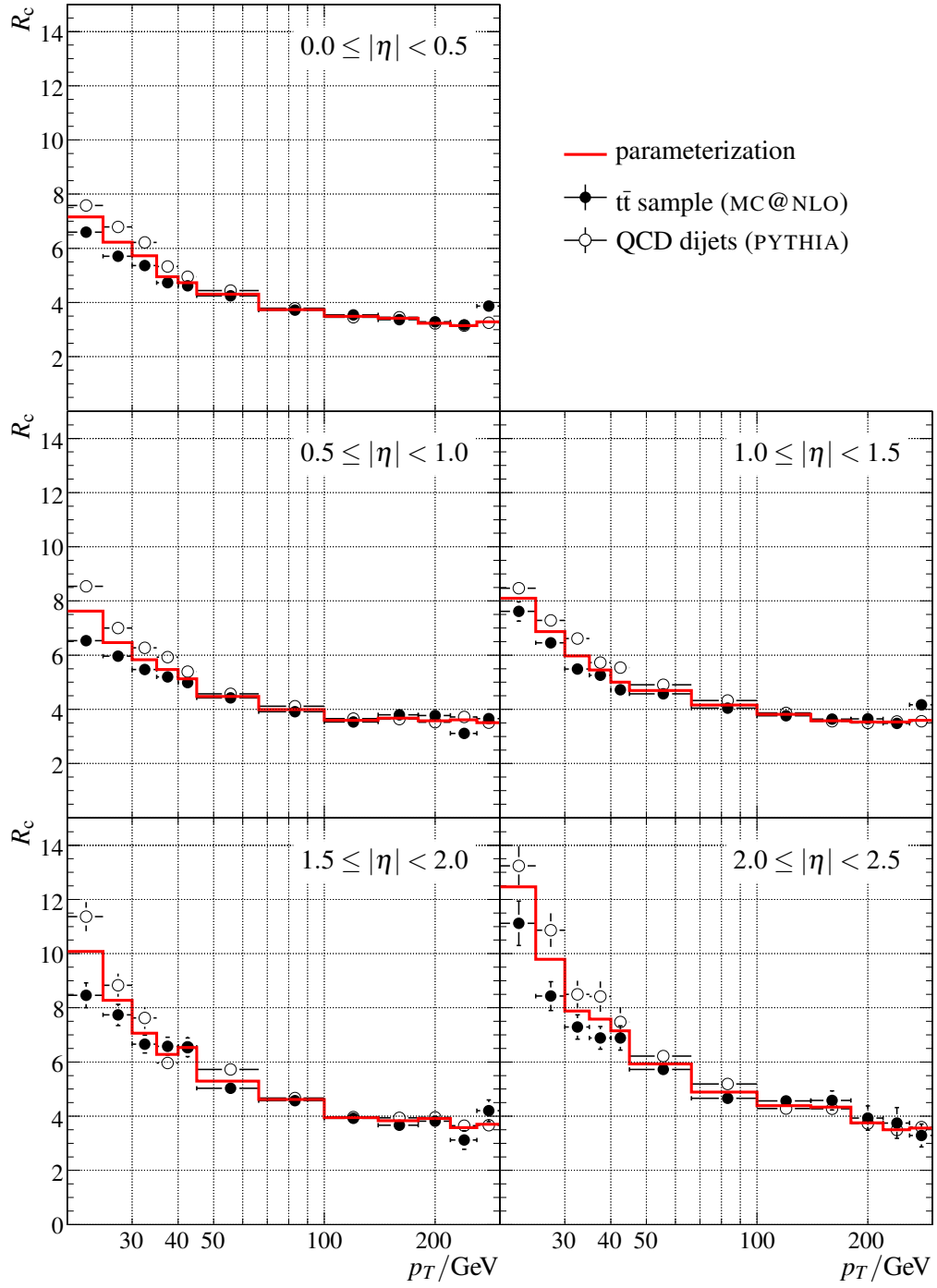


Figure 9.37: Parameterization of the c jet rejection for a weight-cut of four in dependence of p_T in five $|\eta|$ bins (red line). Closed circles: $t\bar{t}$ (1tW ℓ f, MC@NLO), open circles: QCD dijet (PYTHIA) samples.

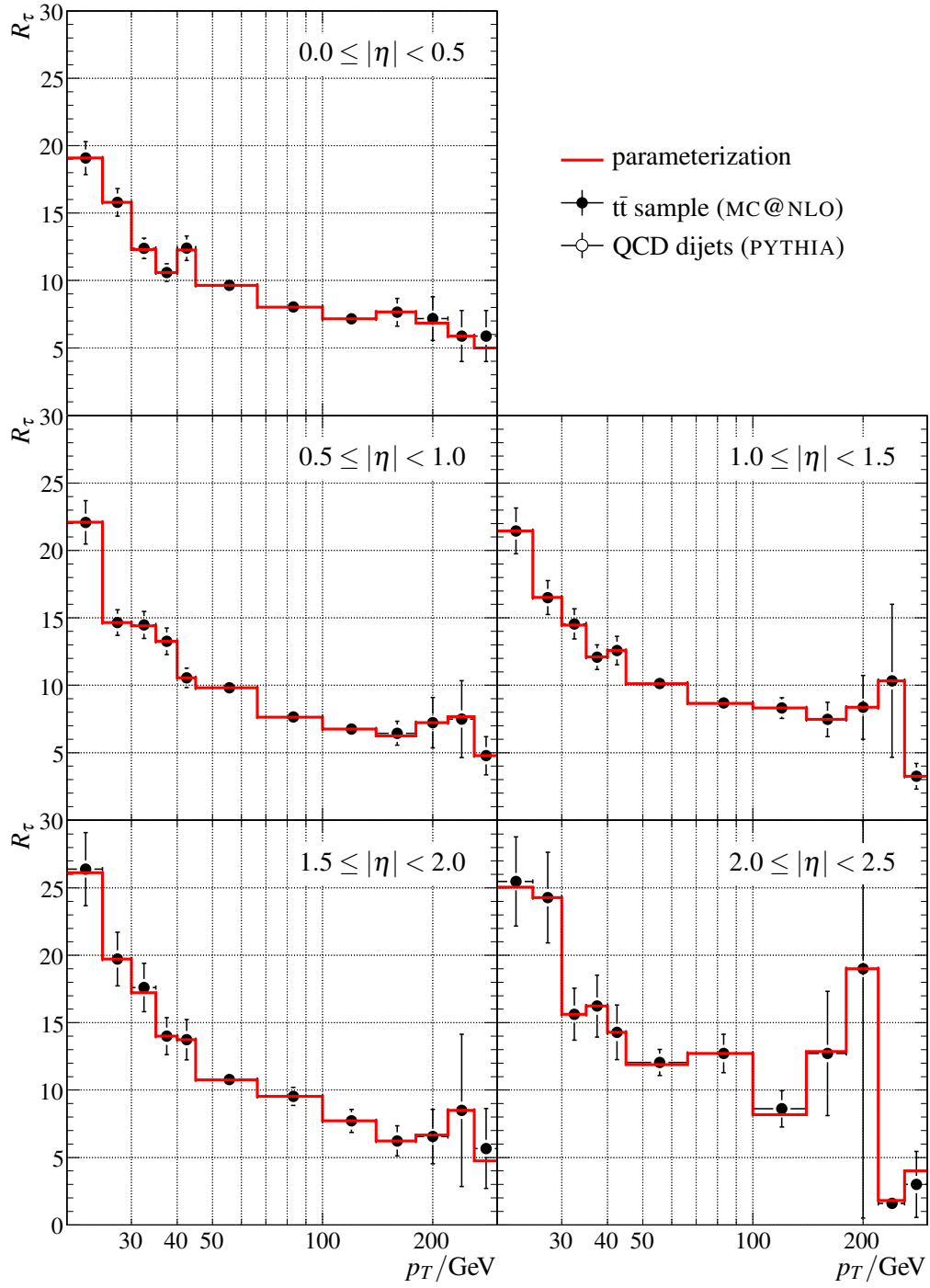


Figure 9.38: Parameterization of the τ jet rejection for a weight-cut of four in dependence of p_T in five $|\eta|$ bins (red line). Closed circles: $t\bar{t}$ (1tW ℓ f, MC@NLO), open circles: QCD dijet (PYTHIA) samples.

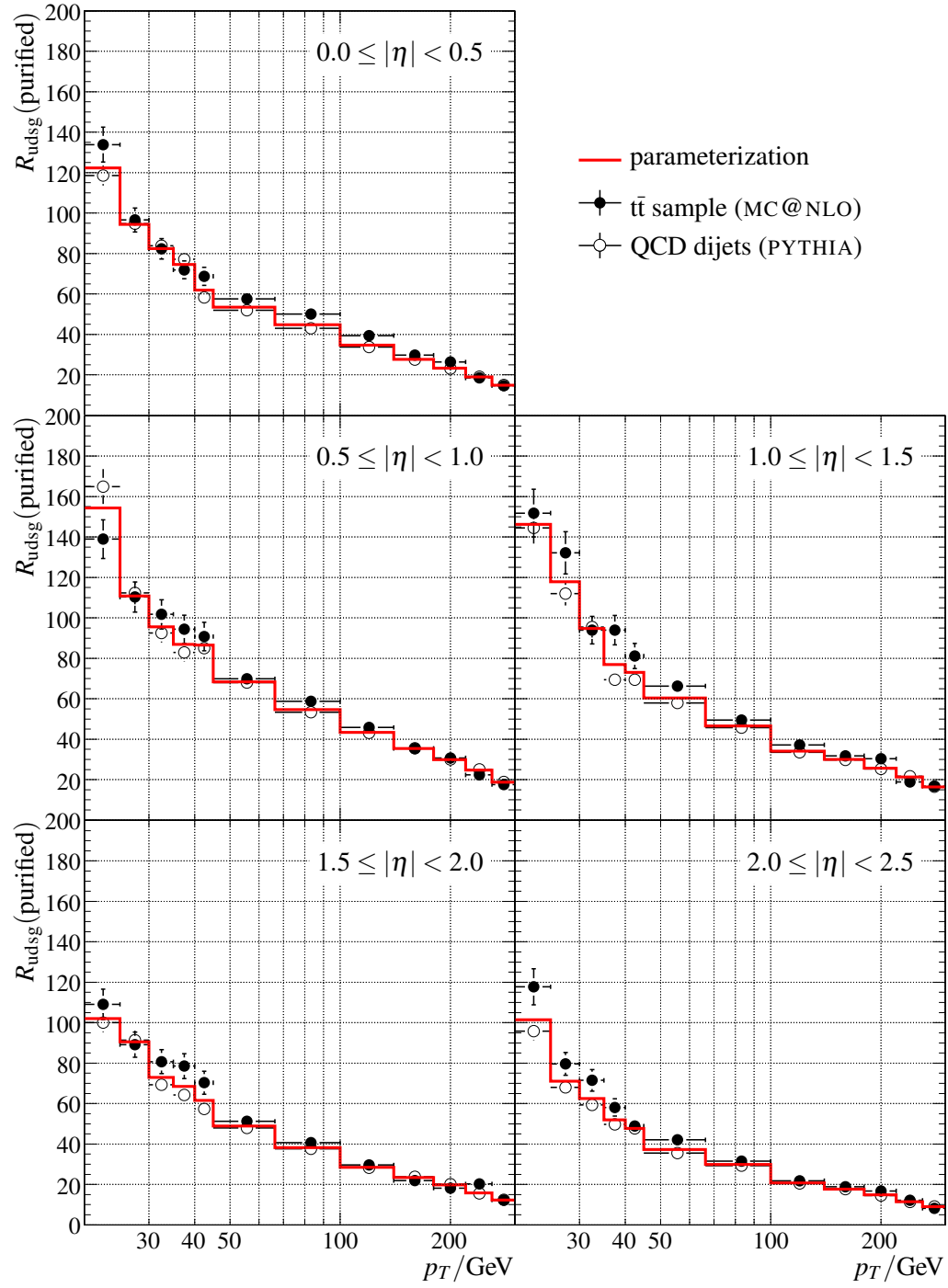


Figure 9.39: Parameterization of the purified udsg jet rejection for a weight-cut of four in dependence of p_T in five $|\eta|$ bins (red line). Closed circles: $t\bar{t}$ ($1tW\ell f$, MC@NLO), open circles: QCD dijet (PYTHIA) samples.

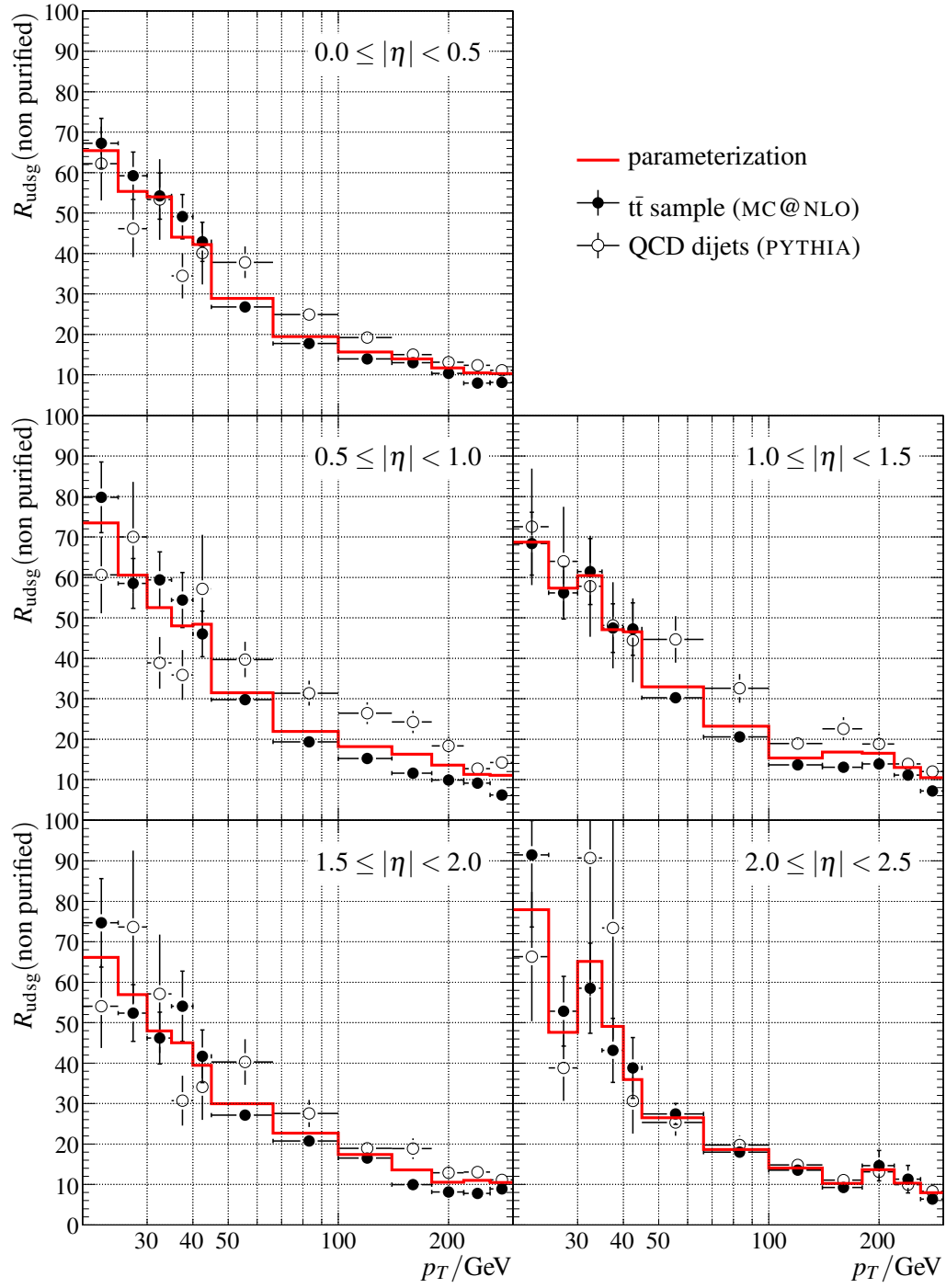


Figure 9.40: Parameterization of the non-purified udsg jet rejection for a weight-cut of four in dependence of p_T in five $|\eta|$ bins (red line). Closed circles: $t\bar{t}$ (1tWℓf, MC@NLO), open circles: QCD dijet (PYTHIA) samples.

9.3.4 Comparison between FULLSIM and ATLFAST

The performance of the parameterization is compared between FULLSIM and ATLFAST by requiring at least one tagged jet within $|\eta| < 2.5$ and with $p_T > 20$ GeV using a weight cut of four. This is done after a preselection cut consisting of requiring exactly one $\mu^+\mu^-$ pair, both isolated and with $p_T > 20$ GeV. Instead of comparing the total efficiencies it is more useful to compare the accepted differential cross sections in the p_T of the jet that caused the event to be tagged. In this way also the jet reconstruction efficiency is probed directly, as there might be correlations between the probability of a jet being tagged and the probability of being reconstructed at all. This procedure would show any deviations simultaneously.

Figure 9.41 shows the differential distributions of the leading tagged jet for different true flavors of the jet and in signal and background samples. It should be noted that the ATLFAST samples and FULLSIM samples are normalized independently from each other and not normalized to the same accepted total cross section.

The overall agreement between FULLSIM and ATLFAST is very good. Most of the differences are already present at the jet reconstruction level and are not caused by the parameterization.

For the signal sample, the agreement is almost perfect.

The same is true for the $Z^0 b\bar{b}$ and $Z^0 + b$ samples. Here some disagreement is present at low transverse momentum for tagged udsg jets. This is caused in part by the parameterization, but also by the differences remaining in the jet reconstruction efficiency. However, the total accepted cross section is completely dominated by true b jets, which are described perfectly.

For $t\bar{t}$ the shape of the p_T distribution of leading tagged true b jets is slightly different, an effect that is already present before tagging. The influence on the accepted total cross section is however small.

The biggest differences remain for the $Z^0 + \text{light}$ sample, but due to the small statistics in FULLSIM, conclusions are difficult. First, as expected in this sample, all three different jet flavors play an important role. The tagged true b jets show a tendency to be overestimated by ATLFAST. However, this contribution to the total accepted cross section of this sample is only about 10%, so a mismodeling here does not have a large influence. For leading tagged true c jets a discrepancy at low p_T is visible. This is caused by both the uncertainties on the b -tagging parameterization and by the residual differences in the jet reconstruction at low p_T . The rate of leading true udsg jets is slightly overestimated by the re-parameterized ATLFAST. This somewhat compensates the underestimated cross section for leading true c jets. However, this effect is only on the 10% level. With the limited statistics it can not be proven that it is significant and it has to be covered by a systematic uncertainty.

Overall the modified parameterized b -tagging in ATLFAST works satisfactory. Some differences between ATLFAST and FULLSIM remain, but this is to be expected in this simple approach of random b -tagging.

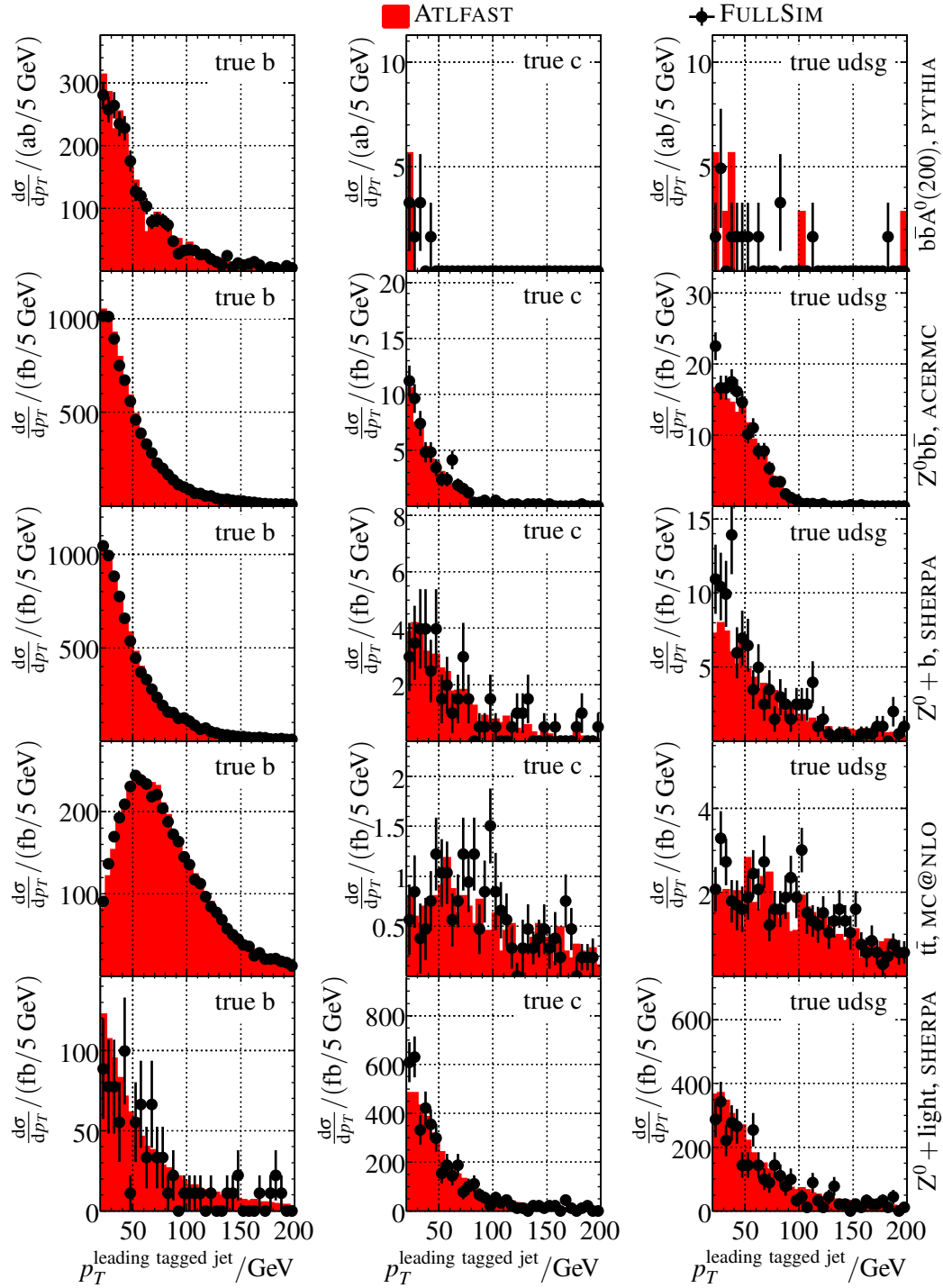


Figure 9.41: Differential distributions of the leading tagged jet normalized to the accepted cross section after preselection cuts. Left column: Leading tagged jet is a true b jet, middle column: true c jet, right column: true udsg jet. Solid histogram: Re-parameterized ATLFAST, datapoints: FULLSIM. From top to bottom: $b\bar{b}A^0$ ($M_{A^0} = 200$ GeV, PYTHIA), $Z^0 b\bar{b}$ (ACERMC), $Z^0 + b$ (SHERPA), $t\bar{t}$ ($2\mu f$, MC@NLO), $Z^0 + \text{light}$ (SHERPA).

9.3.5 Influence of Pile-Up

Pile-up can have a significant impact on the b -tagging performance: First of all, the additional calorimetric energy can have an influence on the jet energy scale. This can lead to miscalibration effects just as discussed in Section 9.2.6. Second, since in the case of pile-up more than one primary vertex is expected in the event, the resolution of the primary vertex reconstruction, and thus the resolution on impact parameters might be degraded. In this way the b -tagging working point is effectively shifted.

The influence of pile-up is studied using the available Monte Carlo samples with simulated pile-up. These consist of significantly less events than those without pile-up. Also, for the $Z^0 + \text{light}$ and the $Z^0 + b$ samples no pile-up simulation is available. Instead of the $Z^0 + \text{light}$ sample, an inclusive Z^0 sample simulated with PYTHIA is used. This also contains true b jets and cannot be naively combined with $Z^0 b\bar{b}$, as this would lead to double-counting of contributions. The comparison is again done on the level of distributions of tagged jets. It is shown in Figure 9.42 in dependence of the true jet flavor for a weight cut of four.

For signal events, almost no difference is visible. The b jet rate is lower at low transverse momentum, but this effect is smaller than 10%. For $Z^0 b\bar{b}$ and $t\bar{t}$, which are still completely dominated by true b jets, a similar effect is seen. For the inclusive Z^0 sample, the contribution of both true b and true c jets becomes smaller at low p_T . For true udsg jets, the effects are in the opposite direction: Their contribution increases by about 10%. All these effects are significant, but have only limited influence on the overall picture, because the backgrounds consist both of b and udsg jets. So parts of the backgrounds are decreased by pile-up, but other contributions are enhanced.

The altered working point when pile-up is included might make a re-optimization of cuts necessary. For example, if it turns out that for the same b jet efficiency the udsg jet rejection is degraded very significantly, it might be worthwhile to move to a somewhat lower efficiency for b jets but higher rejection of udsg jets. This warrants further investigation in future ATLAS software releases, where also misalignment effects and updated b -tagging algorithms are available. These can have quantitatively similar effect as the inclusion of pile-up. To avoid pile-up effects it might also be necessary to increase the cut on the p_T of the leading tagged jet, as this avoids parts of the discrepancies.

Pile-up can not be easily included in the ATLFAST description and no effort is done to correct for the found effects. This is also due to the fact that the influence of pile-up effects on b -tagging in ATLAS is still being studied and no final conclusions are available yet. It is very well possible that ways will be found to recover the performance without pile-up. In addition, pile-up leads to additional low p_T jets in the calorimeter, which cannot be described at all in ATLFAST. This is even more complicated due to the fact that at least the EM calorimeter integrates over multiple bunch crossings. So there might actually be jets that are found in the calorimeter, but have no tracks associated in the inner detector, as at least the precision devices (pixel, SCT) integrate only over one bunch crossing. This makes finding an updated parameterization for ATLFAST very difficult and this is not done in this thesis. The b -tagging performance might thus be slightly overestimated.

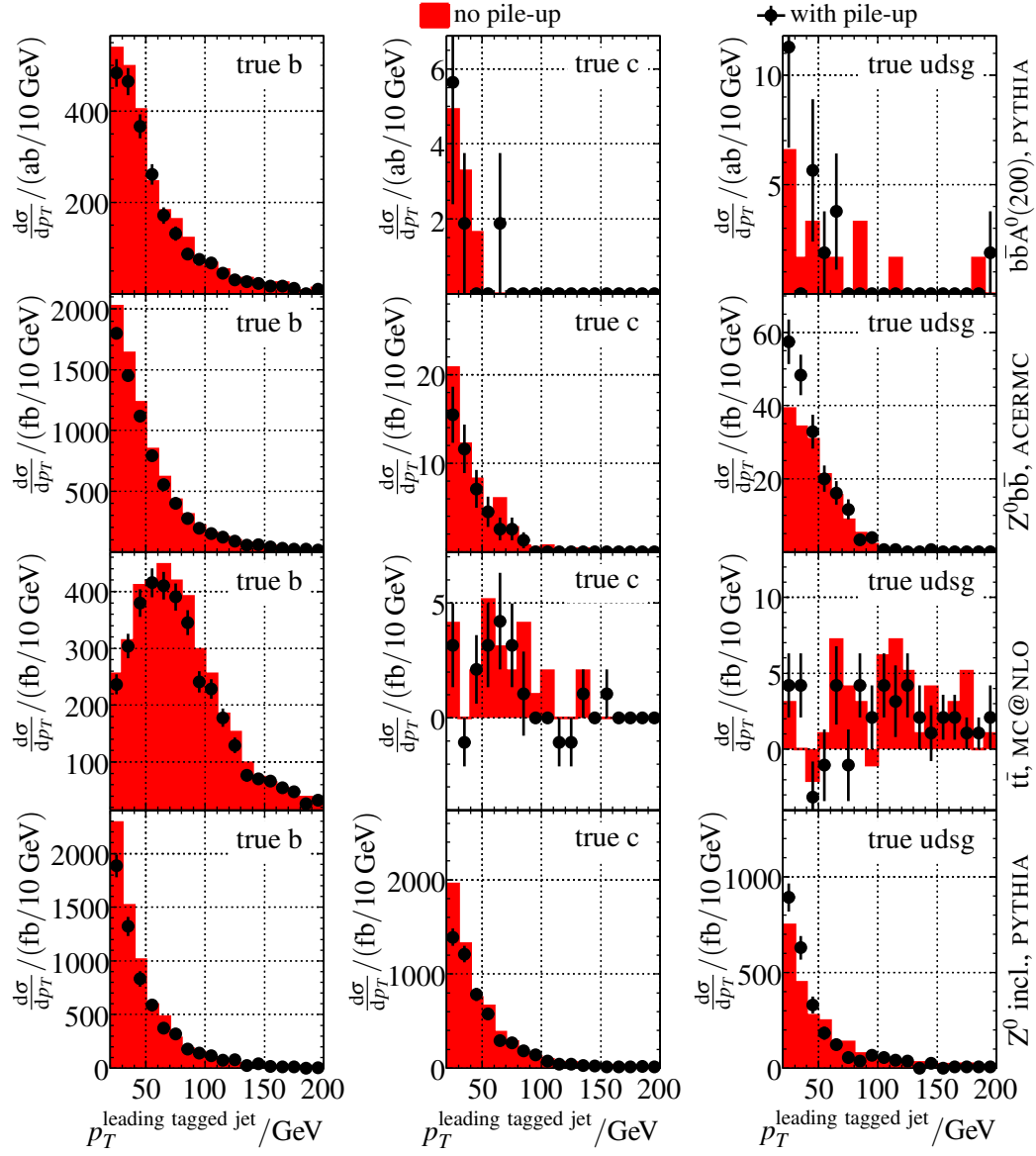


Figure 9.42: Differential distributions of the leading tagged jet normalized to the accepted cross section after preselection cuts. Left column: Leading tagged jet is a true b jet, middle column: true c jet, right column: true udsg jet. Solid histogram: Without pile-up, datapoints: with pile-up. From top to bottom: $b\bar{b}A^0$ ($M_{A^0} = 200$ GeV, PYTHIA), $Z^0b\bar{b}$ (ACERMC), $Z^0 + b$ (SHERPA), $t\bar{t}$ (1tW ℓ f, MC@NLO), Z^0 + light (SHERPA). Negative cross sections for the $t\bar{t}$ sample are due to the negative weight events of MC@NLO and the small statistics of the available sample.

9.3.6 Misalignment

Misalignment of the inner detector has a significant impact on the b -tagging performance. This is due to the fact that the misalignment uncertainties enter directly into the impact parameter resolution. However, in the used ATLAS software release, the actual alignment procedure was not yet available: The Monte Carlo samples are simulated with a randomly misaligned geometry, but are also reconstructed with an exact knowledge of the shifts in the detector components position. In this way, the reconstruction performance corresponds to perfect alignment. The purpose of this procedure was that the same datasets were also reconstructed using the ideal detector geometry, thus corresponding to a simulation of the initial misalignment of ATLAS, as it will be present on day one of data taking. In this way, the software methods to *align* the detector components in themselves and relative to each other could be rehearsed. In this alignment procedure usually the residuals between tracks and associated clusters are minimized. More detail can be found in [148]. The results of this effort are available in newer ATLAS software releases where it is also possible to reconstruct Monte Carlo samples that have been simulated with a misaligned geometry using the aligned geometry, thus giving a more realistic description of the detector performance.

Preliminary estimates by the ATLAS flavor tagging performance group show that the rejection of $udsg$ jets is degraded due to the effects of misalignment, if the b jet efficiency is left constant. To get an estimate of this effect, the rejection of $udsg$ jets is decreased to 70% of the nominal value. For the ATLFast parameterization this is easily implemented as a multiplicative factor. For FULLSIM this effect is estimated by using a different weight cut for $udsg$ jets that corresponds to a decreased average rejection.

9.4 Missing Transverse Energy

The missing transverse energy, \cancel{E}_T , is a crucial signature for a lot of new physics, like SUSY that will be searched for at the LHC. Its reconstruction is rather involved, as it means that all visible particles have to be accounted for and their energy summed vectorially. The \cancel{E}_T vector is then given as the negative of the resulting vector. For its reconstruction a very good calorimeter coverage up to very large $|\eta|$ is crucial, since otherwise particles can escape detection, leading to tails in the distribution of \cancel{E}_T . The forward calorimeters of ATLAS ensure the coverage up to $|\eta| < 4.9$.

In the following, first brief overviews of the \cancel{E}_T reconstruction in detailed reconstruction and in ATLFast are given. Then, a possible simple correction method for ATLFast is presented. Last, the influence of pile-up is discussed.

9.4.1 Reconstruction of \cancel{E}_T in FULLSIM

In a first step, \cancel{E}_T is calculated using the calibrated calorimeter cells, with the global calibration procedure described in Section 9.2.1. The next step is to correct also for muons that leave only a mip signal in the calorimeter and carry a lot of energy away. This is done by using stand-alone muons reconstructed as discussed in Sec. 9.1.1. In this way, the muon

energy loss in the calorimeters is counted only once. To reduce fakes, only good-quality stand-alone muons are used that also have a matched track in the inner detector.

Next, the \cancel{E}_T reconstruction has to be corrected for the energy loss in the cryostat between the barrel EM and tile calorimeter. This is not negligible for high p_T jets (multiple 100 GeV) where it can contribute up to 5% of the jet momentum.

Last, a refined calibration of \cancel{E}_T is performed: All reconstructed high p_T objects in the event are assigned to its globally calibrated calorimeter cells in the following order: electrons, photons, hadronically decaying τ leptons, b jets, light jets and muons. The refined calibration step now replaces the initial contribution of cells associated with an object with the corresponding calibrated object. The main effect of the refined calibration of \cancel{E}_T is that cells belonging to electrons or photons, which are miscalibrated by the global hadronic calibration are set back to the electromagnetic scale and thus calibrated correctly.

Cells not associated to any cluster are included in addition, calibrated globally if they are above a noise cut optimized for \cancel{E}_T measurement.

9.4.2 Reconstruction of \cancel{p}_T in ATLFAST

In ATLFAST the missing transverse momentum \cancel{p}_T is calculated, which should for practical purposes be close to \cancel{E}_T . All reconstructed objects, isolated electrons, photons, muons, taus, jets, and non-isolated muons as well as remaining clusters that did not pass the jet p_T cut are used to calculate \cancel{p}_T . Towers not contained in clusters are also included. Their energy is smeared using the same resolution function as for jets.

9.4.3 ATLFAST Correction

As \cancel{E}_T is a very complicated quantity, it cannot be expected that ATLFAST in the version used in this study can give an adequate description of it. As seen previously, various object resolutions in ATLFAST do not reflect completely the expected detector performance. In the following, a correction procedure is presented that is mostly independent of the other corrections used. This means that e.g. although jets are removed in ATLFAST at random, and their momentum is rescaled, this is not propagated to the \cancel{E}_T measurement. Only the additional smearing of the muon momenta is done before this correction procedure.

Figure 9.43 shows the \cancel{E}_T distributions and resolutions of its x and y components for $b\bar{b}A^0$ ($M_{A^0} = 200$ GeV, PYTHIA) and for $t\bar{t}$ ($2\mu\text{f}$, MC@NLO) after a preselection cut consisting of an isolated $\mu^+\mu^-$ pair, each with $p_T > 20$ GeV. In addition at least one jet with $p_T > 20$ GeV is required, as this can have an influence on the resolution of \cancel{E}_T . The \cancel{E}_T is taken from identical events between FULLSIM and ATLFAST, where the event has to fulfill the mentioned cuts in both simulations.

Obviously the \cancel{E}_T resolution is much better in ATLFAST than in FULLSIM. For the $b\bar{b}A^0$ sample, this leads directly to a \cancel{E}_T distribution that is different between ATLFAST in FULLSIM. For the $t\bar{t}$ sample, the difference in the resolutions is also very well visible, but is not reflected in the \cancel{E}_T distribution itself. This is explained by the fact that $t\bar{t}$ events contain real \cancel{E}_T due to the neutrinos from W decays. In contrast to this, $b\bar{b}A^0$ events, with the A^0 decaying to muons do not contain intrinsic \cancel{E}_T , and are thus completely dominated

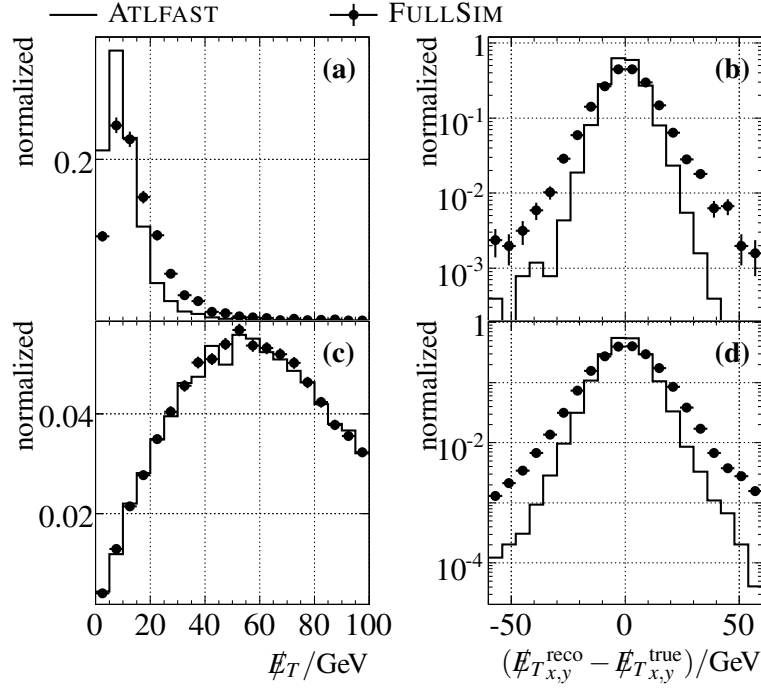


Figure 9.43: Left: Distribution of E_T after preselection cuts, including at least one reconstructed jet. Right: Distribution of the difference of the x and y components of the reconstructed E_T to the true E_T . Solid line: ATLFast. Points: FullSim. (a) and (b): $b\bar{b}A^0$ ($M_{A^0} = 200$ GeV, PYTHIA). (c) and (d): $t\bar{t}$ ($2\mu f$, MC@NLO).

by the resolution of E_T . The difference in the E_T distributions is thus much larger for this type of events, as well as for the $Z^0 + \text{light}$ and $Z^0 + b$ backgrounds. There is a small discrepancy in E_T for $t\bar{t}$ between ATLFast and FullSim, but this is not very significant and does not play any role in the analysis. The resolution of E_T seems to be worse in the $t\bar{t}$ sample. This can be explained by the larger hadronic activity in $t\bar{t}$ events. As the E_T resolution is expected to be proportional to $\sqrt{H_T}$, this leads to a worse E_T reconstruction.

The mismodeling in ATLFast is corrected using a simple scaling procedure: The x and y components of E_T are recalculated according to the following formula:

$$E_{T,x,y}^{\text{new}} = s \cdot (E_{T,x,y}^{\text{old}} - E_{T,x,y}^{\text{true}}) + E_{T,x,y}^{\text{true}}, \quad (9.17)$$

where s is a rescaling factor for the fake E_T component. In this way the E_T resolution is worsened artificially. The parameter s is chosen to be 1.4 in order to provide the largest amount of compatibility between different datasets. To take into account remaining differences, a conservative systematic uncertainty of 0.2 on s is assumed. The result of this rescaling procedure is shown in Figure 9.44.

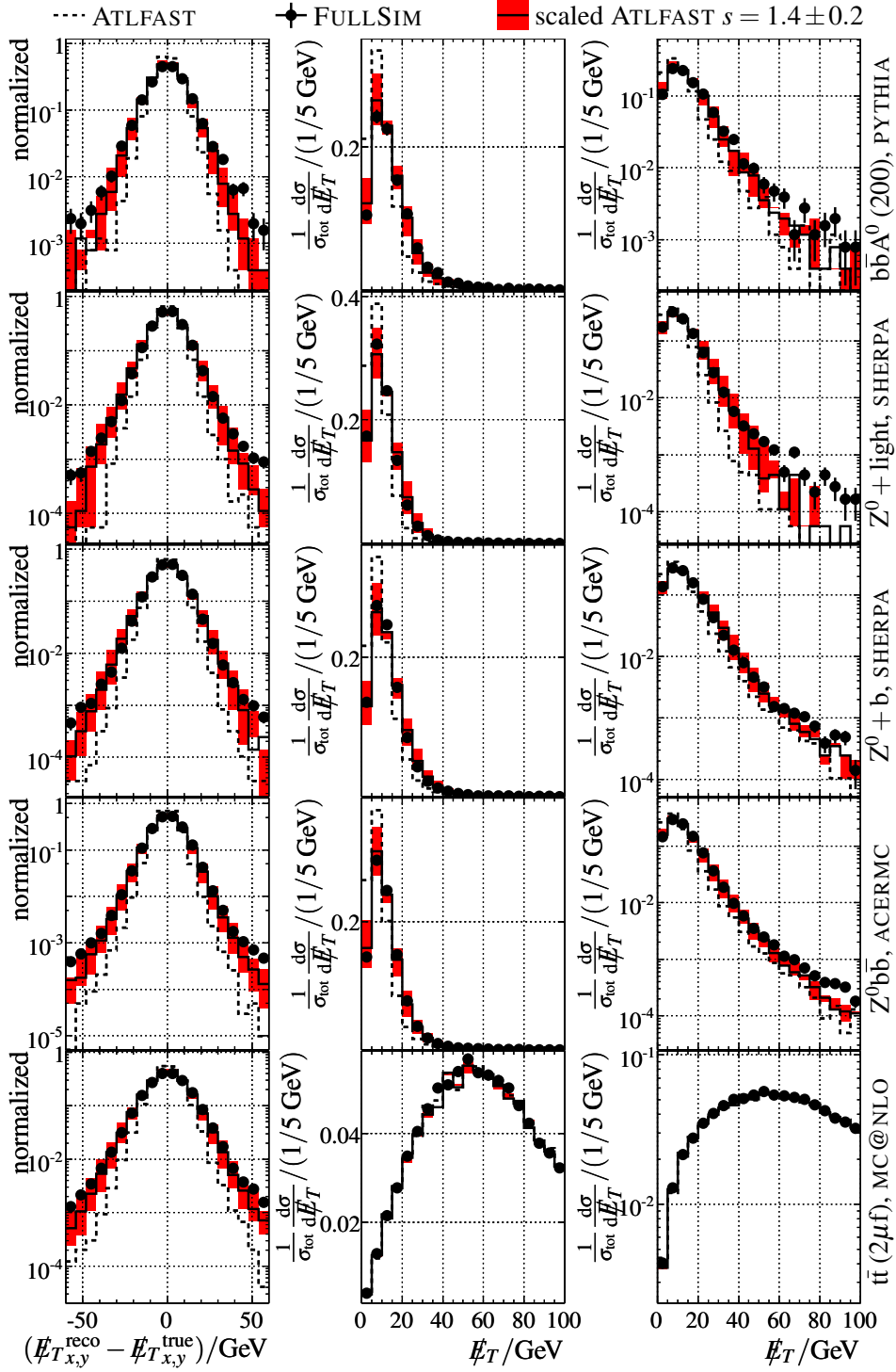


Figure 9.44: Distribution of the fake \cancel{E}_T x and y components (left column) and of the \cancel{E}_T distribution (middle and right columns) after the described preselection cuts in different Monte Carlo samples. Dashed line: Unrescaled ATLFast, solid line with gray (red) shaded area: rescaled ATLFast with $s = 1.4 \pm 0.2$, points: FULLSIM.

On the whole, the simple scaling procedure works remarkably well. The modified \cancel{E}_T distributions are in good agreement between ATLFast and FULLSIM. The main part of the fake \cancel{E}_T component distribution is reproduced. Only the tails towards very high fake \cancel{E}_T components is not described at all, resulting in tails in the \cancel{E}_T distribution that cannot be modeled in this simple approach. Otherwise the uncertainty on s is clearly a bit conservative. However, in this way, some of the effects of the more pronounced tails in FULLSIM are taken properly into account. To understand how this uncertainty affects the analysis, first the usage of \cancel{E}_T in this analysis has to be discussed: The missing transverse energy is only used as a separating variable between signal and $t\bar{t}$ events, since these two classes have very different distributions due to the neutrinos present in $t\bar{t}$ events. The separation is done by only allowing a maximum \cancel{E}_T of a certain value. The influence on the selection efficiency of such a \cancel{E}_T cut is shown in Table 9.7 for \cancel{E}_T cuts of 30 and 40 GeV.

The efficiency in FULLSIM is for all samples more or less within the uncertainties covered by the variation of s . Only for the signal and the $t\bar{t}$ sample very slight deviations are visible. For the $t\bar{t}$ sample, this small deviation is already present before the rescaling procedure. On the whole, the resulting acceptance uncertainties are about 3% at most. They are smaller for the larger \cancel{E}_T cut, since it is very efficient for signal and the Z^0 samples, that don't have real \cancel{E}_T . A further correction is not necessary.

sample	$\cancel{E}_T <$	(rescaled) ATLFast $\epsilon_{\text{ATLFast}}/\%$				FULLSIM
		$s = 1.0$	$s = 1.2$	$s = 1.4$	$s = 1.6$	$\epsilon_{\text{FULLSIM}}/\%$
$b\bar{b}A^0$ (200)	30 GeV	96.1 ± 0.4	94.8 ± 0.4	92.7 ± 0.5	90.2 ± 0.6	89.1 ± 0.6
	PYTHIA 40 GeV	98.2 ± 0.3	97.5 ± 0.3	96.9 ± 0.3	95.6 ± 0.4	94.7 ± 0.4
$Z^0 + \text{light}$	30 GeV	99.5 ± 0.1	98.7 ± 0.1	97.4 ± 0.1	95.2 ± 0.2	96.8 ± 0.1
	SHERPA 40 GeV	99.9 ± 0.1	99.7 ± 0.1	99.4 ± 0.1	98.8 ± 0.1	98.6 ± 0.1
$Z^0 + b$	30 GeV	96.9 ± 0.1	95.7 ± 0.1	93.6 ± 0.1	91.0 ± 0.2	94 ± 0.1
	SHERPA 40 GeV	98.8 ± 0.1	98.5 ± 0.1	97.9 ± 0.1	97 ± 0.1	97.4 ± 0.1
$Z^0 b\bar{b}$	30 GeV	97.7 ± 0.1	96.9 ± 0.1	95.7 ± 0.1	94.0 ± 0.1	95.1 ± 0.1
	ACERMC 40 GeV	99.1 ± 0.1	98.8 ± 0.1	98.5 ± 0.1	98.0 ± 0.1	98.0 ± 0.1
$t\bar{t}$ ($2\mu f$)	30 GeV	14.1 ± 0.2	14.0 ± 0.2	13.9 ± 0.2	13.8 ± 0.2	14.2 ± 0.2
	MC@NLO 40 GeV	23.4 ± 0.2	23.2 ± 0.2	23.0 ± 0.2	22.8 ± 0.2	23.7 ± 0.2

Table 9.7: Efficiencies relative to the described preselection cuts for \cancel{E}_T cuts of 30 and 40 GeV in different Monte Carlo samples for ATLFast without \cancel{E}_T scaling ($s = 1.0$), $s = 1.2$, $s = 1.4$ and $s = 1.6$, and in FULLSIM.

9.4.4 Influence of Pile-Up

So far, no effects from pile-up events on the \cancel{E}_T reconstruction have been discussed. However, in the case of pile-up, additional energy is deposited in the calorimeter that leads to a drastic degradation of the \cancel{E}_T resolution. The decay channel studied in this channel is extremely sensitive to these effects, as the \cancel{E}_T distribution is completely dominated by the resolution and not by true missing transverse energy. Figure 9.45 shows the \cancel{E}_T distribution and the components of the fake \cancel{E}_T for FULLSIM and for ATLFAST rescaled with the previously found rescaling factor of 1.4. A change in resolution is clearly visible.

This additional effect can be taken into account by increasing the rescaling factor to 2.4. Again, the systematic uncertainty is estimated conservatively to 0.3, which was chosen to cover possible differences between the shapes of the \cancel{E}_T distributions and acceptances of a \cancel{E}_T cut in FULLSIM and ATLFAST. Figure 9.46 shows the resolutions and \cancel{E}_T distributions for the available FULLSIM Monte Carlo samples that include pile-up simulation.

Signal and $Z^0 b\bar{b}$ are adequately described within the systematic uncertainty. For the inclusive Z^0 sample, the shapes of the distributions are not described completely. However, the tail of the \cancel{E}_T is described very well. For the $t\bar{t}$ sample the only significant deviations are in the region of large \cancel{E}_T , which is irrelevant for the analysis.

Table 9.8 lists the efficiencies of two different \cancel{E}_T cuts on these samples. Obviously, ATLFAST without any scaling gives a very bad approximation of the efficiency of the \cancel{E}_T cut. The rescaled results of ATLFAST are in good agreement with FULLSIM within uncertainties. The only barely significant deviation is for the $t\bar{t}$ sample, where the rescaled ATLFAST underestimates the efficiency by about 5% for the \cancel{E}_T cut of 40 GeV.

The uncertainties incurred by the scaling procedure become significantly larger, especially for the \cancel{E}_T cut of 30 GeV, where they are on the order of 10% of the efficiency itself. However, the efficiency for signal events is severely reduced to less than 80% when pile-up is included if the \cancel{E}_T cut is placed at 30 GeV. Considering the uncertainties in the pile-up

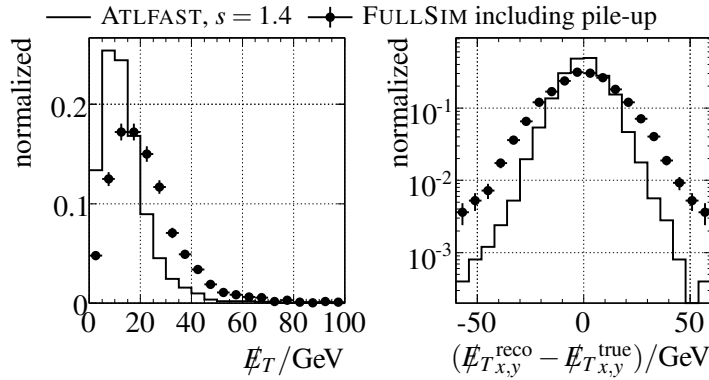


Figure 9.45: Left: Distribution of \cancel{E}_T after preselection cuts, including at least one reconstructed jet. Right: Distribution of the difference of the x and y components of the reconstructed \cancel{E}_T to the true \cancel{E}_T . Solid line: ATLFAST, rescaled with $s = 1.4$. Points: FULLSIM including pile-up simulation. $b\bar{b}A^0$ ($M_{A^0} = 200$ GeV, PYTHIA).

simulation, it is not feasible to place a cut at this low value. Rather, only higher cut values are feasible at the moment, as long as the real \cancel{E}_T reconstruction performance of ATLAS is not studied in more detail in collider data. For the higher cut of 40 GeV, the systematic uncertainties on the scaling factor correspond to uncertainties of the efficiencies of about 3%.

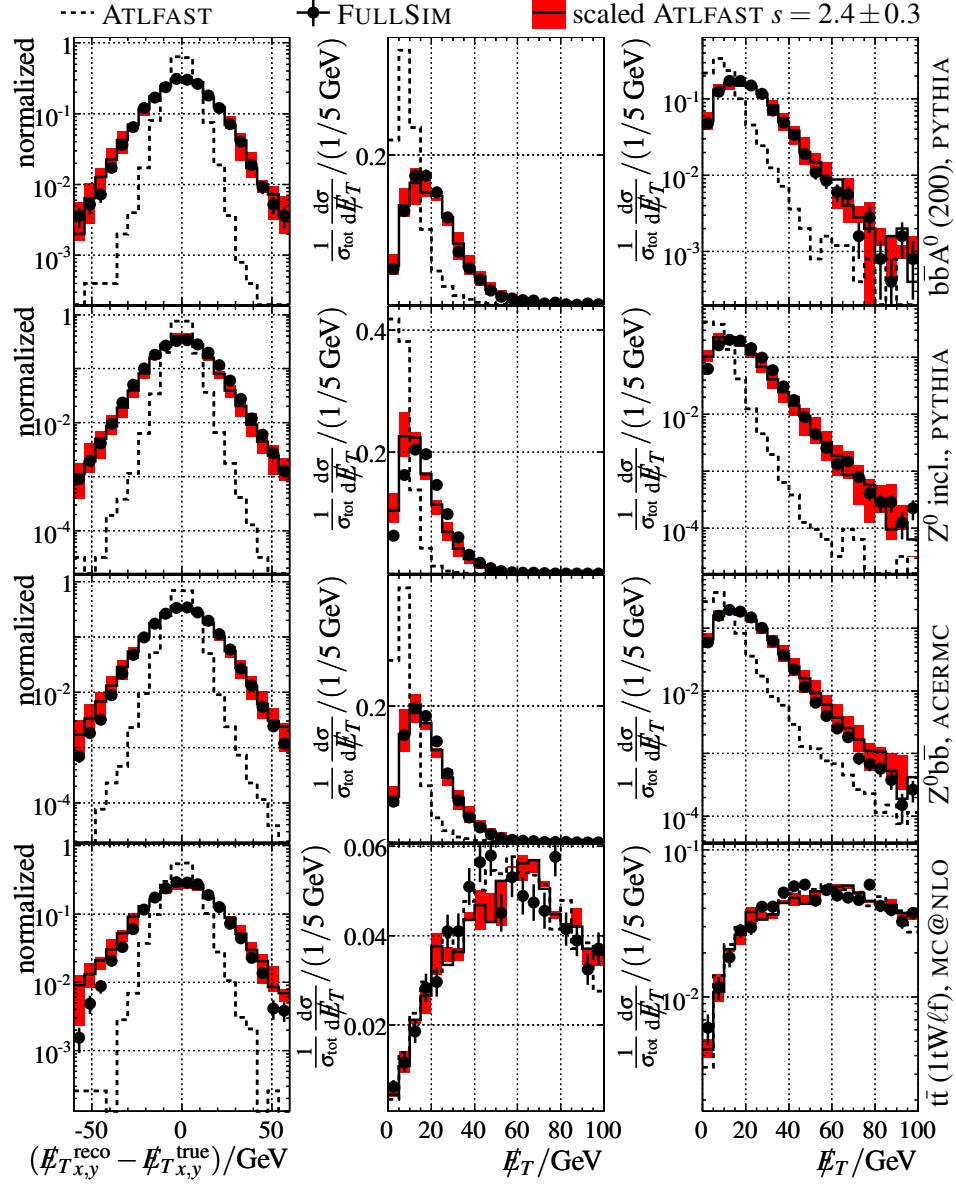


Figure 9.46: Distribution of the fake \cancel{E}_T x and y components (left column) and of the \cancel{E}_T distribution (middle and right columns) after the described preselection cuts in different Monte Carlo samples.. Dashed line: Unrescaled ATLFAST, solid line with gray (red) shaded area: rescaled ATLFAST with $s = 2.4 \pm 0.3$, points: FULLSIM including pile-up simulation.

sample	$\cancel{E}_T <$	(rescaled) ATLFAST $\epsilon_{\text{ATLFAST}}/\%$				FULLSIM
		$s = 1.0$	$s = 2.1$	$s = 2.4$	$s = 2.7$	$\epsilon_{\text{FULLSIM}}/\%$
$b\bar{b}A^0$ (200)	30 GeV	96.6 ± 0.4	82.8 ± 0.8	75.9 ± 0.9	69.3 ± 0.9	78.3 ± 0.8
PYTHIA	40 GeV	98.6 ± 0.2	92.7 ± 0.5	89.2 ± 0.6	85.4 ± 0.7	90.3 ± 0.6
Z^0 incl.	30 GeV	99.6 ± 0.1	93.5 ± 0.1	89.8 ± 0.2	85.6 ± 0.2	86.9 ± 0.2
PYTHIA	40 GeV	99.9 ± 0.1	97.9 ± 0.1	96.4 ± 0.1	94.3 ± 0.1	96.0 ± 0.1
$Z^0 b\bar{b}$	30 GeV	97.7 ± 0.1	87.9 ± 0.2	82.7 ± 0.2	77.3 ± 0.3	84.8 ± 0.2
ACERMC	40 GeV	99.1 ± 0.1	95.6 ± 0.1	93.2 ± 0.2	90.2 ± 0.2	94.6 ± 0.1
$t\bar{t}$	30 GeV	14.1 ± 0.6	13.5 ± 0.5	13.4 ± 0.5	13.3 ± 0.5	13.5 ± 0.5
MC@NLO	40 GeV	22.5 ± 0.7	21.7 ± 0.7	21.4 ± 0.7	21.1 ± 0.7	22.7 ± 0.7

Table 9.8: Efficiencies relative to the described preselection cuts for \cancel{E}_T cuts of 30 and 40 GeV in different Monte Carlo samples for ATLFAST without \cancel{E}_T scaling ($s = 1.0$), $s = 2.1$, $s = 2.4$ and $s = 2.7$, and in FULLSIM including pile-up simulation.

9.5 Electrons, Photons, and Hadronic Taus

Electrons, photons and hadronically decaying τ leptons are not explicitly used in this analysis. They enter the analysis only indirectly. No detailed performance studies of these objects have been done, and no corrections to the ATLFAST default algorithms are applied. Within this section, a very brief summary of the reconstruction of these objects in FULLSIM and in ATLFAST is given.

9.5.1 Electrons and Photons

The detailed algorithms to reconstruct electrons and photons can be found in [149] and [150]. In addition, in [65] a detailed description of the expected performance using an updated detector description is given.

Electromagnetic objects are characterized by the fact that they deposit all their energy in the EM calorimeter. Electrons can be distinguished from photons by requiring a track reconstructed in the ID.

The standard reconstruction algorithm starts by identifying the electromagnetic shower in the calorimeter. This is done by using information about the transverse and longitudinal shower shapes. In addition, isolation variables are used. For electrons, a spatial match between a track in the inner detector fulfilling certain quality criteria, among them a hit in the innermost pixel layer to reject photon conversions, is required. Using high threshold hits of the TRT can increase the rejection of hadrons even further.

In addition to this cluster based algorithm to identify electrons, also a track seeded algorithm is used to identify primarily low p_T electrons and electrons in jets.

Electrons and photons are not used directly in this thesis, they only enter the analysis in the calculation of \cancel{E}_T and in the overlap removal procedure discussed below. The default cuts of the HIGHPTVIEW package (version 00-00-46) are used. For electrons, these correspond to a set of tight cuts both on the shape of the calorimeter shower and the inner detector track. No requirement on the number of high threshold TRT hits is made. This does not fully correspond to the official definition of an ATLAS tight electron (which imposes cuts on the TRT hits), but the effect on the analysis is negligible. Likewise the shower shape cuts placed on photons do not fully correspond to the official ATLAS cuts, but also in this case the differences of relevance for this analysis are negligible.

In ATLFAST, electrons and photons are reconstructed based on truth information. The energies of the true electrons and photons are smeared using appropriate smearing functions. Then an isolation criterion similar to the one for muons is applied, with the difference being that the transverse energy of the smeared object is subtracted from the one in the isolation cone. In addition, clusters in the calorimeter within $\Delta R < 0.15$ of the candidate are removed so that they cannot be reconstructed as jets. For photons in addition the direction in η is smeared.

9.5.2 Hadronic Taus

Hadronically decaying τ leptons can be reconstructed either using the information from the inner detector or from the resulting entries in the calorimeter. A track based algorithm [151] is available, adopting an energy flow type approach to avoid double counting of track energy with calorimetric information. It is optimized for low to medium transverse visible transverse energies ($10 < E_T < 80$ GeV), corresponding to the momentum range of interest in $W \rightarrow \tau \nu$ and $Z^0 \rightarrow \tau \tau$. The alternative is a calorimeter-based algorithm [152], which uses calorimeter clusters and has been optimized for visible transverse energies above 30 GeV. This algorithm combines the information into a likelihood based discriminant that is used to select tau candidates. It is used in this analysis, although, just as for electrons and photons, hadronic taus enter the analysis only indirectly and their influence is negligible.

In ATLFAST the calorimeter based algorithm is available in the form of a parameterization of efficiencies and fake probabilities for QCD jets.

9.6 Overlap Removal

In FULLSIM an object can be reconstructed more than once. For example, an electron can be reconstructed by the electron identification. In addition, e.g. the jet finding algorithm used will also use the calorimeter cluster caused by the electron and might reconstruct it as a jet. To remove such ambiguities, an *overlap removal* procedure based on closeness of objects in (η, ϕ) space is used. Reconstructed muons are never removed, which can be motivated by the fact that the probability of a muon faking any other type of object with large transverse momentum is very small. The remaining objects are used in the following sequence: Electrons, photons, hadronic taus, jets. Overlap is removed with any of the objects that are in front in this sequence using an association cone of $\Delta R = 0.1$, except for jets,

where a larger cone of $\Delta R = 0.3$ is used. As mentioned above, the cuts used for electrons, photons and hadronic taus have not been tuned from the default in HIGHPTVIEW, version 00-00-46. As a consequence, the jets happen to depend slightly also on these parameters, as they can be removed due to overlap with any of these objects. However, this is a small effect: At most 2% of all jet candidates are removed due to this requirement. Even if this number is taken as a conservative estimate on the jet reconstruction efficiency, the effect on the results presented in this analysis are minuscule. In addition, as in the analysis it is asked for a high p_T b jet, the probability of these being falsely identified as an electron, photon or hadronic tau is expected to be very small. Also, the rate of reconstructed electrons, photons or hadronic taus is very small, less than 1% of all selected signal events have any of these objects with a transverse momentum of 20 GeV or more.

“Selection of crews is always been somewhat of a mystery. “

Robert L. Crippen, former NASA Astronaut, 1937–present

10

Event Selection

After having examined the object-wise performance of the event reconstruction, this chapter presents the selection of events. First, it is useful to briefly recall the expected signal signature and its differences from the signatures of the backgrounds.

Signal events have two well isolated muons, for b-associated Higgs boson production two b jets at low transverse momentum and no significant missing transverse energy. No additional hard jet activity can be expected.

The $t\bar{t}$ background can also contain two muons (from W decays) and b jets (from top quark decays). However, in this case the jets will have a higher transverse momentum, as they come from the decay of a heavy particle. In addition, due to the neutrinos in the final state, $t\bar{t}$ events will tend to have significant missing transverse energy. The same is true for the tW background.

The $Z^0 + b$ and $Z^0 + \text{light}$ background are in many respects very similar to the signal events. For the case of the b-associated signal production, some separation from $Z^0 + \text{light}$ is possible by requiring a jet to be tagged as a b jet.

The last important difference is the invariant mass of the produced muon pair: For the signal processes it has to be close to the Higgs boson mass. For the background processes, the invariant mass distribution differs significantly: For $Z^0 + b$ and $Z^0 + \text{light}$ most of the events will be close to the mass of the Z^0 , with only a small fraction of all events having higher masses in the region where they would contribute to the background. For $t\bar{t}$ and tW the two muons do not originate from the same particle decay, so their invariant mass cannot be expected to peak at a particular value.

In the following the event selection is presented. Due to the small statistics of the background samples in FULLSIM, it is based on ATLFast samples with all corrections as described in the previous chapter applied.

10.1 Preselection

In a preselection procedure, the basic signature of the signal is used to suppress any backgrounds that have not even been simulated for this analysis and that are very clearly distin-

sample	exactly one $\mu^+\mu^-$ pair		more than one $\mu^+\mu^-$ pair	
	ATLFAST	FULLSIM	ATLFAST	FULLSIM
$b\bar{b}A^0$ (200-30)	74.5 ± 0.4	74.7 ± 0.7	0	0
$Z^0 + \text{light}$ (SHERPA)	69.25 ± 0.02	66.2 ± 0.2	$2 \cdot 10^{-5} \pm 2 \cdot 10^{-5}$	0.003 ± 0.002
$Z^0 + b$ (SHERPA)	65.97 ± 0.04	63.6 ± 0.2	0.0038 ± 0.0005	0.044 ± 0.007
$t\bar{t}$ ($2\mu f$, MC@NLO)	8.92 ± 0.02	9.00 ± 0.03	0.0012 ± 0.0002	0.013 ± 0.001

Table 10.1: Fractions of events (in %) with exactly one and more than one $\mu^+\mu^-$ pair, with each muon isolated and within $|\eta| < 2.5$ and $p_T > 20$ GeV.

guishable. As both the b-associated and the direct production mode result in two isolated muons with a high transverse momentum, the preselection requirements are chosen as:

- Exactly one reconstructed $\mu^+\mu^-$ pair.
- Both muons isolated.
- Both muons in $|\eta| < 2.5$ and having $p_T > 20$ GeV.

By these requirements it is ensured that no unsimulated backgrounds are of any importance. It is assumed that QCD multijet backgrounds are negligible due to the muon isolation requirement. In addition, any background from the production of a W boson with jets is assumed to be small¹.

In addition, in Chapter 9 the performance of the muon reconstruction was compared between ATLFAST and FULLSIM for the above phase space cuts and found to be similar. Muons with lower transverse momentum are not guaranteed to show the same behavior in ATLFAST and in FULLSIM. In fact the muon reconstruction efficiency for muons with $p_T < 20$ GeV is still 100% in ATLFAST. This can not be taken into account by a simple rescaling factor.

By requiring exactly one $\mu^+\mu^-$ pair, any ambiguities in the Higgs boson reconstruction are resolved. Table 10.1 shows the fractions of events with exactly one and more than one $\mu^+\mu^-$ pair for signal and background. The fraction of events with more than one Higgs boson candidate is completely negligible, both in ATLFAST and in FULLSIM.

Figure 10.1 shows the invariant mass distribution obtained after the preselection cuts for the background processes $Z^0 + \text{light}$, $Z^0 + b$, $t\bar{t}$, tW , WW , and Z^0Z^0 stacked on top of each other and in addition the expected contribution from an A^0 boson with $\tan\beta = 30$ for six different input masses. It should be noted that in almost all the parameter space either the h^0 or H^0 boson is mass-degenerate with the A^0 boson which increases the signal cross section. However, this is not needed for the analysis optimization.

Obviously the most important background is $Z^0 + \text{light}$ after the preselection cuts. $Z^0 + b$, $t\bar{t}$, and WW contribute only slightly. The other backgrounds are already negligible at

¹The W+jets background could only be relevant if a muon is faked or a muon from a hadron decay fakes isolation.

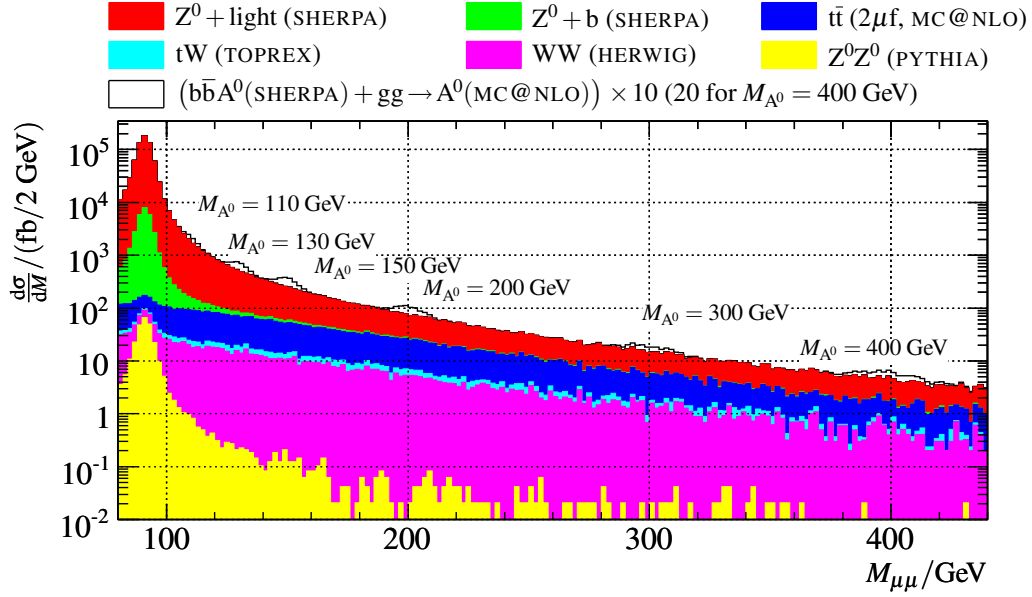


Figure 10.1: Stacked dimuon invariant mass distribution after preselection cuts. Open Histograms: Six different A^0 boson signals for $\tan\beta = 30$, $b\bar{b}A^0$ and $gg \rightarrow A^0$ added, scaled by a factor of 10 (20 for $M_{A^0} = 400$ GeV). Backgrounds from top to bottom: $Z^0 + \text{light}$ (red), $Z^0 + b$ (green), $t\bar{t}$ (dark blue), tW (light blue), WW (magenta), and $Z^0 Z^0 \rightarrow \mu\mu q\bar{q}$ (yellow).

this selection step. They are retained during the analysis optimization and in the final background count, but their differential distributions of discriminating variables are not shown in the following to keep the figures readable.

In the following a simple cut based selection is applied. The goal of this procedure is to reduce the background contributions while at the same time retaining as much of the signal as possible. Several ways of optimization are possible, however, within this work it is chosen to optimize the discovery reach of the analysis. The figure of merit that one should optimize is the expected significance of a signal for a given integrated luminosity. Assuming poissonian statistics, the significance for an unit integrated luminosity can be approximated by:

$$\mathcal{S} = \sigma_{\text{sig}} / \sqrt{\sigma_{\text{bkg}}}, \quad (10.1)$$

where σ_{sig} and σ_{bkg} are the accepted signal and background cross sections. The square root of the accepted background cross section is a measure of the expected statistical fluctuations of the background for an unit integrated luminosity. The expected significance for a given integrated luminosity can be obtained by scaling the cross sections with the luminosity. The significance can be interpreted as a probability of the background to fluctuate to the level of the signal. It is commonly translated into gaussian confidence intervals, which

is only valid for large numbers of background events. Commonly a significance of five, corresponding to a fluctuation probability of $2.87 \cdot 10^{-7}$ is defined as the level of discovery. In Appendix C.2 a different method to estimate the significance based on a frequentist construction of confidence intervals is discussed.

As evident from Figure 10.1 the invariant mass spectra are very different between the individual contributions: The backgrounds show a generally falling spectrum above a mass of 100 GeV. The $Z^0 + \text{light}$, $Z^0 + b$, and $Z^0 Z^0$ samples show the Z^0 resonance and for higher masses an exponentially falling tail due to the contribution of virtual photons. The invariant mass shapes of $Z^0 + \text{light}$ and $Z^0 + b$ are slightly different. This is explained on the one hand by the fact that the coupling of the Z^0 and the photon are different between up-type and down-type quarks. This changes the relative contributions of the Z^0 and the virtual photon in the samples. Another effect can come from the different evolutions of the parton distribution functions with the factorization scale, as the $Z^0 + \text{light}$ and the $Z^0 + b$ processes depend on different parton densities.

The $t\bar{t}$ contribution, just as the one from tW , shows a less steeply falling spectrum. This means that these backgrounds are more important at high candidate masses than for small masses.

The signal samples exhibit, as expected, peaks at the nominal generated mass. Its width is dependent on the mass itself, due to resolution effects.

Simply optimizing the expected significance over the whole mass range is not a sensible option, as differential distributions used for discrimination might depend on the candidate mass. To avoid this effect, the significance is only optimized after applying a mass window cut around the Higgs boson mass of twice the reconstructed width of the Higgs boson resonance to both sides of the nominal mass (two-sigma window). In this way it is ensured that only the background contribution around the analyzed Higgs boson mass is taken into account, and thus any mass dependencies of discriminating variables are disentangled.

In the following the dependence of the size of this mass window of the Higgs boson mass and its width is discussed.

10.2 Mass Window

Figure 10.2 shows the invariant dimuon masses after the preselection in the $b\bar{b}A^0$ channel for six different masses of the A^0 , all for $\tan\beta = 30$. Gaussian functions are fitted to the central part of the spectrum. The fit is performed by restricting the area to be fitted first to an interval around the input Higgs boson mass with a half width of 10% of the mass. The size of this interval is subsequently lowered and the fit repeated until the fit probability is larger than 5%. In this way an automated procedure for determining the reconstructed width is available.

The shape of the resonance can only approximatively be described by a Gaussian. This is due to the fact that it has different components: The detector resolution, which should be described by a Gaussian, and the natural width of the Higgs boson, which is a Breit-Wigner (or Lorentz) distribution. The result of folding a Lorentz distribution with a Gaussian is

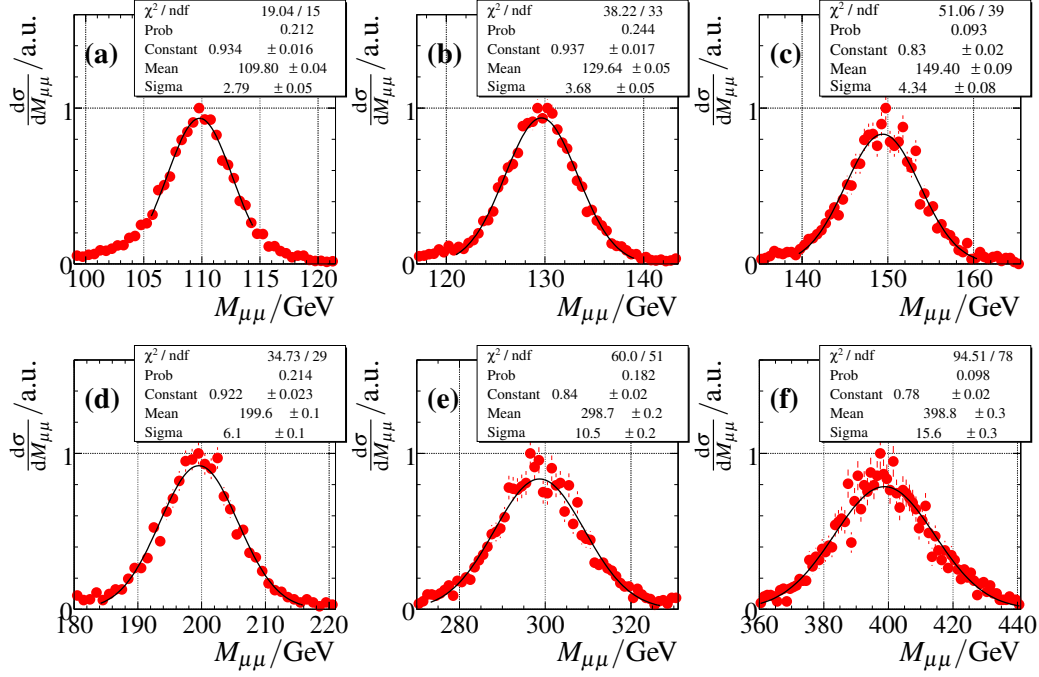


Figure 10.2: Invariant dimuon mass distributions after preselection cuts for $b\bar{b}A^0$ samples simulated with SHERPA in corrected ATLAST for different masses of the A^0 : (a) $M_{A^0} = 110$ GeV, (b) 130 GeV, (c) 150 GeV, (d) 200 GeV, (e) 300 GeV, (f) 400 GeV, all $\tan\beta = 30$. Black lines are the result of a gaussian fit as described in the text.

called a *Voigt* profile. Similar to the Breit-Wigner distribution, its variance is not defined. Fitting the mass distribution with a simple Gaussian is only an approximation that can be expected to be best if the total resolution is dominated by the detector resolution, which should be the case for small natural widths. In addition, also non-Gaussian effects can be present in the mass resolution itself.

The width of the reconstructed mass peak increases with the mass. This is a direct consequence of the muon momentum resolution, which is linearly dependent on p_T . The mean value is slightly smaller than the input mass, but the shift is at most one tenth of the width, and thus negligible. In addition, due to QED final state radiation off the muons, a significant radiation tail towards lower masses is visible. The dependence of the width of the reconstructed resonance on the total decay width of the Higgs boson is shown in Figure 10.3 for six different masses along with fitted functions to be used as an interpolation.

The fit consists of an intrinsic mass resolution σ_M , which dominates the width for small natural widths Γ_{tot} and a term proportional to the width (Γ_{tot}/g) added in quadrature. Although this functional form is only an approximation of the behavior of the Voigt function, it nevertheless yields a usable interpolation.

In order to obtain a prediction for the Gaussian part of the resonance width on the input mass and natural width, the fit parameters have to be interpolated between the different input masses. This is shown in Figure 10.4, where the interpolation is parameterized by

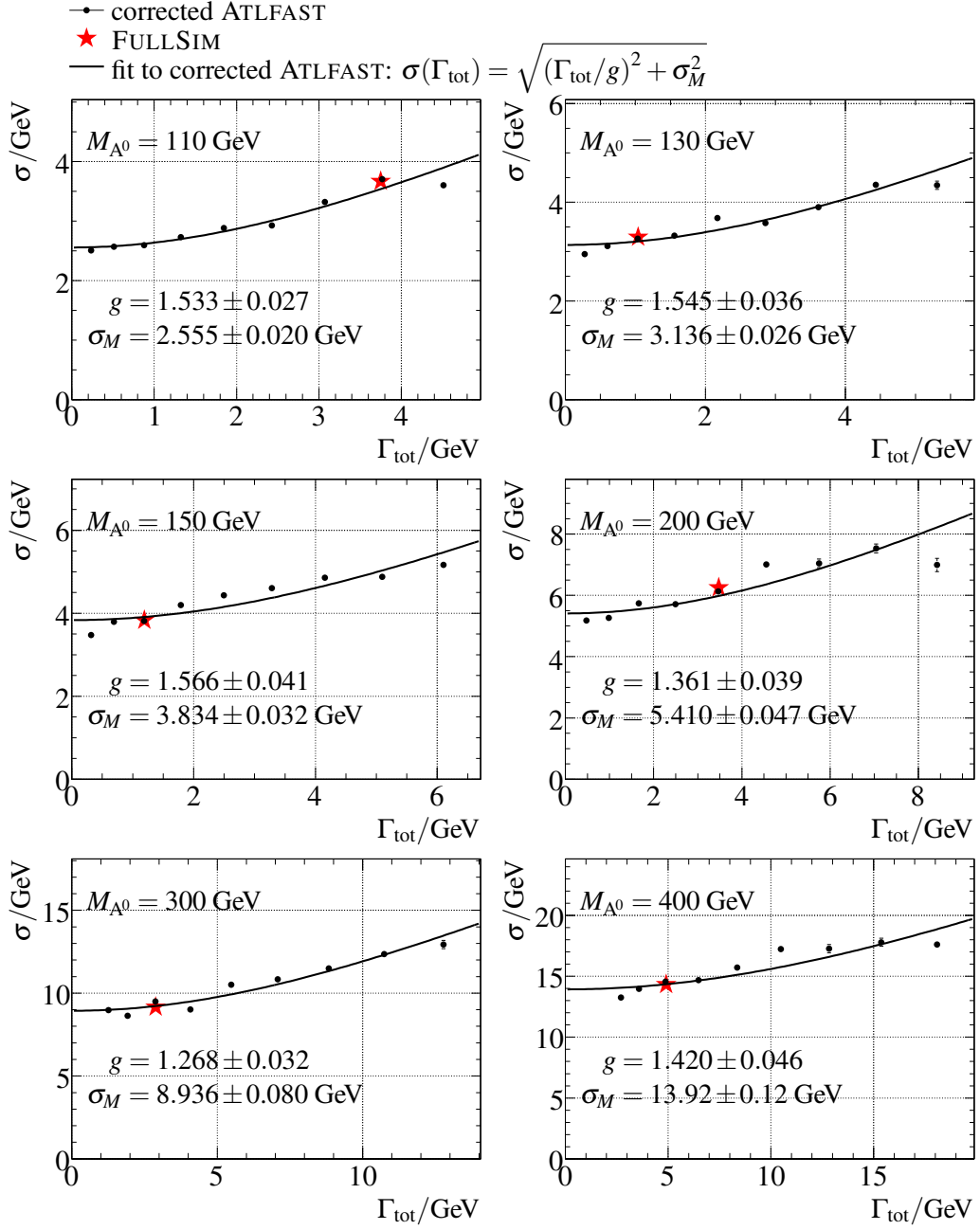


Figure 10.3: Fitted widths of the reconstructed Higgs boson mass in dependence of the natural width of the Higgs boson for different Higgs boson masses (points). The line is a fit to the points. Stars show the reconstructed widths in FULLSIM.

second order polynomials. The dashed lines show 5% uncertainty bands for the interpolation of g and 2.5% for σ_M . The mass resolution σ_M rises almost linearly with the input

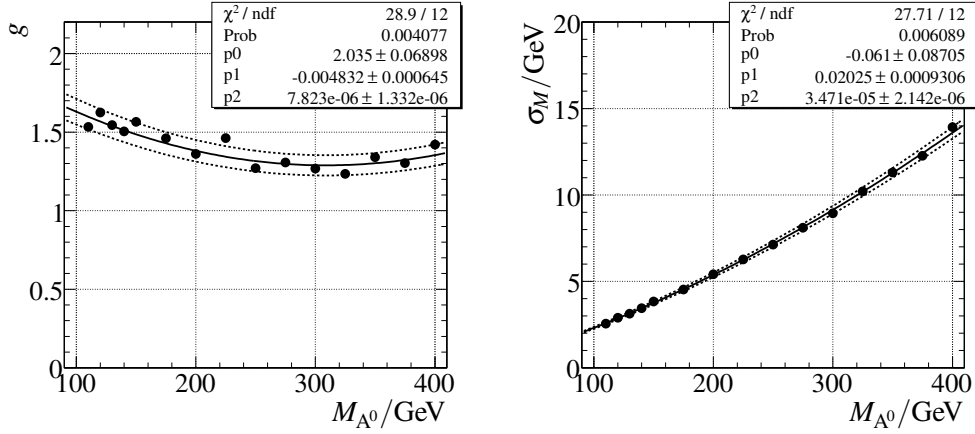


Figure 10.4: Dependence of fit parameters on the Higgs boson mass. Left: g , right: σ_M . Solid lines: Fitted second order polynomials. Dashed lines: $\pm 5\%$ (left) and $\pm 2.5\%$ uncertainty regions (right).

mass. This is expected since the muon momentum resolution rises linearly with p_T . The χ^2 probabilities of the fits are rather small. Especially for the parameter g some deviations are visible. Also no explanation for the mass dependence of g is found. It seems that g is higher for small M_{A^0} . However, the differences between the interpolation functions and the measured values are at most about 5%, which is used as a conservative systematic uncertainty on g . The differences could very well be from the approximation of a Voigt profile by a Gaussian in the central part. The parameter g is mostly determined by the value with the largest natural width, and is thus very susceptible to statistical fluctuations.

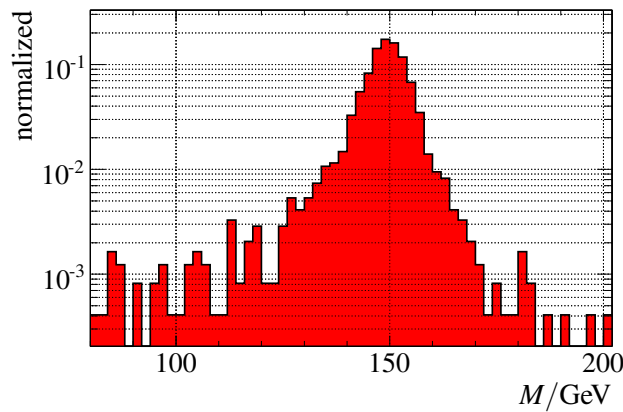


Figure 10.5: Invariant mass distribution for a $b\bar{b}A^0$ sample ($M_{A^0} = 150 \text{ GeV}$, $\tan\beta = 30$) after preselection requirements.

10.2.1 The Mass Tail

One important feature of the mass distribution is a quite long tail towards small masses from the nominal Higgs boson mass. The cause of it is not completely understood: It is either possible that it is caused by significant QED final state radiation (inner bremsstrahlung) of the muons, or possibly caused by the long tail of the Breit-Wigner distribution combined with the higher cross section for smaller masses.

Figure 10.5 shows the invariant mass distribution for a $b\bar{b}A^0$ sample ($M_{A^0} = 150$ GeV, $\tan\beta = 30$), where the tail is clearly visible.

As a consequence, the approximation of a mass window via the Gaussian part does not yield exactly the same efficiency as for a Gaussian. For a two-sided two-sigma mass window, about 85% of all signal event lie inside this window around the generated mass, for a two-sided three-sigma window this content is about 91%.

10.3 Signatures with at least one tagged Jet

As the background and signal properties are very different between events with and without a tagged b jet, the analysis is split into two exclusive subanalyses already at this early stage by requiring at least one tagged b jet (weight-cut of four, IP3D+SV1 tagging algorithm, $p_T > 20$ GeV, $|\eta| < 2.5$). The b-tagged analysis is in the following also called Analysis I.

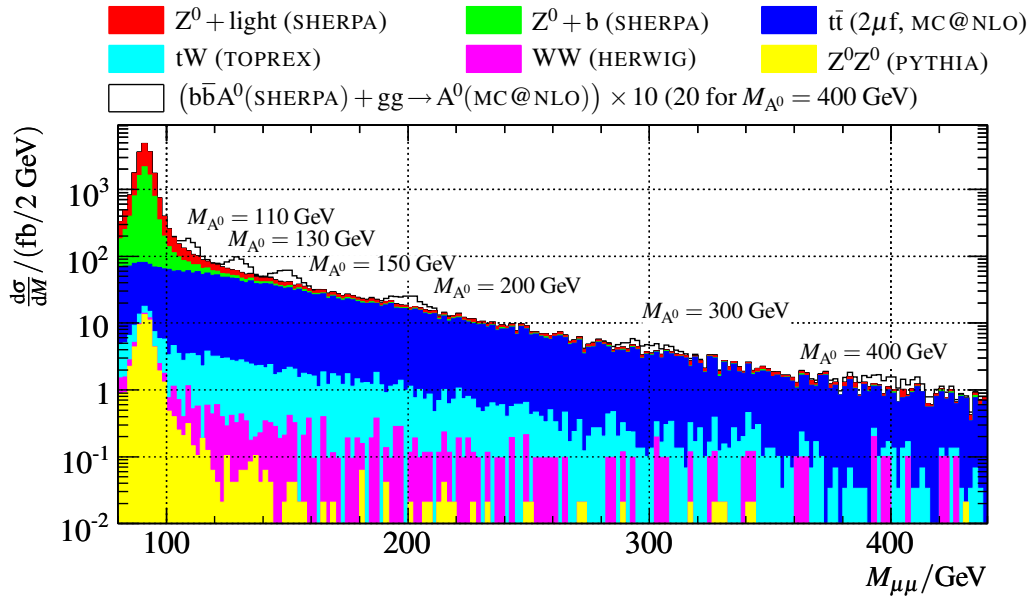


Figure 10.6: Stacked dimuon invariant mass distribution after preselection cuts and requiring at least one b tagged jet ($p_T > 20$ GeV, $w > 4$). Open Histograms: Six different A^0 boson signals for $\tan\beta = 30$, $b\bar{b}A^0$ and $gg \rightarrow A^0$ added together, scaled by a factor of 10 (20 for $M_{A^0} = 400$ GeV). Backgrounds from top to bottom: $Z^0 + \text{light}$ (red), $Z^0 + b$ (green), $t\bar{t}$ (dark blue), tW (light blue), WW (magenta), and $Z^0 Z^0 \rightarrow \mu\mu q\bar{q}$ (yellow).

Figure 10.6 shows the invariant mass distribution for signal and background samples after this requirement.

The b tag already significantly reduces the b-associated production mode as the b-jets from it are predominantly soft. The contribution from direct production is negligible at this stage. But also the $Z^0 + \text{light}$ background is reduced by more than one order of magnitude. The $Z^0 + b$ background is affected similarly as the signal. The $t\bar{t}$ background on the other hand is not suppressed as much as the signal process, as the b-jets in $t\bar{t}$ tend to be harder than in $b\bar{b}A^0$. At high masses (above ≈ 130 GeV) the $t\bar{t}$ background now dominates.

The $Z^0 + \text{light}$ and $Z^0 + b$ backgrounds cannot be reduced significantly further, as otherwise they share exactly the signal characteristics.

Consequently, the only background that can be further reduced is the $t\bar{t}$ background, which also differs significantly from the signal process in several variables. These are discussed in the following. For clarity, the WW and Z^0Z^0 backgrounds are not shown in the following when the differential distributions used are discussed. They are already completely negligible at this stage of the analysis. Nevertheless, they are taken into account when the expected significance is optimized.

In the following subsections, first the individual cut variables are discussed. Later, the cut optimization is presented in Section 10.3.4.

10.3.1 Missing Transverse Energy

One important difference between signal and $t\bar{t}$ events is the presence of neutrinos from W boson decays. These lead to a large missing transverse energy, as they are not detected. Figure 10.7 (a) shows the distributions of \cancel{E}_T (see also Section 9.4 for the major background processes and for a signal sample (only $b\bar{b}A^0$, $M_{A^0} = 150$ GeV) in ATLFAST with an \cancel{E}_T rescaling factor of $s = 2.4$ to simulate pile-up contributions. Clearly the larger \cancel{E}_T in the $t\bar{t}$ sample is visible. A cut on requiring a maximum \cancel{E}_T can suppress the $t\bar{t}$ background.

However, as it turns out the distribution of \cancel{E}_T is dependent of the Higgs boson mass, as shown in Figure 10.7 (b). This is due to harder spectra of the b jet and larger overall hadronic activity, as discussed in the next section, thus leading to a worse \cancel{E}_T resolution. The consequence is that for large masses the same cut on \cancel{E}_T will have a smaller signal selection efficiency than for smaller Higgs boson masses. Unfortunately, the $t\bar{t}$ background is most important at high masses. This means that the separation power of \cancel{E}_T is diminished exactly in the region where it is needed most.

Since at low Higgs boson masses the influence of the Z^0 background contributions is more important, it can be expected that a cut on \cancel{E}_T will give the small improvements in this region, as the Z^0 backgrounds are affected similarly as the signal. But also for high masses, a cut on \cancel{E}_T will have a diminished effect. There is a region of intermediate masses where a cut on \cancel{E}_T is most effective.

Figure 10.8 show a comparison between FULLSIM and ATLFAST for the \cancel{E}_T distributions after the preselection cuts for three selected signal samples and the three major background contributions for. As no pile-up samples are available for the FULLSIM samples, a scale factor $s = 1.4$ is used for the ATLFAST samples. All distributions show satisfactory agreement within uncertainties.

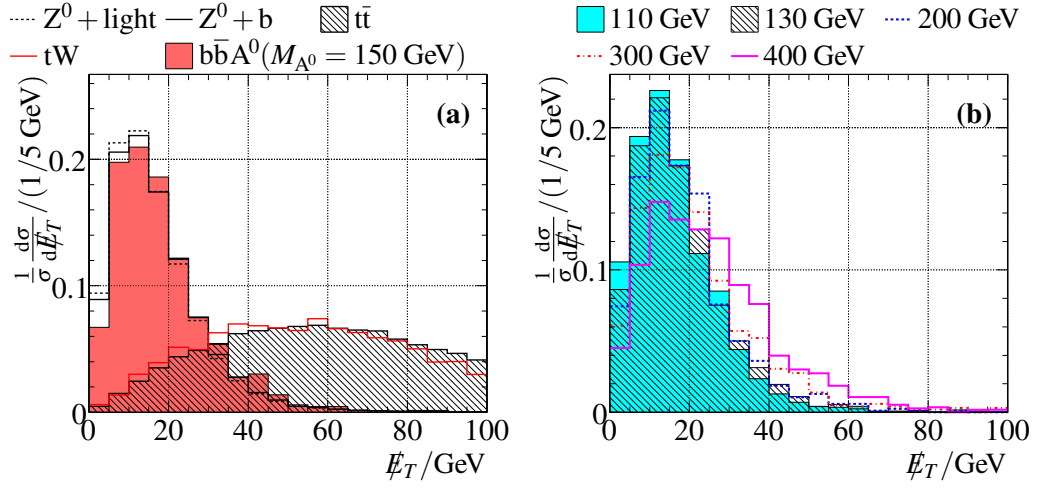


Figure 10.7: (a) Distributions of E_T after the preselection and b tag for background samples and a signal sample ($b\bar{b}A^0$, SHERPA, $M_{A^0} = 150 \text{ GeV}$, $\tan\beta = 30$). (b) Distributions of E_T after the preselection for five other Higgs boson masses (all $b\bar{b}A^0$, $\tan\beta = 30$).

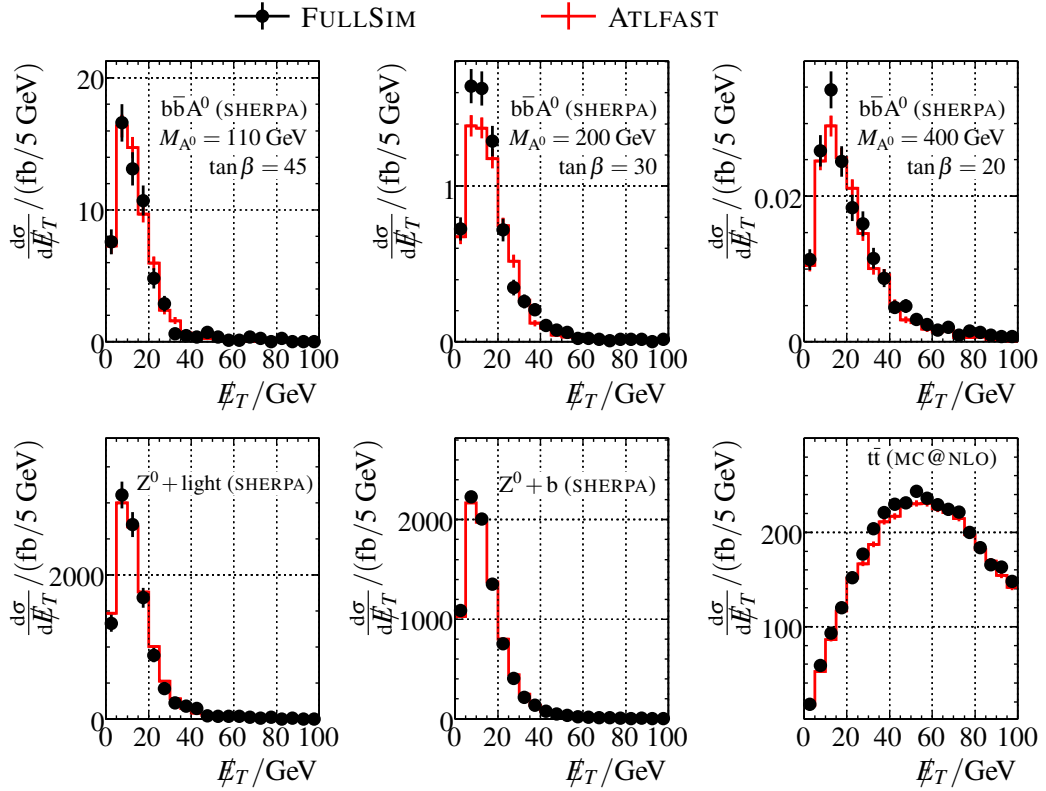


Figure 10.8: Distributions of E_T in signal and background samples after preselection cuts and requiring at least one b tagged jet. Red crosses without markers: ATLFast ($s = 1.4$), points with error bars: FULLSIM (no pile-up simulation).

10.3.2 Hadronic Activity

In addition to the presence of hard final state neutrinos, $t\bar{t}$ events can also be identified by a larger overall hadronic activity and harder b jets, as the b jets produced in $t\bar{t}$ events originate from the decay of the heavy top quark. These variables can also be used to separate signal from the $t\bar{t}$ background.

Momentum of the b-Tagged Jet

Figure 10.9 (a) shows the p_T distribution of the leading b tagged jet in the event for background samples and one selected signal sample. The tagged jets in $t\bar{t}$ events show a much harder p_T spectrum. In contrast to the naive expectation, the tagged b-jet p_T spectrum in $Z^0 + \text{light}$ events is slightly harder than for $Z^0 + b$. This can be explained by the fact that the rejection of udsg jets falls very rapidly with p_T , thus biasing the p_T distribution of b-tagged jets to higher values. For signal events, as in the case of \cancel{E}_T , the p_T distribution of the b jets tends to be harder for larger Higgs boson masses, as shown in Figure 10.9 (b).

The distributions of the leading b jet after the preselection cuts in FULLSIM and ATLFASST were already discussed in Figure 9.41, p. 169. Good agreement between ATLFASST and FULLSIM was achieved. Figure 10.10 shows again the cross section normalized distributions of the leading tagged jet in ATLFASST and FULLSIM for three different Higgs boson masses and the three major background samples. Also in this case the agreement is good. Only for the signal sample with $M_{A^0} = 400$ GeV a small deviation is visible, but is mostly in the overall normalization. This effect is covered by the systematic uncertainty on the muon reconstruction correction applied to ATLFASST.

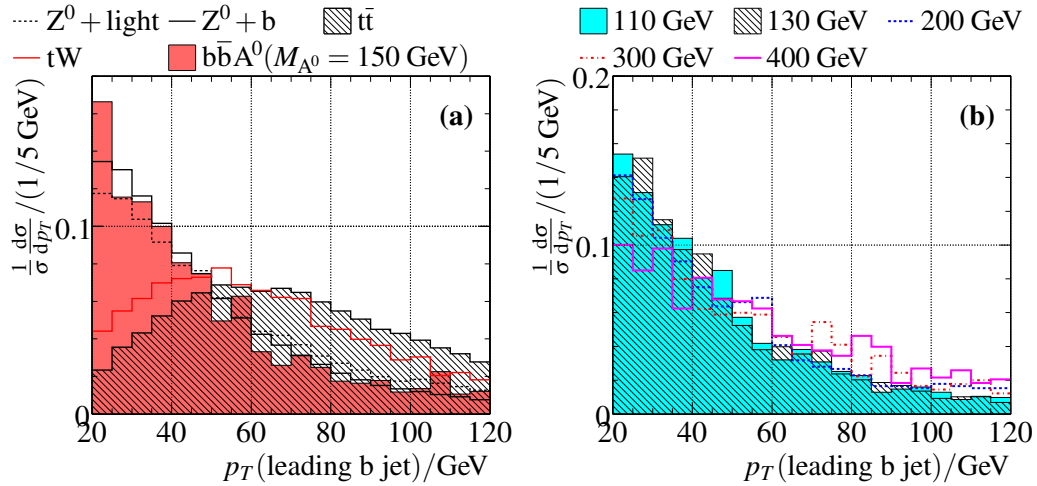


Figure 10.9: a) Distributions of the leading b tagged jet p_T (weight > 4 , $p_T > 20$ GeV, $|\eta| < 2.5$) after the preselection for background samples and a signal sample ($b\bar{b}A^0$, SHERPA $M_{A^0} = 150$ GeV, $\tan\beta = 30$). (b) Distributions of the leading b tagged jet p_T after the preselection for five other Higgs boson masses, all for $b\bar{b}A^0$, SHERPA, $\tan\beta = 30$.

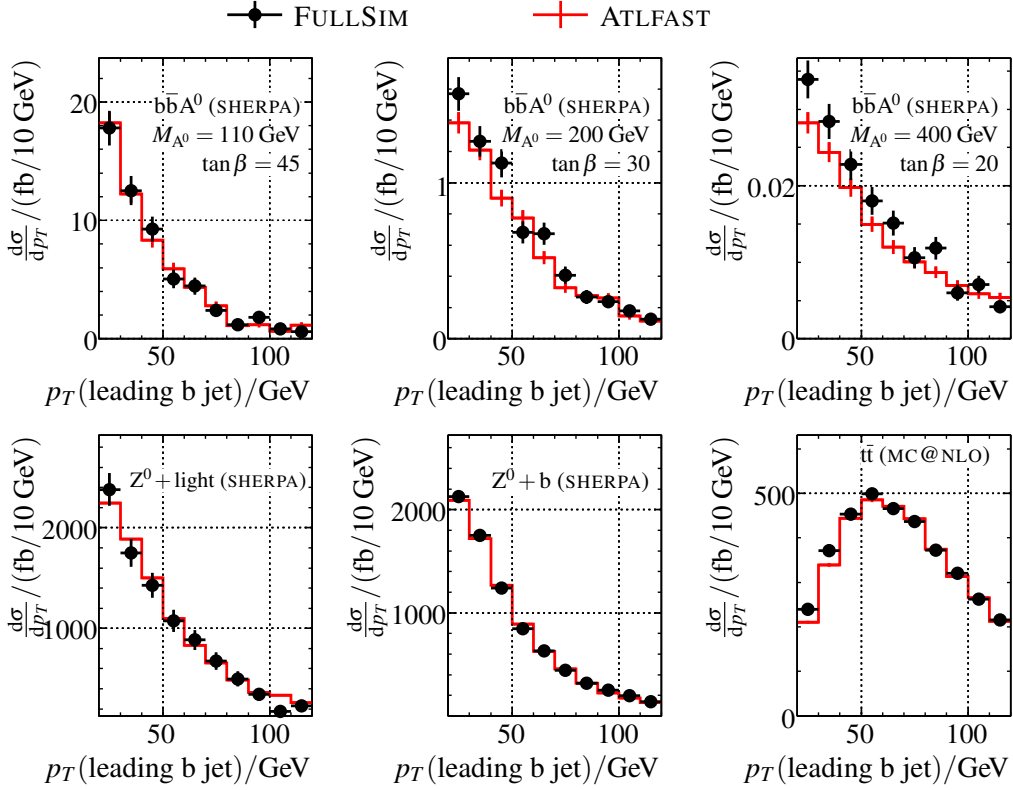


Figure 10.10: Distributions of the leading b tagged jet (weight > 4 , $p_T > 20$ GeV, $|\eta| < 2.5$) in signal and background samples after preselection cuts and requiring at least one b tagged jet. Red crosses without markers: ATLFAST, points with error bars: FULLSIM.

Scalar Sum of Jet Momenta

The scalar sum of the jet momenta, H_T , is also well suited to distinguish between signal and $t\bar{t}$ background events. In a way, it already includes the information from the p_T distribution of the leading b jet, as this one is included in the calculation of H_T . In addition, H_T takes into account that there is also a second hard b jet in a $t\bar{t}$ event. This second b jet might not be tagged as a b jet, either because of limited efficiency or because it might lie outside the acceptance of the inner detector.

Figure 10.11 (a) shows the distribution of H_T for background and one selected signal sample. Figure 10.11 (b) shows the distribution of H_T in signal samples for different Higgs boson masses. As expected, the $t\bar{t}$ background shows larger H_T values than the signal and Z^0 samples. Also, H_T is dependent on the Higgs boson mass. Again, at very large Higgs boson masses, a cut on H_T will have a diminished signal selection efficiency. However, one should keep in mind that due to the harder spectrum of the b jets, the selection efficiency for at least one tagged b jet is higher for larger Higgs boson masses, as the b tagging efficiency increases with p_T and more jets pass the cut on the transverse momentum of 20 GeV. This will counter somewhat the smaller selection efficiency of a cut on H_T .

Figure 10.12 shows a comparison between FULLSIM and ATLFAST of the H_T distributions for three selected signal samples and the three major background contributions. The agreement is good.

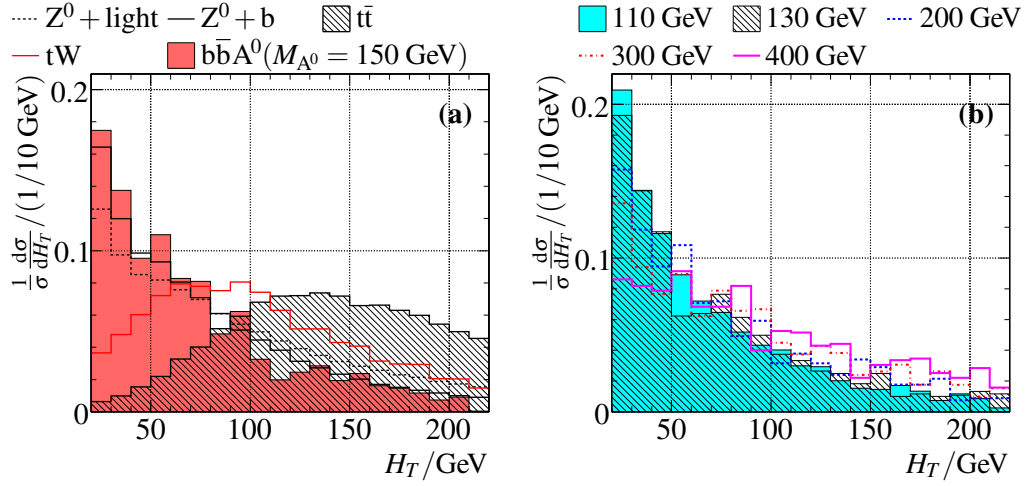


Figure 10.11: (a) Distributions of H_T after the preselection and b tag for background samples and a signal sample ($b\bar{b}A^0$, SHERPA $M_{A^0} = 150 \text{ GeV}$, $\tan\beta = 30$). (b) Distributions of H_T after the preselection for five other Higgs boson masses, (all $b\bar{b}A^0$, $\tan\beta = 30$).

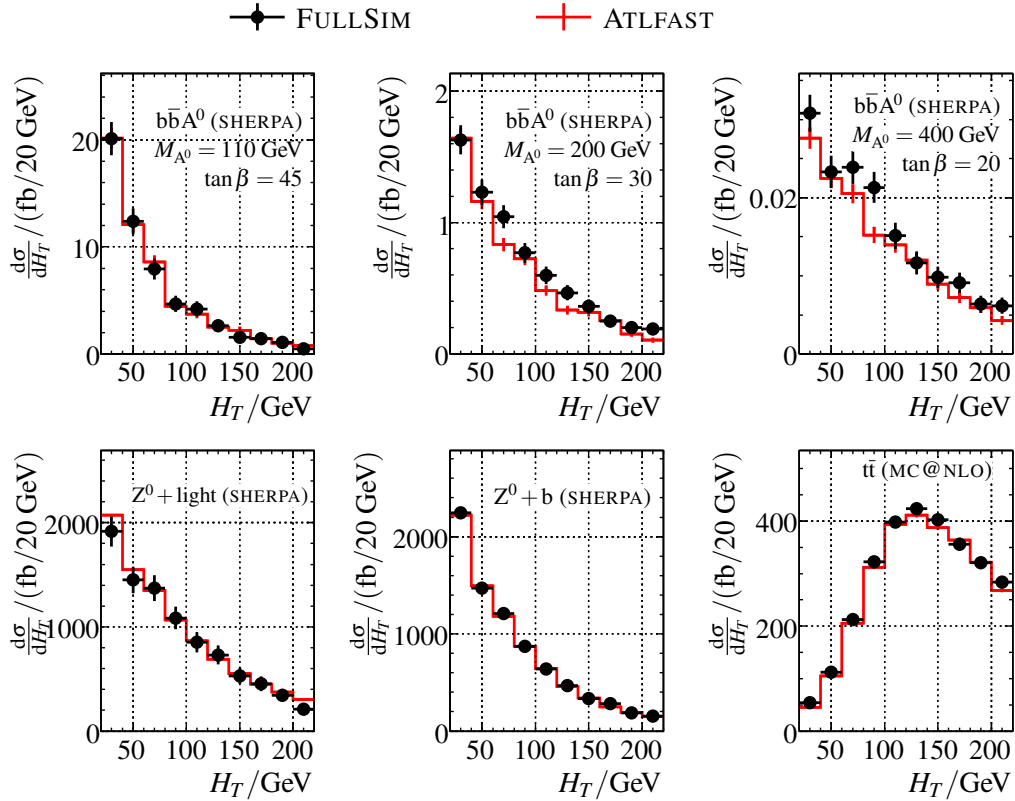


Figure 10.12: Distributions of H_T in signal and background samples after preselection cuts and requiring at least one b tagged jet. Red crosses without markers: ATLFast, points with error bars: FULLSIM.

10.3.3 Muonic Variables

The last class of variables that can be used for the event selection, are those connected to the muons. However, after the preselection cuts, the remaining variables do not offer a large separation power between signal and background.

Muon Transverse Momentum

Figure 10.13 shows the muon transverse momentum distribution of background and signal samples. Obviously, the muon p_T distribution is strongly correlated with the mass of the dimuon system. In order for the muons to have a large invariant mass, they tend to have a harder p_T spectrum due to simple kinematics. Placing a higher cut than the preselection

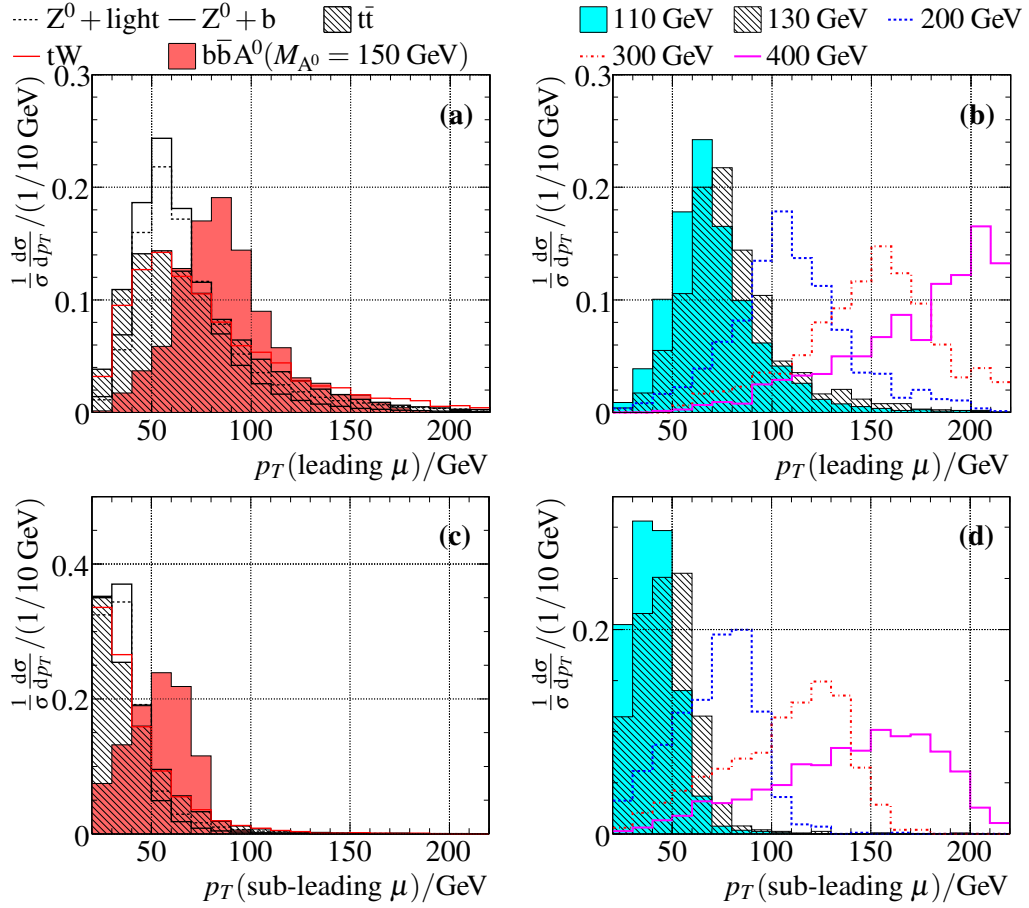


Figure 10.13: (a) Distributions of the p_T of the leading muon after the preselection and b tag for background samples and a signal sample ($b\bar{b}A^0$, SHERPA, $M_{A^0} = 150 \text{ GeV}$, $\tan\beta = 30$). (b) Distributions of the p_T of the leading muon after the preselection for six different Higgs boson masses, all $b\bar{b}A^0$, SHERPA, $\tan\beta = 30$. (c) and (d): As (a) and (b), but for the p_T of the sub-leading muon.

cut of 20 GeV on the muon transverse momentum would simply remove events with small invariant masses. This would only distort the invariant mass spectrum, but provide no gain in expected significance. Higgs bosons with low masses yield a smaller reconstruction efficiency from the cut on the muon transverse momentum. For these small masses, the distribution of the sub-leading muon is clearly already cut on significantly. To increase the efficiency for very small Higgs boson masses, an analysis using a smaller cut on the muon p_T would be more suitable. However, due to the encountered differences between ATLFast and FullSim, this is not feasible in this work.

In addition, the trigger requirement is matched to muons with $p_T > 20$ GeV. Cutting lower on the momentum of the sub-leading muon might increase the selection efficiency slightly, but at the same time the trigger efficiency might be lower, thus compensating to some extent. For a more detailed discussion of the trigger requirements, see Section 10.5.

Acoplanarity

Another variable that is potentially of interest is the acoplanarity A . It is defined as the absolute value of the sine of the opening angle between the two muons in the transverse plane:

$$A = |\sin \Delta\phi_{\mu\mu}|. \quad (10.2)$$

Its name originates from the fact that it is zero if the two muons and the z axis lie in the same plane.

In $t\bar{t}$ events, the two muons do not come from the same parent particle, so the opening angle can in principle take any value. In signal events on the other hand, the two muons come from the decay of the Higgs boson. If the Higgs boson has a small transverse momentum, they are emitted back to back ($\Delta\phi = \pi$).

Figure 10.14 shows the distributions of the acoplanarity for signal and background events. The peak at one for the background samples is in part caused by the non-linearity of the sine function, but also the distribution of $\Delta\phi_{\mu\mu}$ is not flat. At first glance, this variable seems to provide some separation power. However, it has to be remembered that at this stage already a tagged b jet is required. As the Higgs boson in the signal events has to recoil against this jet, it is already boosted in the transverse plane and the opening angle between the two muons is in general smaller than π , thus diminishing the separation. Although one would expect this effect to be less important for higher masses, here the b jets are harder, somewhat compensating the higher mass. The acoplanarity is also correlated to H_T and the p_T of the leading b jet, as it effectively also suppresses hard jets that the Higgs boson recoils against.

The acoplanarity is correlated with the candidate mass also in the background samples. Requiring a higher candidate mass biases the muons to be more back-to-back in the transverse plane, as in this case they have a higher invariant mass for a given transverse momentum. This is shown in Figure 10.15, where the correlation is visible. Clearly, the acoplanarity does not peak as pronounced at one for high masses as for low masses.

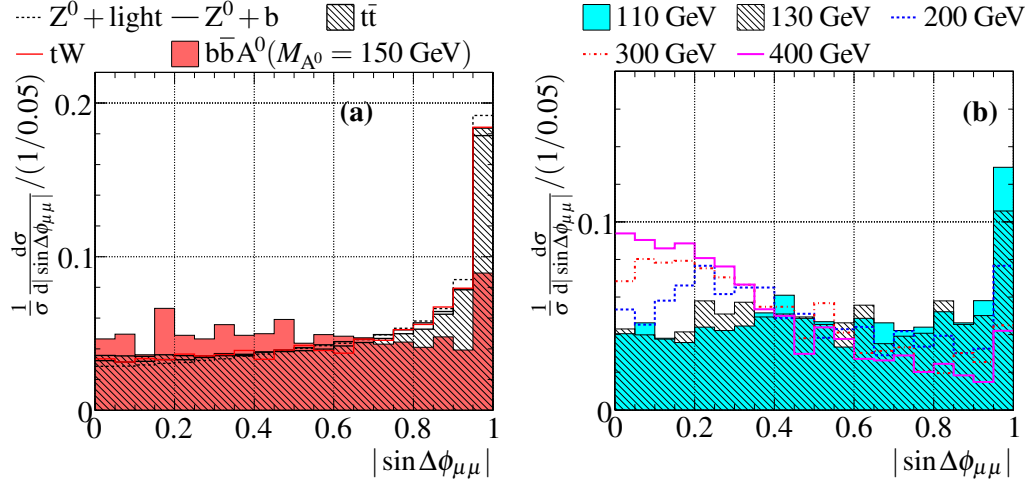


Figure 10.14: (a) Distributions of the acoplanarity after the preselection and b tag for background samples and a signal sample ($b\bar{b}A^0$, SHERPA, $M_{A^0} = 150 \text{ GeV}$, $\tan\beta = 30$). (b) Distributions of the acoplanarity after the preselection for five other Higgs boson masses (all $b\bar{b}A^0$, SHERPA, $\tan\beta = 30$).

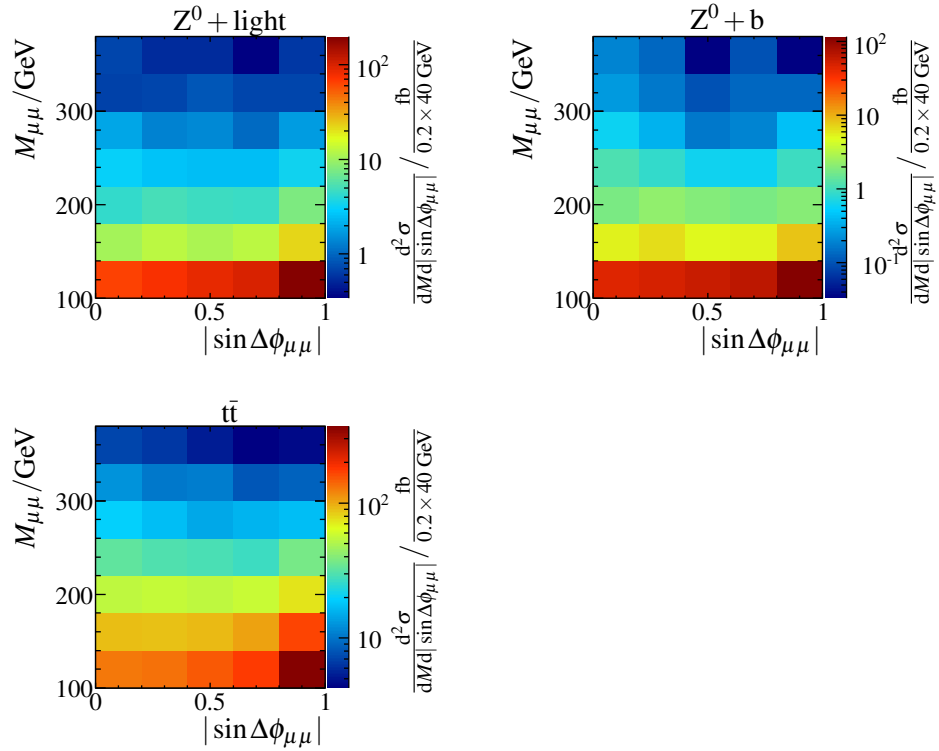


Figure 10.15: Distribution of the acoplanarity versus the candidate mass in the three major background contributions after preselection and b tag requirement.

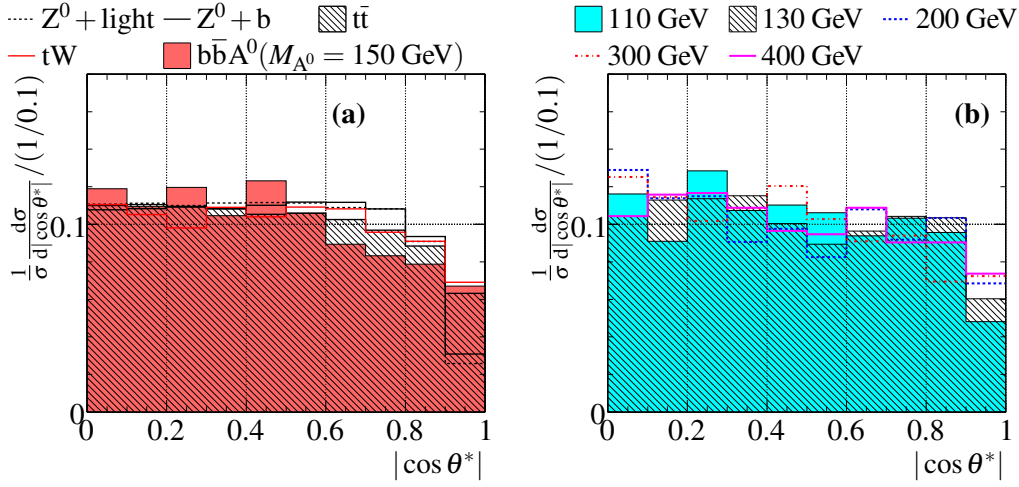


Figure 10.16: (a) Distributions of $|\cos \theta^*|$ after the preselection and b tag for background samples and a signal sample ($b\bar{b}A^0$, SHERPA, $M_{A^0} = 150 \text{ GeV}$, $\tan \beta = 30$). (b) Distributions of $|\cos \theta^*|$ after the preselection for five other Higgs boson masses (all $b\bar{b}A^0$, SHERPA, $\tan \beta = 30$).

Gottfried-Jackson Angle

One last potentially useful variable is the Gottfried-Jackson angle $\cos \theta^*$ [153]. It is defined as the polar angle between one of the two muons and the flight direction of the dimuon system in the rest frame of the dimuon system. It contains basic information about the production mechanism of the two muons. As the two muons in the case of $t\bar{t}$ events do not even originate from the same particle, there might be differences in this variable.

Figure 10.16 shows the distribution of $\cos \theta^*$ in signal and background samples. Some differences in the distributions are visible, but these are rather small and might not be useful in a cut based analysis. The mass dependence of this variable is not investigated further, as it is not used in the following.

10.3.4 Selection

As described above, the selection cuts are now optimized in mass windows around the nominal Higgs boson mass. Six different Higgs boson masses are used to obtain a working selection over a broad mass range. The cuts are not optimized separately for each tested Higgs boson mass. In order to take correlations of different cut variables into account, the cuts are optimized in an iterative way: Already optimized cuts are applied before optimizing the next cut. In addition, after optimization, each cut is re-optimized by removing and retuning it. This procedure is repeated until stability is reached. The expected sensitivities shown in the following are for the optimized cuts except the one under study.

An alternative to this cut-based selection would be to use a multivariate selection method, which could combine one or more variable into a single discriminating variable. However, as discussed before, the distribution of a lot of the possible input variables change

significantly with the candidate mass. This complicates the possible use of a multivariate technique unnecessarily and it is not applied in this thesis.

The optimized cuts are rather simple:

$$p_T(\text{both } \mu) > 20 \text{ GeV} \quad (10.3)$$

$$p_T(\text{leading b jet, weight} > 4) > 20 \text{ GeV} \quad (10.4)$$

$$\cancel{E}_T < 40 \text{ GeV} \quad (10.5)$$

$$H_T < 80 \text{ GeV} \quad (10.6)$$

$$p_T(\text{leading b jet}) < 80 \text{ GeV} \quad (\text{already included in } H_T \text{ cut}) \quad (10.7)$$

$$A \leq 1 \quad (\text{i.e. no cut}) \quad (10.8)$$

$$\cos \theta^* \leq 1 \quad (\text{i.e. no cut}). \quad (10.9)$$

Figure 10.17 shows the expected sensitivities in dependence of the cuts when all other cuts are left at the standard values. As expected, placing a harder cut on the muon transverse momenta does not increase the sensitivity, even for the higher masses. For the cuts on \cancel{E}_T and H_T , as discussed, most improvement by placing a cut on these variables occurs at intermediate Higgs boson masses (i.e. around 200 GeV). For very low or very high masses the improvement is much smaller due to the different background composition and signal distributions.

The acoplanarity and Gottfried-Jackson angle do not provide any additional way to improve the sensitivity. Only for the very high Higgs boson mass of 400 GeV a cut on these two variables might improve the sensitivity. However, this is just barely visible within the Monte Carlo statistics. As the signal cross section is anyway very low for these high masses, no attempt is done to do a designated analysis for the high Higgs boson masses.

Figure 10.18 shows the invariant mass distribution after the selection. Clearly, the $t\bar{t}$ background has been largely reduced. Even for intermediate masses it is now on the same level as $Z^0 + \text{light}$ and $Z^0 + b$.

Table 10.2 shows the accepted cross sections after each selection step for backgrounds and Table 10.3 for signal samples.

The event selection efficiencies range from between 5.5% and 7.5%. They are highest for intermediate masses. At lower masses, both the muons and the b jets are softer. At high masses, the cuts used to reject $t\bar{t}$ background decrease the selection efficiency.

Figure 10.19 shows the invariant mass distributions for six selected $(M_{A^0}, \tan \beta)$ points in the M_{h^0} -max scenario normalized to an integrated luminosity of 30 fb^{-1} . The A^0 is always mass degenerate with either the h^0 or the H^0 . Only for $M_{A^0} = 130 \text{ GeV}$ do all three neutral Higgs bosons contribute significantly to the signal.

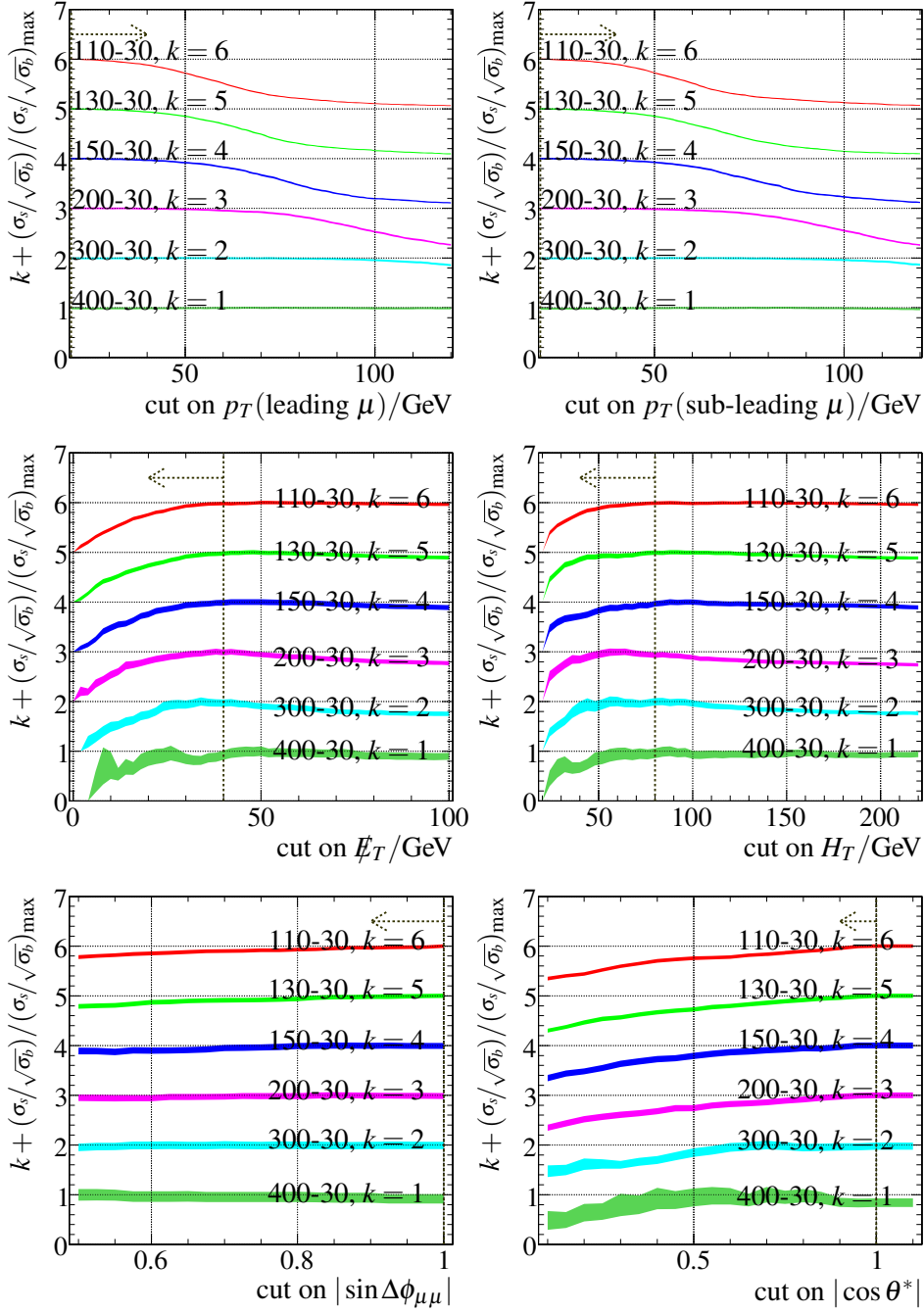


Figure 10.17: Dependence of the expected significance in a mass window for six different Higgs boson masses (all for $\tan\beta = 30$) on the cut on the p_T of the leading μ (top left), the p_T of the sub-leading μ (top right), \cancel{E}_T (middle left), H_T (middle right), the acoplanarity (bottom left), and the Gottfried Jackson angle (bottom right). The size of the bands corresponds to the statistical uncertainty. The dashed lines with errors indicate the chosen cuts.

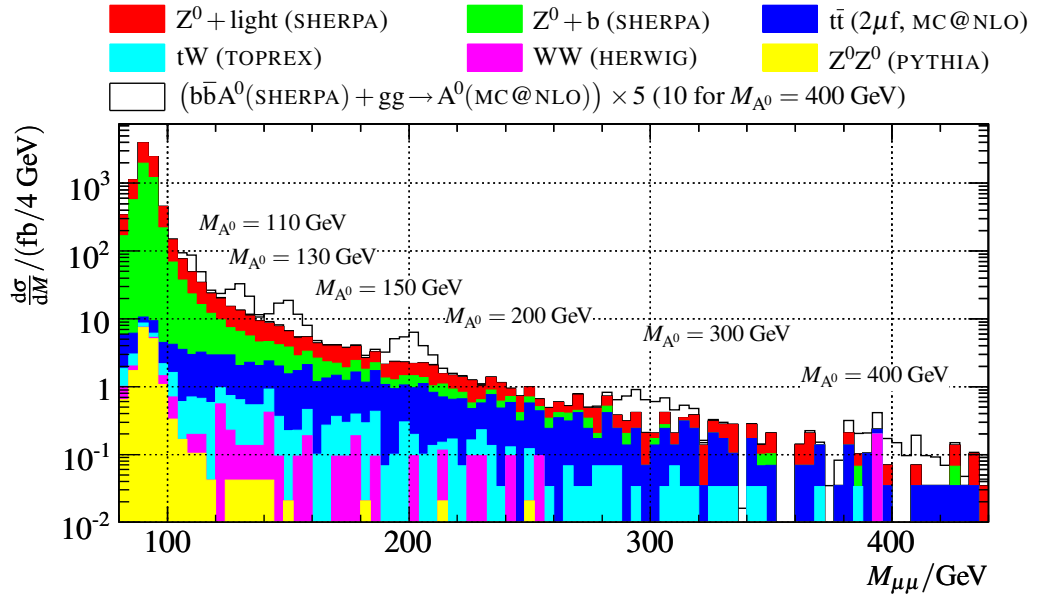


Figure 10.18: Stacked dimuon invariant mass distribution after selection cuts (b tagged analysis). Open Histograms: Six different A^0 boson signals for $\tan\beta = 30$, $b\bar{b}A^0$ and $gg \rightarrow A^0$ added, scaled by a factor of 5 (10 for $M_{A^0} = 400 \text{ GeV}$). Backgrounds from top to bottom: $Z^0 + \text{light}$ (red), $Z^0 + b$ (green), $t\bar{t}$ (dark blue), tW (light blue), WW (magenta), and $Z^0 Z^0 \rightarrow \mu\mu q\bar{q}$ (yellow).

Cut	$\varepsilon \times \sigma / \text{fb}$						Σ
	$Z^0 + \text{light}$ (SHERPA, $2\ell\text{f}$)	$Z^0 + \text{b}$ (SHERPA, $2\ell\text{f}$)	$t\bar{t}$ (MC@NLO, $2\mu\text{f}$)	$t\text{W}$ (TOPREX, $2\ell\text{f}$)	WW (HERWIG, $1\ell\text{f}$)	$Z^0 Z^0$ (PYTHIA, $2\ell\text{f}$)	
All events	1010225	47070	60300	11790	43840	521	1173750
Preselection	699800 ± 150	31050 ± 30	5400 ± 20	401 ± 4	1750 ± 10	278 ± 2	738700 ± 160
$\geq 1 \text{ b jet}$	11080 ± 20	8400 ± 20	4350 ± 10	243 ± 3	35 ± 2	57 ± 1	24165 ± 30
$\cancel{E}_T < 40 \text{ GeV}$	9730 ± 20	7400 ± 20	929 ± 7	64 ± 2	12 ± 1	51 ± 1	18186.0 ± 29
$H_T < 80 \text{ GeV}$	4660 ± 10	4496 ± 12	97 ± 2	25 ± 1	8 ± 1	18 ± 1	9304 ± 16
$\Delta M(110 \text{ GeV})$	75 ± 2	61 ± 1	7.3 ± 0.6	1.4 ± 0.2	0.2 ± 0.1	0.31 ± 0.08	145.2 ± 2.3
$\Delta M(130 \text{ GeV})$	24 ± 1	15.2 ± 0.7	6.5 ± 0.6	1.7 ± 0.2	0.6 ± 0.2	0.15 ± 0.06	48.2 ± 1.4
$\Delta M(150 \text{ GeV})$	12.7 ± 0.7	7.9 ± 0.5	6.5 ± 0.5	1.1 ± 0.2	0.5 ± 0.2	0.06 ± 0.04	28.8 ± 1.0
$\Delta M(200 \text{ GeV})$	5.3 ± 0.4	1.9 ± 0.3	5.4 ± 0.5	0.8 ± 0.2	0.1 ± 0.1	0	13.0 ± 0.7
$\Delta M(300 \text{ GeV})$	1.2 ± 0.2	0.23 ± 0.09	1.9 ± 0.3	0.3 ± 0.1	0	0	3.8 ± 0.4
$\Delta M(400 \text{ GeV})$	0.24 ± 0.09	0.07 ± 0.05	0.6 ± 0.2	0.07 ± 0.05	0.2 ± 0.1	0	1.0 ± 0.2

Table 10.2: Accepted background cross sections after each selection step and after the mass window cuts (Analysis I) for ATLFAS background samples. The cross section before all cuts already includes the event filter efficiencies. All numbers in fb. Uncertainties are statistical only.

$(M_{A^0}/\text{GeV}, \tan\beta)$	$\varepsilon \times \sigma/\text{fb}$					
	$b\bar{b}A^0, A^0 \rightarrow \mu\mu$ (SHERPA)					
	(110,30)	(130,30)	(150,30)	(200,30)	(300,30)	(400,30)
All events	242.9	148.0	95.45	37.4	8.0	2.18
Preselection	145 ± 2	92.3 ± 1.2	61.8 ± 1.1	24.5 ± 0.4	5.45 ± 0.09	1.49 ± 0.03
≥ 1 b jet	27.6 ± 0.7	18.9 ± 0.5	13.6 ± 0.5	6.4 ± 0.2	1.63 ± 0.05	0.50 ± 0.02
$\cancel{E}_T < 40$ GeV	24.6 ± 0.6	16.4 ± 0.5	11.6 ± 0.5	5.5 ± 0.2	1.28 ± 0.05	0.33 ± 0.01
$H_T < 80$ GeV	17.1 ± 0.5	10.5 ± 0.4	7.8 ± 0.4	3.3 ± 0.2	0.67 ± 0.03	0.15 ± 0.01
ΔM	13.9 ± 0.5	9.0 ± 0.4	6.5 ± 0.4	2.8 ± 0.2	0.59 ± 0.03	0.12 ± 0.01
Efficiency/%	5.7 ± 0.1	6.1 ± 0.2	6.8 ± 0.4	7.5 ± 0.4	7.4 ± 0.4	5.5 ± 0.3
$(M_{A^0}/\text{GeV}, \tan\beta)$	$gg \rightarrow A^0, A^0 \rightarrow \mu\mu$ (MC@NLO)					
	(110,30)	(130,30)	(150,30)	(200,30)	(300,30)	(400,30)
	(110,30)	(130,30)	(150,30)	(200,30)	(300,30)	(400,30)
All events	85.6	38.7	19.2	4.36	0.39	0.089
Preselection	47 ± 1	23 ± 1	11.8 ± 0.3	2.7 ± 0.1	0.24 ± 0.01	0.06 ± 0.01
≥ 1 b jet	0.8 ± 0.1	0.5 ± 0.1	0.3 ± 0.1	0.06 ± 0.01	0.01 ± 0.01	0.01 ± 0.01
$\cancel{E}_T < 40$ GeV	0.6 ± 0.1	0.4 ± 0.1	0.2 ± 0.1	0.05 ± 0.01	0.01 ± 0.01	0
$H_T < 80$ GeV	0.2 ± 0.1	0.2 ± 0.1	0.1 ± 0.1	0.02 ± 0.01	0.01 ± 0.01	0
ΔM	0.2 ± 0.1	0.2 ± 0.1	0.1 ± 0.1	0.01 ± 0.01	0.01 ± 0.01	0
Efficiency/%	all $\leq 0.5\%$					

Table 10.3: Accepted cross sections after each analysis step (Analysis I) and in the mass window for ATLFAST signal samples. No event filters were applied for these samples. All numbers in fb.

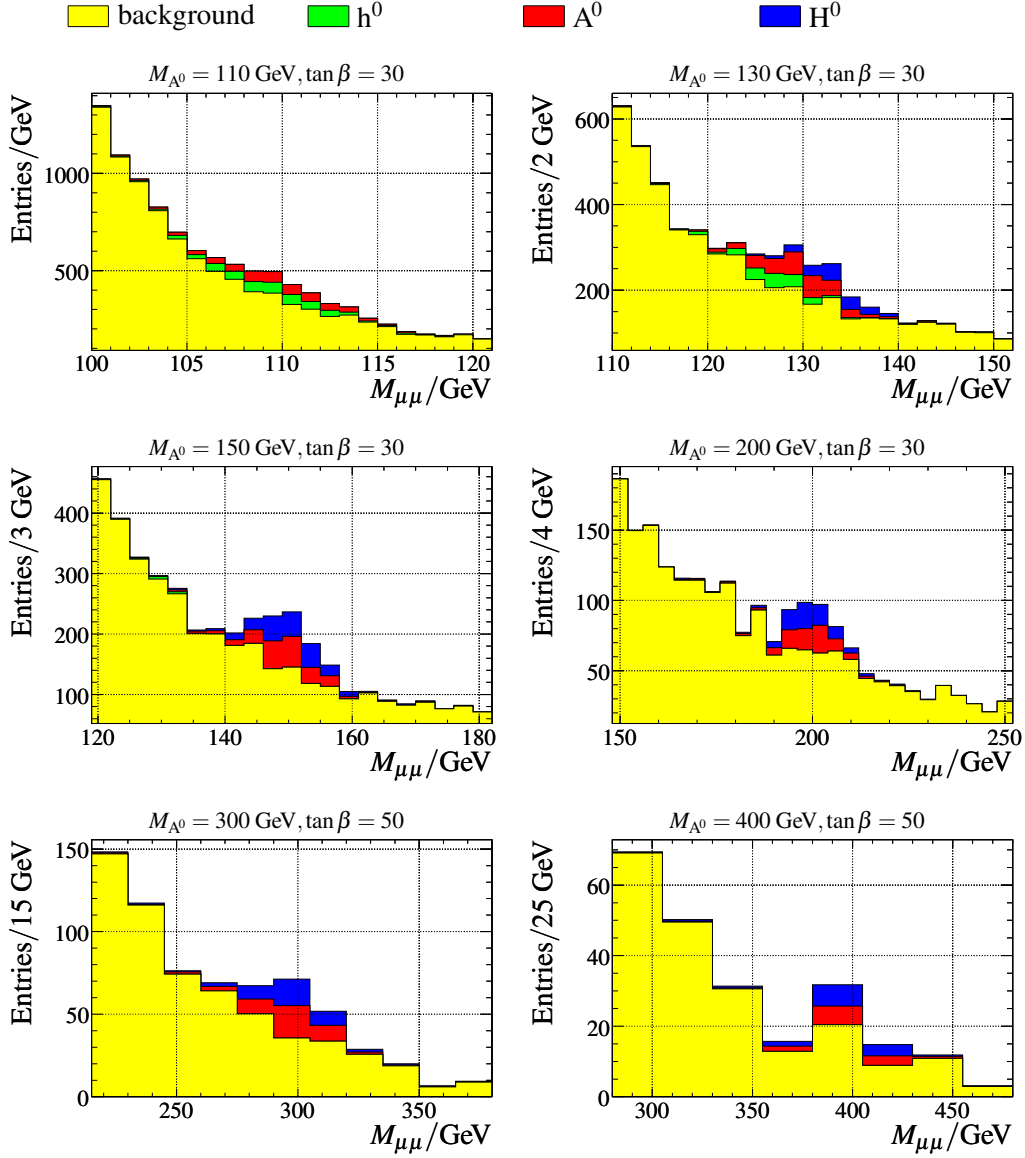


Figure 10.19: Invariant mass distributions for six selected $(M_{A^0}, \tan \beta)$ points in Analysis I for an integrated luminosity of 30 fb^{-1} . Trigger efficiency is included (see Section 10.5).

10.3.5 Influence of the Weight Cut

Last, the influence of the weight-cut applied to define b jets is investigated. The used cut $\text{weight} > 4$ is in a way arbitrary, but is also used in [135].

Using a much higher cut on the combined b -tagging weight would decrease the rate of fake b jets from u or c jets decisively. But at the same time, also the efficiency to tag a b jet would be diminished. On the other hand, applying a softer cut would increase the rate of fake b -tagged jets, while at the same time increasing the signal efficiency. In between

weight-cut	$b\bar{b}A^0, M_{A^0} = 150 \text{ GeV}$	$\varepsilon \times \sigma / \text{fb}$			
		$Z^0 + \text{light}$	$Z^0 + b$	$t\bar{t}$	total bkg.
2	3.2 ± 0.2	10.4 ± 0.6	2.2 ± 0.3	6.0 ± 0.5	18.6 ± 0.8
4	2.8 ± 0.1	5.3 ± 0.4	1.9 ± 0.3	5.4 ± 0.5	12.6 ± 0.9
6	2.4 ± 0.1	3.0 ± 0.3	1.5 ± 0.2	4.9 ± 0.5	9.4 ± 0.6

Table 10.4: Accepted cross sections after all selection cuts and within the mass window for $M_{A^0} = 200 \text{ GeV}$, $\tan\beta = 30$ for three different weight-cuts.

is an optimal working point for the analysis. Table 10.4 shows the accepted cross sections inside the two sigma mass window for a Higgs boson mass of 200 GeV for signal and the three major background contributions. Obviously, especially the $Z^0 + \text{light}$ background depends very much on the weight-cut, but also the signal selection efficiency is influenced significantly.

Figure 10.20 shows the expected significances after all selection cuts in dependence of the weight-cut. The chosen weight-cut of four is close to the optimum. For small Higgs boson masses a small improvement on the order of 2% of the significance might be feasible by choosing a weight-cut of five. This is due to the fact that at such low masses the contribution of $Z^0 + \text{light}$ is largest and a better rejection of the $Z^0 + \text{light}$ background could increase the significance in spite of the smaller signal efficiency.

The possible improvement of 2% is much smaller than the systematic uncertainties. In addition, choosing a higher weight-cut would increase the statistical uncertainty of the ATLFAST parameterization of the rejection, since less udsg jets would pass the weight-cut in the (small) Monte Carlo samples used to derive the parameterization. As the expected significances show a very broad plateau around the optimal working point, the exact choice of the weight-cut has only a small influence on the final result.

10.4 Signatures without tagged Jets

A second analysis, called Analysis II in the following, is performed on all events that do not contain a b tagged jet with the described cuts. This is done to retain a complementary analysis, since the signal selection efficiencies are rather low. In this way it is made sure that the optimal sensitivity is reached.

After vetoing any tagged b jets, the main background is $Z^0 + \text{light}$. All other background contributions are almost negligible in comparison, only WW contributes a little especially for high masses. As a consequence, the variables that were used to discriminate against the $t\bar{t}$ background are only of very limited use. Figure 10.21 shows the result of an optimization attempt for the cut on \cancel{E}_T . Obviously, the \cancel{E}_T cut is of no use anymore. Anyhow, a cut at 50 GeV is applied in the following to suppress the $t\bar{t}$ and WW backgrounds. Although this diminishes somehow the significance for very large Higgs boson masses,

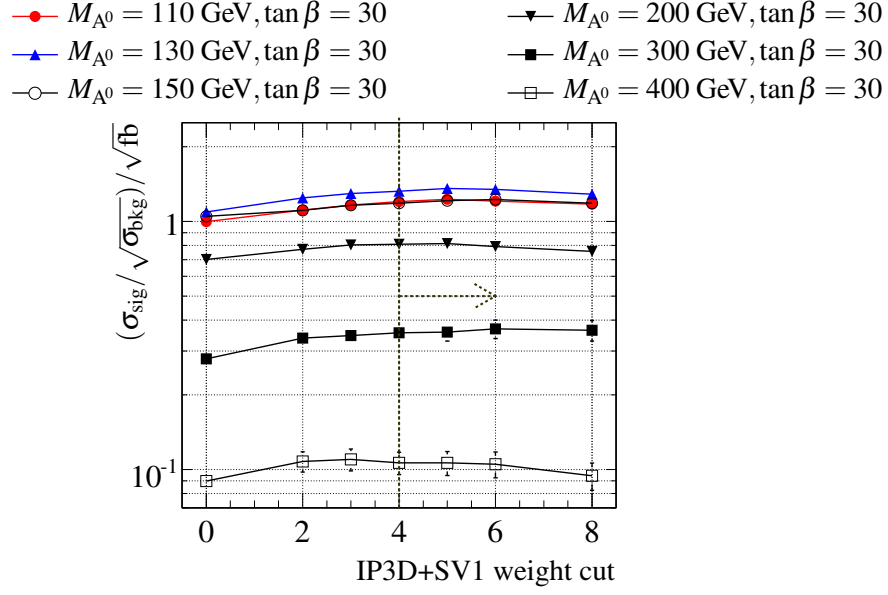


Figure 10.20: Dependence of the expected significance after selection cuts for different Higgs boson masses in dependence of the b -tagging weight-cut. The dashed line with arrow indicates the chosen cut.

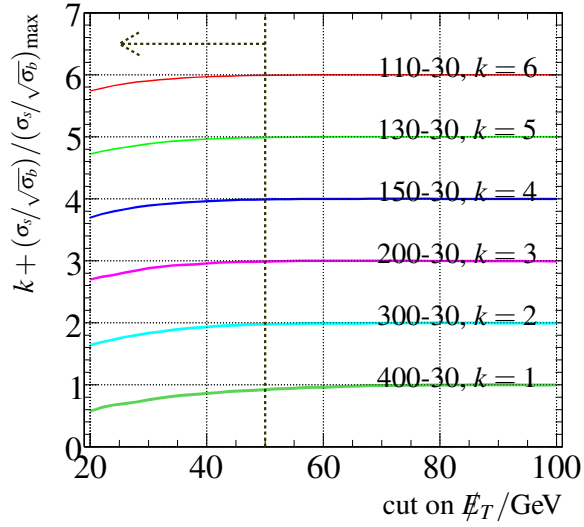


Figure 10.21: Cut optimization of the cut on E_T in the non- b tagged analysis for six different Higgs boson masses as indicated. The dashed line with arrow indicated the chosen cut.

this cut ensures that no possibly unsimulated background, e.g. the production of SUSY

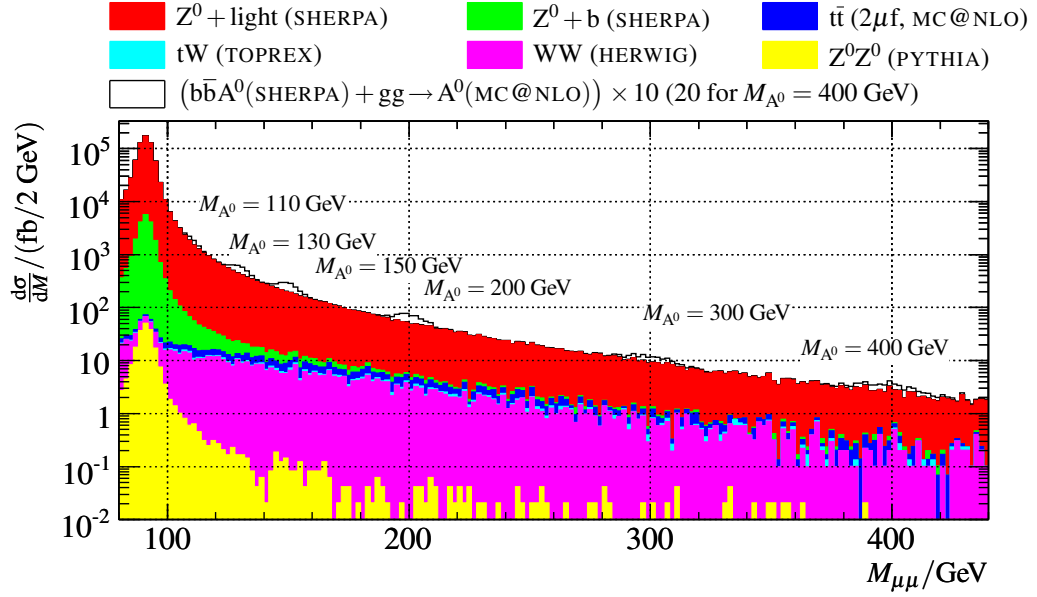


Figure 10.22: Stacked dimuon invariant mass distribution after applying the selection without b tag requirement. Open Histograms: Six different A^0 boson signals for $\tan\beta = 30$, $b\bar{b}A^0$ and $gg \rightarrow A^0$ added, scaled by a factor of 10 (20 for $M_{A^0} = 400$ GeV). Backgrounds from top to bottom: $Z^0 + \text{light}$ (red), $Z^0 + b$ (green), $t\bar{t}$ (dark blue), tW (light blue), WW (magenta), and $Z^0 Z^0 \rightarrow \mu\mu q\bar{q}$ (yellow).

particles, which would contain a large \cancel{E}_T , enters the analysis. For masses below 300 GeV this cut has almost no effect on the significance.

Figure 10.22 shows the invariant mass distribution after these cuts. The $Z^0 + \text{light}$ background now dominates the background contribution. The $Z^0 + b$ background also contributes significantly. The $t\bar{t}$ and tW backgrounds are much smaller for this analysis. WW has now a contribution larger than as $t\bar{t}$, but is still very small. It contributes maximal 10% of the total background rate. Tables 10.5 and 10.6 show the accepted cross sections after the selection steps for background and signal samples in ATLFast.

Figure 10.23 shows the invariant mass distributions for six selected $(M_{A^0}, \tan\beta)$ points in the M_{h^0} -max scenario normalized to an integrated luminosity of 30 fb^{-1} . Obviously the signal to background ratio is much worse than in Analysis I. Nevertheless, because of the higher signal selection efficiency, Analysis II also retains a perceivable statistical power.

Cut	$\varepsilon \times \sigma / \text{fb}$						Σ
	$Z^0 + \text{light}$ (SHERPA, $2\ell\text{f}$)	$Z^0 + \text{b}$ (SHERPA, $2\ell\text{f}$)	$t\bar{t}$ (MC@NLO, $2\mu\text{f}$)	$t\text{W}$ (TOPREX, $2\ell\text{f}$)	WW (HERWIG, $1\ell\text{f}$)	$Z^0 Z^0$ (PYTHIA, $2\ell\text{f}$)	
All events	1010225	47070	60300	11790	43840	521	1173750
Preselection	699780 ± 150	31050 ± 30	5400 ± 20	401 ± 4	1750 ± 10	278 ± 2	738679 ± 155
$< 1 \text{ b jet}$	688700 ± 150	22650 ± 30	1054 ± 7	158 ± 2	1710 ± 10	220 ± 2	714492 ± 153
$\cancel{E}_T < 50 \text{ GeV}$	680200 ± 150	22130 ± 30	340 ± 4	62 ± 2	1015 ± 10	215 ± 2	703962 ± 153
$\Delta M(110 \text{ GeV})$	9800 ± 20	272 ± 3	25 ± 1	4.6 ± 0.4	67 ± 3	3.4 ± 0.3	10172 ± 20
$\Delta M(130 \text{ GeV})$	3100 ± 10	69 ± 2	24 ± 1	3.8 ± 0.4	68 ± 3	1.1 ± 0.2	3266 ± 11
$\Delta M(150 \text{ GeV})$	1607 ± 7	34 ± 1	24 ± 1	4.4 ± 0.4	55 ± 2	0.9 ± 0.1	1725 ± 8
$\Delta M(200 \text{ GeV})$	571 ± 4	7.7 ± 0.5	16 ± 1	2.8 ± 0.3	38 ± 2	0.3 ± 0.1	636 ± 5
$\Delta M(300 \text{ GeV})$	174 ± 2	1.5 ± 0.2	5.0 ± 0.5	1.0 ± 0.2	16 ± 1	0.2 ± 0.1	198 ± 3
$\Delta M(400 \text{ GeV})$	71 ± 2	0.8 ± 0.2	2.6 ± 0.3	0.5 ± 0.1	5.2 ± 0.7	0.02 ± 0.02	80 ± 2

Table 10.5: Accepted background cross sections after each selection step and after the mass window cuts (Analysis II) for ATLFAST background samples. The cross section before all cuts already includes the event filter efficiencies. All numbers in fb. Uncertainties are statistical only.

Cut	$\varepsilon \times \sigma/\text{fb}$ $b\bar{b}A^0, A^0 \rightarrow \mu\mu$					
	110-30	130-30	150-30	200-30	300-30	400-30
All events	242.9	148.0	95.45	37.4	8.0	2.18
Preselection	145 ± 2	92.3 ± 1.2	61.8 ± 1.1	24.5 ± 0.4	5.45 ± 0.09	1.49 ± 0.03
$< 1 \text{ b jet}$	117 ± 1	73.4 ± 1.0	48.2 ± 1.0	18.0 ± 0.4	3.82 ± 0.08	0.99 ± 0.02
$\cancel{E}_T < 50 \text{ GeV}$	114 ± 1	71.6 ± 1.0	46.8 ± 0.9	17.4 ± 0.4	3.51 ± 0.07	0.83 ± 0.02
ΔM	94 ± 1	60.7 ± 0.9	39.7 ± 0.9	14.7 ± 0.3	2.97 ± 0.07	0.70 ± 0.02
Efficiency/%	38.7 ± 0.4	41.0 ± 0.5	41.5 ± 0.7	39.3 ± 0.7	37.1 ± 0.7	32.1 ± 0.7

Cut	$gg \rightarrow A^0, A^0 \rightarrow \mu\mu$					
	110-30	130-30	150-30	200-30	300-30	400-30
All events	85.6	38.7	19.2	4.36	0.39	0.089
Preselection	47 ± 1	23 ± 1	11.8 ± 0.3	2.7 ± 0.1	0.24 ± 0.01	0.055 ± 0.001
$< 1 \text{ b jet}$	46 ± 1	22.1 ± 0.5	11.6 ± 0.3	2.64 ± 0.06	0.239 ± 0.005	0.053 ± 0.001
$\cancel{E}_T < 50 \text{ GeV}$	45 ± 1	21.5 ± 0.5	11.3 ± 0.3	2.54 ± 0.06	0.220 ± 0.005	0.043 ± 0.001
ΔM	38 ± 1	18.5 ± 0.5	9.85 ± 0.24	2.25 ± 0.05	0.197 ± 0.005	0.038 ± 0.001
Efficiency/%	44.4 ± 0.7	47.8 ± 0.8	51.3 ± 0.8	51.6 ± 0.8	50.5 ± 0.8	42.7 ± 0.7

Table 10.6: Accepted cross sections after each analysis step (Analysis II) and in the mass window for ATLFAS signal samples. No event filters were applied for these samples. All numbers in fb.

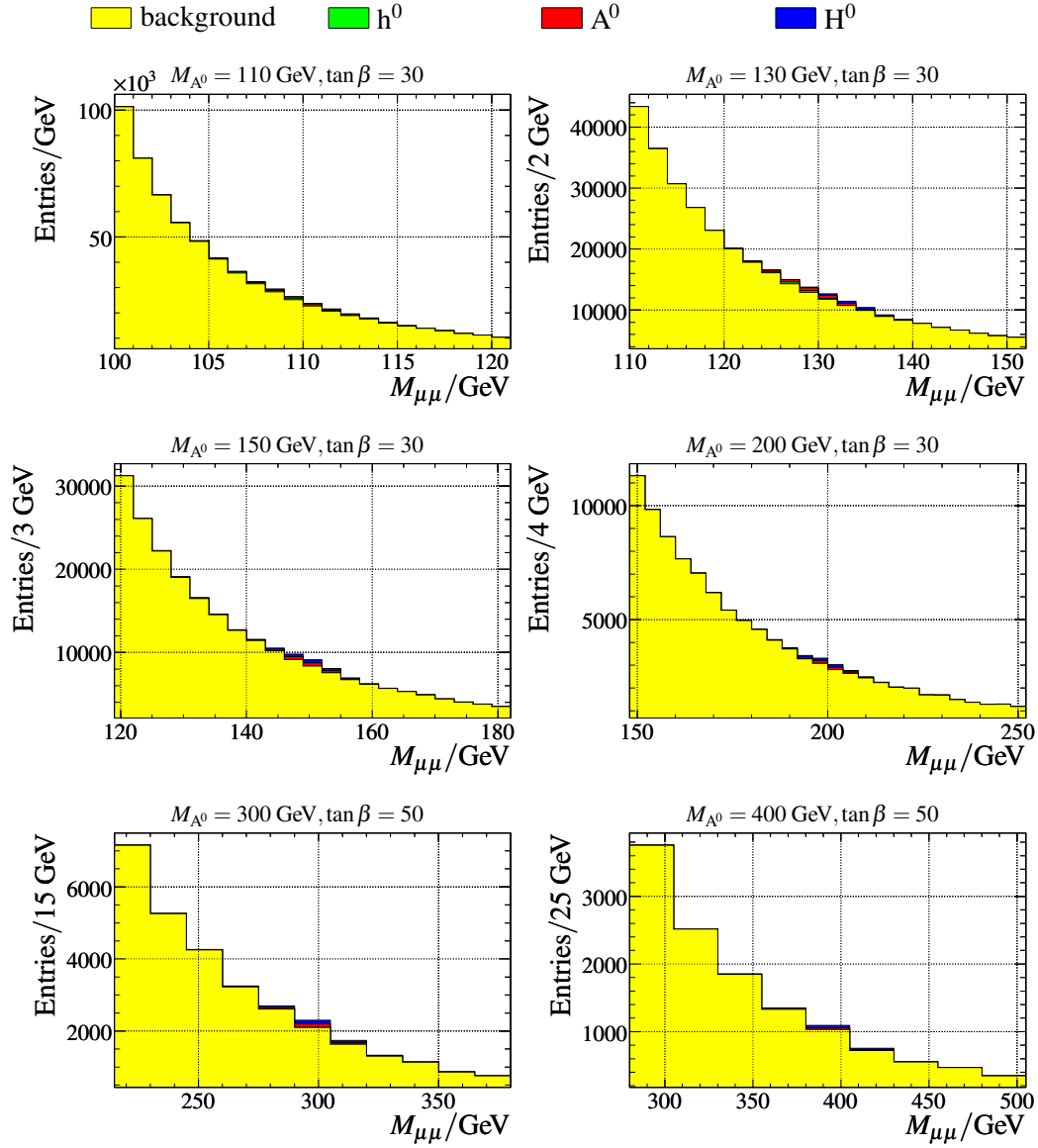


Figure 10.23: Invariant mass distributions for six selected $(M_{A^0}, \tan \beta)$ points in Analysis I for an integrated luminosity of 30 fb^{-1} . Trigger efficiency is included (see Section 10.5).

10.5 Trigger Requirements

The event selections presented in the previous sections are based solely on the performance of offline objects. However, in order for events to be analyzed at all by the ATLAS offline software, they first have to be recorded and stored on permanent storage. This is done by the ATLAS trigger and data acquisition system, as described in Chapter 5. Due to the high interaction rate, a lot of events have to be discarded here. The total interaction rate at an

instantaneous luminosity of $10^{33} \text{ cm}^{-2} \text{ s}^{-1}$ is about 100 MHz, with a bunch crossing rate of 40 MHz. The Level 1 (L1) trigger has to reduce this rate to about 45 kHz, the Level 2 (L2) trigger to 1 kHz, and the Event Filter (EF) to 200 Hz, which is the event rate to permanent storage.

In the following the effect of the trigger on the final event selection is discussed. This is only possible in FULLSIM, in which also a detailed simulation of the trigger sequence is included.

Instead of evaluating the trigger efficiency for all signal and background events without any kind of selection, it is for this study sufficient to regard only the probability to trigger an event if a certain kind of selection is already applied, since only this will be of interest for analysis purposes. Events that cannot be selected by the offline event selection, but can be triggered anyway are not of interest for the evaluation of the trigger.

Since the event selection first employs the signature of two high p_T muons in the final state, the most reliable trigger item is a single high p_T muon with $p_T > 20 \text{ GeV}$ (`mu20`). At the L1 trigger stage, it consists of requiring coincidences in muon trigger chambers corresponding to certain p_T ranges. Further, the L1 trigger defines the regions of interest (RoI) for the next trigger stages. The L2 trigger starts from the RoI's, extracts the related detector information from these regions, and uses measurements from the muon precision chambers to perform a fast track reconstruction. In addition the reconstructed tracks are associated with tracks from the inner detector. At the EF level, the track reconstruction is performed in a more sophisticated way to yield a better p_T measurement and further reject fake muons. More information about the capabilities of the ATLAS muon trigger system can be found in [65, 154].

It is expected that this trigger will remain viable, i.e. unprescaled² up to luminosities of $10^{32} \text{ cm}^{-2} \text{ s}^{-1}$. At higher luminosities, the input rates into and the output rate out of the EF may become too large and it will require prescaling or a significantly higher trigger threshold. The output rate of the EF is expected to be about 200 Hz for a luminosity of $10^{33} \text{ cm}^{-2} \text{ s}^{-1}$ [154]. This may be circumvented by requiring a muon isolation requirement already at the L2 and EF level. However, the corresponding trigger (`mu20i`) was not yet available in the ATLAS software release used for the simulation and reconstruction of the used FULLSIM samples. The effect of the isolation requirement on the trigger efficiency is not evaluated and assumed to be small, as the preselection cuts already require muon isolation.

Figure 10.24 shows the fraction of muons in the $Z^0 + \text{light}$ sample fulfilling the muon selection criteria used in the analysis with $p_T > 20 \text{ GeV}$ that also have a L1 RoI reconstructed in dependence of p_T , $|\eta|$ and ϕ . The average reconstruction efficiency at L1 is about 87%. It is mainly limited by the geometrical acceptance: Beyond $|\eta| = 2.4$ no trigger chambers are present. The same is true in the feet region of the muon spectrometer, which lead to inefficiencies for $|\eta| < 1.2$ and $\phi \approx -3/8\pi$ and $-5/8\pi$. Some of these inefficiencies are expected to be recovered when additional trigger chambers are installed, that are not part of the detector layout used for the event simulation. The L1 muon efficiency is expected to rise by about 3% from the increased acceptance.

²A prescale factor is a rejection factor that enables a trigger item in only a fraction of bunch crossings.

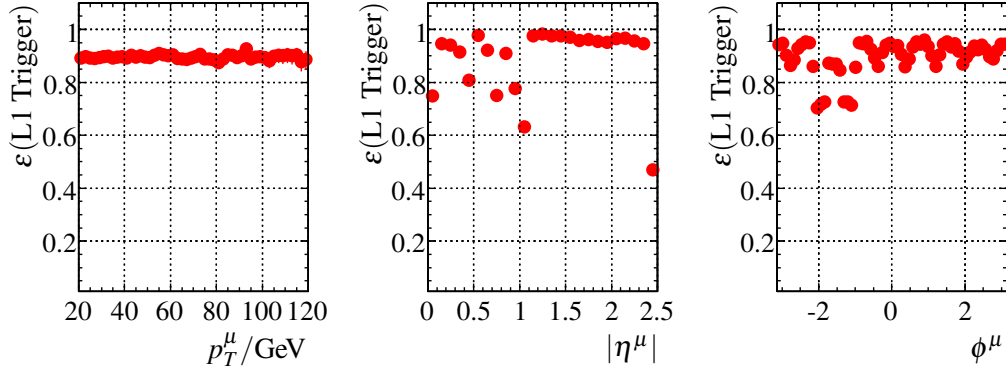


Figure 10.24: L1 single-muon trigger efficiency (threshold: $p_T = 20$ GeV) in the Z^0 + light sample in dependence of p_T , $|\eta|$, and ϕ wrt. offline muons with the isolation requirement used in this work.

sample	after					
	Preselection L1	L2	EF	L1	all selection cuts L2	EF
$t\bar{t}$	98.1 ± 0.1	96.6 ± 0.1	95.8 ± 0.1	98.4 ± 0.4	96.5 ± 0.6	96.1 ± 0.7
Z^0 + light	98.0 ± 0.1	96.5 ± 0.1	95.8 ± 0.1	98.8 ± 0.6	96.8 ± 0.9	95.8 ± 1.0
Z^0 + b	97.9 ± 0.1	96.4 ± 0.1	95.7 ± 0.1	97.9 ± 0.1	96.6 ± 0.2	96.0 ± 0.2
$b\bar{b}A^0$ (SHERPA)						
$M_{A^0} =$						
110 GeV	97.9 ± 0.3	96.7 ± 0.4	95.9 ± 0.4	97.5 ± 0.9	96.9 ± 1.0	96.9 ± 1.0
130 GeV	98.2 ± 0.2	97.2 ± 0.3	96.5 ± 0.3	98.0 ± 0.7	96.8 ± 0.8	96.4 ± 0.9
150 GeV	97.5 ± 0.3	96.0 ± 0.3	95.2 ± 0.4	97.8 ± 0.6	96.3 ± 0.8	95.5 ± 0.9
200 GeV	98.1 ± 0.2	97.1 ± 0.3	96.3 ± 0.3	97.3 ± 0.7	96.3 ± 0.8	95.9 ± 0.8
300 GeV	97.9 ± 0.3	96.7 ± 0.4	95.7 ± 0.4	97.6 ± 0.8	96.4 ± 1.0	95.5 ± 1.1
400 GeV	97.9 ± 0.3	96.7 ± 0.3	96.1 ± 0.4	97.6 ± 0.8	95.9 ± 1.0	95.7 ± 1.1

Table 10.7: Cumulative event trigger efficiencies (in %) with respect to the preselection and the full selection criteria (b tagged analysis) after L1, L2, and the EF.

As the selection criteria require two muons with a transverse momentum of at least 20 GeV, it can be expected that the L1 trigger efficiency for such events is around $1 - 0.13^2 \approx 0.98$. The trigger efficiencies have been evaluated for different signal and background samples, both after the L1, L2, and the final EF stage. They are shown in Table 10.7 after the preselection cuts and after the cuts of the full selection of Analysis I (b tag). The final trigger efficiency is about 96% and is independent of the event sample and whether only the preselection cuts or other cuts are applied. This is because the additional cuts do

not significantly influence the muon kinematics. The same is found for the cuts of Analysis II (b veto). As the trigger efficiency with respect to the offline selection criteria is the same for signal and background contributions, it is taken into account as a simple multiplicative factor for the final event yield, also in the ATLFast samples. The trigger efficiency of 96% corresponds to a reduction of the discovery significance of about 2%, which is almost negligible.

Figure 10.25 shows the efficiency in dependence of the invariant mass for the three major background contributions and after the different selection criteria. Within the statistics the efficiency does not depend on the invariant dimuon mass, and thus introduces no bias in the shape of the invariant mass spectrum of the background.

This discussion of the trigger efficiency assumes, as mentioned, the assumption that the $\mu 20i$ trigger performs comparably to the $\mu 20$ trigger in terms of efficiency with respect to the selection criteria, while at the same time providing enough rejection power to be run unrescaled even at luminosities of $10^{33} \text{ cm}^{-2} \text{ s}^{-1}$. If this is not the case, the threshold of the single muon trigger has to be raised. This can be expected to be rather unproblematic for high Higgs boson masses, but low mass Higgs bosons might be affected significantly.

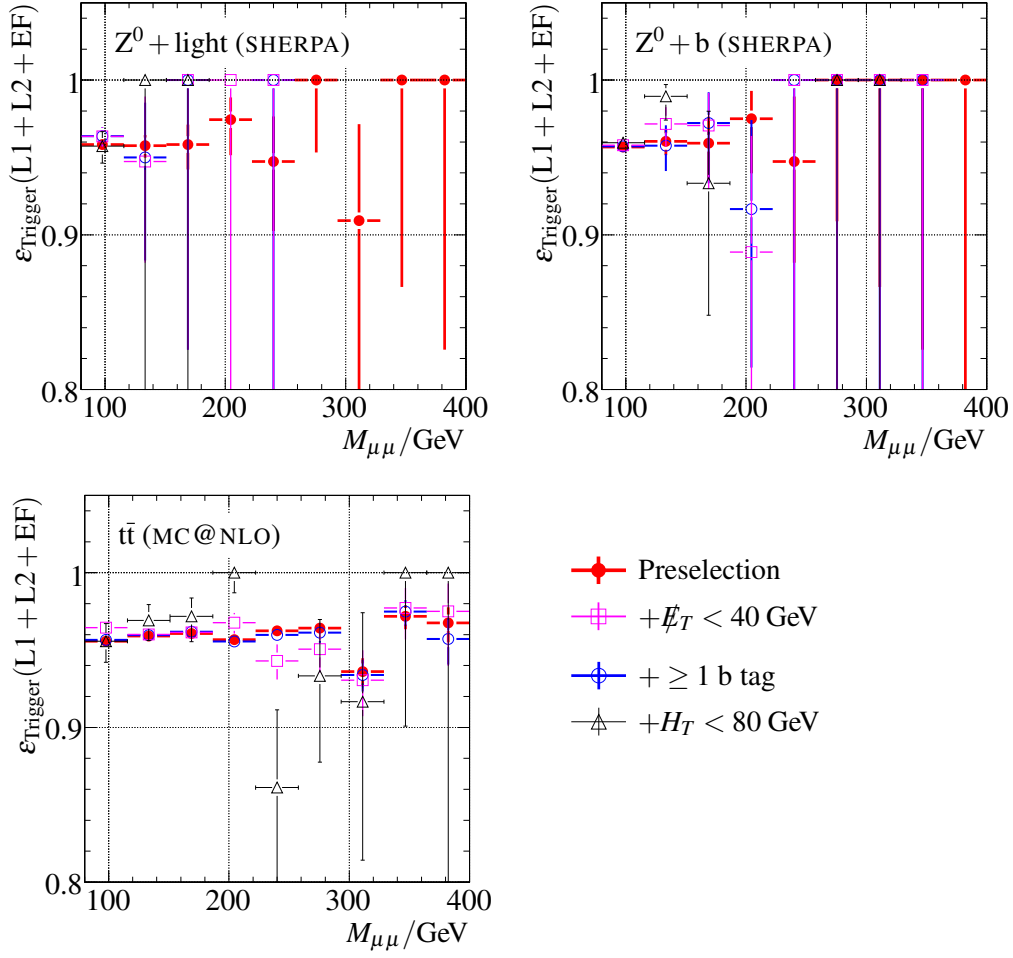


Figure 10.25: Trigger efficiencies for the three major background samples in dependence of the invariant dimuon mass after the different selection criteria.

“For my part I know nothing with any certainty, but the sight of the stars makes me dream.”

Vincent van Gogh, 1853–1890

11

Systematic Uncertainties

The two selections presented in the previous chapters have been performed using the current ATLAS software, with all the corrections derived in Chapter 9 applied to the ATLFast samples. Nevertheless, in the real experiment, the reconstruction performance of the ATLAS detector will only be measured with a limited statistical and systematical accuracy. This has to be reflected in detector and simulation related systematic uncertainties on the event yields predicted by the Monte Carlo simulations. Also the prediction of the Monte Carlo generators and the theoretical predictions of production cross sections have a limited accuracy.

The estimation of the systematic uncertainties especially on the background yields has a very direct consequence on the search strategy of for the neutral MSSM Higgs bosons: If the systematic uncertainties on the background yield would be much smaller than the expected statistical fluctuations of the background, it would be possible to very accurately predict the number of background events from the Monte Carlo simulation, subtract this number from the number of observed events and get instantly a discovery significance. If the background uncertainties are not small, they would have to be taken into account when subtracting the background using Monte Carlo and would largely diminish the sensitivity. In this case, a completely data-driven approach might be helpful to reduce the uncertainties.

In the following, the systematic uncertainties are discussed and their influence on the expected event yields calculated and presented.

11.1 Normalization Uncertainties

The first class of systematical uncertainties influences the total normalization of the event samples. Among these are theoretical uncertainties as well as the experimental uncertainty of the luminosity determination.

11.1.1 Luminosity Uncertainty

The expected accuracy of the luminosity measurement has a direct impact on the event yield. The determination of the integrated luminosity at a hadron collider is very complicated. In contrast to an e^+e^- collider like LEP, no precisely calculable reference process like Bhabha scattering ($e^+e^- \rightarrow e^+e^-$) exists. The only reference available is the total inelastic pp cross section, which has never been measured at a center-of-mass energy of 14 TeV and is only known with a very low accuracy by extrapolation from lower energies.

At the start-up of ATLAS only a very rough measurement of the relative luminosity from machine parameters (bunch currents, beam profile,...) and the LUCID detector will be available. Using special runs of the LHC machine in 2009 and later, the ultimate systematic uncertainty can be reduced to 5%. The ALFA detector is expected to provide a measurement of the luminosity by measuring elastic scattering in the Coulomb-Nuclear interference region. This will be done using special runs of the LHC with a special beam optics setup (see Sec. 5.6.3). The accuracy of this measurement is expected to be about 3%. A similar accuracy could be reached using the optical theorem if an external measurement of the total cross section is available. This might be provided by the TOTEM [63] experiment.

In the following, as the analysis results and the discovery potential are discussed for an integrated luminosity of 30 fb^{-1} , a systematic uncertainty of 3% on the integrated luminosity is assumed. This uncertainty is 100% correlated between all event samples.

11.1.2 Theory Uncertainties

Another normalization uncertainty comes from the fact that the cross sections used in this thesis are known only to a certain accuracy. Parts of these uncertainties will be reduced in the future once LHC runs and the cross sections are measured. However, until this is the case, estimates of the theory uncertainty obtained by scale and pdf variations, as discussed in Chapters 7 and 8 have to be used as a systematic uncertainty. These are summarized in Table 11.1 for the background processes and signal processes at selected masses. As described in Section 7.1.7, the cross sections for b-associated production in the analysis requiring zero b tagged jets are assigned an additional 15% uncertainty due to the uncertainty of the normalization procedure.

Although in principle some of the scale choices used in calculating the cross sections might be correlated between some of the used predictions, this uncertainty is assumed to be uncorrelated between the samples.

11.1.3 Monte Carlo Statistical Uncertainty

The used Monte Carlo samples have a limited size. For this analysis they correspond to about 30 fb^{-1} for all background processes. Due to this limited Monte Carlo statistics, the event yields can only be predicted with a limited precision, which has to be accounted for. In principle this contribution can be lowered by generating more Monte Carlo events, but

	$Z^0 + \text{light}$	$Z^0 + b$	$t\bar{t}$	tW	WW	$Z^0 Z^0$	
$(\Delta\sigma/\sigma)/\%$	$^{+6}_{-8}$	$^{+11}_{-13}$	± 12	± 3	± 20	± 20	
$b\bar{b}A^0, M_{A^0} = \dots \text{ GeV, Analysis I (b tag)}$							
	110	130	150	200	300	400	$gg \rightarrow A^0$
$(\Delta\sigma/\sigma)/\%$	$^{+21}_{-25}$	$^{+18}_{-22}$	$^{+16}_{-20}$	$^{+14}_{-17}$	$^{+12}_{-13}$	$^{+11}_{-12}$	± 15
$b\bar{b}A^0, M_{A^0} = \dots \text{ GeV, Analysis II (b tag veto)}$							
	110	130	150	200	300	400	$gg \rightarrow A^0$
$(\Delta\sigma/\sigma)/\%$	$^{+26}_{-29}$	$^{+23}_{-27}$	$^{+22}_{-25}$	$^{+21}_{-23}$	$^{+19}_{-20}$	$^{+19}_{-19}$	± 15

Table 11.1: Theoretical uncertainties on production cross sections for background processes and signal processes at selected masses.

Analysis I (b tag)						
MC statistical uncertainty in mass window for $M =$						
Sample	110 GeV	130 GeV	150 GeV	200 GeV	300 GeV	400 GeV
$Z^0 + \text{light}$	± 2	± 4	± 5	± 8	± 17	± 38
$Z^0 + b$	± 2	± 5	± 7	± 13	± 38	± 71
$t\bar{t}$	± 8	± 9	± 8	± 9	± 15	± 27
$b\bar{b}A^0$	± 3	± 4	± 5	± 5	± 5	± 6
Analysis II (b tag veto)						
MC statistical uncertainty in mass window for $M =$						
Sample	110 GeV	130 GeV	150 GeV	200 GeV	300 GeV	400 GeV
$Z^0 + \text{light}$	± 0.2	± 0.3	± 0.5	± 0.8	± 1.4	± 2.2
$Z^0 + b$	± 1.1	± 2.2	± 3.1	± 6.5	± 15	± 20
$t\bar{t}$	± 4	± 4	± 4	± 5	± 10	± 13
$b\bar{b}A^0$	± 1	± 2	± 2	± 2	± 2	± 3
$gg \rightarrow A^0$	± 3	± 3	± 2	± 2	± 2	± 2

Table 11.2: Monte Carlo relative statistical uncertainties (in %) inside the mass windows after event selection for the two analyses. Only the major background processes are shown.

in practice the data statistics will never be matched by the Monte Carlo statistics. Due

to the large resource requirements of the detector simulation, and due to limited storage space, it is planned to simulate only about 25% of the data statistics [92].

The MC statistical uncertainty can be estimated by using the square root of the quadratic weight sum as an estimate, thus assuming poissonian statistics. Table 11.2 lists these uncertainties for the main backgrounds and exemplary signal samples in the mass windows as used in Chapter 10. Although the background samples correspond to an integrated luminosity of about 30 fb^{-1} , the statistical uncertainty of the MC estimate becomes sizable, especially for high masses in the b tagged analysis. In the analysis vetoing a tagged b jet, the MC statistical uncertainty becomes much smaller due to the larger event selection efficiencies.

Due to the random nature of the MC statistical uncertainties, these are uncorrelated between all samples.

11.2 Uncertainties of the Event Selection

Another source of uncertainties are the detector properties and how well the response and reconstruction can be determined from data. The level of understanding of the ATLAS detector properties is a function of the integrated luminosity itself, since in general reconstruction efficiencies and resolutions will be determined in data. Within the recently concluded computing system commissioning (CSC) effort [135], the ATLAS combined performance working groups have provided estimates of the level of understanding of the different reconstructed objects for a given luminosity. These estimates are used in the following assuming an integrated luminosity of 10 fb^{-1} . For lower integrated luminosities these estimates can be assumed to be too optimistic. For larger integrated luminosities it is well possible that a better performance can be achieved in the real experiment.

In the following the detector and simulation related systematic uncertainties and their impact on the event selection efficiencies are discussed. The uncertainties are in part implemented as scaling or smearing factors to reconstructed objects in the Monte Carlo samples. When comparing the efficiencies with and without such a variation applied, it has to be kept in mind that the event selection efficiencies are correlated. Appendix C shows a calculation of the error on the relative change of event selection efficiencies in such a case. Wherever possible, instead of applying a change to objects that can have a random influence, instead analytical expressions are preferred to avoid incurring additional statistical components that are correlated to the Monte Carlo statistical uncertainty.

Only the three major backgrounds, $Z^0 + \text{light}$, $Z^0 + b$, and $t\bar{t}$, as well as the signal processes are discussed. The uncertainties on the less important backgrounds (tW , WW , Z^0Z^0) can be expected to be of the same order, but due to the limited Monte Carlo statistics it is even more difficult to make adequate comparisons.

11.2.1 Muons

The muon reconstruction efficiency is expected to be known to within 1%. In the data this can be measured using the “tag and probe” method, in which the decay $Z^0 \rightarrow \mu^+ \mu^-$ is

reconstructed by requiring only one muon and a track in the inner detector. In this way the track can be ensured to originate from a muon and the muon reconstruction efficiency can be determined from data.

For ATLFAST, this uncertainty is increased to $\pm 2\%$ as indicated in Section 9.1.5 to account for the different isolation efficiencies between FULLSIM and ATLFAST.

The uncertainty of the muon reconstruction efficiency can be taken into account analytically: Since two muons are required, it enters quadratically, leading to an uncertainty of 4% on the event selection efficiency. Influences e.g. on the \cancel{E}_T reconstruction due to removed muons are neglected, since the selected events will still contain two muons, that most of the times come from the decay of a heavy boson. As the only other source of muons are heavy flavor decays, and the muons from these have a small transverse momentum, the influence if these are not reconstructed is expected to be small.

In addition to the uncertainty common to all candidate masses, as discussed in Section 9.1.5, a mass dependent uncertainty due to the difference of the isolation efficiencies between FULLSIM and ATLFAST is taken into account. Approximative values of this uncertainty are listed in Table 11.3.

The muon energy scale is assumed to be known within 1% using $Z^0 \rightarrow \mu^+ \mu^-$ decays. Noting that this corresponds to a shift of the mass of the Z^0 of almost 1 GeV, this is clearly a very conservative estimate given the large Z^0 production cross section. However, the energy scale has to be extrapolated to regions of transverse momenta that are not populated by Z^0 decays. This will be done using Monte Carlo simulation, thus incurring an additional systematic uncertainty.

The 1% is retained as conservative estimate also for large integrated luminosities. It is implemented by scaling the four vector of each reconstructed muon by 1.01 and 0.99. The change of p_T is also propagated to the measurement of \cancel{E}_T . This can have an effect on the cut on the muon p_T and on \cancel{E}_T . In addition, the candidate mass is also shifted by 1%.

The uncertainty on the muon momentum resolution is simulated by applying an additional Gaussian smearing of $1/p_T$ according to:

$$\sigma(1/p_T)/(1/\text{GeV}) = 0.011/(p_T/\text{GeV}) \oplus 0.00017. \quad (11.1)$$

The first term enhances the coulomb smearing term due to multiple scattering and decreases the muon momentum resolution from 2.3% to 2.5%. The second term increases the contributions from the residual misalignment and has only an influence on muons with a p_T in the TeV range, where the effective resolution is doubled.

M/GeV	110	130	150	200	300	400
$(\Delta\epsilon/\epsilon)/\%$	-3.3	-2.8	-2.2	-0.8	+1.7	+4.6

Table 11.3: Mass window dependent uncertainties of the event selection efficiencies due to differences between FULLSIM and ATLFAST in the muon isolation efficiency (see Section 9.1.5).

Using a mass window, this has a small effect on the selection efficiency of the signal, since events might migrate outside the mass window. This can be expected to be less pronounced for the background processes, since the mass spectrum does not show a peak in the mass window, but rather continues smoothly through it.

Figure 11.1 shows the uncertainties on the event selection efficiencies inside the mass windows for the two analyses and signal and background processes. The numerical values can be found in Appendix D.

The most significant influence of the energy scale variation is found in the low mass region for the Z^0 samples. This can be easily understood, as these samples show a very steeply falling mass spectrum. Shifting the mass e.g. in the upwards direction, as it is done when the energy scale is enhanced, will result in more events entering the applied

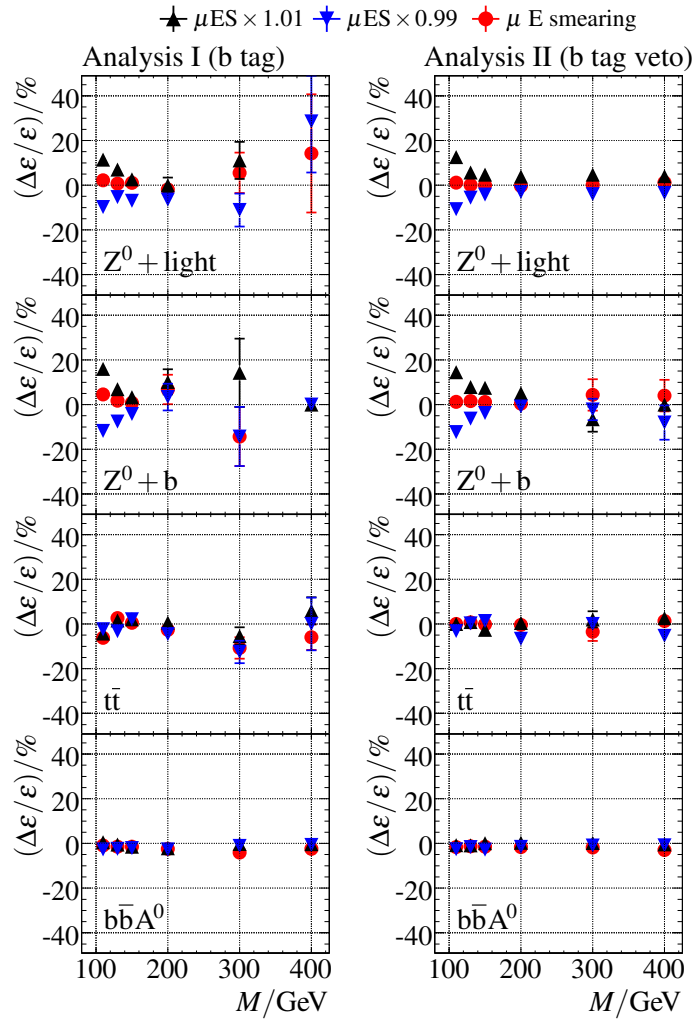


Figure 11.1: Graphical representation of the systematic uncertainties of the muon energy scale (μ ES) and energy resolution (μ E smearing).

mass window than leaving and vice versa. The effect is less pronounced for high masses, as the slope of the spectrum gets smaller. The $t\bar{t}$ and signal samples are only very weakly influenced by the applied variations. This can be understood, as the applied mass windows correspond to about 6 to 10% of the central values. A shift or a smearing of 1% has only a small effect.

11.2.2 Jets

The determination of the jet energy scale will be a major factor for the ATLAS physics program. It will be measured in-situ using a number of processes, e.g. the production of a photon and a jet, where from the known electromagnetic energy scale, the jet energy scale can be inferred by requiring momentum conservation in the transverse plane. Preliminary estimates assume a systematic uncertainty of the jet energy scale of $\pm 7\%$ within $|\eta| < 3.2$ and $\pm 15\%$ for $|\eta| > 3.2$.

The uncertainty on the jet energy resolution is estimated by applying a Gaussian smearing to the jet energies according to:

$$\sigma(E)/\text{GeV} = 0.45 \cdot \sqrt{E/\text{GeV}} \quad (|\eta| < 3.2) \quad (11.2)$$

$$\sigma(E)/\text{GeV} = 0.63 \cdot \sqrt{E/\text{GeV}} \quad (|\eta| > 3.2) \quad (11.3)$$

In both cases the changes are propagated to the \cancel{E}_T measurement. For the jet energy scale, only a 5% contribution is propagated to \cancel{E}_T , as preliminary studies [155] have shown that although the jet energy scale might be uncertain to a larger amount, the influence on the \cancel{E}_T measurement can be estimated more accurately. Since most of the jets in the samples of relevance are central jets, this does not make a large difference.

Figure 11.2 shows the resulting changes in the event selection efficiencies. the jet energy resolution shows only a small effect. The changes to the jet energy scale have a very significant influence especially on the $t\bar{t}$ sample, where it causes a +30%, -20% uncertainty for the b tagged analysis¹ and $\pm 10\%$ in the analysis vetoing tagged jets. Smaller deviations are seen for the Z^0 samples and the signal samples, especially for high masses.

This behavior is actually caused primarily by the cuts on H_T , which is applied in the b tagged analysis, and \cancel{E}_T , which is applied in both analyses, although at different values.

Figure 11.3 shows the distributions of the p_T of the leading tagged jet, \cancel{E}_T , and H_T in the $t\bar{t}$ sample after preselection and requiring at least one tagged jet. Clearly the jet energy scale affects all three of them, especially H_T which is shifted by exactly the jet energy scale uncertainty. As the applied cut ($H_T < 80$ GeV) is placed in the steepest part of the spectrum, this has a huge influence on the $t\bar{t}$ sample. For the Z^0 and signal samples, the cut on H_T is placed more in the tail of the distribution, except for the high masses, and the effect of the jet energy scale shift is less pronounced.

A smaller effect is also seen in the influence on \cancel{E}_T . This is also more pronounced for $t\bar{t}$, since the jets in $t\bar{t}$ have a larger transverse momentum and are more numerous than in the other samples.

¹The seemingly smaller changes for higher masses are not statistically significant.

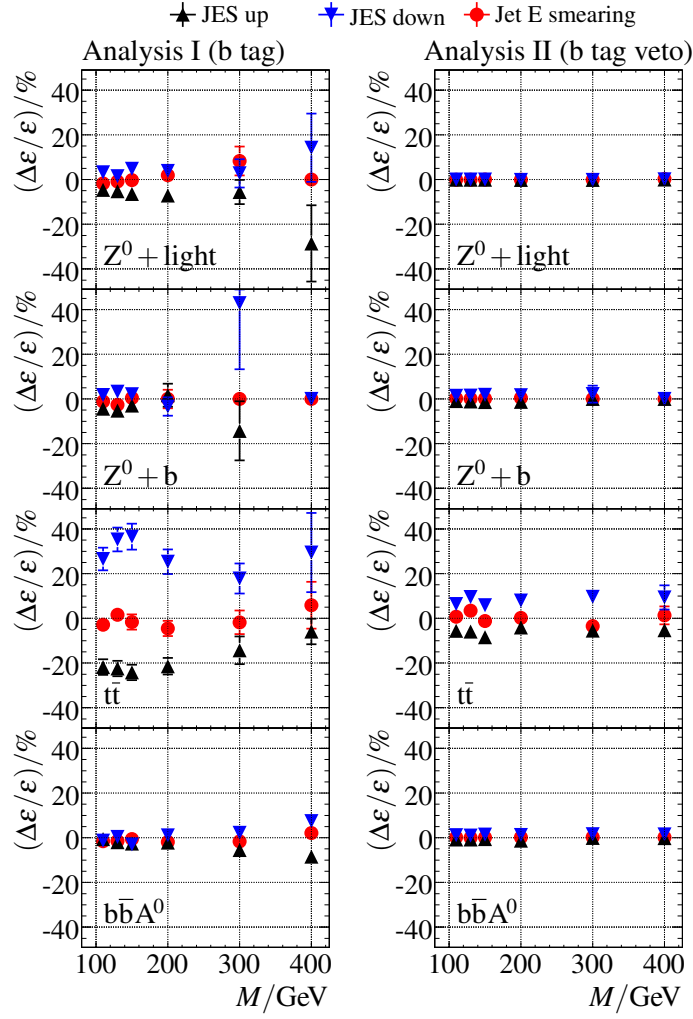


Figure 11.2: Graphical representation of the systematic uncertainties of the jet energy scale (JES) and energy resolution (Jet E smearing).

11.2.3 B Tagging

The estimation of systematic uncertainties for b -tagging is still in its infancy. Preliminary estimates show that the b jet efficiency and c jet efficiency should be controllable to within 5%. This more or less agrees with the differences seen between the different samples used to derive the ATLFASST parameterization. This uncertainty is assumed to be fully correlated between b and c jets, since both types of jets contain true lifetime information and are not dominated by resolution.

As described in Section 9.3.6 the udsg jet rejection is decreased artificially to 70% of the actual value to simulate the influence of the residual misalignment. This is expected to be known to within $\pm 14\%$, equaling 60% and 80% of the nominal rejection rate. In

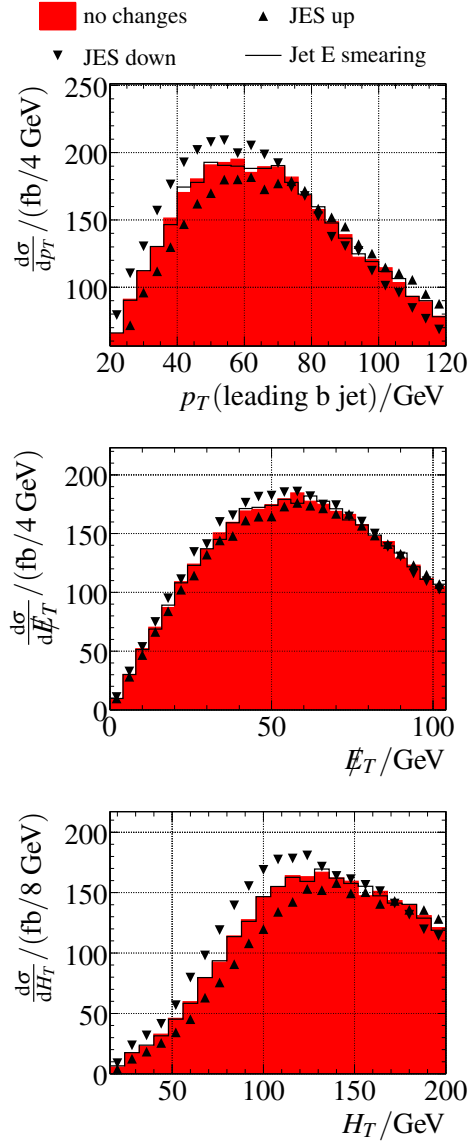


Figure 11.3: Distributions of the p_T of the leading b tagged jet (left), E_T (middle), and H_T (right) in the $t\bar{t}$ sample after preselection and b tag requirement with and without jet reconstruction systematic uncertainties.

order to take into account the differences observed between the two samples to derive the parameterization and possible inaccuracies of the statistical b -tagging in ATLFAST, this uncertainty is inflated to 20%, corresponding to 56% and 84% of the nominal rejection without misalignment effects.

Figure 11.4 shows the resulting uncertainties inside the mass windows of the two analyses.

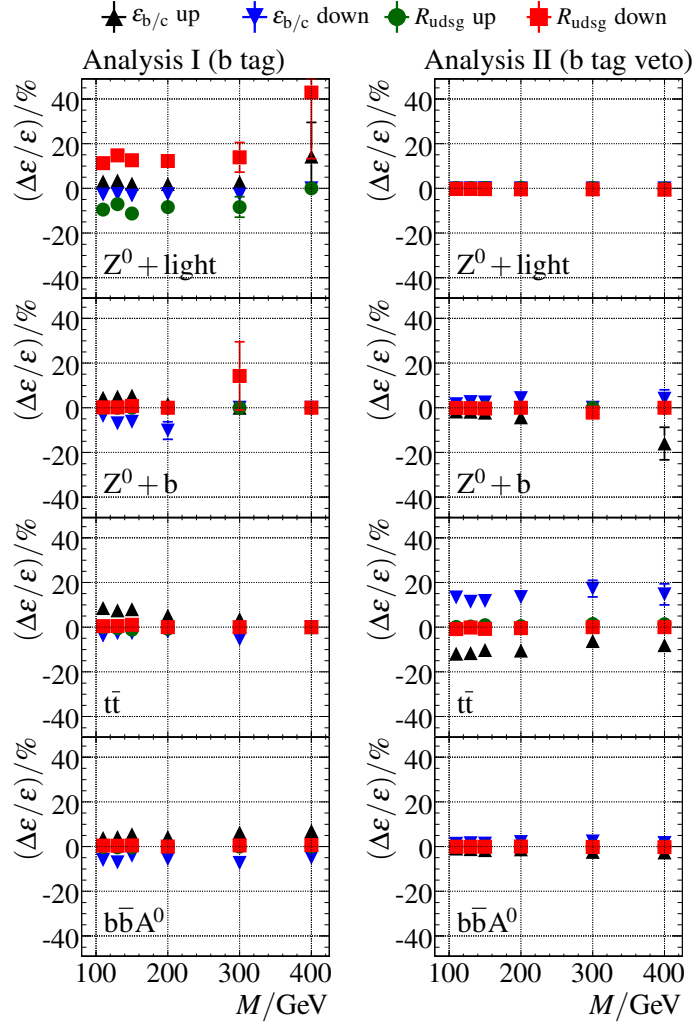


Figure 11.4: Graphical representation of the systematic uncertainties of the b -tagging.

As expected, the $b\bar{b}A^0$ signal samples, the $t\bar{t}$ background and the $Z^0 + b$ background are only affected by the b efficiency. In the case of $t\bar{t}$, this even leads to a large uncertainty in the analysis vetoing a tagged b jet. This is caused by the fact that the efficiency to have at least one tagged b jet in $t\bar{t}$ events is very high, since they contain two high p_T b jets. Thus the rate of the remaining, untagged events depends strongly on the b efficiency.

The $Z^0 + \text{light}$ sample shows dependence both on the b/c efficiency and the u ds g rejection. As seen before, it contains both true c and u ds g jets, so this is not unexpected. The $Z^0 + \text{light}$ background is the dominant background for the analysis with zero b jets. However, since the probability to tag an u ds g or c jet is very low anyway, the influence of the b -tagging systematic uncertainties is very small in this case.

11.2.4 Missing Transverse Energy

As the missing transverse energy is itself composed of all visible objects (and taking the negative), it is assumed that the described rescaling and smearing of the other objects is sufficient to describe the systematic uncertainties on \cancel{E}_T . The soft component of \cancel{E}_T , that does not belong to reconstructed high p_T objects, but to unclustered energy, is not smeared in addition.

For the ATLFast simulation, the uncertainty on the scaling factor s as described in Section 9.4 needs to be taken into account. This is also some measure on the yet unknown total inelastic pp cross section at LHC energies, which is directly correlated to the average number of pile-up events.

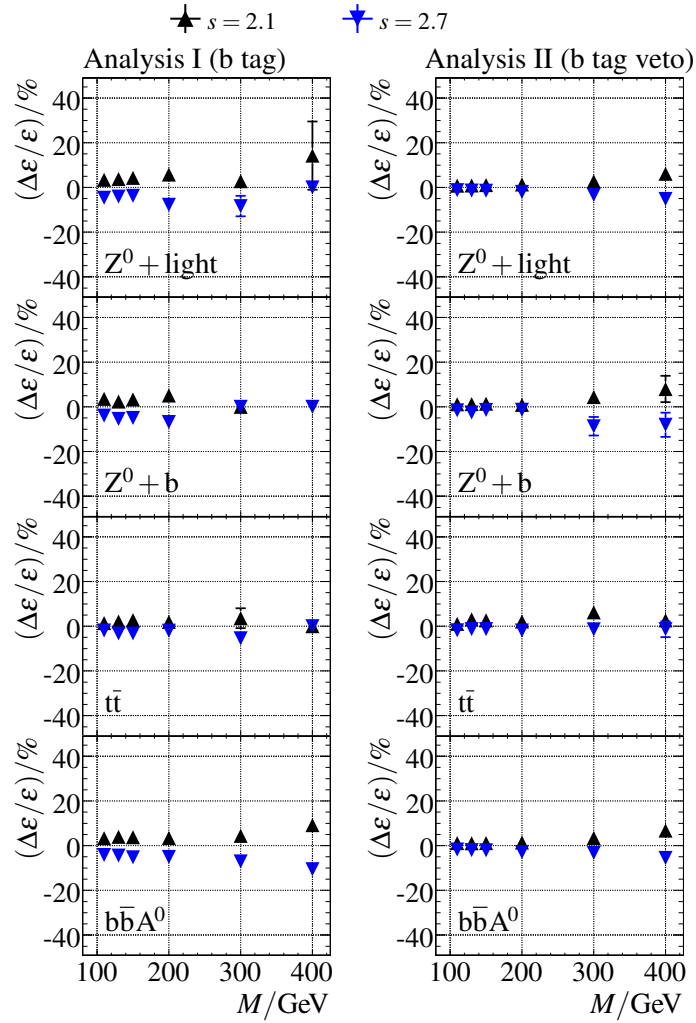


Figure 11.5: Graphical representation of the systematic uncertainties of the \cancel{E}_T rescaling description in ATLFast including pile-up effects ($s = 2.4 \pm 0.3$).

Figure 11.5 shows the resulting uncertainties. Compared to other uncertainties, it has only a small influence. For large masses, uncertainties of 10% on the signal selection efficiencies can be seen. This is due to the worse \cancel{E}_T resolution at high masses, which is by itself caused by harder jets, as discussed in Section 10.3.2.

11.2.5 Electrons, Photons, and Hadronic Taus

Although electrons, photons and hadronically decaying tau leptons are not used directly within this analysis, they might have a small indirect influence due to their contribution to \cancel{E}_T . The expected uncertainties of energy scales, resolutions and reconstruction efficiencies are shortly discussed in the following.

The electron and photon reconstruction efficiencies are expected to be known to a level of 0.2%.

The energy scale of electrons and photons is expected to be known with an accuracy of 0.5%. This will be mainly determined by reconstructing the decay $Z^0 \rightarrow e^+e^-$ and using the very precisely known mass of the Z^0 to calibrate the electromagnetic energy scale.

The uncertainty on the electromagnetic energy resolution can be approximated by a gaussian energy smearing of electrons and photons according to $\sigma(E_T) = 0.0073 \cdot E_T$. In this way the constant term of the calorimetric energy measurement is enhanced.

For the software release used in this analysis, no systematic uncertainties for tau lepton reconstruction are available. As an estimate, an uncertainty on the energy scale of $\pm 5\%$ and on the energy resolution according to $\sigma(E)/\text{GeV} = 0.45 \cdot \sqrt{E/\text{GeV}}$ is used.

All these systematic variations have been investigated and found to be completely negligible, as expected.

11.3 Summary on Systematic Uncertainties

As shown, the systematic uncertainties on the prediction of the signal and background rate, both experimental and theoretical, are of the order of a few 10%. This means that they are not negligible, especially in Analysis II (b tag veto), where the background statistics will be very high, and thus the background relative statistical uncertainty rather low.

Predicting the background solely from Monte Carlo would thus diminish the discovery potential quite significantly. In addition to this, since no one has yet measured proton-proton collisions at $\sqrt{s} = 14$ TeV, other unexpected effects might occur in real data.

Instead it is necessary to try and extract the background directly from the data itself. In the muonic decay mode of the Higgs boson, this is actually made easier by the very good mass resolution. This is discussed in the next chapter.

“If you are distressed by anything external, the pain is not due to the thing itself but to your own estimate of it; and this you have the power to revoke at any moment.”

Marcus Aurelius, 121–180

12

Background Estimation from Data

As described in Chapter 11, the systematic uncertainties on the event yields predicted by Monte Carlo simulations are rather large and of the order of a few dozen percent. In order to claim a discovery of the neutral Higgs bosons of the MSSM in the muonic decay mode, the background contribution needs to be predicted with a much larger precision.

The statistical fluctuations of the background itself are proportional to the square root of the number of background events, and thus the relative statistical uncertainty becomes smaller with increasing luminosity. However, the relative systematic uncertainties, if unconstrained by data, are constant and will thus limit the sensitivity for a discovery of a Higgs boson already for low to moderate integrated luminosities.

An alternative to estimating the background contribution from Monte Carlo simulation is to estimate it from the data itself. Although no ATLAS data is available yet, within this chapter a method to estimate the background from the data is discussed. The Monte Carlo simulation is used just as if it was real data. An integrated luminosity of 30 fb^{-1} , corresponding to three years of LHC operation at a luminosity of $10^{33} \text{ cm}^{-2} \text{ s}^{-1}$, is assumed and also reflected in the size of the used Monte Carlo samples to obtain similar statistical fluctuations.

The merit of a data based procedure to estimate the background is that it is only barely influenced by the systematic uncertainties presented in Chapter 11. This is immediately obvious for the theoretical uncertainties of the event selection. But also the detector related systematic uncertainties do play a smaller role in this case, as it can be assumed that these affect the data used to estimate the background in the same way as the region of interest.

In the following, first some basic principles of background estimation from data are discussed. Then a sideband fit based method is presented in more detail and validated.

12.1 Basic Methods

For any data based background estimation technique a way has to be found to obtain an event sample that can be normalized to the expected background and which does not contain significant signal contributions.

Two basic methods can be envisaged to obtain a sample like this: Either one uses a different final state, which is not populated by the signal, or one uses the same final state but uses a different set of cuts designed to select background, but not signal.

12.1.1 Different Final States

For the study of Higgs bosons decaying into muons, two different approaches to obtain the background from data in different final states have been proposed. The first is to use identified $Z^0 \rightarrow e^+e^-$ events, using the same analysis cuts as for the signal, except replacing the requirements for muons with those for electrons. It was first proposed in [108]. As the coupling of the Higgs bosons to the almost massless electron is strongly suppressed compared to the muon ($\approx 1/40000$), the resulting event sample can be considered background free. The only differences between the $\mu^+\mu^-$ and the e^+e^- final state might then be due to different reconstruction efficiencies for electrons and muons and different mass resolutions, which would have an effect on the invariant mass distribution of the background. In addition, electrons emit a larger amount of inner bremsstrahlung, and a method to recombine the emitted photons with the electron candidates needs to be implemented. Using this method the shape of the invariant mass spectrum can be predicted to within 10% [108].

Another method aiming at estimating the $t\bar{t}$ contribution is proposed in [135]. In this alternative way, the $e\mu$ final state is used. As neither the Z^0 , nor the Higgs bosons can decay into this final state, only the $t\bar{t}$ (and tW) backgrounds can be estimated in this way¹. Also in this case an accuracy of the order of 10% is expected.

Common to both methods is that in order to work, the mass resolution has to be close to each other in the $\mu^+\mu^-$ sample and in the control sample. Both types of control samples contain electron final states. However, no high statistics FULLSIM samples for $Z^0 \rightarrow e^+e^-$ and $t\bar{t}$ are available and the electron reconstruction properties have not been compared between FULLSIM and ATLFAST for this study. For example, in the standard ATLAS reconstruction, electrons in the transition region between the barrel and end-cap regions of the calorimeters are discarded due to the extra material in this region. This is not matched at all in ATLFAST, where the electron reconstruction efficiency is 100% over the whole acceptance region. In addition, in ATLFAST a detailed study of the recovery of hard bremsstrahlung photons is not possible, at least not in a way that it would resemble the FULLSIM simulation.

12.1.2 Same Final State

Another possibility to measure the background from data would be to retain the same final state ($\mu^+\mu^-$), but to either change some cuts to obtain background enriched samples, or to obtain the background by a fit to the mass sidebands.

Obtaining control samples by reversing some cuts is only feasible in the analysis where a b tag is required. In the non b tagged analysis (Analysis II), the dominant background,

¹In principle also the $Z^0 \rightarrow \tau\tau \rightarrow e\mu + 4\nu$ final state remains, but this contributes only for very low masses and can be neglected.

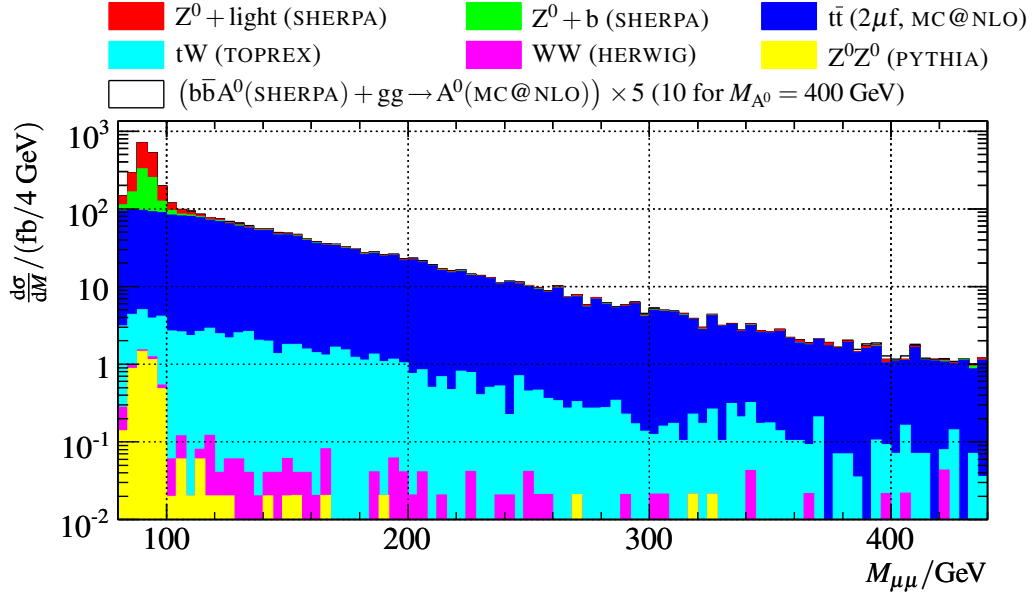


Figure 12.1: Stacked dimuon invariant mass distribution after selection cuts (b tagged analysis) with reversed cuts on \cancel{E}_T and H_T . Open Histograms: Six different A^0 boson signals for $\tan\beta = 30$, $b\bar{b}A^0$ and $gg \rightarrow A^0$ added, scaled by a factor of 5 (10 for $M_{A^0} = 400$ GeV). Backgrounds from top to bottom: $Z^0 + \text{light}$ (red), $Z^0 + b$ (green), $t\bar{t}$ (dark blue), tW (light blue), WW (magenta), and $Z^0Z^0 \rightarrow \mu\mu q\bar{q}$ (yellow).

$Z^0 + \text{light}$, is not reduced significantly by the applied cut on \cancel{E}_T . Reversing this cut would not enrich the $Z^0 + \text{light}$ background.

On the other hand, in the analysis requiring at least one b tag (Analysis I), the cuts aimed against $t\bar{t}$ background (\cancel{E}_T , H_T) can be reversed. Figure 12.1 shows the invariant mass distribution after requiring $\cancel{E}_T > 40$ GeV and $H_T > 80$ GeV. Obviously, the $t\bar{t}$ background is enriched significantly by these cuts, the other backgrounds (and the signal) are negligible for masses above ≈ 110 GeV.

Figure 12.2 shows a comparison of the invariant mass distribution of the $t\bar{t}$ sample with the standard cuts applied and with the anti- $t\bar{t}$ cuts reversed. Good agreement can be achieved in this way and a sample from which the shape of the $t\bar{t}$ background can be estimated is thus available. The selection efficiencies are very different between using the normal and the reversed cuts on \cancel{E}_T and H_T , but the $t\bar{t}$ mass shape could for example be used in a template fit to the data with the normal cuts to obtain also the normalization. But in this case also the Z^0 contributions would be needed to make a complete fit to the data.

However, the other background distributions are not that easily measurable: The Z^0 backgrounds have kinematics very similar to the signal. One possibility would be to reverse the b -tagging weight cut, thus requiring at least one jet with weight < 4 and $p_T > 20$ GeV, $|\eta| < 2.5$. In this way the $Z^0 + \text{light}$ background is enhanced drastically. Figure 12.3 shows the invariant mass distributions of the $Z^0 + \text{light}$, the $Z^0 + b$ sample,

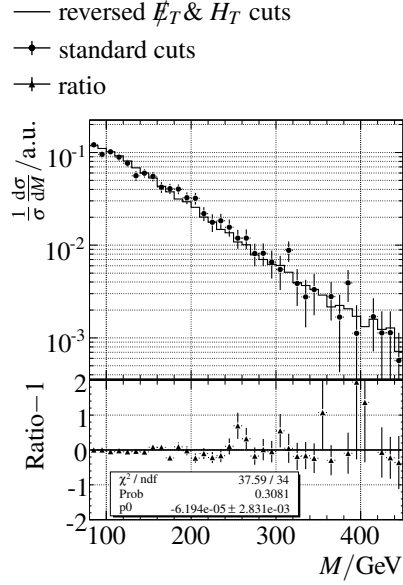


Figure 12.2: Top: Invariant mass distributions for the standard selection (circles with error bars) and with reversed cuts on \cancel{E}_T and H_T (line). Bottom: Ratio (subtracted by -1) between the two distributions (triangles with error bars) and a fit of a constant (line).

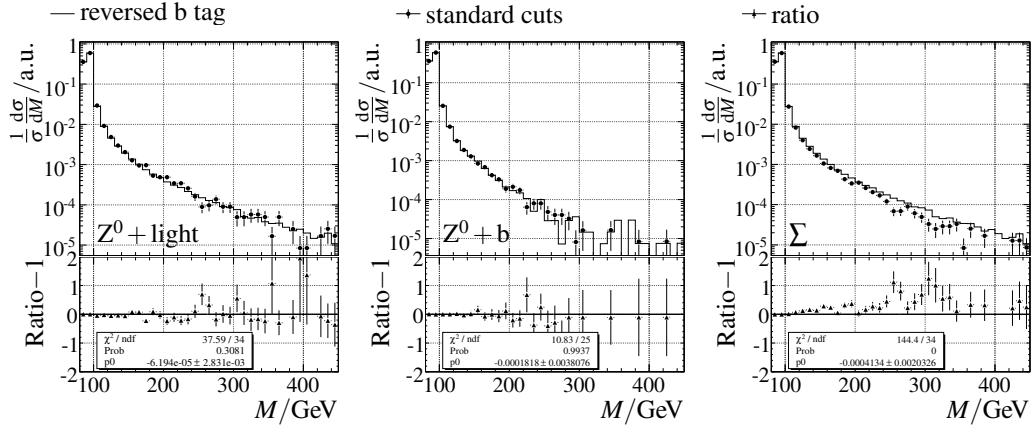


Figure 12.3: Top: Invariant mass distributions for the standard selection (circles with error bars) and with reversed b -tagging weight cut (line). Bottom: Ratio (subtracted by -1) between the two distributions (triangles with error bars) and a fit of a constant (line). From left to right: Only $Z^0 + \text{light}$, only $Z^0 + b$, and the sum of the two samples.

and of their sum with the standard b -tagging cut and the reversed one. Clearly, taking each of the two Z^0 backgrounds separately, a good agreement can be obtained. However, in their sum, the invariant mass distributions of the control sample and the signal region are different. This actually just reflects the difference in the mass distributions between $Z^0 + \text{light}$ and $Z^0 + b$, which is caused by the fact that quarks of different flavor (up-type or down-type) couple differently to the Z^0 and the photon. In addition the two processes depend on different parton densities. Reversing the weight-cut changes the ratio between $Z^0 + \text{light}$ and $Z^0 + b$, thus also changing the invariant mass distribution. In addition, a b tagged reversed sample is not free of any signal contribution. Thus no effective control sample for the Z^0 backgrounds could be found.

An alternative to the construction of control samples by reversing cuts is to use the shape of the invariant mass distribution after the selection cuts. The background contributions show a generally smooth distribution, while the signal would show up as a peak in a limited region of invariant masses. Using a parameterization of the background shape, it is possible to fit the background contribution directly in the data. This can be either done simultaneously for the signal and the background, or by excluding a mass window from the fit region and extrapolating the background fit into the mass window to estimate the background. As a simultaneous fit of signal and background would require prior knowledge of the shape of the signal mass distribution, this is not used in the following. A priori the number of Higgs bosons, their width, and their separation in mass cannot be known, thus a mass shape is not available.

Obviously such a method is prone to run into problems with low statistics for the background, as a stable fit to the background shape will not be easily possible. This problem is not addressed in this thesis, as all results in the following will be given for an integrated luminosity of 30 fb^{-1} , where the background statistics is large enough to perform such a fit. At smaller luminosities the susceptibility to statistical fluctuations would be larger.

12.2 Basic Fit Strategy

The basic procedure applied to extract the background as from real data is the following:

1. A multi-parameter function is used to describe the shape of the background contribution. The function has to be versatile enough to be able to describe differences between data and Monte Carlo. As the background contributions in the two analyses are significantly different, the background parameterizations do not necessarily need to be the same.

As a large range of Higgs boson masses is studied (from about 110 GeV to 400 GeV), it might be necessary to apply different parameterizations for different regions of the spectrum.

A priori it cannot be ensured that the parameterization found in Monte Carlo events will also work on real data. However, signal free final states as described above will give a control sample for this procedure. In this work the background parameterizations are tested exclusively on the $\mu^+\mu^-$ final state using Monte Carlo simulations.

2. A test mass and natural width of the Higgs resonance is assumed. According to the parameterization of the reconstructed width in dependence of mass and natural width of the Higgs boson (cf. Section 10.2), a two-sided two-sigma mass window is constructed. In principle the size of the mass window is arbitrary and could be optimized to yield the best sensitivity. However, cutting very close to the peak position would lead to very large systematic uncertainties, as the cut would be placed in a very steep part of the mass spectrum. Using a two-sigma mass window ensures that the procedure is more robust against mismodelling of the shape of the Higgs boson resonance.
3. The background parameterization is fitted to the mass spectrum, excluding a two-sided *three*-sigma region around the test mass. The excluded region is chosen larger than the signal region to ensure that the signal contribution in the fit is almost negligible.

The fit is performed as a binned χ^2 fit. As a consequence the number of events per bin has to be large enough to ensure that the χ^2 fit is a good approximation. In principle the procedure is not limited to a binned χ^2 fit. However, in this Monte Carlo analysis parts of the background samples contain weighted events with negative weights. Performing an unbinned likelihood fit on such event samples is possible, but would involve a more complicated likelihood function and an analytical expression of the covariance matrix, which is impossible for some of the used parameterizations, since they involve non-analytical functions, such as the Voigt function. In real data this would not be a limitation, since obviously real events do not have negative weights.

4. The fitted function is integrated numerically inside the two-sigma mass window. In this way the prediction of the background contribution is found. In addition, the error on the integral is evaluated numerically using the complete covariance matrix of the fit parameters, using the routines available in the ROOT [156] package.

12.3 Analysis I (b tag)

The background parameterization chosen in Analysis I (b tag), is motivated by the background composition: The Z^0 backgrounds show a peak at the Z^0 mass that is smeared by the detector resolution. For higher masses they, as well as the $t\bar{t}$ background, exhibit an exponentially falling spectrum. This is produced on the one hand by the influence of the virtual photon exchange, but also by the fact that for higher invariant masses the parton distribution functions are probed at different x and Q^2 , thus changing the cross section.

12.3.1 Background Parameterization

The background parameterization is chosen to be the sum of a Voigt profile, which is the convolution of a Breit-Wigner distribution with a Gaussian with the same central value, and an exponentially falling part:

$$bkg(x; N_1, N_2, M, \Gamma, \kappa, \tau) = N_1 \cdot \frac{1}{x} \text{Voigt}(x; M, \Gamma, \kappa \cdot M) + N_2 \cdot \exp(-x/\tau), \quad (12.1)$$

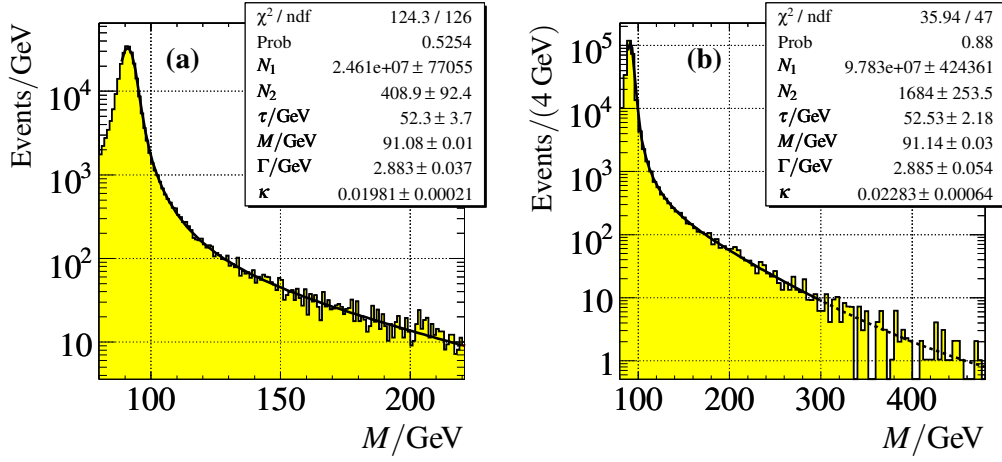


Figure 12.4: Background parameterizations in the b tagged analysis fitted to the whole allowed range. (a) Low mass region, (b) high mass region. Masses above 300 GeV are excluded from the fit, as shown by the dashed line.

N_1 and N_2 describe normalization parameters, Γ is the width of the Breit-Wigner of the Voigt profile, $\sigma = \kappa \cdot M$ the width of the Gaussian part, M the central value, and τ the slope parameter of the exponential. The $1/x$ damping factor for the Voigt profile ensures that it does not contribute too much in the high mass region. All six parameters are left floating in the fit, as in principle the resolutions are unknown. In addition, in this way differences in the background shape between Monte Carlo and data could also be accounted for.

As the fit is done as a binned χ^2 fit, in principle the bin width has to be chosen as small as affordable, while still retaining enough statistics to remain in the gaussian limit. As a consequence, the sample is divided into a low mass region, where enough statistics is available to keep a very fine binning, and a high mass region, where a coarser binning is applied.

The low mass region extends from 88 GeV to 220 GeV, and here the binning is fixed at a width of 1 GeV. Figure 12.4 (a) shows the parameterization applied to the whole region, with only the background Monte Carlo shown.

The fitted mass of the Voigt profile is close to the nominal mass of the Z^0 boson, however the fitted width of the Breit-Wigner part is slightly larger than the true value of 2.5 GeV. This shows that the mass shape cannot be explained completely by a pure Z^0 resonance smeared with the detector resolution, but also contains other contributions which are taken into account phenomenologically.

An extension to higher masses is not possible due to the small statistics. In addition it is required that the lower end of the signal mass window is above 94 GeV, in order to retain enough parts of the spectrum to obtain a reliable estimate. This region is used up to central values of the mass window of 160 GeV.

For central values of the mass window of more than 160 GeV the binning is chosen as 4 GeV and the fit region extended up to 300 GeV. The fit to the whole region is shown in

Figure 12.4 (b). The value of 160 GeV to separate between these two regions was chosen so that the expected uncertainties of the background prediction are the same at this point when choosing the one or the other binning and fit range. If the fit with a finer beginning would be continued to larger masses, it would perform worse as the sideband to the right of the mass window becomes too small. Extending the fit with a coarser binning to lower masses also gives worse performance since it is not able to define the shape of the Voigt profile very accurately due to its worse resolution. At a mass of 160 GeV, the two approaches work similarly.

For masses beyond 300 GeV the fitted mass spectrum is extrapolated only from the lower mass side, as in this region the statistics is too small to fit reliably on both sides of the excluded region.

12.3.2 Fit performance

In the following the performance of the fit is reviewed in dependence of the center of the signal mass window and its chosen width. As described above, its width is determined by the expected width of the Higgs boson resonance, and also possibly the separation between two or three different Higgs bosons contributing. To express the performance independent of these parameters, the dependence on the width is examined as a function of the width divided by the width for a single resonance dominated by detector resolution ($\Gamma_{\text{Higgs}} = 0$).

Figure 12.5 shows exemplarily the background contribution with the signals from the three neutral Higgs bosons on top for $M_{A^0} = 130$ GeV and 200 GeV for $\tan\beta = 30$ in the M_{h^0} -max scenario. The applied outer and inner mass windows are shown. They consist of the combined two respectively three-sigma windows of all Higgs bosons of relevance.

Subsequently, the performance of the fit is studied using the background-only sample with a signal mass window excluded from the fit. The following quantities are of interest, that are shown in Figure 12.6 in dependence of the central value M_{center} and the width of the mass window:

- a) The deviation between the background predicted by the fit and the actual background in the two-sigma mass window. To take the statistical uncertainties into account, this is normalized by dividing by the quadratic sum of two uncertainties: The statistical uncertainty ΔB_{true} of the number of background events and the uncertainty ΔB_{fit} on the number of events predicted by the fit. As the two-sigma region is excluded from the fit, these two are independent of each other. For a large number of background events inside the mass window, and for an unbiased behavior of the fit, this quantity should deviate from zero according to a standard Gaussian with width one and central value zero. Indeed this is the case within statistics. It should be noted that there is a high degree of correlation between fit results for different central values and widths of the mass window, as most of the bins used in the fit are identical. The largest deviations are of the order of two sigma. For example around a mass of 200 GeV there seems to be a slight upward fluctuation in the background, which shows up as a vertical band in the figure, as this fluctuation is seen more or less independent of the width of the mass window. Overall no evidence of a possible bias is seen.

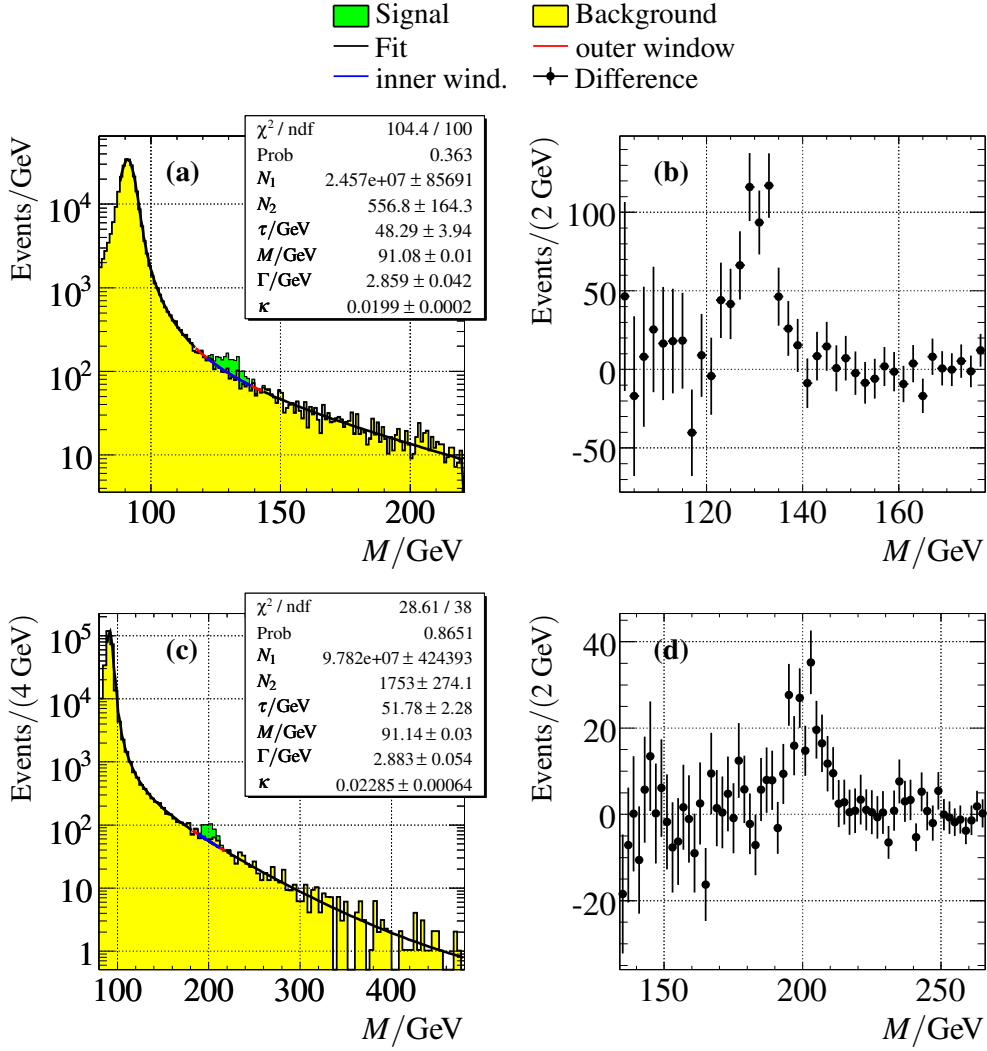


Figure 12.5: Sideband fits to the invariant mass spectrum in Analysis I (b tagged) including background (left column) and after background subtraction (right column). (a) and (b): $M_{A^0} = 130 \text{ GeV}, \tan \beta = 30$, (c) and (d): $M_{A^0} = 200 \text{ GeV}, \tan \beta = 30$. Exclusion windows are the combined three- and two-sigma regions of all Higgs bosons contributing significantly. Error bars of the background subtracted spectrum are correlated.

- b) The χ^2 probability of the fit (\mathcal{P}_{χ^2}) is rather large for all chosen mass windows. Also the upwards fluctuation of the background around 200 GeV is seen in the fit probability, since \mathcal{P}_{χ^2} slightly increases if this region is excluded. For very high masses the fit probability becomes constant, as the fitted function is extrapolated and nothing changes anymore.
- c) The relative uncertainty of the background prediction $\Delta B_{\text{fit}}/B$ ranges between about 0.5 and 9%. It is smallest for masses around 110 GeV and rises gradually for larger masses. In fact it becomes largest around 300 GeV for large widths of the mass window. As 300 GeV marks the end of the fit region, this coincides with the smallest available region for the fit. For very low masses the relative uncertainty also becomes larger, as less events are available in the left sideband region.
- d) The ratio between the uncertainty of the fit prediction for the background rate and the statistical uncertainty of the background itself is plotted. For a lot of the chosen mass windows the uncertainty from the fit is smaller or of the same order as the statistical uncertainty. Only for very small masses and very large widths of the mass window, fit uncertainties much larger than the statistical uncertainty are observed. This is again due the poorly constrained Z^0 peak.

It should be noted that large widths of the mass window will mostly be needed only for very large natural Higgs boson widths. This coincides with large $\tan\beta$ and corresponds to large production cross sections as well. This will compensate the degradation of sensitivity due to the larger mass window somehow.

12.4 Analysis II (b tag veto)

For Analysis II (b veto), the background composition is found to be very different, since it is dominated completely by the $Z^0 + \text{light}$ contribution. The parameterization obtained for the b tagged analysis does not allow for a stable fit anymore. In addition, no parameterization was found that allows to fit also below or on the Z^0 peak. In a sense the larger background contribution now also leads to a more problematic fitting procedure, since instead on the level of a few percent, the statistical fluctuations in the background are now on the level of a few permille.

12.4.1 Parameterization

As for the Analysis I, the fit procedure is divided into two different regions, separated at a central value of the mass window of 175 GeV. This value is again chosen to yield similar uncertainties if either of the two procedures is applied.

For masses below 175 GeV a function very similar to Eq. 12.1 is used:

$$bkg(x; N_1, N_2, M, \Gamma, \kappa, \tau) = N_1 \cdot \text{Voigt}(x; M, \Gamma, \kappa \cdot M) + N_2 \cdot \exp(-x^{\frac{1}{4}}/\tau), \quad (12.2)$$

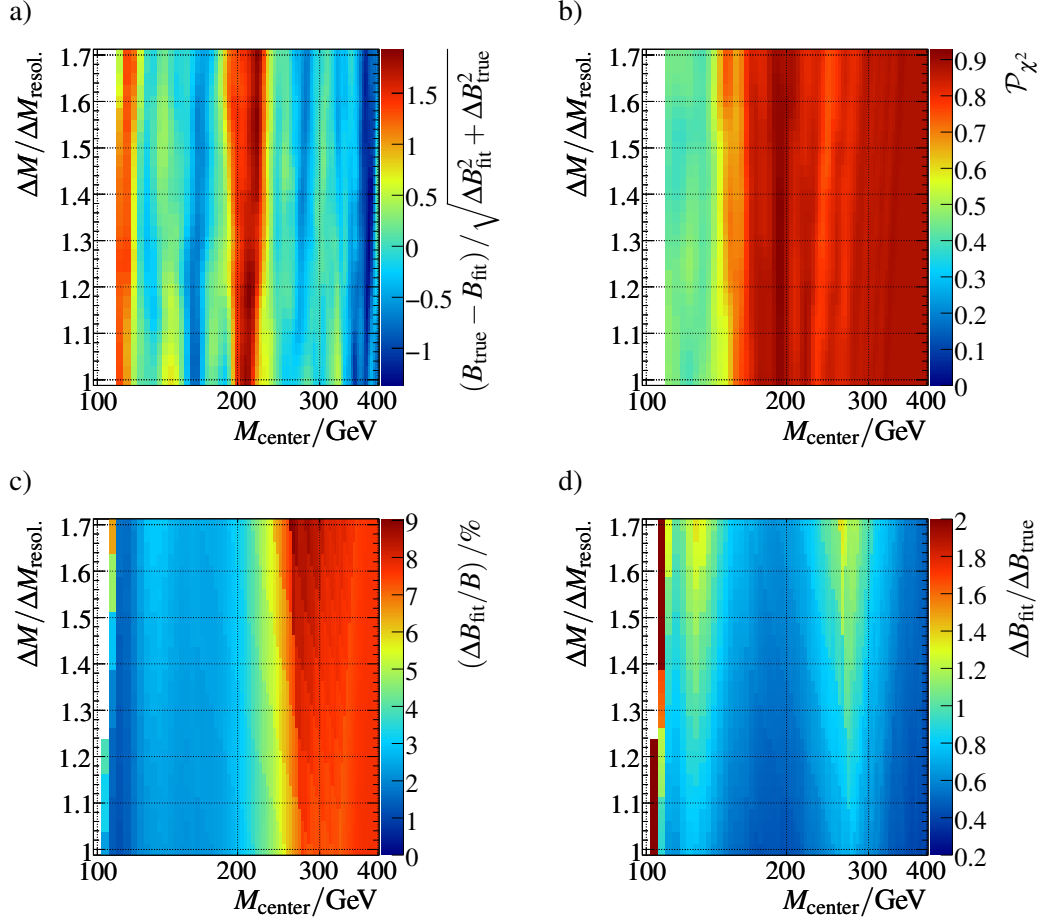


Figure 12.6: Performance of the background fit for Analysis I (b tagged) in dependence of the center of the chosen mass window (M_{center}) and its width normalized to the detector resolution ($\Delta M / \Delta M_{\text{resol.}}$) as described in the text. a): Deviation between true and fitted number of events in the inner mass window normalized to the combined uncertainty. b): χ^2 probability of the fit. c): Relative uncertainty of the background prediction in the inner mass window from the fit. d): Background uncertainty from the fit divided by the statistical uncertainty of the background inside the inner mass window.

the only change being a modification of the exponential fall-off. The fit is performed between 95 and 250 GeV and the bin width is chosen as 1 GeV. If the outer mass window would exclude the mass bins at 99 GeV or below from the fit, the parameter point is discarded from the analysis, as otherwise a stable and unbiased fit is found to be impossible. The fitted parameterization is shown in Figure 12.7 (a).

For the higher masses, a completely phenomenological function is used:

$$bkg(x; A, B, C, D, E, F) = D \cdot \exp \left(1 + C \cdot x / \text{GeV} + \frac{A}{x / \text{GeV} - B} + \frac{E}{(x / \text{GeV})^2 - F} \right) \quad (12.3)$$

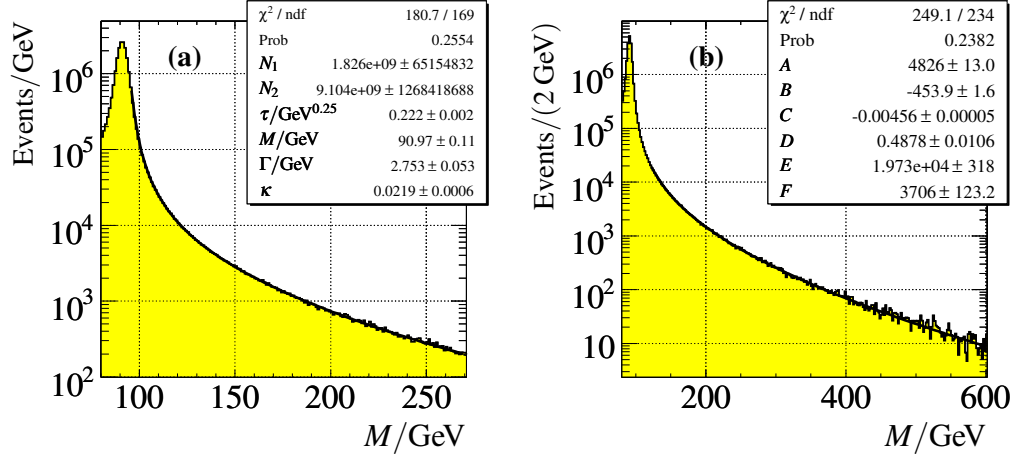


Figure 12.7: Background parameterizations in Analysis II (b tag veto) fitted to the whole allowed range. (a) Low mass region, (b) high mass region.

The second term in the exponential function again describes a normal exponential fall-off, the others parameterize the deviation due to the influence of the Z^0 . The fit is performed between 120 and 600 GeV with a bin width of 2 GeV. It is shown in the whole range in Figure 12.7 (b).

12.4.2 Fit Performance

Figure 12.8 shows the background, the fit and the two and three-sigma regions along with the signals on top for $M_{A^0} = 130$ GeV and 200 GeV for $\tan \beta = 30$ in the M_{h^0} -max scenario. Although the signal contributions is not visible by eye due to the large background level, the signal peak is clearly visible after background subtraction.

The performance of the fit is evaluated as in the case for the b tagged analysis and is shown in Figure 12.9.

- Again some deviations between the fit predictions and the actual background inside the inner mass window are visible as vertical bands in the plot. Around 200 GeV a deficit of events is visible and around 270 GeV an excess is visible. The deviations are at most of about 2.7 sigma. Keeping in mind the large number of bins entering this fit, and that the probability of a 2.7 sigma fluctuation is about 0.3%, this is not a sign of a significant problem.
- The χ^2 probability is again satisfactory in all regions.
- The uncertainty of the predicted background rates are significantly smaller than for the b tagged analysis, but this is a direct result of the much larger overall event rate. If the fit uncertainty is compared to the statistical uncertainty, a similar result as for the b tagged analysis is obtained. For high masses the fit sometimes fails to reach convergence. This could probably be fixed by choosing different start parameters, but

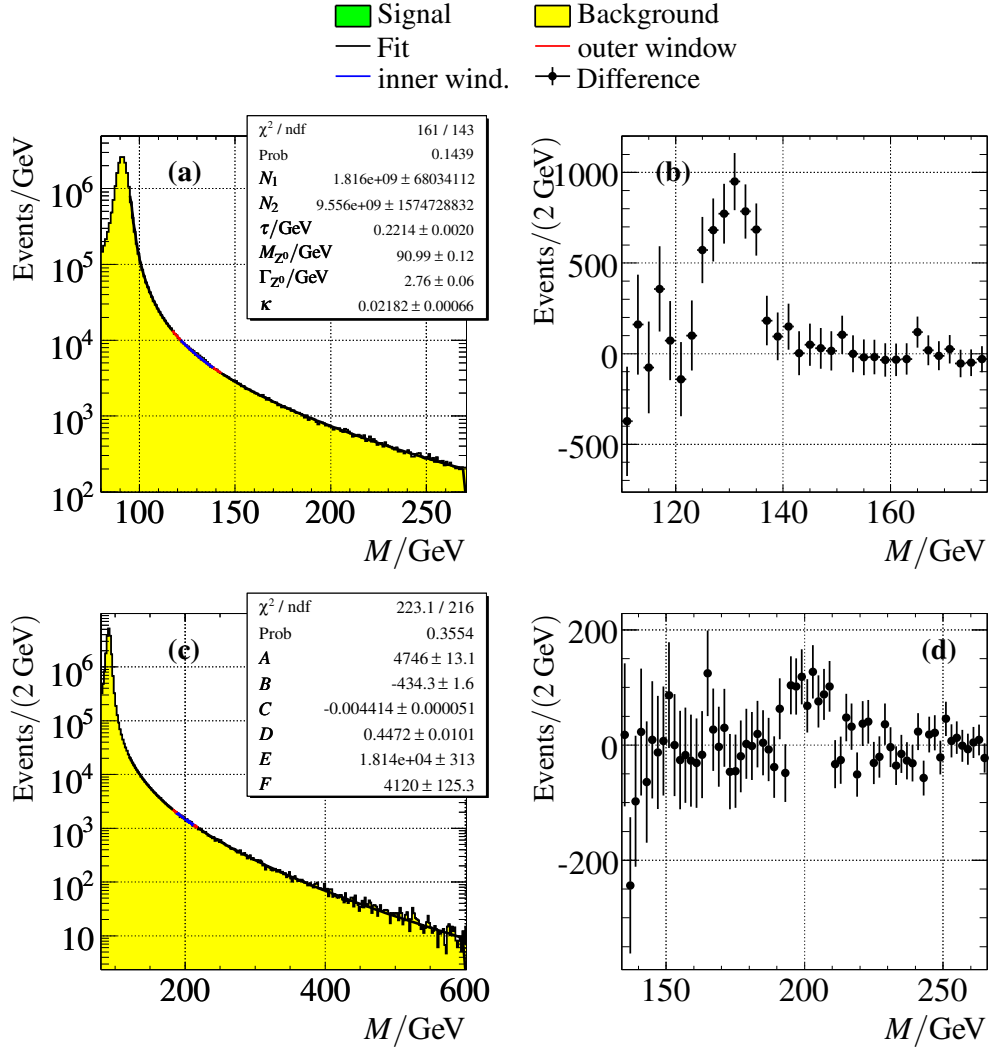


Figure 12.8: Sideband fits to the invariant mass spectrum in Analysis II (b tag veto) including background (left column) and after background subtraction (right column). (a) and (b): $M_{A^0} = 130$ GeV, $\tan\beta = 30$, (c) and (d): $M_{A^0} = 200$ GeV, $\tan\beta = 30$. Exclusion windows are the combined three and two-sigma regions of all Higgs bosons contributing significantly. Error bars of the background subtracted spectrum are correlated.

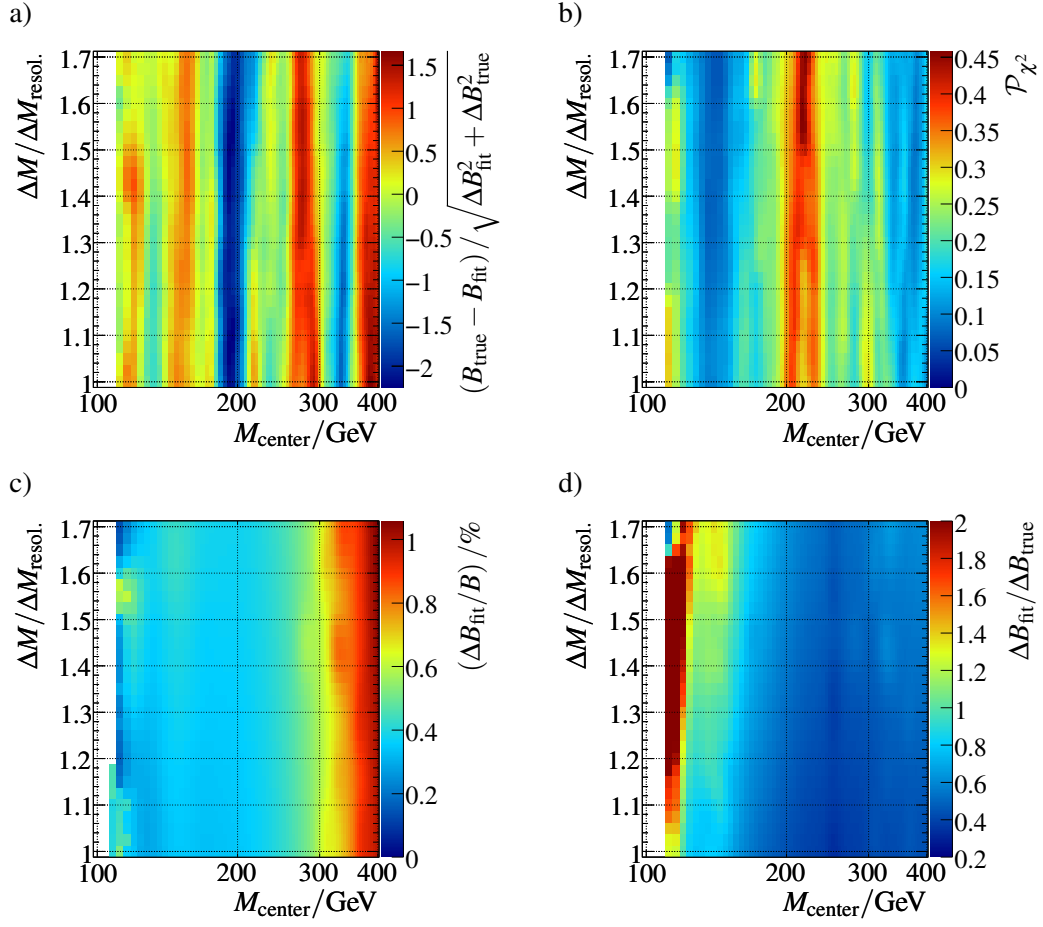


Figure 12.9: Performance of the background fit for Analysis II (b veto) in dependence of the center of the chosen mass window (M_{center}) and its width normalized to the detector resolution ($\Delta M/\Delta M_{\text{resol.}}$) as described in the text. a): Deviation between true and fitted number of events in the inner mass window normalized to the combined uncertainty. b): χ^2 probability of the fit. c): Relative uncertainty of the background prediction in the inner mass window from the fit. d): Background uncertainty from the fit divided by the statistical uncertainty of the background inside the inner mass window.

this was not done in in this automated procedure. Instead the histogram in the figure has been smoothed by a kernel smoothing algorithm as implemented in ROOT [156].

- d) Compared to the statistical uncertainty of the background contribution, for almost all mass windows the fit yields a smaller uncertainty than the statistical uncertainty. Only for the very small masses it performs significantly worse. This is a direct consequence of the much larger number of background events and the smaller fit region compared to Analysis I.

For centers of the mass window close to 110 GeV it is observed that the fit becomes unstable. Small variations of the start parameters in this case lead to large differences in

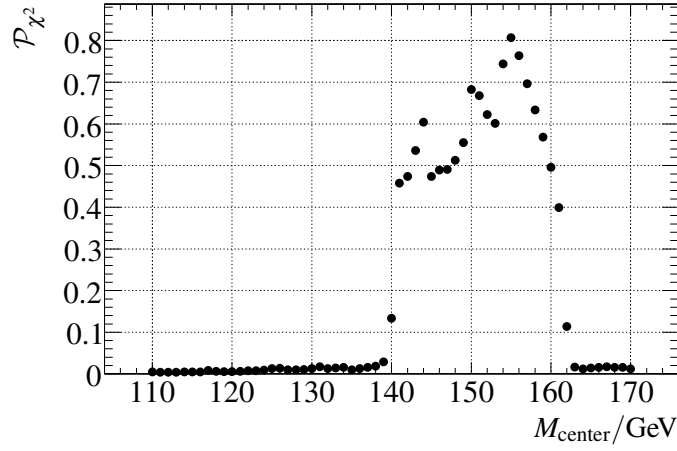


Figure 12.10: Fit χ^2 probability in dependence of the center of the mass window excluded from the background fit for analysis I in the presence of a signal ($M_{A^0} = 150$ GeV, $\tan\beta = 20$).

the convergence behavior and can yield very different result if the fit is performed in an automated procedure. Especially the covariance matrix is not always computed accurately. This chaotic behavior becomes even worse for larger mass windows. In the final analysis presented in the next chapter, the low mass region are therefor excluded from the analysis. Only Analysis I contributes in this case.

12.5 Floating Higgs Boson Mass

The methods described above make use of a fixed mass window used to define a signal region to be excluded from the background fit. However, in the real experiment, the mass of the Higgs boson(s) is not known a priori, except if they are discovered first in another decay and/or production channel, e.g. in their decay into τ leptons. However, also with an unknown Higgs boson mass, the region to be excluded from the fit can be found from the data itself.

The procedure described in the following makes use of the fact that in presence of a signal peak on top of the spectrum, a background-only fit to the spectrum including the peak will yield a very low χ^2 probability.

In order to make use of this, one could simply move the mass window with a width fixed to the one corresponding detector resolution and test different masses. The real Higgs boson mass will show up as a region with a higher χ^2 probability. This can in the following be excluded from the fit and be analyzed if it is possibly due to the presence of a Higgs boson.

The procedure is exemplified in the following for $M_{A^0} = 150$ GeV, $\tan\beta = 20$ in the M_{h^0} -max scenario. Figure 12.10 shows the χ^2 probability in dependence of the center of

the mass window for analysis I. Clearly a wide minimum of higher χ^2 probabilities around the mass of the Higgs bosons is visible.

This method is also prone to detect statistical fluctuations of the background. However, these should not be able to reach the discovery threshold after being excluded from the fit.

12.6 Influence of the Mass Tail

As discussed in Section 10.2.1, about 9% of all signal events are still outside the three-sigma mass window due to the long mass tail towards low invariant dimuon masses. Anyway, in the fit procedure it was assumed that the signal contribution outside the three-sigma mass window is negligible.

This might lead to a possible bias of the fit, as it is no longer ensured that the background contribution inside the mass window is predicted correctly. As a signal contribution in the sideband can only shift the prediction upwards, this would actually mean that the background is overestimated. Thus the fit procedure on data is conservative, as if one claims a discovery based on a background that is estimated too high, the real signal significance would be even larger.

The fit bias was checked using signal Monte Carlo at discrete points of M_{A^0} and $\tan\beta$ in the M_{h^0} -max scenario. The fit was performed using signal plus background and only background. The deviations between the two background predictions in the inner mass window have been compared. The largest effect is seen for very low masses in Analysis II, where the background might be overestimated by one standard deviation of the statistical uncertainty of the background. For Analysis I and for large masses, a much more stable behavior is seen, where the bias is at most half a standard deviation.

Also the fit probability is not influenced significantly by the signal contribution outside the sidebands.

“It soon became obvious that we were but on the threshold of the discovery. “

Howard Carter, 1874–1939

13

Discovery Potential

In this chapter the discovery potential of the ATLAS experiment for neutral Higgs bosons of the MSSM in the muonic decay mode is discussed assuming an integrated luminosity of 30 fb^{-1} . The previous three chapters build the basis for this study: The events have to be selected with a certain efficiency for signal and background, the systematic uncertainties on these have to enter the calculation of a significance and due to the proposed method of extracting the background from data it is possible to significantly increase the discovery potential compared to extracting the background using the Monte Carlo simulation.

The discovery potential is reported in dependence of M_{A^0} and $\tan\beta$ for the four CP conserving benchmark scenarios described in Section 2.4.1. As it was not possible to generate signal Monte Carlo at each parameter point, a scan procedure has to be devised. The signal reconstruction efficiency is parameterized as a function of the mass of the Higgs boson. The same is done for the fraction of signal events falling into the two-sided two-sigma mass window, with the width determined according to the parameterization described in Section 10.2. In this way the signal contribution inside the applied mass window can be determined for each Higgs boson mass. The systematic uncertainties of the signal selection efficiencies are taken into account by constructing separate parameterizations for each of the experimental systematic uncertainties. This procedure is discussed in the first section.

The background contribution inside the assumed mass window is determined using the sideband fit described in Chapter 12. The systematic uncertainties are taken into account by re-performing the fit with a systematic variation, as described in Chapter 11. This has the advantage that the resulting variation in the expected background rate is less susceptible to statistical fluctuations, since the fit regions are much larger than the two-sigma mass windows in which the systematic uncertainties were evaluated in Chapter 11.

The expected significance for discovery of a signal is calculated using an approximated *profile likelihood* method, which is briefly discussed. As the background extraction using a sideband fit is actually independent of the systematic uncertainties, these do not directly enter the calculation of the significance. In a way, the sideband fit encompasses a measurement of the unknown parameters, like the background cross sections and the reconstruction efficiencies. These experimental and theoretical uncertainties instead have to

be seen as a measure of the unknown real performance of ATLAS and the real behavior of proton proton collisions at $\sqrt{s} = 14$ TeV. They are taken into account by varying the signal and background contributions and adding the resulting variation of the signal significance in quadrature.

13.1 Parameterization of Signal Efficiencies

To be able to perform a quasi-continuous scan of the $(M_{A^0}, \tan\beta)$ plane, the selection efficiencies for the two analyses have to be parameterized for the two contributing signal processes $b\bar{b}A^0$ and $gg \rightarrow A^0$. In this way, the different benchmark scenarios can be scanned without generating separate Monte Carlo samples for each scan point.

For practical purposes, the signal selection efficiency is separated into two parts: First the selection efficiency without requiring any cut on the invariant dimuon mass, then the efficiency to reconstruct the mass inside a specified mass window. For the background contributions such a parameterization is not necessary, since the background is independent of M_{A^0} and $\tan\beta$.

The parameterizations are derived using ATLFast Monte Carlo samples, including all corrections shown in Chapter 9. Different masses of the A^0 boson and $\tan\beta$ have been simulated, thus giving a representative region of masses and widths of the studied Higgs bosons. It has to be noted that the natural widths used to simulate these samples have been calculated with an older version of FEYNHIGGS 2.5.1. In the parameter scan, FEYNHIGGS 2.6.4 is used, which includes better predictions and also has some programming errors removed, mostly affecting Higgs bosons with masses above the top quark mass.

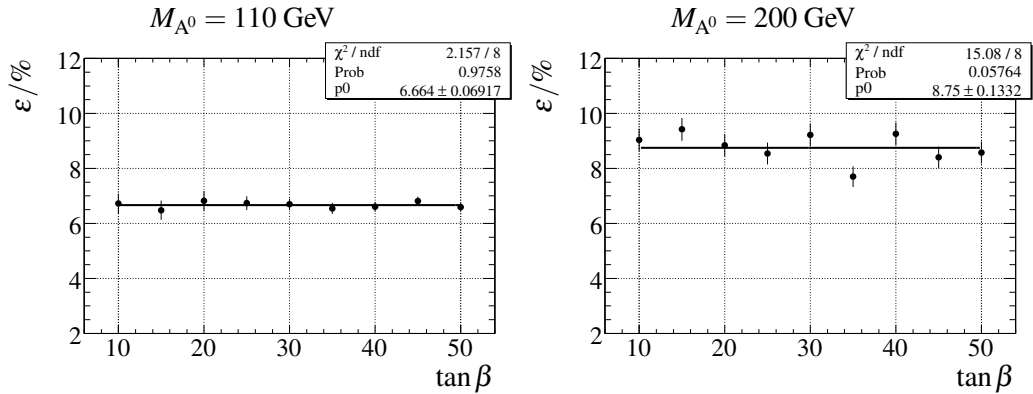


Figure 13.1: Mean selection efficiencies for $b\bar{b}A^0$ events (M_{h^0} -max scenario, FEYNHIGGS 2.5.1) in Analysis I (b tag) in dependence of $\tan\beta$ for $M_{A^0} = 110$ GeV and $M_{A^0} = 200$ GeV. The line shows the fit of a constant to the data points.

13.1.1 Parameterization of Selection Efficiencies

As the selection criteria presented in Chapter 10 without requiring a mass window do not directly make use of the Higgs boson mass, it can be expected that the selection efficiencies are mostly independent of the width of the Higgs boson, as long as the width is not of the same order as the mass itself. The width of the MSSM Higgs bosons in the studied range of parameters is only influenced by $\tan\beta$, so it is sufficient to check its independence of $\tan\beta$. This is shown in Figure 13.1 for Analysis I (b tag) for two different Higgs boson masses along with a fitted constant function, thus obtaining a weighted average of the individual efficiencies. The mean efficiency is obviously not independent of the Higgs boson mass. This is expected, as shown in Chapter 10. For example lower Higgs boson masses yield softer muons and b jets than higher masses. For very high Higgs boson masses the efficiency will drop again due to the influence of the harder jet p_T spectrum on H_T and \cancel{E}_T .

For the $gg \rightarrow A^0$ sample and for Analysis II similar results are achieved, i.e. no significant dependence of the selection efficiency on the Higgs boson width is observed. To obtain a parameterization in dependence of the mass the mean efficiency is fitted with a third order polynomial. This is shown in Figure 13.2 for the two signal production channels and the two analyses. To account for possible deviations from this parameterization, a $\pm 2\%$ systematic uncertainty is assigned to this parameterization. As shown in Figure 13.2, this completely covers the deviations of the mean efficiencies from the parameterization, and also accounts for the bad χ^2 in the fit of the $gg \rightarrow A^0$ contribution in Analysis II. Compared to a theory uncertainty of the signal cross section of at best 15%, this is a negligible uncertainty.

The detector related systematic uncertainties discussed in Chapter 11 are taken into account by obtaining a new parameterization with this systematic variation applied. Also for these parameterizations no significant deviations within the 2% uncertainty are observed. As described in Chapter 11, only the systematic uncertainties that directly influence the shapes of the cut variables are taken into account in this way. For example the influence of the uncertainty of the muon reconstruction efficiency is simulated using a multiplicative correction of the selection efficiencies.

Using a fitted parameterization also reduces the statistical component of the systematic uncertainties, as a larger effective dataset is used when determining the parameterization.

13.1.2 Parameterization of the Mass Window Efficiency

Apart from the selection efficiency, also the fraction of signal events falling into a given mass window needs to be parameterized. As described in Section 10.2, a parameterization of the Gaussian width of the signal is available. However, this is only an approximation, as a large non-Gaussian contribution is clearly evident, especially in the form of a mass tail towards lower masses.

In addition, though the number of signal and background events is counted in a two-sigma mass window around the nominal Higgs boson mass, in large parts of the parameter space the contributing Higgs bosons are not completely mass-degenerate. Although a com-

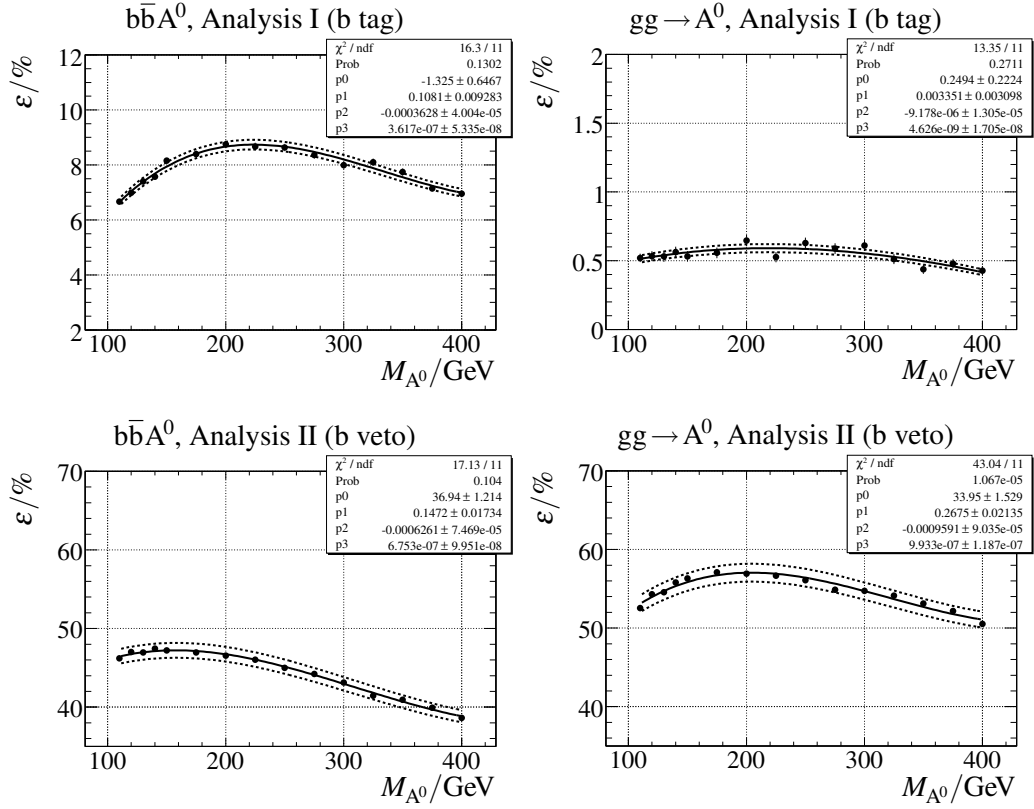


Figure 13.2: Mean reconstruction efficiencies in dependence of the Higgs boson mass (points) for the two Higgs boson production channels and the two analyses. Solid line: Fitted parameterization. Dashed lines: $\pm 2\%$ uncertainty region.

binned two-sigma window is used, this does not necessarily lead to a symmetric two-sigma window for the individual Higgs bosons. This is especially true in the case of the intense coupling region (see Section 2.4.4), where all three neutral Higgs bosons are close to each other in mass.

To take this into account, the selection efficiency of a more or less arbitrary mass window cut is needed. In the following this is constructed as a look-up table, where the efficiencies as a function of various borders of the mass window normalized to the parameterized Gaussian width is recorded.

The dependence of the mass window efficiency on the natural width of the Higgs boson is checked in the same way as for the selection efficiency. Figure 13.3 shows the efficiency versus $\tan\beta$ to reconstruct the Higgs boson in a symmetric two-sigma window around its nominal mass for $bb\bar{b}A^0$ events in Analysis II (b veto) for two selected input masses. Analysis I as well as $gg \rightarrow A^0$ events yield similar results within statistics.

Obviously, the mass window efficiency retains a small dependency on the width of the Higgs boson, and thus indirectly on $\tan\beta$. However, this is a small effect. It is caused by

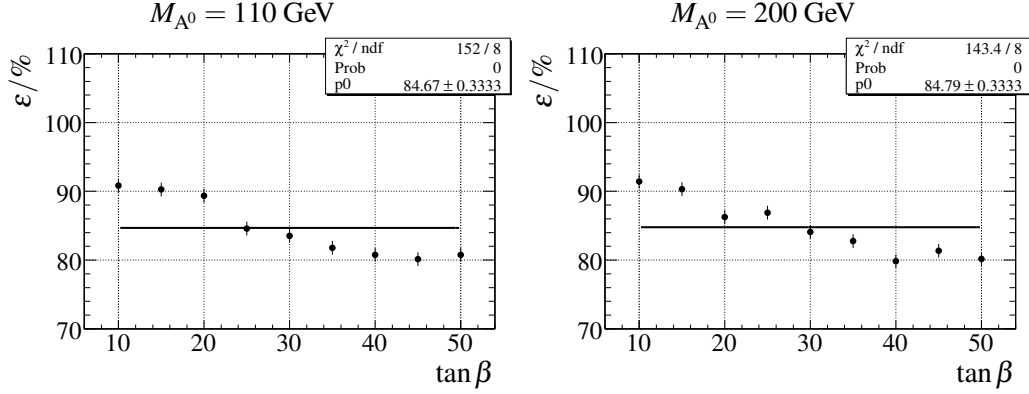


Figure 13.3: Relative reconstruction efficiency of a symmetric two-sigma mass window for $b\bar{b}A^0$ events in Analysis II (b veto) in the M_{h^0} -max scenario for different $\tan \beta$. Left: $M_{A^0} = 110$ GeV, right: $M_{A^0} = 200$ GeV. The line shows the average of the points.

deviations from the Gaussian shape that could not be taken into account in the parameterization of the reconstructed widths.

Taking the average reconstruction efficiency yields about 85% for the chosen mass window. The remaining dependence on the natural width can be taken fully into account by a 5% systematic uncertainty on this number. This is still a small uncertainty compared to the theoretical uncertainties of the signal cross sections.

The average efficiency is determined by fitting a constant to the $\tan \beta$ dependence as shown in Figure 13.3. In this fit the uncertainties of each data point are assumed to be the same, in order to yield an average efficiency that is not biased by different Monte Carlo sample sizes or selection efficiencies. As a consequence of this procedure, the χ^2 of this fit is meaningless. If the 5% systematic uncertainty would be taken into account, it would even lead to a very low χ^2 in all cases, since it is a very conservative estimate.

This mean mass window efficiency is a little bit too low for small widths (small $\tan \beta$) and a little bit too high for large natural widths of the Higgs boson. However, in the region of intermediate $\tan \beta$ it agrees much better than 5% with the true values. It should be noted that this at most 5% bias enters linearly into the calculated significance. As the signal cross section in a very good approximation is proportional to $\tan^2 \beta$, this corresponds to a 2.5% bias on the discovery potential in $\tan \beta$. This 5% uncertainty on the signal rate is supposed to be 100% correlated with the uncertainty on the predicted mass window, as described in Section 10.2.

The average efficiencies are shown in Figure 13.4 versus the mass of the Higgs boson. Within the assumed 5% uncertainty the values for different masses agree very well and an average efficiency is again determined by fitting a constant. Again, since equal uncertainties are assumed before, the χ^2 of this fit is meaningless.

The deviations from a constant are largest for the symmetric two-sigma mass window, the symmetric two-sigma. Figure 13.5 shows the dependence on $\tan \beta$ for an asymmetric and larger mass window. As the efficiency itself is significantly larger, the dependence is much smaller. In principle, a lower systematic uncertainty could be used for the larger

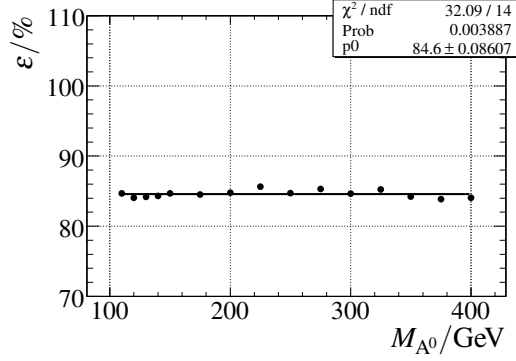


Figure 13.4: Average efficiencies for the symmetric two-sigma mass window versus the Higgs boson mass (data points) and fit of a constant function (line).

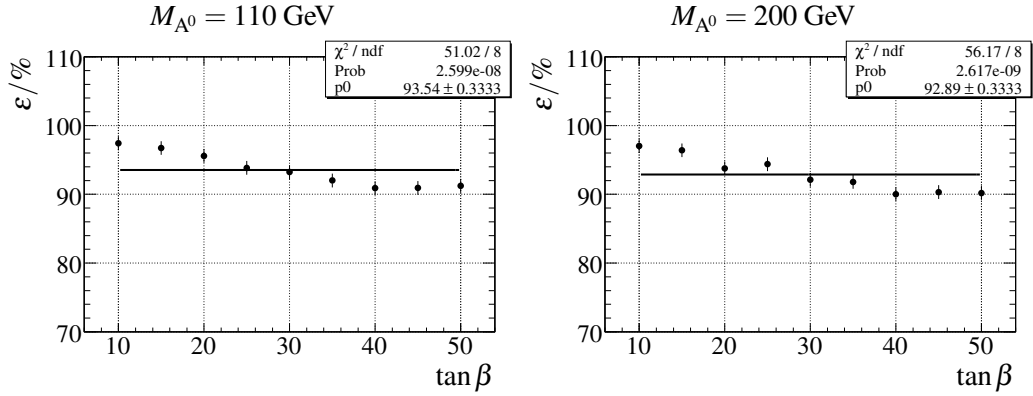


Figure 13.5: Relative reconstruction efficiency of an asymmetric mass window (-4 sigma, $+3$ sigma) for $b\bar{b}A^0$ events in Analysis II (b veto) in the M_{h^0} -max scenario for different $\tan\beta$. Left: $M_{A^0} = 110$ GeV, right: $M_{A^0} = 200$ GeV. The line shows a fit to the points with assumed equal uncertainties.

mass windows. To keep a conservative estimate, the $\pm 5\%$ is retained also for larger mass windows, but the efficiency is not allowed to be larger than unity.

On the other hand, if the mass window would be chosen even smaller than two sigma, the uncertainty would be much larger, as the cut would be placed in a much steeper part of the mass spectrum. Unless the line shape is under very good control, a harder cut has to be avoided.

The influence of the systematic uncertainties described in Chapter 11 on the mass window efficiency is in most cases negligible. Only the uncertainties on the muon energy scale and resolution have a small influence. However, this is much smaller than the assumed flat 5% uncertainty and is neglected in the following. Only the influence of the muon energy resolution smearing is kept as a systematic uncertainty of -1.7% , which is determined for the two-sigma mass window, where this effect is again largest.

The described procedure of first obtaining an efficiency averaged over all $\tan\beta$ and then deriving from these an averaged one over all masses is used to produce a look-up

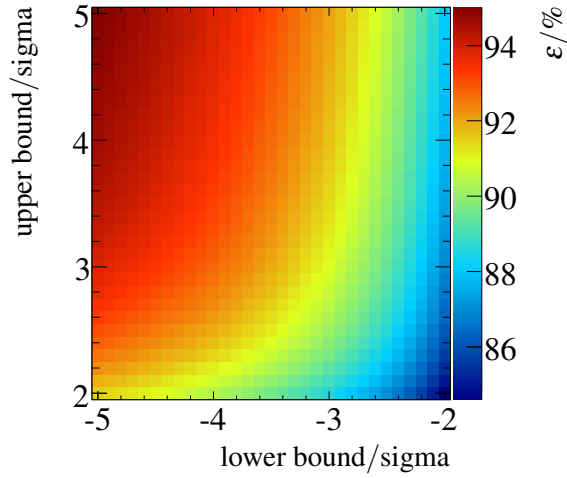


Figure 13.6: Selection efficiency of the mass window in dependence on the lower and upper bounds in units of the parameterized Gaussian width.

table of possibly asymmetric mass windows. It is shown graphically in Figure 13.6. The mass window selection efficiency ranges between 84% and 95%. Also a slight asymmetry between the lower and the upper end of the mass window is visible, corresponding to the observed mass tail towards lower masses.

13.2 Choice of Mass Window

The size of the mass window parameterized previously only corresponds to a single Higgs boson resonance. However, as shown in Chapter 2, for large $\tan\beta$, at least one of the scalar Higgs bosons (h^0, H^0) will be close to the pseudoscalar A^0 in mass and also similar in its properties. However, the mass degeneracy is only perfect for infinite $\tan\beta$. In the following, the discovery potential is evaluated in an effective two-sigma region that encompasses all Higgs bosons of relevance.

To decide which Higgs bosons contribute, the following algorithm is used: The A^0 is always taken into account, as it will always couple to b quarks and muons with a coupling proportional to $\tan\beta$, regardless of the properties of the specific benchmark scenario, and thus will always contribute to the signal. To decide, which of the other two neutral Higgs bosons are included, the expected significance considering the h^0 or H^0 alone is calculated in the S/\sqrt{B} approximation. If this significance is within 20% of the contribution of the A^0 , or if it exceeds a significance of two, the scalar boson under consideration is also used in the following. The second requirement ensures that the background extraction from the sideband fit does not have a significant signal contribution.

For each of the contributing Higgs bosons, the two- and three-sigma regions are calculated. The fit for the background extraction is then performed excluding the combined three-sigma interval, and the number of background events is predicted in the combined

two-sigma region. Along with the parameterized signal selection efficiency the expected significance can be calculated, by counting the number of background and signal events inside the inner mass window.

As described above, this method only tests a certain MSSM benchmark scenario, as the predicted masses and widths for the neutral Higgs bosons for a given $(M_{A^0}, \tan\beta)$ point enter the search strategy. A search strategy independent on the assumed model is beyond the scope of this work. In general, one would consider a rather large mass window excluded from the background fit, to search for a generic Higgs boson resonance.

13.3 Scan Procedure

Now all components for a scan of the $(M_{A^0}, \tan\beta)$ plane are ready: The signal selection efficiencies are parameterized, a method to extract the background from data has been presented, and thus it is possible to predict the expected level of background, and an expected uncertainty on its measurement, as well as the expected number of signal events.

The scan procedure is thus very simple: For each scan point, the contributing Higgs bosons are determined, the mass window, as described in the previous section, is constructed and the expected number of accepted signal events is calculated.

To determine the number of background events, instead of counting the number of background events in the mass window, the fitting procedure as discussed in Chapter 12 is applied and the number predicted by the fit is used. As the Monte Carlo samples used in this work have the same statistics as the expected data, the statistical fluctuations of the Monte Carlo samples are not negligible. By using the number predicted by the fit, the sensitivity to these purely statistical fluctuations is reduced, since effectively the background contribution is smoothed. As shown in Chapter 12, the background fit yields an unbiased prediction of the background yield, but only without any signal contribution. To be able to perform the scan, the fit is nevertheless performed using a signal-free, background-only sample. It will therefore predict slightly less background than it will in the real experiment in case of a signal. In the real experiment, this slight bias will be subtracted from the signal, if present, thus decreasing the sensitivity. It should be noted that this procedure will be conservative, as the background might be over-estimated. However, since in the scan it is assumed that the background is correctly predicted by the fit procedure, the discovery significances will be slightly overestimated compared to the real experiment. In case that it will be possible to reduce the signal contribution outside the three-sigma mass window, not only the fit bias would be reduced, but also the signal efficiency inside the mass window could be increased. In this way, it might easily happen that in the real experiment, the effect of the fit bias could be overcome with more systematic studies. In the scan presented in this thesis the fit bias in presence of signal is neglected. The possible influence of this neglect on the discovery potential is discussed in Section 13.5.1.

13.3.1 Fit Stability

As already discussed in Chapter 12, the fit for the background extraction in Analysis II becomes unstable for mass windows very close to the Z^0 peak, since in this case the left part of the sidebands becomes very small, and the content of the few bins below the mass window have a large influence on the outcome of the fit. As it turns out, this leads to unexpected instabilities in the fitting procedure for Analysis II. The fit shows a trend towards chaotic behavior, where small changes of the initial conditions have a large influence on the outcome of the fit, and more importantly the accuracy of the calculated covariance matrix. But exactly this covariance matrix is used to determine the uncertainty on the number of background events, and has a potentially large influence on the calculation of the expected significance.

To ensure that this chaotic behavior does not have an influence on the analysis, instead the lower range of allowed A^0 masses is restricted. The ranges of M_{A^0} and $\tan\beta$ in the scan of the benchmark scenarios for the two analyses is listed in Table 13.1. Also in the other parts of the parameter space, the fit procedure for Analysis II sometimes does fail to reach convergence. Since in such an automated procedure it is not possible to treat each failed fit manually, the appearing inaccuracies of the expected significances are later accounted for by smoothing the distributions.

The M_{h^0} -max and no-mixing scenarios are a lot easier for fitting the background in the low mass range compared to the small α_{eff} and gluophobic scenarios. This is because the mass-degeneracy is best in these two scenarios, as discussed in Section 2.4.5.

For the no-mixing scenario the Higgs boson widths are a bit larger for a given $\tan\beta$ value compared to the M_{h^0} -max scenario, thus the effect is a more pronounced.

In the small α_{eff} scenario, the mass degeneracy between the h^0 and the A^0 is lifted by radiative corrections. So in contrast to e.g. in the M_{h^0} -max scenario, both the A^0 and the h^0 couple strongly to down-type fermions, thus contribute to the signal, yet are not mass degenerate. As a consequence, the mass window excluded in the background fit has to be made larger than for the M_{h^0} -max scenario, thus destabilizing the fit procedure. In addition the center of the mass window is then significantly lower than the mass of the A^0 .

scenario	Analysis I (b tag)		Analysis II (b tag)	
	M_{A^0}/GeV	$\tan\beta$	M_{A^0}/GeV	$\tan\beta$
M_{h^0} -max	110–400	10–50	117–400	10–50
no-mixing	111–400	10–50	119–400	10–50
gluophobic	112–400	10–50	125–400	10–50
small α_{eff}	113–400	10–50	125–400	10–50

Table 13.1: Ranges of the mass of the A^0 and $\tan\beta$ allowed in the scans of the four CP conserving benchmark scenarios.

In the gluophobic scenario, the same effect is observed.

It should be noted that the lower ranges of M_{A^0} are significantly above the exclusion bound from LEP [31]. This does not necessarily mean that Higgs bosons in this region of parameter space cannot be discovered by ATLAS, but in this analysis with the used background subtraction technique going to lower masses is not feasible.

13.4 Calculation of Significances

The method used up to now to estimate signal significances (S/\sqrt{B}) is only an approximation of the general discovery significances that is only valid for a large number of signal and background events, so that a Gaussian approximation is valid. Commonly a discovery is defined by the probability of the expected background to fluctuate to the level of the signal. A five-sigma discovery is declared if this probability is smaller than $2.87 \cdot 10^{-7}$.

However, as presented previously, the levels of background and signal events in the two analyses vary strongly with the signal mass under consideration due to the steeply falling invariant mass spectrum of the background contributions. In addition, the S/\sqrt{B} approximation does not allow to include background uncertainties in a direct way, and also does not ensure correct coverage of the resulting confidence interval.

Instead, a method based on the so-called *profile likelihood* is used, which is described in more detail in Appendix C.2. It is based on the general method presented in [157] and [158], and has been modified by the ATLAS statistics working group [159]. It is based on a fully frequentist approach with some approximations, that has been shown to give good coverage of confidence intervals [157, 158]. In addition it provides the possibility to include background uncertainties in a direct way. Also with this method, a significance corresponding to the quantiles of the Gaussian distribution is constructed.

13.4.1 Inclusion of Systematic Uncertainties

The experimental and theoretical systematic uncertainties presented in Chapter 11 don't have a direct influence on the expected significances, as the background can be measured from data. In this way, the only uncertainty entering the discovery sensitivity is the one obtained from the fit of the background prediction in the inner mass window.

However, the experimental and theoretical uncertainties represent the possible differences between the prediction of the outcome of the experiment and the real outcome. As the real experiment is not yet running, they have to be taken into account as an uncertainty of the predicted discovery significances.

This is done by applying the complete scan procedure again, with one systematic variation, e.g. a lower jet energy scale, applied. This is done simultaneously for signal and background, as well as for the two analyses to take into account correlations between the different systematic uncertainties.

$(M_{A^0}, \tan \beta) =$ Analysis	(120 GeV, 30)			(300 GeV, 50)		
	I	II	$I \oplus II$	I	II	$I \oplus II$
μ energy scale $\times 1.01$	-2.4	-9.4	-5.4	+0.2	-1.4	-0.5
μ energy scale down $\times 0.99$	+2.8	+4.2	+3.4	+4.5	+1.4	+3.0
μ resolution smearing	-0.1	-5.2	-2.3	+0.6	-1.8	-0.5
muon isolation shape	-1.3	-0.9	-1.1	+0.5	+0.7	+0.6
muon efficiency +2%	+0.9	-1.8	-0.3	+1.0	+0.6	+0.8
muon efficiency -2%	-1.4	-3.7	-2.4	-1.1	-2.4	-1.8
jet energy scale $\times 1.07/1.15$	+2.6	-0.7	+1.1	+1.0	-0.5	+0.2
jet energy scale $\times 0.95/0.85$	-5.3	+0.9	-2.4	-0.9	+0.6	-0.1
jet resolution smearing	-1.4	+0.0	-0.8	+2.3	+0.1	+1.2
$\epsilon_b \times 1.05$	+2.7	-0.8	+1.1	+5.2	-1.5	+1.9
$\epsilon_b \times 0.95$	-3.0	+0.7	-1.2	-3.6	+1.5	-1.0
$R_{\text{udsg}} \times 1.2$	+1.9	-0.1	+0.9	-0.1	+0.0	-0.1
$R_{\text{udsg}} \times 0.8$	-1.6	+0.0	-0.8	+0.7	+0.0	+0.3
$\cancel{E}_T: s = 2.1$	+1.0	+0.4	+0.7	+5.2	+1.7	+3.5
$\cancel{E}_T: s = 2.7$	-2.9	-1.1	-2.1	-0.6	-2.4	-1.5
Luminosity $\times 1.03$	+0.3	+0.7	+0.5	+0.8	+1.1	+0.9
Luminosity $\times 0.97$	-0.9	-0.9	-0.9	-0.8	-1.2	-1.0
mass window larger	+2.9	+1.9	+2.5	+0.6	+3.3	+2.0
mass window smaller	-3.2	-3.1	-3.1	-2.9	-3.4	-3.1
total experimental (up)	+6.1	+4.9	+4.8	+9.3	+4.6	+5.8
total experimental (down)	-8.4	-12.2	-8.3	-5.0	-5.8	-4.3

Table 13.2: Experimental uncertainties (in %) on the predicted significances for two selected scan points in the M_{h^0} -max scenario.

The significances at each scan point are recalculated. The differences to the significance without a systematic variation are added quadratically to obtain a total uncertainty on the predicted significance.

Table 13.2 and 13.3 show the experimental and theoretical uncertainties on the predicted significances for two selected scan points. Obviously, the total uncertainty is dominated by the uncertainty of the signal cross section of the $b\bar{b}A^0$ process. The experimental uncertainties only contribute significantly for large masses in Analysis I.

A good example of the behavior of the significances is given by the jet energy scale. Although it was observed that especially the $t\bar{t}$ background is influenced very strongly by

$(M_{A^0}, \tan \beta) =$ Analysis	(120 GeV, 30)			(300 GeV, 50)		
	I	II	$I \oplus II$	I	II	$I \oplus II$
$\sigma(t\bar{t}) \times 0.88$	+0.7	-0.2	+0.3	+4.4	+0.1	+2.3
$\sigma(t\bar{t}) \times 1.12$	-0.9	+0.0	-0.5	-4.2	-0.2	-2.2
$\sigma(tW) \times 0.97$	-0.4	+0.0	-0.1	+0.0	+0.0	+0.0
$\sigma(tW) \times 1.03$	+0.0	-0.2	-0.1	+0.0	+0.0	+0.0
$\sigma(WW) \times 0.8$	-0.2	+0.2	+0.0	+0.8	+1.1	+0.9
$\sigma(WW) \times 1.2$	-0.2	-0.2	-0.2	-0.7	-1.2	-1.0
$\sigma(Z^0 Z^0) \times 0.8$	-0.4	-0.3	-0.3	+0.0	+0.0	+0.0
$\sigma(Z^0 Z^0) \times 1.2$	+0.0	-0.1	-0.1	+0.0	+0.0	+0.0
$\sigma(Z^0 + b) \times 0.87$	+2.6	+0.1	+1.5	+0.5	+0.0	+0.3
$\sigma(Z^0 + b) \times 1.1$	-2.2	-0.2	-1.3	-0.5	+0.0	-0.3
$\sigma(Z^0 + \text{light}) \times 0.92$	+2.1	+6.0	+3.9	+1.0	+4.1	+2.5
$\sigma(Z^0 + \text{light}) \times 1.06$	-2.0	-4.4	-3.0	-0.8	-2.9	-1.8
$\sigma(b\bar{b}A^0)$ up	+17.9	+19.7	+18.7	+9.7	+17.3	+13.6
$\sigma(b\bar{b}A^0)$ down	-22.3	-22.5	-22.4	-11.5	-18.4	-14.9
$\sigma(gg \rightarrow A^0) \times 1.15$	+0.2	+2.8	+1.3	+0.0	+0.8	+0.4
$\sigma(gg \rightarrow A^0) \times 0.85$	-0.2	-2.8	-1.3	+0.0	-0.8	-0.4
total theoretical up	+18.3	+20.8	+19.3	+10.9	+17.9	+14.1
total theoretical down	-22.5	-23.2	-22.8	-12.4	-18.7	-15.3

Table 13.3: Theoretical uncertainties (in %) on the predicted significances for two selected scan points in the M_{h^0} -max scenario.

this uncertainty, its impact on the significances is very limited. This is caused by two facts: First, also the signal shows a similar behavior, its rate increases or decreases in the same general direction as the backgrounds. Second, if more background enters through a systematic variation, it also means that the number of events in the sideband regions becomes larger. This leads to a better prediction of the background in the inner mass window due to the larger sideband statistics. This counterbalances the effects of the systematic uncertainties of the event yields on the expected significances somewhat.

This method also takes care of possible numerical instabilities of the fit procedure, since each of these variations corresponds to a small change of the input parameters, thus also covering random fluctuations from possible fit failures. These effects are later smoothed out to obtain mean significances of parameter regions, so the significance in a region is decreased if the fit fails regularly in it.

13.5 Results

The expected significances are shown in Figures 13.7 and 13.8 for the two analyses and in Figure 13.9 for the combination of these two. They have been smoothed by a kernel algorithm, as implemented in ROOT [156].

The significances are in general higher for larger $\tan\beta$ and low masses of the A^0 . This is a direct consequence of the production cross section, which is enhanced for large $\tan\beta$ and falls off very fast with the mass of the Higgs boson.

The other visible structures in the significances can be explained either by mass values of the A^0 , where Analysis II is switched off due to getting too close to the lower end of the fit region, or due to regions where more than two Higgs bosons contribute and the mass window has to be chosen larger as a consequence, thus allowing for more background and a worse background measurement.

For example in the M_{h^0} -max scenario, around $M_{A^0} = 130$ GeV all three Higgs bosons contribute simultaneously. For the small α_{eff} scenario, the change-over between h^0 and H^0 happens over a comparatively small range of A^0 masses, and thus is barely visible around 120 GeV.

In the gluophobic scenario the very rapid drop of significances is explained by the fact that here the change-over between h^0 and H^0 is very slow, thus the mass window has to be chosen very large already very early.

One other structure visible is a stripe of lower significances around $M_{A^0} = 200$ GeV for Analysis II. It runs over a certain range in $\tan\beta$ and disappears again. It has been identified as a region where the background fit has difficulties to converge. In principle, this could be fixed by using different fitting techniques or varying the starting points for the fit. In this work, this region is manually smoothed out using linear extrapolation between the adjacent regions. There is no reason to expect that the fit cannot converge if treated more extensively.

The 5σ discovery contours are shown in Figures 13.10 to 13.12, along with its combined experimental and theoretical uncertainties in both directions. Also shown are the regions of parameter space excluded by LEP [31] and by the currently most sensitive single analysis of the CDF collaboration [51]¹. It should be noted that the LEP limits shown have been calculated in [31] using a mass of the top quark of 174.3 GeV, while in the scan of this study the latest result of 172.5 GeV [1] has been used. Also shown is the contour obtained if the background could be predicted with complete accuracy, to show the power of the analyses.

Some general observations valid for all four scenarios can be done:

1. Analysis I is more sensitive at low masses than Analysis II. This is because the background fit can be extended to lower masses and allows this analysis to work properly also at low masses.
2. For intermediate to high masses Analysis II contributes more or less as much as Analysis I. Combining the two analyses allows to significantly increase the region of a possible discovery.

¹The CDF collaboration has not interpreted its data in the gluophobic or small α_{eff} scenario.

3. As expected from the significances, the analyses are less sensitive if more than two, or non-mass degenerate, Higgs bosons have to be covered.
4. For Analysis I a worsening of the discovery contour is visible just below 300 GeV. This is because starting in this region, the background prediction is extrapolated to higher masses. If the mass window is in this region, it reduces the range available to fit the background, thus worsening the significance. The effect is largest for the no-mixing scenario, as here for a given $\tan\beta$ the total width of the Higgs bosons is largest, and thus also the width of the mass window.

In the following the results of the four benchmark scenarios are discussed in more detail.

- The M_{h^0} -max scenario shows the best discovery potential for low masses. This is because in this scenario at low masses, the h^0 and A^0 are almost perfectly mass degenerate, thus the fit window becomes very small. In the intense coupling region around $M_{A^0} = 130$ GeV the Higgs bosons could be discovered if $\tan\beta$ is larger than about 20. For slightly higher masses, even lower $\tan\beta$ are explorable.
- The discovery region for Higgs bosons around 150 GeV is even slightly larger in the no-mixing scenario compared to the M_{h^0} -max scenario. This is because of a slightly larger signal cross section, which is a consequence of different radiative corrections in this scenario.
- In the gluophobic scenario, the drop-off in sensitivity for lower masses is much more pronounced. Also for the higher masses, the discovery region is slightly smaller than for the first two scenarios. One visible feature is the steeper slope of the discovery region for masses above 290 GeV. This can be traced back to the MSSM particle spectrum generated by FEYNHIGGS: In this scenario the lightest stop squark, the \tilde{t}_1 is very light, with a mass of about 145 GeV. The H^0 boson can then decay into $\tilde{t}_1\tilde{t}_1^*$. This becomes the dominant decay mode of the H^0 , increasing its total width significantly, and reducing branching fraction of the muonic decay mode. The A^0 boson cannot decay to $\tilde{t}_1\tilde{t}_1^*$ because of the different CP quantum number.
- In the small α_{eff} scenario, as discussed previously, the discovery potential at low masses is diminished due to the larger separation between h^0 and A^0 , thus forcing a larger mass window. Also, the difference between the discovery contour with and without uncertainty of the background prediction is larger, which is again due to the larger mass window. For high masses, this scenario is very similar to the other ones.

Overall, more or less independent on the scenario, one or more of the neutral Higgs bosons can be discovered in the muonic decay mode at the LHC for low masses down to $\tan\beta$ about 20 using a dataset of 30 fb^{-1} of well understood data. The systematic uncertainties on this prediction are dominated by the uncertainties of the main signal process, the b associated production mode. Very low M_{A^0} are not accessible with the analysis presented in this work. To close the gap between the LEP limits and this analysis, either different Higgs boson production and decay channels, or a dedicated analysis dealing with a Higgs boson almost on top of the Z^0 resonance would have to be devised, in which this background is predicted from data with high accuracy.

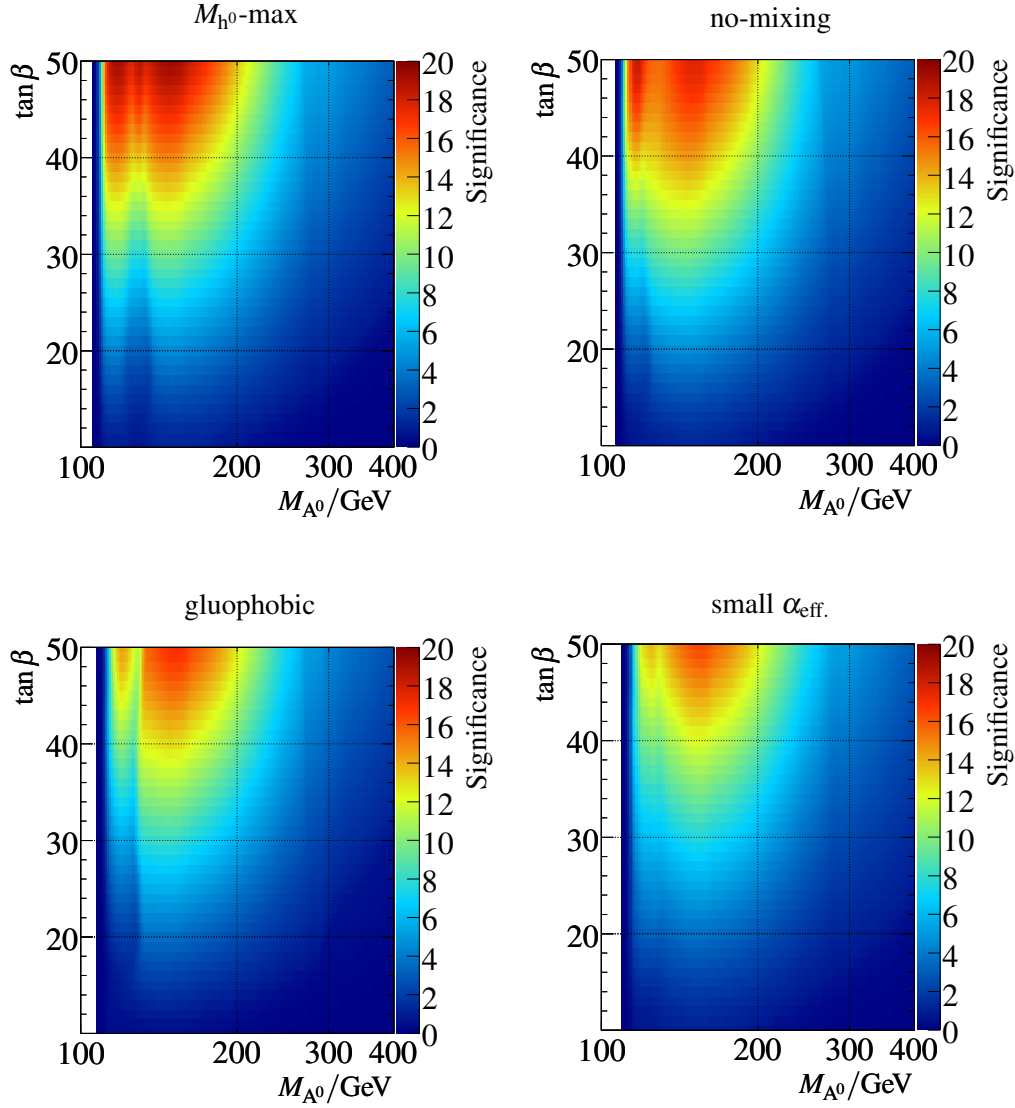


Figure 13.7: Expected discovery significances for Analysis I (b tag) with the central signal efficiencies and background contributions in the $(M_{A^0}, \tan \beta)$ plane in the four CP conserving benchmark scenarios assuming an integrated luminosity of 30 fb^{-1} .

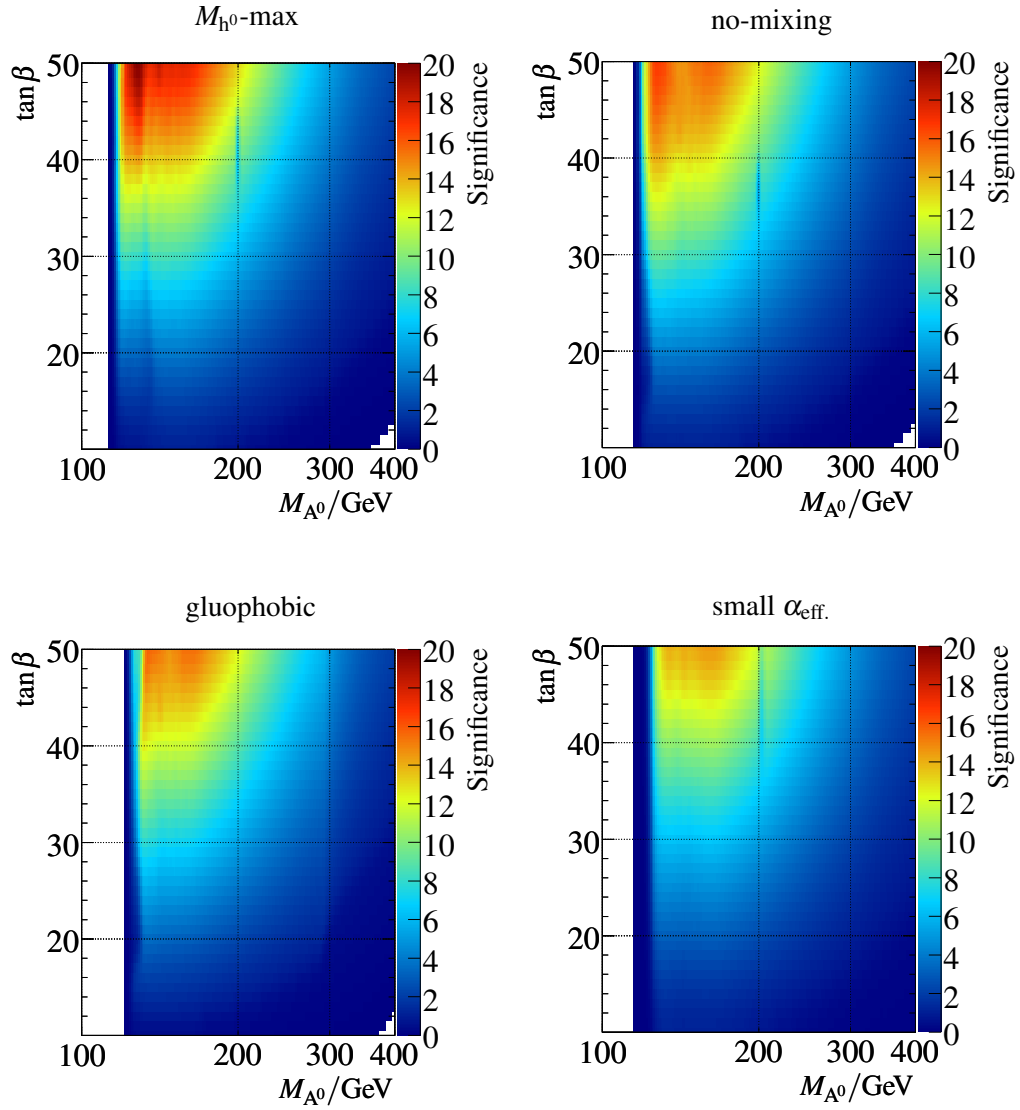


Figure 13.8: Expected discovery significances for Analysis II (b veto) with the central signal efficiencies and background contributions in the $(M_{A^0}, \tan\beta)$ plane in the four CP conserving benchmark scenarios assuming an integrated luminosity of 30 fb^{-1} .

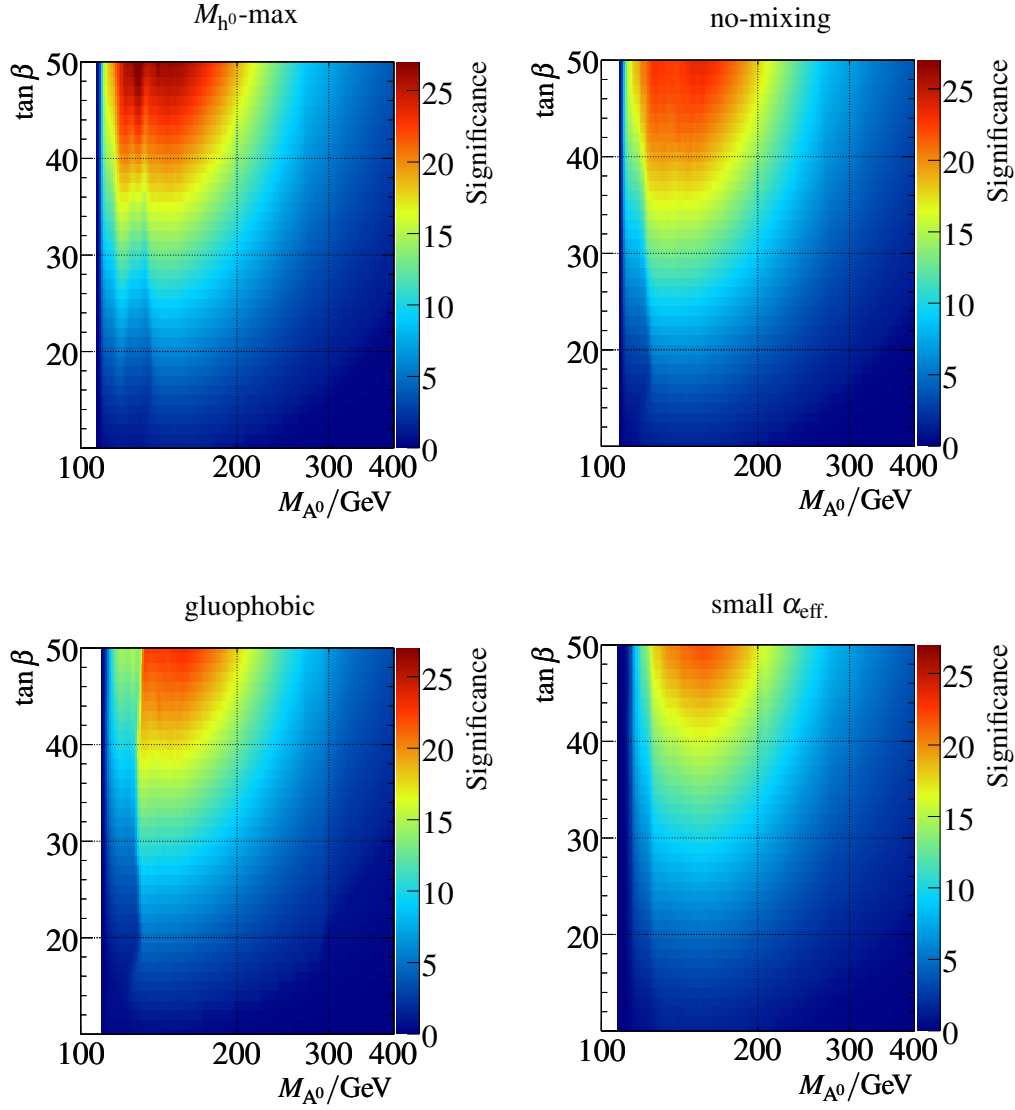


Figure 13.9: Expected discovery significances for the combination of Analysis I and II with the central signal efficiencies and background contributions in the $(M_{A^0}, \tan \beta)$ plane in the four CP conserving benchmark scenarios assuming an integrated luminosity of 30 fb^{-1} .

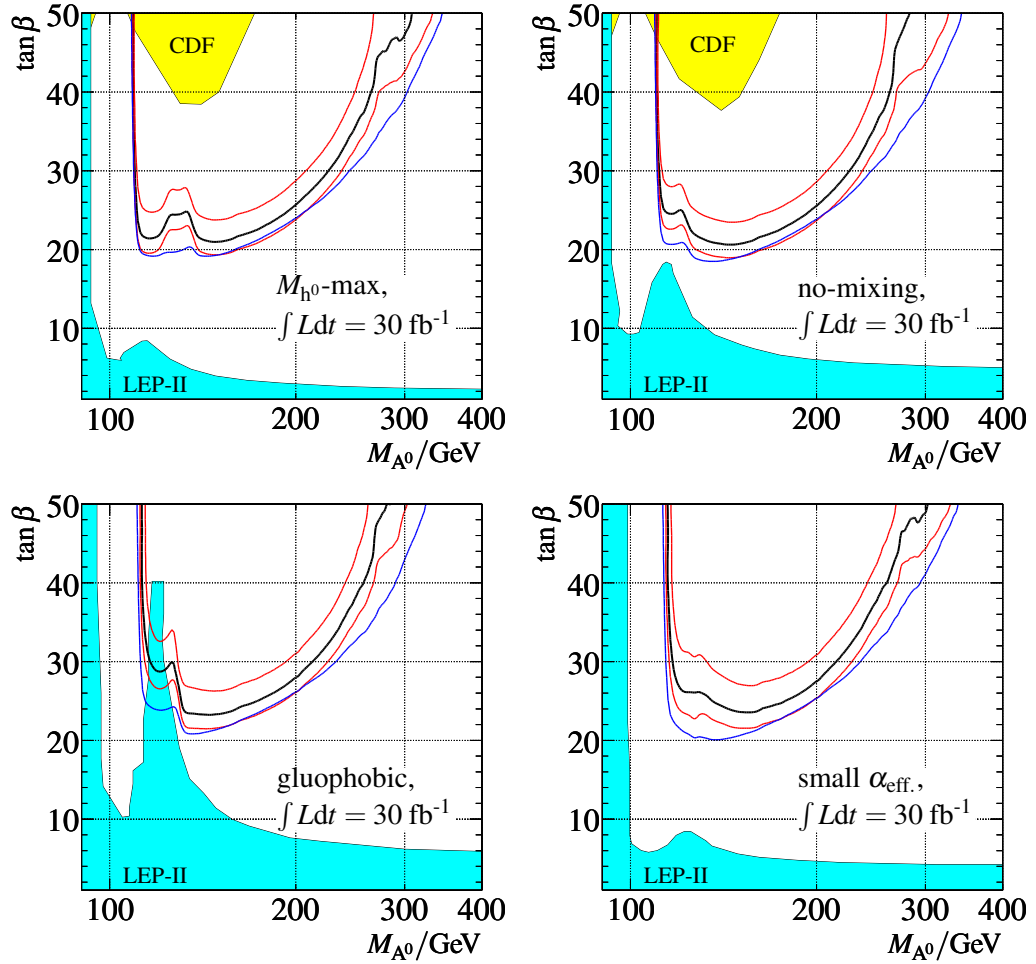


Figure 13.10: Discovery potential for Analysis I (b tag) in the $(M_{A^0}, \tan\beta)$ plane in the four CP conserving benchmark scenarios assuming an integrated luminosity of 30 fb^{-1} . Black line: 5σ contour level, red lines: 5σ contours when applying theoretical and experimental uncertainties (both directions), blue line: 5σ contour if the background is assumed to be known without uncertainties. Yellow shaded area: Excluded by CDF [51], blue shaded area: excluded by the LEP experiments [31] at the 95% confidence level. The LEP exclusion contour in the gluophobic scenario is truncated at $\tan\beta = 40$.

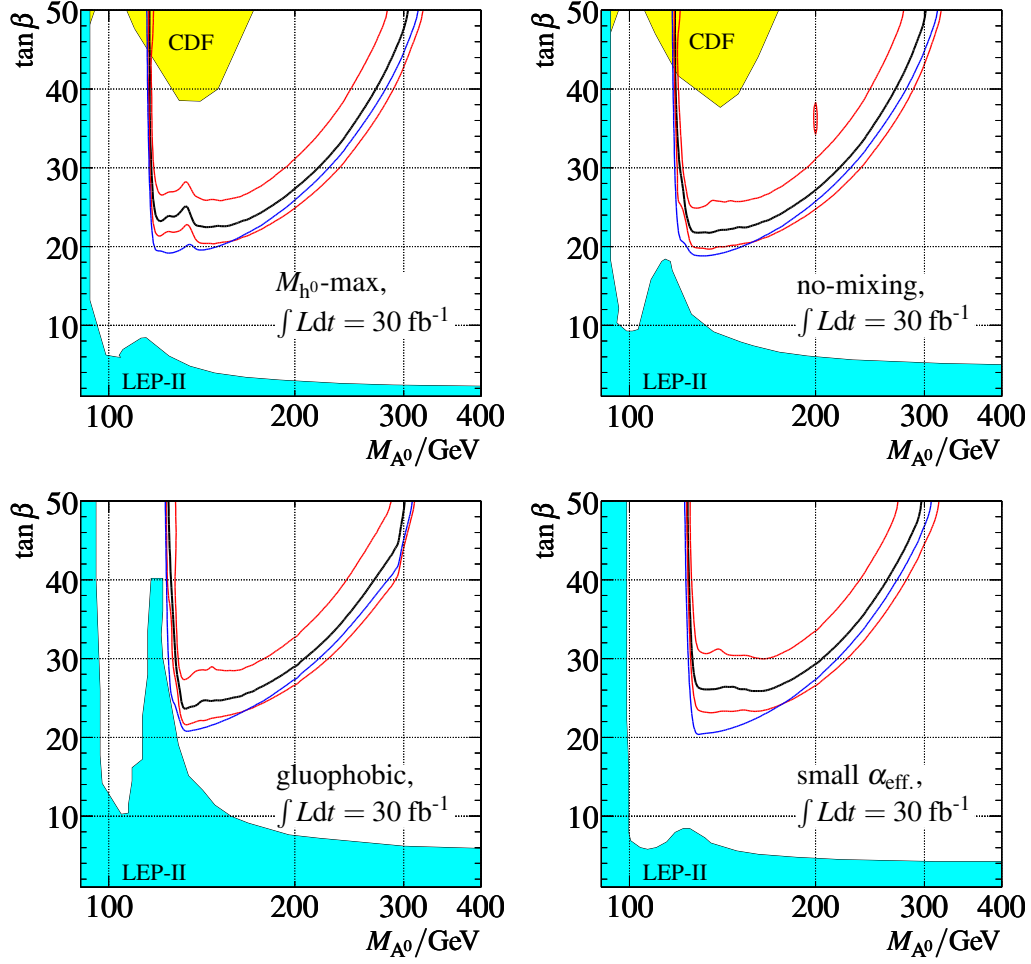


Figure 13.11: Discovery potential for Analysis II (b veto) in the $(M_{A^0}, \tan \beta)$ plane in the four CP conserving benchmark scenarios assuming an integrated luminosity of 30 fb^{-1} . Black line: 5σ contour level, red lines: 5σ contours when applying theoretical and experimental uncertainties (both directions), blue line: 5σ contour if the background is assumed to be known without uncertainties. Yellow shaded area: Excluded by CDF [51], blue shaded area: excluded by the LEP experiments [31] at the 95% confidence level. The LEP exclusion contour in the gluophobic scenario is truncated at $\tan \beta = 40$.

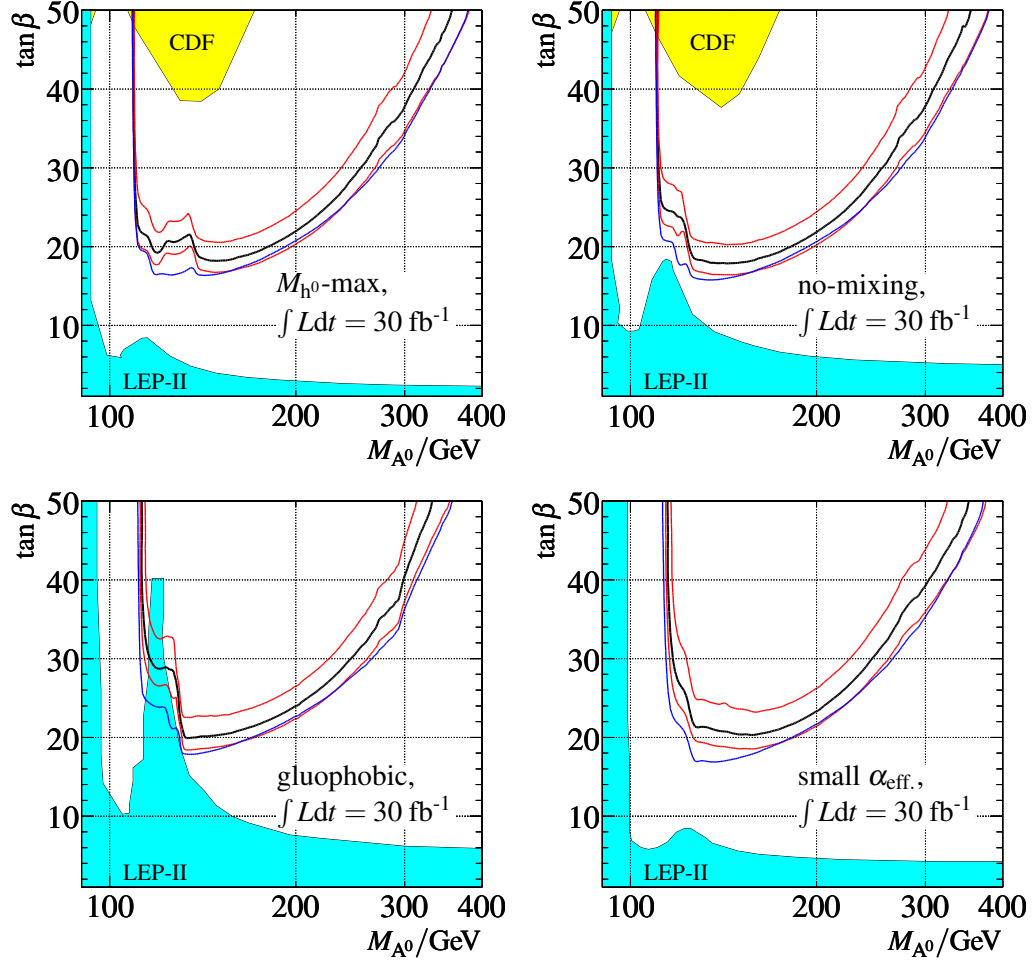


Figure 13.12: Discovery potential for the combination of Analysis I and II in the $(M_{A^0}, \tan\beta)$ plane in the four CP conserving benchmark scenarios assuming an integrated luminosity of 30 fb^{-1} . Black line: 5σ contour level, red lines: 5σ contours when applying theoretical and experimental uncertainties (both directions), blue line: 5σ contour if the background is assumed to be known without uncertainties. Yellow shaded area: Excluded by CDF [51], blue shaded area: excluded by the LEP experiments [31] at the 95% confidence level. The LEP exclusion contour in the gluophobic scenario is truncated at $\tan\beta = 40$.

13.5.1 Influence of the Mass Tail

In the scan procedure any contribution of the signal outside the three-sigma mass window has been neglected. As discussed in Section 10.2.1, this means that the result of the scan does not represent the true experiment when the fit is applied to a sample with real signal content. In this case the fit would yield a slightly too large background prediction, thus reducing the effective signal yield and at the same time slightly increasing the background contribution inside the two-sigma mass window.

This effect cannot be taken into account easily during the scan procedure. As the size of the fit bias depends on the signal yield, the resulting shift in the significances is dependent on the significances themselves. To analyze the impact of the effect the significances have been evaluated at a few selected points in the vicinity of the 5σ discovery contour level. At these points signal Monte Carlo samples are to the background, the fit is redone and the background prediction subtracted from the combined background and signal contribution inside the two-sigma (inner) mass window. The significances are evaluated once for the case when the fit is done to a signal plus background sample and once when only the background is fitted and the signal is not diminished by the fit bias.

The resulting relative differences of the significances are listed in Table 13.4.

The difference between performing the fit with and without signal included in the spectrum is very small for Analysis I. At most, the significance changes by 5% in the region of a 5σ discovery. This is a lot smaller than the systematic uncertainties, which are dominated by the uncertainty of the signal cross section. For low M_{A^0} this would correspond to a shift of the discoverable $\tan\beta$ of at most 0.5, which is negligible.

For Analysis II large effects can be seen for small masses. This is again due to the smaller lever arm of the left sideband. If there is a signal pollution in it, it can have a larger influence than in the case of larger lever arms. However, at small masses, where the effect is largest, the combined significance is dominated by Analysis I anyway, so this would not change the overall picture. For larger masses, deviations of the order of at most 10% are seen.

Keeping in mind that the $b\bar{b}A^0$ cross section in Analysis II was assigned a very conservative additional 15% systematic uncertainty due to the matching scale effect, this is again a very small effect. It would correspond to a shift of the reachable $\tan\beta$ of between one at small masses and 2.5 to 3 at large masses.

A correction for this effect is not applied, as the reason for mass tail is not completely clear. Also there seems to be a statistical component in the observed shifts, that is not easily quantifiable. It might be possible that the mass distribution in real data is different. Already a slightly smaller tail would be sufficient to remedy the effect altogether. This is caused by the fact that if events in the mass tail move to the actual center of the distribution, this at the same times increases the signal selection efficiency inside the two-sigma mass window and reduces the fit bias in a twofold way.

Analysis I		Analysis II	
$(M_{A^0}, \tan \beta)$	$\frac{S_{\text{unbiased}} - S_{\text{biased}}}{S_{\text{biased}}}$	$(M_{A^0}, \tan \beta)$	$\frac{S_{\text{unbiased}} - S_{\text{biased}}}{S_{\text{biased}}}$
(110, 20)	-3.1%	(120, 25)	-14%
(130, 25)	-3.5%	(130, 25)	-1%
(150, 20)	-3.2%	(150, 20)	-9%
(200, 35)	-1.5%	(200, 30)	-1%
(250, 35)	-4.0%	(250, 35)	-2%
(300, 50)	-1.0%	(300, 50)	-7%

Table 13.4: Relative change in significances if the background fit is performed without any signal contribution (S_{unbiased}) and if performed with the actual background contributing (S_{biased}) in the M_{h^0} -max scenario of the two analyses. The points have been chosen to be close to the 5σ discovery contour.

13.5.2 Possible Improvements

The method presented in this thesis can probably be improved on to improve the discovery potential of the neutral MSSM Higgs bosons. In the background extraction and significance calculation, all that is used is the number of events in the inner mass window. However, there is additional information in the shape of the invariant mass distribution. This could be taken into account in a shape-sensitive analysis. A statistical fluctuation is very unlikely to produce a peak shaped just like the expected signal.

However, such a shape analysis would need good knowledge of the shape of the mass resolution and in principle would also need to assume a separation and widths of the contributing Higgs bosons. A shape analysis is not done in this work.

13.6 Resolving Multiple Higgs Bosons

One of the most astonishing features of the studied decay channel is the very good dimuon mass resolution. This already helped to efficiently reduce the background contributions and allowed for a sideband fit to measure the background in data.

However, in the MSSM parameter scan presented in the previous section, the mass window was chosen to encompass all contributing Higgs bosons, and not to separate them from each other.

In certain parts of the parameter space it might be possible to actually observe the neutral MSSM Higgs bosons separately. For this, first the separation between them has to be large, then the states have to couple strongly to b quarks to be visible in b associated production, and last the reconstructed widths of the resonances have to be small enough so that they can be observed separately. Unfortunately, these parameters are contradicting. The signal rate is much larger for large $\tan \beta$, thus increasing the overall chance of a discovery. But at the same time the mass difference of the neutral Higgs bosons becomes

smaller and the natural decay width becomes larger. In addition for larger $\tan\beta$ the cross-over between the h^0 and the H^0 to couplings similar to the Standard Model Higgs boson happens in a smaller mass interval. All this makes the observation of multiple Higgs boson states difficult.

To quantify this, the mass difference between the h^0 or H^0 with the A^0 is calculated. The mass resolution and natural widths are taken into account by normalizing this difference to the quadratic sum of the reconstructed widths according to the parameterization discussed in Section 10.2:

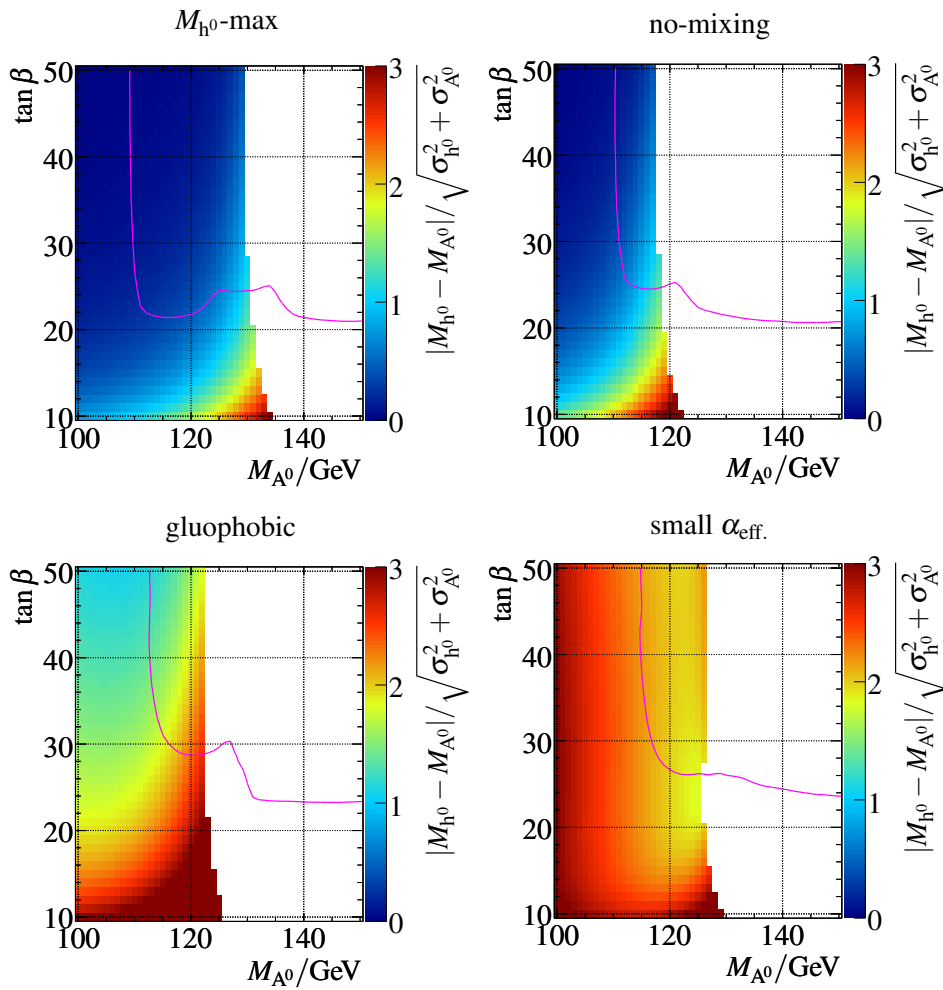


Figure 13.13: Mass difference between the h^0 and the A^0 boson divided by the quadratic sum of the reconstructed widths in the $(M_{A^0}, \tan\beta)$ plane for the four CP conserving benchmark scenarios. A point is only filled if the partial width of the h^0 into $b\bar{b}$ is at least one third of the one of the A^0 . The magenta line is the 5σ discovery contour of Analysis I.

$$\Delta M_{\text{norm}} = \frac{|M_\phi - M_{A^0}|}{\sqrt{\sigma_\phi^2 + \sigma_{A^0}^2}} \quad (13.1)$$

To take into account only neutral Higgs bosons produced significantly in b associated production, the partial width of the h^0 or H^0 is required to be at least one third of the one of the A^0 boson.

Figures 13.13 and 13.14 show the results in the four benchmark scenarios. The discovery contour for Analysis I using 30 fb^{-1} is superimposed. Analysis II is not used in this

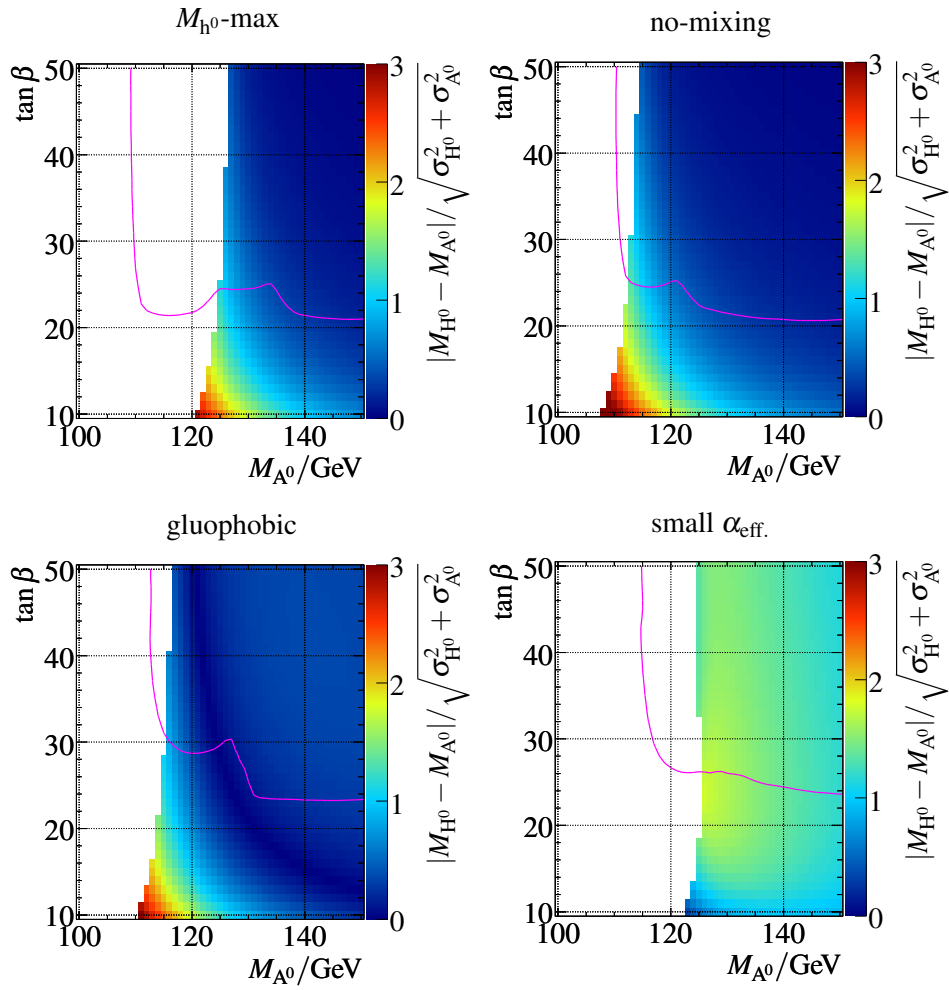


Figure 13.14: Mass difference between the H^0 and the A^0 boson divided by the quadratic sum of the reconstructed widths in the $(M_{A^0}, \tan\beta)$ plane for the four CP conserving benchmark scenarios. A point is only filled if the partial width of the H^0 into $b\bar{b}$ is at least one third of the one of the A^0 . The magenta line is the 5σ discovery contour of Analysis I.

study due to the far worse signal to background ratio, which has not a large influence on the discovery potential, but is important to be able to separate the two Higgs boson states. In the M_{h^0} -max and no-mixing scenarios, a separation between two or three Higgs boson states is not possible. For a large separation, $\tan\beta$ has to be in the low range, which is not within the discovery region.

The situation is a lot different in the gluophobic and the small $\alpha_{\text{eff.}}$ scenarios. Due to the lifted mass degeneracy in these scenarios, the separation between the h^0 and the A^0 might be on the level of more than two standard deviations for $M_{A^0} \approx 120$ GeV. For the small $\alpha_{\text{eff.}}$ scenario, the separation becomes even larger for very small masses of the A^0 boson due to the increasing mass resolution. However, the h^0 would then sit right on top of the Z^0 resonance and a discovery is not possible.

To illustrate how the signal on top of the backgrounds with the largest separations in the small $\alpha_{\text{eff.}}$ and the gluophobic scenario look, Figure 13.15 shows the invariant mass spectrum for $M_{A^0} = 120$ GeV and $\tan\beta = 35$ for the two scenarios. If the background can be subtracted, indeed the two mass peaks might be separated somewhat. However, the separation is no way perfect. A very good understanding of the invariant mass resolution will be necessary to exploit the rather large separation and claim a discovery of two separate Higgs boson states.

In addition to a possible separation of the different Higgs boson states, a very good understood dimuon mass resolution might allow to reconstruct the Higgs width. For large $\tan\beta$, as shown in Section 10.2, the natural width does contribute to the width of the reconstructed resonance. By using a well known dimuon detector resolution and a good modeling of the effects of QED final state radiation, it might be possible to unfold the background subtracted mass spectrum and obtain a measurement of the Higgs bosons natural line width. This would allow a measurement of $\tan\beta$ if a specific MSSM parameter point is chosen. However, such a measurement of $\tan\beta$ would be limited by the theory input: Without knowing all other 104 MSSM parameters, a one-to-one relation between

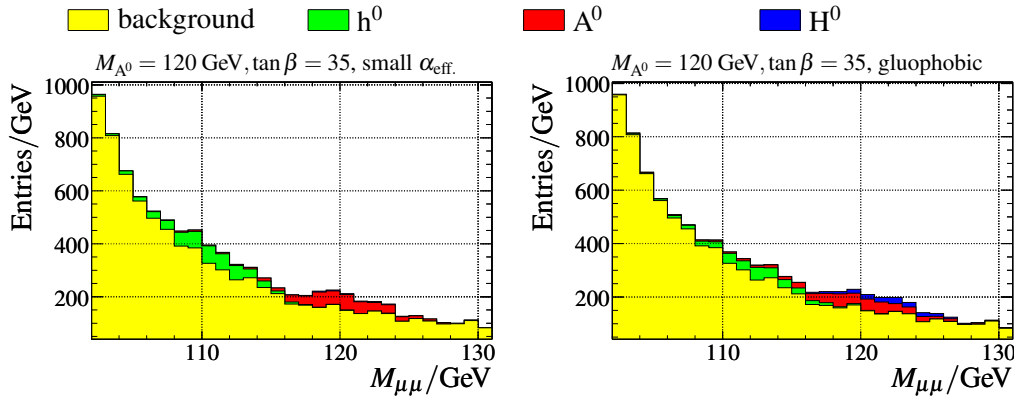


Figure 13.15: Invariant mass spectra for $M_{A^0} = 120$ GeV, $\tan\beta = 35$ in the small $\alpha_{\text{eff.}}$ (left) and the gluophobic (right) scenarios for an integrated luminosity of 30 fb^{-1} indicating background and signal contributions.

the Higgs boson width and $\tan\beta$ is not available, so a measurement of $\tan\beta$ can only be done if a specific scenario is assumed.

“I think and think for months and years. Ninety-nine times, the conclusion is false. The hundredth time I am right.”

Albert Einstein, 1879–1955

14

Conclusions and Outlook

In this work a Monte Carlo study of neutral MSSM Higgs bosons decaying into muons at the ATLAS experiment is presented.

Within this study special emphasis has been placed on the usage of novel Monte Carlo tools that promise to give a better description of the proton-proton collisions that will soon start at the Large Hadron Collider. The SHERPA generator has been validated within this thesis for its usage in b-associated Higgs boson production. A method to normalize its output to higher order calculations is proposed. Also the background processes relevant for this study are normalized to higher order calculations.

Correction procedures for the ATLAS fast detector simulation are devised that lead to a better agreement with the detailed simulation and reconstruction.

A cut-based event selection consisting of two sub-analyses is implemented and optimized for the discovery of the neutral Higgs bosons of the MSSM in parameter regions with large $\tan\beta$. The large theoretical and experimental uncertainties make a data-based method to extract the background desirable. A sideband fit is used on the simulated data to evaluate this possibility.

The ATLAS discovery potential for neutral Higgs bosons of the MSSM is evaluated in the four CP conserving benchmark scenarios of [33]. The result is shown for the M_{h^0} -max scenario in Figure 14.1 assuming an integrated luminosity of 30 fb^{-1} . For the other benchmark scenarios similar regions of the MSSM parameter space allow for a discovery.

The sensitivity of ATLAS to the neutral Higgs bosons of the MSSM is overall much larger than the one of the LEP [31] and Tevatron experiments [50–53].

Low masses of the pseudoscalar Higgs boson A^0 just above the LEP exclusion limit are not accessible using the applied background extraction method, as the signal peak would be

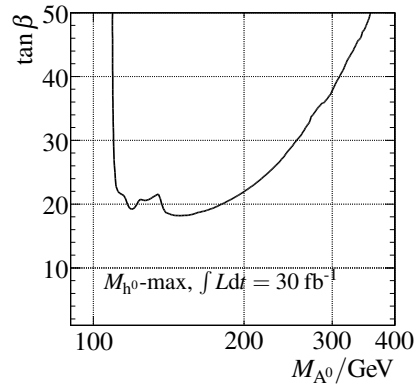


Figure 14.1: Discovery region in the $(M_{A^0}, \tan\beta)$ plane.

too close to the Z^0 peak. For this region a dedicated analysis would be needed to discover the MSSM Higgs bosons in the muonic decay mode.

For large masses of the A^0 and for small $\tan\beta$, the MSSM Higgs bosons will not be observable at the LHC in the muonic decay mode. But also in this case, at least one Higgs boson will be in the discovery reach of other production and decay channels.

The first collisions at the LHC are expected in the near future. This collider with its unprecedented center-of-mass energy and luminosity will be a major step in experimental particle physics, as it opens a new energy scale for the direct study. The Standard Model Higgs boson, if it exists, will definitely be discovered at the LHC. Also in the MSSM at least one Higgs boson will be discovered, if this model is realized in nature.

Before these big expectations can be met, the detectors like ATLAS, which are in themselves immensely complex devices, have to be calibrated and understood first. Also the event and detector simulation programs will have to be compared to the real output of the experiments and changed where necessary. As never before proton-proton collisions at the LHC center-of-mass energy have been observed in a collider experiment, it can be expected that significant tuning of the event simulation will be necessary to get the simulation in agreement with the data.

At the same time it will be of utmost importance to first observe Standard Model processes at the LHC and verify that their properties are as expected. Standard Model processes like Z^0 or $t\bar{t}$ production will provide ideal standard candles for calibration of the detector and for verification of the reconstruction performance.

After this initial period of detector calibration and understanding is passed, the time will come to probe the mechanism of mass generation for the first time. Also, in addition to Higgs bosons, either in the Standard Model or the MSSM, ATLAS will be sensitive to a lot of other phenomena beyond the Standard Model. The production of superpartners of the Standard Model particles is just one example, but also e.g. extra space-time dimensions will be in the discovery reach of the LHC experiments.

The LHC will finally put an end to the quest for the Higgs boson, but this will only be the start of the next steps: If only one Higgs boson is observed, it will be necessary to check whether it is the Standard Model Higgs boson, or if it is only one of the five Higgs bosons predicted in supersymmetry. If supersymmetry is discovered, immediately the question of the SUSY breaking mechanism has to be asked. A lot of these questions can already be probed at the LHC, but a hadron collider it is not well suited for the precise measurements necessary to answer these questions. The proposed International Linear Collider, which would be an e^+e^- collider reaching a center-of-mass energy of up to 1 TeV would be very well suited to perform these precision measurement.

“We are driven to the conclusion that the Hamiltonian method for strong interaction is dead and must be buried, although of course with deserved honor.”

Lev Davidovich Landau, 1908–1968



Strong Interactions as Gauge Theory

The interaction of quarks with each other can be described within a local gauge theory. It is called Quantum Chromodynamics (QCD) and is based on the $SU(3)_C$ gauge group. It is a non-abelian group, just as $SU(2)$, and as a consequence the gauge bosons, the gluons, carry color themselves and interact with each other. The gluons are massless particles. The short range of strong interactions is in contrast to weak interactions not caused by the high mass of the gauge bosons. Rather it is caused by the fact that QCD is an asymptotic free theory [160], which means that the coupling constant α_s decreases with energy. At low scales the coupling constant gets close to unity and the theory is no longer perturbative. As a consequence there are no free quarks or gluons, rather they are *confined* inside colorless hadrons¹. More detail about QCD as a gauge theory can be found in in Ref. [161].

Starting from the free Lagrangian in Eq. 2.1, where it has to be kept in mind that the fermion now also carries a color charge, the gauge transformation is now expressed by a rotation in color space:

$$\psi(x) \rightarrow e^{i\vec{\alpha}(x)\vec{T}} \psi(x) \quad (\text{A.1})$$

Here $\vec{\alpha}(x)$ are eight phase factors and \vec{T} is a set of eight linearly independent traceless 3×3 matrices, which are the generators of the $SU(3)$ group and can be represented by the Gell-Mann matrices. In order to achieve gauge invariance, one has to introduce eight gauge fields \vec{G}_μ and the covariant derivative is defined as

$$D_\mu = \partial_\mu + i g_s \vec{T} \vec{G}_\mu, \quad (\text{A.2})$$

¹It should be noted that the ultimate proof of the existence of confinement is not yet done.

where g_s is the coupling constant of QCD. One important change is that in contrast to the $U(1)$ case the generators of the group do not commute

$$[T_a, T_b] = i \sum_c f_{abc} T_{abc} \quad (\text{A.3})$$

where f_{abc} are the structure constants of the group. Due to this non-abelian structure, the gauge transformation for the gauge fields has to be modified:

$$G_\mu^a \rightarrow G_\mu^a - \frac{1}{g_s} \partial_\mu \alpha_a - \sum_{b,c} f_{abc} \alpha_b G_\mu^c. \quad (\text{A.4})$$

In addition the field strength tensors for the gauge fields are written as:

$$G_{\mu\nu}^a = \partial_\mu G_\nu^a - \partial_\nu G_\mu^a - g_s \sum_{b,c} f_{abc} G_\mu^b G_\nu^c. \quad (\text{A.5})$$

The final gauge invariant Lagrangian then reads

$$\mathcal{L}_{QCD} = \bar{\psi} i \gamma^\mu \partial_\mu \psi - m_f \bar{\psi} \psi - g_s \sum_a (\bar{\psi} \gamma^\mu T_a \psi) G_\mu^a - \frac{1}{4} \sum_a G_{\mu\nu}^a G_a^{\mu\nu}, \quad (\text{A.6})$$

which has the same basic structure as the one for QED. One important difference is that the last term also contains interactions between the gauge bosons themselves. The gauge bosons are called gluons and carry color charge themselves. As there are eight independent phase transformations possible, eight gluon fields are needed to obtain gauge invariance. Just as for the photon in QED, the gluon is predicted to be massless. Experimentally, the gluon mass has to be lower than a few MeV [162].

“Here come the Jets, like a bat out of hell...”

Stephen Sondheim, 1930–present, *West Side Story*, Act 1: “Jet Song”

B

Jet Algorithms

The purpose of a jet algorithm is to cluster any input objects for nearness within a certain spatial region. These might be for examples the hadrons arising from the hadronization of a high p_T parton. The concept of jet algorithms is very general, as a lot of different input objects can be used, as long as they can be converted into a four-momentum like quantity. A jet can be composed for example of the stable hadrons of a Monte Carlo generator, the tracks of charged particles as measured in a tracking detector, or the cells or clusters in a calorimeter.

A lot of different jet algorithms have been designed. They basically only differ in the type of *resolution variable* to define the nearness of two input objects, and in the way in which two objects designated by the algorithm are added together, which is called the *recombination scheme*. A lot more detail can be found in [71].

B.1 Recombination Schemes

The default in ATLAS is the E scheme. Here two objects i, j are added as four vectors:

$$p(i, j) = p(i) + p(j) \quad (\text{B.1})$$

This results in general in massive final states. As only in the limit of massless particles the pseudorapidity is equal to the rapidity $y = \frac{1}{2} \log \frac{E+p_z}{E-p_z}$, the latter has to be used in this recombination scheme.

An alternative is the *Snowmass*, or E_T scheme. Here the transverse energies are added:

$$E_T(i, j) = E_T(i) + E_T(j), \quad (\text{B.2})$$

and the combined objects pseudorapidity and azimuthal angle are set to the E_T weighted mean of the two input objects:

$$\eta(i, j) = \frac{E_T(i)\eta(i) + E_T(j)\eta(j)}{E_T(i, j)} \quad \phi(i, j) = \frac{E_T(i)\phi(i) + E_T(j)\phi(j)}{E_T(i, j)}. \quad (\text{B.3})$$

The combined objects are then set massless.

B.2 Clustering algorithms

The clustering algorithms used in this thesis differ in the used resolution variable. The cone algorithm defines the nearness of two particles as an angular distance in (η, ϕ) space. The k_{\perp} algorithm defines nearness in a *relative* momentum space.

B.2.1 Cone algorithm

The basis of the the cone algorithm is a to define a fixed-size region in (η, ϕ) that defines a jet. A cone jet has thus a well defined boundary. The basic algorithm works like this:

1. From the list of input object for the jet reconstruction, objects are selected if their transverse energy is greater than a specified value E_T^{seed} . These are called 'seeds' and are sorted in descending E_T order.
2. The next highest E_T seed is taken. All objects that have a distance in (η, ϕ) space to the seed of less than R are combined with it. R is a parameter of the jet algorithm. This is repeated until the (η, ϕ) direction of the combined object does not change anymore.
3. If this combined object was not yet found from a previous seed, the cone is added to the list of protojets. Then step 2 is repeated with the next seed.
4. After all seeds have been processed, one is left with a list of protojets that may overlap with each other. Overlapping jets are merged into one jet, if the shared fraction of the transverse energy is larger than a certain fraction f . If the shared transverse energy is less, the objects in the overlap are assigned to the nearest jet. This split/merge algorithm is done in an iterative way starting with the highest E_T protojet, which means that one jet can also undergo multiple splits and merges.
5. The remaining protojets are retained as a jet.

The seeded cone algorithm thus has a three parameters: R , E_T^{seed} and f . It has the advantage of being a fast jet algorithm, and that it has well defined boundaries. From the theoretical point of view, it has unwanted features: It is not *infrared safe*, which means that it is sensitive to soft radiation which can lead to spurious jets. Seedless cone algorithms have much better theoretical behaviour, but are not yet used by ATLAS.

B.2.2 k_{\perp} Algorithm

The k_{\perp} algorithm uses a relative transverse momentum as a distance measure. It can be used in an inclusive or an exclusive mode. The inclusive algorithm is the following defined as¹ [163]:

¹There exist variations of the used distance measure that differ in detail, but not in the basic properties of the jet algorithm.

1. For every pair of input objects (i, j) a distance parameter is defined²:

$$d_{ij} = \min(p_{Ti}, p_{Tj}) \frac{\Delta R_{ij}}{D}, \quad (\text{B.4})$$

where D is a parameter of the algorithm and R_{ij} their distance in (η, ϕ) space. It can be shown that for small angular separations, this is equivalent to the relative transverse momentum of the two objects.

2. For every single object i the distance to the beam is defined as:

$$d_i = p_{Ti} \quad (\text{B.5})$$

3. If of all d_{ij} and d_i , the smallest one is a d_{ij} , the objects i and j are merged together to some recombination scheme as for the cone jet algorithm. Otherwise, if it is a d_i , then object i is removed from the list of objects and added to the list of jets.
4. The first three steps are repeated until all objects have been removed from the input list.

The inclusive k_\perp algorithm has just one parameter: D . It can be interpreted in (η, ϕ) space as the minimal distance of two jets. However, as any input object is uniquely assigned to a jet, the boundaries of the jets are not well defined in (η, ϕ) space.

In addition to this inclusive algorithm, there is an exclusive algorithm that either forces the jet algorithm to cluster the input objects into a specified number of jets, or introduces a minimal transverse momentum that each jet has to fulfill with respect to the Z axis or relative to another jet. This exclusive algorithm works like this [77]:

1. The same distance parameters as in the inclusive case are calculated. Objects are merged as long as $\min(d_i, d_{ij}) < d_{\text{cut}}$.
2. If the minimum is a d_i , it is merged with the beam and not added to the list of jets. It can in a way be called a beam jet, in which one is no longer interested.
3. These steps are repeated iteratively until $d_{\text{min}} > d_{\text{cut}}$. The final state hard jets left fulfill $p_T > d_{\text{cut}}$ is left.

The k_\perp algorithm has the advantage of having well defined theoretical properties, e.g. infrared safety. The drawback is more on the experimentalists side, as the fuzzy boundaries of the jets make these difficult to calibrate. Also it is in its original implementation very slow, compared to the seeded cone algorithm. A new implementation, the Fast k_\perp algorithm [164] uses an advanced method for clustering that speeds up the process while retaining the nice theory behavior.

²Actually the definition in [163] differs in the way that here the square root of the resolution variables is used, which makes no difference for the algorithm itself.

“There are three kinds of lies: lies, damned lies, and statistics.”

Attributed to Benjamin Disraeli, 1804–1881

C

Statistical Methods

C.1 Statistical Component of Systematic Variations

As described in Chapter 11, the systematic uncertainties of the analysis selection efficiencies have been estimated by applying systematic changes to certain event properties, e.g. smearing the momentum of muons or changing the jet energy scale. The effect of this variation gives a direct influence on the event selection efficiency. This can be quantified by quoting

$$\Delta\epsilon_{\text{relative}} = \frac{\epsilon_{\text{systematic}} - \epsilon_{\text{standard}}}{\epsilon_{\text{standard}}}, \quad (\text{C.1})$$

where $\epsilon_{\text{systematic}}$ and $\epsilon_{\text{standard}}$ are the event selection efficiencies or the event yields when the systematic variation is applied and when not. The systematic variation can have multiple effects on the event selection efficiencies. In a way, the analysis with and without the variation can be seen as two different analyses. However, they act on the same events, and so there is a high level of correlation between the two samples. As a consequence, one also has to quote a statistical uncertainty on this ratio, which is calculated in the following.

Suppose that the event sample is divided into four exclusive, not overlapping subsamples, with number of events n_1 to n_4 , $\sum_i n_i = N$. Suppose that one of two analyses selects n_1 and n_2 , the other n_2 and n_3 , and that n_2 is selected by both. Due to the exclusive nature of the subsamples, the properties of the event selection can be described by a *multinomial* distribution, with each event having a probability p_i to be placed in category i . In an experiment, the estimator for the p_i is given by n_i/N . The variance of the selected event numbers of each subclass is given by:

$$V(n_i) = \text{cov}(n_i, n_i) = N \cdot p_i(1 - p_i), \quad (\text{C.2})$$

and the covariances are given by:

$$\text{cov}(n_i, n_j) = -N \cdot p_i \cdot p_j \quad (i \neq j). \quad (\text{C.3})$$

The relative change of selection efficiency is now given by (modulo a -1 , which has no influence on the uncertainty):

$$Y = \frac{n_1 + n_2}{n_2 + n_3} \quad (\text{C.4})$$

The variance of Y is then given by,

$$V(Y) = \sum_{i=1}^3 \sum_{j=1}^3 \frac{\partial Y}{\partial n_i} \frac{\partial Y}{\partial n_j} V_{ij}(n_1, n_2, n_3), \quad (\text{C.5})$$

where V_{ij} is the covariance matrix. The partial derivatives are given by:

$$\frac{\partial Y}{\partial n_1} = \frac{n_2 + n_3}{(n_2 + n_3)^2} \quad \frac{\partial Y}{\partial n_2} = \frac{n_3 - n_1}{(n_2 + n_3)^2} \quad \frac{\partial Y}{\partial n_3} = \frac{-(n_1 + n_2)}{(n_2 + n_3)^2}. \quad (\text{C.6})$$

Introducing the short notation $n_2 + n_3 = k$ and inserting this into Eq. C.5 yields:

$$V(Y) = \frac{1}{k^2} N \frac{n_1}{N} \left(1 - \frac{n_1}{N}\right) \quad (\text{C.7})$$

$$+ \frac{(n_3 - n_1)^2}{k^4} N \frac{n_2}{N} \left(1 - \frac{n_2}{N}\right) \quad (\text{C.8})$$

$$+ \frac{(n_1 + n_2)^2}{k^4} N \frac{n_3}{N} \left(1 - \frac{n_3}{N}\right) \quad (\text{C.9})$$

$$+ 2 \cdot \frac{n_3 - n_1}{k^3} \cdot \left(-N \frac{n_1}{N} \frac{n_2}{N}\right) \quad (\text{C.10})$$

$$+ 2 \cdot \frac{-n_1 + n_2}{k^3} \cdot \left(-N \frac{n_1}{N} \frac{n_3}{N}\right) \quad (\text{C.11})$$

$$+ 2 \cdot \frac{-(n_3 - n_1)(n_1 + n_2)}{k^3} \cdot \left(-N \frac{n_2}{N} \frac{n_3}{N}\right) \quad (\text{C.12})$$

$$= \frac{1}{k^4} (n_2 + n_3)^2 n_1 \left(1 - \frac{n_1}{N}\right) \quad (\text{C.13})$$

$$+ \frac{1}{k^4} (n_3 - n_1)^2 n_2 \left(1 - \frac{n_2}{N}\right) \quad (\text{C.14})$$

$$+ \frac{1}{k^4} (n_1 + n_2)^2 n_3 \left(1 - \frac{n_3}{N}\right) \quad (\text{C.15})$$

$$- 2 \frac{1}{k^4} (n_3 - n_1)(n_2 + n_3) n_1 \frac{n_2}{N} \quad (\text{C.16})$$

$$+ 2 \frac{1}{k^4} (n_2 + n_3)(n_1 + n_2) n_1 \frac{n_3}{N} \quad (\text{C.17})$$

$$+ 2 \frac{1}{k^4} (n_3 - n_1)(n_1 + n_2) n_2 \frac{n_3}{N} \quad (\text{C.18})$$

The resulting terms can now be divided into terms that retain a direct dependency on N , and those without. The former are all proportional to $1/N$. Simple arithmetics show that all these terms cancel each other exactly to zero. The final result no longer depends on N and is given by:

$$V(Y) = \frac{1}{(n_2 + n_3)^4} \{ (n_2 + n_3)^2 \cdot n_1 + (n_3 - n_1)^2 \cdot n_2 + (n_1 + n_2)^2 \cdot n_3 \}. \quad (\text{C.19})$$

The statistical uncertainty on Y is then given by $\sqrt{V(Y)}$. It should be noted that this remarkably simple result is of exactly the same form as if using the naive approach of assuming each subclass to be independent, the uncertainty on the event number to be simply $\sqrt{n_i}$, and then using error propagation neglecting any correlations. For the interested reader it should be noted that exactly the same ansatz yields the uncertainty on event selection efficiencies just as the correct calculation using binomial statistics. A possible general proof that the method of dividing the sample in mutually exclusive subclasses and applying error propagation neglecting any correlations yields the same result as using multinomial statistics is beyond the scope of this thesis.

C.2 Calculation of Discovery Significances

In this section the method used in this work to estimate the expected significances is briefly discussed.

C.2.1 Introduction

In the experiment an discovery can only be made if the probability for a false positive signal, thus falsely claiming a discovery if there is no signal, is low. This probability is called in statistics a type I error probability. Commonly the type I error probability is required to be lower than $2.87 \cdot 10^{-7}$, corresponding to the 5σ confidence interval of a Gaussian.

One very easy measure of the discovery significance is S/\sqrt{B} , where S is the number of signal and B the number of background events, which was already used in the optimization procedure. However, this method has several drawbacks: It is only an approximation that does not necessarily ensure correct coverage of the confidence intervals for arbitrary numbers of signal and background events. Furthermore, it only takes into account the statistical uncertainty of the background events, as evidenced by \sqrt{B} . However, in the experiment, the number of background events can only be predicted with a certain accuracy ΔB , be it with Monte Carlo simulation or a data based method, as described in the previous chapter. These additional parameters in the model, that are not of interest for the outcome of the experiment, are also called *nuisance parameters*. Another example would be a signal efficiency that is only known with a limited accuracy.

C.2.2 The Profile Likelihood

As an alternative to the estimate of the significance using the simple measure as above, a more sophisticated method based on a likelihood ratio test is used. It is based on the so-called *profile likelihood* that is discussed in the context of construction of confidence intervals in the presence of nuisance parameters in [157]. The following short discussion of the method is based on [158], where the application of this method is presented in the context of testing for a signal.

The general problem is based on a likelihood ratio test. Denoting the measured data as \vec{x} , that is supposed to be randomly distributed according to a probability density function $p(\vec{x}; \vec{\theta})$ where $\vec{\theta}$ is a vector of parameters within the possible parameter space Θ . The likelihood function, giving the likelihood of a parameter set $\vec{\theta}$ if \vec{x} is measured, is given by $L(\vec{\theta}|\vec{x}) = p(\vec{x}; \vec{\theta})$.

Two different hypothesis are now tested against each other: The null hypothesis $\vec{\theta} \in \Theta_0$ (no signal) against the hypothesis of non-zero signal contribution ($\vec{\theta} \in \bar{\Theta}_0$). The likelihood ratio test statistic is then given by:

$$\lambda(\vec{x}) = \frac{\sup_{\Theta_0} L(\vec{\theta}|\vec{x})}{\sup_{\Theta} L(\vec{\theta}|\vec{x})}, \quad (\text{C.20})$$

where in the numerator the likelihood function is maximized over the set of parameters assuming the null hypothesis and in the denominator for the whole parameter space. The likelihood ratio test is then done in the way that the null hypothesis is rejected if $\lambda(\vec{x}) \leq c$, where c is related to the type I error probability. In [165] and [166] it is shown that in case of a correct null hypothesis (i.e. no signal), $-2 \ln \lambda(\vec{x})$ is approximately distributed as a χ^2 distribution with the number of parameters given by the differences between the number of free parameters in the null hypothesis and in the whole parameter space. In this way the corresponding cut-off values for claiming a discovery can be calculated easily from the tabulated values of the χ^2 distribution.

C.2.3 Probability Model

The model used in this thesis to calculate the efficiency is based on a counting experiment with background and efficiency. Suppose that n events are selected, which can be modeled as a random variable N with a Poisson distribution of rate $\varepsilon s + b$, where b is the background only rate, s the signal contribution, and ε the signal selection efficiency. The background rate is assumed to be measured independently as y , for example in sidebands, or from Monte Carlo. This can be modeled as a random variable Y as a Poisson distribution with mean value τb , where τ is the relative size between the sidebands and the signal region or between the Monte Carlo sample and the data sample. The background rate in the signal region is then estimated as y/τ . In addition the efficiency z is estimated from Monte Carlo and is modeled as a Gaussian N with mean ε and standard deviation σ_ε . The joint

probability is then given by:

$$p(n, y, z; \varepsilon, s, b) = \frac{(\varepsilon s + b)^n}{n!} \exp\{-(\varepsilon s + b)\} \frac{(\tau b)^y}{y!} \exp\{-\tau b\} \frac{1}{\sqrt{2\pi}\sigma_\varepsilon} \exp\left\{-\frac{1}{2} \frac{(z - \varepsilon)^2}{\sigma_\varepsilon^2}\right\}. \quad (\text{C.21})$$

Within this probability model, s is the parameter of interest and ε and b are nuisance parameters.

The denominator of the likelihood ratio test statistic is maximized by the maximum likelihood estimators (MLE) of ε, s, b , which are given as $\hat{s} = n - y/\tau$, $\hat{b} = y\tau$ and $\hat{\varepsilon} = z$. The null hypothesis is defined by $s = 0$ and maximizing the likelihood in the two remaining parameters yields the estimators $\tilde{b} = \frac{n+y}{1+\tau}$ and $\tilde{\varepsilon} = z$. The test statistic is then given by [158]:

$$\lambda(n, y, z) = \frac{p(n, y, z | 0, \tilde{b}, \tilde{\varepsilon})}{p(n, y, z | \hat{s}, \hat{b}, \hat{\varepsilon})} = \frac{\left(\frac{n+y}{1+\tau}\right)^{n+y} \tau^y}{n^n y^y}. \quad (\text{C.22})$$

It should be noted that the test statistic does not retain a direct dependence on the estimate of the signal selection efficiency z . This comes from the fact that under the null hypothesis there are no signal events. The efficiency has an indirect influence on the power of the analysis in the sense that it determines the number of events entering the test.

Evidently the full parameter space has three free parameters, while the null hypothesis has s fixed to zero, thus reducing this to two. Accordingly, the logarithm of the test statistic (multiplied by minus two) is distributed as a χ^2 with one degree of freedom and this number can be converted into a significance by taking the square root of it:

$$S = \sqrt{-2 \log \lambda(n, x, y)} \quad (\text{C.23})$$

Multiple decay channels or independent analyses can be combined by multiplying the individual channels likelihood functions, respectively their test statistics.

C.2.4 Application in the Analysis

The significances in the analysis described in this thesis are calculated according to the procedure described above. The number of signal events S is estimated from the signal Monte Carlo prediction, the number of expected background events B is taken from the sideband fit, along with its relative uncertainty $r = \Delta B/B$. Obviously, the analysis with the sideband based background prediction bears some resemblance of counting events in a sideband, but it is not exactly the same. An alternative way to model the background prediction would be a Gaussian with mean B and rms ΔB . Also in this case, the profile likelihood method could be used to obtain a likelihood ratio test statistic. However, instead an approximation is used with the Poisson modeling as above, motivated by [159]: The standard deviation of the Poisson distribution as given in Eq. C.21 is given by $\sqrt{\tau b}$. This is required to be equal to the uncertainty of the background prediction $r \cdot \tau b$. Using $\tau = 1/r^2 b$ gives the appropriate approximation. In this way the relative level of fluctuations of the

Poisson or a Gaussian distribution are the same, and the Poisson distribution corresponds to finding an effective size of the sidebands compared to the signal region.

The final numbers entering in the significance calculation as in the model described above are:

$$n = S + B \quad (\text{C.24})$$

$$y = \tau \cdot B \quad (\text{C.25})$$

$$\tau = \frac{1}{(\Delta B/B)^2 B} \quad (\text{C.26})$$

This procedure has been shown in [159] to yield a good approximation of the extracted significances compared to a Gaussian probability function of the auxiliary background measurement.

C.2.5 Comment on Setting Limits

It should be noted that the described procedure cannot be used directly for placing exclusion limits on the signal rate. Excluding a given production cross section at a certain confidence level is a different question than claiming a discovery. Here one is interested in the probability that an assumed signal rate fluctuates downwards to the level of the observed rate. This is equivalent to the type II error probability. In principle this can also be tackled using the profile likelihood technique. However, in this case also the uncertainty on the signal selection efficiency obviously has to enter the exclusion limit. Expected exclusion limits are not given in this thesis.

“It’s clearly a budget. It’s got a lot of numbers in it.”

George W. Bush, 1946–present

D

Tables of Systematic Uncertainties

As described in Chapter 11, the systematic uncertainties of the event selection efficiencies have been evaluated. Table D.1 summarizes the detector related systematic uncertainties. In the following the numerical values that have been omitted in Chapter 11 are given.

		FULLSIM	ATLFAST
Muons	reco. efficiency	$\pm 1\%$	$\pm 2\%$
	energy scale	$\pm 1\%$	$\pm 1\%$
	energy resolution	$\sigma(\frac{1}{p_T})/\text{GeV}^{-1} = \frac{0.011}{p_T/\text{GeV}} \oplus 0.0017$	
Jets	energy scale ($ \eta < 3.2$)	$\pm 7\%$	$\pm 7\%$
	energy scale ($ \eta > 3.2$)	$\pm 15\%$	$\pm 15\%$
	energy resolution ($ \eta < 3.2$)	$\sigma(E)/\text{GeV} = 0.45 \cdot \sqrt{E/\text{GeV}}$	
	energy resolution ($ \eta > 3.2$)	$\sigma(E)/\text{GeV} = 0.63 \cdot \sqrt{E/\text{GeV}}$	
b -tagging	ϵ_b	$\pm 5\%$	$\pm 5\%$
	R_c	$\pm 5\%$	$\pm 5\%$
	R_{udsg}	$\pm 14\%$	$\pm 20\%$
\cancel{E}_T	pile-up	—	$s = 2.4 \pm 0.3$
	no pile-up	—	$s = 1.4 \pm 0.2$

Table D.1: Summary of detector and simulation related systematic uncertainties.

D.1 Analysis I (b tag)

Syst.	Mass window for $M =$					
	110 GeV	130 GeV	150 GeV	200 GeV	300 GeV	400 GeV
Muons						
$ES+$	$+11.5 \pm 1.1$	$+7 \pm 1.8$	$+2.7 \pm 2.1$	$+0 \pm 3.4$	$+11.1 \pm 8.3$	$+57.1 \pm 35.8$
$ES-$	-9.6 ± 0.9	-5.2 ± 1.5	-6.9 ± 2	-6.4 ± 2.8	-11 ± 7.4	$+28.6 \pm 22.9$
resol.	$+2.2 \pm 0.9$	$+0.7 \pm 1.6$	$+1.1 \pm 2.1$	-1.8 ± 2.5	$+5.6 \pm 9$	$+14.3 \pm 26.5$
ϵ_μ				± 4		
shape	-3.3	-2.8	-2.2	-0.8	+1.7	+4.6
Jets						
$ES+$	-4.5 ± 0.7	-5.1 ± 1.4	-6.3 ± 1.8	-7 ± 3	-5.5 ± 5.4	-28.5 ± 17.1
$ES-$	$+3.2 \pm 0.9$	$+1.5 \pm 1.5$	$+4.8 \pm 2.1$	$+3.9 \pm 3.4$	$+2.8 \pm 6.3$	$+14.3 \pm 15.3$
resol.	-1.6 ± 0.6	-0.7 ± 1.2	-0.2 ± 1.5	$+1.9 \pm 2.7$	$+8.3 \pm 6.5$	$+0 \pm 0$
b tag						
$\epsilon_{b/c}+$	$+3.1 \pm 0.4$	$+3.5 \pm 0.7$	$+2.1 \pm 0.8$	$+1.9 \pm 1.1$	$+2.8 \pm 2.8$	$+14.3 \pm 15.3$
$\epsilon_{b/c}-$	-2.7 ± 0.4	-2.4 ± 0.6	-3.1 ± 0.9	-2.5 ± 1.3	-2.7 ± 2.7	$+0 \pm 0$
$R_{\text{udsg}}+$	-9.4 ± 0.6	-6.9 ± 1	-11.1 ± 1.6	-8.3 ± 2.2	-8.2 ± 4.6	$+0 \pm 0$
$R_{\text{udsg}}-$	$+11.3 \pm 0.8$	$+14.7 \pm 1.5$	$+12.6 \pm 1.9$	$+12.3 \pm 3$	$+13.9 \pm 6.6$	$+42.9 \pm 29.6$
\cancel{E}_T						
$s = 2.1$	$+3.4 \pm 0.4$	$+3.8 \pm 0.7$	$+4.3 \pm 1.1$	$+5.8 \pm 2$	$+2.8 \pm 2.8$	$+14.3 \pm 15.3$
$s = 2.7$	-4.5 ± 0.4	-4 ± 0.7	-3.6 ± 1	-7.6 ± 2.1	-8.2 ± 4.6	$+0 \pm 0$
MC_{stat}	± 2.1	± 3.7	± 5.2	± 8.0	± 16.7	± 37.8

Table D.2: Systematic uncertainties (in %) for $Z^0 + \text{light}$, analysis requiring at least one tagged jet.

Syst.	Mass window for $M =$					
	110 GeV	130 GeV	150 GeV	200 GeV	300 GeV	400 GeV
Muons						
$ES+$	$+16 \pm 1.3$	$+6.9 \pm 2$	$+3.3 \pm 2.5$	$+10.2 \pm 5.6$	$+14.3 \pm 15.3$	$+0 \pm 0$
$ES-$	-11.7 ± 1	-7.5 ± 2	-4.1 ± 2.7	3.4 ± 6	-14.2 ± 13.2	$+0 \pm 0$
resol.	$+4.5 \pm 1.1$	$+1.7 \pm 1.9$	$+0.8 \pm 2.4$	$+6.8 \pm 6.6$	-14.2 ± 13.2	-49.9 ± 35.4
ϵ_μ				± 4		
shape	-3.3	-2.8	-2.2	-0.8	$+1.6$	$+4.7$
Jets						
$ES+$	-4.2 ± 0.8	-5.1 ± 1.7	-2.8 ± 2.2	$+1.7 \pm 5.1$	-14.2 ± 13.2	-99.9 ± 0
$ES-$	$+1.7 \pm 0.9$	$+3.2 \pm 1.9$	$+2.1 \pm 2.6$	-3.3 ± 4.1	$+42.9 \pm 29.6$	$+0 \pm 0$
resol.	-1 ± 0.7	-2.5 ± 1.5	$+0.4 \pm 1.8$	$+0 \pm 4.2$	$+0 \pm 0$	$+0 \pm 0$
b tag						
$\epsilon_{b/c}+$	$+4.5 \pm 0.5$	$+5 \pm 1.1$	$+5.4 \pm 1.5$	$+1.7 \pm 1.7$	$+0 \pm 0$	$+100 \pm 100$
$\epsilon_{b/c}-$	-3.5 ± 0.4	-6.8 ± 1.2	-6.2 ± 1.6	-10.1 ± 3.9	$+0 \pm 0$	$+0 \pm 0$
$R_{uds}+$	$+0 \pm 0.1$	$+0 \pm 0$	$+0 \pm 0$	$+0 \pm 0$	$+0 \pm 0$	$+0 \pm 0$
$R_{uds}-$	$+0.2 \pm 0.1$	$+0.2 \pm 0.2$	$+0.8 \pm 0.6$	$+0 \pm 0$	$+14.3 \pm 15.3$	$+0 \pm 0$
\cancel{E}_T						
$s = 2.1$	$+3.6 \pm 0.4$	$+2.4 \pm 0.7$	$+3.3 \pm 1.2$	$+5.1 \pm 3$	$+0 \pm 0$	$+50 \pm 61.2$
$s = 2.7$	-3.8 ± 0.4	-5.3 ± 1.1	-4.9 ± 1.4	-6.7 ± 3.3	$+0 \pm 0$	$+0 \pm 0$
MC_{stat}	± 2.3	± 4.6	± 6.5	± 12.9	± 37.8	± 70.7

Table D.3: Systematic uncertainties (in %) for $Z^0 + b$, analysis requiring at least one tagged jet.

Syst.	Mass window for $M =$					
	110 GeV	130 GeV	150 GeV	200 GeV	300 GeV	400 GeV
Muons						
$ES+$	-4.2 ± 2.9	$+1.6 \pm 2.6$	$+2.2 \pm 3.2$	$+0.6 \pm 3.4$	-5.3 ± 3.9	$+5.9 \pm 6.1$
$ES-$	-2.3 ± 2.8	-3.1 ± 3.4	$+2.2 \pm 2.8$	-4.4 ± 3	-12.4 ± 5	$+0 \pm 11.8$
resol.	-6.1 ± 2.4	$+2.7 \pm 2.6$	$+0.5 \pm 3.1$	-2.5 ± 2.7	-10.6 ± 4.8	-5.8 ± 5.7
ϵ_μ				± 4		
shape	-3.3	-2.8	-2.2	-0.8	+1.8	+4.4
Jets						
$ES+$	-21.7 ± 3.5	-22.4 ± 3.5	-24.1 ± 3.5	-21.3 ± 3.7	-14.2 ± 6.2	-5.8 ± 5.7
$ES-$	$+26.5 \pm 5.1$	$+35.3 \pm 5.4$	$+36.6 \pm 5.8$	$+25.3 \pm 5.5$	$+17.9 \pm 6.7$	$+29.4 \pm 17.7$
resol.	-2.7 ± 3.3	$+1.6 \pm 3.3$	-1.5 ± 3.4	-4.4 ± 3.4	-1.7 ± 5.3	$+5.9 \pm 10.5$
b tag						
$\epsilon_{b/c}+$	$+8.5 \pm 2.1$	$+7.5 \pm 2.1$	$+8.1 \pm 2.2$	$+5.2 \pm 1.9$	$+3.6 \pm 2.6$	$+0 \pm 0$
$\epsilon_{b/c}-$	-3.7 ± 1.3	-2.6 ± 1.2	-2.6 ± 1.2	-1.8 ± 1.1	-5.3 ± 3	$+0 \pm 0$
$R_{uds}g+$	$+0 \pm 0$	-0.4 ± 0.5	-1 ± 0.8	-0.5 ± 0.6	$+0 \pm 0$	$+0 \pm 0$
$R_{uds}g-$	$+0.5 \pm 0.5$	$+0.5 \pm 0.5$	$+1.1 \pm 0.8$	$+0 \pm 0$	$+0 \pm 0$	$+0 \pm 0$
\cancel{E}_T						
$s = 2.1$	1.4 ± 2.1	$+2.1 \pm 2.5$	$+2.7 \pm 2$	$+1.9 \pm 2.2$	$+3.6 \pm 4.5$	$+0 \pm 0$
$s = 2.7$	-1.8 ± 2.1	-3.1 ± 2	-3.1 ± 2.1	-1.8 ± 1.7	-5.3 ± 3	$+0 \pm 0$
MC_{stat}	± 8.0	± 8.8	± 8.4	± 8.9	± 14.9	± 27.0

Table D.4: Systematic uncertainties (in %) for $t\bar{t}$, analysis requiring at least one tagged jet.

Syst.	Mass window for $M =$					
	110 GeV	130 GeV	150 GeV	200 GeV	300 GeV	400 GeV
Muons						
$ES+$	$+0.6 \pm 0.9$	-0.4 ± 0.8	-1.4 ± 1.3	-2 ± 1.1	-0.2 ± 0.7	-0.3 ± 0.9
$ES-$	-2.6 ± 0.9	-2.4 ± 1	-1.9 ± 1.2	-2.6 ± 1	-1 ± 0.8	-0.6 ± 0.7
resol.	-0.8 ± 0.8	-1.4 ± 1	-1.4 ± 1	-2.3 ± 1.3	-4 ± 1	-2.4 ± 1.2
ϵ_μ				± 4		
shape	-3.3	-2.7	-2.2	-0.8	+1.8	+4.5
Jets						
$ES+$	-0.5 ± 1	-1.9 ± 1.3	-2.5 ± 1.8	-2 ± 1.8	-5.3 ± 1.6	-8.4 ± 2.1
$ES-$	-1.2 ± 1.3	$+0.3 \pm 1.5$	-2.8 ± 2.2	$+1.1 \pm 1.9$	$+2.2 \pm 2$	$+7.4 \pm 2.8$
resol.	-1.4 ± 1	-1.4 ± 1.2	-0.5 ± 1.5	-1.8 ± 1.5	-1.5 ± 1.5	$+2.1 \pm 1.9$
b tag						
$\epsilon_{b/c}+$	$+3.8 \pm 0.7$	$+4.3 \pm 0.9$	$+5.6 \pm 1.3$	$+4.3 \pm 1.1$	$+6.3 \pm 1.3$	$+7.0 \pm 1.6$
$\epsilon_{b/c}-$	-5.9 ± 0.8	-7 ± 1	-4 ± 1.1	-5.5 ± 1.2	-7.3 ± 1.4	-4.8 ± 1.3
$R_{uds}+$	-0.1 ± 0.2	-0.2 ± 0.2	-0.2 ± 0.3	$+0 \pm 0$	$+0 \pm 0$	$+0 \pm 0$
$R_{uds}-$	$+0.5 \pm 0.2$	$+0.3 \pm 0.2$	$+0.6 \pm 0.4$	$+0 \pm 0$	$+0.5 \pm 0.4$	$+0.7 \pm 0.5$
\cancel{E}_T						
$s = 2.1$	$+3.4 \pm 0.6$	$+3.9 \pm 0.8$	$+3.8 \pm 1.1$	$+3.5 \pm 1$	$+4.4 \pm 1.2$	$+9.2 \pm 1.9$
$s = 2.7$	-4.1 ± 0.7	-4.3 ± 0.8	-5.2 ± 1.2	-5 ± 1.1	-7 ± 1.3	-10.5 ± 1.8
MC_{stat}	± 3.4	± 4.1	± 5.4	± 5.2	± 5.2	± 5.9

Table D.5: Systematic uncertainties (in %) for $b\bar{b}A^0$, analysis requiring at least one tagged jet.

D.2 Analysis II (b tag veto)

Syst.	Mass window for $M =$					
	110 GeV	130 GeV	150 GeV	200 GeV	300 GeV	400 GeV
Muons						
$ES+$	$+12.6 \pm 0.1$	$+5.7 \pm 0.1$	$+4.8 \pm 0.2$	$+3.9 \pm 0.3$	$+4.7 \pm 0.6$	$+4 \pm 0.9$
$ES-$	-10.7 ± 0.1	-5.5 ± 0.1	-4.1 ± 0.2	-2.9 ± 0.3	-3.9 ± 0.5	-3.4 ± 0.7
resol.	$+1.1 \pm 0.1$	$+0.1 \pm 0.1$	$+0.1 \pm 0.2$	-0.2 ± 0.3	$+0.2 \pm 0.6$	$+1.2 \pm 1.1$
ϵ_μ				± 4		
shape	-3.3	-2.8	-2.2	-0.9	+1.7	+4.5
Jets						
$ES+$	$+0 \pm 0$	$+0 \pm 0$	$+0 \pm 0$	$+0 \pm 0.1$	-0.1 ± 0.2	$+0 \pm 0.3$
$ES-$	$+0 \pm 0$	$+0 \pm 0$	$+0 \pm 0$	-0.1 ± 0.1	$+0 \pm 0.2$	$+0.1 \pm 0.3$
resol.	$+0 \pm 0$	$+0 \pm 0$	$+0 \pm 0$	$+0 \pm 0.1$	$+0 \pm 0.1$	$+0.3 \pm 0.2$
b tag						
$\epsilon_{b/c}+$	$+0 \pm 0$	$+0 \pm 0$	$+0 \pm 0$	$+0 \pm 0$	$+0 \pm 0$	$+0 \pm 0.1$
$\epsilon_{b/c}-$	$+0 \pm 0$	$+0.1 \pm 0$	$+0.1 \pm 0$	$+0 \pm 0$	$+0 \pm 0$	$+0 \pm 0$
$R_{\text{udsg}}+$	$+0.2 \pm 0$	$+0.2 \pm 0$	$+0.2 \pm 0$	$+0.2 \pm 0$	$+0.2 \pm 0.1$	$+0 \pm 0$
$R_{\text{udsg}}-$	-0.1 ± 0	-0.2 ± 0	-0.2 ± 0	-0.3 ± 0	-0.3 ± 0.1	-0.5 ± 0.2
\cancel{E}_T						
$s = 2.1$	$+0.8 \pm 0$	$+0.9 \pm 0$	$+1 \pm 0$	$+1.4 \pm 0.1$	$+2.7 \pm 0.2$	$+6.1 \pm 0.6$
$s = 2.7$	-1.1 ± 0	-1.3 ± 0	-1.4 ± 0.1	-1.9 ± 0.1	-3.2 ± 0.3	-5 ± 0.5
MC_{stat}	± 0.2	± 0.3	± 0.5	± 0.8	± 1.4	± 2.2

Table D.6: Systematic uncertainties (in %) for $Z^0 + \text{light}$, analysis requiring zero tagged jets.

Syst.	Mass window for $M =$					
	110 GeV	130 GeV	150 GeV	200 GeV	300 GeV	400 GeV
Muons						
$ES+$	$+14.6 \pm 0.6$	$+7.8 \pm 1$	$+7.6 \pm 1.4$	$+5.1 \pm 2.8$	-6.4 ± 5.6	$+0 \pm 0$
$ES-$	-12.2 ± 0.5	-6.2 ± 0.9	-3.6 ± 1.2	-0.8 ± 2.5	-2.1 ± 4.8	-7.9 ± 7.7
resol.	$+1.2 \pm 0.5$	$+1.6 \pm 0.9$	$+1.2 \pm 1.2$	$+0.4 \pm 2.7$	$+4.3 \pm 7$	$+4 \pm 7.1$
ϵ_μ				± 4		
shape	-3.3	-2.8	-2.2	-0.9	+1.8	+4.4
Jets						
$ES+$	-0.8 ± 0.1	-1 ± 0.2	-1.3 ± 0.4	-1.2 ± 0.9	$+0 \pm 0$	$+0 \pm 0$
$ES-$	$+1.4 \pm 0.2$	$+1.5 \pm 0.3$	$+1.9 \pm 0.5$	$+1.7 \pm 0.9$	$+2.2 \pm 3.8$	$+0 \pm 0$
resol.	$+0.3 \pm 0.1$	$+0.1 \pm 0.3$	$+0.1 \pm 0.4$	$+0.4 \pm 0.7$	$+0 \pm 3.1$	$+0 \pm 0$
b tag						
$\epsilon_{b/c}+$	-1.6 ± 0.1	-1.7 ± 0.3	-2.1 ± 0.5	-4.2 ± 1.3	$+0 \pm 0$	-15.9 ± 7.3
$\epsilon_{b/c}-$	$+1.5 \pm 0.1$	$+2.5 \pm 0.4$	$+2.4 \pm 0.5$	$+4.3 \pm 1.4$	$+0 \pm 0$	$+4 \pm 4.1$
$R_{uds}g+$	$+0.1 \pm 0$	$+0.1 \pm 0.1$	$+0.1 \pm 0.1$	$+0 \pm 0$	$+0 \pm 0$	$+0 \pm 0$
$R_{uds}g-$	$+0 \pm 0$	$+0 \pm 0.1$	-0.2 ± 0.2	$+0 \pm 0$	-2.1 ± 2.2	$+0 \pm 0$
\cancel{E}_T						
$s = 2.1$	$+1.1 \pm 0.1$	$+1.3 \pm 0.2$	$+1.4 \pm 0.4$	$+0.9 \pm 0.6$	$+4.3 \pm 3.1$	$+8 \pm 5.9$
$s = 2.7$	-1.5 ± 0.1	-2.4 ± 0.3	-1.3 ± 0.4	-1.2 ± 0.7	-8.6 ± 4.2	-7.9 ± 5.4
MC _{stat}	± 1.1	± 2.2	± 3.1	± 6.5	± 14.7	± 20.0

Table D.7: Systematic uncertainties (in %) for $Z^0 + b$, analysis requiring zero tagged jets.

Syst.	Mass window for $M =$					
	110 GeV	130 GeV	150 GeV	200 GeV	300 GeV	400 GeV
Muons						
$ES+$	$+0 \pm 1.5$	$+0.9 \pm 1.7$	-2.5 ± 1.6	$+0.4 \pm 1.5$	$+2.1 \pm 3.6$	$+2.7 \pm 3.3$
$ES-$	-3 ± 1.7	$+0.3 \pm 1.5$	$+1.3 \pm 1.5$	-6.5 ± 1.8	$+0 \pm 3.4$	-5.2 ± 2.6
resol.	$+0 \pm 1.5$	$+0.7 \pm 1.6$	$+0 \pm 1.5$	-0.3 ± 1.7	-3.3 ± 4.1	$+1.3 \pm 0$
ϵ_μ				± 4		
shape	-3.3	-2.7	-2.2	-0.8	+1.8	+4.4
Jets						
$ES+$	-5.5 ± 0.9	-5.8 ± 1.2	-8.4 ± 1.2	-4 ± 1.3	-5.4 ± 2.5	-5.2 ± 3.2
$ES-$	$+6.4 \pm 1.1$	$+9.6 \pm 1.3$	$+5.8 \pm 1.1$	$+7.9 \pm 1.6$	$+9.7 \pm 2.7$	$+9.3 \pm 5.4$
resol.	$+0.7 \pm 1.1$	$+3.4 \pm 1.3$	-1.1 ± 1.3	$+0.2 \pm 1.2$	-3.3 ± 2.8	$+1.3 \pm 4$
b tag						
$\epsilon_{b/c}+$	-11.8 ± 1.2	-11.5 ± 1.2	-10.1 ± 1.2	-10.4 ± 1.4	-6.1 ± 2	-7.9 ± 3.1
$\epsilon_{b/c}-$	$+13.3 \pm 1.4$	$+11.3 \pm 1.4$	$+11.7 \pm 1.4$	$+13.5 \pm 1.8$	$+17.2 \pm 3.7$	$+14.7 \pm 4.7$
$R_{uds}g+$	$+0.1 \pm 0.1$	$+0.3 \pm 0.2$	$+0.9 \pm 0.4$	$+0.4 \pm 0.3$	$+1.4 \pm 1$	$+1.3 \pm 1.3$
$R_{uds}g-$	-0.7 ± 0.3	0 ± 0.1	-0.6 ± 0.3	-0.3 ± 0.3	$+0 \pm 0$	$+0 \pm 0$
\cancel{E}_T						
$s = 2.1$	$+1.1 \pm 0.8$	$+3.1 \pm 1$	$+2.6 \pm 1$	$+2.1 \pm 1$	$+6.2 \pm 1.2$	$+2.7 \pm 2.7$
$s = 2.7$	-1.7 ± 0.9	-1.2 ± 0.9	-1.2 ± 0.9	-1.8 ± 1.1	-1.3 ± 2.4	-1.2 ± 3.5
MC_{stat}	± 4.2	± 4.4	± 4.3	± 5.2	± 10.0	± 13.1

Table D.8: Systematic uncertainties (in %) for $t\bar{t}$, analysis requiring zero tagged jets.

Syst.	Mass window for $M =$					
	110 GeV	130 GeV	150 GeV	200 GeV	300 GeV	400 GeV
Muons						
$ES+$	-0.6 ± 0.3	-0.8 ± 0.3	$+0.1 \pm 0.5$	$+0.3 \pm 0.4$	$+0.2 \pm 0.4$	-0.3 ± 0.4
$ES-$	-2.5 ± 0.3	-1.5 ± 0.3	-2.6 ± 0.5	-1.5 ± 0.5	-0.9 ± 0.5	-0.8 ± 0.5
resol.	-1.5 ± 0.3	-1.2 ± 0.3	-1.3 ± 0.4	-1.5 ± 0.5	-1.7 ± 0.6	-2.9 ± 0.6
ϵ_μ				± 4		
shape	-3.3	-2.7	-2.2	-0.8	+1.8	+4.5
Jets						
$ES+$	-0.7 ± 0.1	-0.7 ± 0.2	-0.5 ± 0.2	-1.2 ± 0.3	0 ± 0.3	-0.1 ± 0.3
$ES-$	$+1.1 \pm 0.2$	$+1 \pm 0.2$	$+1.4 \pm 0.3$	$+1.2 \pm 0.3$	$+1.6 \pm 0.4$	$+1.5 \pm 0.4$
resol.	$+0.2 \pm 0.1$	$+0 \pm 0.1$	$+0.1 \pm 0.2$	$+0.2 \pm 0.3$	$+0.3 \pm 0.3$	$+0.2 \pm 0.3$
b tag						
$\epsilon_{b/c}+$	-0.8 ± 0.1	-1 ± 0.2	-1.5 ± 0.3	-1.1 ± 0.2	-2.2 ± 0.3	-2.5 ± 0.4
$\epsilon_{b/c}-$	$+1.2 \pm 0.1$	$+1.5 \pm 0.2$	$+1.3 \pm 0.3$	$+2 \pm 0.3$	2.3 ± 0.4	$+1.6 \pm 0.3$
$R_{uds}g+$	$+0 \pm 0$	$+0 \pm 0$	$+0.1 \pm 0.1$	$+0.1 \pm 0.1$	$+0.1 \pm 0.1$	$+0 \pm 0$
$R_{uds}g-$	$+0 \pm 0$	$+0 \pm 0$	$+0 \pm 0.1$	$+0 \pm 0$	-0.1 ± 0.1	-0.1 ± 0.1
\cancel{E}_T						
$s = 2.1$	$+1.1 \pm 0.1$	$+1.1 \pm 0.2$	$+1.2 \pm 0.2$	$+1.4 \pm 0.3$	$+3.4 \pm 0.4$	$+6.7 \pm 0.7$
$s = 2.7$	-1.7 ± 0.2	-1.9 ± 0.2	-2 ± 0.3	-2.8 ± 0.4	-3.1 ± 0.4	-5.4 ± 0.6
MC _{stat}	± 1.3	± 1.6	± 2.2	± 2.3	± 2.3	± 2.5

Table D.9: Systematic uncertainties (in %) for $b\bar{b}A^0$, analysis requiring zero tagged jets.

Syst.	Mass window for $M =$					
	110 GeV	130 GeV	150 GeV	200 GeV	300 GeV	400 GeV
Muons						
$ES+$	-0.2 ± 0.6	$+0.5 \pm 0.5$	-1.3 ± 0.5	-0.1 ± 0.4	$+0 \pm 0.4$	$+0 \pm 0.4$
$ES-$	-1.7 ± 0.6	-2 ± 0.5	-1.8 ± 0.4	-2.1 ± 0.4	-1.1 ± 0.4	-0.7 ± 0.4
resol.	-0.6 ± 0.6	-0.9 ± 0.5	-1.7 ± 0.5	-1.4 ± 0.4	-2.9 ± 0.5	-3.7 ± 0.6
ϵ_μ				± 4		
shape	-3.3	-2.7	-2.2	-0.8	+1.8	+4.5
Jets						
$ES+$	$+0 \pm 0.2$	$+0 \pm 0.1$	-0.2 ± 0.1	-0.6 ± 0.2	$+0.7 \pm 0.3$	-0.5 ± 0.4
$ES-$	-0.2 ± 0.2	-0.3 ± 0.2	$+0.1 \pm 0.2$	-0.4 ± 0.2	-0.8 ± 0.3	-0.9 ± 0.4
resol.	$+0 \pm 0.1$	$+0 \pm 0.1$	$+0 \pm 0.1$	-0.1 ± 0.2	$+0 \pm 0.2$	-0.1 ± 0.3
b tag						
$\epsilon_{b/c+}$	$+0 \pm 0$	$+0.1 \pm 0$	$+0 \pm 0$	-0.1 ± 0.1	$+0 \pm 0.1$	$+0 \pm 0.1$
$\epsilon_{b/c-}$	$+0 \pm 0$	$+0 \pm 0$	$+0 \pm 0$	$+0 \pm 0$	$+0 \pm 0$	$+0 \pm 0$
R_{uds+}	$+0.2 \pm 0.1$	$+0.2 \pm 0.1$	$+0.2 \pm 0.1$	$+0 \pm 0$	$+0.6 \pm 0.2$	$+0.5 \pm 0.2$
R_{uds-}	-0.1 ± 0.1	-0.2 ± 0.1	-0.3 ± 0.1	-0.1 ± 0.1	-0.2 ± 0.1	-0.6 ± 0.2
\cancel{E}_T						
$s = 2.1$	$+1.1 \pm 0.3$	$+1 \pm 0.2$	$+1.3 \pm 0.2$	$+1.9 \pm 0.3$	$+3.1 \pm 0.4$	$+7.3 \pm 0.6$
$s = 2.7$	-1.8 ± 0.3	-1.7 ± 0.3	-2.1 ± 0.3	-2.7 ± 0.4	-3.8 ± 0.4	-6.1 ± 0.5
MC_{stat}	± 2.6	± 2.5	± 2.4	± 2.3	± 2.3	± 2.4

Table D.10: Systematic uncertainties (in %) for $gg \rightarrow A^0$, analysis requiring zero tagged jets.

Bibliography

- [1] CDF and DØ Collaborations, *A Combination of CDF and DØ Results on the Mass of the Top Quark*, arXiv:0803.1683 [hep-ex].
- [2] A. Einstein, *The foundation of the general theory of relativity*, Annalen Phys. **49** (1916) 769–822.
- [3] Particle Data Group, W. M. Yao *et al.*, *Review of particle physics*, J. Phys. **G33** (2006) 1–1232, and 2007 partial update for 2008: <http://pdg.lbl.gov>.
- [4] G. 't Hooft, *Renormalizable Lagrangians for massive Yang-Mills fields*, Nucl. Phys. **B35** (1971) 167–188;
G. 't Hooft, *Renormalization of Massless Yang-Mills Fields*, Nucl. Phys. **B33** (1971) 173–199;
M. J. G. Veltman, *Perturbation theory of massive Yang-Mills fields*, Nucl. Phys. **B7** (1968) 637–650.
- [5] S. L. Glashow, *Partial Symmetries of Weak Interactions*, Nucl. Phys. **22** (1961) 579–588;
S. Weinberg, *A Model of Leptons*, Phys. Rev. Lett. **19** (1967) 1264–1266;
A. Salam, in *Elementary Particle Theory*, p. 367 Almqvist and Wiksell, Stockholm, 1968.
- [6] T. D. Lee and C.-N. Yang, *Question of Parity Conservation in Weak Interactions*, Phys. Rev. **104** (1956) 254–258.
- [7] C. S. Wu, E. Ambler, R. W. Hayward, D. D. Hoppes, and R. P. Hudson, *Experimental Test of Parity Conservation in Beta Decay*, Phys. Rev. **105** (1957) 1413–1414.
- [8] A. Pich, *The standard model of electroweak interactions*, hep-ph/0502010.
- [9] Super-Kamiokande Collaboration, Y. Fukuda *et al.*, *Evidence for oscillation of atmospheric neutrinos*, Phys. Rev. Lett. **81** (1998) 1562–1567, hep-ex/9807003.
- [10] KamLAND Collaboration, K. Eguchi *et al.*, *First results from KamLAND: Evidence for reactor anti-neutrino disappearance*, Phys. Rev. Lett. **90** (2003) 021802, hep-ex/0212021.
- [11] K2K Collaboration, M. H. Ahn *et al.*, *Indications of neutrino oscillation in a 250 km long-baseline experiment*, Phys. Rev. Lett. **90** (2003) 041801, hep-ex/0212007.
- [12] SNO Collaboration, Q. R. Ahmad *et al.*, *Direct evidence for neutrino flavor transformation from neutral-current interactions in the Sudbury Neutrino Observatory*, Phys. Rev. Lett. **89** (2002) 011301, nucl-ex/0204008.

- [13] P. W. Higgs, *Broken symmetries, massless particles and gauge fields*, Phys. Lett. **12** (1964) 132–133;
P. W. Higgs, *Broken symmetries and the masses of the gauge bosons*, Phys. Rev. Lett. **13** (1964) 508–509;
F. Englert and R. Brout, *Broken symmetry and the mass of gauge vector mesons*, Phys. Rev. Lett. **13** (1964) 321–322;
G. S. Guralnik, C. R. Hagen, and T. W. B. Kibble, *Global conservation laws and massless particles*, Phys. Rev. Lett. **13** (1964) 585–587;
P. W. Higgs, *Spontaneous Symmetry Breakdown Without Massless Bosons*, Phys. Rev. **145** (1966) 1156–1163;
T. W. B. Kibble, *Symmetry breaking in non-Abelian gauge theories*, Phys. Rev. **155** (1967) 1554–1561.
- [14] E. Fermi, *An attempt of a theory of beta radiation. 1*, Z. Phys. **88** (1934) 161–177.
- [15] K. Riesselmann, *Limitations of a standard model Higgs boson*, hep-ph/9711456.
- [16] M. Spira and P. M. Zerwas, *Electroweak symmetry breaking and Higgs physics*, hep-ph/9803257.
- [17] H. P. Nilles, *Supersymmetry, Supergravity and Particle Physics*, Phys. Rept. **110** (1984) 1.
- [18] M. Drees, *An introduction to supersymmetry*, hep-ph/9611409.
- [19] E. Witten, *Dynamical Breaking of Supersymmetry*, Nucl. Phys. **B188** (1981) 513;
S. Dimopoulos, S. Raby, and F. Wilczek, *Supersymmetry and the Scale of Unification*, Phys. Rev. **D24** (1981) 1681–1683;
S. Dimopoulos and H. Georgi, *Softly Broken Supersymmetry and SU(5)*, Nucl. Phys. **B193** (1981) 150;
N. Sakai, *Naturalness in Supersymmetric Guts*, Zeit. Phys. **C11** (1981) 153.
- [20] H. Baer and X. Tata, *Weak scale supersymmetry: From superfields to scattering events*, Cambridge, UK: Univ. Pr. (2006) 537 p.
- [21] R. Haag, J. T. Lopuszanski, and M. Sohnius, *All Possible Generators of Supersymmetries of the S Matrix*, Nucl. Phys. **B88** (1975) 257.
- [22] I. Simonsen, *A Review of minimal supersymmetric electroweak theory*, hep-ph/9506369.
- [23] J. R. Ellis, *Beyond the standard model for hillwalkers*, hep-ph/9812235.
- [24] WMAP Collaboration, D. N. Spergel *et al.*, *Wilkinson Microwave Anisotropy Probe (WMAP) three year results: Implications for cosmology*, Astrophys. J. Suppl. **170** (2007) 377, astro-ph/0603449.
- [25] D. I. Kazakov, *Beyond the standard model (in search of supersymmetry)*, hep-ph/0012288.
- [26] H. P. Nilles, *Dynamically Broken Supergravity and the Hierarchy Problem*, Phys. Lett. **B115** (1982) 193;
A. H. Chamseddine, R. Arnowitt, and P. Nath, *Locally Supersymmetric Grand Unification*, Phys. Rev. Lett. **49** (1982) 970;

- P. Nath, R. Arnowitt, and A. H. Chamseddine, *Gauge Hierarchy in Supergravity Guts*, Nucl. Phys. **B227** (1983) 121;
- R. Barbieri, S. Ferrara, and C. A. Savoy, *Gauge Models with Spontaneously Broken Local Supersymmetry*, Phys. Lett. **B119** (1982) 343;
- E. Cremmer, P. Fayet, and L. Girardello, *Gravity Induced Supersymmetry Breaking and Low-Energy Mass Spectrum*, Phys. Lett. **B122** (1983) 41;
- L. E. Ibanez, *Locally Supersymmetric SU(5) Grand Unification*, Phys. Lett. **B118** (1982) 73;
- H. P. Nilles, M. Srednicki, and D. Wyler, *Weak Interaction Breakdown Induced by Supergravity*, Phys. Lett. **B120** (1983) 346.
- [27] M. Dine and A. E. Nelson, *Dynamical supersymmetry breaking at low-energies*, Phys. Rev. **D48** (1993) 1277–1287, hep-ph/9303230;
- M. Dine, A. E. Nelson, and Y. Shirman, *Low-energy dynamical supersymmetry breaking simplified*, Phys. Rev. **D51** (1995) 1362–1370, hep-ph/9408384;
- M. Dine, A. E. Nelson, Y. Nir, and Y. Shirman, *New tools for low-energy dynamical supersymmetry breaking*, Phys. Rev. **D53** (1996) 2658–2669, hep-ph/9507378.
- [28] L. Randall and R. Sundrum, *Out of this world supersymmetry breaking*, Nucl. Phys. **B557** (1999) 79–118, hep-th/9810155;
- G. F. Giudice, M. A. Luty, H. Murayama, and R. Rattazzi, *Gaugino mass without singlets*, JHEP **12** (1998) 027, hep-ph/9810442.
- [29] D. E. Kaplan, G. D. Kribs, and M. Schmaltz, *Supersymmetry breaking through transparent extra dimensions*, Phys. Rev. **D62** (2000) 035010, hep-ph/9911293;
- Z. Chacko, M. A. Luty, A. E. Nelson, and E. Ponton, *Gaugino mediated supersymmetry breaking*, JHEP **01** (2000) 003, hep-ph/9911323.
- [30] H. E. Haber, *The status of the minimal supersymmetric standard model and beyond*, Nucl. Phys. Proc. Suppl. **62** (1998) 469–484, hep-ph/9709450.
- [31] ALEPH, DELPHI, L3, and OPAL Collaborations and LEP Working Group for Higgs Boson Searches, S. Schael *et al.*, *Search for neutral MSSM Higgs bosons at LEP*, Eur. Phys. J. **C47** (2006) 547–587, arXiv:hep-ex/0602042.
- [32] B. C. Allanach *et al.*, *The Snowmass points and slopes: Benchmarks for SUSY searches*, hep-ph/0202233.
- [33] M. S. Carena, S. Heinemeyer, C. E. M. Wagner, and G. Weiglein, *Suggestions for benchmark scenarios for MSSM Higgs boson searches at hadron colliders*, Eur. Phys. J. **C26** (2003) 601–607, hep-ph/0202167.
- [34] M. S. Carena, S. Heinemeyer, C. E. M. Wagner, and G. Weiglein, *Suggestions for improved benchmark scenarios for Higgs- boson searches at LEP2*, hep-ph/9912223.
- [35] A. Djouadi, *Squark effects on Higgs boson production and decay at the LHC*, Phys. Lett. **B435** (1998) 101–108, hep-ph/9806315.
- [36] M. S. Carena, J. R. Ellis, A. Pilaftsis, and C. E. M. Wagner, *CP-violating MSSM Higgs bosons in the light of LEP 2*, Phys. Lett. **B495** (2000) 155–163, hep-ph/0009212.

- [37] M. Frank *et al.*, *The Higgs boson masses and mixings of the complex MSSM in the Feynman-diagrammatic approach*, JHEP **02** (2007) 047, hep-ph/0611326;
G. Degrandi, S. Heinemeyer, W. Hollik, P. Slavich, and G. Weiglein, *Towards high-precision predictions for the MSSM Higgs sector*, Eur. Phys. J. **C28** (2003) 133–143, hep-ph/0212020;
S. Heinemeyer, W. Hollik, and G. Weiglein, *The masses of the neutral CP-even Higgs bosons in the MSSM: Accurate analysis at the two-loop level*, Eur. Phys. J. **C9** (1999) 343–366, hep-ph/9812472;
S. Heinemeyer, W. Hollik, and G. Weiglein, *FeynHiggs: A program for the calculation of the masses of the neutral CP-even Higgs bosons in the MSSM*, Comput. Phys. Commun. **124** (2000) 76–89, hep-ph/9812320.
- [38] M. S. Carena, S. Heinemeyer, C. E. M. Wagner, and G. Weiglein, *MSSM Higgs boson searches at the Tevatron and the LHC: Impact of different benchmark scenarios*, Eur. Phys. J. **C45** (2006) 797–814, arXiv:hep-ph/0511023.
- [39] ALEPH, DELPHI, L3, and OPAL Collaborations and LEP Working Group for Higgs boson searches, R. Barate *et al.*, *Search for the standard model Higgs boson at LEP*, Phys. Lett. **B565** (2003) 61–75, arXiv:hep-ex/0306033.
- [40] V. D. Barger, M. S. Berger, P. Ohmann, and R. J. N. Phillips, *Phenomenological implications of the $m(t)$ RGE fixed point for SUSY Higgs boson searches*, Phys. Lett. **B314** (1993) 351–356, hep-ph/9304295;
M. S. Carena, S. Pokorski, and C. E. M. Wagner, *On the unification of couplings in the minimal supersymmetric Standard Model*, Nucl. Phys. **B406** (1993) 59–89, hep-ph/9303202.
- [41] M. Battaglia *et al.*, *Proposed post-LEP benchmarks for supersymmetry*, Eur. Phys. J. **C22** (2001) 535–561, hep-ph/0106204.
- [42] E. Boos, A. Djouadi, M. Muhlleitner, and A. Vologdin, *The MSSM Higgs bosons in the intense-coupling regime*, Phys. Rev. **D66** (2002) 055004, hep-ph/0205160.
- [43] ALEPH, DELPHI, L3, and OPAL Collaborations and LEP Electroweak Working Group, J. Alcaraz *et al.*, *Precision Electroweak Measurements and Constraints on the Standard Model*, arXiv:0712.0929 [hep-ex].
- [44] LEP Electroweak Working Group, *Update Winter 2008*, <http://lepewwg.web.cern.ch/LEPEWWG/>.
- [45] CDF Collaboration, F. Abe *et al.*, *The CDF detector: an overview*, Nucl. Instr. Meth. **A271** (1988) 387–403.
- [46] DØ Collaboration, V. M. Abazov *et al.*, *The upgraded DØ detector*, Nucl. Instrum. Meth. **A565** (2006) 463–537, physics/0507191.
- [47] CDF and DØ Collaborations (The TEVNPH Working Group for the Collaborations), *Combined CDF and DØ Upper Limits on Standard Model Higgs-Boson Production with up to 2.4 fb⁻¹ of data*, arXiv:0804.3423 [hep-ex].
- [48] S. Asai *et al.*, *Prospects for the search for a standard model Higgs boson in ATLAS using vector boson fusion*, Eur. Phys. J. **C32S2** (2004) 19–54, hep-ph/0402254.

- [49] O. Buchmüller *et al.*, *Prediction for the Lightest Higgs Boson Mass in the CMSSM using Indirect Experimental Constraints*, Phys. Lett. **B657** (2007) 87–94, arXiv:0707.3447 [hep-ph].
- [50] CDF Collaboration, *Search for Higgs Bosons Produced in Association with b -Quarks*, CDF Note 8954.
- [51] CDF Collaboration, *Search for Neutral MSSM Higgs Decaying to Tau Pairs with 1.8 fb^{-1} of Data*, CDF Note 9071.
- [52] DØ Collaboration, V. M. Abazov *et al.*, *Search for neutral Higgs bosons decaying to τ pairs in $p\bar{p}$ collisions at $\sqrt{s} = 1.96\text{ TeV}$* , Phys. Rev. Lett. **97** (2006) 121802, hep-ex/0605009.
- [53] DØ Collaboration, *Search for Neutral Higgs Bosons at High $\tan\beta$ in multi-jet Events*, DØ Note 5503-CONF.
- [54] M. Schumacher, *Investigation of the discovery potential for Higgs bosons of the minimal supersymmetric extension of the standard model (MSSM) with ATLAS*, hep-ph/0410112;
V. Büscher and K. Jakobs, *Higgs boson searches at hadron colliders*, Int. J. Mod. Phys. **A20** (2005) 2523–2602, hep-ph/0504099.
- [55] E. Accomando *et al.*, *Workshop on CP studies and non-standard Higgs physics*, hep-ph/0608079.
- [56] LHC Study Group, T. S. Pettersson, P. Lefèvre, *et al.*, *The Large Hadron Collider: Conceptual design*, CERN-AC-95-05-LHC.
- [57] P. Ferracin, *Mechanical and magnetic analysis of the Large Hadron Collider main dipole*, PhD thesis, Torino TU, 2002.
- [58] CMS Collaboration, M. Della Negra *et al.*, *CMS: The Compact Muon Solenoid: Letter of intent for a general purpose detector at the LHC*, CERN-LHCC-92-03;
CMS, the Compact Muon Solenoid: Technical proposal, CERN-LHCC-94-38.
- [59] ATLAS Collaboration, *ATLAS: Detector and physics performance technical design report. Volume 1*, CERN-LHCC-99-14.
- [60] LHCb Collaboration, S. Amato *et al.*, *LHCb technical proposal*, CERN-LHCC-98-04.
- [61] ALICE Collaboration, P. Giubellino, *The ALICE detector at LHC*, Nucl. Instrum. Meth. **A344** (1994) 27–38.
- [62] O. Adriani *et al.*, *LHCf experiment: Technical Design Report*, CERN-LHCC-2006-004.
- [63] TOTEM Collaboration, V. Berardi *et al.*, *TOTEM: Technical design report. Total cross section, elastic scattering and diffraction dissociation at the Large Hadron Collider at CERN*, CERN-LHCC-2004-002.
- [64] J. M. Campbell, J. W. Huston, and W. J. Stirling, *Hard interactions of quarks and gluons: A primer for LHC physics*, Rept. Prog. Phys. **70** (2007) 89, hep-ph/0611148.

- [65] ATLAS Collaboration, G. Aad *et al.*, *The ATLAS Experiment at the CERN Large Hadron Collider*, accepted by JINST.
- [66] S. Ask, *Status of the Forward Physics Projects in ATLAS*, arXiv:0706.0644 [hep-ex].
- [67] J. Pinfold, *Plans for the very forward region of ATLAS: The lucid luminosity monitor*, Prepared for 9th ICATPP Conference on Astroparticle, Particle, Space Physics, Detectors and Medical Physics Applications, Villa Erba, Como, Italy, 17-21 Oct 2005.
- [68] M. Dobbs and J. B. Hansen, *The HepMC C++ Monte Carlo event record for High Energy Physics*, Comput. Phys. Commun. **134** (2001) 41–46.
- [69] J. C. Collins and D. E. Soper, *The Theorems of Perturbative QCD*, Ann. Rev. Nucl. Part. Sci. **37** (1987) 383–409.
- [70] V. N. Gribov and L. N. Lipatov, *$e^+ e^-$ pair annihilation and deep inelastic $e p$ scattering in perturbation theory*, Sov. J. Nucl. Phys. **15** (1972) 675–684;
Y. L. Dokshitzer, *Calculation of the Structure Functions for Deep Inelastic Scattering and $e^+ e^-$ Annihilation by Perturbation Theory in Quantum Chromodynamics. (In Russian)*, Sov. Phys. JETP **46** (1977) 641–653;
G. Altarelli and G. Parisi, *Asymptotic Freedom in Parton Language*, Nucl. Phys. **B126** (1977) 298.
- [71] G. C. Blazey *et al.*, *Run II jet physics*, hep-ex/0005012.
- [72] T. Sjostrand, *Monte Carlo generators*, hep-ph/0611247.
- [73] V. V. Sudakov, *Vertex parts at very high-energies in quantum electrodynamics*, Sov. Phys. JETP **3** (1956) 65–71.
- [74] F. Krauss, *Matrix elements and parton showers in hadronic interactions*, JHEP **08** (2002) 015, hep-ph/0205283.
- [75] S. Catani, F. Krauss, R. Kuhn, and B. R. Webber, *QCD matrix elements + parton showers*, JHEP **11** (2001) 063, hep-ph/0109231.
- [76] S. Catani, Y. L. Dokshitzer, M. Olsson, G. Turnock, and B. R. Webber, *New clustering algorithm for multi - jet cross-sections in $e^+ e^-$ annihilation*, Phys. Lett. **B269** (1991) 432–438.
- [77] S. Catani, Y. L. Dokshitzer, M. H. Seymour, and B. R. Webber, *Longitudinally invariant $K(t)$ clustering algorithms for hadron hadron collisions*, Nucl. Phys. **B406** (1993) 187–224.
- [78] L. Lonnblad, *Correcting the colour-dipole cascade model with fixed order matrix elements*, JHEP **05** (2002) 046, hep-ph/0112284.
- [79] S. Höche *et al.*, *Matching parton showers and matrix elements*, hep-ph/0602031.
- [80] T. Gleisberg *et al.*, *SHERPA 1.alpha., a proof-of-concept version*, JHEP **02** (2004) 056, hep-ph/0311263.

-
- [81] S. Frixione and B. R. Webber, *Matching NLO QCD computations and parton shower simulations*, JHEP **06** (2002) 029, hep-ph/0204244;
S. Frixione, P. Nason, and B. R. Webber, *Matching NLO QCD and parton showers in heavy flavour production*, JHEP **08** (2003) 007, hep-ph/0305252.
- [82] T. Sjostrand and M. van Zijl, *A Multiple Interaction Model for the Event Structure in Hadron Collisions*, Phys. Rev. **D36** (1987) 2019.
- [83] S. Alekhin *et al.*, *HERA and the LHC - A workshop on the implications of HERA for LHC physics: Proceedings Part A*, hep-ph/0601012.
- [84] T. Sjostrand *et al.*, *High-energy-physics event generation with PYTHIA 6.1*, Comput. Phys. Commun. **135** (2001) 238–259, hep-ph/0010017.
- [85] G. Corcella *et al.*, *HERWIG 6: An event generator for hadron emission reactions with interfering gluons (including supersymmetric processes)*, JHEP **01** (2001) 010, hep-ph/0011363.
- [86] J. M. Butterworth, J. R. Forshaw, and M. H. Seymour, *Multiparton interactions in photoproduction at HERA*, Z. Phys. **C72** (1996) 637–646, hep-ph/9601371.
- [87] J. S. Virzi, private communication and presentations in ATLAS Monte Carlo generators meetings.
- [88] B. P. Kersevan and E. Richter-Was, *The Monte Carlo event generator AcerMC version 2.0 with interfaces to PYTHIA 6.2 and HERWIG 6.5*, hep-ph/0405247.
- [89] S. R. Slabospitsky and L. Sonnenschein, *TopReX generator (version 3.25): Short manual*, Comput. Phys. Commun. **148** (2002) 87–102, hep-ph/0201292.
- [90] S. Jadach, J. H. Kuhn, and Z. Was, *TAUOLA: A Library of Monte Carlo programs to simulate decays of polarized tau leptons*, Comput. Phys. Commun. **64** (1990) 275–299.
- [91] E. Barberio and Z. Was, *PHOTOS: A Universal Monte Carlo for QED radiative corrections. Version 2.0*, Comput. Phys. Commun. **79** (1994) 291–308.
- [92] ATLAS Collaboration, G. Duckeck (editor) *et al.*, *ATLAS computing: Technical design report*, CERN-LHCC-2005-022, ATLAS-TDR-017.
- [93] GEANT4 Collaboration, S. Agostinelli *et al.*, *GEANT4: A simulation toolkit*, Nucl. Instrum. Meth. **A506** (2003) 250–303;
J. Allison *et al.*, *Geant4 developments and applications*, IEEE Trans. Nucl. Sci. **53** (2006) 270.
- [94] CERN, *Computing in High Energy Physics and Nuclear Physics 2004*, CERN, Geneva, 2005.
- [95] E. Barberio *et al.*, *The Geant4-Based ATLAS Fast Electromagnetic Shower Simulation*, ATL-SOFT-CONF-2007-002.
- [96] C. Zeitnitz and T. A. Gabriel, *The GEANT - CALOR interface and benchmark calculations of ZEUS test calorimeters*, Nucl. Instrum. Meth. **A349** (1994) 106–111.
-

- [97] A. Ferrari, P. R. Sala, A. Fasso, and J. Ranft, *FLUKA: A multi-particle transport code (Program version 2005)*, CERN-2005-010.
- [98] E. Richter-Was, D. Froidevaux, and L. Poggioli, *ATLFAST 2.0 a fast simulation package for ATLAS*, ATL-PHYS-98-131.
- [99] D. Cavalli *et al.*, *Performance of the ATLAS fast simulation ATLFAST*, ATL-PHYS-INT-2007-005.
- [100] K. A. Assamagan *et al.*, *The Higgs working group: Summary report 2003*, hep-ph/0406152.
- [101] R. V. Harlander and W. B. Kilgore, *Higgs boson production in bottom quark fusion at next-to-next-to-leading order*, Phys. Rev. **D68** (2003) 013001, hep-ph/0304035.
- [102] S. Dittmaier, M. Kramer, and M. Spira, *Higgs radiation off bottom quarks at the Tevatron and the LHC*, Phys. Rev. **D70** (2004) 074010, hep-ph/0309204.
- [103] S. Dawson, C. B. Jackson, L. Reina, and D. Wackeroth, *Exclusive Higgs boson production with bottom quarks at hadron colliders*, Phys. Rev. **D69** (2004) 074027, hep-ph/0311067.
- [104] M. Spira, private communication.
- [105] M. Spira, *Higgs radiation off bottom quarks at hadron colliders*, Prepared for 12th International Workshop on Deep Inelastic Scattering (DIS 2004), Strbske Pleso, Slovakia, 14-18 Apr 2004.
- [106] J. Campbell, R. K. Ellis, F. Maltoni, and S. Willenbrock, *Higgs boson production in association with a single bottom quark*, Phys. Rev. **D67** (2003) 095002, hep-ph/0204093.
- [107] S. Dawson, C. B. Jackson, L. Reina, and D. Wackeroth, *Higgs boson production with one bottom quark jet at hadron colliders*, Phys. Rev. Lett. **94** (2005) 031802, hep-ph/0408077.
- [108] S. Gentile, H. Bilokon, V. Chiarella, and G. Nicoletti, *The ATLAS discovery potential for MSSM neutral Higgs bosons decaying to a $\mu^+\mu^-$ pair in the mass range up to 130 GeV*, Eur. Phys. J. **C52** (2007) 229–245, arXiv:0705.2801 [hep-ex].
- [109] D. Cavalli and P. Bosatelli, *Combined Analysis of A/H to $\mu^+\mu^-$ Events from Direct and Associated bbA Production*, ATL-PHYS-2000-001.
- [110] F. Krauss, private communication.
- [111] T. Sjostrand, private communication.
- [112] J. Campbell and K. Ellis, <http://mcfm.fnal.gov>.
- [113] A. D. Martin, R. G. Roberts, W. J. Stirling, and R. S. Thorne, *Uncertainties of predictions from parton distributions. I: Experimental errors. ((T))*, Eur. Phys. J. **C28** (2003) 455–473, arXiv:hep-ph/0211080.
- [114] R. S. Thorne, A. D. Martin, W. J. Stirling, and R. G. Roberts, *Update of MRST parton distributions*, arXiv:hep-ph/0407311.

-
- [115] J. Pumplin *et al.*, *New generation of parton distributions with uncertainties from global QCD analysis*, JHEP **07** (2002) 012, hep-ph/0201195.
- [116] R. V. Harlander and W. B. Kilgore, *Next-to-next-to-leading order Higgs production at hadron colliders*, Phys. Rev. Lett. **88** (2002) 201801, hep-ph/0201206.
- [117] C. Anastasiou and K. Melnikov, *Higgs boson production at hadron colliders in NNLO QCD*, Nucl. Phys. **B646** (2002) 220–256, hep-ph/0207004.
- [118] C. Anastasiou, K. Melnikov, and F. Petriello, *Higgs boson production at hadron colliders: Differential cross sections through next-to-next-to-leading order*, Phys. Rev. Lett. **93** (2004) 262002, hep-ph/0409088.
- [119] U. Aglietti, R. Bonciani, G. Degrassi, and A. Vicini, *Two-loop light fermion contribution to Higgs production and decays*, Phys. Lett. **B595** (2004) 432–441, hep-ph/0404071.
- [120] G. Degrassi and F. Maltoni, *Two-loop electroweak corrections to Higgs production at hadron colliders*, Phys. Lett. **B600** (2004) 255–260, hep-ph/0407249.
- [121] S. Catani, D. de Florian, M. Grazzini, and P. Nason, *Soft-gluon resummation for Higgs boson production at hadron colliders*, JHEP **07** (2003) 028, hep-ph/0306211.
- [122] F. Maltoni *et al.*, <http://maltoni.home.cern.ch/maltoni/TeV4LHC>.
- [123] S. Heinemeyer, A. Nikitenko, and G. Weiglein, *Heavy MSSM Higgs Bosons at CMS: 'LHC wedge' and Higgs-Mass Precision*, arXiv:0710.3109 [hep-ph].
- [124] DØ Collaboration, *Z + jet production in the DØ experiment: A comparison between data and the PYTHIA and SHERPA Monte Carlos*, DØ Note 5066-CONF.
- [125] K. Melnikov and F. Petriello, *Electroweak gauge boson production at hadron colliders through $O(\alpha(s)^2)$* , Phys. Rev. **D74** (2006) 114017, hep-ph/0609070.
- [126] S. I. Alekhin, *The NNLO predictions for the rates of the W / Z production in (anti)-p p collisions*, hep-ph/0307219.
- [127] B. P. Kersevan and I. Hinchliffe, *A consistent prescription for the production involving massive quarks in hadron collisions*, JHEP **09** (2006) 033, hep-ph/0603068.
- [128] F. Maltoni, T. McElmurry, and S. Willenbrock, *Inclusive production of a Higgs or Z boson in association with heavy quarks*, Phys. Rev. **D72** (2005) 074024, hep-ph/0505014.
- [129] J. Campbell, R. K. Ellis, F. Maltoni, and S. Willenbrock, *Associated production of a Z boson and a single heavy- quark jet*, Phys. Rev. **D69** (2004) 074021, hep-ph/0312024.
- [130] N. Kidonakis and R. Vogt, *Next-to-next-to-leading order soft-gluon corrections in top quark hadroproduction*, Phys. Rev. **D68** (2003) 114014, hep-ph/0308222.
- [131] R. Bonciani, S. Catani, M. L. Mangano, and P. Nason, *NLL resummation of the heavy-quark hadroproduction cross- section*, Nucl. Phys. **B529** (1998) 424–450, hep-ph/9801375.
-

- [132] J. Campbell and F. Tramontano, *Next-to-leading order corrections to $W t$ production and decay*, Nucl. Phys. **B726** (2005) 109–130, hep-ph/0506289.
- [133] J. M. Campbell and R. K. Ellis, *An update on vector boson pair production at hadron colliders*, Phys. Rev. **D60** (1999) 113006, hep-ph/9905386.
- [134] S. Hassani *et al.*, *A muon identification and combined reconstruction procedure for the ATLAS detector at the LHC using the (MUONBOY, STACO, MuTag) reconstruction packages*, Nucl. Instrum. Meth. **A572** (2007) 77–79.
- [135] ATLAS Collaboration, *The expected performance of the ATLAS experiment – Detector, Trigger and Physics* –, to be published as CERN Report.
- [136] H1 Calorimeter Group, B. Andrieu *et al.*, *Results from pion calibration runs for the H1 liquid argon calorimeter and comparisons with simulations*, Nucl. Instrum. Meth. **A336** (1993) 499–509.
- [137] ATLAS Liquid Argon EMEC/HEC Collaboration, C. Cojocaru *et al.*, *Hadronic calibration of the ATLAS liquid argon end-cap calorimeter in the pseudorapidity region $1.6 < |\eta| < 1.8$ in beam tests*, Nucl. Instrum. Meth. **A531** (2004) 481–514, arXiv:physics/0407009.
- [138] H1 Collaboration, I. Abt *et al.*, *The Tracking, calorimeter and muon detectors of the H1 experiment at HERA*, Nucl. Instrum. Meth. **A386** (1997) 348–396.
- [139] S. Horvat, private communication.
- [140] CLEO Collaboration, G. Brandenburg *et al.*, *Charged track multiplicity in B meson decay*, Phys. Rev. **D61** (2000) 072002, arXiv:hep-ex/9907057.
- [141] V. Vuillemin *et al.*, *Inclusive Studies of D Meson Decays at the PSI-prime-prime (3772)*, Phys. Rev. Lett. **41** (1978) 1149.
- [142] T. Cornelissen, M. Elsing, S. Fleischmann, W. Liebig, E. Moyse, and A. Salzburger, *Concepts, Design and Implementation of the ATLAS New Tracking (NEWT)*, ATL-SOFT-PUB-2007-007.
- [143] ATLAS Collaboration, P. Ferrari, *Tracking and vertexing at ATLAS*, arXiv:0707.3071 [physics.ins-det].
- [144] ATLAS Collaboration, *ATLAS inner detector: Technical design report. Vol. 1*, CERN-LHCC-97-16.
- [145] ATLAS Collaboration, *ATLAS inner detector: Technical design report. Vol. 2*, CERN-LHCC-97-17.
- [146] T. Göpfert, private communication.
- [147] S. Corréard, V. Kostyukhin, J. Lévêque, A. Rozanov, and J. B. De Vivie de Régie, *b -tagging with DC1 data*, ATL-PHYS-2004-006.
- [148] P. Brückman, A. Hicheur, and S. J. Haywood, *Global χ^2 approach to the Alignment of the ATLAS Silicon Tracking Detectors*, ATL-INDET-PUB-2005-002; F. Heinemann, *Track Based Alignment of the ATLAS Silicon Detectors with the Robust Alignment Algorithm*, ATL-INDET-PUB-2007-011.

-
- [149] F. Derue and C. Serfon, *Electron/jet separation with DC1 data*, ATL-PHYS-PUB-2005-016.
- [150] M. Escalier, F. Derue, L. Fayard, M. Kado, B. Laforge, C. Reifen, and G. Unal, *Photon/jet separation with DC1 data*, ATL-PHYS-PUB-2005-018.
- [151] E. Richter-Was and T. Szymocha, *Hadronic tau identification with track based approach the $Z \rightarrow \tau\tau$, $W \rightarrow \tau\nu$ and dijet events from DC1 data samples*, ATL-PHYS-PUB-2005-005.
- [152] M. Heldmann and D. Cavalli, *An improved tau-Identification for the ATLAS experiment*, ATL-PHYS-PUB-2006-008.
- [153] K. Gottfried and J. D. Jackson, *On the Connection between production mechanism and decay of resonances at high-energies*, Nuovo Cim. **33** (1964) 309–330.
- [154] A. Sidoti *et al.*, *The ATLAS Muon Trigger “Slice”*, ATL-DAQ-CONF-2007-014.
- [155] K. Cranmer, *HG3: VBF Higgs to Tau Tau*. Presentation in ATLAS Higgs Working Group Meeting: <http://indico.cern.ch/getFile.py/access?contribId=5&resId=0&materialId=slides&confId=27015>.
- [156] R. Brun and F. Rademakers, *ROOT: An object oriented data analysis framework*, Nucl. Instrum. Meth. **A389** (1997) 81–86.
- [157] W. A. Rolke, A. M. Lopez, and J. Conrad, *Confidence Intervals with Frequentist Treatment of Statistical and Systematic Uncertainties*, Nucl. Instrum. Meth. **A551** (2005) 493–503, arXiv:physics/0403059.
- [158] W. A. Rolke and A. M. Lopez, *A Test for the Presence of a Signal*, arXiv:physics/0606006.
- [159] E. Gross, *The Profile Likelihood for Significance Calculation*. Talk in ATLAS Higgs Working Group Meeting: <http://indico.cern.ch/getFile.py/access?contribId=25&resId=0&materialId=slides&confId=16862>.
- [160] D. J. Gross and F. Wilczek, *Ultraviolet Behaviour of non-abelian Gauge Theories*, Phys. Rev. Lett. **30** (1973) 1343–1346;
D. J. Gross and F. Wilczek, *Asymptotically Free Gauge Theories. 1*, Phys. Rev. **D8** (1973) 3633–3652;
H. D. Politzer, *Reliable Perturbative Results for Strong Interactions?*, Phys. Rev. Lett. **30** (1973) 1346–1349;
H. D. Politzer, *Asymptotic Freedom: An Approach to Strong Interactions*, Phys. Rept. **14** (1974) 129–180.
- [161] G. Ecker, *Quantum chromodynamics*, hep-ph/0604165.
- [162] F. J. Yndurain, *Limits on the mass of the gluon*, Phys. Lett. **B345** (1995) 524–526.
- [163] S. D. Ellis and D. E. Soper, *Successive combination jet algorithm for hadron collisions*, Phys. Rev. **D48** (1993) 3160–3166, hep-ph/9305266.
- [164] M. Cacciari and G. P. Salam, *Dispelling the N^3 myth for the $k(t)$ jet-finder*, Phys. Lett. **B641** (2006) 57–61, arXiv:hep-ph/0512210.
-

- [165] A. Stuart, J. K. Ord, and S. Arnold, *Advanced Theory of Statistics, Volume 2A: Classical Inference and the Linear Model* Oxford University Press, London, 1999.
- [166] G. Casella and R. L. Berger, *Statistical Inference, 2nd Edition* Duxberry Press, 2002.

Danksagung/Acknowledgements

Nun, jetzt ist es 5:30, und da muß noch eine Danksagung hin. Im voraus bitte ich alle, die ich hierbei vergessen sollte um Verzeihung – im Zweifelsfall handle ich einfach nur in Umnachtung. Nach insgesamt zwei Universitäten, zwei (oder drei) Experimenten, und diversen (vier ?) Bürowechseln, kann eine solche Danksagung eigentlich nur unvollständig sein.

Zuallererst möchte ich mich bei meinen Eltern für die gar nicht zu groß zu bewertende andauernde Unterstützung danken. Ohne Euch wären insbesondere die letzten Monate dieser Doktorarbeit überhaupt nicht möglich gewesen.

Bei Professor Michael Kobel möchte ich mich für die Gelegenheit, diese Arbeit in seiner Arbeitsgruppe angefertigt haben zu dürfen, sowie für seine Geduld mit mir bedanken. Die Termineintragungen in “Belgrad, Bratislava, Budapest, Ljubljana, Prag” werde ich in Zukunft vermissen.

Professor Markus Schumacher und Dr. Frank Krauss danke ich für die freundliche Übernahme der weiteren Gutachten. Ich weiss, das die Begutachtung dieser Arbeit einen beachtlichen Leidensdruck verursacht haben dürfte.

Bei allen Bonner Opalis, Atlanten, Silab-Mitarbeitern, und DØ’ern und besonders auch bei Professor Wermes möchte ich mich für lange Jahre angenehmer Institutsatmosphäre bedanken, auch wenn ich meine Promotion nicht in Bonn beendet habe.

Bei den Dresdener Babaren und Atlanten bedanke ich mich ganz herzlich für eine herzliche Aufnahme im schönen Sachsen. Die netten “Käffchen” in der Sonne haben immer viel weitergeholfen. Besonders erwähnen möchte ich Rainer Schwierz und Andreas Petzold, ohne deren tatkräftigen hard- und softwaretechnischen Einsatz bestimmt nichts funktionieren würde, und diese Arbeit sicherlich nie fertig geworden wäre.

Markus Schumacher danke ich weiterhin für seine stetige Bereitschaft zu Diskussionen jeglicher Natur - sei es physikalisch oder nicht-physikalisch. Dein stetiger Einsatz soll mir ein Vorbild für die Zukunft sein.

Frank Krauss und den anderen Sherpas, besonders Steffen Schumann, danke ich für die Ansprechbarkeit, auch wenn am Montag der nächste Release rauskommen sollte.

Für das Korrekturlesen dieses Manuskripts bedanke ich mich bei Thomas Göpfert, Verena Klose, Kathrin Leonhardt, Andreas Ludwig, Andreas Petzold, Marek Schönherr, Dr. Wolfgang Mader und nicht zuletzt meinem Bürogenossen und Chefkorrekturleser Peter Steinbach. Ohne Eure Anstrengungen wären mit Sicherheit noch viel mehr Fehler in diesem Werk.

The members of the DØ SMT group deserve a special thanks, as with them I learned what it means to really participate in an experiment. Of all the people I have worked with

during my stay at Fermilab, I would like to thank especially Petros Rapidis, Eric Kajfasz, Harald Fox, Andrei Nomerotski, Ron Lipton, Frederick "Fritz" Bartlett, Markus Klute, and Breese Quinn. Working with you on getting the SMT running was a most rewarding experience. Even if we had to clean these fanout boards with toothbrushes.

Der Studienstiftung des Deutschen Volkes danke ich für die finanzielle Unterstützung.

Wie bereits erwähnt, ist diese Auflistung sicherlich lückenhaft. Deshalb hiermit an alle, die ich nicht namentlich erwähnen konnte:

Danke ! Thank you !

Versicherung

Hiermit versichere ich, dass ich die vorliegende Arbeit ohne unzulässige Hilfe Dritter und ohne Benutzung anderer als der angegebenen Hilfsmittel angefertigt habe; die aus fremden Quellen direkt oder indirekt übernommenen Gedanken sind als solche kenntlich gemacht. Die Arbeit wurde bisher weder im Inland noch im Ausland in gleicher oder ähnlicher Form einer anderen Prüfungsbehörde vorgelegt.

Diese Arbeit wurde am Institut für Kern- und Teilchenphysik der Technischen Universität Dresden unter wissenschaftlicher Betreuung von Prof. Dr. Michael Kobel angefertigt.

Es haben keine früheren erfolglosen Promotionsverfahren stattgefunden.

Ich erkenne die Promotionsordnung der Fakultät Mathematik und Naturwissenschaften an der Technischen Universität Dresden vom 20. März 2000, in der Fassung der vom Fakultätsrat am 19.06.2002 und 12.07.2002 beschlossenen und mit Erlass des Sächsischen Staatsministeriums für Wissenschaft und Kunst vom 18.03.2003 genehmigten Änderungen gemäß Satzung vom 16.04.2003, an.

Dresden, den 25.07.2008

Markus Warsinsky